Fuel Aging in Storage and Transportation (FAST): Accelerated Characterization and Performance Assessment of the Used Nuclear Fuel Storage System

Fuel Cycle
Integrated Research Project

Sean McDeavitt
Texas A&M University

In collaboration with:
Boise State University
North Carolina State University
University of Florida
University of Illinois at Urbana – Champaign
University of Wisconsin - Madison

JC De La Garza, Federal POC
Brady Hanson, Technical POC
Seigfied Stockinger, Technical POC

NEUP | Nuclear Energy University Programs

U.S. Department of Energy

Fuel Aging in Storage and Transportation (FAST): Accelerated Characterization and Performance Assessment of the Used Nuclear Fuel Storage System

FINAL REPORT

Submitted: August 2, 2016

Editor:

Dr. Sean M. McDeavitt, Associate Professor of Nuclear Engineering
Department of Nuclear Engineering, Texas A&M University
117 D.L. Houston Building, College Station, TX
E-mail: *mcdeavitt@tamu.edu*, Phone: 979/862-1745

Contributing Authors (alphabetical):

Jonathan D. Almer[11], Carl Beyer[9], Jake Blanchard[6], Giuseppe Brunetti[8], Darryl Butt[2], Howie Choset[7], Changwoo Do[10], Jacob Eapen[3], Xiaochun Han[5], Brent Heuser[5], Mike Hurley[2], Brian Jaques[2], Boopathy Kombaiah[3], Zachary D. Kriz[5], Kuan-Che Lan[5], Jun-Li Lin[5], Sin Ming Loo[2], Drew Lysne[2], Zhenqiang (Jack) Ma[6], John Calvin Martinez[1], Sean M. McDeavitt[1], K. L. Murty[3], Prithwish K. Nandi[3], Vikram Patel[2], Apu Sarkar[3], Kumar Sridharan[6], James Stubbins[5], James Tulenko[4], Yong Yang[4], John Youngsman[2],

1. *Texas A&M University*
2. *Boise State University*
3. *North Carolina State University*
4. *University of Florida*
5. *University of Illinois at Urbana-Champaign*
6. *University of Wisconsin-Madison*
7. *Carnegie Mellon University*
8. *University of Pisa, Italy*
9. *Pacific Northwest National Laboratory*
10. *Oak Ridge National Laboratory*
11. *Argonne National Laboratory*

TABLE OF CONTENTS

Program Overview

This Integrated Research Project (IRP) was established to characterize key limiting phenomena related to the performance of used nuclear fuel (UNF) storage systems. This was an applied engineering project with a specific application in view (i.e., UNF dry storage). The completed tasks made use of a mixture of basic science and engineering methods. The overall objective was to create, or enable the creation of, predictive tools in the form of observation methods, phenomenological models, and databases that will enable the design, installation, and licensing of dry UNF storage systems that will be capable of containing UNF for extended period of time.

The project was divided four distinct, yet synergistic, technical mission areas (TMAs), as summarized below. The key technical results and findings from each of the TMAs are summarized in Sections 2 through 5.

Technical Mission Area 1: Low Temperature Creep
This mission focused on the low temperature creep of UNF cladding that may be enabled by decay heat from fission products and stresses from internal pressures. The major objectives were (1) to obtain data using highly oxidized/hydrided tubing under relevant stresses and temperatures, (2) to characterize and translate that data to enable input to FRAPCON and other codes that may be modified to predict UNF behavior in dry storage, and (3) to formulate atomistic simulations to better understand long term creep behavior.

Technical Mission Area 2: Hydrogen Behavior and Delayed Hydride Cracking
This mission focused on the characterization and understanding of delayed hydride cracking (DHC) in spent Zircaloy cladding. The DHC mechanism is generally attributed to local hydride precipitation at stress risers present on the surface of the cladding. Samples with low and high hydrogen loadings were prepared and studiedusing various methods.

Technical Mission Area 3: UNF Canister Corrosion
This mission was focused on recognized gaps in understanding mechanisms relevant to the corrosion degradation of the UNF canisters in various environments. The methods employed included: 1) electrochemical corrosion testing, 2) stress corrosion cracking (SCC) studies, 3) characterization of the corrosion of welds, bolted joints, and seals under prototypic conditions, and 4) integration the results of corrosion tests and microstructural analyses.

Technical Mission Area 4: Novel System Monitoring
The focus of this mission was to develop in-situ prognostic monitoring methods to verify the condition of the UNF and the internal canister environment without having to break the seal of the inner cask. This included the development of self-powered sensing methods to continuously monitor the cask system and provide physical, safety, and security information during.

> **REPORT FORMAT NOTE:**
> This document is large with several components from several authors. In order to expedite reporting, the original formatting is retained to avoid transcription errors. Figures, Tables, and References will designated sequentially within each section.

Context and Motivations

Nuclear energy systems continue to be a significant component of the United States energy portfolio. However, open questions regarding the final disposition of used nuclear fuel (UNF) represent a continued challenge to the long-term viability of nuclear energy. Even the most uninterested members of the public understand that the key question that persists is "what are we going to do about the waste?" Even more, two recent events raised the global national awareness of the significance of and need for safe storage of used nuclear fuel: 1) the termination of proposed deep geologic repository at Yucca Mt., NV and 2) the events at the Fukushima Nuclear Power Plants following the tragic earthquake and tsunami in Japan in March 2011.

The termination of the Yucca Mountain Project re-opened the dialog within the U.S. regarding UNF reprocessing as well as the strategy and potential selection for a real high level waste disposal site. With the termination of the project, UNF continues to accumulate at 99 operating commercial nuclear reactors in the U.S. Used fuel is initially stored in storage pools and then relocated to dry cask storage after sufficient time has passed to allow cooling via radioactive decay (Fig. 1.1). The present regulatory basis for dry cask storage is 60 years but longer storage times will likely become necessary as the U.S. Department of Energy (DOE) and Nuclear Regulatory Commission (NRC) evaluate repository and reprocessing components under the modified open cycle strategy.
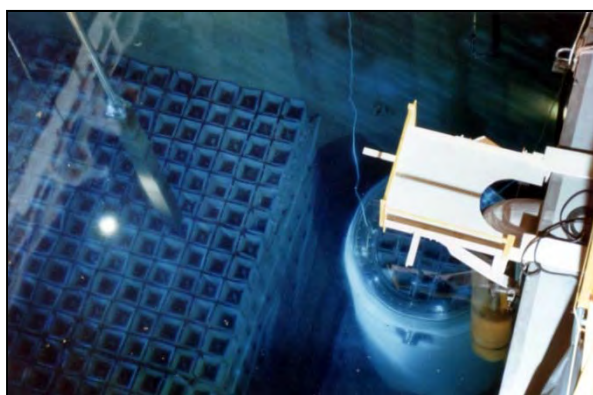

Figure 1.1. Photos of a) used nuclear fuel being loaded into an interim spent fuel storage cask and b) a collection of UNF casks on a dry cask storage platform [1].

Recovery is still ongoing after the serious radiological events at the Fukushima Nuclear Power Plants that evolved following the catastrophic earthquake and tsunami in Japan. One of the challenges this severe natural disaster has revealed is that the latent energy and radioactive

materials contained in UNF must be controlled and safeguarded against conceivable and inconceivable events. While there were many challenges during this incident, the disruption of the fuel storage pool in Unit 4 revealed the extent of the latent energy that continues to be released from UNF even after the fuel is removed from the reactor. The long-term storage of UNF is a paramount issue of international importance.

As UNF storage times are projected to extend beyond 60 years, the trend in the commercial power production industry is to push fuel to higher and higher burnup (>45GWD/t). This creates a UNF storage challenge as higher burnup increases cladding degradation, fission product concentrations, and other phenomena that will affect storage performance. The U.S. DOE is supporting research at the national laboratory level in order to create a comprehensive strategy that addresses these challenges [2-4]. The work reported here was carried out make a significant contribution to this strategy.

Waste Canister Systems

Dry storage technology for UNF has been evolving over the past three decades [1]. The initial regulatory framework in the United States was published under 10CFR72 [5] in 1980 with a modification in 1990 to grant a general license for dry storage to sites that already hold a 10CFR50 [6] operating license. Over the past 30 years a variety of Independent Spent Fuel Storage Installations (ISFSIs) have been put into service, initially as experimental programs but eventually as formal storage strategies. With the variety of approaches it is difficult to describe a nominal cask system.

Some of the first storage containers, such as the older CASTOR V/21, Westinghouse MC-10, Transnuclear TN-24P, and NAC I28 systems, were vertical storage systems used to demonstrate the method. Many of the current designs are vertical as well, but horizontal storage systems such as the Nutech Horizontal Modular Storage (NUHOMS) method. The early systems were only designed for storage and the expectation is that such dry cask systems will have to be repackaged for transportation. Later systems were designed to be multi-purpose containers to serve as dry storage, transportation, and disposal canisters. Figure 1.2 shows a representative collection of dry storage designs; there are multiple variations for many of these systems that are designed to contain differing numbers of fuel assemblies.
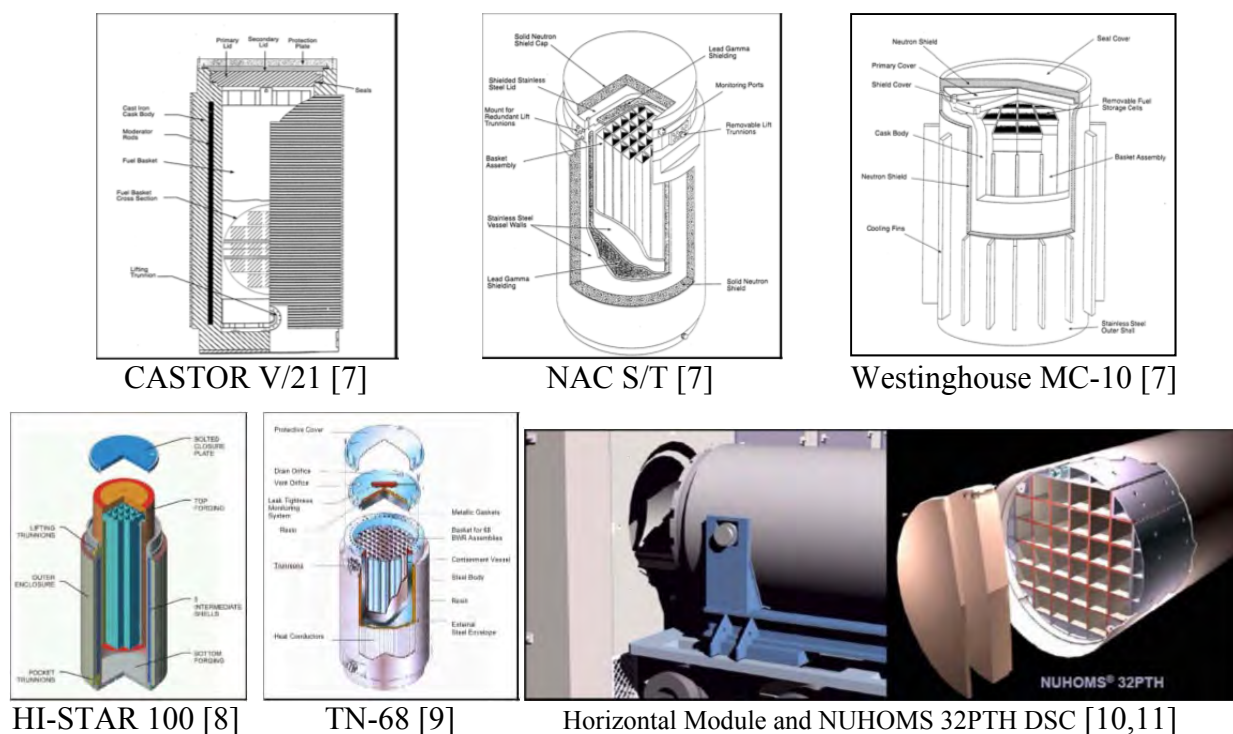
CASTOR V/21 [7]   NAC S/T [7]   Westinghouse MC-10 [7]

HI-STAR 100 [8]   TN-68 [9]   Horizontal Module and NUHOMS 32PTH DSC [10,11]

Figure 1.2.   Schematics of selected dry storage canisters and systems (old systems).

References (Section 1.0)

[1]   *Industry Spent Fuel Storage Handbook*, Electric Power Research Institute, Palo Alto, CA, (July 2010).

[2]   CSNF Waste Form Degradation: Summary Abstraction, Bechtel SAIC Company, LLC, Las Vegas, NV, ANL-EBS-MD-000015 REV 02 (August 2004).

[3]   *High-Burnup Fuel Issues for Long-Term Dry Storage and Transportation*, white paper to DOE/NE Fuel Cycle Technologies Program, Office of Used Fuel Disposition Research and Development, Argonne National Laboratory, August 27, 2010 (Updated December 3, 2010).

[4]   B.Hansen, C. Stockman, J. Wagner, S. Birk, A. Alsaed, N, Iyer, and B. Halsey, "Preliminary DOE Gap Analyses and R&D Needs," presentation to the EPRI Extended Storage Collaboration Project, Charlotte, NC (Dec. 7-8, 2010).

[5]   10CFR72, Title 10, U.S. Code of Federal Regulations, Part 72 "Licensing Requirements for the Independent Storage of Spent Nuclear Fuel, High-Level Radioactive Waste, and Reactor-Related Greater Than Class C Waste."

[6]   10CFR50, Title 10, U.S. Code of Federal Regulations, Part 50 "Domestic Licensing of Production and Utilization Facilities."

[7]   *Industry Spent Fuel Storage Handbook*, NEI 98-01 (May 1998).

[8]   K.P. Singh, Holtech International,"Safety and Security of HLW Storage and Transport in the 21st Century," NEI Dry Storage Information Forum (May 3-4, 2004).

[9]   F.Bailly, Areva, Inc., "Spent Fuel Storage and Transportation Technologies," Nevada Workshop, Pahrump, NV (June 9, 2005).

[10]   T. Neider, Transnuclear, Inc., "The Transnuclear Future Licensing Objectives and New Project Overviews," NEI Dry Storage Information Forum (May 10, 2005).

[11]   T. Neider, Transnuclear, Inc., "Transnuclear Recent Operational Experience," NEI Dry Storage Information Forum (May 13, 2008).

1.0   Summary of Key Results and Findings from TMA-1: Low Temperature Creep

Introduction

Since the mid-1980s when spent fuel pools began to reach their capacity at nuclear plants operating companies have had to find alternative options for spent fuel storage. The main two options consist of increasing the spent fuel pool size and casking the fuel assemblies for dry storage either on site or at a repository. With the closing of Yucca Mountain in 2011 there are no fuel repositories in the United States, as such casked dry storage is becoming more and more significant in the United States as the total fuel amounts will eventually surpass the capacity for wet storage.

During storage, fuel cladding is at risk of failure from several processes, among them creep failure is considered the most important. Though the rate at which creep occurs within the cladding is low, over the course of twenty to forty years accumulated damage in the cladding can cause failure. Because temperature and pressure determine the rate at which creep occurs over the lifetime of a cask the Determining Allowable Temperatures in Inert and Nitrogen Gases code (DATING) routine was developed to determine an allowable temperature and pressure combinations for dry storage.

During storage the cladding experiences a decreasing internal temperature, and thus a decreasing creep rate throughout its life time. However unexpected temperature events, such as repackaging, re immersion into a fuel pool, or failures of the cask cooling system can occur. These events could potentially cause a temperature spike within the contained assemblies which could spike the creep rate and thus affect the overall expected lifetime of the cladding.

The DATING routine works well for standard cases of storage, however off-normal temperature events are not well incorporated into the system. This study aims to reproduce the DATING routine using updated creep equations in order to look at the effect off normal temperature events have on allowable temperature limits for zirconium based cladding. Zircaloy-4 will be used for several creep tests at varying temperatures and pressures expected to be seen during storage, updated creep equations will be fit to the data to better allow for changing temperature conditions in the code, and finally the effects of several off temperature conditions will be looked at for potential storage risks.

The following sections are detailed reports presented from TMA1 contributors in their original format (to maintain clarity).

Nuclear Energy University Program

IRP - Fuel Aging in Storage and Transportation (FAST) : Accelerated Characterization and Performance Assessment of the Used Nuclear Fuel Storage System

Technical Mission Area 1 – Low Temperature Creep

Final Report

by

Dr. K. Linga (KL) Murty, Principal Investigator
Dr. Apu Sarkar, Post-Doctoral Research Associate
Dr. Boopathy Kombaiah, Graduate Student (PhD, 5/2015)

Objective

Technical Mission Area 1 – Low Temperature Creep

This mission's focus is on the low temperature creep of UNF cladding enabled by decay heat from fission products and stresses from internal pressures. Systematic studies will characterize the low-temperature low-stress mechanisms relevant to dry storage.

The major objectives are:

1. to obtain data using highly oxidized/hydrided tubing under relevant stresses and temperatures,
2. to characterize and translate that data to enable input to FRAPCON and other codes that may be modified to predict UNF behavior in dry storage, and
3. to formulate atomistic simulations to better understanding of the long term creep behavior with emphasis on effects of oxygen and hydrogen as well as neutron irradiation.

One of the main tasks of the team at North Carolina State University is on the characterization of creep mechanisms under internal pressurization of Zircaloy cladding with emphasis on transitions in creep mechanisms so that a knowledgeable extrapolation of high stress data to low stresses of relevance to dry storage conditions can be made. To this end, creep of Zircaloy-4 and HANA4 cladding tubes were studied using internal pressurization tests at varied temperatures and hoop stresses. In addition, hydriding of HANA4 cladding tubes was developed and some preliminary creep tests of hydride tubing were performed. Finally, current experimental findings along with very limited experimental data in the recent literature on internal pressurization creep of irradiated Zirlo cladding are used in predicting the accumulated plastic hoop strains during dry storage of used nuclear fuel (UNF).

Model predictions clearly reveal the influence of temperature and internal pressure history of the SNF from the time they are removed from the water pool and transferred to dry storage. Effects of hydriding and neutron radiation exposure are seen to result in lower creep rates and creep strains accumulated during dry storage of UNF. Main conclusions are that further experimental studies are needed in the following two areas:

1. Effect of hydriding on low temperature creep of Zircaloy cladding at low stresses where viscous creep (creep rate proportional to stress) becomes dominant
2. Internal pressurization creep of irradiated cladding especially at low stresses where viscous creep (creep rate proportional to stress) becomes dominant

This report consists of the following four experimental and modeling studies:

1. Creep mechanisms of recrystallized Zircaloy-4
2. Creep mechanisms in HANA4 alloy tubing
3. Effect of hydrogenation on creep of HANA4 cladding
4. Zircaloy creep mechanisms – Application to dry storage of UNF.

<p style="text-align:center">**TABLE OF CONTENTS**</p>

RESEARCH DISSEMINATION

LIST OF PUBLICATIONS

1) B. Kombaiah and K. Linga Murty, "Coble, Orowan Strengthening and Dislocation Climb mechanisms in a Nb-modified Zircaloy cladding", accepted in *Metallurgical and Materials Transactions A*.

2) B. Kombaiah and K. Linga Murty (2015). "High temperature creep and deformation microstructures in recrystallized Zircaloy-4." Philosophical Magazine 95(15): 1656-1679.

3) B. Kombaiah and K. Linga Murty, "Dislocation cross slip controlled creep in Zircaloy-4 at high stresses", *Materials Science & Engineering A*, 623 (2015) 114–123.

4) A. Sarkar, K. Boopathy, J. Eapen and K.L. Murty, "Creep behavior of hydrogenated Zirconium alloys", *J. of Materials Engineering and Performance*, 23 (2014) 3649-3656.

LIST OF CONFERENCE PRESENTATIONS

1) B. Kombaiah, A. Sarkar and K.L. Murty, "Transitions in creep mechanisms of Zircaloy 4", 143th Annual Meeting and Exhibition, TMS 2014, San Diego, California.

2) K.L. Murty and B. Kombaiah, "Transitions in creep mechanisms in low c/a-ratio HCP metals", *19th International Symposium, Plasticity 2013*, Nassau, Bahamas.

3) A.Sarkar, B. Kombaiah, J. Eapen, K. L. Murty, "Effect of hydrogen on creep behavior of Zirconium alloys", LWR Fuel Performance Meeting Top Fuel 2013, Charlotte, NC, USA.

4) B. Kombaiah, C.S. Seok and K. Linga Murty, "Burst, Ring and Biaxial Creep of Zircaloy Cladding – Applications to Dimensional Change Predictions during Dry Storage", *MS&T conference 2012*, Pittsburgh, USA.

5) K. Linga Murty, C.S. Seok and B. Kombaiah, "Burst and Biaxial Creep of Thin-Walled Tubing of Low c/a-Ratio HCP Metals", *6th International Conference on Creep, Fatigue and Creep-Fatigue Interaction [CF-6]*, Kalpakkam, India, 2012.

1 Transitions in creep mechanisms of recrystallized Zircaloy-4

1.1 Introduction

Zirconium and its alloys have a rich history of serving light water reactors as fuel claddings and other structural components for several decades owing to their attractive properties, such as low absorption cross section for thermal neutrons, good aqueous corrosion resistance and sufficient strength at high temperature. In particular, claddings, spacer grids and intermediate flow mixers of light water reactors (LWR), channels in boiling water reactors (BWR) and calandria tubes in pressurized heavy water reactors (PHWR) are fabricated of Zircaloy-4, an alloy of Sn, Cr, Fe and Zr [1]. Creep deformation of these components during service as well as spent fuel storage has been regarded as a potential limiting factor of their structural integrity under the variable conditions of stress, temperature and material microstructure. Therefore, the creep life of the zirconium alloys subjected to these conditions becomes a critical parameter for nuclear reactor design, and its accurate prediction inevitably requires the comprehension of transitions in creep mechanisms as lower stresses are approached that are relevant to dry storage conditions [2, 3]. For instance, FRAPCON mechanical model employed for predicting the creep strain accumulated in the reactor components requires mechanistic-based creep rate equations, encompassing stress and temperature as major variables, as a principal input [4].

In spite of extensive investigations conducted on the creep deformation of α-Zirconium and its alloys, the micro-mechanisms controlling the creep rate associated with low stresses as well as high stresses were not unequivocally pointed out [2, 5]. For instance, several mechanisms have been proposed to be controlling the creep rate at the intermediate stress range in the temperature vicinity of 0.3-0.5 T_m (T_m is the melting point in Kelvin) for α-Zirconium and its alloys such as Zircaloy-2 and Zircaloy-4, which have tin as a major alloying element: non-conservative motion of jogs in the screw dislocations [6-8], dislocation glide process [8-10], and Climb of edge dislocations [11, 12]. The creep data from all these investigations exhibited stress exponent (*n*) ranging 3-9 and the creep activation energy (Q_c) values, in most cases, being close to the activation energy for self-diffusion in α-Zirconium (Q_l), 270 kJ/mol. Further, Murty et al followed by Matsuo et al determined that the creep rate of Zircaloy-4 could be fit with a power law function of *sinh(σ/E)* in the range of 49 MPa to 344 MPa at the temperatures around 400 °C with an activation energy of 260 kJ/mol and attested a self-diffusion controlled mechanism to be responsible for creep deformation [13, 14].

Hayes et al reviewed the creep data of α-Zirconium, Zircaloy-2 and Zircaloy-4 collected from several investigations to uncover the rate-controlling mechanism in the power law regime by plotting the creep rates as BMD plots – dimensionless parameters of diffusion coefficient-compensated creep rate versus modulus compensated stress – and obtained a stress exponent of 6.4, 4.8 and 5.0 respectively [5, 15]. A stress-independent creep activation energy was assumed to be ~270 kJ/mol that has been found to best condense the creep rate data into a single line. Depending upon these observations, they have ascribed dislocation climb, as opposed to dislocation glide, being responsible for controlling the creep deformation at the intermediate

2

stresses based upon the mechanistic creep parameters. A combination of – n~4.8-6.4 and Q_c~Q_l – could, however, be indicative of not only edge dislocation climb but also non-conservative motion of jogs on screw dislocations as a governing mechanism. For instance, Morrow et al and Moon et al conducted creep tests on Zircaloy-4 over a range of temperature and stress conditions, 260-593 °C and 26-196 MPa respectively, and considered the modified Jogged-Screw model (MJSD) based upon the deformation microstructure exhibiting a distribution of jog-heights characteristic of the creep process controlled by the glide of jogged-screw dislocations; a good agreement between the predictions by the model and the experimental creep rates was obtained [6, 16].

A transition from dislocation-mediated mechanisms at high stresses to diffusional flow at low stresses has been noted in Zirconium alloys as generally found in many materials. At low stresses, the steady state creep rate was shown to have a linear dependency on the applied stress with a stress exponent of 1 making the deformation like that of Newtonian viscous flow. For α-Zirconium with small grain size (up to 50μm), Coble creep, wherein creep is the result of stress-directed diffusion of vacancies along grain boundaries, was proposed to be the dominant creep mechanism based upon the equivalency of the creep activation energy with that for grain boundary self-diffusion at 5-13 MPa and 425-620 °C [17, 18]. On the other hand, Fiala and Čadek have determined a good correlation between the creep rates and the predictions by the Ashby-Verdell model [19], which was derived based upon the creep deformation being controlled by grain boundary sliding accommodated by non-uniform diffusional flow of vacancies along grain boundaries, for α-Zirconium specimens with grain size in the range of 48-113 μm at the low stress range (4×10^{-6}E to 4.6×10^{-4}E) and low homologous temperatures (0.4-0.5T_m) [8, 20]. As well, the steady state creep rate data have demonstrated an inverse linear dependence to the cubic power of the grain size, which complied with the model. However, on analyzing the creep data pertinent to the low stresses collectively from the preceding studies, Hayes et al have identified that the normalization of the steady state creep rates with the grain size with a power of 1 condensed them closely on a single line instead of a power of 3 when plotted with the normalized stress on the abscissa. This lead them to question the applicability of the Coble creep model as well as the Ashby-Verdell model to the low stress creep deformation of α-Zirconium with smaller grain size, <90 μm.

Addition of alloying elements to α-Zirconium can alter its creep mechanisms operative at the low stress regime. For instance, Prasad et al have investigated the creep behavior of pure α-Zirconium and Zircaloy-2 which has Sn, Fe, Cr and Ni as alloy constituents, both having an equal grain size of ~17 μm at stresses to a maximum of 5.9 MPa and 600-720 °C [17]. While the creep activation energy value for α-Zirconium was measured to be of 102.8 kJ/mol, it increased to 267 kJ/mol for Zircaloy-2, indicating the dominant creep mechanism respectively to be Coble creep and Nabarro-Herring creep (N-H), wherein creep is the result of stress-directed flow of vacancies through the lattice. Since the grain sizes in these materials are similar, the origin of the transition in creep mechanism has been ascribed to the sluggishness in grain boundary diffusion arising due to the presence of more refractory $Zr(Cr, Fe)_2$ type precipitates at the grain boundaries of Zircaloy-2. The low stress creep data of Zircaloy-4 was, however, not found in the literature.

3

In the light of the above discussions, it can inferred that there is no clear agreement on the rate governing mechanisms in α-Zirconium and its alloys at low as well as intermediate stresses. One of the shortcomings of several investigations on elucidating the creep mechanisms in these alloys is the lack of detailed microstructural analysis of the deformed specimens using transmission electron microscopy (TEM) in support of the creep data. The objective of this study is to investigate the creep behavior of Zircaloy-4 in the low and intermediate stress regimes with a focus on uncovering the rate-controlling creep mechanism(s). At first, possible creep mechanisms have been short-listed based upon the mechanistic creep parameters such as stress exponent and activation energy determined from the uniaxial tensile creep tests of Zircaloy-4 conducted over a range of temperature and stress conditions, 500-600 °C and $2.56 \times 10^{-4}E - 2.8 \times 10^{-3}E$ respectively. Following that, an extensive analysis of the dislocation substructures in the microstructure of the crept specimens using TEM was undertaken to ascertain the dominant creep mechanism. Furthermore, the experimental creep rates were compared with the predictions of standard creep models to validate the rate-controlling mechanisms over the testing conditions.

1.2 Materials and experiments

The chemical composition of the Zircaloy-4 sheet tested in this study is given in Table 1.1. Uniaxial tensile creep specimens were machined out from the sheet by keeping the rolling direction along the loading axis of the specimens. The gauge dimension of the specimens was 25.4 x 6.2 x 1.2 mm³. The specimens were recrystallized at 700 °C for 4 hours under Argon atmosphere. The polarized-optical micrographs revealed an equiaxed grain structure as shown in Figure 1.1a. The average grain size measured using the linear intercept method of about 350 grains was 8.5 μm with a standard deviation of 4.4 μm.
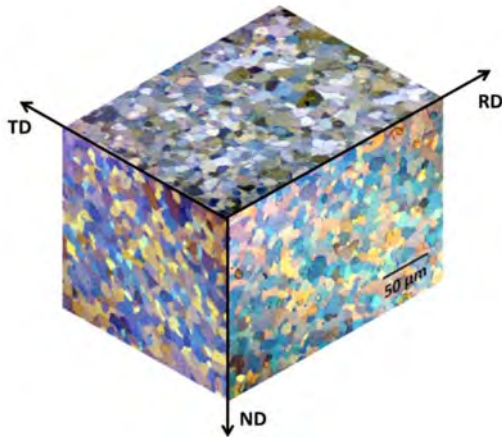
Figure 1.1a. Optical micrographs of the annealed Zircaloy-4 sheet
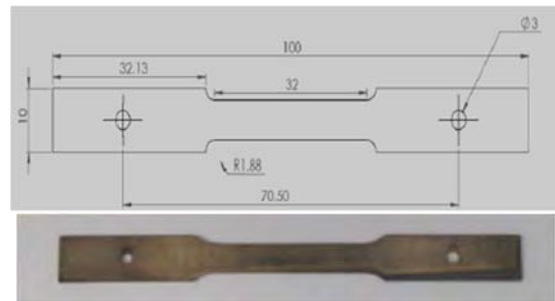
Figure 1.2b. Zircaloy-4 sheet creep tensile specimen drawing and a photograph

Figure 1.1b includes a drawing and a photograph of creep specimens machined from Zircaloy-4 sheet. Uniaxial tensile creep tests were carried out in a constant load lever arm tester (Figure 1.1c) by applying a range of stresses, $2.56 \times 10^{-4}E - 2.8 \times 10^{-3}E$, at three different temperatures: 500 °C, 550 °C and 600 °C. The test temperatures were achieved by heating the specimens inside a three-zone furnace that was connected to an ATS® temperature controller. A

4

K-type thermocouple wire was wound on the gauge section of the specimen in order to measure and control the temperature accurately within a range of ±1 K. The extension of the gauge length during creep tests was measured by a Linear Variable Capacitor (LVC) and extensometer assembly; the LVC could accurately measure an extension of as low as 2 µm. Once the steady state creep was attained, the creep testes were stopped by switching off the furnace and cooling the specimen down to room temperature under air flow to preserve the deformation microstructure.

Table 1.1.
Chemical composition of Zircaloy-4 tested in this study

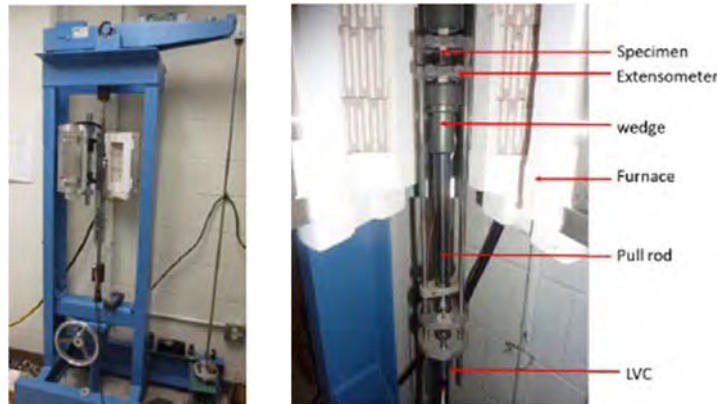| Element	Amount
Tin	1.62%
Iron	0.23%
Chromium	0.11%
Oxygen	1158 ppm

Figure 1.3c. Lever arm tester employed for uniaxial creep testing (a) and a close-up view of the tensile specimen attached with the extensometer (b)

The microstructures of the unstrained samples as well as crept samples were analyzed by means of TEM with an objective to comprehend the underlying creep mechanisms. For synthesizing TEM thin specimens, the sheets with a thickness of about 1 mm were initially dissolved in an etching solution, consisting of 45 ml nitric acid, 10 ml hydrofluoric acid in 45 ml water, to bring down the thickness to about 200 µm. Following that, the sheets were slowly polished using 800 grit sand papers till a thickness of ~100 µm is reached. The preceding procedure avoids any artificial dislocations generated in the disc from coarse polishing. Discs with 3 mm diameter were then cut using a mechanical punch and were polished using a model 110 Fischione automatic twin-jet polisher to produce the final specimens at -60 °C by applying a voltage of 25 V using the following electrolytic solution: 30 ml sulfuric acid and 1 ml hydrofluoric acid in 470 ml methanol. A 200 KeV JEOL 2000FX TEM equipped with a double tilt-holder was utilized for imaging.

TEM micrographs of the unstrained sample revealed fully recrystallized grains with a low dislocation density that is characteristic of an annealed microstructure as shown in Figure 1.2. The few dislocations were observed to be long and fairly straight without forming any sort of tangles or sub-boundaries. Dislocation density (ρ) in the unstrained specimen as well as crept samples were measured from their TEM micrographs using the following relation,

5

$$\rho = \alpha \frac{0.5j}{A} \tag{1.1}$$

where j is the number of intersections of the dislocations on the foil surface, A is the area of the micrograph and α is a correction factor that assumes a value between 1 and 2 corresponding to completely parallel and completely random dislocations respectively [6]. The dislocation density in the unstrained sample was estimated to be in the range of $1.6 \times 10^{11} - 4.3 \times 10^{11}/m^2$, which is similar to the value of dislocation density estimated in annealed materials [21].
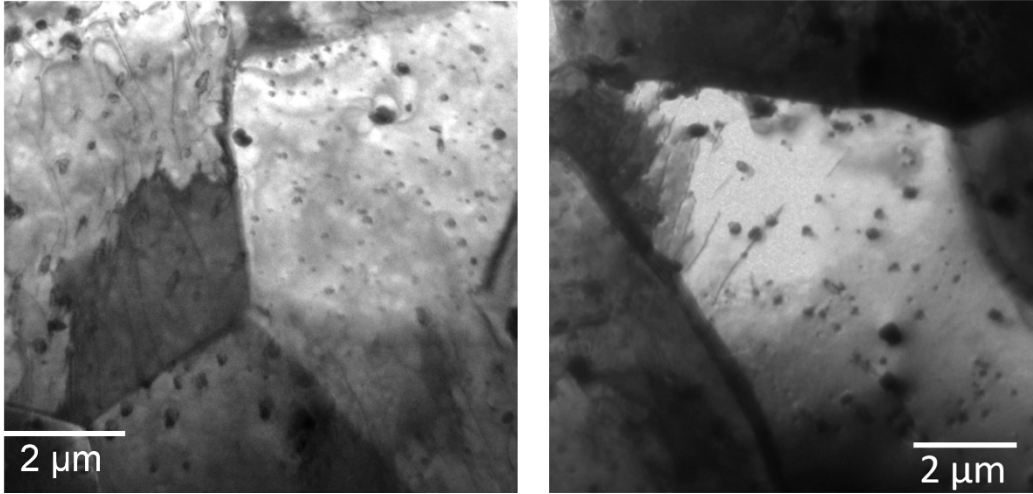
Figure1.4. Representative TEM micrographs of Zircaloy-4 before creep depicting recrystallized grains with few straight dislocations
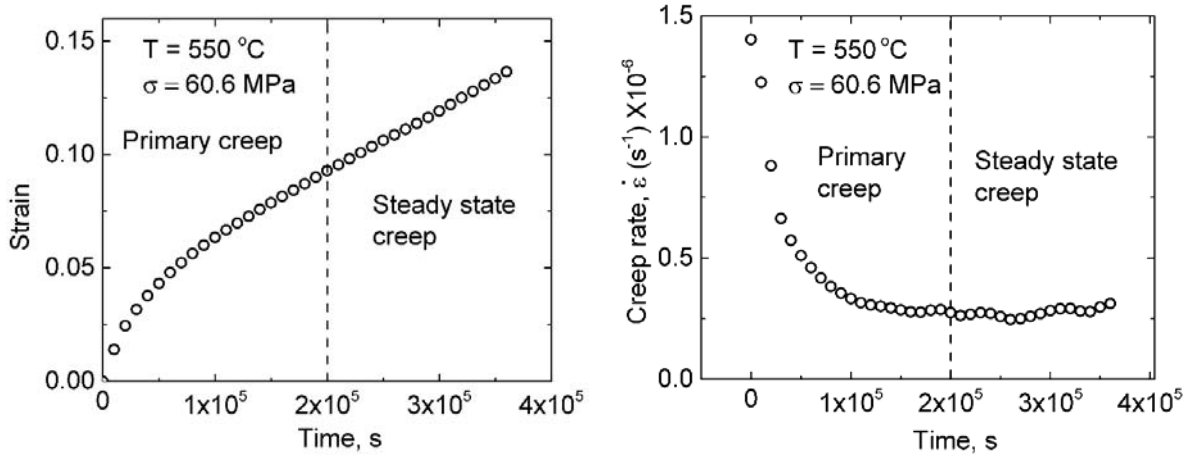
Figure 1.5. Representative creep curve of Zircaloy-4 obtained at 550 °C and 60.6 MPa (left) and the derivative plot showing a transition from the primary creep to the steady state creep (right)

1.3 Results and discussion

1.3.1 Stress exponent

A creep curve and its derivative plot for an applied stress of 60.6 MPa at 550 °C representing the creep curves at high stresses are given in Figure 1.3. A decrease in the creep rate with respect to the time followed by a steady state creep rate demarcated the primary creep regime from the steady state creep regime, pointing out dislocation-assisted creep deformation at

6

high stresses. As well, it can be suggested that the recovery rate during the steady state creep regime equally compensates the effects of work hardening originated from the dislocation interactions [22]. In contrast to the creep curves at high stresses, the creep curves exhibited little primary creep at low stresses and the entire strain is nearly achieved through the steady state deformation as shown by the curve at 15.3 MPa and 550 °C in Figure 1.4. Such kind of deformation can point out the occurrence of viscous flow mechanism in which stress-directed diffusion of vacancies results in strain.
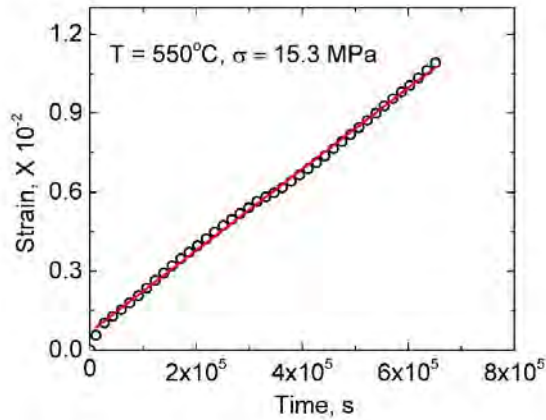

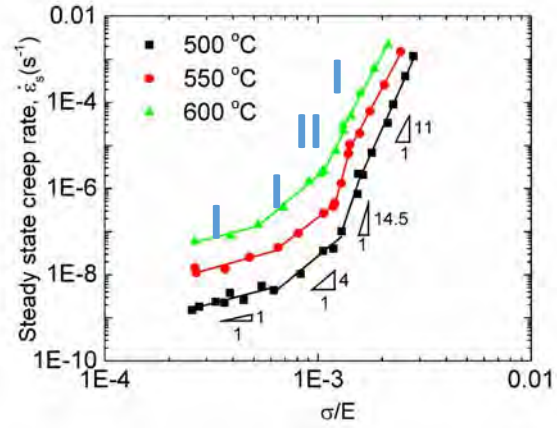Figure 1.6. Representative creep curve obtained at 550 °C and 15.3 MPa.

Figure 1.7. Steady state creep rate versus modulus -compensated stress plot

The steady state creep rates and the total strain along with the stresses and temperatures employed in the tests are given in Table 1.2. The steady state creep rate data were further analyzed to note the rate controlling mechanisms at the testing conditions. At the outset, two important creep parameters namely stress exponent (n) and activation energy (Q_c) were obtained from the general creep equation relating the steady state creep rate ($\dot{\varepsilon}_s$) with the applied stress (σ) and temperature (T in K) that can be stated as,

$$\dot{\varepsilon}_s = \frac{AEb}{kT} \left(\frac{\sigma}{E}\right)^n e^{-\frac{Q_c}{RT}}, \tag{1.2}$$

$$E = 98.82 - 0.076(T - 273) \, GPa . \tag{1.3}$$

In equation (1.2), A is a constant, E is the temperature-dependent elastic modulus of Zircaloy-4, b is the burgers vector ($3.23 \times 10^{-10} m$), k is the Boltzmann's constant and R is the gas constant. The stress exponent is then equivalent to the slope of the log-log plot between the steady state creep-rate versus the modulus compensated stress which is shown in Figure 1.5 and four regimes (I to IV) have been identified with the stress exponents of 1, 4, 14.5 and 9-11 as the applied stress increases.

The subsequent sections will be dealing with the analyses of the creep data pertained to regimes I and II at first, followed by regime III and finally regime IV.

7

Table 1.2. Stress, steady state creep rates and total strain at the three different test temperatures.

500 °C			550 °C			600 °C		
σ, MPa	σ/E	$\dot{\varepsilon}_s$, s^{-1}	σ, MPa	σ/E	$\dot{\varepsilon}_s$, s^{-1}	σ, MPa	σ/E	$\dot{\varepsilon}_s$, s^{-1}
15.6	2.56X 10^{-4}	1.5 X 10^{-9}	15.1	2.65 X 10^{-4}	1.5 X 10^{-8}	14.1	2.65 X 10^{-4}	6.0 X 10^{-8}
16.9	2.78 X 10^{-4}	1.8 X 10^{-9}	15.3	2.68 X 10^{-4}	1.1 X 10^{-8}	20.8	3.90 X 10^{-4}	8.0 X 10^{-8}
20.1	3.30 X 10^{-4}	2.4 X 10^{-9}	20.8	3.65 X 10^{-4}	1.4 X 10^{-8}	27.8	5.22 X 10^{-4}	1.5 X 10^{-7}
22.2	3.65 X 10^{-4}	2.3 X 10^{-9}	21.0	3.68 X 10^{-4}	1.4 X 10^{-8}	36.6	6.88 X 10^{-4}	3.6 X 10^{-7}
23.5	3.86 X 10^{-4}	3.8 X 10^{-9}	27.2	4.77 X 10^{-4}	2.5 X 10^{-8}	48.3	9.07 X 10^{-4}	1.4 X 10^{-6}
27.3	4.49 X 10^{-4}	2.6 X 10^{-9}	37.1	6.51 X 10^{-4}	4.3 X 10^{-8}	54.8	1.03 X 10^{-3}	2.2 X 10^{-6}
33.1	5.44X 10^{-4}	5.5 X 10^{-9}	46.1	8.08 X 10^{-4}	9.2 X 10^{-8}	56.0	1.05 X 10^{-3}	2.5 X 10^{-6}
37.8	6.22 X 10^{-4}	4.4 X 10^{-9}	60.6	1.06 X 10^{-3}	2.7 X 10^{-7}	56.6	1.06 X 10^{-3}	2.6 X 10^{-6}
50.3	8.27X 10^{-4}	1.1 X 10^{-8}	67.3	1.18 X 10^{-3}	3.8 X 10^{-7}	64.5	1.21 X 10^{-3}	7.5 X 10^{-6}
64.3	1.06 X 10^{-3}	3.6 X 10^{-8}	68.3	1.20 X 10^{-3}	4.6 X 10^{-7}	70	1.32 X 10^{-3}	3.0 x 10^{-5}
71.8	1.18 X 10^{-3}	4.0 X 10^{-8}	73.3	1.29 X 10^{-3}	1.3 x 10^{-6}	70	1.32 X 10^{-3}	2.2 x 10^{-5}
78.5	1.29 X 10^{-3}	1.0 X 10^{-7}	79.5	1.39 X 10^{-3}	6.5 x 10^{-6}	76	1.43 X 10^{-3}	4.8 x 10^{-5}
93.2	1.53 X 10^{-3}	7.5 X 10^{-7}	79	1.39 X 10^{-3}	6.3 x 10^{-6}	84	1.58 X 10^{-3}	1.6 x 10^{-4}
94	1.55 X 10^{-3}	2.2 x 10^{-6}	80.5	1.41 X 10^{-3}	1.1 x 10^{-5}	97.5	1.83 X 10^{-3}	6.1 x 10^{-4}
99	1.63 X 10^{-3}	2.1 x 10^{-6}	80.5	1.41 X 10^{-3}	1.0 x 10^{-5}	113.5	2.13 X 10^{-3}	2.2 x 10^{-3}
109	1.79 X 10^{-3}	6.7 x 10^{-6}	89.5	1.57 X 10^{-3}	1.9 x 10^{-5}			
129	2.12 X 10^{-3}	3.3 x 10^{-5}	100	1.75 X 10^{-3}	6.2 x 10^{-5}			
137	2.25 X 10^{-3}	8.9 x 10^{-5}	117	2.05 X 10^{-3}	2.5 x 10^{-4}			
156	2.56 X 10^{-3}	4.0 x 10^{-4}	139	2.44 X 10^{-3}	1.5 x 10^{-3}			
170	2.80 X 10^{-3}	1.2 x 10^{-3}						

σ–Stress, E–Elastic Modulus, $\dot{\varepsilon}_s$ –Steady state creep rate, ε–Totalstrain

8

1.3.2 Creep mechanisms in Regime I and II

A stress exponent of 4.1±0.2 at high stresses transits into a value of 1.3±0.2 at low stresses which are referred to as regime II and regime I respectively. At a constant modulus-compensated stress, the general creep equation (1.2) can simply be written as,

$$\dot{\varepsilon}_s = A_0 e^{-\frac{Q_c}{RT}}, \qquad\qquad\qquad (1.4)$$

where A_0 is a function of the applied stress. The activation energy was then calculated from the slope of a semi-logarithmic plot of the steady state creep rate versus the inverse of temperature as shown in Figure 1.6 and plotted as a function of the modulus compensated stress in Figure 1.7. The activation energy value for regime I was calculated to be 196±2 kJ/mol, whereas the activation energy value increased to 240±6 kJ/mol for regime II. Also, it can be seen that the activation energy values remain constant vis-à-vis the applied stress within a regime. The activation energy for creep for regime I, 196 kJ/mol, resides close to the activation energy value for self-diffusion along grain boundary in α-Zirconium determined from diffusion experiments (Q_{gb}=188 kJ/mol) [23]. Notably, the activation energy data for self-diffusion along grain boundary in Zircaloy-4 is not available in the literature. On the other hand, the higher activation energy value for creep determined for regime II, 240 kJ/mol, lies in the range of the activation energy for lattice self-diffusion in Zr-1.3%Sn determined using the tracer method (Q_l=259 kJ/mol) [24]. Moreover, the ratio of the creep activation energy value for regime I to that for regime II is 0.8, which agrees with the general observation that $Q_{gb} = 0.5\text{-}0.8Q_l$.
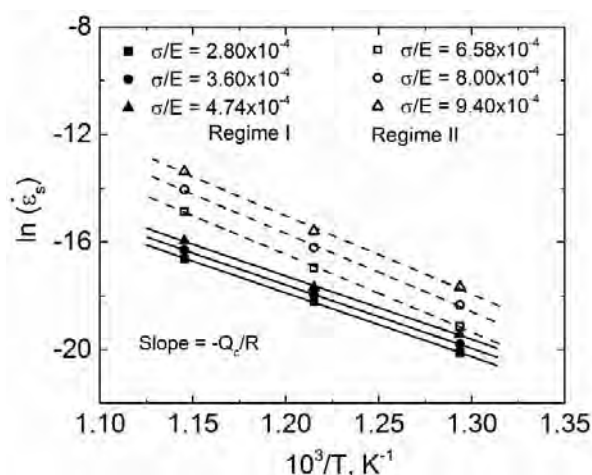
Figure 1.8. Arrhenius plots at different stresses (regimes I and II)
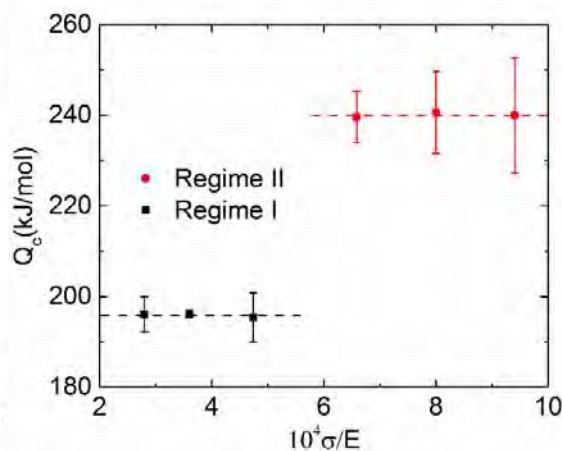
Figure 1.9. Creep activation energy as a function of applied stress in regimes I and II

Figure 1.8 shows the plot of the steady state creep rates normalized by the lattice diffusivity, $D_l = 5 \times 10^{-4} \exp(-259000/RT)$, versus modulus-compensated stress [24]; it can be seen that the normalization converges the creep rates in regime II fall closely in a single line whereas it separates out the creep rates in regime I depicting the effect of temperature on the transition in creep mechanisms. Further, grain boundary sliding (GBS) – controlled regime with a stress exponent of 2, which usually exists between the viscous diffusion creep regime at low stresses and the dislocation-assisted creep regime at high stresses as suggested by Langdon, is absent in Zircaloy-4 [25, 26].

9
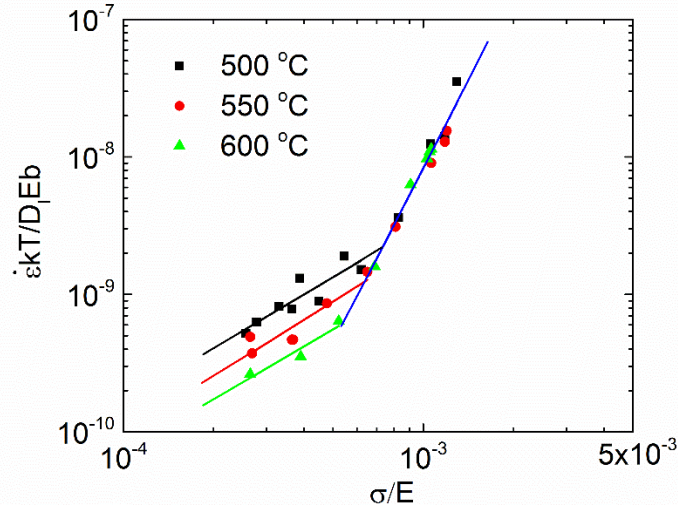
Figure 1.10. Normalized steady state creep rate versus normalized stress

Possible creep mechanism(s)

A stress exponent close to 1 in conjunction with a stress-independent activation energy for creep similar to the activation energy for self-diffusion along the grain boundary in zirconium generally indicates Coble creep as the rate controlling mechanism in regime I [27]. Also, other common Newtonian flow mechanisms such as N-H creep [28], and Harper-Dorn (H-D) creep [29] wherein creep is produced as a result of viscous flow due to dislocations, can be negated as the prominent creep mechanisms since an activation energy equivalent to that for lattice self-diffusion is warranted for such creep processes. Moreover, these viscous flow processes in general would become prominent in materials with large grain sizes. For instance, Novotný et al [30] have demonstrated based on the creep data on alpha-zirconium at the temperature range, 500 °C to 750 °C, and the stresses ranging from $4 \times 10^{-6} - 9 \times 10^{-5} G$ that H-D creep operates significantly only when the grain size is larger than 125 μm and that Coble creep dictates the creep rates in alpha-zirconium with finer grain size. Congruous with this observation, Bernstein et al have earlier shown Coble creep to be active in alpha-zirconium and Zircaloy-2 with grain sizes 50 μm and 10 μm respectively at 520-620 °C and low stresses [18]. Therefore, a smaller grain size of 8.5 μm present in the Zircaloy-4 sheet tested in this study further favors the negligence of N-H creep and H-D creep as viable mechanisms in regime I.

On the other hand, a combination of n~1 and Q_c~Q_{gb} can be ascribed not only to Coble creep but also to the slip-band model developed by Spingarn-Nix, wherein creep is controlled by climb of dislocations assisted by diffusion of atoms along grain boundaries [31]. For instance, Gollapudi et al have obtained n~1 and Q_c~Q_{gb} for Ti-3Al-2.5V at low stresses; however, the predictions by the Coble creep model have fallen below the experimental creep rates by about seven orders of magnitude [32]. Further analysis of the deformation microstructures in TEM exhibiting parallel slip-bands joining with grain boundaries and a good consensus between the experimental creep rates with the model predictions attested the creep mechanism based upon the slip-band model to the viscous creep regime in Ti-3Al-2.5V. A similar creep behavior might be expected in Zircaloy-4 as

10

well on account of its similar crystal structure (HCP) with a low c/a ratio (<1.633) as per the Ti alloy.

In regime II, a stronger dependency of the creep rate on the applied stress with n=4.1 points out a dislocation-mediated mechanism to be governing the creep rate. Additionally, having a stress-independent creep activation energy equivalent to that for lattice self-diffusion in regime II, any of the dynamic recovery processes based on dislocation climb [33] or glide of jogged screw dislocations [34], which necessitate exchange of vacancies between edge dislocation core and surrounding lattice, can be generally considered for the rate controlling process. Meanwhile, dislocation glide controlled creep, which is generally associated with n~3 and Q_c~Q_l, cannot be disregarded in regime II. For instance, despite of the creep data on α-Zirconium from Pahutová and Čadek exhibiting n=6.3 and Q_c~Q_l, they have suggested an interpretation in which dislocation glide-controlled creep is attested to the power law regime by incorporating an effective stress into the analysis [10]. The effective stress was obtained by subtracting the internal stress due to the dislocations present within the system to the external applied stress. In the analysis, the stress exponent of 6.3 determined using the applied stress was reduced to a value of 2-4 when the effective stress was considered in evaluating the stress dependence.

In order therefore to establish the appropriate creep mechanism for regimes I and II from the ones suggested by the mechanistic creep parameters of Zircaloy-4, analyses of the deformation microstructures in TEM as well as validation of the experimental creep rates using standard models are undertaken.
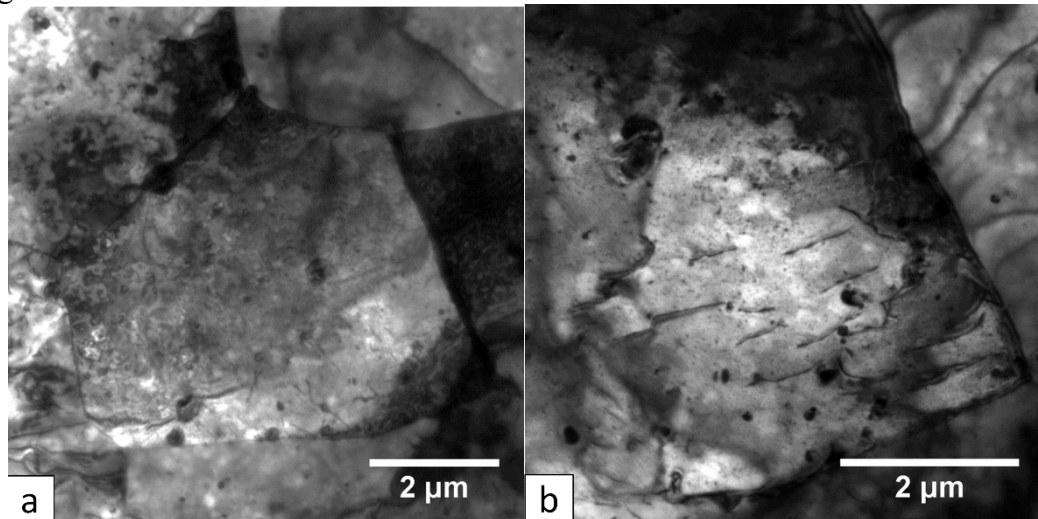
Figure 1.11. Representative TEM micrographs of the specimen deformed initially at 550 °C and 15.3 MPa for a strain of 1.1% and lastly at 550 °C and 10 MPa for a strain of 1.1% in regime I.

Regime I

Microstructural characterization

Figure 1.9 shows representative TEM micrographs of the specimen deformed in two test conditions in regime I: firstly at 550 °C and 15.3 MPa up to 1.1% strain followed by a change in stress to 10 MPa for another 1.1% strain. The microstructural

11

characteristics of the specimen deformed in regime I were observed to be quite akin to that of the unstrained specimen; the crept microstructure revealed no dislocation sub-boundaries or tangles and was estimated to possess a dislocation density of $(4.3 \pm 2.8) \times 10^{11}/m^2$ which is similar to the value obtained for the unstrained specimen. Neither the microstructure exhibited any slip bands as observed by Gollapudi et al in the viscous deformation regime of Ti-3Al-2.5V in compliance with the slip band model [35]. These observations suggest that the strain accumulated in the specimen deformed in the viscous creep regime perhaps resulted from the diffusion of vacancies/atoms but not involving any dislocation slip. Therefore, Coble creep was deemed as the rate controlling mechanism in regime I as pointed out by the stress exponent and activation energy.

Coble creep model

Further, the experimental creep rates in regime I were compared with the theoretical Coble creep model in order to verify its applicability to Zirclaoy-4 using the following equation [36],

$$\frac{\dot{\varepsilon}kT}{D_{gb}Eb} = (100 \pm 50)\left(\frac{b}{d}\right)^3\left(\frac{\sigma}{E}\right) \tag{1.5}$$

$$D_{gb} = D_{0gb}\exp\left(-\frac{Q_{gb}}{RT}\right), \tag{1.6}$$

where d is the average grain size (8.5 μm), D_{gb} is the diffusivity along the grain boundary in Zircaloy-4, D_{ogb} and Q_{gb} are the diffusivity coefficient and the activation energy for grain boundary self-diffusion, which assumed the values of $10^{-3}m^2/s$ and 188 kJ/mol respectively as determined for α-Zr from radioactive tracer data [23] and the rest are as described earlier. As shown in Figure 1.10, though the experimental results fall ~4 times higher than the theoretical predictions, it can be considered as a reasonable agreement between them further substantiating Coble creep-controlled deformation in regime I of Zircaloy-4 considering the fact that the constant in Eq. 5 for Coble creep mechanism was noted to be anywhere between 50-150 [27, 37].
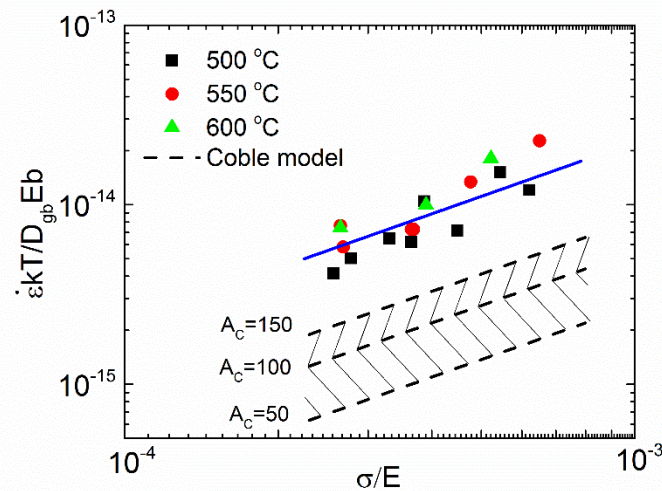

Figure 1.12. Comparison of the experimental results of regime I with the predictions by Coble creep model

12

The identification of Coble creep as the dominant mechanism for Zircaloy-4 at the low stress range falls in line with the creep behavior of α-Zr with small grain sizes (<50 μm) as reported by Bernstein et al [17] and Fiala and Čadek [17, 18]. However, on analyzing the creep data together from the investigations stated above, Ruano et al have argued in support of grain boundary sliding (GBS) controlled creep at low stresses in α-Zr by portraying a close agreement between the GBS model and the experimental results, albeit a stress exponent of 1 was obtained for the creep data, whereas GBS controlled creep requires n=2 [17, 18, 20, 38]. In fact, Ruano et al have suggested against the existence of diffusion creep-controlled deformation in both metals and ceramics [39]. In contrast to this, the application of GBS model to the creep data of Zircaloy-4 in this study can be negated based upon the two following observations. Firstly, TEM analyses of the deformed specimen reveal no signatures pertinent to GBS controlled creep, which can result in distinct dislocation pile-ups against grain boundaries as well as a high dislocation activity adjacent to grain boundaries in the deformation microstructure as noted by Gollapudi et al in the GBS regime of Ti-3Al-2.5V [35]. Secondly, there exists a good compliance of the experimental results to Coble creep model as depicted in Figure 1.10.
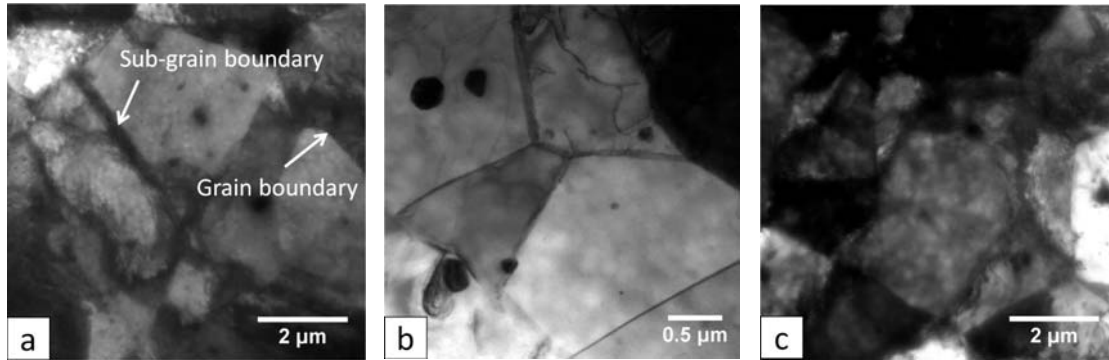
Figure 1.13. Representative TEM micrographs depicting sub-grains in the specimens deformed at a) 550 °C and 46.1 MPa (σ/E=8.08 × 10^{-4}), b) 600 °C and 54.8 MPa (σ/E=1.03 × 10^{-3}) and c) 500 °C and 78.5 MPa ($\sigma/E = 1.29 × 10^{-3}$) in regime II

Regime II

Microstructural characterization

The steady state deformation microstructures of the specimens deformed in regime II consisted of well-developed sub-grains bounded by dislocations within grains as shown in Figure 1.11. Inside the sub-grains, the dislocation density was evidently low. All the dislocations in Zircaloy-4 became invisible while imaging in two beam condition with $g = <0002>$ suggesting that the burgers vector of these dislocations to be of $\frac{a}{3} < 2\bar{1}\bar{1}0 >$ type according to the invisibility condition $g.b = 0$, where g is the reflecting vector. This observation remains consistent with the general agreement that the predominant slip system in zirconium and its alloys is prismatic slip of $\frac{a}{3} < 2\bar{1}\bar{1}0 > \{01\bar{1}0\}$ type on account of their low c/a ratio.

The dislocations present at the sub-grain boundaries were analyzed to assess their characters using higher magnification micrographs. It was revealed that two kinds of

13

dislocation morphologies were present in the sub-boundaries. Figure 1.12 shows one such kind of sub-boundary in which straight dislocations are stacked on each other. It can be seen from the trace analysis using the diffraction pattern that $g = [2\bar{1}\bar{1}0]$ is perpendicular to the plane on which the dislocation line vector lies demonstrating that these dislocations have pure edge character and thus the sub-boundaries formed by these dislocations are of pure tilt type.
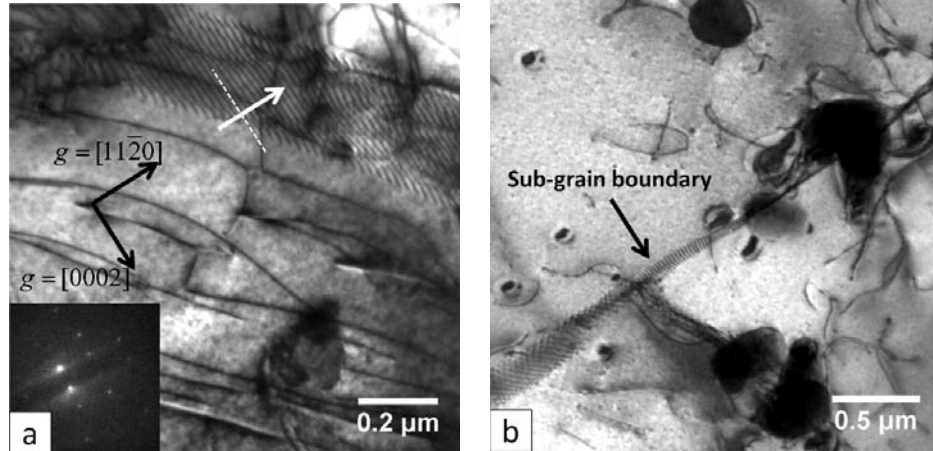
Figure 1.14. Sub-boundary consisting of edge dislocations in the specimens crept at a) 500 °C and 64.3 MPa and b) 500 °C and 78.5 MPa in regime II. The $[1\bar{1}00]$ diffraction pattern shows the orientation of the grain. The dashed line depicts the cut section of the plane on which the dislocation line vector lies, which is perpendicular to the <a> direction in the left image.
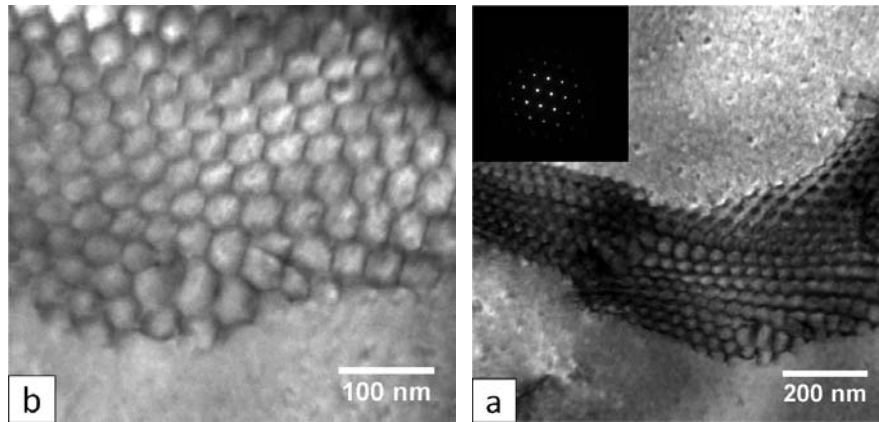
Figure 1.15. a) A TEM micrograph depicting dislocations forming hexagonal network on the plane normal to $[11\bar{2}3]$ crystallographic axis in the specimen deformed at 500 °C and 64.3 MPa. The inset shows the diffraction pattern of $[11\bar{2}3]$. b) A TEM micrograph at a higher magnification showing the dislocation network

Figure 1.13 exhibits another kind of sub-boundary that was observed in the bright field images recorded using the direct beam parallel to the $[11\bar{2}3]$ zone axis. It can be seen that the dislocations formed into a hexagonal network on the image plane. The burgers vectors of the dislocations forming this network were determined with the aid of tilting experiments and using the invisibility criterion.

14

Figure 1.16. (a-c) TEM images recorded in two-beam conditions using the *g* vectors mentioned on the image and their schematics depicting the invisible (blue) and the visible (red) dislocation lines of the hexagonal network of dislocations shown in Figure 1.13
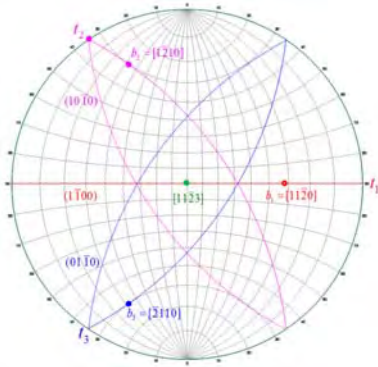
Figure 1.17.
The stereographic projection of the HCP structure with [$11\bar{2}3$] as the normal axis showing the angular relation between the Burgers vectors (b), the dislocation line vectors (t) and the slip planes of the network dislocations

Figure 1.14 shows a set of bright field images of the dislocation network recorded in two-beam condition with the *g* vectors [$1\bar{1}00$], [$10\bar{1}\bar{1}$] and [$01\bar{1}\bar{1}$] respectively. As can be seen, for each *g* vector, a pair of dislocation lines in each hexagonal loop of dislocations becomes invisible by satisfying the invisibility criterion. Since all the dislocations imaged in the two-beam condition with $g =< 0002 >$ vector become invisible, the burgers vectors of the invi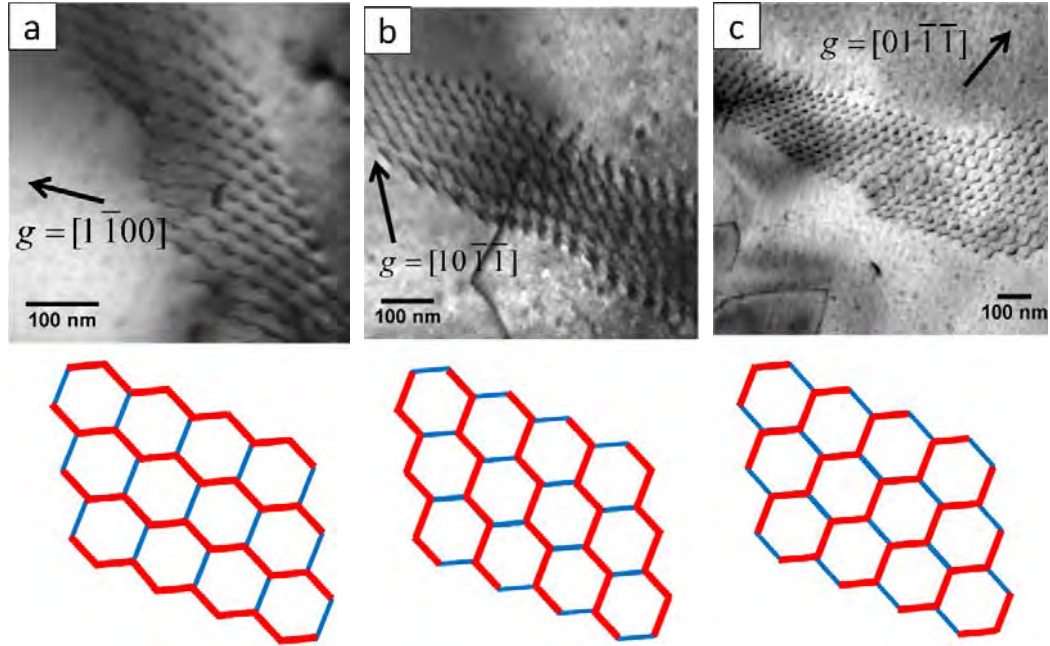sible dislocation lines in the two-beam images with the *g* vectors [$1\bar{1}00$], [$10\bar{1}\bar{1}$] and [$01\bar{1}\bar{1}$] are respectively calculated to be $\frac{a}{3}[11\bar{2}0]$, $\frac{a}{3}[1\bar{2}10]$ and $\frac{a}{3}[\bar{2}110]$. These dislocations can then be assumed to lie on the prism (slip) planes ($1\bar{1}00$), ($10\bar{1}0$) and ($01\bar{1}0$) respectively. Furthermore, the line vectors of these dislocations are nothing but the intersection of their slip planes with the plane normal to the [$11\bar{2}3$] axis on which the two dimensional dislocation networks spread. The stereographic projection with [$11\bar{2}3$] as normal axis was then utilized to calculate the angle between the burgers vector and the dislocation line vector, which was obtained to be 33° for all the dislocations (Figure 1.15). These dislocations in the network were therefore characterized as <a> type mixed dislocations.

15

Formation of this network comprising of mixed dislocations could be explained with a two-step process which is quite analogous to the formation of screw dislocation network in Zircaloy-4 as described in detail elsewhere [40]: Firstly, an interaction between two <a> type mixed dislocations gliding on their respective prism planes produces the third type of <a> type dislocation according to the following relation (Figure 1.16):

$$\frac{a}{3}[2\bar{1}\bar{1}0] + \frac{a}{3}[\bar{1}2\bar{1}0] = \frac{a}{3}[11\bar{2}0] \qquad (1.7)$$

Secondly, the network of dislocations formed by this reaction interrupts the glide of the upcoming dislocations on their slip planes. Further glide would be possible only when the network dislocations move out of the glide planes through a dynamic recovery process. Owing to the mixed nature of these dislocations, they would possibly recover by dislocation climb [31] on the plane that is normal to the $<11\bar{2}3>$ axis as observed in this study. A representative TEM micrograph serving as an evidence for the process described above is given in Figure 1.16c. It shows a couple dislocations, noted as A and B, interacting with an array of parallel dislocations, noted as C. While the dislocation 'B' appears to have just interacted with 'C' dislocations, the dislocation 'A' has already reacted with 'C' dislocations to form a network of dislocations, which could possibly be in the course of climbing down to get annihilated with the opposite dislocations.
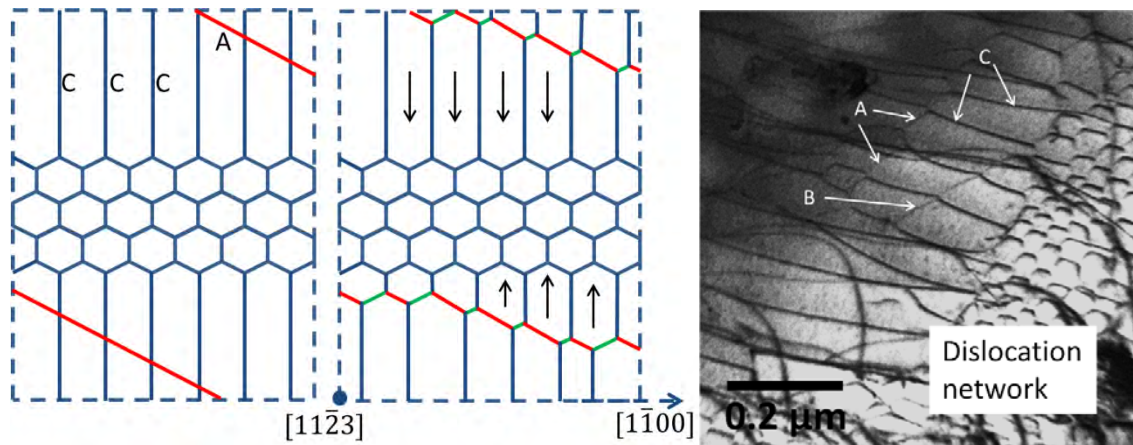
Figure 1.18. (a-b) Schematic diagram depicting the formation of hexagonal network dislocations. Each type of <a> dislocations is marked by different colors. (c) TEM micrograph showing the interaction of dislocations 'A' and 'B' with 'C' while forming the network possibly aided by dislocation climb in the specimen crept at 78.5 MPa and 550 °C.

The sub-boundaries consisting of pure edge dislocations as well as hexagonal network of mixed dislocations revealed by the TEM analyses of the crept specimens indicate that the steady state creep rate is controlled by dislocation climb mechanism in regime II [33, 41].

Sub-grain size versus stress

The average sub-grain size (δ) in several materials where creep is controlled by the dislocation climb has been found to have a dependency on the normalized shear stress (τ/G) through a relationship of the form [37],

$$\frac{\delta}{b} = K \left(\frac{\tau}{G}\right)^{-r} \qquad (1.8)$$

16

where K and r are constants whose values were empirically estimated to be 10-20 and 1 respectively for several materials [42]. Thus, the sub-grain size exhibits an inverse linear relationship with the applied stress when the creep is controlled by dislocation climb. In our study, the areas of the sub-grains were measured from the TEM micrographs of the specimens deformed at the stresses of 46.1 MPa, 54.8 MPa and 78.5 MPa respectively at 550 °C, 600 °C and 500 °C and converted into the diameter by assuming the area to be circular. As many as 25-30 sub-grains were measured for each applied stress and the average sub-grain sizes with their standard deviations are given in Table 1.3. Further, the sub-grain sizes are presented as a logarithmical plot between normalized sub-grain size versus normalized shear stress in Figure 1.17. The normal stress (σ) and the shear stress (τ) are related as $\tau = \sigma/M$, where M is the Taylor factor and taken to be 4 for Zircaloy-4 [43]. From this plot, the values of K and r were found to be 15 and 0.9 respectively showing a good agreement with the empirical relation that has been found to be applicable for the dislocation climb mechanism. Moreover, the results show that the dependency of the sub-grain size on the normalized stress still holds regardless of the different test temperatures.

Table 1.3.
Sub-grain sizes measured from the specimens deformed in regime II.

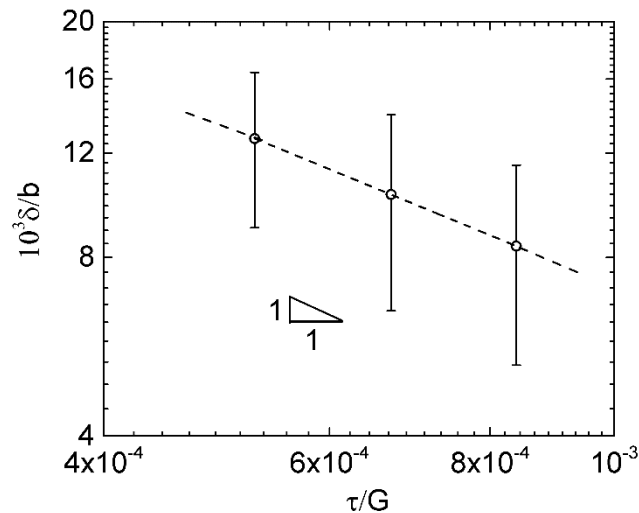| Stress (σ), MPa	Shear stress (τ), MPa	Test temperature, °C	τ/G	Sub-grain Size (δ), µm	$10^{-3}\delta/b$
46.1	11.5	550	5.25×10^{-4}	4.1 ± 1.2	12.7 ± 3.7
54.8	13.7	600	6.70×10^{-4}	3.3 ± 1.2	10.2 ± 3.7
78.5	19.6	500	8.39×10^{-4}	2.7 ± 1.0	8.4 ± 3.1

Figure 1.19. Normalized sub-grain size versus normalized shear stress

17

The Weertman model

The sub-grain boundaries comprised of dislocations observed in the TEM analyses of the crept specimens in regime II are congruous with the assumptions of the dislocation climb model derived by Weertman [41]. According to this model, the dislocations generated at various dislocation sources under the application of stress glide on their slip plane until they are blocked by the dislocations from other sources, thus forming dislocation dipoles. The dipoles are further annihilated by the dislocations climbing toward each other through diffusion of vacancies which ultimately create sub-boundaries within grains. The glide and climb of dislocations are sequential processes and hence the slower process, which is the later one namely climb, controls the rate of deformation. However, the macroscopic strain itself is primarily the resultant of the dislocation glide. Weertman derived the following equation for predicting the creep rate in materials involving dislocation climb [41],

$$\dot{\varepsilon} = \alpha \left(\frac{D_l}{b^{3.5} M^{0.5}} \right) \left(\frac{\sigma}{G} \right)^{4.5} \left(\frac{G\Omega}{kT} \right) \tag{1.9}$$

where M is the number of active dislocation sources in a unit volume, G is the shear modulus, Ω is the atomic volume, α is a constant whose values are in the range 0.015 $< \alpha <$0.33, $D_l = D_0 \exp \left(-\frac{Q_l}{RT} \right)$ and the rest are as described before. In order to derive the stress exponent of 4.5 in the equation, which has been observed in the 'Class M' materials whose deformation is controlled by dislocation climb, Weertman imposed an adhoc assumption of a constant dislocation source density (M) being operative independent of the applied stress. Disregarding such assumption would give a stress exponent of 3. Weertman defended this assumption by arguing that the number of active dislocation sources would be reduced continuously during the course of deformation through the inactivation of the sources belonging to smaller pile up of dislocations by neighboring larger pile up of dislocations [41]. As a result, the number of active dislocation sources would eventually become the smallest possible as that in well-annealed materials regardless of the deformation stress. The value of M can then be obtained using the following equation derived geometrically [44],

$$M = 0.27 \rho^{1.5} \tag{1.10}$$

where ρ is the dislocation density in fully annealed material. Assigning the value of dislocation density determined in the unstrained Zircaloy-4 ($4.3 \times 10^{11}/m^2$) for ρ in equation (1.10), the value of 'M' is calculated to be $7.6 \times 10^{16}/m^3$, which lies within the range of M values calculated by Weertman, $3.6 \times 10^{14} - 1.8 \times 10^{17}/m^3$. Substituting $M = 7.6 \times 10^{16}/m^3$, $\alpha \sim 0.1$, $\Omega = 0.7b^3$ and $G = E/2.6$ renders equation (1.10) in the form of,

$$\frac{\dot{\varepsilon} kT}{D_l E b} = 1.22 \times 10^6 \left(\frac{\sigma}{E} \right)^{4.5} \tag{1.11}$$

Figure 1.18 compares the normalized creep rates in regime II from the experiments with the ones predicted by equation (1.11) based upon the Weertman model. The lattice diffusivity coefficient (D_0) and the lattice diffusion activation energy (Q_l) of $5 \times 10^{-4} m^2/s$ and $259 \, kJ/mol$ respectively were determined using radioactive tracers in Zr-1.3% Sn alloy [24]. A good agreement between the experimental results with the model predictions further substantiates dislocation climb-controlled creep to be operative in regime II of Zircaloy-4.
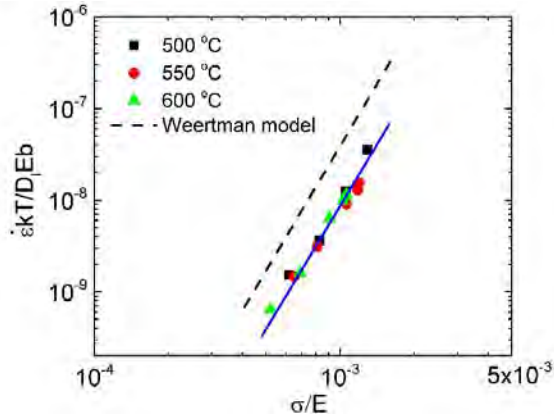
18

Figure 1.20.
Comparison of the experimental results of regime II with the predictions by the Weertman model.

1.3.3 Creep mechanism in regime IV

The stress exponent decreased from a value of ~11 at 500°C to ~9.3 at higher temperatures of 550°C and 600°C in regime IV. The activation energies were calculated using Arrhenius plots as given in Figure 1.19 and plotted as a function of the modulus-compensated stress in Figure 1.20. The errors in the activation energy values were estimated from the standard errors in the slope parameter of the linear fits in Figure 1.19.
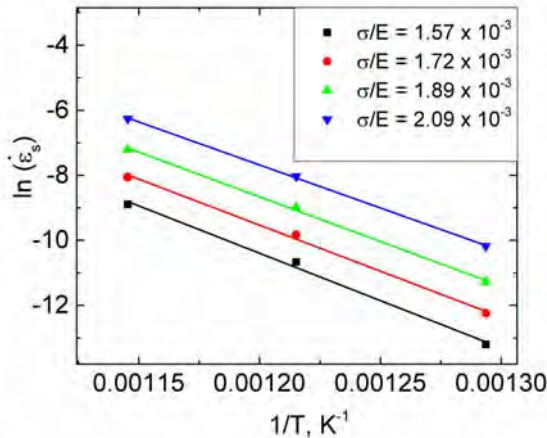
Figure 1.19. Arrhenius plots at various applied stresses
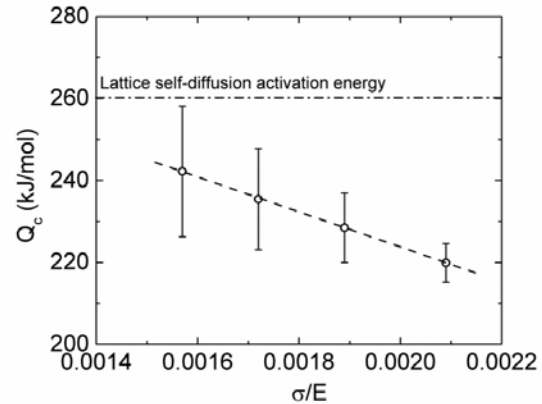
Figure 1.20. Activation energy for creep as a function of the applied stress

The activation energy for the creep (Q_C) deformation was found to be slightly decreasing as the applied stress increases: 242±16 kJ/mol at a stress of $1.57 \times 10^{-3}E$ to 220±5 kJ/mol at a stress of $2.1 \times 10^{-3}E$. The activation energy for the lattice self-diffusion (Q_{SD}) of Zr in Zr-1.3%Sn alloy was estimated to be 260 kJ/mol [24]. While Q_C at lower stresses is comparable to Q_{SD}, it, however, deviates from Q_{SD} to a lower value at higher stresses exhibiting a stress-dependent activation energy. Therefore, the rate controlling mechanism under the test conditions should account for this stress-dependence of the activation energy obtained from the experimental data. However, it is established that the activation energy for the lattice diffusion-controlled recovery processes such as dislocation climb or glide of jogged screw dislocations is independent of the applied stress [33, 45, 46]. In view of this, considering these processes as the rate controlling mechanisms under the present test conditions for Zircaloy-4 becomes unviable. On the other hand, Raj et al [47] showed that a mechanistic transition from the high temperature climb to the low

19

temperature climb could lead to a regime in which the activation energy would linearly decrease with the applied stress. However, such a regime would possess a stress exponent of around 7, which is clearly not the case in our data. Some thermally activated mechanisms such as recovery by cross slip of screw dislocations [48, 49] or glide controlled creep [33, 50], in which the dislocations overcome the obstacles by stress assistance exhibit a stress dependent activation energy and can be the rate controlling process for Zircaloy-4 in the testing conditions.

Microstructural observations

TEM micrographs of the annealed Zircaloy-4 revealed fully recrystallized grains with a low dislocation density characteristic of an annealed microstructure as shown in Figure 1.21. The few dislocations were observed to be long and fairly straight without forming any sort of tangles or sub-boundaries.

(a)   (b)
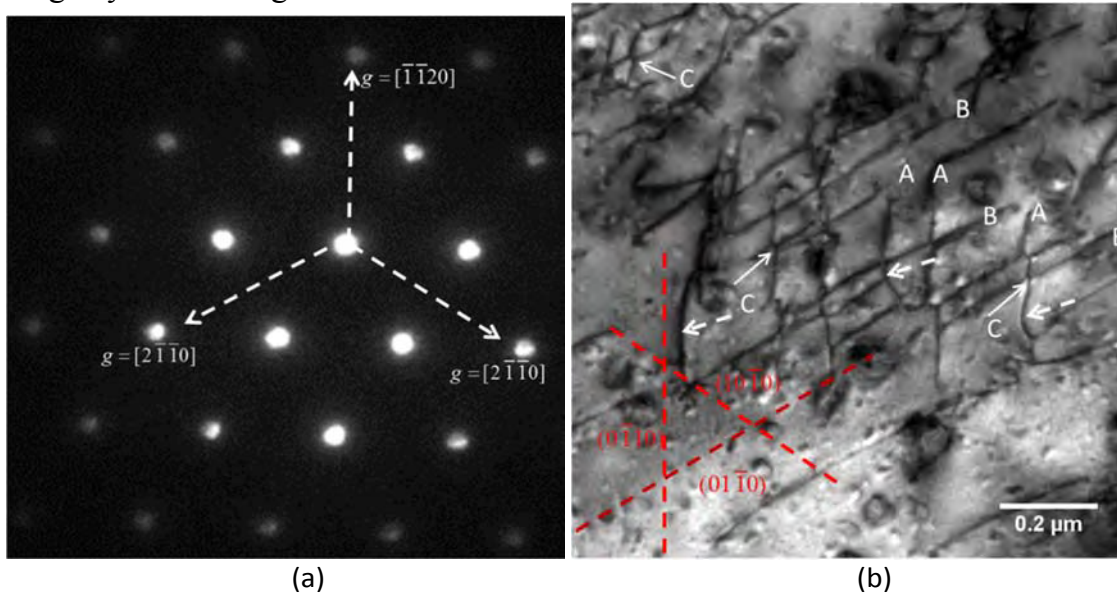
Figure1.21. TEM images of the specimen crept at 550 °C and 79 MPa.
(a) [0001] Zone axis pattern showing the crystal orientation of the grain;
the dashed lines point out the directions of the $g = < 2\bar{1}\bar{1}0 >$ vectors.
(b) A bright field image showing two families of screw dislocations, noted as A and B, interacting and producing a third family of screw dislocations, noted as C, developing a dislocation network; the dashed lines indicate the traces of $\{10\bar{1}0\}$ planes. The dashed arrows point at the dislocations with a curvature on the basal plane suggesting their slip on the plane.

Representative TEM micrographs of the specimens creep tested in the range of temperature and stress conditions used here are given in Figure 1.21 and 1.22. The microstructures consisted of dense hexagonal networks of dislocations on the basal planes, which were connected to the grain boundary, as shown in Figs. 9 and 10. In addition to that, edge dislocation sub-boundaries, though not fully developed, were observed sporadically. The dislocation network became invisible while imaging in a two beam condition with the g = <0002> vector, indicating that the network consists of only <a> type dislocations according to the $g.b=0$ invisibility criterion. Therefore the Burgers vector of these dislocations is $\frac{a}{3} < 2\bar{1}\bar{1}0 >$, where *a* is the lattice constant. Figure 1.21

20

shows observably an initial stage of dislocation network formation. It can be seen that the long dislocation segments are clearly parallel to the traces of the $g = < 2\bar{1}\bar{1}0 >$ vectors on the basal plane revealing that the dislocations are pure screw dislocations predominantly lying on the prism planes, $\{01\bar{1}0\}$. Our analysis is in line with the general observation that $< 2\bar{1}\bar{1}0 > \{01\bar{1}0\}$ is the dominant slip system in Zircaloy-4 owing to its low c/a ratio [51, 52].

Figure1.22. A bright field TEM image of the specimen crept at 550 °C and 79 MPa depicting a dense screw dislocation network formed on the basal planes. The network is connected to the grain boundary on the left.

Formation of dislocation network

Our TEM analysis indicates that the formation of dense screw dislocation network is the result of the dislocations interacting on the basal planes and, followed by the occurrence of a dynamic recovery process of the screw dislocations, possibly through cross slip. As can be seen in Figure 1.21, dislocations with two different <a> Burgers vectors, which are noted as A and B, lying on two prism planes intersect each other on the basal plane and produce a third type of dislocations with a different <a> type Burgers vector on the third prism plane, which is noted as C. Such a dislocation reaction is energetically favorable according to the well-known Frank's rule since the total line energy (proportional to b^2) can be proportionally reduced from $2a^2$ to a^2 by the reaction,

$$\frac{a}{3} < 2\bar{1}\bar{1}0 > + \frac{a}{3} < \bar{1}2\bar{1}0 > = \frac{a}{3} < 11\bar{2}0 > \qquad (1.12)$$

This reaction could occur from the dislocations gliding on several parallel slip planes leading to the formation of a two dimensional dislocation network. A schematic of the process is shown in Figure 1.24. Such screw dislocation networks can be characterized as pure twist boundaries.

The dislocation reactions and the subsequent formation of dislocation networks can act as obstacles for the gliding dislocations on the prism planes. Further glide of the

dislocations could only be possible when the dislocations involved in the formation of the network move out of their original slip plane assisted by a recovery process. Since the dislocations possess predominantly the screw character, they necessitate cross-slipping along the basal plane to recover and can get annihilated by combining with dislocations with opposite Burgers vectors. The screw dislocations forming the network are observed to form curvatures on the basal plane in Figure 1.21 and 1.22, indicating that the dislocations are cross-slipping on the basal planes.
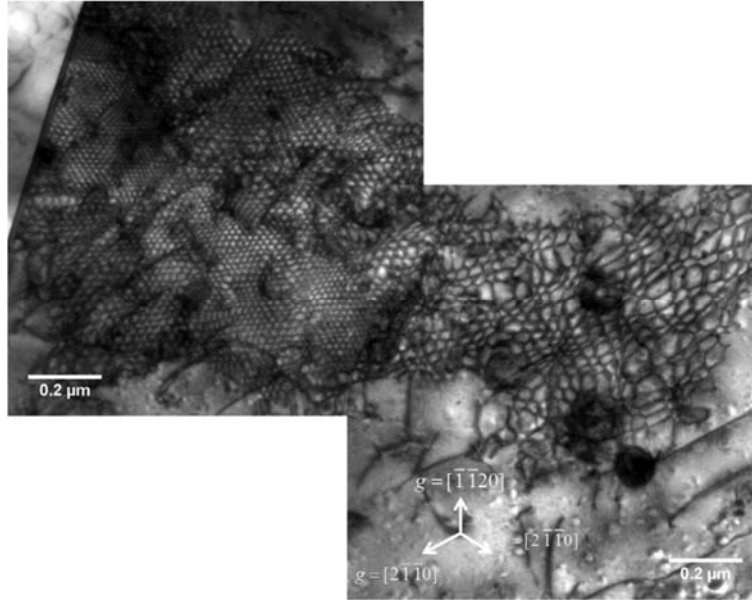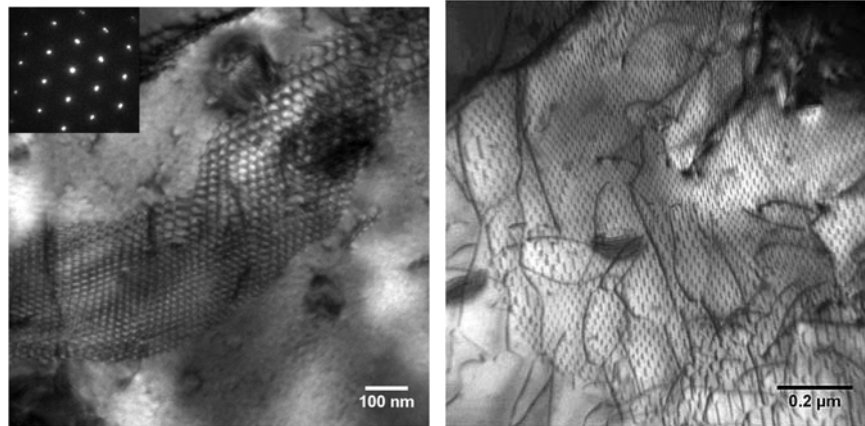

Figure 1.23. Bright field TEM images of the specimen crept at 550 °C and 117 MPa showing a dense screw dislocation network formed on the basal planes. The inset shows the [0001] zone axis pattern indicating the orientation of the grain. In image on the right, note that one set of dislocations becomes invisible because they satisfy the invisibility criterion.
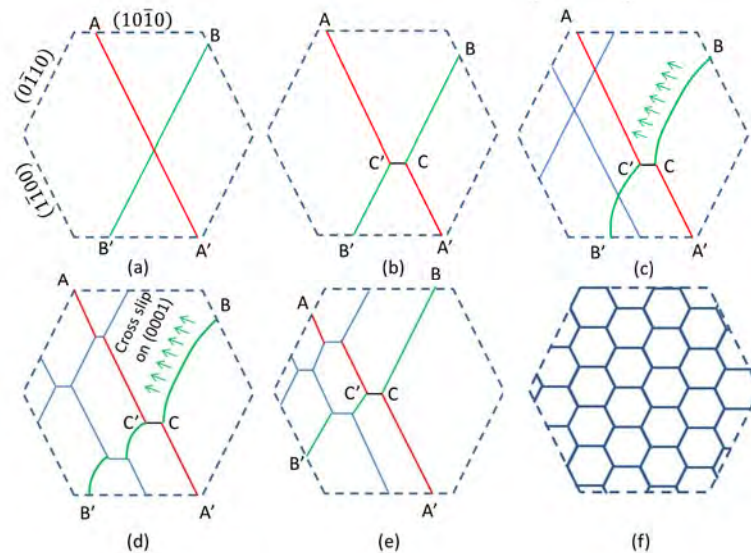
Figure 1.24. A Schematic representation of the sequence of the screw dislocation network formation on the basal planes: (a) & (b) Interaction of two screw dislocations, AA' and BB', gliding on their respective prism planes produces a third screw dislocation, CC'; (c) BC and BC' screw dislocations cross slip on the basal plane; (d-f) More interactions between dislocations and cross-slip leading to the formation of hexagonal dislocation network.

Ecob et al [30] and Armas et al [53, 54] observed similar dislocation networks in Zircaloy-4 deformed at high temperatures (700-800 °C). Further, Ecob et al [53] argued

22

that the dislocations in the network possibly moved out of the slip planes by diffusion assisted climb of the edge character originated from the curvature of the screw dislocations. However, it is more plausible that the screw dislocations change their glide planes via the cross slip process as noted in several investigations on different materials [49]. Moreover, the absence of well-developed sub-grains formed by the edge dislocations and the stress-dependent activation energy suggest against the dislocation climb as the rate-controlling process in the range of stresses and temperatures investigated in this study. The possibility of the glide of jogged screw dislocations being the rate-controlling mechanism is not considered owing to a non-significant presence of jogged screw dislocations in the microstructure as well as the stress dependent activation energy. At high temperatures, the easy flow of vacancies could facilitate the glide of the jogged portion of the screw dislocations making it an insignificant process, which is also substantiated by the TEM observations of screw dislocations forming networks. Moon et al [16] reported a similar observation in the crept Zircaloy-4 specimens at the temperatures above 500°C. An extensive occurrence of screw dislocation network on the basal planes and the stress-dependent activation energy, which is suggestive of a thermally assisted mechanism to be controlling the creep deformation, lead us to consider the cross slip as a rate controlling mechanism.
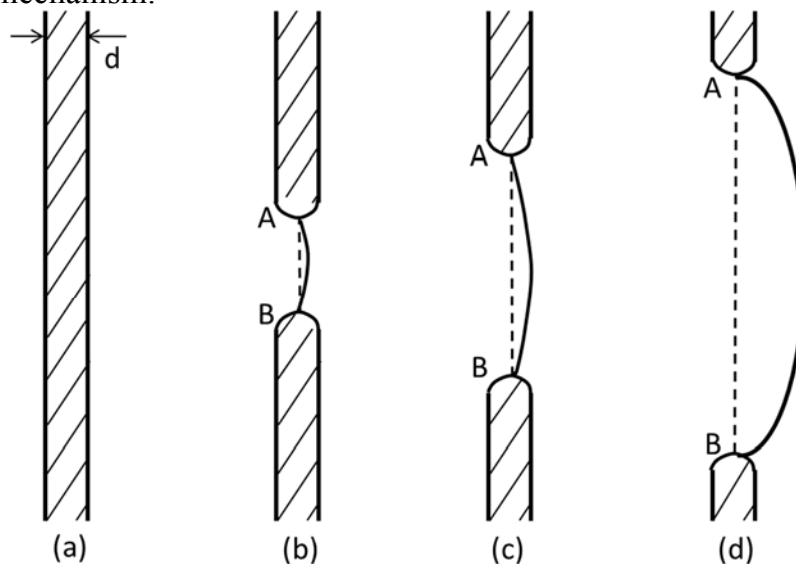
Figure 1.25. Cross slip of a screw dislocation according to Friedel's model:
(a) screw dislocation partials with a spacing of *d* on the glide plane; (b) constriction of the partials at points A and B and recombination of the partials between A and B; (c) and (d) the recombined part of the dislocation expands on the cross slip plane by the applied stress [20].

Cross slip as the rate controlling mechanism

Cross slip has been proposed as the rate controlling mechanism in several FCC [55, 56] and HCP metals such as Magnesium and Zinc [57, 58]. Very few studies, however, treated the cross slip of screw dislocations as a viable mechanism for deformation in zirconium in high temperature quasi-static tensile testing [59, 60]. The models for cross slip mechanism were developed by Friedel [48] and Poirier [49]. Friedel considered a case of a screw dislocation cross-slipping from the basal plane to the prismatic plane in

23

HCP materials. He argued that the partials of the screw dislocation on the glide plane must initiate constriction at a point and recombine over a length of AB to be able expand onto the new plane as depicted in Figure 1.24. Consequently, the activation energy for cross-slip (U), as derived by Friedel, encompassed the energy necessary for the constriction and the recombination of the partials. The activation energy for cross slip was obtained in the form of [48, 57, 58],

$$U = U_C + const\ \tau^{-1} = U_c + \frac{2^{5/2} R^{3/2} \Gamma^{1/2}}{3b\tau}$$
(1.13)

where U_c is the energy of formation of a constriction, R is the recombination energy per unit length, Γ is the energy of an undissociated dislocation per unit length and τ is the shear stress on the prism plane.

For the cross-slip controlled deformation, the shear strain rate is given by [58],

$$\dot{\gamma} = \frac{\lambda A b^4 v_0 \tau^2}{8R\Gamma} \exp\left(-\frac{U_C}{kT}\right) \exp\left(-\frac{2^{5/2} R^{3/2} \Gamma^{1/2}}{3b\tau kT}\right)$$
(1.14)

where λ is the total length of screw dislocations on the cross-slip plane per unit volume and A is the average area swept out per process.
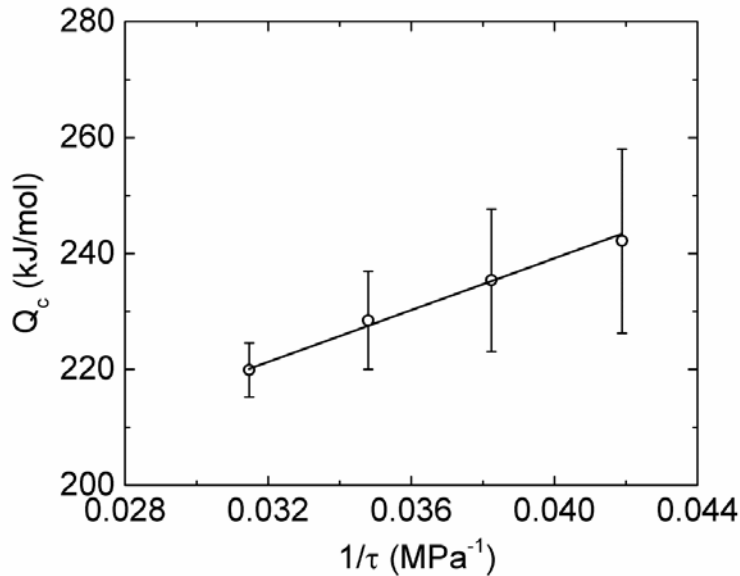
Figure 1.26. Activation energy for creep as a function of the inverse of the shear stress

Poirier [49] derived a constitutive equation for the cross-slip controlled deformation which is essentially similar to the equation by Friedel [48],

$$\dot{\varepsilon} = \dot{\varepsilon}_{0,CS} \left(\frac{\sigma}{\mu}\right)^2 exp - \left(\frac{Q_{CS}(\sigma,\gamma_F)}{kT}\right)$$
(1.15)

where $\dot{\varepsilon}_{0,CS}$ is a constant, Q_{CS} is the activation energy for cross slip, which is a function of the applied stress (σ) and the stacking fault energy (γ_F) and μ is the shear modulus. Though Friedel developed the model considering screw dislocations cross slipping from the basal planes to the prism planes, it should be applied to the prism to basal cross slip in Zr as well while considering the symmetrical nature of such processes [59].

24

According to equation (1.13), a plot between U and $1/\tau$ would be linear with the intercept on the energy coordinate and the slope to be equivalent to the constriction energy and the second term in U consisting of the recombination energy respectively when the deformation was controlled by the cross slip mechanism. In Figure 1.26, the activation energy for Zircaloy-4 is plotted against the inverse of the shear stress. It can be seen that the data can well be fitted with the linear equation,

$$U = (150 \pm 4) + \left(\frac{2236 \pm 124}{\tau}\right) kJ/mol \qquad (1.16)$$

Comparing it to equation (1.13), the constriction energy U_c comes out to be 150±4 kJ/mol. The amount of energy that is required for constricting a pair of partial screw dislocations is primarily a function of the separation between the partials, which has an inverse dependence on the stacking fault energy. The constriction energy can be equated to the separation between the partial dislocations using the Stroh's equation [48, 61] as,

$$U_C = \frac{\mu b^2 d}{30}\left(ln\frac{d}{b}\right)^{1/2} \qquad (1.17)$$

where, d is the separation between the partials. Substituting $U_C = 150\ kJ/mol$ obtained from the creep data, $b = 3.23\ X\ 10^{-10}m$ and μ for Zircaloy-4 at 500°C = 23.4 GPa, the value of d is calculated to be $22.0\ X\ 10^{-10}\ m$, which is equivalent to $6.8b$. Sastry et al [62] estimated the separation between the partial dislocations of <a> type screw dislocations on the prism planes using X-Ray diffraction method and obtained the values of 2.6b, 5.4b, 7.4b and 9.8b for zirconium with 0%, 0.7%, 3% and 5% of tin respectively while Zircaloy-4 tested in our study has 1.62% of tin. The results of the separation between partials of the screw dislocations that were estimated by Sastry et al [62] and that derived in this study exhibited good agreement as shown in Figure 1.27. Moreover, the constriction energy is in agreement with the earlier estimate of 142 kJ/mol for Zirconium single crystals through tensile tests by Akhtar [59] and it is also comparable to the values of 134 kJ/mol, 147 kJ/mol reported for magnesium by Vagarali et al [57] and Flynn et al [58], respectively, and of 159 kJ/mol obtained for zinc by Gilman et al [63].
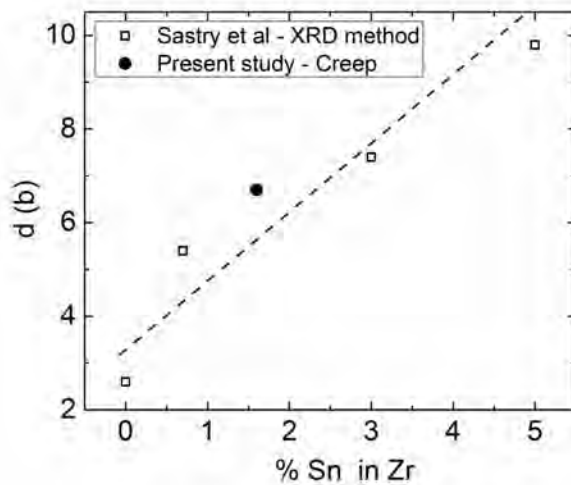
Figure 1.27.
Separation between the partial dislocations as a function of the percentage of Sn in Zr

25

Activation volume of deformation in regime IV

The activation volume of the dominant deformation process occurring at various flow stresses in the temperature range of 500 – 600 °C was estimated from the stress relaxation experiments, which were conducted using an Instron universal tester. A three-zone furnace similar to the one used for the creep tests was employed for heating the specimen. A K-type thermocouple was attached to the specimen for accurate test temperature measurement. The stress relaxation experiment consisted of deforming the specimen plastically at a nominal strain rate of $10^{-3} s^{-1}$, arresting the crosshead movement at a flow stress and recording the stress drop over about 300s. After 300s of stress relaxation, the specimen was again deformed to a higher flow stress and allowed to relax as shown in Figure 1.28a. The activation volume as a function of flow stress was calculated by fitting the plots of stress drop ($\Delta\sigma$) versus time (t) as shown in Figure 1.28b [64, 65],

$$-\Delta\sigma = \frac{MkT}{V^*}\ln\left(1 + \frac{t_0}{t}\right),$$ (1.18)

where M is the Taylor factor which relates the normal stress (σ) to the shear stress (τ) as $\tau = \sigma/M$ and M is taken to be 4 for Zircaloy-4 [43]; it is interesting to note that M for many materials is usually considered to be 2 and this higher value seems to stem from the commonly observed crystallographic textures of Zircaloys [52]. In equation (1.18), V^* is the apparent activation volume for the thermally activated process and t_0 is the time constant. The true activation volume (V), as derived by Vagarali et al [57], can be estimated from the apparent activation volume as follows,

$$V = V^* - \frac{2kT}{\tau}.$$ (1.19)

The variance in the yield strength of Zircloy-4 with temperature in the range of 500 °C – 600 °C was obtained from the initial loading in the stress relaxation tests.

(a)   (b)
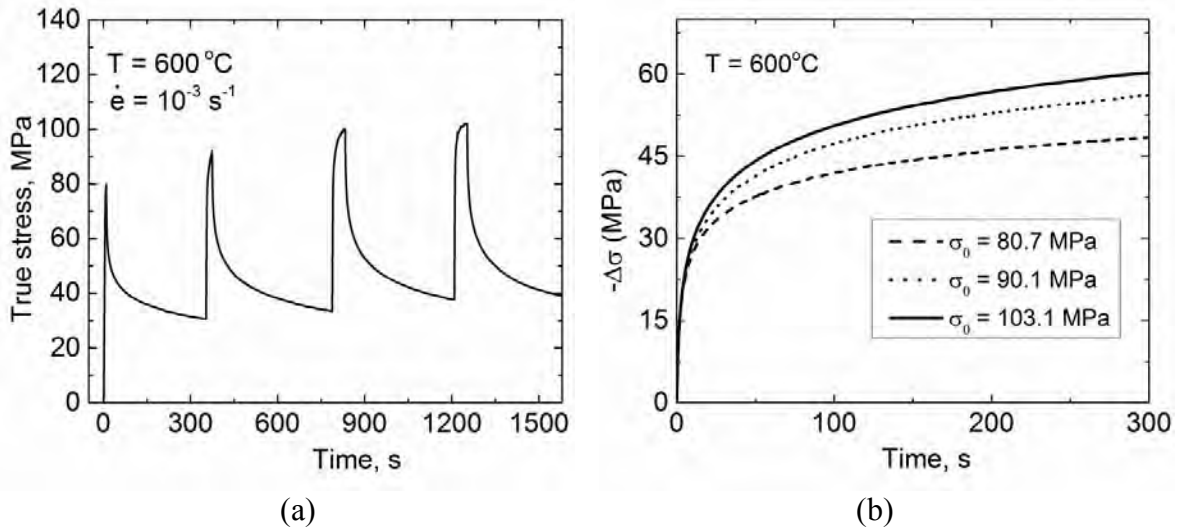
Figure 1.28. True stress versus time plot for the stress relaxation experiment conducted at 600°C (a) and Change in true stress versus time for various initial stresses (b)

26

Figure 1.29 depicts the true activation volume derived from the stress relaxation tests as a function of the flow stress in the temperature range of 500-600 °C. The true activation volume, which spreads in the range of $70b^3$-$190b^3$, shows an inverse dependency on the stress and it, however, remains quite independent of the test temperature. The trend of change in the activation volume values with the stress and the temperature for Zircaloy-4 is consistent with that reported for many materials [66]. The decrease in the activation volume with stress suggests that a stress-assisted thermally activated mechanism like cross slip is the dominant deformation process at the test conditions. The true activation volume values in the range of $70b^3$-$190b^3$ are in fairly good agreement with a cross-slip process [56, 64].
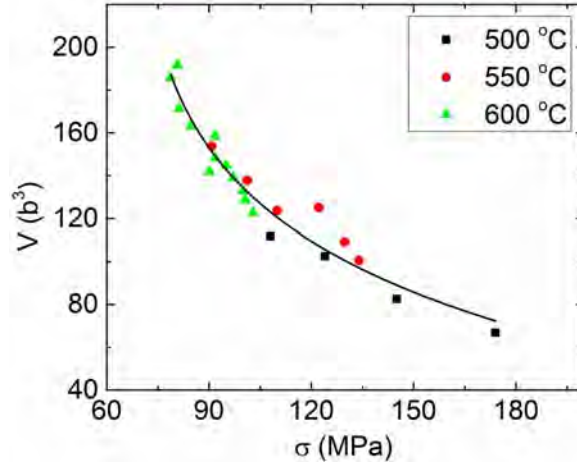
Figure 1.29. True activation volume versus stress at various temperatures.
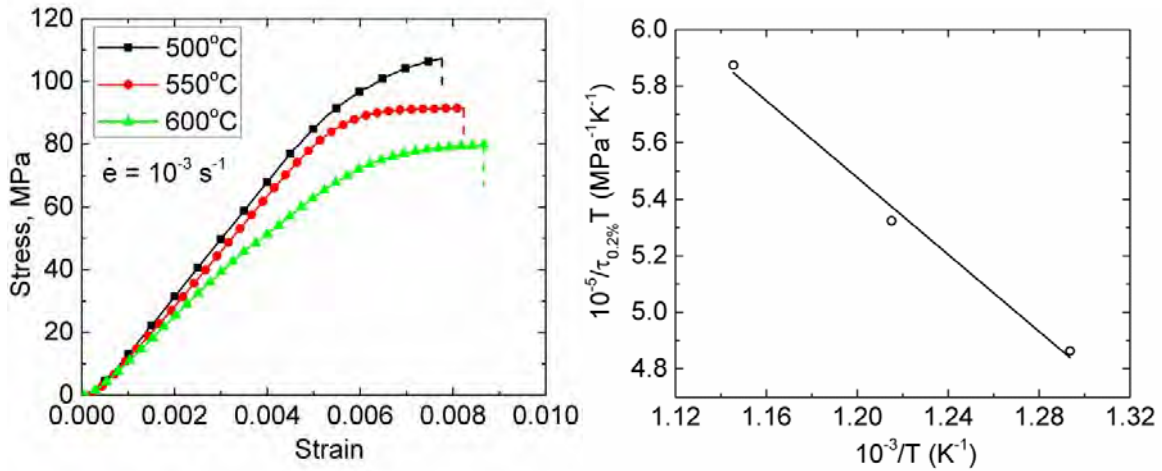
Figure 1.30. Loading portion the stress-strain curves from the relaxation tests (left) and $1/\tau T$ versus $1/T$ plot (right) where τ is the shear stress at the 0.2% yield point

Temperature dependence of the yield strength

Rearranging the rate equation (1.14) for the cross slip mechanism gives,

$$\frac{1}{\tau T} = \frac{3bk}{2^{5/2}R^{3/2}\Gamma^{1/2}} \ln\frac{\lambda Ab^4 v_0}{8R\Gamma\dot{\gamma}} + \frac{3bk \ln\tau}{2^{5/2}R^{3/2}\Gamma^{1/2}} - \frac{3bU_C}{2^{5/2}R^{3/2}\Gamma^{1/2}T} \tag{1.20}$$

27

At a constant-rate deformation, the first term on the right hand side of the equation becomes constant and the second term only varies modestly with respect to the applied stress. Therefore, $1/\tau T$ should decrease almost linearly with $1/T$. The 0.2% yield strength obtained from the tensile tests in the temperature range 500-600 °C, as shown in Figure 1.30, are plotted as $1/\tau T$ versus $1/T$ and it shows a linearly decreasing trend, which is in consensus with the prediction of the cross-slip rate equation. We note from the slope that,

$$\frac{3bU_C}{2^{5/2}R^{3/2}\Gamma^{1/2}} = (6.8 \pm 0.6) X 10^{-2} \, MPa^{-1}$$
(1.21)

or

$$\frac{U_C}{R^{3/2}\Gamma^{1/2}} = 397 \pm 35 \, m/N \tag{1.22}$$

The error in this value was obtained from the standard error in the slope parameter of the linear fit in Figure 1.30b.

On the other hand, the effect of change in strain rate on the stress for the mechanism of cross slip can be computed by differentiating the rate equation [58],

$$\beta = \frac{\partial ln\dot{\gamma}}{\partial \tau} = \frac{2}{\tau} + \frac{2^{5/2}R^{3/2}\Gamma^{1/2}}{3bkT\tau^2} \tag{1.23}$$

Or

$$R^{3/2}\Gamma^{1/2} = \frac{3bkT\tau^2\beta}{2^{5/2}} - \frac{3bkT\tau}{2^{3/2}}$$
(1.24)

The value of β can then be calculated from the activation volume data at various stresses as,

$$\beta = \frac{\partial ln\dot{\gamma}}{\partial \tau} = \frac{V^*}{kT}$$
(1.25)

Substituting the values of β and τ at the yield strength obtained from the stress relaxation tests respectively at various temperatures in equation (1.24) gives an average value of,

$$R^{3/2}\Gamma^{1/2} = (4.6 \pm 0.3) X \, 10^{-22} \, J^2/m^2$$

Table 1.4.

Parameters used in the calculation of $R^{\frac{3}{2}}\Gamma^{\frac{1}{2}}$.
Note that the errors in the activation volume values are the 95% prediction intervals of the power law fit in the plot between the apparent activation volume and the stress.

$T, °C$	$\sigma_{0.2\%}, MPa$	$\tau_{0.2\%}, MPa$	V^*, b^3	$R^{\frac{3}{2}}X10^{-22}, J^2 m^{-2}$
500	106.4	26.6	150 ± 18	5.2 ± 0.7
550	91.3	22.8	179 ± 18	4.5 ± 0.5
600	78.0	19.5	226 ± 21	4.2 ± 0.5

28

The parameters used in computing the value of $R^{3/2}\Gamma^{1/2}$ are given in Table 1.4. Applying this value in equation (1.22), the constriction energy is calculated to be 110±10 kJ/mol while the constriction energy is calculated to be 150±4 kJ/mol from the creep data. Further, substituting the value of $R^{3/2}\Gamma^{1/2}$ and τ value at the yield stress at 500 °C in the second term in the activation energy (U) equation (1.13) yields,

$$\frac{2^{5/2}R^{3/2}\Gamma^{1/2}}{3b\tau} = (1.17 \pm 0.08) \, X \, 10^{-25} \, MPa \, m^3 = 71 \pm 5 \, kJ/\, mol$$

Similarly, from the creep data, the value of the second term in U at the yield stress at 500 °C is estimated to be 84±5 kJ/mol from equation . Both the constriction energy value and the second term in U consisting of the recombination energy calculated from the tensile and relaxation tests are comparable with the values obtained from the creep tests.

A reasonable compliance of the creep and tensile data of Zircaloy-4 at high stresses with Friedel's cross-slip model for HCP materials suggests that the cross-slip of screw dislocations, as a recovery process, controls the creep rate of Zircaloy-4 and, possibly, of other zirconium alloys. This observation is also substantiated by our TEM analysis, which revealed an extensive prism slip with cross-slip on basal planes by screw dislocations forming networks. Poirier [49] postulated that climb of edge dislocations and cross slip of screw dislocations, should be occurring as the recovery mechanisms in parallel to produce the strain in materials. He further argued that cross-slip becomes dominant especially at high stresses at a given temperature in materials for which the activation energy for the cross-slip is less than that of the self diffusion. The creep data of Zircaloy-4 seem to follow a similar trend with cross-slip dominating at high stresses and diffusion controlled mechanisms such as dislocation climb or non-conservative glide of jogs on screw dislocations dominating at the intermediate stress levels as reported in several investigations [15, 16].

1.3.4 Creep mechanisms in regime III

With stress exponents ranging 9.5-18 and creep activation energy of 302 kJ/mol which is slightly higher than the activation energy for self-diffusion, regime III spreads over a narrow stress range of 10-15 MPa. The deformation microstructures revealed the presence of sub-boundaries consisting of edge dislocations as well as screw dislocations (Figure 1.31). Though the microstructural evidences depict climb of edge dislocations and cross-slip of screw dislocations occurring, the rate-controlling mechanism could not be singled out based on the available data. Further research in regime III is warranted to arrive at a reasonable conclusion on the rate-controlling mechanism.

1.4 Conclusions

Uniaxial creep tests were performed on Zircaloy-4 tensile specimens with an average grain size of 8.5 μm in the stress range, $2.56 \times 10^{-4}E - 2.8 \times 10^{-3}E$, where E is the elastic modulus at three temperatures (500 °C, 550 °C and 600 °C) with an objective to uncover the rate-controlling mechanism(s). Four regimes (I to IV) have been identified with the stress exponents of 1, 4, 14.5 and 9-11 as the applied stress increases. TEM analyses of the

29

deformation microstructures and validation of the experimental creep rates with standard creep models were undertaken to uncover the dominant creep mechanisms in regimes I - IV.
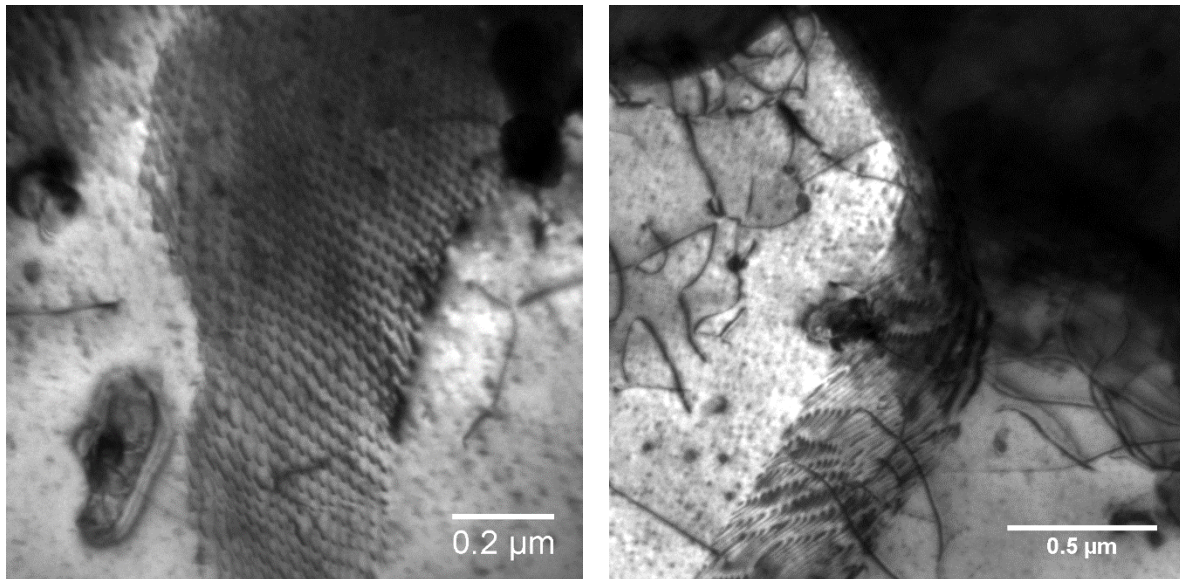
Figure 1.31. TEM micrographs showing hexagonal network consisting of screw dislocations and a sub-boundary produced by edge dislocations

Regime I:

 at low stresses transits into regime II with *n=4.1* and $Q_c=240$ kJ/mol at high stresses. The activation energies were determined to be independent of the applied stress within a regime. A stress exponent close 1 and a stress-independent creep activation energy in range of that for self-diffusion along the grain boundary in α-Zr (188 kJ/mol) suggests any of Coble creep or the Slip-band mechanism proposed by Spingarn and Nix to be the rate-controlling mechanism in regime I. A stress exponent of 4.1 and a stress-independent creep activation energy being close to the activation energy for lattice self-diffusion in Zr-1.3%Sn indicate that any of dislocation climb and glide of jogged screw dislocations can be the rate-controlling process in regime II. Furthermore, TEM analyses of the deformation microstructures and validation of the experimental creep rates with standard creep models were undertaken to uncover the dominant creep mechanisms in regime I and II.

Coble creep mechanism was identified to be the rate-controlling mechanism in regime I based on the following observations:

(a) Stress exponent close to *1* and *$Q_c=196$ kJ/mol* in range of the activation energy for self-diffusion along the grain boundary in α-Zr (188 kJ/mol)
(b) The deformation microstructures of the specimens deformed even up to 2% in regime I were noted to have dislocation densities close to that of the unstrained Zircaloy-4. The TEM micrographs revealed no slip-bands or sub-grains suggesting the strain accumulation through diffusional creep mechanisms.
(c) A good agreement between the experimental creep rates with the predictions by the Coble creep model was obtained.

30

Regime II:

Edge dislocation climb was attested to regime II as the rate-controlling mechanism based on the following observations:

(a) Stress exponent close to 4 and Q_c=240 kJ/mol in range of the activation energy for self-diffusion along the lattice in α-Zr (259 kJ/mol).
(b) The TEM micrographs of the deformation microstructures in regime II exhibited sub-grains within grains. The sub-grains were determined to be bounded by pure tilt boundaries and hexagonal dislocation networks comprised of mixed type dislocations indicating dislocation climb as the rate-controlling process.
(c) The sub-grain sizes in regime II followed an inverse linear relationship with the applied stress regardless of the test temperature.
(d) The experimental creep rates in regime II were in good agreement with the predictions of the Weertman dislocation climb model.

Regime III:

The rate controlling mechanism could not be underscored based on the available creep and microstructural data.

Regime IV:

A stress exponent in the range of 9.3-11 and a stress-dependent activation energy in the range of 220-242 kJ/mol were obtained. Following observations substantiate the cross-slip of screw dislocations as the rate controlling mechanism in Zircaloy-4 over the test conditions,

1. The stress-dependent activation energy obtained from the creep data can be written in the following form, as derived in Friedel's model, which encompasses the activation energies for the constriction and the recombination of screw dislocations,
$$U = (150 \pm 4) + \left(\frac{2236 \pm 124}{\tau}\right) kJ/mol$$
2. The constriction energy of 150 kJ/mol obtained from creep data is in good agreement with the values reported in the literature for zirconium and several HCP materials.
3. The activation volume values measured from the stress relaxation experiments in the temperature and stress ranges similar to the creep test conditions are $70b^3$-$190b^3$, which are in consensus with a cross slip process.
4. The yield strength of Zircaloy-4 in the temperature range of 500-600 °C determined from the tensile tests were found to be in line with the constitutive equation given by the Friedel model namely $1/\tau T$ linearly decreasing with $1/T$.
5. The activation energy values for the constriction and the recombination of the screw dislocations were calculated from the tensile and the activation volume data from relaxation tests; they are comparable to the activation energy values obtained from the creep data.

31

2 Creep mechanisms in HANA-4 using internal pressurization of closed end tubes

2.1 Introduction

Zirconium alloys have found extensive applications in nuclear reactors as fuel rods and structural materials for several decades owing to their attractive properties such as sufficient mechanical strength at high temperatures, good corrosion resistance and, more importantly, low absorption cross section for thermal neutrons. In particular, Zircaloy-2 and Zircaloy-4 with major alloying elements of Sn, Fe and Cr have been serving boiling water reactors (BWR) and pressurized water reactors (PWR) respectively for several decades [52]. However, with the advent of using these cladding materials for extended burn-up as well as Generation-IV reactor design concepts, the materials inside the reactors are expected to function reliably at higher temperatures, higher neutron doses and extremely corrosive environment for far longer times [67]. This critically demands for improved microstructural design in reactor structural materials through various methods such as altering composition and processing routes to attain better properties. One such attempt towards realizing this goal was to add Niobium with Zircaloys for achieving an improved long-term corrosion resistance and mechanical properties without losing the neutron absorption characteristics, the attributes which are generally ascribed to the distribution of β-Nb precipitates in the microstructure [68, 69]. For instance, Zr-2.5%Nb pressure tubes are currently used in pressurized heavy water reactors (PHWR). As well, Nb-modified Zr cladding alloys such as Zirlo and M5 have been developed in the USA and Europe for applications in modern PWRs [67]. Along this line, the Zircaloy fuel cladding team at Korea Atomic Energy Research Institute (KAERI) has recently developed several Zr-Nb cladding alloys, known as HANA (High performance Alloy for Nuclear Applications) alloys, with optimum composition and processing conditions to enhance their structural properties [70-73]. The out-of-pile and in-pile performance evaluations of these alloys demonstrated their improved corrosion resistance as well as mechanical properties than Ziracloy-4 probably due to the effect of finely distributed second phase precipitates in HANA claddings [74].

Among several possible performance degradation phenomena occurring in nuclear fuel cladding materials such as creep, stress-corrosion cracking and delayed-hydrogen cracking, creep is regarded as the prime degradation mechanism. Further, knowledge on transitions in creep mechanisms becomes essential not only in predicting the life times of fuel claddings conservatively but also can be useful in designing microstructures with better creep resistance [1, 2]. To this end, several investigations were undertaken to comprehend the creep behavior of Zr-Nb alloys which were recently reviewed by Charit and Murty for different Zr-Nb based alloys with an emphasis on the transitions in creep mechanisms over a range of stress and temperature conditions [3, 68, 75-79]. From the review, a common trend that can be noted in all the Zr-Nb based alloys considered vis-à-vis the change in stress exponent (n) as a function of the applied stress is as following: n=1 at low stresses changes to n=3 at intermediate stresses, which then transits into a n=5-7 regime at high stresses. Based on the analyses of the stress exponent values in combination with the creep activation energies in the three regimes, the rate-controlling mechanisms for the creep deformation have been proposed. For instance, Coble creep, which is a Newtonian viscous flow mechanism, was attested to the n=1 regime at low stresses for Zr-Nb alloys with fine grain size, lesser than < 10 μm. In the intermediate regime that behaves like the

32

natural power law creep with n=3, viscous glide mechanism mediated by dragging of dislocations by niobium solutes has been suggested as the rate-controlling process while climb of edge dislocations at high stresses. However, TEM analyses of the deformation microstructures in support of the viscous dragging mechanism was undertaken by only a very few studies. For example, Murty et al showed dislocations uniformly distributed throughout the zirconium matrix without forming into sub-boundary or networks, possibly indicating viscous glide mechanism to be operative in the n=3 regime [80, 81]. However, at the temperatures of interest, Nb exhibits distinct precipite formation with very little solid solubility in Zr thereby rendering doubt as to the locking of the dislocations by Nb solid solutes. As the applied stress becomes larger than a critical stress of about $7.5 \times 10^{-4}E$, which is sufficient to break away the dislocations bounded by the niobium solutes [82], the creep deformation of Zr-Nb alloys was postulated to be controlled by dislocation climb, which is now the slower process between glide and climb acting sequentially. In this regime, the crept microstructures revealing sub-grains bounded by dislocations [78] and dislocation networks [68] in TEM micrographs were ascribed to the occurrence of dislocation-climb controlled process. In addition, the activation energies determined for n=3 and n=5-7 regimes were found to be close to the lattice self-diffusion activation energy in α-Zr since both glide and climb are controlled by solute atom diffusion and self-diffusion that are noted to have similar activation energies. Based on these observations, it can be argued that Zr-Nb alloys behave like a class-A alloys during creep at intermediate stresses, whereas they act as a class-M alloy at high stresses similar to α-zirconium and its alloys with tin as major alloying element such as Zircaloy-2 and Zircaloy-4 [5, 15] .

Though there exists a consistency in the mechanistic creep parameters like stress exponent and activation energy at a range of stresses in several Zr-Nb alloys, more detailed analyses of the deformation microstructure are warranted to unambiguously detect the rate-controlling mechanisms. With this in mind, the creep behavior of HANA-4 (Zr-1.5%Nb alloy) cladding, which is a potential candidate for nuclear fuel claddings, has been investigated with a focus on identifying the transitions in creep mechanisms along with emphasis on deformation microstructures. Biaxial creep tests on HANA-4 tubes were conducted using internal pressurization of closed-end tubes, which simulates similar loading conditions experienced by fuel claddings in reactors, to gather the steady state creep data over a range of stress and temperature conditions. From the analysis, the creep data of HANA-4 was noted to follow a similar trend observed in other Zr-Nb alloys with respect to the variance of stress exponent as a function of stress (n=1, n=3 and n=4.5 respectively at low, intermediate and high stresses) as well as the activation energies being equivalent to that for the lattice self-diffusion in α-Zr in the n=3 and n=4.5 regimes. However, it is postulated from the analyses of the deformation microstructures using TEM that dislocations bypassing the β-Nb precipitates in HANA-4 through the climb process is the rate-controlling mechanism, as against the usually-perceived viscous glide mechanism, in the n=3 regime. Furthermore, the recovery of dislocations by climb, as suggested by the pillbox model from Weertman, is proposed as the dominant mechanism in the n=4.5 regime [33]. The stress at the point of transition from the n=3 regime to the n=4.5 regime has been identified as the critical stress required by dislocations to bypass the precipitates in HANA-4 via the well-known Orowan mechanism [83, 84]. For the first time, we show that the creep behavior of a Zr-Nb alloy is similar to that of certain precipitation-hardened materials; but not of a class-A alloy.

33

2.2 Materials and Experiments

HANA 4 tubes with an outer diameter (D_o) of 9.50 mm and a wall thickness (t) of 0.57 mm were received from Korea Atomic Energy Research Institute (KAERI) in cold-worked and stress relieved condition. The chemical composition of the tubing is given in table 2.1. The as-received tubes were annealed at 537 °C for 4 hours inside a vacuum furnace continuously purged with argon gas to reduce their oxidation. The annealing temperature was chosen so that the creep tests with temperature as high as 500 °C in this study could be carried out with little microstructural changes. Grain size distributions are characterized using EBSD and Figure 2.1a compiles the inverse pole figure maps of grain orientations and grain size distributions of the annealed material that yielded a mean grain size of 3.6 μm.

With an outer diameter to wall thickness ratio of lesser than 0.1, the thin-wall approximation, i.e. radial stress is negligible, can be applied to the HANA tubing. Biaxial creep testes were then carried out vis-à-vis closed-end internal pressurization of the tubes which gives rise to a stress ratio (i.e. hoop stress to axial stress) of 2:1. Figure 2.1b includes an example of the biaxial creep specimen and internal pressurization biaxial creep equipment with in-situ hoop strain measurement using a laser telemetric extensometer.

Table 2.1. Chemical composition of HANA-4 tested in this study

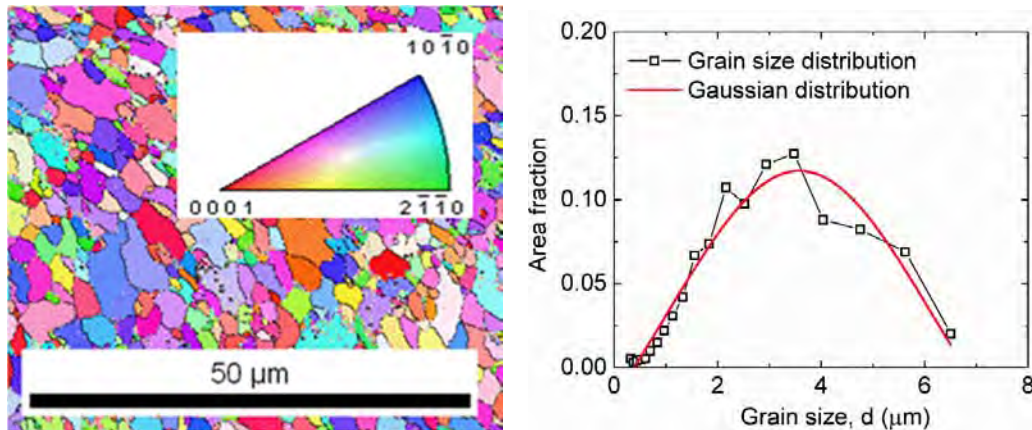| Element	Amount
Niobium	1.5 %
Tin	0.4 %
Iron	0.2 %
Chromium	0.1 %
Oxygen	1100 ppm
Silicon	100 ppm
Zirconium	Rest

Figure 2.1a. Inverse pole figure maps depicting the grain orientation in the annealed HANA-4 tubing at 537 °C for 4 hours with inset of the orientation legend (left) and the grain size distribution calculated from the inverse pole figure map revealing an average grain size of about 3.8 μm (right)
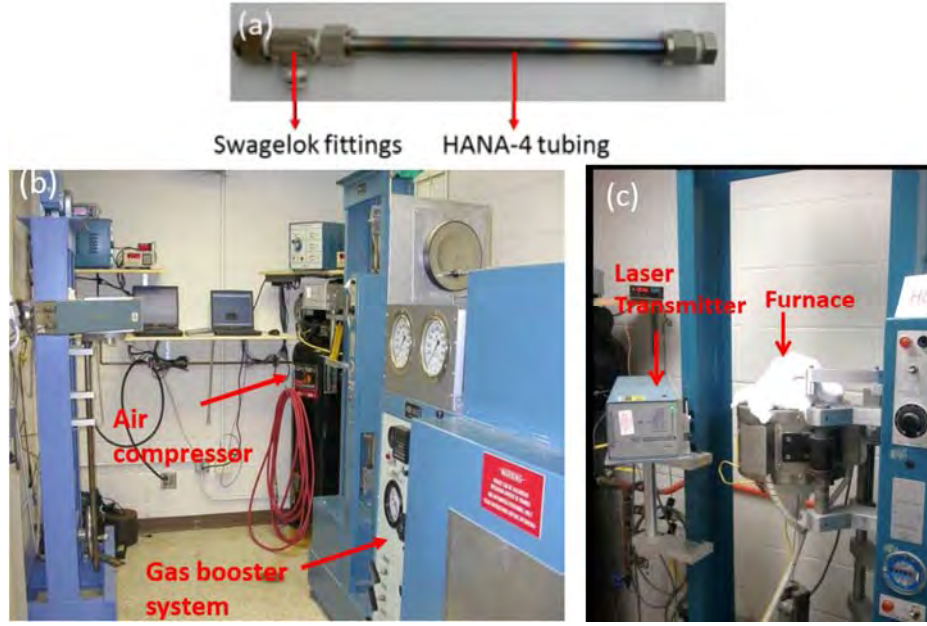
34

Figure 2.1b. Biaxial creep specimen of HANA-4 tubing (top),
Air compressor and gas booster system capable of generating 17,000 psi pressure to supply the
required pressure for the biaxial creep tests (b) and
Biaxial creep set-up showing the lasermike and the furnace (c)

The hoop (σ_θ) and axial stresses (σ_H) were calculated using the relations,

$$\sigma_\theta = \frac{pr}{t}, \tag{2.1a}$$

$$\sigma_H = \frac{pr}{2t}, \tag{2.1b}$$

where r is the mean radius and p is the argon pressure inside tube. Biaxial creep testing of HANA-4 tubing was carried out by applying a range of hoop stresses, 8.38×10^{-5}E - 2.87×10^{-3}E, at temperatures, 400 °C, 450 °C and 500 °C. The biaxial creep specimens were prepared by closing the ends of the tubes with Swagelok fittings except for an inlet to internally pressurize with argon gas. A gas pressurization system comprising of a gas booster and an air compressor capable of generating up to 17,000 psi of argon pressure was utilized as a source to supply the pressure to attain the required hoop stress. Before each creep test, it was ensured that the specimen could hold up the set pressure without any gas leakage. The test temperatures were attained by heating the specimen using a one-zone furnace that was connected to an ATS® temperature controller. Two K-type thermocouple wires were wound on the specimen in order to measure and control the temperature accurately within a range of ±3 K. The diametrical expansion (ΔD_o) of the tubing during creep test was *in-situ* measured by a non-contact Beta lasermike with an accuracy of as low as 2.5 μm and was continuously logged by a computer. The hoop strain (ε) was then measured using the relation,

$$\varepsilon = \frac{\Delta r}{r} \tag{2.2}$$

Since the axial strains produced in tube specimen under the biaxial loading with 2:1 stress ratio are negligible, only the hoop strain was measured for further analysis [35]. Once the steady state creep rates were achieved, the creep tests were stopped by cooling the specimen down to room

35

temperature using forced air-flow under loaded condition in order to preserve the deformation microstructures.

Since the tube specimens were heated in the atmospheric air without any protection for oxidation during the creep tests, any thickness variation originated from the oxide scale formation could be added up to the creep induced diametrical expansion by the lasermike resulting in a wrong interpretation of the data. However, it was noted from oxidation experiments, in which HANA 4 tubing was heated in the atmospheric air without the application of pressure that the thickness increment arising solely from the oxide scale formation is negligible for the test temperatures employed here. For instance, heating the HANA 4 tubing at 525 °C for 20 days increased its thickness by only about 0.4 µm owing to the formation of oxide scale, which is an insignificant ($\varepsilon_\theta \cong 10^{-5}$) fraction of the diametrical expansion obtained from our creep tests.

The microstructures of the specimens before and after creep were characterized using TEM with an objective to detect the dominant mechanism operative under the testing conditions. To this end, the walls of the tube specimens were sectioned using a low speed saw and polished using 800 fine grit sand-papers down to ~100 µm thick flat sheet for synthesizing TEM thin specimens. The flat sheets were then punched using a mechanical punch into 3 mm disks, which were further polished using a model 110 Fischione automated twin-jet polisher to produce the final thin specimens at -60 °C by applying a voltage of 25 V using the following electrolytic solution: 30 ml sulfuric acid and 1 ml hydrofluoric acid in 470 ml methanol. A 200 KeV JEOL 2010F TEM equipped with a double tilt-holder was employed for imaging the microstructures. In addition, compositional analysis of the secondary phases in this alloy was conducted using energy dispersive X-ray spectroscopy (EDS) mapping in a 200 KeV aberration-corrected FEI Titan G2 microscope with an X-FEG source and ChemiSTEM technology which was operated under scanning transmission electron microscope (STEM) mode. The EDS maps were recorded over areas of 108×101 nm in 420×392 pixels for about 20 mins.

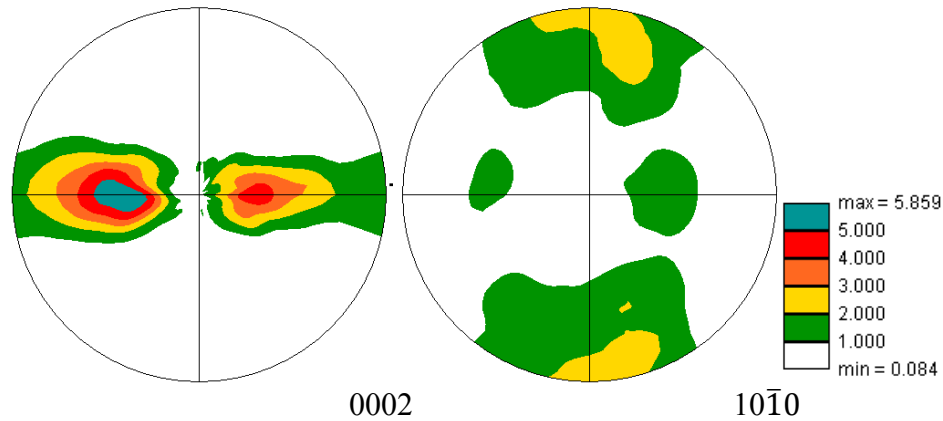0002   10$\bar{1}$0

Figure 2.2. Pole figures of (0002) and (10$\bar{1}$0) with the thickness direction (r) at the center along with axial direction (z) on the top and hoop (q) at 90º along the horizontal direction of annealed HANA-4 tubing with the legend showing intensity distribution.

36

2.3 Results

2.3.1 Microstructure of annealed HANA-4

Figure 2.1a presents the inverse pole figure map of the annealed HANA 4 from which grain size distribution and pole (basal and prism) figures (Figure 2.2) were evaluated. An average grain size of about 3.6±2.5 µm was determined by fitting the plot of grain size versus area fraction with a Gaussian distribution function. From the pole figures, it can be seen that the annealed HANA 4 possessed a texture which is comparable to the one that was observed in zirconium alloys [85]. The basal poles were noted to be aligned at an angle of about ±20-40º from the radial direction towards the hoop direction as seen in Figure 2.2. On the other hand, the maximum intensity of the prism poles existed at a slightly tilted angle from the axial direction.

TEM micrographs of the annealed HANA-4, given in Figure 2.3, revealed recrystallized grains with a low density of dislocations without forming any entangles or sub-boundaries. Additionally, second phase precipitates, most of them in rounded shape, were observed to be distributed throughout grain interiors as well as at grain boundaries. The size of the precipitates of about 500 numbers in different grains were measured from the micrographs using the ImageJ software. The size distribution of precipitates complied with a log-normal distribution with an average diameter (d) of about 63 ± 35 nm as shown in Figure 2.4. Similarly, the precipitate size distribution in the HANA-4 tubing crept at 450 °C and 50 MPa for 5 days in regime II was determined from the measurements of about 500 precipitates (Figure 2.4), which also complied to a log-normal distribution with an average precipitate diameter of 57±34 nm. As seen, no statistically significant change in the precipitate size distribution is determined in the HANA-4 tube after a prolonged heating indicating the presence of stable precipitates. Further, energy dispersive X-ray spectroscopy (EDS) elemental maps of a precipitate surrounded by the matrix are presented in Figure 2.5.
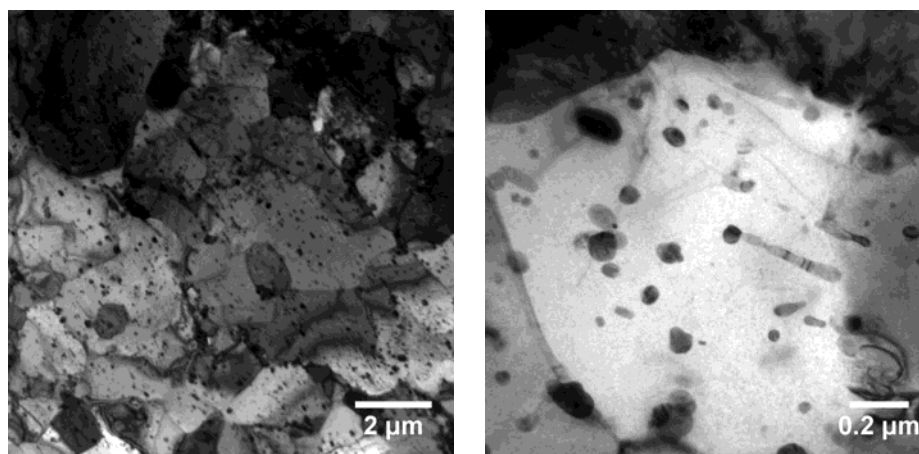
Figure 2.3. Representative TEM micrographs of annealed HANA-4 showing recrystallized grains with fine precipitates distributed throughout the matrix

It is quite evident from the maps that the precipitates are composed of niobium as the major element. The quantitative analysis of the elements determined by the software provided the chemical composition of the precipitates to be Nb-82.6%, Zr-17%, Cr-0.2% and Fe-0.2%.

37
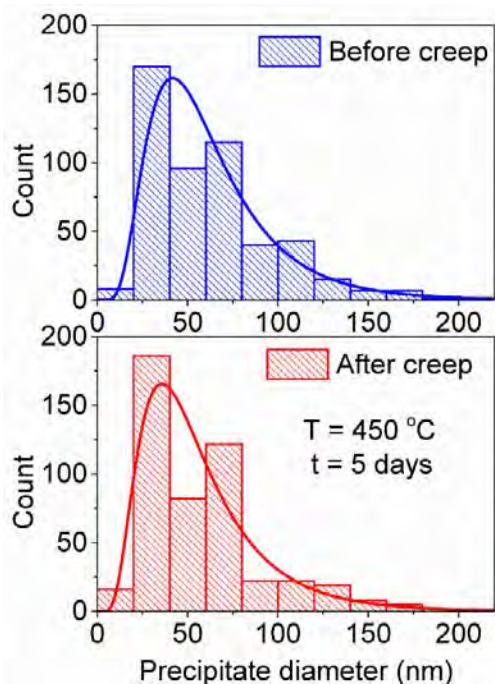
Figure 2.4.
The size distribution of the precipitates in HANA-4 before creep (top) and after crept at 450 °C for 5 days (bottom)
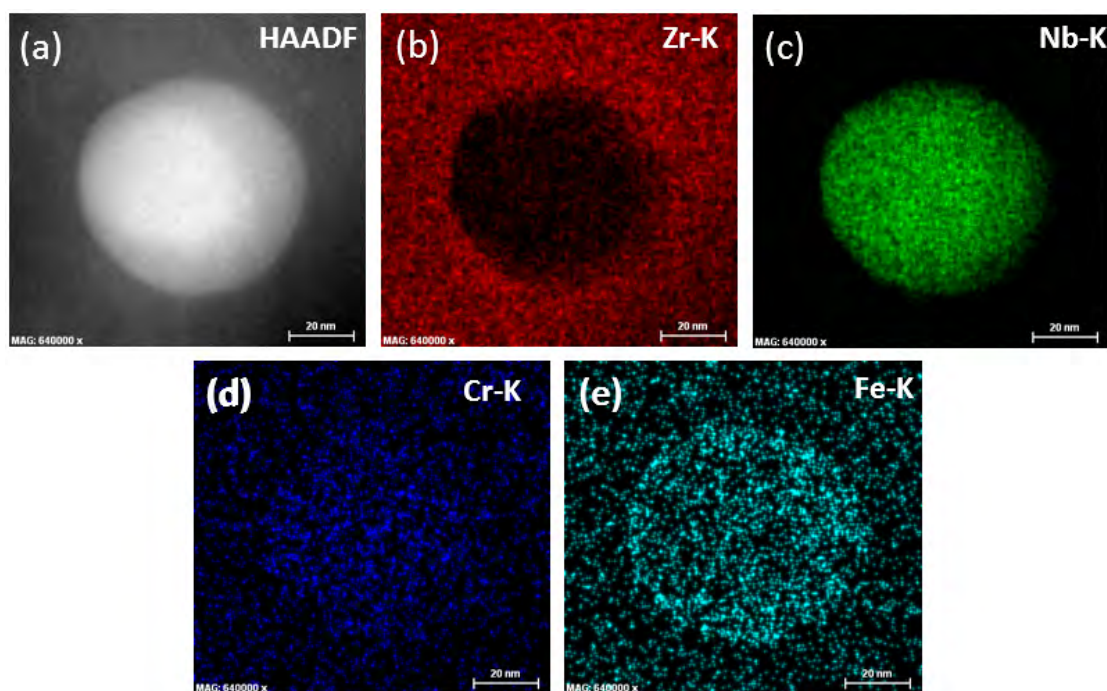
Figure 2.5. a) HAADF-STEM image of a precipitate surrounded by the matrix. (b)-(e) EDS elemental mapping of the precipitate and the matrix

The diffraction patterns obtained from the precipitates confirm that they have BCC crystal structure as depicted in Figure 2.6. The preceding analyses indicate that these are β-Nb (BCC) second phase precipitates, which are generally present in Zr-Nb alloys owing to a very low solubility of Nb in Zr at room temperature according to the Zr-Nb phase diagram (Figure 2.7)

38

[86-88]. As well, similar second phase precipitates were observed to be present in HANA-6 alloys (Zr-1.1%Nb), which are processed in a similar way like that of HANA-4 [74].
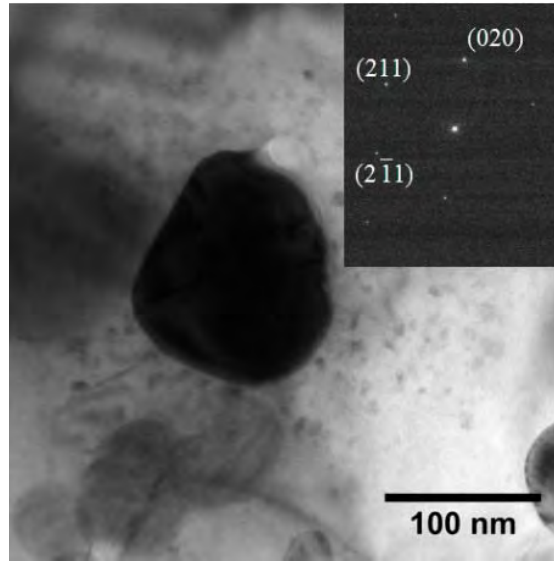
Figure 2.6. Diffraction pattern obtained from the precipitate indexed with the reflections of BCC crystal structure. The zone axis of the pattern is along $[10\bar{2}]$
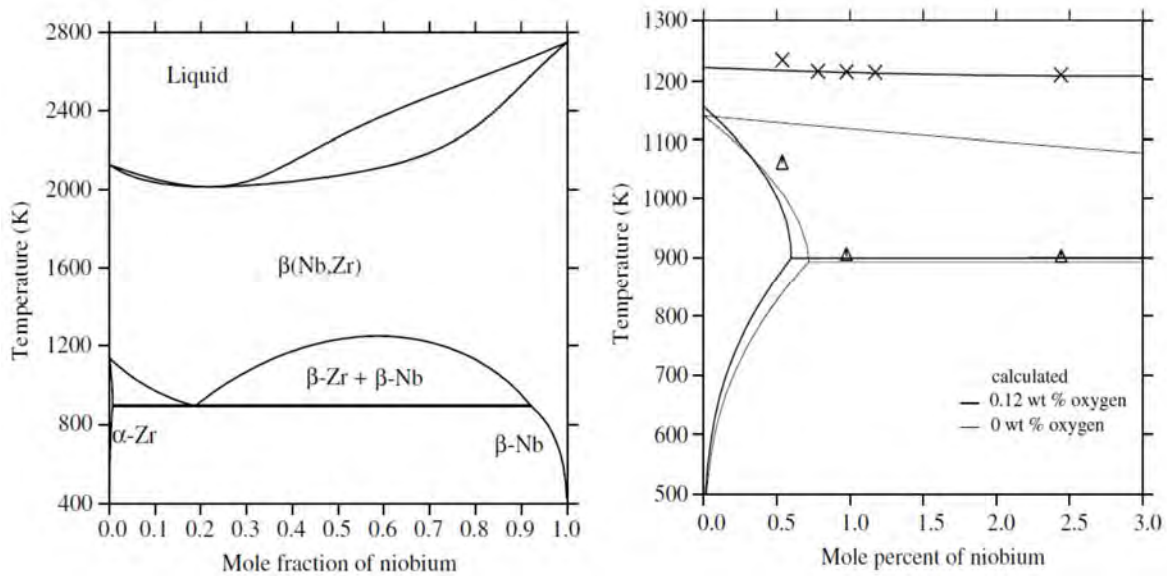
Figure 2.7. Zr-Nb phase diagram (left) and an expanded view of the Zr-rich side in the Zr-Nb phase diagram (right) [29]

2.3.2   Stress exponent and activation energy

Figure 2.8 shows a representative creep curve of a specimen deformed at 100 MPa and 450 °C. The creep curves in general exhibited the primary creep regime initially, wherein the creep rate showed a decreasing trend with time, and followed by the steady state creep regime, wherein the creep rate became time-invariant. The steady state creep rates and the total strain

39

along with the stresses and temperatures employed in the tests are given in Table 2.2. The steady state creep rate data were further analyzed to note the rate controlling mechanisms at the testing conditions. At the outset, two important creep parameters namely stress exponent (n) and activation energy (Q_c) were obtained from the general creep equation relating the steady state creep rate ($\dot{\varepsilon}_s$) with the applied stress (σ) and temperature (T in K) that can be stated as,

$$\dot{\varepsilon}_s = \frac{AEb}{kT}\left(\frac{\sigma}{E}\right)^n e^{-\frac{Q_c}{RT}}, \tag{2.3a}$$

$$E = 95.92 - 0.0629(T - 273)\ GPa\ . \tag{2.3b}$$

In equation (2.3a), A is a constant, E is the temperature-dependent elastic modulus of Zr-2.5% Nb [89], b is the burgers vector ($3.23 \times 10^{-10}m$), k is the Boltzmann's constant and R is the gas constant.
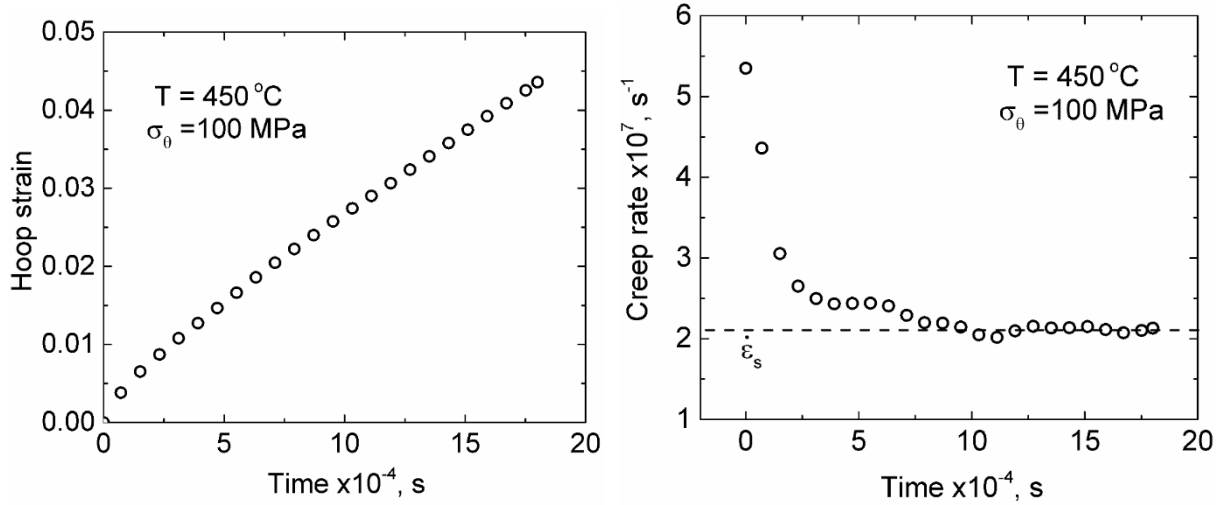
Figure 2.8. The creep curve of HANA-4 at 100 MPa and 450 °C (left) and creep-rate versus time plot showing the steady state creep rate (right)

From equation (2.3a), the stress exponent is equivalent to the slope of the log-log plot between the steady state creep-rate versus the modulus compensated stress at a constant temperature which is shown in Figure 2.9. As seen from the plot pertained to the tests at 500 °C, n is 0.6±0.3 at low stresses which changes to 4.2±0.1 at high stresses passing through n=2.9±0.1 at the intermediate stress regime indicating transitions in creep mechanisms as the applied stress increases. These regimes will be referred to as regime I, II and III at low, intermediate and high stresses respectively. A similar trend can be observed at 450 °C and 400 °C as well except for the absence of the creep data at lower stresses.

At a constant modulus-compensated stress, the general creep equation (2.3a) can simply be written as,

$$\dot{\varepsilon}_s = A_0 e^{-\frac{Q_c}{RT}}. \tag{2.4}$$

where A_0 is a function of the applied stress. The activation energy was then calculated from the slope of a semi-logarithmic plot of the steady state creep rate versus the inverse of temperature as shown in Figure 2.10. A creep activation energy value of 226 kJ/mol was determined for both regimes II and III. However, the activation energy for regime I

40

could not be assessed owing to the lack of creep data at lower temperatures. The activation energy estimated for regimes II and III is somewhat lesser than the activation energy for lattice self-diffusion for α-Zr determined by radioactive tracer experiments, which is 259 kJ/mol [24]. This value is comparable to the lattice diffusion activation energiesof 213 kJ/mol and 234 kJ/mol obtained from creep experiments in Zr-1%Nb alloys by Voeikov et al [68] and Alymov et al [79] respectively. Further the creep data is presented as the plot of the steady state creep rates normalized by the lattice diffusivity ($D_l = D_0 \exp\left(-\frac{Q_c}{RT}\right)$) versus the modulus-compensated stress in Figure 2.11. The diffusion coefficient, D_0, and Q_c assumed the values of $5 \times 10^{-4} m^2/s$ and 259 kJ/mol respectively as determined for Zr-1.3%Sn from radioactive tracer data [24]. It can be seen in this figure that the steady state creep rates obtained at different test temperatures overlapped well showing the transitions in the value of stress exponents and possibly in creep mechanisms as the applied hoop stress increases; Regime I with a stress exponent close to 1 transits into regime II with n~3 at a stress of about $2.95 \times 10^{-4}E$, which further changes to regime III with n~4.5 at about $8.22 \times 10^{-4}E$.
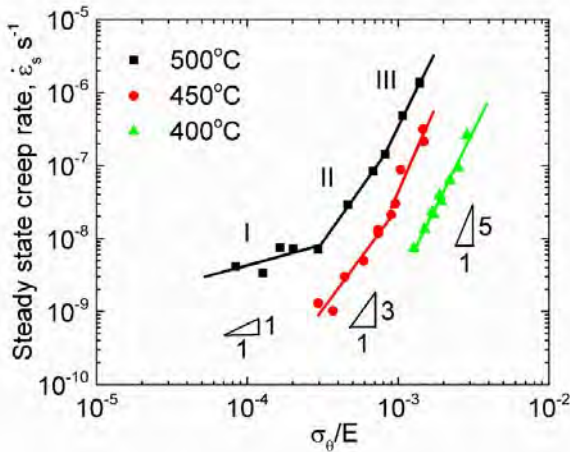

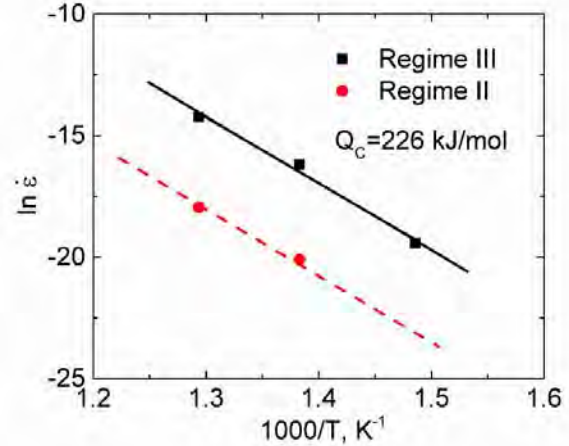Figure 2.9. Steady state creep rate versus modulus-compensated hoop stress

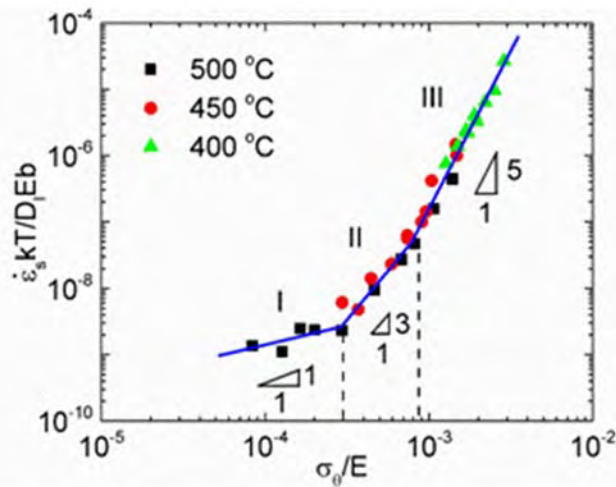Figure 2.10. Arrhenius plots at a constant normalized stress (regimes II and III)

Figure 2.11. Normalized steady state creep rate versus normalized hoop stress

41

Table 2.2. Stress, steady state creep rates and total strain at the three different test temperatures.

400 °C				450 °C				500 °C			
σ_θ, MPa	σ_θ/E	$\dot{\varepsilon}_s$, s^{-1}	ε, %	σ_θ, MPa	σ_θ/E	$\dot{\varepsilon}_s$, s-1	ε, %	σ_θ, MPa	σ_θ/E	$\dot{\varepsilon}_s$, s-1	ε, %
90	1.27×10^{-3}	7.3×10^{-9}	0.8	20	2.96×10^{-4}	1.3×10^{-9}	0.2	5.4	8.38×10^{-5}	4.2×10^{-9}	0.4
106	1.50×10^{-3}	1.3×10^{-8}	1.2	25	3.70×10^{-4}	1.0×10^{-9}	0.5	8.2	1.27×10^{-4}	3.4×10^{-9}	0.6
119	1.68×10^{-3}	2.3×10^{-8}	0.6	30	4.44×10^{-4}	3.0×10^{-9}	0.2	10.6	1.64×10^{-4}	7.5×10^{-9}	1.1
122	1.72×10^{-3}	2.1×10^{-8}	1.5	40	5.92×10^{-4}	5.0×10^{-9}	0.2	13	2.02×10^{-4}	7.3×10^{-9}	0.9
134	1.89×10^{-3}	3.9×10^{-8}	0.6	50	7.39×10^{-4}	1.2×10^{-8}	0.5	19	2.95×10^{-4}	7.1×10^{-9}	0.4
137.5	1.94×10^{-3}	3.2×10^{-8}	1.1	50	7.39×10^{-4}	1.3×10^{-8}	0.6	30	4.65×10^{-4}	2.9×10^{-8}	1.2
156	2.20×10^{-3}	6.2×10^{-8}	1.7	61	9.02×10^{-4}	2.1×10^{-8}	0.5	44	6.82×10^{-4}	8.3×10^{-8}	1.2
177	2.50×10^{-3}	9.3×10^{-8}	1.5	65	9.61×10^{-4}	3.0×10^{-8}	0.2	53	8.22×10^{-4}	1.4×10^{-7}	2.8
203	2.87×10^{-3}	2.6×10^{-8}	2.1	70	1.04×10^{-3}	8.8×10^{-8}	1.7	69	1.07×10^{-3}	4.8×10^{-7}	4.9
				99	1.46×10^{-3}	3.1×10^{-7}	4.5	90	1.40×10^{-3}	1.4×10^{-6}	7.4
				100	1.48×10^{-3}	2.1×10^{-7}	4.4	90	1.40×10^{-3}	1.3×10^{-6}	10.8

σ_θ – Hoop stress, E – Elastic Modulus, $\dot{\varepsilon}_s$ – Steady state creep rate, ε – Total strain

42

2.3.3 Crept Microstructures

The deformation microstructure of the specimens crept in regime II revealed dislocations distributed throughout the matrix with little sub-boundaries formation as seen in Figure 2.12a. A predominant number of dislocations were observed to be pinned at the precipitates with the unpinned portion of the dislocation lines advanced further with bows (curves) in the matrix as seen in Figure 2.12b. Further, the dislocations were imaged using weak-beam dark field technique in order to observe the interaction of the dislocation lines with the precipitates (Figure 2.13). It can be seen from the micrographs that dislocations were captured while bypassing the precipitates possibly assisted by dislocation climb process, which are marked as 'A'. As well, dislocation lines were observed to be partially wrapping around the precipitates in a way they are in the process of bypassing the precipitates through Orowan bowing, which are marked as 'B'. The curvature formed by the dislocations in between precipitates generally indicates the direction in which the shear stress acts on the dislocation line.

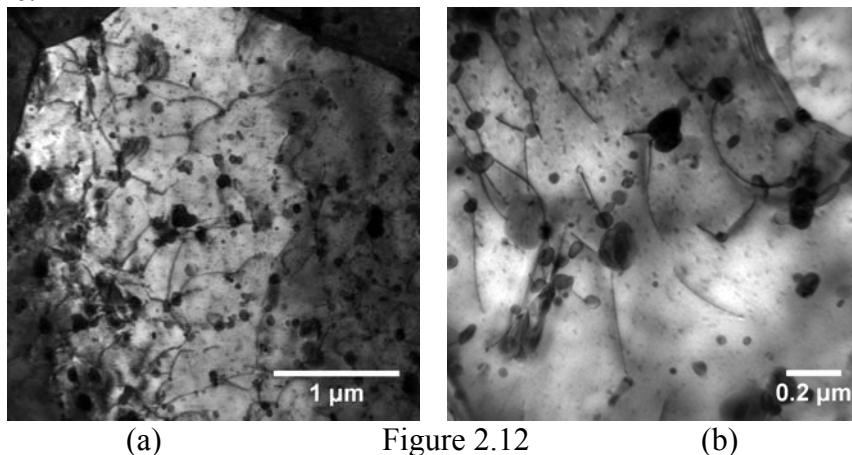(a)   Figure 2.12   (b)

TEM micrographs of the crept specimen at 50 MPa and 450 °C in regime II (n=3)
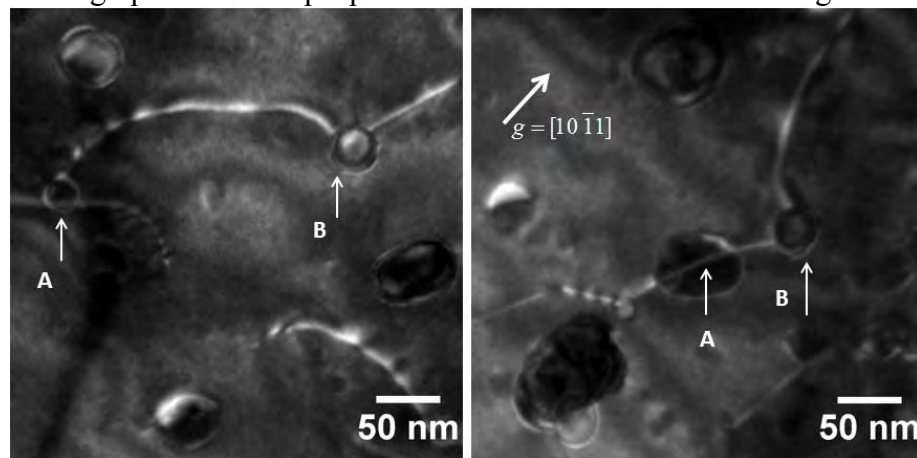

Figure 2.13. Weak beam dark field TEM images showing dislocations climbing over precipitates

<div align="center">43</div>

On the other hand, the micrographs of the crept specimen in regime III showed dislocations forming hexagonal networks as well as sub-grain boundaries which were distinctly absent in regime II (Figure 2.14). Further, the dislocation density inside the sub-grains was evidently low. These observations suggest that the dislocations could overcome the precipitates in regime III at a relative ease making the interruption by them probably an insignificant process towards the rate controlling mechanism.
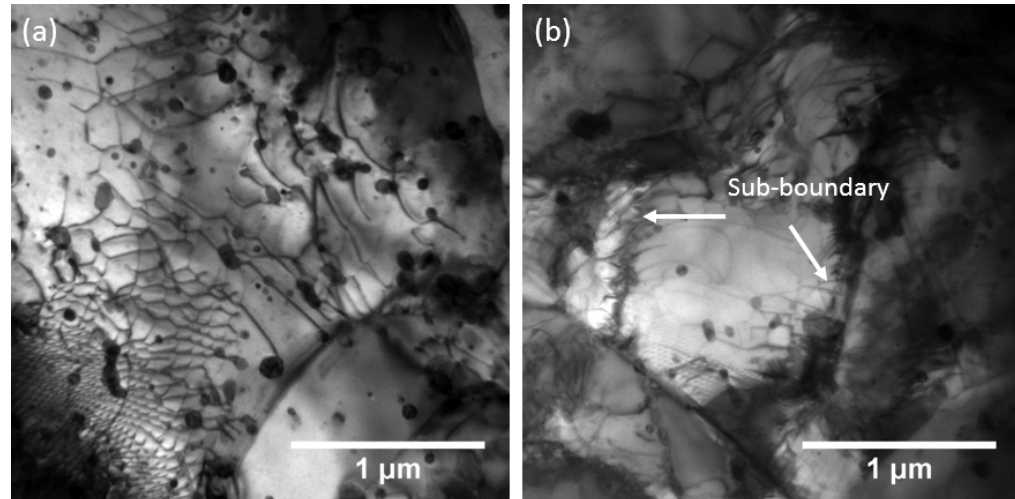
Figure 2.14.
TEM micrographs of the crept specimen at 99 MPa and 450 °C in regime III (n=4.5). Dislocations forming into networks inside grains (a) and dislocations forming into sub-boundaries with lesser dislocation density inside the sub-grain (b)

2.4 Discussion

2.4.1 Rate controlling mechanism in regime I

A stress exponent close to 1 at low stresses indicates that any of the diffusional creep mechanisms such as Coble creep, Nabarro- Herring (N-H) creep or Harper-Dorn (H-D) creep can be the dominant mechanism [27, 29, 90, 91]. But pointing out the exact rate-controlling mechanism necessitates the activation energy data or the knowledge of the dependency of the creep rate on the change in grain size (inverse grain size exponent), which are unavailable for regime I [92]. However, it can be suggested based on the earlier studies on zirconium alloys that Coble creep is more likely the rate-controlling mechanism owing to the distribution of fine grain size in HANA-4, which has an average of 3.6 μm. Generally, N-H creep and H-D creep are the dominant mechanisms in materials with intermediate and large grain sizes respectively. For instance, the creep data of α-Zr from Novotný et al exhibited an inverse grain size exponent of ~3 up to a grain size of 125 μm suggesting Coble creep to be active at 600 °C [30]. In specimens with larger grain size than 125 μm, the inverse grain size exponent value reduced to zero indicating that H-D creep is the rate-governing mechanism. Also in an unpublished work of the authors [93] , Coble creep was found to be operable in Zircaloy-4 with an average grain size of 8.5 μm at low stresses in the temperature range of 500-600 °C based on the observation that the creep activation energy value (196 kJ/mol) lied closed to

44

the grain-boundary diffusion energy (188 kJ/mol) in α-Zr determined using radioactive tracer data [23]. Further, the experimental creep results in regime I are compared with the predictions by the Coble creep model given by the relation,

$$\frac{\dot{\varepsilon}_s kT}{D_{gb} Eb} = (100 \pm 50) \left(\frac{b}{d}\right)^3 \left(\frac{\sigma}{E}\right)^1 \tag{2.5a}$$

$$D_{gb} = D_{0gb} \exp\left(-\frac{Q_{gb}}{RT}\right), \tag{2.5b}$$

where, A_c is a constant which was derived to be equal to (100 ± 50) [27, 37], d is the average grain size (3.6 μm) and D_{gb} is the grain boundary diffusivity. D_{0gb} and Q_{gb} are the grain boundary diffusivity coefficient and the grain boundary diffusion activation energy, which have the values of $10^{-3} m^2/s$ and $188\ kJ/mol$ determined for α-Zr using radioactive tracer data [23]. Additionally, the predictions by the models for N-H creep [91] and H-D creep [94] were calculated using equations (2.6) and (2.7) respectively,

$$\frac{\dot{\varepsilon}_s kT}{D_l Eb} = 12 \left(\frac{b}{d}\right)^2 \left(\frac{\sigma}{E}\right)^1 \tag{2.6}$$

$$\frac{\dot{\varepsilon}_s kT}{D_l Eb} = 4 \times 10^{-11} \left(\frac{\sigma}{E}\right)^1 \tag{2.7}$$

Figure 2.15 compares the experimental creep rates in regime I with the model predictions for Coble, N-H and H-D creep mechanisms as a BMD plot. As seen, the predictions by the Coble creep model exhibit an excellent correlation with the experimental results, thus substantiating the dominance of the Coble creep mechanism in HANA-4 at low stresses. On the other hand, the creep rates predicted by the N-H and the H-D models fell about 2 and 5 orders of magnitude respectively below the creep rates measured in regime I. Therefore, these mechanisms are not considered to be rate controlling in the HANA-4 tubing.
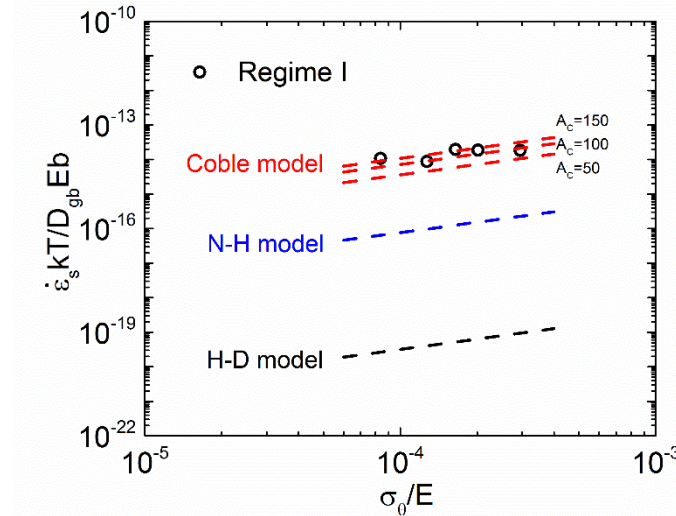

Figure 2.15. Comparison of the experimental creep rates with the Coble creep model

2.4.2 Rate controlling mechanism in regime II

A stress exponent of 3 with the creep activation energy equivalent to that of the lattice self-diffusion activation energy in regime II generally points to dislocation glide or microcreep as the rate controlling mechanism [95] as pointed out earlier. In fact, the creep deformation of several Nb added Zircaloys in n=3 regime has been ascribed to dislocation glide controlled mechanism arising from locking of gliding dislocations by niobium solute atoms [68], which was as well validated by TEM micrographs revealing uniform distribution of dislocations in grain interior. Although the deformation microstructures of HANA-4 in regime II showed dislocations presented throughout the matrix, it is quite evident from the micrographs that those dislocations were pinned at the precipitates (Figure 2.12a). This indicates that dislocations could more likely move at ease while gliding in between two consecutive precipitates without being locked by niobium solute atoms, if anything present. Moreover, very limited solubility of niobium in zirconium (0.3 wt% of Nb at 500 °C) possibly leaves little solute atoms available in the matrix for locking dislocations to reduce their glide rate. Based on these observations, dislocation glide resulting from solute locking as the rate controlling mechanism, which has been generally attested to the n=3 regime in Zr-Nb alloys, becomes questionable in regime II of HANA-4 alloy. It is worth pointing out here that while Sn is present as solid solution in Zr, Zircaloy-4 was shown not to exhibit viscous glide creep [1, 93]. On the other hand, dislocations bypassing the precipitates, which is the slower process, can be the rate-governing mechanism in regime II.
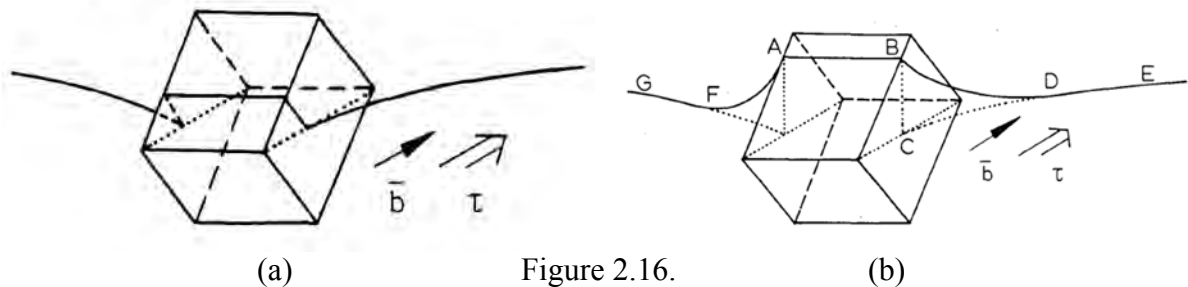
(a)   Figure 2.16.   (b)

Schematic diagrams depicting local climb (a) and general climb of dislocation (b) over cubical precipitate. [51]

An activation energy equivalent to that for the lattice self-diffusion in conjunction with the observation of dislocations passing over the precipitates in the crept microstructure (Figure 2.13) indicate that dislocation climb over the Nb-rich precipitates as the rate-controlling mechanism in regime II. Dislocation climb over obstacles as the rate controlling mechanism has been extensively investigated especially in precipitation hardened and dispersion strengthened materials [84, 96-103]. Local climb and general climb are the two mechanisms that have been often postulated as the modes of dislocations bypassing second phase particles at relatively low stresses and high temperatures, wherein diffusion occurs at a reasonably faster rate [22, 98]. In local climb, the dislocation line assumes the profile of the particle at the particle-matrix interface while the rest of the dislocation line glides on the slip plane thus creating a sharp curvature (Figure 2.16a). On the other hand, in the case of general climb, the dislocation line outside the particle gets relaxed by forming a smooth curvature at

the interface through diffusion of vacancies to the core (Figure 2.16b). Though both these mechanisms were suggested to be operative in precipitation hardened as well as dispersion strengthened materials through experiments and mathematical models, it necessitates a discrete analysis to figure out from which one of these mechanisms is operative in HANA-4, which has not been attempted here [22]. However, Rösler and Arzt demonstrated using their model that general climb is favorable energetically and predominates when dislocations bypass precipitates in materials with low volume fraction of precipitates and without any long range attractive dislocation-precipitate interactions [98]. The force of the attractive or repulsive interaction between matrix and precipitates increases proportional to the difference in their physical parameters, namely, lattice parameter and shear modulus, which are listed for HANA-4 in Table 2.3. As seen from Table 2.3, the lattice parameter and the shear modulus of the zirconium matrix and the β-Nb precipitates lie closely indicating that the dislocation-particle interaction would be likely small. Also, HANA-4 has a low volume fraction of β-Nb precipitates in accordance with the assumption of the model. It can be therefore conjectured that general climb occurs predominantly in regime II of HANA-4. As well, Roser and Arzt derived a stress exponent of 3-4 for the general climb controlled creep regime, which matches with the stress exponent of 3 obtained in regime II further substantiating dislocation climb, as opposed to dislocation glide, as the rate-controlling mechanism in HANA-4 [98].

2.4.3 Rate-controlling mechanism in regime III

A stress exponent of ~4.5 and an activation energy close to the lattice self-diffusion activation energy in regime III indicate edge dislocation climb as the rate controlling mechanism, whose mathematical formulation was derived by Weertman [33, 104]. According to this model, dislocations glide with less resistance on their slip plane till they arrive closer to other dislocations with the opposite burgers vectors in the parallel slip planes and form dislocation dipoles. Further, these dislocations climb up or down to combine and get annihilated thus allowing further glide to proceed. Between these sequential processes of glide and climb, the later proceeds at a slower rate thus controlling the deformation process. The rate equation derived by Weertman based on these assumptions has the following form [41],

$$\dot{\varepsilon}_S = \alpha \left(\frac{D_l}{b^{3.5}M^{0.5}} \right) \left(\frac{\sigma}{G} \right)^{4.5} \left(\frac{G\Omega}{kT} \right) \tag{2.8}$$

where α is a constant whose values are in the range $0.015 < \alpha < 0.33$, M is the number of active dislocation sources in a unit volume, G is the shear modulus , Ω is the atomic volume, $D_l = 5 \times 10^{-4} \exp\left(-\frac{25900}{RT} \right) m^2/s$ [24] and the rest are as described before. As noted, the stress exponent was derived to be 4.5. The value of M can be related to the dislocation density in the annealed material under consideration as [44],

$$M = 0.27\rho^{1.5} \tag{2.9}$$

The value of M was earlier estimated for annealed Zircaloy-4 to be about, $7.6 \times 10^{16}/m^3$, which could be applicable to annealed HANA-4 as well [93]. Substituting $\alpha \sim 0.1$ and

47

$\Omega \sim 0.7b^3$ and $E = 2.6G$ with other values, equation (2.8) can be written in the BMD format as,

$$\frac{\dot{\varepsilon}_s kT}{D_l Eb} = 1.22 \times 10^6 \left(\frac{\sigma}{E}\right)^{4.5} \tag{2.10}$$

The experimental creep results in regime III were then compared with the Weertman model as given in equation (2.10) (Figure 2.17), which shows a good correlation between them indicating climb of edge dislocations as the rate-controlling mechanism in regime III of HANA-4. Further, an important signature in the crept microstructure of the dislocation climb controlled process is the formation of sub-grain boundaries and dislocation networks, which were as well observed in the HANA-4 specimens deformed in regime III (Figure 2.14).
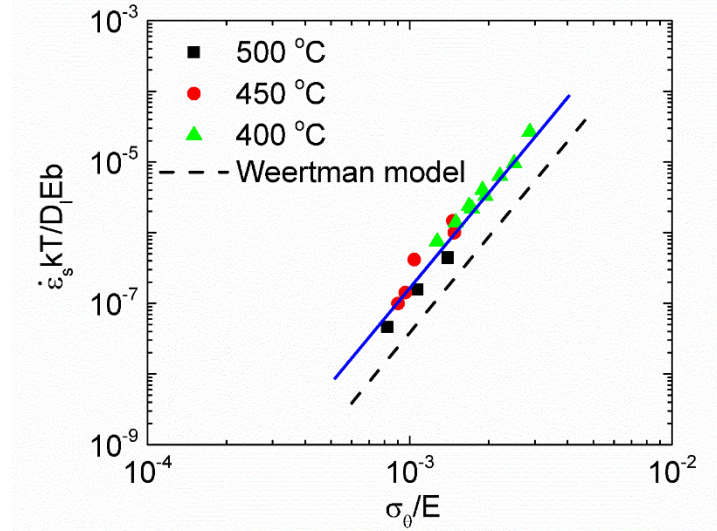
Figure 2.17. Comparison of the experimental creep rates in regime III with the Weertman climb model.

Based on the analyses of the creep data and the microstructural evidences, it can be suggested that dislocation climb is the rate-controlling mechanism in both regimes II and III respectively at low and high stresses. Notably, the activation energies for creep in regimes II and III are similar which are close to the lattice self-diffusion activation energy, thus supporting this proposition. However, the difference between the climb processes in regimes II and III would be that only the segments of dislocations approaching the precipitates would climb over them to bypass (a local phenomenon) and then start gliding on the same slip plane as the former one, whereas the entire dislocation line would climb to get annihilated or to form sub-boundaries on the parallel slip planes in the latter case (a global phenomenon).

2.4.4 Transition from regime II to regime III

A question arises as to what causes the transition from regime II at low stresses to regime III at high stresses. It can be argued that dislocations start overcoming the precipitates through a mechanism other than the climb process in regime III above the hoop stress of about $8.22 \times 10^{-4}E$. At high enough stresses, precipitate shearing and Orowan bowing

48

between precipitates, which are essentially athermal processes, are generally considered to be operative for bypassing precipitates by dislocations. In the case of precipitate shearing, the shear stress required to break away from the precipitates can be calculated from the particle strength which may originate from various hardening mechanisms such as misfit strengthening, chemical strengthening, modulus hardening and order hardening [84]. Since the β-Nb precipitates in HANA-4 have no ordered structure as noticed from the diffraction pattern, only the strengthening owing to the other mechanisms can be considered for calculating the shearing stress of the precipitates. The strengthening (σ_m) contributed by the misfit (ε) between matrix and precipitate can be determined using the relations [108] ,

$$\sigma_m = M\chi(\varepsilon\mu)^{3/2}\left(\frac{<r>fb}{T}\right) \quad , \tag{2.11a}$$

$$\varepsilon = \frac{2}{3}\left(\frac{a_p - a}{a}\right) \quad , \tag{2.11b}$$

where M is the Taylor factor that generally assumed a value of 4 for zirconium alloys in the case of uniaxial tensile testing. However, the value of M for biaxial loading is not available in the literature. Therefore, M is assumed to be 4 here. χ is a constant whose value is 2.5, μ is the shear modulus at the test temperature, $<r>$ and f are the average radius and the volume fraction of precipitates, T is the line tension of dislocations, which is roughly equal to $\frac{1}{2}\mu b^2$ and a and a_p are the lattice parameters of the matrix and precipitate respectively. The value of $<r>$ is 32 nm obtained from the precipitate size distribution. The volume fraction (f) of the β-Nb precipitates corresponding to 1.5wt% of Nb in HANA-4 calculated from Zr-Nb phase diagram using the lever rule is about 1% at 450 °C. Substituting the values of μ, a and a_p given in Table 2.3, the stress required to shear the β-Nb precipitates that are hardened by the misfit is calculated to be 363 MPa at 450 °C. For comparison, the effective stress at the transition point between regimes II and III calculated from the hoop stress using the Von Mises criteria is 53 MPa, which is about seven times smaller than the shearing stress of the precipitates hardened by the misfit. With respect to the chemical strengthening mechanism, a simple model equating the work done by the dislocations to create the new particle-matrix interface owing to particle shear would give the following relation for calculating the stress (σ_c) required for particle shearing [109],

$$\sigma_c = \frac{M\pi\gamma_s<r>}{2b\lambda} \quad , \tag{2.12a}$$

and

$$\lambda = \left(\sqrt{\frac{\pi}{f}} - 2\right)\sqrt{\frac{2}{3}}<r>. \tag{2.12b}$$

Here γ_s is the particle-matrix interfacial energy and λ is the average inter-precipitate spacing. The interfacial energy for the Zr matrix and β-Nb precipitates was obtained from the literature to be $0.19 \, J/m^2$ [106, 110], which is assumed for the newly formed interface due to particle sharing in HANA-4 as well. Thus, the stress required to shear the β-Nb precipitates in HANA-4 was calculated to be 308 MPa. Similarly, the stress (σ_{mo}) needed to shear the precipitates strengthened by modulus hardening can be stated as [111],

49

$$\sigma_{mo} = 0.0055 M \left(\frac{f}{T}\right) \left(\mu_p - \mu\right)^{\frac{3}{2}} b \left(\frac{<r>}{b}\right)^{\frac{3m}{2}-1} , \tag{2.13}$$

where μ_p and μ are the shear modulus of the precipitate and matrix respectively and m is a constant whose value is equal to 0.85. Substituting the modulus values from Table 2.3, the stress required to shear the β-Nb precipitates strengthened by modulus hardening is determined to be about 301 MPa, which, similar to the case of misfit hardening and chemical strengthening, is several times higher than the observed stress at the transition between regimes II and III from the creep experiments. Based on these calculations, the precipitate shearing as a mechanism to bypass the precipitates in regime III of HANA-4 can be discounted. In addition, the crept microstructure of the specimens from regime III still revealed essentially rounded precipitates supporting that the particle shearing is not an active mechanism for dislocations to bypass the precipitates in regime III.

Table 2.3 Lattice parameters and shear modulus of the Zr matrix and β-Nb precipitates

Parameter	Zr matrix	β-Nb precipitates
Lattice parameter, Å	a=3.23 [105]	a_p = 3.28 [106]
Shear modulus at 450 °C, GPa	μ = 25 [89]	μ_p = 30 [107]
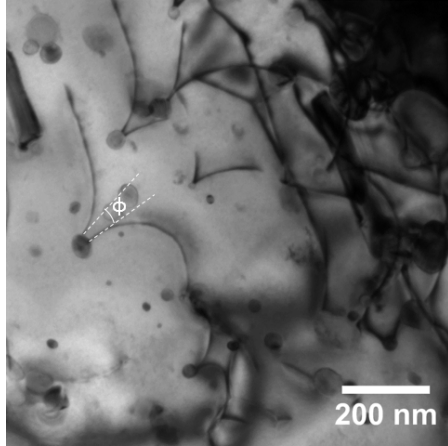
Figure 2.18.
TEM micrograph of the crept specimen at 99 MPa and 450 °C in regime III (n=4.5) showing dislocations pinned by the precipitates. As seen, the breaking angle (φ) is close to zero for all dislocations suggesting that they might bypass the precipitates through the Orowan mechanism.

The second kind of mechanism by which dislocations can bypass precipitates is through the well-known Orowan bowing, for which the required stress (σ_{O-A}) is given by the Orowan-Ashby model [83],

$$\sigma_{O-A} = M \frac{0.83\mu b}{2\pi(1-\nu)^{0.5}} \frac{1}{\lambda} \ln\left(\frac{\sqrt{\frac{2}{3}}<r>}{2b}\right) , \tag{2.14}$$

where ν is the Poisson ratio (0.34). A similar volume fraction of the precipitates (1%) is assumed at 500 °C since the difference between them is insignificant. Substituting the other values of the parameters in equation (2.14), the stresses necessary for the Orowan-bypass are determined to be 51 MPa and 48 MPa respectively at 450 °C and 500 °C. On the other side,

50

the effective stress at the transition point between regimes II and III are obtained to be 53 MPa and 43 MPa at 450 °C and 500 °C respectively. A good agreement between the experimental stress values with the ones calculated from the Orowan-Ashby model indicates that the dislocations bypass the precipitates through the Orowan-bowing mechanism in regime III and also, unlike in regime II, dislocations bypassing the precipitates using climb is not the rate-controlling mechanism in regime III. Additionally, the dislocations, which were still pinned by the precipitates in regime III, were observed to make a breaking angle (ϕ) – the angle between the two arms of the dislocations bowing around the precipitate as depicted in Figure 2.18 – close to zero suggesting that the precipitates might act as impenetrable obstacles. As a result, it is likely that the dislocation arms might pinch off to cross the precipitates through the Orowan bowing mechanism [84].

2.4.5   Creep threshold stress

A distinct feature that has been noted in the creep behavior of several precipitation hardened and dispersion hardened materials is the existence of a threshold stress at the low stress levels, below which the creep rate would drop at an increasing rate to a negligible value. The origin of such a threshold stress can be related to any of particle shearing, dislocation climb-controlled bypass or dislocation-particle detachment [97]. According to the model by Rösler and Arzt [98], which was derived for the general climb of dislocations over precipitates, an expression for the creep threshold stress (σ_{th}) was obtained in the form of,

$$\frac{\sigma_{th}}{\sigma_{O-A}} = \frac{<r>}{2\lambda} .$$
(2.15)

The origin of the threshold stress was attributed to the stress required for a small increment in the length of the dislocation line while climbing, which is necessary to keep up a minimum energy configuration. This relation given in equation (2.15) could be applied to HANA-4 since general climb of dislocations has been suggested to occur in regime II. Accordingly, the threshold stress for HANA-4 calculated using equation (2.15) is about 4 MPa in all the test temperatures employed in this study if the very small difference in the stress values arising due to the variance in temperatures is neglected. However, as seen from the creep data of HANA-4 at 500 °C, the creep rates in regime II transit into regime I, where diffusional creep mechanism was suggested to be operative, at a stress of 19 MPa. It can thus be argued that the threshold stress arising from the general climb process in regime II would not be revealed in the case of HANA-4. Alternately, Coble creep has become the rate-controlling step at low stresses as shown by the model predictions. This can be justified by considering the fact that general climb and Coble creep mechanisms proceed in parallel and that the faster mechanism would dictate the creep rate. Thus, Coble creep proceeds at a faster rate than the dislocation-based mechanism below the applied stress of 19 MPa.

2.5   Conclusions

The creep behavior of newly-developed HANA-4 (Zr-1.5% alloy) cladding has been investigated with a focus on identifying the transitions in creep mechanisms. Biaxial creep tests on HANA-4 tubes were conducted using internal pressurization of closed-end tubes to gather the steady state creep data over a range of hoop stresses, $8.38 \times 10^{-5}E - 2.87 \times$

$10^{-3}E$, at three different temperatures: 400 °C, 450 °C and 500 °C. The mechanistic creep parameters such as stress exponent (n) and activation energy (Q_C) were then determined from steady state creep rates. Based on the variance in stress exponent with respect to the applied stress, three regimes have been identified: a stress exponent close to 1 at low stresses increased to 3 at the intermediate stresses, which became 4.5 at high stresses. These regimes are referred to as I, II and III respectively. An activation energy value of 226 kJ/mol was evaluated for regimes II and III, which lies close to that for self-diffusion (Q_L) in α-Zr alloys. Further, TEM analyses of crept microstructures and comparison of experiments results with standard models were undertaken to find out the rate-controlling mechanisms. The following are the important observations from this study.

1) In regime 1, Coble creep has been suggested as the dominant mechanism based upon the stress exponent close to 1 and the fine grain size in HANA-4. As well, a good correlation between the experimental rates in regime I with the Coble creep model predictions substantiated the proposal.

2) At intermediate stresses, the crept microstructure revealed a uniform distribution of dislocations throughout grain interior pinned by the precipitates suggesting that dislocations bypassing precipitates is the slower process than the glide between precipitates. Further, n=3 and $Q_C=Q_L$ in regime II indicates dislocations climbing over the precipitates as the rate-controlling mechanism in accordance with the model by Rösler and Arzt. Thus, for the first time, we show that the creep behavior of a Zr-Nb alloy is similar to that of certain precipitation-hardened materials but not of a class-A alloy (viscous glide or microcreep).

3) With n=4.5 and $Q_C=Q_L$ in regime III that occurred at high stresses, recovery of dislocations through climb as characterized by the Weertman model is identified as the rate-controlling mechanism. A good prediction of the experimental creep rates by the Weertman model and the TEM analyses, which revealed sub-boundaries and networks formed by dislocations, support the proposed mechanism.

4) The critical stress of transition from regime II to regime III was found to be equivalent to that required for the activation of the Orowan bypass mechanism by which dislocations could bypass the precipitates without an involvement of the dislocation climb process.

5) A low creep threshold stress of ~4 MPa was estimated based on the general climb model of Rösler and Arzt at the test temperatures. However, the threshold stress possibly would not be revealed at the calculated stress owing to the dominance of Coble creep at these low stress levels (<19 MPa) at 500 °C.

52

3   Effect of hydrogenation on the creep behavior of HANA-4

Abstract

The effect of hydrogenation of the biaxial creep behavior of HANA-4 was studied using internal pressurization of closed end tubes by applying a range of hoop stresses (27 MPa to 156 MPa) at two temperatures: 400 °C and 500 °C. Two HANA-4 tubes were hydrogenated using the electrolytic method respectively with ~387 ppm and ~715 ppm of hydrogen while HANA-4 tubes without hydrogenation were utilized as the test specimens for comparison.   Further, high temperature XRD experiments were conducted on the hydrogenated HANA-4 specimens to detect the dissolution limit of the hydride phase. A collective examination of the results of the creep tests and the XRD experiments shows that hydrogen fully present in the solid solution at the creep temperature enhances the creep rate of HANA-4, whereas hydrogen present as both hydride and dissolved hydrogen reduces the creep rate regardless of the applied stress. The rationale behind the creep behavior of hydrogenated HANA-4 has been suggested from models.

3.1   Introduction

Zirconium (Zr) alloys are the backbone materials for the water-cooled thermal reactors. They are used for fuel-element cladding and in-core structural components in water-cooled nuclear reactors. Low neutron absorption cross-section, attractive mechanical properties and good corrosion resistance make Zr-based alloys the best possible cladding material in modern thermal nuclear reactors [52]. Over the years, various alloying elements have been added in Zr to make alloys to sustain in the highly diverse atmosphere in the nuclear reactor for long time. Zircaloys with Sn and Fe as primary alloying elements are widely used as fuel cladding material. Zr2.5%Nb alloy is used as pressure tube material for pressurized heavy water reactors (PHWRs). There are some new generation Zr alloys used in nuclear applications like Zirlo (Zircaloy with Nb), M5 (Zr-1Nb), etc. All these alloys used in the reactor undergo several degradation mechanisms including radiation damage, corrosion, etc. These limit their life in the reactor as well as during dry storage of UNF.
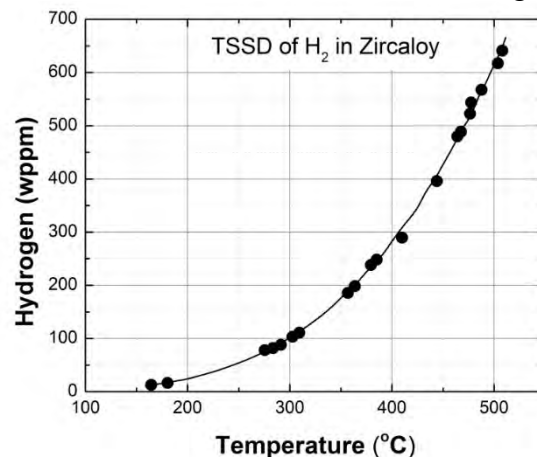

Figure 3.1. Terminal Solid Solubility curve of H in Zircaloy-2 [3]

53

Water (Light or Heavy) is used as coolant and moderator in the thermal reactors. In the reactor environment, Hydrogen (H_2) is released from water either due to radiolysis or from the following corrosion reaction with Zr:

$$Zr + 2H_2O \rightarrow ZrO_2 + 2H_2 \tag{3.1}$$

Zr is an exothermic occluder of hydrogen, which means that hydrogen is more stable in solution in the Zr matrix than it is as hydrogen gas. Enthalpy of solution for H_2 in Zr is -12.2 kcal/mole for hexagonal closed packed (hcp) α-Zr [112]. Therefore, Zr alloys pick up the hydrogen generated in the coolant. Solubility of H_2 in a Zr alloy is dependent on temperature. Hydrogen atoms are located at tetrahedral sites in the hcp zirconium lattice up to solubility limit. The maximum solubility of H_2 in Zr is described by Terminal Solid Solubility (TSS) and Figure 3.1 shows the variation of TSS for dissolution of H_2 in Zircaloy [113].
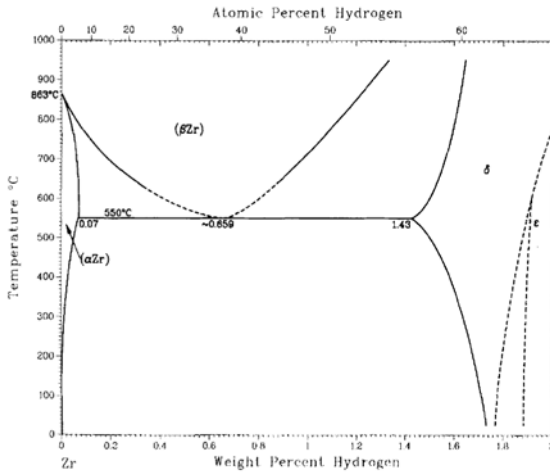

Figure 3.2. Zr-H phase diagram [4]

Table 3.1. Physical Characteristics of hydrides in Zr [5]

Hydride	Crystal Structure	Lattice parameters (nm)
δ	FCC	a = 0.4778
γ	Tetragonal	a = 0.4596 c = 0.4778
ε	Tetragonal	a = 0.4980 c = 0.4445

It can be seen that at lower temperatures hydrogen has very low solubility in Zircaloy but with increasing temperature it increases almost in an exponential fashion. This behavior is similar in other Zr alloys. Once the H_2 concentration exceeds the TSS limit, hydride precipitates are formed in the alloy. Figure 3.2 shows the Zr-H phase diagram [114]. It shows that depending on the H_2 concentration and temperature, different types of precipitates are formed. Physical characteristics of different hydrides in Zr system are listed in Table 3.1 [115]. Among these three types of hydrides, δ-hydrides are most commonly observed. Hydride acquires plate shaped morphology and the broad face of the hydride plate coincides with certain crystallographic plane of hcp α-Zr crystal, which is called the habit plane.

Creep is considered to be one of the important degradation mechanisms of the nuclear structural materials during reactor operating and repository conditions [9]. The reactor components are designed to operate at stresses well below the yield stress at normal conditions. Therefore the only significant deformation is time dependent. The cladding and pressure tubes used in the reactors are subjected to various thermal and multi-axial stress conditions inside the reactor. During normal operation, a typical water reactor core experiences temperatures in the range of 290-350°°C and a system pressure of 15-16 MPa. In

54

addition, there are other sources of stresses e.g. the pressure of the coolant, internal pressure due to released fission gases, pellet-cladding mechanical interaction, etc. Creep-rupture is considered to be a potential cladding failure mode during dry storage [2]. The parameters that determine the possibility of creep rupture are: the cladding temperature during cask drying, depending on the drying procedure, the evolution of cladding temperature during long time storage depending on burnup and the previous cooling time, the cladding stresses due to the internal gas pressures depending on cladding wall, fuel duty and burnup, the creep strength of the cladding material that depends on its condition and composition. During vacuum drying after loading of the fuel into the cask, temperatures of 360-500°C may exist for hours depending on the drying procedure. During long time storage the temperature decreases from an initial value of 300-400°C to significantly lower values. The cladding hoop stress also decreases as a consequence of the decreasing temperature of the internal gas during this period. The initial value of hoop stress is in a range of 60-120 MPa.

The factors which are considered to affect the creep mechanism under dry storage condition are: Thermal creep, Effect of hydrogen on thermal creep, Effect of irradiation hardening on thermal creep, Irradiation damage recovery during the initial drying cycle(s) and during subsequent long term dry storage. Among them, the effect of hydrogen on the creep behavior of zirconium alloys is the interest of this study. Several investigations have thus far focused on understanding the effect of hydrogen on creep of various zirconium alloys, which have been reviewed by Sarkar et al [116]. For instance, Setoyama and Yamanaka have carried out indentation creep experiments on pure Zr specimens charged with 50, 144 and 185 ppm levels of hydrogen at 420 °C and 100-200 MPa [117]. The results revealed an increase in creep rate with the hydrogen amount without altering the stress exponents considerably, which suggested activation of similar creep mechanism in the specimens tested. It has to be emphasized that all the hydrogenated zirconium specimens in this study had hydrogen in the solid solution at 420 °C, which is the dissolution limit for ~350 ppm of hydrogen according to the TSS curve in Figure 3.1. A similar observation of increase in the creep rates was made from the creep experiments conducted by Bouffioux et al [118, 119] in annealed Zircaloy-4 sheet with 180 ppm of hydrogen at the stress of 120 MPa and at the temperature of 400 °C, at which the entire hydrogen dissolves into the solid solution. However, the creep rate was noted to be lesser for a Zircaloy-4 sheet with an increased hydrogen content of 500 ppm than the as-received Zircaloy-4 under similar test conditions. Hydrogen would be completely in the solid solution in the former case, whereas some of it would be precipitated as zirconium hydride in the latter case at the creep temperature of 400 °C. These results suggest that hydrogen in solid solution during creep would enhance the creep rate and, on the other hand, hydrogen present as precipitated hydride would reduce the creep rate in zirconium alloys. The preceding inference has been demonstrated to be applicable to several zirconium alloys using creep experiments and computational modeling [120, 121].

The objective of this study is to investigate the effect of hydrogen on the biaxial creep behavior of HANA-4, a recently developed Zr-1.5%Nb alloy by Korea Atomic Energy Research Institute (KAERI) for fuel cladding applications in advanced nuclear reactors [70-

55

73]. The biaxial creep behavior of annealed HANA-4 tubing has been studied recently at the temperature range 400 °C-500 °C with an emphasis on the transitions in creep mechanisms with the applied stress [122]. However, the data on how hydrogenation of HANA-4 would alter its creep deformation is not available in the literature. To this end, two HANA-4 tubes were hydrogenated using the electrolytic method respectively with ~387 ppm and ~715 ppm of hydrogen. Biaxial creep experiments were carried out through internal pressurization of closed-end tubes by applying a range of hoop stresses at two temperatures: 400 °C and 500 °C. Further, high temperature XRD experiments were conducted on the hydrogenated HANA-4 specimens to detect the dissolution limit of the hydride phase. A collective examination of the results of the creep tests and the XRD experiments confirms that hydrogen fully present in solid solution at the creep temperatures enhances the creep rate of HANA-4, while hydrogen present as both hydride and dissolved hydrogen reduces the creep rate regardless of the applied stress, which is in line with the previous investigations on this subject.

3.2   Materials and experiments

HANA 4 tubes with an outer diameter (D_o) of 9.50 mm and a wall thickness (t) of 0.57 mm were received from KAERI in cold-worked and stress relieved condition. The as-received tubes were annealed at 537 °C for 4 hours inside a vacuum furnace continuously purged with argon gas to reduce their oxidation. The chemical composition and the microstructural analysis of annealed HANA-4 vis-à-vis grain-size distribution, texture measurements and β-Nb precipitate size distribution were presented in Section 4.2.

3.2.1   Electrolytic hydrogenation process

A schematic diagram and a photograph of the electrolytic set-up used for hydrogenation are shown in Figure 3.3. A flow chart depicting the sequence of the hydrogenation process and an image of a hydrogenated HANA-4 are given in Figure 3.4. HANA-4 tubes in cold worked-stress relieved condition were charged with hydrogen using the electrolytic method in which the tubing was suspended into an electrolyte of 0.4 N sulphuric acid solution and connected to the negative terminal of a constant current source as cathode [123]. A lead cylinder as anode was suspended in a way that its inner wall remains at equidistant from the HANA-4 tubing, which helps in attaining a constant current density across the surface of the tubing. In principle, the hydrogen positive ions from the sulphuric acid solution would migrate to the tubing that is cathode and react with its surface to form an outer layer of zirconium hydride. The tubing and the lead cylinder were earlier cleaned thoroughly to remove any foreign matter from their surface such as oxide scale, dirt and grease in order to accomplish a proper current flow through the circuit as well as to facilitate a good adherence of the hydride layer on the tube surface. To this end, pickling of HANA-4 tubing was carried out by immersing it into an acidic solution consisting of 45 vol% nitric acid, 45 vol% water and 10 vol% hydrofluoric acid for few seconds. The pickling process was also useful in removing any scratches present on both outside and inside surfaces of the tubing. Further, the surfaces of the lead cylinder were polished using sand-papers started with coarse (300) to fine grit (800) to remove any oxide scale present. Subsequently, the tubing

and the lead cylinder were cleaned separately using an ultrasonic cleaner for 20 mins each by immersing first into acetone and then into ethanol for degreasing their surfaces.

As shown in Figure 3.3, a constant current density of 0.2 A/cm^2 was supplied through the electrolytic set-up. The electrolyte bath was maintained at a temperature of 65 °C using a heater and an immersion thermometer and was constantly stirred using a magnetic stirrer to uphold its chemical and thermal homogeneity. Figure 3.4 summarizes the procedure used in the hydrogenation process and includes a typical hydrogenated tubing. Using this method, two tubes were charged with hydrogen by running the electrolytic process for 2 days and 7 days respectively, which produced a layer of zirconium hydride on the surfaces with thicknesses of 20 μm and 30 μm respectively. An X-Ray diffraction (XRD) scanning on the surface of the tubing revealed that the hydride layer composed of $ZrH_{1.6}$ (δ-hydride) having FCC crystal structure (Figure 3.5).
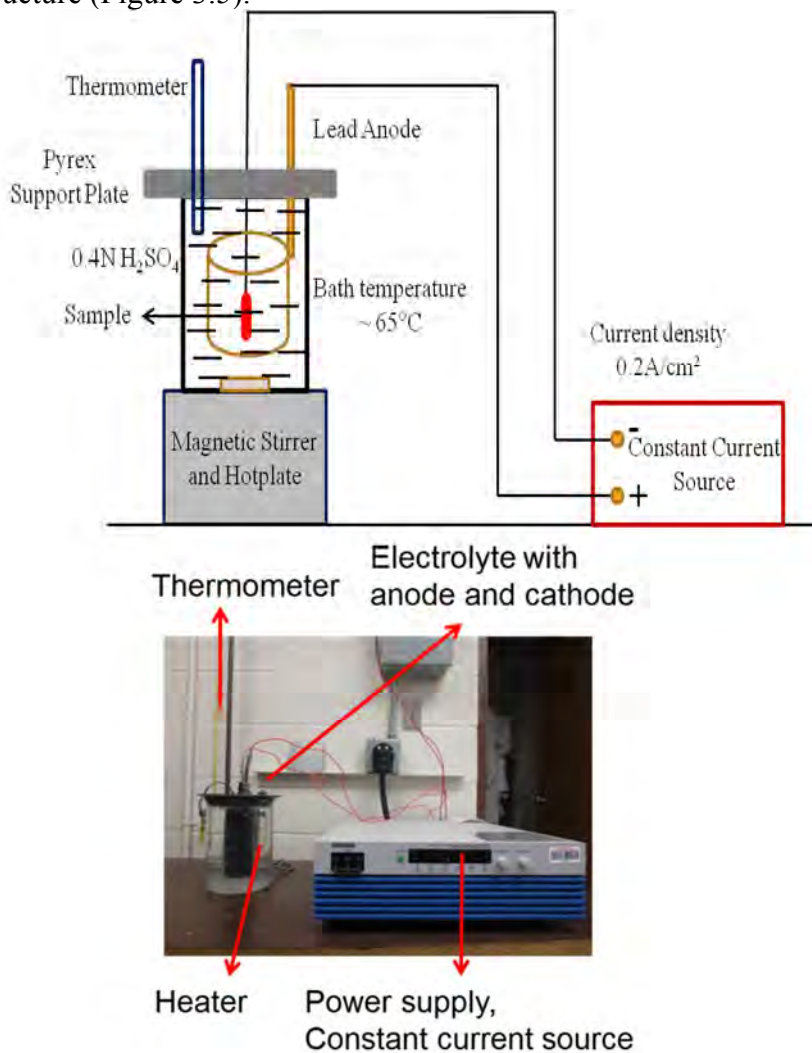

Figure 3.3. Schematic diagram (top) and photograph of the electrolytic set-up (bottom) used for hydrogenation of HANA-4 tubing
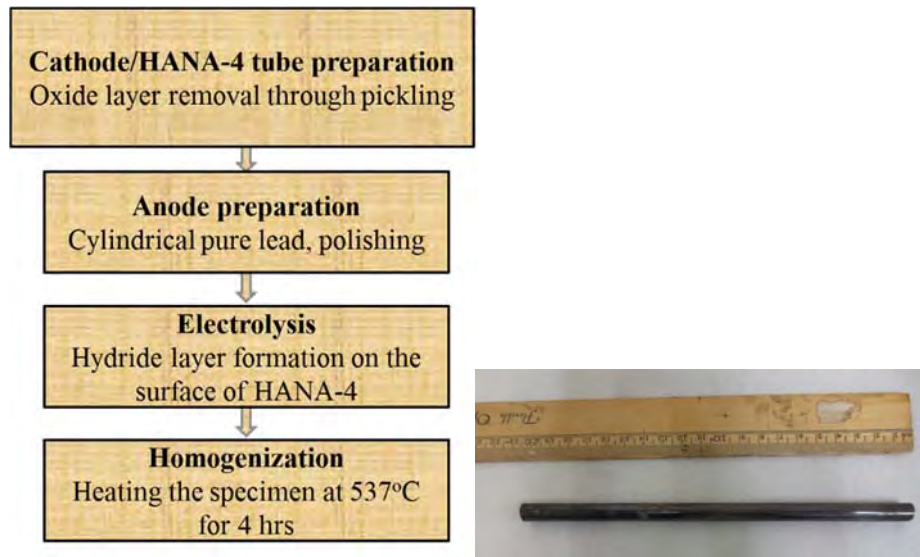
57

Figure 3.4. Flow chart (left) depicting the sequence of the hydrogenation process and a hydrogenated HANA-4 tubing
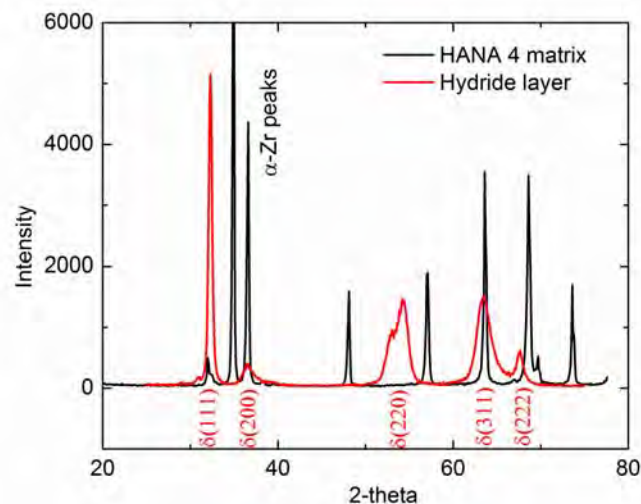

Figure 3.5. XRD patterns obtained from the HANA matrix and the hydride layer at the surface of HANA-4 tubing formed by the electrolytic method

The tubes with hydride layer were then annealed at 537 °C for 4 hours inside a vacuum furnace continuously purged with argon gas to reduce their oxidation. The annealing step served two purposes: firstly, the thermal annealing process activates the diffusion of hydrogen from the outer hydride layer into the HANA-4 matrix, which leads to the formation of hydrides into a rim structure spread across the tube wall as shown in Figure 3.6. Secondly, the annealing process facilitates a direct comparison between the creep data obtained from hydrogenated HANA-4 and HANA-4 without hydrogenation which were annealed at identical conditions. Further, samples cut from the hydrogenated tubes were consigned to Applied Testing Services (ATS), Georgia, for quantifying the hydrogen amount in them

58

through inert gas fusion method. According to the analysis, the average hydrogen amounts were determined to be 387 ppm and 715 ppm in the tubes that were in the electrolytic process respectively for 2 days and 7 days. These tubes are hereafter referred to as H-387 and H-715 respectively. The HANA-4 tubes without hydrogenation, which were utilized as controlled specimens in the creep experiments, will be referred to as HANA-4.
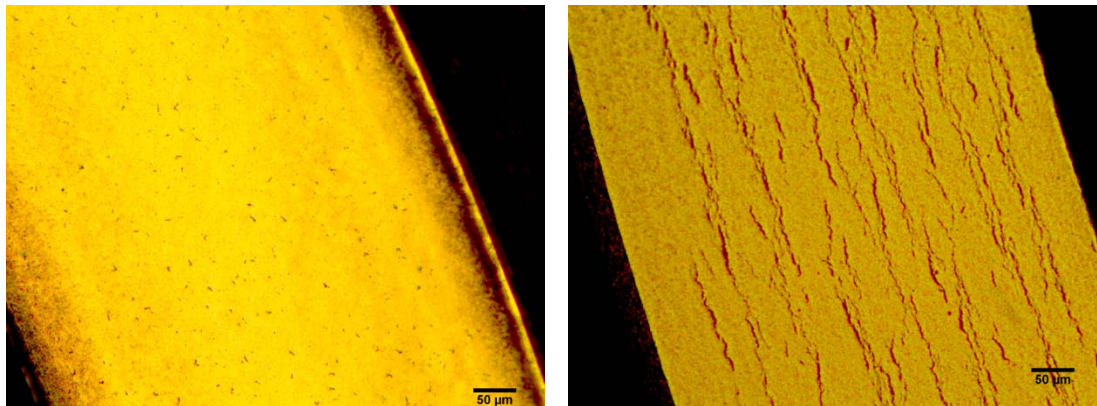

Figure 3.6. Optical micrographs of as received HANA-4 (left) and hydrogenated HANA-4 (right) with ~387 ppm of hydrogen

3.2.2 High temperature XRD experiments

It has been shown from the previous investigations that the state in which hydrogen present in zirconium alloys, dissolved in solid solution and precipitated hydride, could influence their creep behavior [118, 119]. Therefore, a knowledge on the state of hydrogen in microstructure during creep becomes essential. As seen from Figure 3.1, the solubility of hydrogen in zirconium matrix was found to increase exponentially with the raise in temperature [124, 125]. It is relevant to note that alloying elements, especially niobium, were found to enhance the TSS of hydrogen in zirconium [126]. Being alloyed with niobium, it could be expected for HANA-4 to have higher solubility limits for hydrogen than the zirconium alloys without niobium. In order to detect the TSS of hydrogen in HANA-4, high temperature X-ray diffraction experiments were conducted on the hydrogenated tubes using a Panalytical Empyrean diffractometer equipped with a high temperature holder which is capable of heating specimens up to 1200 °C in vacuum or argon atmosphere and simultaneously collecting the diffraction data. The diffractometer is equipped with a special line detector (PIXcel[1D]) capable of collecting diffractograms at faster rate with low noise than the conventional detectors. The diffraction experiments on the H-387 and H-715 specimens were carried out by heating them at a rate of 10 °C/min to above their hydride dissolution temperature. The XRD scanning over the 2θ range of 31°-33.5° to capture the (111) δ-hydride peak was programmed to take place for every 10 °C in isothermal condition. The change in peak intensity was observed as a function of temperature.

3.2.3 Biaxial creep tests

The hydrogenated tubes with their ends closed using Swagelok fittings were bi-axially crept by internally pressurizing them with argon gas to various hoop stresses to

59

determine the steady state creep rates at two temperatures: 400 °C and 500 °C. The test matrix for the H-387, H-715 and HANA-4 specimens is given in Table 3.2. In the case hydrogenated HANA-4, all creep tests were conducted on each single specimen of H-387 and H-715 by changing the applied stress and/or the temperature once the steady state creep rate was attained in the previous test.

3.3   Results

3.3.1   High temperature XRD results

The results of the high temperature XRD experiments conducted on the hydrogenated HANA-4 specimens are shown as intensity versus 2-theta plots at various temperatures and temperature versus 2-theta plot which portrays the peak intensity using a color scheme in Figures 3.7 and 3.8 respectively for H-387 and H-715. As seen from the figures 3.7a and 3.7b pertained to H-387, the intensity of the hydride peak keeps lowering down till it disappears into the background intensity at about 395 °C, which is the dissolution limit of the hydride phase according to the XRD experiment. However, the intensity of the peak originating the zirconium matrix exists without any significant change for the entire range temperature applied in the experiment. Another notable feature associated with the hydride peak is its shifting towards higher 2-theta with the temperature rise, indicating that the lattice parameter of the hydride phase decreases on heating.
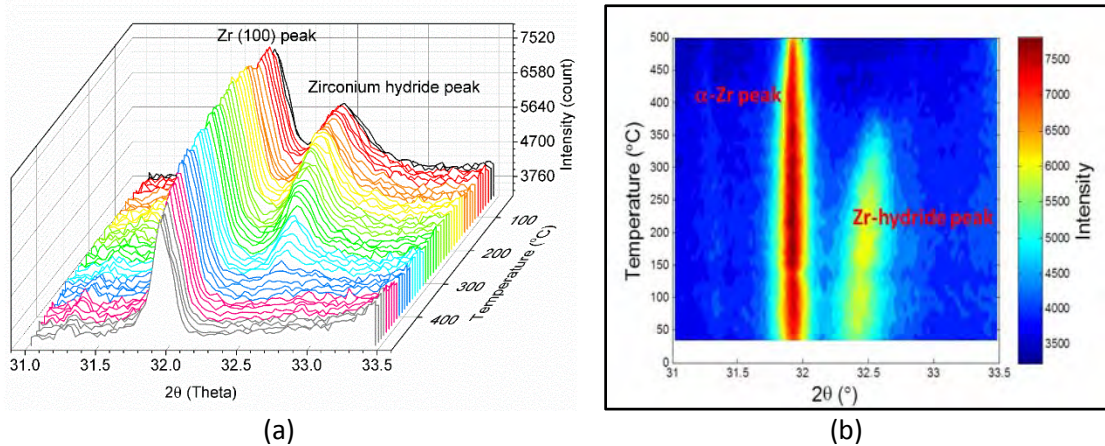

| (a) | (b) |

Figure 3.7. XRD data (a) and a contour plot (b) as a function of temperature and for H387

In the case of H-715, the intensity of the zirconium hydride peak appears till the temperature reaches to about 535 °C (Figures 3.8a and 3.8b). Based on the XRD results, the dissolution limits of the hydride phase in the hydrogenated HANA-4 specimens with 387 ppm and 715 ppm of hydrogen respectively are about 395 °C and 535 °C. However, a detection limit of ~3% pertaining to XRD phase analysis suggests that the actual dissolution limits could be higher than that determined from the XRD experiments. In view of this, H-387 could possess some hydride phase with major portion of hydrogen dissolved into the solid solution during creep at 400 °C. However, the entire hydrogen in H-387 would be dissolved into the solid solution during the creep tests at 500 °C. On the other hand, H-715 would have its hydrogen as hydride as well as in the solid solution during the creep tests both at 400 °C and 500 °C.

60

Table 3.2. The test matrix and creep results of unhydrogenated and hydrogenated HANA-4.

Unhydrogenated HANA-4				Hydrogenated HANA-4 (387 ppm)				Hydrogenated HANA-4 (715 ppm)			
T, °C	σ_θ, MPa	$\dot{\varepsilon}_s$, s^{-1}	ε, %	T, °C	σ_θ, MPa	$\dot{\varepsilon}_s$, s^{-1}	ε, %	T, °C	σ_θ, MPa	$\dot{\varepsilon}_s$, s^{-1}	ε, %
400	90	7.3×10^{-9}	0.8	400	90	4.0×10^{-9}	0.3	400	90	2.3×10^{-9}	0.3
400	122	2.1×10^{-8}	1.5	400	121	1.1×10^{-8}	0.8	400	121	6.8×10^{-9}	0.3
400	156	6.2×10^{-8}	1.7	400	150	3.7×10^{-8}	0.6	400	151	2.2×10^{-8}	0.4
500	30	2.9×10^{-8}	1.2	500	27	2.7×10^{-8}	1.2	500	35	2.3×10^{-8}	1.1
500	44	8.3×10^{-8}	1.2	500	43	1.2×10^{-7}	2.6	500	45	3.8×10^{-8}	0.7
500	53	1.4×10^{-7}	2.8	500	53	2.3×10^{-7}	1.5	500	54	7.2×10^{-8}	0.5
500	69	4.8×10^{-7}	4.9	500	70	8.1×10^{-7}	1.9	500	72	2.0×10^{-7}	0.7
500	90	1.4×10^{-6}	7.4	500	90	2.8×10^{-6}	2.6	500	90	5.5×10^{-7}	0.5
500	90	1.3×10^{-6}	10.8								

T- Temperature, σ_θ – Hoop stress, E – Elastic Modulus, $\dot{\varepsilon}_s$ – Steady state creep rate, ε – Total strain

3.3.2 Biaxial creep results

The representative creep curves of H-387 and H-715 obtained at 400 °C and 500 °C are given in Figure 3.9. The creep curves of the controlled specimen HANA-4 obtained under similar testing conditions of stress and temperature are also added in Figure 3.9. As seen from the creep curves at 121 MPa and 400 °C, the creep strain accumulated at a given time and, as a result the steady state creep rate become lesser as the hydrogen content increases in HANA-4. A similar trend has been observed for the tests at various stresses at 400 °C for the H-387 specimen. In contrast to this, as the test temperature is raised to 500 °C, the H-387 specimen crept at a higher steady state creep rate than HANA-4 as shown in the representative creep curve at 53 MPa and 500 °C in Figure 3.9b. In the case of H-715 specimen, the accumulated creep strain and the steady state creep rate were determined to be at the lower side than that of HANA-4 at both 400 °C and 500 °C (Figure 3.9). These trends are similar for varied stresses as noted below.
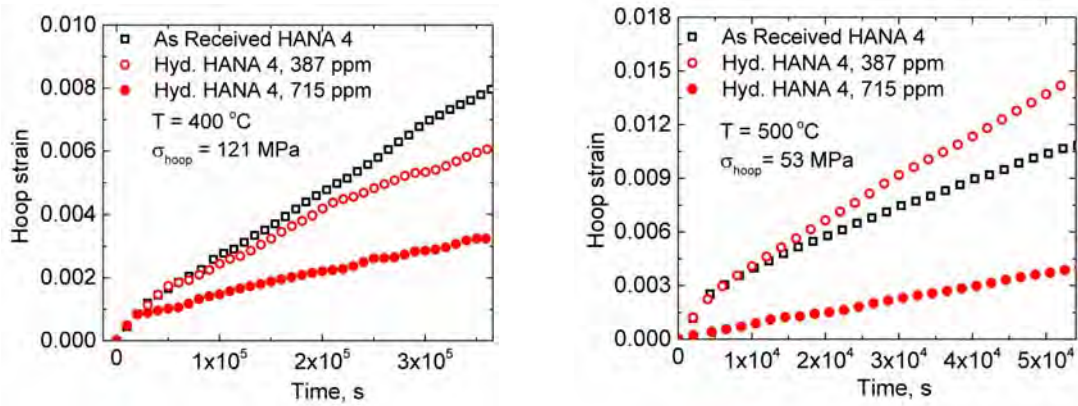

Figure 3.8. Creep curves for annealed and hydrided HANA-4 at 121 MPa and 400 °C (left) and 53 MPa and 500 °C (right)

The steady state creep rates of the H-387 and H-715 specimens calculated at the stress and temperature conditions employed in this study are listed in Table 3.2. As noted, the steady state creep rates of H-387 and H-715 were reduced by about 2 and 3 times from that of HANA-4 at 400 °C. In the creep tests conducted at 500 °C, the steady state creep rates of the H-387 specimen increased by up to 2 times, while the creep rates of H-715 specimen decreased by 1.3-2.6 times than that of HANA-4. The steady state creep rate data were further analyzed to obtain the true stress exponent (n) from the general creep equation relating the steady state creep rate ($\dot{\varepsilon}_s$) with applied stress (σ) and temperature (T in K) that can be stated as,

$$\dot{\varepsilon}_S = \frac{AEb}{kT} \left(\frac{\sigma}{E}\right)^n e^{-\frac{Q_c}{RT}}, \tag{6.2a}$$

$$E = 95.92 - 0.0629(T - 273)\ GPa. \tag{6.2b}$$

In equation (2a), A is a constant, E is the temperature-dependent elastic modulus of Zr-2.5% Nb [89], b is the burgers vector ($3.23 \times 10^{-10} m$), k is the Boltzmann's constant and R is the gas constant. At a constant temperature and assuming the elastic-modulus to be invariant of hydrogenation, equation (2a) can be written in the form of,

$$\dot{\varepsilon}_s = A_1\ \sigma^n \tag{6.3}$$

62

From equation (3), the stress exponent is equivalent to the slope of the log-log plot between the steady state creep-rate versus the stress at a constant temperature as shown in Figure 3.10. The stress exponents obtained for the specimens with their corresponding stress ranges and temperatures are listed in Table 3.3, from which it can be noted that hydrogenation of HANA-4 with hydrogen amounts as high as 715 ppm used in this study has no considerable effect on the stress exponents obtained over the testing conditions. At 500 °C, an average stress exponent of 2.8 at the low stress range (27 MPa–53 MPa) increased to 4.3 at high stresses (53 MPa–90 MPa) for all the three specimens. From the creep tests conducted at high stresses and at 400 °C, an average stress exponent of 4.1 was estimated.
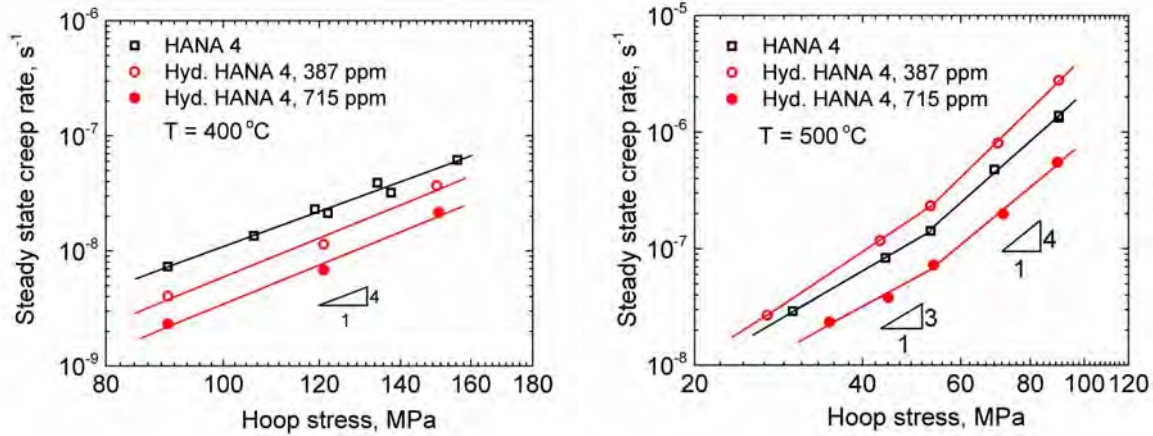

Figure 3.9. Steady state creep rate versus hoop stress at 400 °C (left) and 500 °C (right)

Table 3.3.
Stress exponents of HANA-4, H-387 and H-715 at various stresses and temperatures

Specimen	Stress exponent (n)		
	$T = 400$ °C σ_θ=90 - 156 MPa	$T = 500$ °C σ_θ=27 - 53 MPa	$T = 500$ °C σ_θ=53 - 90 MPa
HANA-4	3.8 ± 0.2	2.8 ± 0.03	4.7 ± 0.1
H387 (387 ppm of H)	4.3 ± 0.5	3.2 ± 0.03	4.2 ± 0.1
H715 (715 ppm of H)	4.3 ± 0.2	2.6 ± 0.4	1.0 ± 0.3

3.4 Discussion

It has been recently demonstrated that dislocation bypassing the β-Nb precipitates distributed in the microstructure through climb as the rate-controlling mechanism in the n=3 regime changes to dynamic recovery of edge dislocations by climb in the n=4.5 regime in HANA-4 [122]. The stress at the transition between these regimes at 500 °C was found to be equal to the stress required for dislocations to bypass the precipitates through the Orowan bowing mechanism. Based on the similar stress exponent values noted for HANA-4 and hydrogenated HANA-4 within the range of applied stresses (Table 3.4), it can be inferred that hydrogen present within the concentrations employed in this study would not alter the rate-creep mechanisms in HANA-4. As noted, the n=3 regime changes to the n=4.5 regime at a stress of ~53 MPa in all the HANA-4 and hydrogenated HANA-4 specimens at 500 °C indicating that the

63

presence of hydrogen has no influence on the critical stress required for the activation of Orowan mechanism.

In order to comprehend the effect of hydrogen on the steady state creep rates of HANA-4, a collective examination of the results of the creep tests and the high temperature XRD experiments on HANA-4 and hydrogenated HANA-4 was undertaken. While the hydrogenated HANA-4 specimen possess the zirconium hydride phase under the test temperature regardless of the amount of dissolved hydrogen, its creep rate is reduced in comparison with HANA-4. For instance, both the hydrogenated specimens (H-387 and H-715) would possess zirconium hydride distributed in the microstructure during the creep tests at 400 °C resulting in a decrease in the creep rates (Figure 3.10a). This observation is also applicable to the reduced creep rate measured for the H-715 specimen crept at the temperature of 500 °C (Figure 3.10b), at which the hydride phase is retained according to the XRD results. Further, the magnitude of reduction in the creep rate carries a direct proportionality with the amount of hydride present in HANA-4 as discussed earlier. Similar results have been demonstrated from the creep experiments on hydrogenated zirconium alloys in cold-worked stress relieved (CWSR) condition as well as in annealed condition having hydride phase at the test temperatures [118, 119]. For example, Bouffioux et al conducted uniaxial and biaxial creep experiments on Zircaloy-4 cladding tubes in CWSR condition charged with a range of hydrogen concentrations, 100-1100 ppm at room temperatures and at high temperatures, 350 °C and 400 °C [119]. It was revealed that the steady state creep rates of the hydrogenated Zircaloy-4 with hydrides under the test temperature decreased from that of Zircloy-4 as the hydrogen concentration increases. This conclusion has also been extended to the creep behavior of hydrogenated Zircaloy-4 in recrystallized condition [118]. Further, a numerical model developed by Mallipudi et al to investigate the effect of hydrogen on the creep behavior of Zircaloy-4 exhibited a decrease in the creep rate in the presence of hydride phase [127]. A plausible explanation for the reduction in creep rate of zirconium alloys with hydride phase could be attested to the hindrance of dislocation glide by the hydride phase. Owing to this effect, the dislocation velocity in materials with precipitated second phases was calculated to have an inverse relationship with the square of the volume fraction of the second phases in the n=3 regime according to the Rösler and Arzt model [98]. In the case of HANA-4 with the hydride phase during creep, it could be argued that the volume fraction of the hydride phase gets added to the already existing β-Nb precipitates resulting in a decrease in the dislocation velocity and thus the creep rate. Similarly, the presence of hydride phase is expected to prohibit the glide of dislocations and reduces the creep rate in the n=4.5 regime of HANA-4.

In contrast to the preceding observation, the steady state creep rates of HANA-4 were found to be enhanced while hydrogen is fully dissolved into the solid solution as noted from the creep deformation of the H-387 specimen at 500 °C. This result falls in line with that from the creep experiments conducted by Bouffioux et al and that from the numerical modeling by Mallipudi et al on Zircaloy-4 with hydrogen at the test temperatures above the dissolution limit of the hydride phase [118, 127]. An explanation for the increased creep strain could be extracted from the results of ab-initio calculations carried out by Domain et al to investigate the interaction between hydrogen and planar defects in α-Zr-H system [128]. This study has revealed that the atomic hydrogen in zirconium could be favorably trapped at the core of the screw dislocations owing to a strong binding energy between hydrogen and the stacking faults presented in the dislocations. As a result, the planar slip of the dislocations is enhanced in zirconium by the presence of atomic hydrogen possibly leading to a higher creep strain. However, it is interesting to note that hydrogen fully present in the solid solution of CWSR Zirclaoy-4 at the creep

64

temperature was measured to decrease the creep rate unlike in the case of annealed Zircaloy-4, for which the reasons are unknown.

This study shows that the presence of hydrogen as zirconium hydride would be beneficial to HANA-4 claddings as far as the steady state creep deformation is concerned during their in-reactor service and spent fuel storage. Since the creep life time before fracture has an inverse relation to the steady state creep rate according to the Monkman-Grant relationship [129], it can be expected that the creep life time of HANA-4 with hydride phase would be prolonged. Meanwhile, it is critical to note that the steady state creep rate is accelerated in HANA-4 with the presence of hydrogen in the solid solution, which carries a malign effect on its creep life time. Owing to the exponential increase in the TSS of hydrogen in Zr with raise in temperature, it can be predicted that Zr fuel claddings serving under untoward high temperature conditions such as Loss-Of-Coolant-Accident (LOCA) would have a deleterious effect from the dissolved hydrogen in terms of creep deformation. Additionally, hydrogen enhanced creep rate in Zr claddings merits attention while employing them in high temperatures reactors.

3.5 Conclusions

The effect of hydrogen on the biaxial creep behavior of HANA-4, a recently developed Zr-1.5%Nb alloy by KAERI for fuel cladding applications in advanced nuclear reactors was investigated. Two HANA-4 tubes were hydrogenated using the electrolytic method respectively with ~387 ppm and ~715 ppm of hydrogen. Biaxial creep experiments were carried out through internal pressurization of closed-end tubes by applying a range of hoop stresses (27 MPa to 156 MPa) at two temperatures: 400 °C and 500 °C. Further, high temperature XRD experiments were conducted on the hydrogenated HANA-4 specimens to detect the dissolution limit of the hydride phase. A collective examination of the results of the creep tests and the XRD experiments confirms that hydrogen fully present in solid solution at the creep temperatures enhances the creep rate of HANA-4, whereas hydrogen present as both hydride and dissolved hydrogen reduces the creep rate regardless of the applied stress. Preferential segregation of atomic hydrogen to the core of screw dislocations resulting in easy planar slip as proposed by ab-initio calculations was proposed as a possible rationale for the increase in the creep rates in the former case. On the other hand, the zirconium hydride phase acting as obstacles to dislocation glide leads to reduction in the creep rate in the latter case. However, no change in the rate-controlling mechanism in HANA-4 by the influence of hydrogenation has been proposed based on the comparable stress exponents obtained for all the specimens tested under identical conditions of stress and temperature.

65

4 Creep Mechanisms in Zircaloys: Application to dry storage of UNF

We can now apply the formulations described in the previous chapters for creep of Zircaloy-4 and Nb-modified Zircaloys in predicting the changes in hoop strains as a function of time during dry storage for a given set of time dependent temperature following removal from coolant pool and dry storage, and internal pressure due to fission gases. While a relatively modest increase with prolonged decrease in the temperature of the cladding during dry storage (Figure 4.1a) was used by Murty earlier [2], a more recent temperature profile reported by EPRI in a report on 'Spent fuel transportation applications – Assessment of Cladding performance,' is used as in Figure 4.1b [130]. We consider these temperature profiles along with a constant internal pressure of 60 MPa that covers a range of hoop stresses from $5x10^{-4}E$ to $7x10^{-4}E$ where both Zircaloy-4, Zirlo as well as HANA4 alloys exhibited a transition from viscous creep to dislocation dominated creep.
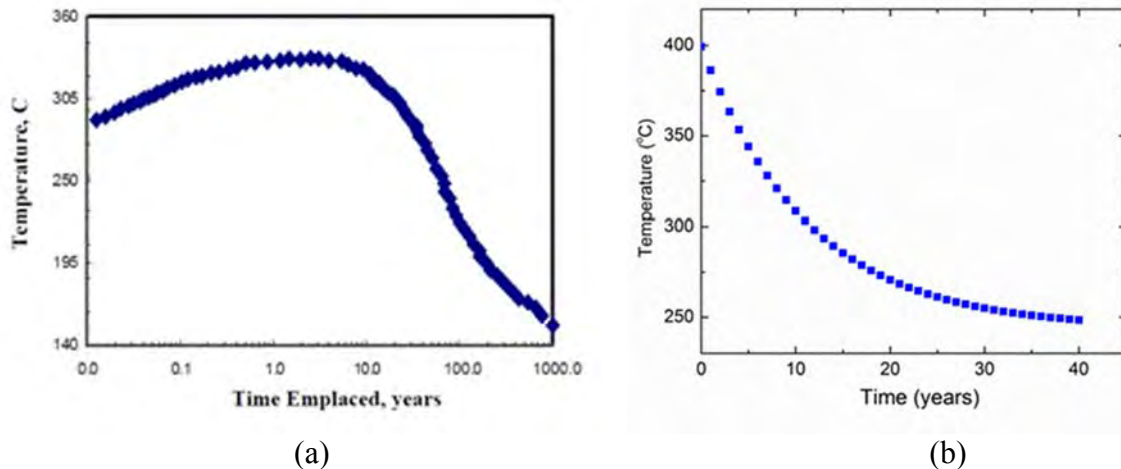

<div align="center">(a)   (b)</div>

Figure 4.1. Time dependences of clad temperature during dry storage
from Murty [2] (a) and EPRI [130] (b)
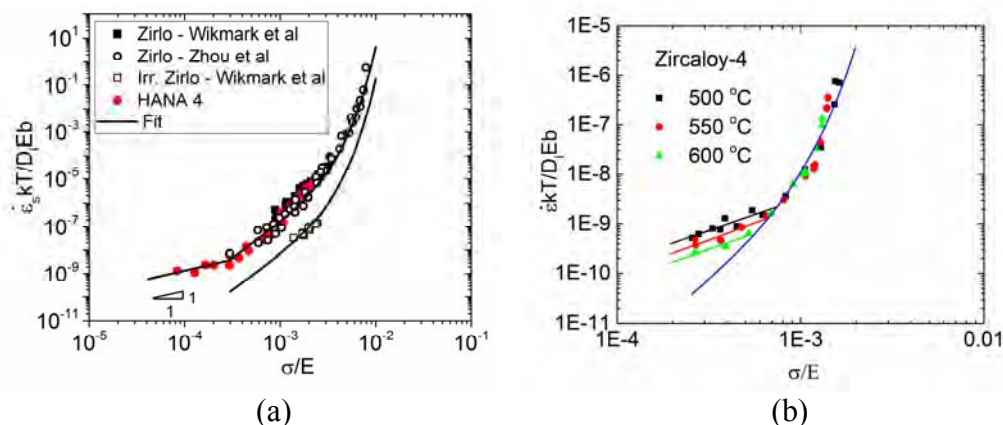

<div align="center">(a)   (b)</div>

Figure 4.2. Biaxial creep data on unirradiaated and irradiated Zirlo, and HANA4 (a) with model fits [131] and uniaxial creep data of Zircaloy-4 (b)

Figures 4.2a and 4.2b document creep results on Nb-modified Zircaloy-4 (both Zirlo and HANA4) and Zircaloy-4 along with model fits. It should be noted that the biaxial creep data of Zirlo obtained by Zhou et al [3]and Wikmark et al [131] correlate well with that of HANA-4

<div align="center">66</div>

tested in our study. The models defining the steady state creep rates pertinent to both diffusion and dislocation creep in these materials are given in Table 4.1. These are of course for steady state values and transient creep as well as transients in creep due to temperature changes need to be considered for dislocation creep mechanisms while they are negligible for diffusion creep operative at low stresses. In the case of dislocation creep, the transient creep strain (ε_T) and steady state creep strain were included in the strain (ε) calculation through the formulation,

$$\varepsilon = \dot{\varepsilon}_s t + \frac{k\varepsilon_T \dot{\varepsilon}_s t}{\varepsilon_T + k\dot{\varepsilon}_s t}$$

(4.1)

In equation 4.1, $\dot{\varepsilon}_s$ is the steady state creep rate and t is the time. k and ε_T assume values of 10 and 0.008 respectively.

Table 4.1. Equations used for calculating strain

Material	Creep Model	Fitting equation
Zircaloy-4	Coble	$\dot{\varepsilon}_{coble} = 693\left(\frac{E}{T}\right)\exp\left(-\frac{22600}{T}\right)\left(\frac{\sigma}{E}\right)^1$ (/hr)
	Dislocation	$\dot{\varepsilon}_{glide} = 11712\left(\frac{E}{T}\right)\exp\left(-\frac{31200}{T}\right)\left[\sinh 1937\left(\frac{\sigma}{E}\right)\right]^3$ (/hr)
Zirlo [131] Zirlo [3] HANA-4 Unirradiated Zirlo	Coble	$\dot{\varepsilon}_{coble} = 6085\left(\frac{E}{T}\right)\exp\left(-\frac{22600}{T}\right)\left(\frac{\sigma}{E}\right)^1$ (/hr)
Zirlo [131] Zirlo [3] HANA-4	Dislocation	$\dot{\varepsilon}_{glide} = 2.5\times10^7\left(\frac{E}{T}\right)\exp\left(-\frac{31200}{T}\right)\left[\sinh 590\left(\frac{\sigma}{E}\right)\right]^3$ (/hr)
Unirradiated Zirlo	Dislocation	$\dot{\varepsilon}_{glide} = 1.3\times10^6\left(\frac{E}{T}\right)\exp\left(-\frac{31200}{T}\right)\left[\sinh 590\left(\frac{\sigma}{E}\right)\right]^3$ (/hr)

Strain hardening model is considered to be applicable in comparison to time hardening although very little difference is noted in the final analyses. More details of the strain calculation can be seen in Refs [2] . A Matlab script written for the strain calculation is given in Appendix 1. Figures 4.3 summarizes the accumulated strains versus time during dry storage for Zircaloy-4 using the two temperature profiles shown in Figures 4.1a and 4.1b. Figures 4.4 and 4.5 summarize the corresponding results for unirradiated Zirlo and HANA-4 and irradiated Zirlo. It is clear that strain accumulations saturate at around 10 years of implacement while irradiation hardening leads to relatively lower levels of accumulated strains by a factor of ~3 as noted for Zirlo. It needs to be emphasized that Coble creep contributes predominantly to the total strain than dislocation creep after about 1year into dry storage for the irradiated Zirlo showing the significance of diffusion creep. These results clearly point out the importance of obtaining relevant creep data following radiation exposures in-reactor.
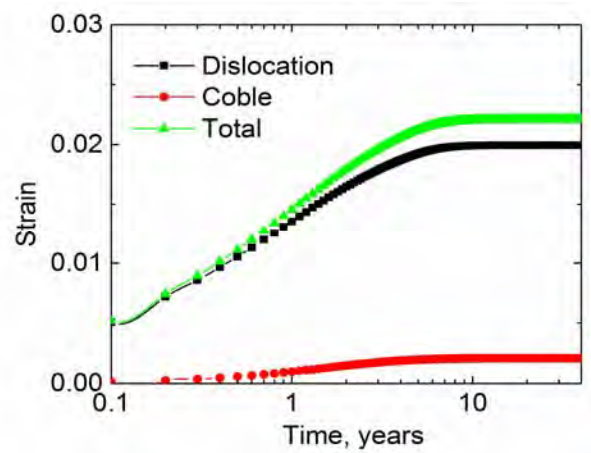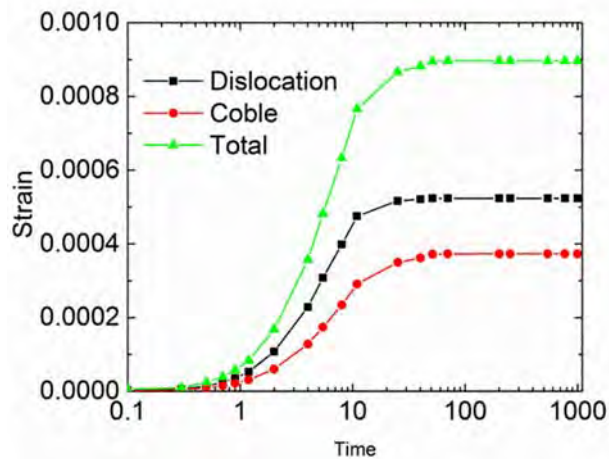
67

Figure 4.3. Creep strain predictions for unirradited Zircaloy-4 using temperature profiles of Figures 4.1a (left) and 4.1b (right)
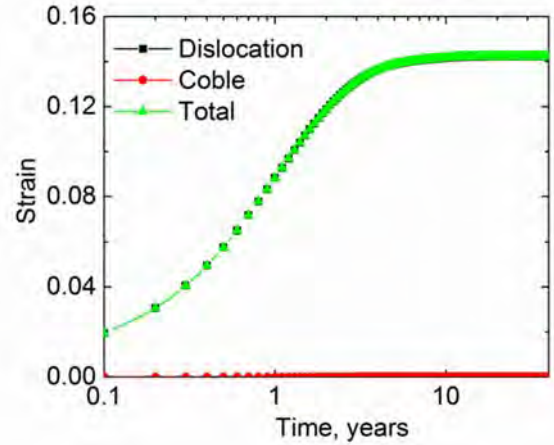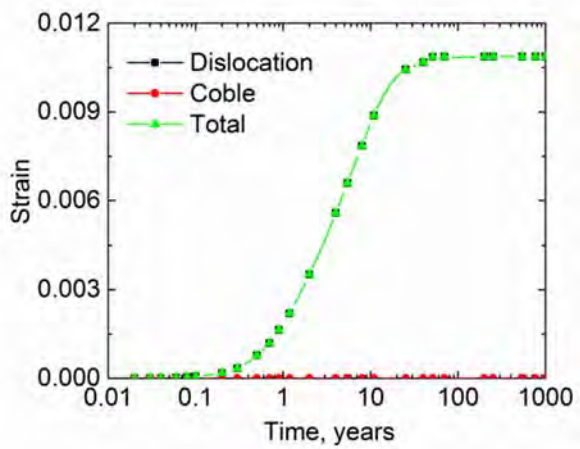

Figure 4.4. Creep strain predictions for unirradited Zirlo using temperature profiles of Figures 4.1a (left) and 4.1b (right)
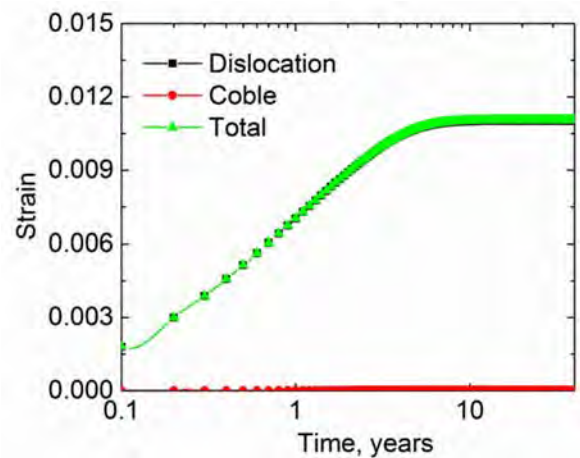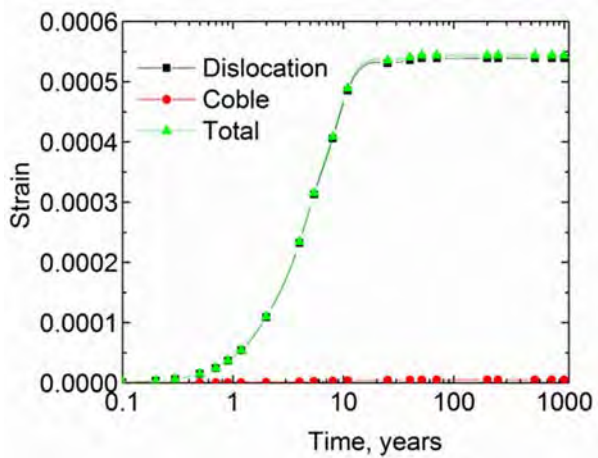

Figure 4.5. Creep strain predictions for irradited Zirlo using temperature profiles of Figures 4.1a (left) and 4.1b (right)

68

Appendix 1:

MATLAB Code for the strain calculation:

```
maxtime = 40; %max time in years
timeint = .1; %years, amount of time between measurements
stress = 60000000; %Pa
% the creep rate equation is in the form of
% rate = glideconst exp(-Qglide/T) (E/T) (sinh (sinhconst*(stress/E)))^3
glideconst = 11712;
%glideconst = 1.26391*10^8;
cobleconst = 693;
Qglide = 31200;
Qcoble = 22600;
sinhconst = 1937;
%sinhconst = 500;
k = 10;
strainT = .008;

%Construct time array
length = maxtime/timeint;
time = zeros(length,1);
x=0;
for i=1:length
    x = x + timeint;
    time(i)= x;
end
%Construct temperature array
temp = zeros(length,1);
for i=1:length
    temp(i) = 517.48 + 155.52*exp(-.0877*time(i)) - .6922575*time(i);
end
%Temp dependent elastic modulus
E = zeros(length,1);
for i=1:length;
    E(i) = (98.82-0.076*temp(i))*1000000000;
end
%Preallocate memory for various arrays
srateglide = zeros(length,1);
sratecoble = zeros(length,1);
scoble_i_i = zeros(length,1);
sglide_i_i = zeros(length,1);
scoble_i_i1 = zeros(length,1);
sglide_i_i1 = zeros(length,1);
straintotal = zeros(length,1);
accglide = zeros(length,1);
acccoble = zeros(length,1);
for i=1:length
    srateglide(i) = glideconst*(E(i)/temp(i))*exp(-
Qglide/temp(i))*(sinh(sinhconst*stress/E(i)))^3;
    sratecoble(i) = cobleconst*(E(i)/temp(i))*exp(-
Qcoble/temp(i))*(stress/E(i));
    sglide_i_i(i) = srateglide(i)*time(i)*365*24 +
(k*strainT*srateglide(i)*time(i)*365*24/(strainT+k*srateglide(i)*time(i)*365*2
4));
    scoble_i_i(i) = sratecoble(i)*time(i)*365*24;
end
for i=2:length
    sglide_i_i1(i) = srateglide(i)*time(i-1)*365*24 +
(k*strainT*srateglide(i)*time(i-1)*365*24/(strainT+k*srateglide(i)*time(i-
1)*365*24));
    scoble_i_i1(i) = sratecoble(i)*time(i-1)*365*24;
end
```

```matlab
accglide(1) = sglide_i_i(1);
acccoble(1) = scoble_i_i(1);
straintotal(1) = accglide(1)+acccoble(1);
for i=2:length
    accglide(i) = accglide(i-1)+sglide_i_i(i) - sglide_i_i1(i);
    acccoble(i) = acccoble(i-1)+scoble_i_i(i) - scoble_i_i1(i);
    straintotal(i) = acccoble(i)+accglide(i);
end
fprintf('Time      Total Strain\n')
for i=1:length;
    fprintf('%f %f\n', time(i),straintotal(i))
end
semilogx(time,straintotal,time,accglide,time,acccoble,'LineWidth',2);
leg = legend('Total Strain', 'Acc. Glide Strain', 'Acc. Coble Strain');
xlabel('Time (yrs)')
ylabel('Total Strain')
title('Total Strain vs. Time')
%Create arrays to write to spreadsheet
titles = {'Time','Temp (K)','Stress (Pa)','Elastic Modulus (Pa)','Glide Strain
Rate (/hr)','Coble Strain Rate (/hr)','Glide Strain','Coble
Strain','Accumulated Glide','Accumulated Coble','Total Strain'};
for i=1:length
    results(i,1)=time(i);
    results(i,2)=temp(i);
    results(i,3)=stress;
    results(i,4)=E(i);
    results(i,5)=srateglide(i);
    results(i,6)=sratecoble(i);
    results(i,7)=sglide_i_i(i);
    results(i,8)=scoble_i_i(i);
    results(i,9)=accglide(i);
    results(i,10)=acccoble(i);
    results(i,11)=straintotal(i);
end
%Write to spreadsheet and the file will be created in the same folder as the
%script
xlswrite('creepresults.xlsx',titles,1)
xlswrite('creepresults.xlsx',results,1,'A2')
```

70

References

[1]   K.L. Murty. Creep studies for Zircaloy life prediction in water reactors, Jom-J Min Met Mat S 51 (1999) 32-39.

[2]   K.L. Murty. The internal pressurization creep of Zr alloys for spent-fuel dry storage feasibility, Jom-J Min Met Mat S 52 (2000) 34-38.

[3]   Y. Zhou, B. Devarajan, K.L. Murty. Short-term rupture studies of Zircaloy-4 and Nb-modified Zircaloy-4 tubing using closed-end internal pressurization, Nucl Eng Des 228 (2004) 3-13.

[4]   F. Feria, L.E. Herranz. Creep assessment of Zry-4 cladded high burnup fuel under dry storage, Progress in Nuclear Energy 53 (2011) 395-400.

[5]   T.A. Hayes, M.E. Kassner. Creep of zirconium and zirconium alloys, Metall Mater Trans A 37A (2006) 2389-2396.

[6]   B.M. Morrow, R.W. Kozar, K.R. Anderson, M.J. Mills. An examination of the use of the Modified Jogged-Screw model for predicting creep behavior in Zircaloy-4, Acta Mater 61 (2013) 4452-4460.

[7]   E.R. Gilbert, S.A. Duran, A.L. Bement. Creep of Zirconium from 50 to 850C. Application-related phenomena in Zirconium and its alloys, ASTM STP 458. Philadelphia, PA: American Society for Testing and Materials, 1969. p.210-225.

[8]   A.J. Ardell, Sherby The steady state creep fo polycrystalline alpha zirconium at elevated temperatures T Metall Soc Aime 239 (1967) 1547-1556.

[9]   S.R. Macewen, R.G. Fleck, E.T.C. Ho, O.T. Woo. Deformation of α-zirconium in the vicinity of 0.5 tinm, MTA 12 (1981) 1751-1759.

[10]   M. Pahutová, J. Čadek. Interpretation of high temperature creep in alpha-zirconium in terms of effective stress and dislocation dynamics, Mater Sci Eng 11 (1973) 151-162.

[11]   M.T. Pérez-Prado, S.R. Barrabes, M.E. Kassner, E. Evangelista. Dynamic restoration mechanisms in α-zirconium at elevated temperatures, Acta Mater 53 (2005) 581-591.

[12]   C. Nam, B.-K. Choi, M.-H. Lee, Y.-H. Jeong. Creep strength of Zircaloy-4 cladding depending on applied stress and annealing temperature, J Nucl Mater 305 (2002) 70-76.

[13]   Y. Matsuo. Thermal Creep of Zircaloy-4 Cladding under Internal Pressure, Journal of Nuclear Science and Technology 24 (1987) 111-119.

[14]   K.L. Murty, S.G. Mcdonald. Tensile, creep and relaxation characteristics of Zircaloy cladding at 385ºC. 6th Int. Conf. Structural Mechanics in Reactor Technology (SMiRT-6). Paris, 1981. p.C2/3.

[15]   T. Hayes, M.E. Kassner, R. Rosen. Steady-state creep of α-zirconium at temperatures up to 850 °C, Metall and Mat Trans A 33 (2002) 337-343.

[16]   J.H. Moon, P.E. Cantonwine, K.R. Anderson, S. Karthikeyan, M.J. Mills. Characterization and modeling of creep mechanisms in Zircaloy-4, J Nucl Mater 353 (2006) 177-189.

[17]   N. Prasad, G. Malakondaiah, P.R. Rao. LOW STRESS CREEP-BEHAVIOR OF ZIRCALOY-2 VIS-A-VIS ZIRCONIUM, Scripta Metallurgica et Materialia 26 (1992) 541-543.

[18]   I.M. Bernstein. Diffusion creep in Zirconium and certain Zirconium alloys T Metall Soc Aime 239 (1967) 1518-1522.

[19]   M.F. Ashby, R.A. Verrall. Diffusion-accommodated flow and superplasticity, Acta Metallurgica 21 (1973) 149-163.

71

[20] J. Fiala, J. Čadek. Creep in zirconium at low stresses and temperatures from 748 to 973 K, Mater Sci Eng 75 (1985) 117-126.

[21] G.K. Williamson, R.E. Smallman. III. Dislocation densities in some annealed and cold-worked metals from measurements on the X-ray debye-scherrer spectrum, Philos Mag 1 (1956) 34-46.

[22] J. Čadek. Creep in metallic materials, Elsevier Science Publishers B. V., Amsterdam, The Netharlands, 1988.

[23] K. Vieregge, R. Willecke, C. Herzig. Grain Boundary Diffusion of Bulk Interstitials in Alpha-Zirconium, Le Journal de Physique Colloques 51 (1990) C1-691-C691-696.

[24] V.S. Lyashenko, V.N. Bykon, L.V. Pavlinov. A study of self-diffusion in Zirconium and its alloys with tin, Fiz. metal. metalloved 8 (1959) 362-369.

[25] T.G. Langdon. Grain boundary sliding as a deformation mechanism during creep, Philos Mag 22 (1970) 689-700.

[26] P. Shahbeigi Roodposhti, A. Sarkar, K.L. Murty. Microstructural development of high temperature deformed AZ31 magnesium alloys, Materials Science and Engineering: A 626 (2015) 195-202.

[27] R.L. Coble. A Model for Boundary Diffusion Controlled Creep in Polycrystalline Materials, J Appl Phys 34 (1963) 1679-1682.

[28] F.R.N. Nabarro. Creep at very low rates, Metall Mater Trans A 33 (2002) 213-218.

[29] J. Harper, J.E. Dorn. Viscous creep of aluminum near its melting temperature, Acta Metallurgica 5 (1957) 654-665.

[30] J. Novotný, J. Fiala, J. Čadek. Harper-Dorn creep in alpha-zirconium, Acta Metallurgica 33 (1985) 905-911.

[31] J.R. Spingarn, W.D. Nix. A model for creep based on the climb of dislocations at grain boundaries, Acta Metallurgica 27 (1979) 171-177.

[32] S. Gollapudi, V. Bhosle, I. Charit, K.L. Murty. Newtonian viscous creep in Ti-3Al-2.5V, Philos Mag 88 (2008) 1357-1367.

[33] J. Weertman. Dislocation climb theory of steady state creep, Transactions of the ASM 61 (1968) 680-694.

[34] G.B. Viswanathan, V.K. Vasudevan, M.J. Mills. Modification of the jogged-screw model for creep of γ-TiAl, Acta Mater 47 (1999) 1399-1411.

[35] S. Gollapudi, I. Charit, K.L. Murty. Creep mechanisms in TI-3Al-2.5V alloy tubing deformed under closed-end internal gas pressurization, Acta Mater 56 (2008) 2406-2419.

[36] K.L. Murty, F.A. Mohamed, J.E. Dorn ✠ . Viscous glide, dislocation climb and newtonian viscous deformation mechanisms of high temperature creep in Al-3Mg, Acta Metallurgica 20 (1972) 1009-1018.

[37] J.E. Bird, A.K. Mukherjee, J.E. Dorn. Correlations between high-temperature creep behavior and structure. In: Brandon DG, Rosen A, (Eds.). Quantitative relation between properties and microstructure Haifa, Israel: Israel University press, 1969. p.255-342.

[38] O.A. Ruano, J. Wadsworth, O.D. Sherby. Low stress creep of α-Zr at intermediate temperatures, Mater Sci Eng 84 (1986) L1-L6.

[39] J. Wadsworth, O.A. Ruano, O.D. Sherby. Deformation by grain boundary sliding and slip creep versus diffusional creep. In: Mishra RS, Mukherjee AK, Murty KL, (Eds.). Creep behavior of advanced materials for the 21st century. San Diego, California: TMS, 1999. p.425-431.

72

[40] B. Kombaiah, K.L. Murty. Dislocation cross-slip controlled creep in Zircaloy-4 at high stresses, Materials Science and Engineering: A 623 (2015) 114-123.

[41] J. Weertman. High temperature creep produced by dislocation motion. In: Mukherjee AK, Li JCM, (Eds.). Rate processes in plastic deformation of materials Cleveland, Ohio: ASM, 1972. p.315-336.

[42] T. Ginter, F. Mohamed. The stress dependence of the subgrain size in aluminium, J Mater Sci 17 (1982) 2007-2012.

[43] J.L. Derep, S. Ibrahim, R. Rouby, G. Fantozzi. DEFORMATION-BEHAVIOR OF ZIRCALOY-4 BETWEEN 77K AND 900-K, Acta Metallurgica 28 (1980) 607-619.

[44] J. Weertman. Creep of Indium, Lead and some of their alloys with various metals, T Metall Soc Aime 218 (1960) 207.

[45] C.R. Barrett, W.D. Nix. A model for steady state creep based on the motion of jogged screw dislocations, Acta Metallurgica 13 (1965) 1247-1258.

[46] J.P. Poirier. Creep of crystals - High temperature deformation processes in metals, ceramics and minerals, Cambridge University Press, London, 1985.

[47] S.V. Raj, T.G. Langdon. Creep behavior of copper at intermediate temperatures—I. Mechanical characteristics, Acta Metallurgica 37 (1989) 843-852.

[48] J. Friedel. Dislocations Interactions and Internal Strains. In: Rassweiler GM, Grube WL, (Eds.). Proceedings of the symposium on Internal stresses and fatigue in metals Detroit and Warren, Mich: Elesevier Publishing Company, 1958. p.220.

[49] J.P. Poirier. On the symmetrical role of cross-slip of screw dislocations and climb of edge dislocations as recovery processes controlling high-temperature creep, Rev. Phys. Appl. (Paris) 11 (1976) 731-738.

[50] J.J. Gilman. Dislocation Mobility in Crystals, J Appl Phys 36 (1965) 3195-3206.

[51] J.E. Bailey. Electron microscope studies of dislocations in deformed zirconium, J Nucl Mater 7 (1962) 300-310.

[52] K. Linga Murty, I. Charit. Texture development and anisotropic deformation of zircaloys, Progress in Nuclear Energy 48 (2006) 325-359.

[53] R.C. Ecob, A.T. Donaldson. A microstructural investigation of steady state creep of zircaloy-4 at 973 K, J Nucl Mater 132 (1985) 110-125.

[54] I. Armas, M. Boček. The analysis of dislocation networks formed in Zircaloy-4 during high temperature creep, J Nucl Mater 115 (1983) 263-270.

[55] N. Jaffe, Dorn, J. E. Effect of stress on the creep rate of high purity Aluminum in the cross-slip region, T Metall Soc Aime 224 (1962) 1167-1173.

[56] D. Caillard, J.L. Martin. Some aspects of cross-slip mechanisms in metals and alloys, J. Phys. France 50 (1989) 2455-2473.

[57] S.S. Vagarali, T.G. Langdon. Deformation mechanisms in h.c.p. metals at elevated temperatures—I. Creep behavior of magnesium, Acta Metallurgica 29 (1981) 1969-1982.

[58] P.W. Flynn, J. Mote, J.E. Dorn. On the thermally activated mechanism of prismatic slip in Magnesium single crystals, T Metall Soc Aime 221 (1961) 1148-1153.

[59] A. Akhtar. Basal slip in zirconium, Acta Metallurgica 21 (1973) 1-11.

[60] J.K. Chakravartty, R. Kapoor, A. Sarkar, S. Banerjee. Dynamic Recrystallization in Zirconium Alloys, Journal of ASTM International 7 (2010).

[61] A.N. Stroh. Constrictions and Jogs in Extended Dislocations, Proceedings of the Physical Society. Section B 67 (1954) 427.

[62] D.H. Sastry, M.J. Luton, J.J. Jonas. Stacking fault energy and its influence on high-temperature plastic flow in Zr-Sn alloys, Philos Mag 30 (1974) 115-127.

[63] J.J. Gilman. Plastic anisotropy of Zinc monocrystals, T Metall Soc Aime 206 (1956) 1326-1336.

[64] A.G. Evans, R.D. Rawlings. The Thermally Activated Deformation of Crystalline Materials, physica status solidi (b) 34 (1969) 9-31.

[65] A. Sarkar, A.H. Alsabbagh, K.L. Murty. Investigation of microstructure and mechanical properties of low dose neutron irradiated HT-9 steel, Annals of Nuclear Energy 65 (2014) 91-96.

[66] N. Balasubramanian, J.C.M. Li. The activation areas for creep deformation, J Mater Sci 5 (1970) 434-444.

[67] K.L. Murty, I. Charit. Structural materials for Gen-IV nuclear reactors: Challenges and opportunities, J Nucl Mater 383 (2008) 189-195.

[68] I. Charit, K.L. Murty. Creep behavior of niobium-modified zirconium alloys, J Nucl Mater 374 (2008) 354-363.

[69] K.L. Murty. Deformation mechanisms and transients in creep of zircaloys: Applications to nuclear technology, T Indian I Metals 53 (2000) 107-120.

[70] H.-G. Kim, I.-H. Kim, B.-K. Choi, J.-Y. Park, Y.-H. Jeong, K.-T. Kim. Study of the corrosion and microstructure with annealing conditions of a beta-quenched HANA-4 alloy, Corrosion Science 52 (2010) 3162-3167.

[71] Y.I. Jung, M.H. Lee, H.G. Kim, J.Y. Park, Y.H. Jeong. Behavior of a recrystallization in HANA-4 and HANA-6 zirconium-based alloys, Journal of Alloys and Compounds 479 (2009) 423-426.

[72] Y.H. Jeong, H.G. Kim, D.J. Kim, B.K. Choi, J.H. Kim. Influence of Nb concentration in the α-matrix on the corrosion behavior of Zr–xNb binary alloys, J Nucl Mater 323 (2003) 72-80.

[73] Y.H. Jeong, K.O. Lee, H.G. Kim. Correlation between microstructure and corrosion behavior of Zr–Nb binary alloy, J Nucl Mater 302 (2002) 9-19.

[74] Y.H. Jeong, S.-Y. Park, M.-H. Lee, B.-K. Choi, J.-H. Baek, J.-Y. Park, J.-H. Kim, H.-G. Kim. Out-of-pile and In-pile Perfomance of Advanded Zirconium Alloys (HANA) for High Burn-up Fuel, Journal of Nuclear Science and Technology 43 (2006) 977-983.

[75] K.L. Murty, J. Ravi, Wiratmo. TRANSITIONS IN CREEP MECHANISMS AND CREEP ANISOTROPY IN ZR-1NB-1SN-0.2FE SHEET, Nucl Eng Des 156 (1995) 359-371.

[76] J.C. Britt, J. Ravi, Wiratmo, K.L. Murty. Mechanical and Creep Anisotropy and Crystallographic Texture of Nb-Modified Zircaloy Sheet, Proceedings of the Sixth International Symposium on Environmental Degradation of Materials in Nuclear Power Systems - Water Reactors (1993) 483-490.

[77] W.R. Thorpe, I.O. Smith. Creep properties of Zr-1wt.%Nb alloy, J Nucl Mater 75 (1978) 209-219.

[78] M. Pahutová, J. Čadek, V. Černý. Steady state creep of Zr・Nb alloys in a temperature interval 350 to 550°C, J Nucl Mater 61 (1976) 285-296.

[79] M.I. Alymov, E.N. Pirogov, L.L. Artyukhina. Steady-state creep of the N-1 alloy in the 650–870°K range, At Energy 62 (1987) 441-444.

[80] K.L. Murty, J. Ravi, Wiratmo. Transitions in creep mechanisms and creep anisotropy in Zr・1Nb・1Sn・0.2Fe sheet, Nucl Eng Des 156 (1995) 359-371.

74

[81]   J. Ravi, K.L. Murty. Transitions in creep mechanisms in a Zr-1 Nb-1 Sn-0.2 Fe sheet. In: Arsenault RJ, Cole D, Sizek H, Liaw P, Parameswaran G, Kostorz G, (Eds.). Johannes Weertman Symposium: TMS Annual Meeting Anaheim, California: The Society, 1996. p.203-209.

[82]   K.L. Murty. Transitional Creep Mechanisms in Al-5mg at High Stresses, Scripta Metallurgica 7 (1973) 899-903.

[83]   E. Orowan. Theory of yield without particle shear. Symposium on Internal Stresses in Metals and Alloys. London, 1948. p.451.

[84]   J.W. Martin. Precipitation Hardening, Butterworth-Heinemann, Oxford, 1998.

[85]   I. Charit, K.L. Murty. Texture and creep anisotropy in zirconium alloys, Mater Sci Forum 539-543 (2007) 3377-3382.

[86]   H. Okamoto. Nb-Zr (Niobium-Zirconium) - Phase diagram updates, Journal of Phase Equilibria 13 (1992) 577.

[87]   R.J. Pérez, A.R. Massih. Thermodynamic evaluation of the Nb–O–Zr system, J Nucl Mater 360 (2007) 242-254.

[88]   A. Guillermet. Thermodynamic Analysis of the Stable Phases in the Zr--Nb System and Calculation of the Phase Diagram, Zeitschrift fur Metailkunde 82 (1991).

[89]   H.E. Rosinger, D.O. Northwood. The elastic properties of zirconium alloy fuel cladding and pressure tubing materials, J Nucl Mater 79 (1979) 170-179.

[90]   C. Herring. Diffusional Viscosity of a Polycrystalline Solid, J Appl Phys 21 (1950) 437-445.

[91]   F.R.N. Nabarro. Report of conference on Strength of Solids London: The Physical Society, 1948.

[92]   K.L. Murty. Viscous Creep in Pb-9 Sn, Mater Sci Eng 14 (1974) 169-177.

[93]   B. Kombaiah, K.L. Murty. High Temperature Creep and Deformation Microstructures in Recrystallized Zircaloy-4, submitted for publication (2015).

[94]   K.L. Murty. Viscous creep in Pb—9 Sn, Mater Sci Eng 14 (1974) 169-177.

[95]   J. Weertman. STEADY-STATE CREEP OF CRYSTALS, J Appl Phys 28 (1957) 1185-1189.

[96]   N.Q. Vo, C.H. Liebscher, M.J.S. Rawlings, M. Asta, D.C. Dunand. Creep properties and microstructure of a precipitation-strengthened ferritic Fe–Al–Ni–Cr alloy, Acta Mater 71 (2014) 89-99.

[97]   E.A. Marquis, D.C. Dunand. Model for creep threshold stress in precipitation-strengthened alloys with coherent particles, Scripta Mater 47 (2002) 503-508.

[98]   J. Rösler, E. Arzt. The kinetics of dislocation climb over hard particles—I. Climb without attractive particle-dislocation interaction, Acta Metallurgica 36 (1988) 1043-1051.

[99]   E. Arzt, J. Rösler. The kinetics of dislocation climb over hard particles—II. Effects of an attractive particle-dislocation interaction, Acta Metallurgica 36 (1988) 1053-1060.

[100] E. Arzt, M.F. Ashby. Threshold stresses in materials containing dispersed particles, Scripta Metallurgica 16 (1982) 1285-1290.

[101] B.G. Clark, I.M. Robertson, L.M. Dougherty, D.C. Ahn, P. Sofronis. High-temperature Dislocation-precipitate Interactions in Al Alloys: An in situ Transmission Electron Microscopy Deformation Study, Journal of Materials Research 20 (2005) 1792-1801.

[102] A. Melander, P.Å. Persson. The strength of a precipitation hardened AlZnMg alloy, Acta Metallurgica 26 (1978) 267-278.

75

[103] R. Lagneborg, B. Bergman. The stress/creep rate behaviour of precipitation-hardened alloys, Metal Science 10 (1976) 20-28.

[104] J. Weertman. STEADY-STATE CREEP THROUGH DISLOCATION CLIMB, J Appl Phys 28 (1957) 362-364.

[105] J. Goldak, L.T. Lloyd, C.S. Barrett. Lattice Parameters, Thermal Expansions, and Grueneisen Coefficients of Zirconium, 4.2 to 1130 K, Physical Review 144 (1966) 478-484.

[106] M. Ivermark, J. Robson, M. Preuss, S.W. Dean. Measurement and Modeling of Second Phase Precipitation Kinetics in Zirconium Niobium Alloys, Journal of ASTM International 7 (2010) 103011.

[107] Y.F. Bychkov, A.N. Rozanov, D.M. Skorov. The normal elastic modulus of alloys of zirconium with niobium, The Soviet Journal of Atomic Energy 2 (1957) 171-175.

[108] B. Jansson, A. Melander. On the critical resolved shear stress from misfitting particles, Scripta Metallurgica 12 (1978) 497-498.

[109] P.G. Shewmon. Transformations in metals McGraw-Hill book company, 1969.

[110] J.D. Robson. Modelling precipitation in zirconium niobium alloys, J Nucl Mater 377 (2008) 415-422.

[111] E. Nembach. Precipitation hardening caused by a difference in shear modulus between particle and matrix, physica status solidi (a) 78 (1983) 571-581.

[112] S. Banerjee, P.K. Mukhopadhyay. Phase Transformations — Examples from Titanium and Zirconium Alloys, Elsevier, Amsterdam, 2005.

[113] G. Östberg. Determination of hydride solubility in alpha phase zirconium, zircaloy-2 and zircaloy 4, J Nucl Mater 5 (1962) 208-215.

[114] E. Zuzek, J.P. Abriata, A. San-Martin, F.D. Manchester. The H-Zr (hydrogen-zirconium) system, Bulletin of Alloy Phase Diagrams 11 (1990) 385-395.

[115] M.P. Puls. The effect of Hydrogen and Hydrides on the integrity of Zirconium alloy components London: Springer-Verlag, 2012.

[116] A. Sarkar, K. Boopathy, J. Eapen, K.L. Murty. Creep Behavior of Hydrogenated Zirconium Alloys, Journal of Materials Engineering and Performance 23 (2014) 3649-3656.

[117] D. Setoyama, S. Yamanaka. Indentation creep study of zirconium hydrogen solid solution, Journal of Alloys and Compounds 379 (2004) 193-197.

[118] N. Rupa, M. Cavel, P. Bouffioux, C. Domain, A. Legris. About the mechanisms governing hydrogen effect on viscoplasticity of unirradiated fully annealed zircaloy-4 sheet, ASTM STP 1423 (2002) 811.

[119] P. Bouffioux, N. Rupa. Impact of Hydrogen on Plasticity and Creep of Unirradiated Zircaloy-4 Cladding Tubes Zirconium in the Nuclear Industry:Twelfth International Symposium ASTM STP 1354, 2000. p.399-422.

[120] R. Kishore. Effect of hydrogen on the creep behavior of Zr–2.5%Nb alloy at 723 K, J Nucl Mater 385 (2009) 591-594.

[121] V. Mallipudi, S. Valance, J. Bertsch. Meso-scale analysis of the creep behavior of hydrogenated Zircaloy-4, Mechanics of Materials 51 (2012) 15-28.

[122] B. Kombaiah, K.L. Murty. Transition in creep mechanisms of HANA-4 tubing, Unpublished (2015).

[123] R.N. Singh, J.K. Chakravartty, S. Banerjee. Hydride induced embrittlement of zirconium alloy pressure tubes, BARC News Letters (2009).

76

[124] A. Motta, L.-Q. Chen. Hydride Formation in Zirconium Alloys, Jom-Us 64 (2012) 1403-1408.

[125] K.B. Colas, A.T. Motta, J.D. Almer, M.R. Daymond, M. Kerr, A.D. Banchik, P. Vizcaino, J.R. Santisteban. In situ study of hydride precipitation kinetics and re-orientation in Zircaloy using synchrotron radiation, Acta Mater 58 (2010) 6575-6583.

[126] M. Ito, K. Ko, H. Muta, M. Uno, S. Yamanaka. Effect of Nb addition on the terminal solid solubility of hydrogen for Zr and Zircaloy-4, Journal of Alloys and Compounds 446–447 (2007) 451-454.

[127] V. Mallipudi, S. Valance, J. Bertsch. Meso-scale analysis of the creep behavior of hydrogenated Zircaloy-4, Mechanics of Materials 51 (2012) 15-28.

[128] C. Domain, R. Besson, A. Legris. Atomic-scale ab initio study of the Zr–H system: II. Interaction of H with plane defects and mechanical properties, Acta Mater 52 (2004) 1495-1502.

[129] F.C. Monkman, N.J. Grant. Proceedings of the ASTM 56 (1956) 593-620.

[130] Spent Fuel Transportation Applications—Assessment of Cladding Performance: A Synthesis Report. Palo Alto, CA: EPRI, 2007.

[131] Wikmark. TESTINGAND MODELING OF LONG-TERM CREEP OFMODERN PWR CLADDING IN DRY STORAGE AND TRANSPORT, Water Reactor Fuel Performance Meeting (2011).

77

DOE Nuclear Energy University Program - IRP

Fuel Aging in Storage and Transportation (FAST): Accelerated Characterization and Performance Assessment of the Used Nuclear Fuel Storage System

Technical Mission Areas:
1 – Low Temperature Creep and
2 – Hydrogen Behavior and Delayed Hydride Cracking

Final Report
7 January 2016

Contributors

Kuan-Che Lan, Graduate Student

Zachary D. Kriz, Graduate Student

Giuseppe Brunetti*,

James F Stubbins, Principal Investigator

Department of Nuclear, Plasma and Radiological Engineering

University of Illinois at Urbana-Champaign

*University of Pisa

Pisa, Italy

Table of Contents

Objectives

Technical Mission Area 1 – Low Temperature Creep

This mission's focus is on the low temperature creep of Used Nuclear Fuel (UNF) cladding enabled by decay heat from fission products and stresses from internal pressures. Systematic studies will characterize the low-temperature low-stress mechanisms relevant to dry storage.

Technical Mission Area 2 – Hydrogen Behavior and Delayed Hydride Cracking

This mission's focus is on the effects of dissolved hydrogen and hydride precipitates on the mechanical properties and deformation behavior of Used Nuclear Fuel (UNF) cladding under long-term storage conditions. Systematic studies will characterize the influence of hydrogen and hydrides on low-temperature creep and creep-rupture mechanisms relevant to dry storage.

1. Influence of zirconium hydride on the creep behavior of Zircaloy-4 cladding for interim dry storage of spent nuclear fuel

1.1. Introduction

Low temperature creep rupture of used nuclear fuel cladding is a concern as a possible failure mechanism during long-term dry storage. Furthermore, high burnup used nuclear fuel (UNF) (>45 GWd/MTU) may face more significant long-term storage issues due to the increase in hydrogen pickup of the cladding and irradiation effects during its service life. Some studies indicates that the hydrogen content of the fuel cladding will close to 750 weight part per million (wppm) as the fuel burnup approach the new limit 62 GWd/MTU, as shown in Fig.1 - 1

In this study, the pressurized tube technique was employed to test the durability of as-hydrided Zircaloy-4 tubular specimens and the influence of zirconium hydride on the biaxial thermal creep behavior of Zircaloy-4 cladding. This approach account for the creep behavior more related to the realistic conditions to which the materials are subject. Test specimens were hydrogen-charged by a thermal cycling process to attain the target hydrogen levels of 300 and 750 wppm. Specimens were exposed in a tube furnace with laboratory air at 573 and 773 K (300° C and 500°C) and were pressurized with high purity argon (99.998%) at a constant internal pressure of 9.8 MPa to generate 65 MPa effective stresses at mid-wall of cladding. To study the biaxial creep behavior for interim dry storage of spent nuclear fuel, creep strain was obtained by measuring the diameter strain at various exposure times, stresses, and temperatures.

The objective of this study is to develop a better understanding of creep performance of hydrided Zircaloy-4 cladding in a relative low stress (< 90 MPa) to support the design basis of interim and long-term dry storage facilities for up to 300 years.
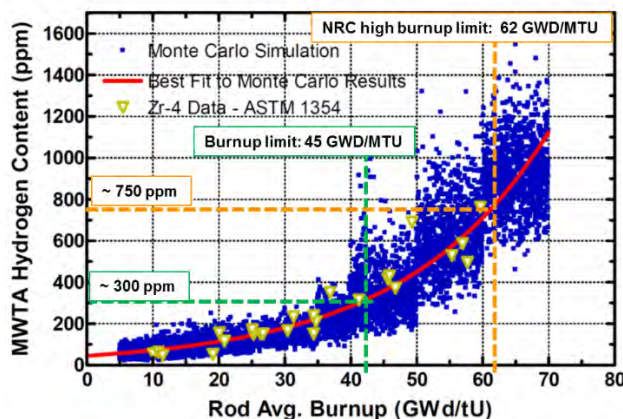

Fig.1 - 1 Hydrogen pick up v.s Fuel burnup [1] [2]

1.2. Creep Mechanism of Zirconium Alloy

Typically, in secondary creep, the strain rate $\dot{\varepsilon}_{II}$ depends on the stress and exponentially on the temperature T:

$$\dot{\varepsilon}_{II} = A\sigma^n \exp\left(-\frac{Q}{RT}\right) \tag{1.1}$$

where A is constant, n is creep stress exponent, σ is external stress, R is gas constant and Q is an activation energy characterizing the creep process. Eq.(1.1) is also called power-law creep. According to this equation, creep is a thermally activated process. Chin and Gilbert [3] firstly considering the deformation mechanism map for zirconium alloy based on theoretical considerations, as shown in Fig.1 - 2. Within the limitation of operation condition of dry storage facility (cladding temperature < 400°C and hoop stress < 90 MPa) [4], four most possible mechanism to dominate steady-state creep behavior are high-temperature climb, low-temperature climbing, Coble creep, and grain boundary sliding mechanism.

Creep mechanism of high-temperature climb and low-temperature climb is categorized as diffusion-controlled dislocation creep, this is, dislocation creep. Dislocation climbing and gliding would be activated at intermediate temperature and external stress. Once dislocation gliding on a slip plane is blocked and later the dislocation overcomes the obstacle by climbing to the next slip plane, the rate control of deformation rate is controlled by dislocation climbing. High-temperature climb mechanism is achieved by lattice diffusion, and creep strain rate is proportion to σ^n, (n = 3 ~ 5). Low-temperature climb mechanism is controlled by transportation via dislocation core diffusion, where the creep strain rate is proportion to σ^{n+2}.

Coble [5] proposed a grain boundary diffusion model to elucidate the creep behavior of polycrystalline materials at extremely low stress condition. Coble creep mechanism is sensitive to grain size and more significant for material with small grains. In addition, at low stress and at high temperature, the vacancy is able to directly diffuse in lattice. This process is called Nabarro-Herring (N-H) creep. [6] [7] Both Coble creep and N-H creep are diffusional creep mechanism, and their creep strain linearly depend on applied stress. Grain boundary sliding happens at low strain rate condition. [8] [9] Different from diffusion creep and dislocation creep, a polycrystalline material is able to deform by relative movement from grain to grain without any change in shape of grain. In the regime of grain boundary sliding, the creep strain rate has a σ^2 dependence.
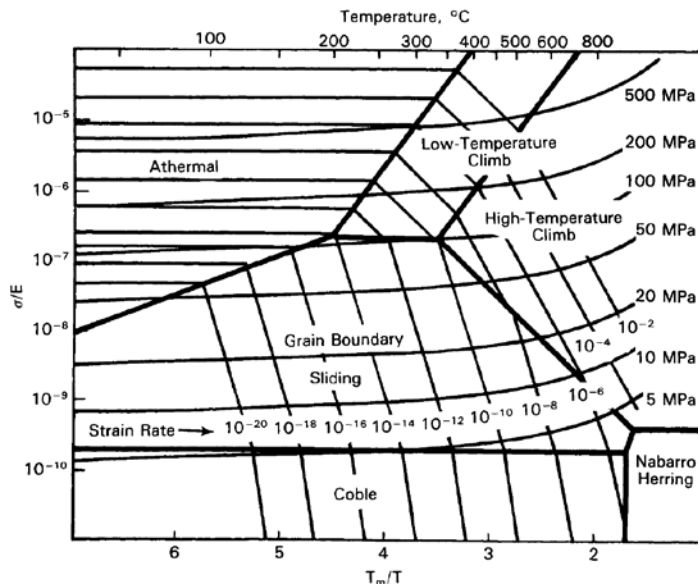
Fig.1 - 2 Deformation map for Zircaloy with constant stress and strain rate contours (strain rate is in s^{-1}) [3].

Existence of hydrogen in zirconium-based alloys impacts the mechanical properties which can degrade the integrity of Zircaloy cladding and further shorten its life.   Hydrogen either in solid solution or in the precipitated hydride phase is considered to influence the creep behavior of Zircaloy. [10]   Boffioux et al. [11] carried out biaxial creep tests using internal pressure technique on hydrided Zircaloy-4 tubes in cold-worked stress-relieved (CWSR) and annealed condition, where the hydrogen content is between 100 and 1100 wppm.   Results of two creep conditions, 400ºC and 140 MPa, and 350ºC and 200 MPa, show higher creep strain rate in control sample (non-hydride tube).   These experimental results indicated that both hydrogen in solid solution and precipitated decrease creep strain rate. However, some TEM observation on different materials found that solute hydrogen would reduce the barrier to the dislocation mobility. [12]

1.3. Material and Experimental Details

1.3.1. Material

Stress-relief annealed (SRA) Zircaloy-4 cladding with an outside diameter of 9.5 mm and wall thickness of 0.58 mm was used in this study.   Its chemical composition is given in Table 1 - 1.

Table 1 - 1 Chemical compositions of Zircaloy-4 cladding tube (weight %)

Sn	Fe	Cr	O	N	C	H	Zr

1.26	0.22	0.12	0.13	0.0029	0.01	0.0007	Balance

1.3.2. Hydrogen Charging Procedures

SRA Zircaloy-4 cladding tube, cut into 13-cm lengths, was first uniformly hydrogen-charged by a thermal cycling process [13]. The specimen was encapsulated with a pre-determined amount of pure hydrogen in a Pyrex capsule of sufficient volume such that a low hydrogen partial pressure could be obtained to avert the formation of hydride layers. The encapsulated cladding specimen was then thermally cycled between 200°C and 300°C for a certain number of cycles, depending on the target hydrogen concentration level. The heating and cooling rates were at 3°C/min and 2°C/min, respectively. The target hydrogen levels ranged are 300 wt. ppm and 750 wt. ppm. Total hydrogen content (radial average) was measured from approximately 5-mm-wide by 4-mm-long slices of cladding rings (approximately 1/4 of circumference) using a hot-vacuum-extraction process in a Horiba® Model EMGA-930 Hydrogen analyzer. The hydrogen content of Zircaloy-4 cladding with target hydrogen level 300 wt. ppm is 302 ± 14 wt. ppm.

1.3.3. Biaxial Creep Test

Using the electron beam welding technique, a 65 mm-long specimen was sealed by two Zircaloy-4 end plugs with a small hole drilled in the 20 mm-long end plugs. 3/8" to 1/8" Swagelok® fittings were used for the reduction union between the specimen and a Haynes 230 tubing. These particular fittings were chosen because of their sealing mechanism (compression ferrules), which grip very tightly and allow an excellent seal. The dimensions of the creep specimen and the photograph of the specimen are shown in Fig.1 - 3.

Fig.1 - 4 and Fig.1 - 5 shows the schematic diagram and photograph of the system. Before exposure of specimen in working environment, a cyclic cleaning with a pressurization followed by then vent was be repeated four times in order to minimize the oxidation of the inner wall during exposure. No protective atmosphere was used to protect the outer surface of the creep tube from oxidation. Firstly, the specimen was inserted into a tube furnace. The furnace MTI-OTF-1200X was then heated to the working temperature, followed by 30 minutes stabilization of the temperature. The temperature was maintained within ± 2 K. Next, a high purity argon gas (99.998%) was employed to pressurize the specimens, and the gas pressure was controlled and monitored by a pressure controller, Mensor CPC6000. At the end of the first isothermal exposure, venting pressure was followed by a cooling process, and finally specimen

was withdrew out of furnace for diameter measurements. The specimens were then reinserted into the furnace for the next exposure. This procedure was repeated for selected exposure intervals. The test matrix of testing temperature and pressure is given in Table 1 - 2. For the convenience of identifying the specimens prepared under a combination of experimental conditions, a designation scheme is devised. Zuvw is a specimen designation: the lower case u = 0, 3, or 7 represents its chemical composition of hydrogen, where 0, 3 and 7 stand for 0 wt ppm, 300 wt .ppm, and 750 wt .ppm, respectively; v = A, B, C or D denotes the effective stress at mid-wall of cladding, where A, B, C or D stand for 65 MPa, 60 MPa, 55MPa, and 40MPa, respectively; and w = 50, 40, 35, or 30 denotes the creep temperature, where 50, 40, 35, and 30 indicates 500°C, 400°C, 350°C, and 300°C respectively. For example, Z3D50 is a specimen with a hydrogen content of 300 wt. ppm, effective stress at mid-wall of 40 MPa and creep temperature of 500°C.

Table 1 - 2 Exposure time of Zircaloy-4 specimen at each test condition

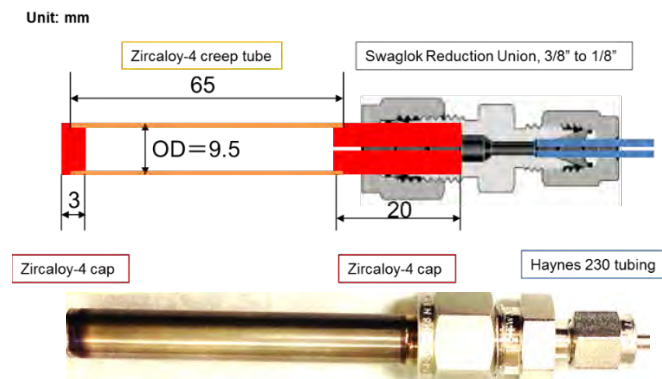| Effective Stress / Internal Pressure (MPa) / (MPa)	500ºC	400ºC	350ºC	300ºC
65 / [9.8]	Until fail	2000	2000	2000
60 / [9.1]	Until fail	-	-	-
55 / [8.3]	Until fail	2000	-	-
40 / [6.1]	Until fail	-	-	-

Fig.1 - 3 Schematic diagram and photograph of the pressurized creep tube.

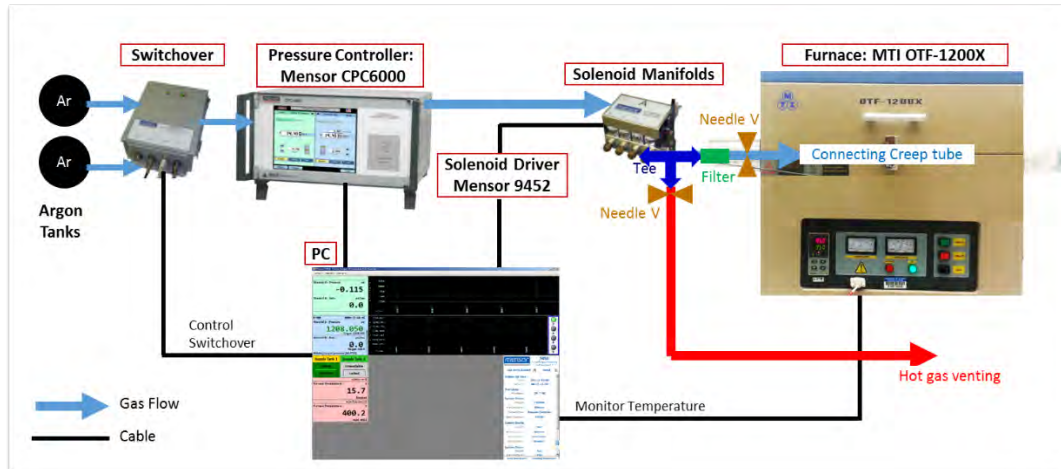Fig.1 - 4 Systematic diagram of biaxial creep test system.

Fig.1 - 5 Overview of biaxial creep test system.

1.3.4. Determination of biaxial creep strain

Before and after each exposure, the outer diameter (OD) of the pressurized creep tubes was measured at room temperature using a laser profilometer with a resolution of 1 μm. These measurements were made at ten locations spaced 2.3 mm apart along the specimen length in the middle of the specimen, and 4 diameters at 45º interval of rotations with respect to a reference mark on the tubing. The mean OD of a tube was computed by averaging the 24 (6×4) measurements made in the middle of the tube specimen to preclude any end effects. Diameter strain was calculated using the equation below:

$$\varepsilon_d = \frac{\Delta D}{D_0} \quad (1)$$

where D_0 is an original diameter before exposure, D is a diameter after exposure, and ε_d is the diameter strain. Effective strain (ε_e) was given by equation (2) [14].

$$\varepsilon_e = \frac{2}{\sqrt{3}}\epsilon_d \quad (2)$$

Mid-wall effective stresses of a pressurized tube were calculated using von Mises distortion energy criterion [15]. This technique uses the original tube dimensions so once the deformation exceeds a few percent, the tube stress levels increase due to the tube wall thinning effects. Since most design limitations require low values of strain, typically less than 1%, the creep values at low strain levels should be useful.

1.4. Results and discussion

Thin foil was cut parallel to the outer surface of the tested specimens, were mechanically ground to a thickness of 300 μm, and followed by investigation of its crystallographic structure using XRD, as shown in Fig.1 - 6   XRD results of as-received specimens depicted in Fig.1 - 7 shows that the crystallinity before and after hydriding process is similar.   Microstructure observation on cross section plane (radial-circumferential plane) using optical microscopy has been presented in Fig.1 - 8.   Obvious hydride phase growth along hoop direction and uniformly distributed through the tube wall thickness.
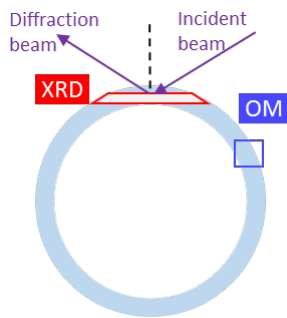
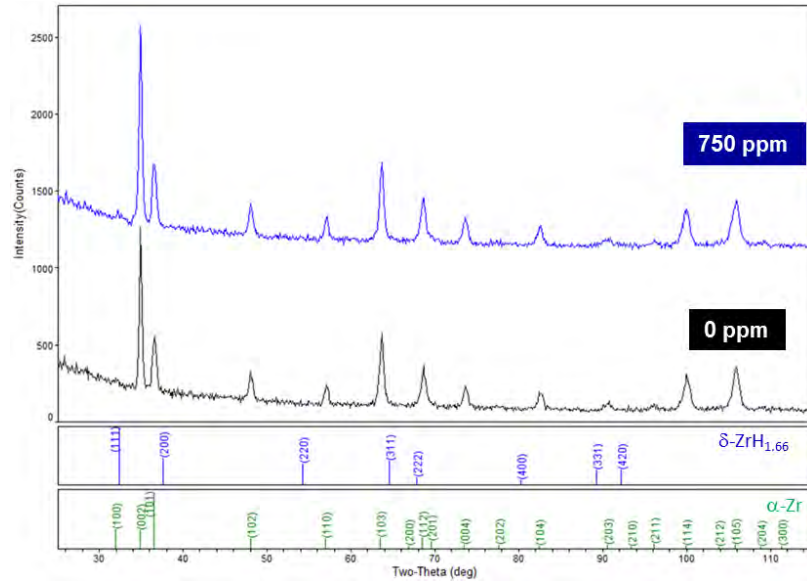Fig.1 - 6 The 3 mm thin foil for XRD investigation and cross section view using optical microscopy (OM).

Fig.1 - 7 XRD results of as-received zircaloy-4 cladding without hydride and 750 wt. ppm hydrogen. There is no significant change between the peak shape of the two specimen.
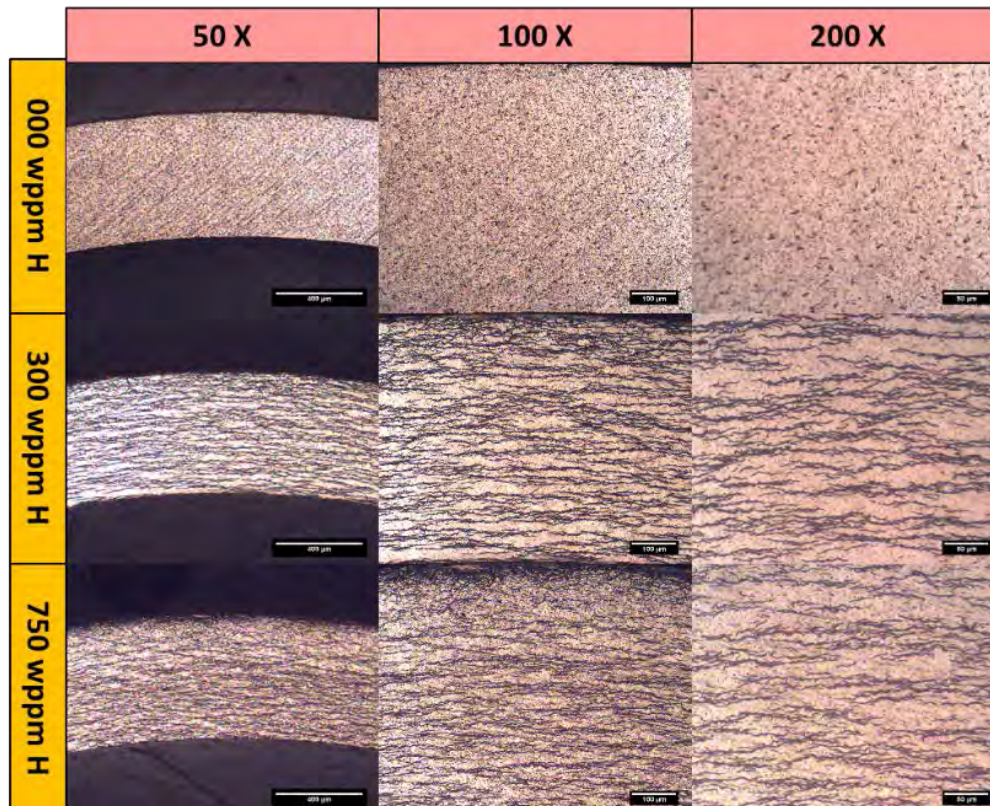

Fig.1 - 8 OM results of as-received zircaloy-4 cladding.

The biaxial creep behaviors of non-hydrided zircaloy-4 cladding are plotted in Fig.1 - 9. It can be seen that as the applied stress decreases, the rupture lifetime increases, as expected. Tests under 400°C are terminated at 2,000 hours and are shown Fig.1 - 9 (b). It can be seen that the creep deformation is still in steady-state regime for the test of the temperature at and under 400°C, and effective stress at mid-wall at and under 65 MPa. Similarly, biaxial creep behaviors of hydrided zircaloy-4 cladding will be separated in the same manner in two group: high temperature group (crept at 500°C) and low temperature group (exposure temperature $\leq$ 400°C).
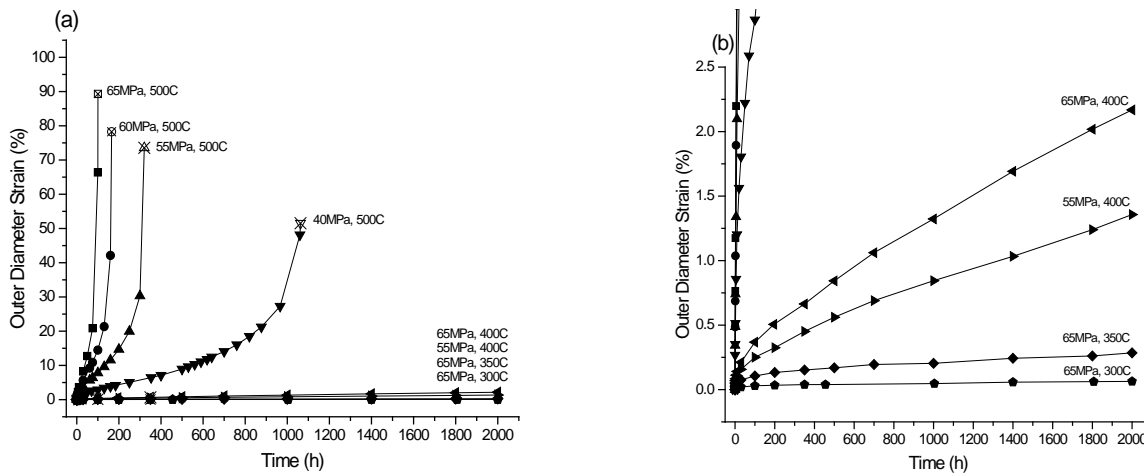

Fig.1 - 9 Diameter strain vs. creep exposure time for Zircaloy-4 cladding at (a) 500°C and (b) 400°C ~ 300°C

Diameter strain as a function of exposure time of Zircaloy-4 cladding with three level of hydrogen content crept at 500°C and applied stress from 65MPa to 40MPa are demonstrated in Fig.1 - 10, Fig.1 - 11, and Fig.1 - 12. It is noted that the rupture time decreases with the increase in hydrogen content of zircaloy-4 cladding, except for the one creep at 40 MPa. Fig.1 - 13 and Fig.1 - 14, Fig.1 - 15, and Fig.1 - 16 represent the low temperature diameter strain behavior at 65MPa and 400°C, at 55MPa and 400°C, 65MPa and 350°C, and at 65MPa and 300°C, respectively. It can be seen that the creep strain of Zircaloy-4 claddings with hydride is significantly smaller than that without hydride.
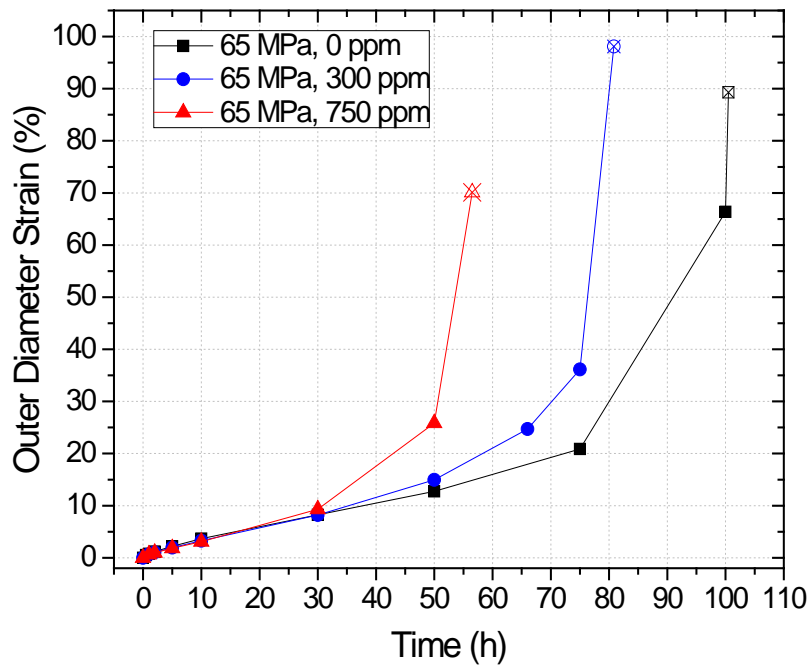
Fig.1 - 10 Diameter strain vs. creep exposure time for Zircaloy-4 cladding with applied stress 65MPa at 500°C

Fig.1 - 11 Diameter strain vs. creep exposure time for Zircaloy-4 cladding with applied stress 55MPa at 500°C

Fig.1 - 12 Diameter strain vs. creep exposure time for Zircaloy-4 cladding with applied stress 40MPa at 500°C
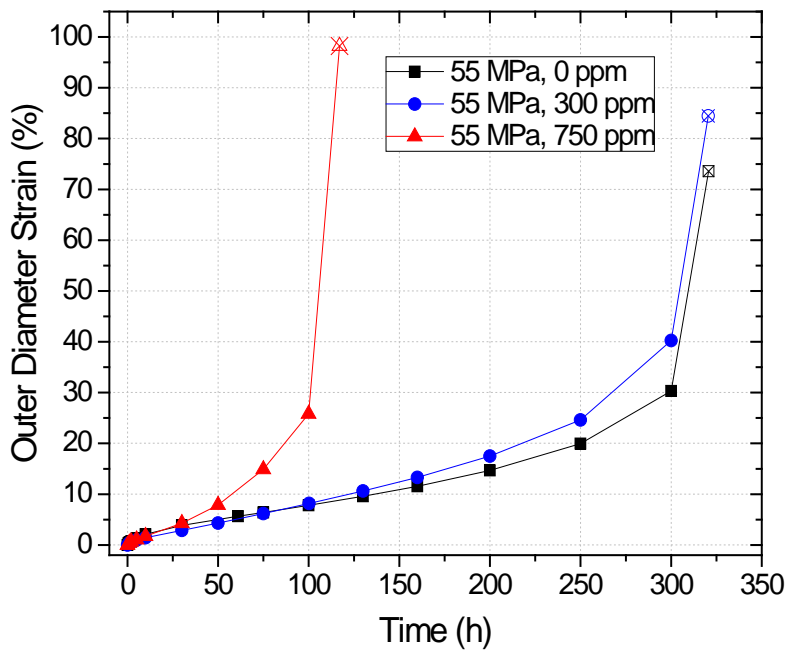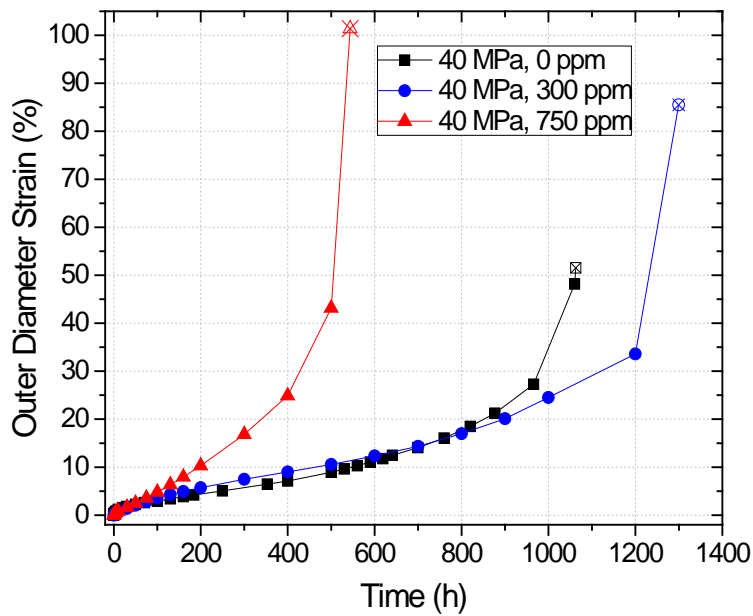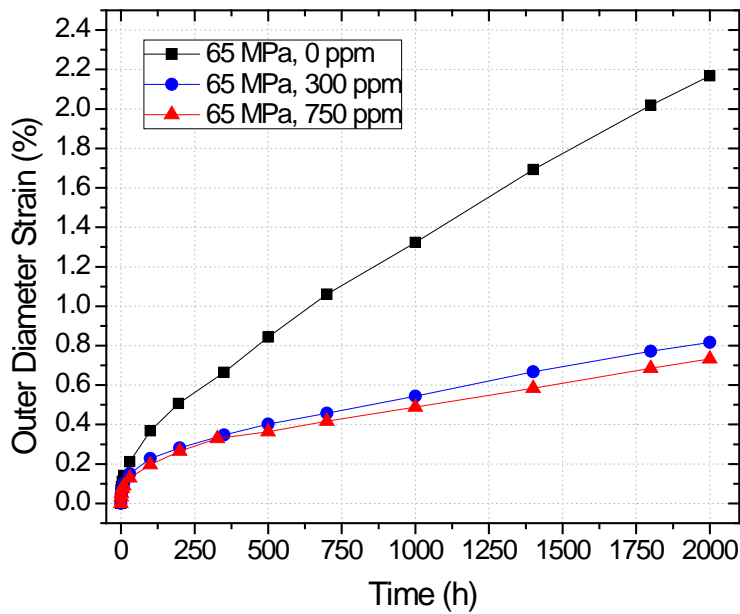

Fig.1 - 13 Diameter strain vs. creep exposure time for Zircaloy-4 cladding with applied stress 65MPa at 400°C
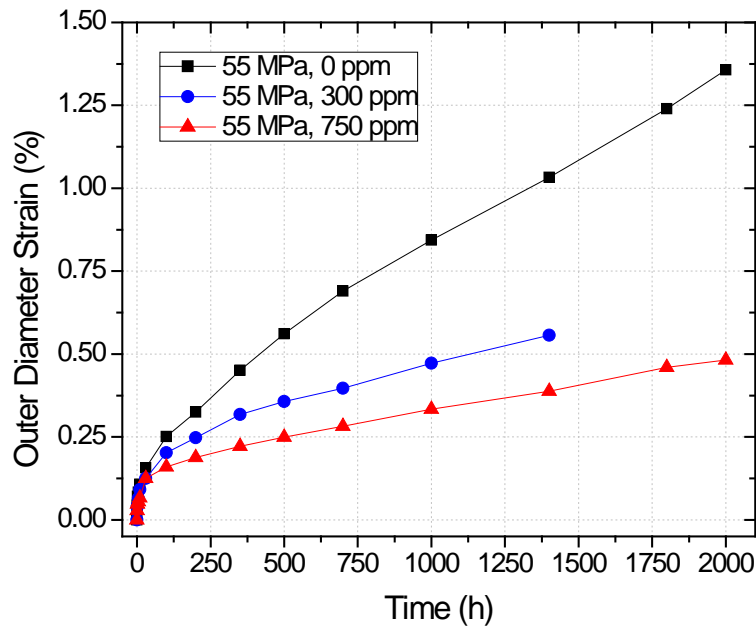
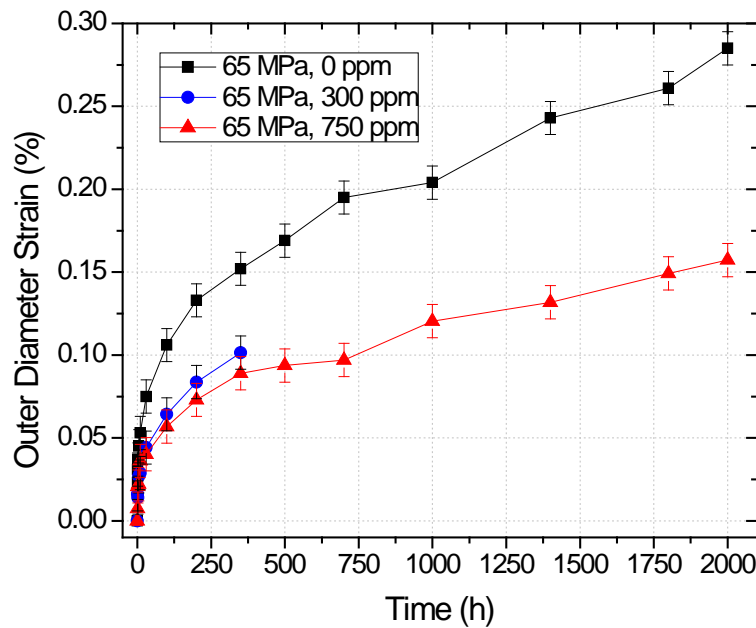Fig.1 - 14 Diameter strain vs. creep exposure time for Zircaloy-4 cladding with at 55MPa and 400°C

Fig.1 - 15 Diameter strain vs. creep exposure time for Zircaloy-4 cladding with at 65MPa and 350°C
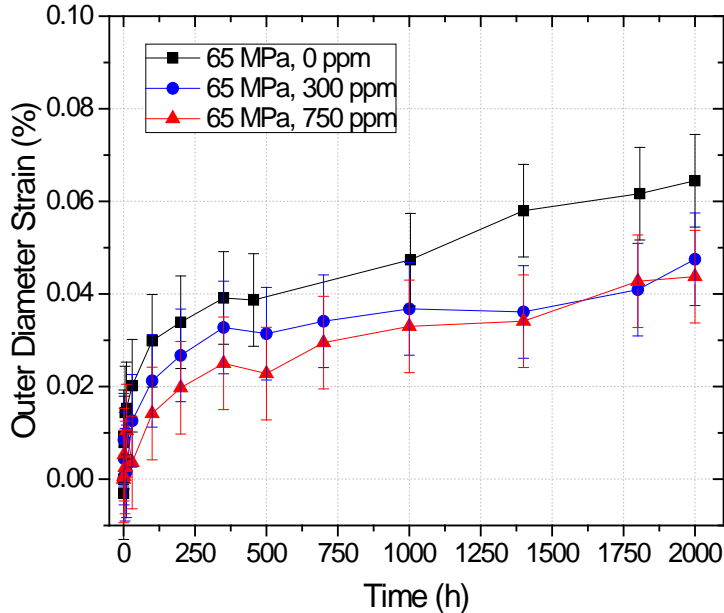
Fig.1 - 16 Diameter strain vs. creep exposure time for Zircaloy-4 cladding at 65MPa and 300°C

To identify the influence of the oxide thickness on the measurement of outer diameter at 500°C, the oxidation test of zircaloy-4 plate has been conducted.   Several 10 mm x 15 mm x 1.6 mm Zircaloy-4 plates were exposed in the air at 500°C for 1 to 100 hours, and oxidation growth as well as the both oxide thickness and weight gain are demonstrated in Fig.1 - 17 and Fig.1 - 16. The phase identification of surface oxide using XRD analysis indicates the oxide layer is composed of monoclinic and tetragonal zirconia, as shown in Fig.1 - 17.   Assuming that the growth of oxide on the zircaloy-4 cladding is similar to that on plate and close to results in Fig.1 - 17 and Fig.1 - 16, the ratio of oxide thickness to the increase in outer diameter is less than 0.2% of the measured diameter strain in 100 hours in 500°C.   It is to say that the overestimation of diameter strain due to oxidation is insignificant.

Fig.1 - 17 Growth of thermal oxide on zircaloy-4 plate in the air at 500°C

Fig.1 - 18 Growth of thermal oxide on zircaloy-4 plate in the air at 500°C

Fig.1 - 19 The XRD patterns for the specimens oxidized in the air at 500°C

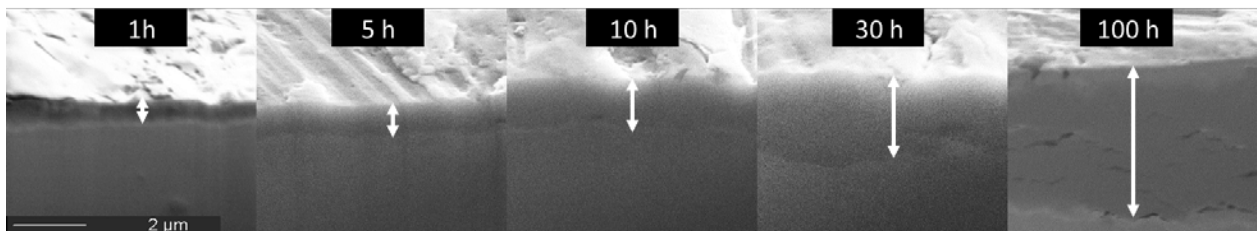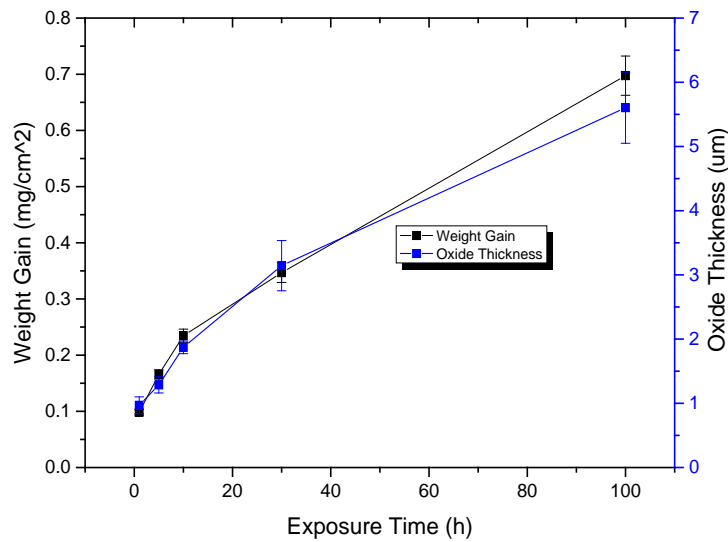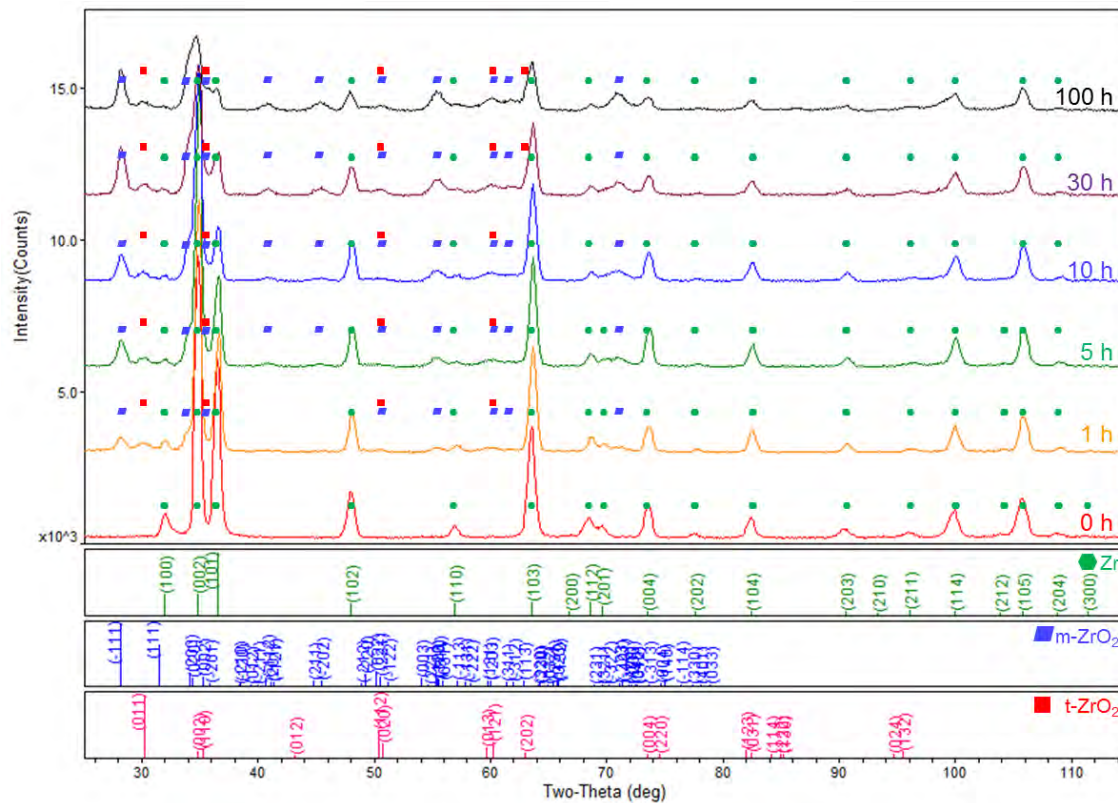Comparing cross sectional images on the normal direction- hoop direction (ND-HD) plane of pre- and post- creep test specimen with 750 wt. ppm which was exposed at 500°C and at 65MPa for 57 hours, hydrid platelets aligned along circumferential direction which is similar to original feature before creep test, no radial hydrides were found.   It signifies that the hydride reorientation induced embrittlement does not account for a shorter creep lifetime.   On the other hand, effect of hydrogen in solid solution to facilitate the movement of dislocation is consistent with the solve stress exponent n=4 in Fig.1 - 18.   A dislocation creep dominated steady-state creep deformation rate would have a σ^n dependence, where n = 3~ 5.
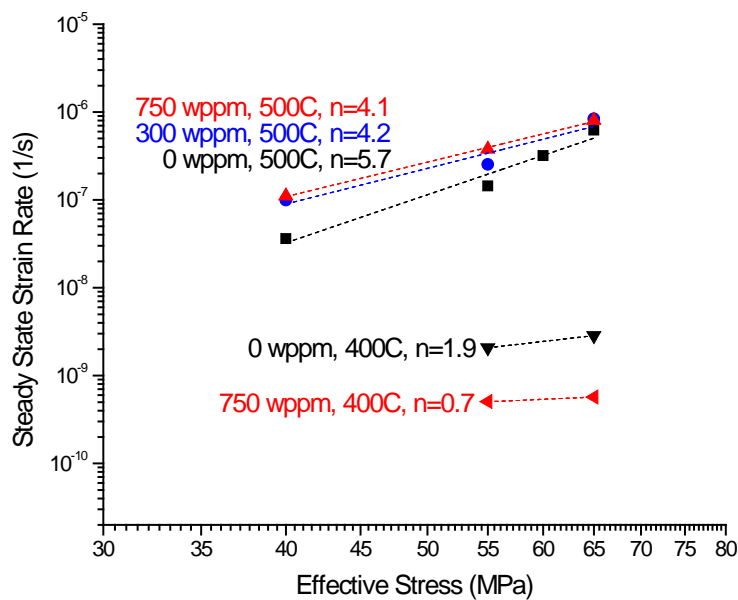
Fig.1 - 20 Stress exponent analysis of zircaloy-4 cladding at 500°C and 400°C

ND-HD cross-sectional images of different place also depicted in Fig.1 - 19.   There is no significant intergranular crack or triple junction void microstructure, which would correlate to creep fracture mechanism, can be observed by optical microscopy.   In addition, cross sectional images on normal direction- longitudinal direction (ND-LD) plane is represented in Fig.1 - 20. It is noted that the hydride density decreased gradually with decrease in the distance between observation location and end cap.   This results indicates that hydrogen diffused toward the end cap.   At location E which is close to the center of specimen, the some hydride near the outer region slightly oriented to the normal direction.
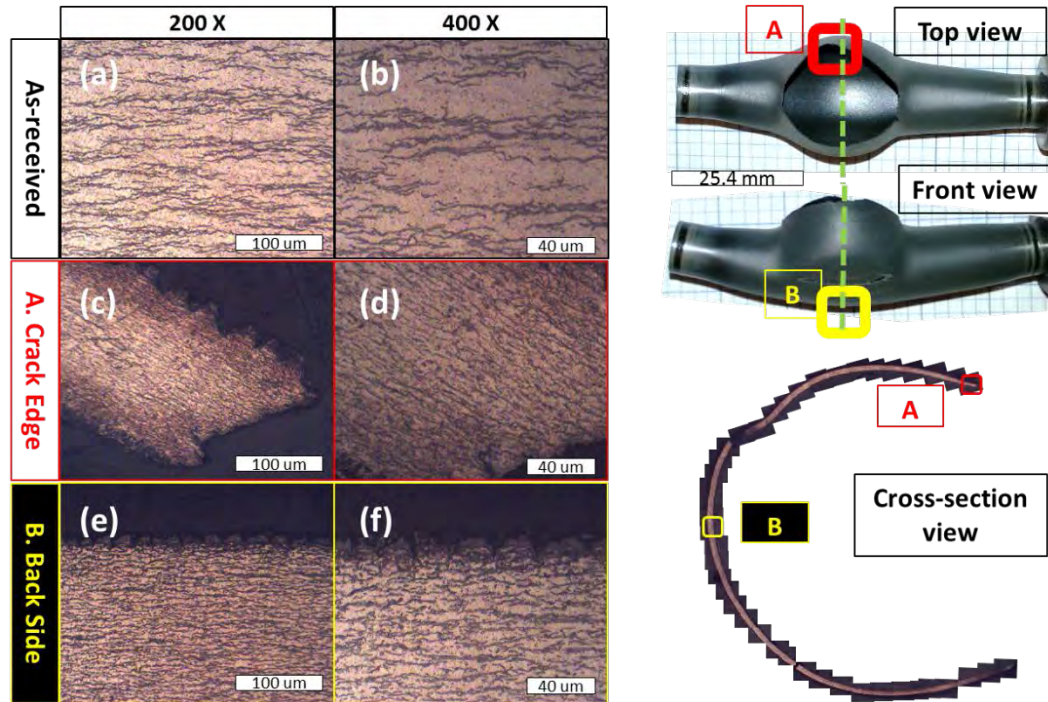
Fig.1 - 21 Cross-sectional images on normal direction - hoop direction (ND-HD) plane of Zircaloy-4 tube with 750 wt. ppm H before and after creep test at 65 MPa, 500°C for 57 hours, and location indication of observation, where the specimen was cut along the green dash line.
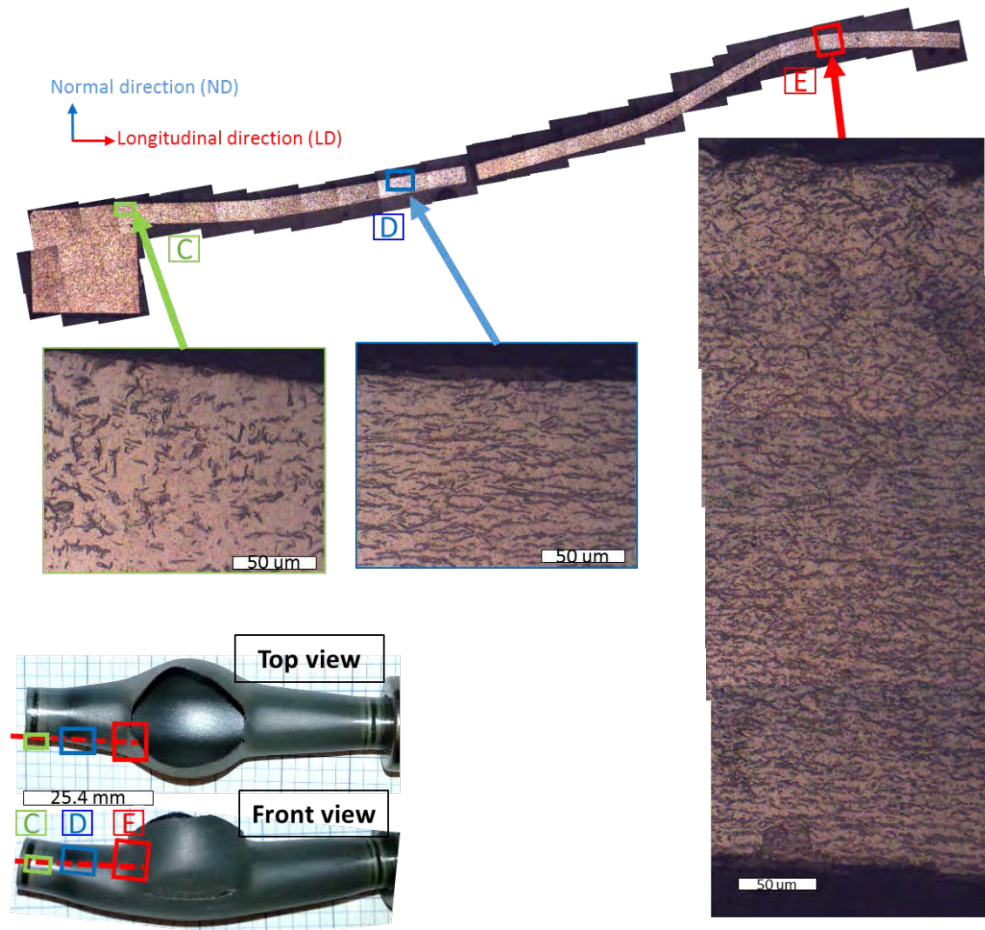
Fig.1 - 22 Cross-sectional images on normal direction - longitudinal direction (ND-LD) plane of Zircaloy-4 tube with 750 wt. ppm H after creep test at 65 MPa, 500°C for 57 hours, and location indication of observation, where the specimen was cut along the red dash line.

Results of the appearance and surface morphology close to the terminals of cladding tube is demonstrated in Fig.1 - 22.   The thickness oxidation of layer at the surface of heat-affected zone (HAZ) by e-beam welding is about 3 um and significantly smaller than that of the place away from HAZ, as the gray layer shown in Fig.1 - 22 (a) and (b).   Oxide on HAZ pointed out by the purple arrow in Fig.1 - 22 (d), looked darker than other places.   Fig.1 - 22 (e) shows the area of HAZ, where the depth is about 750 um.   Enlarged view on the boundary of HAZ in Fig.1 - 22 (f) shows a dense dendritic structure which is an evidence of that this region was influenced by a strong heat gradient.
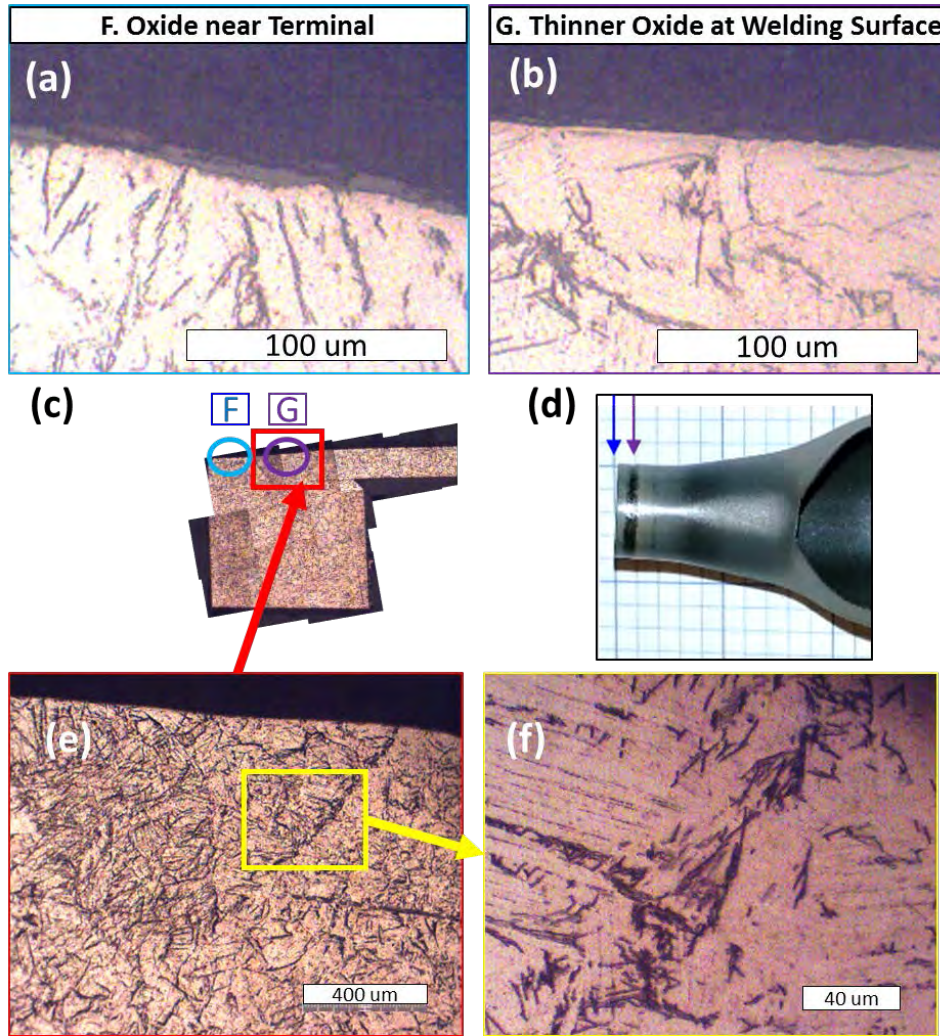
Fig.1 - 23 Cross-sectional images on ND-LD plane around the end cap of Zircaloy-4 tube with 750 wppm H after creep test at 65 MPa, 500°C for 57 hours, and location indication of observation.

To analysis texture evolution before and after biaxial creep test, discs with 3 mm in diameter were cut from the Zircaloy-4 cladding by using a traveling-wire, electrodischarge machine (EDM), and were mechanically polished to 1200 Grit.   Principle directions of specimen with respect to the cladding are demonstrated in Fig.1 - 24.   Direct pole figure of Zr(0002) basal plane of Z0-series and of Z7-sereies before and after creep test at 500°C are shown in Fig.1 - 25 and Fig.1 - 26, respectively.   The typical preferential orientation of Zr(0002) basal plane of CWSR Zircaloy-4 cladding with two apexes inclined $\pm30°$ from radial direction toward circumferential direction can be observed in Fig.1 - 25 (a) and Fig.1 - 26 (a).   After creep testing, the two apexes are closer to each other.   To quantified the texture evolution, Kearns factors [16] are used given as f_{TD}, f_{RD}, and f_{ND}, [17]

$$f_{\text{TD}} = \frac{1}{N} \int_0^{\pi/2} \int_0^{2\pi} I(\chi,\psi)\, sin^3(\chi) sin^2(\psi)\, d\chi\, d\psi$$

$$f_{\text{RD}} = \frac{1}{N} \int_0^{\pi/2} \int_0^{2\pi} I(\chi,\psi)\, sin^3(\chi) cos^2(\psi)\, d\chi\, d\psi$$

$$f_{\text{ND}} = \frac{1}{N} \int_0^{\pi/2} \int_0^{2\pi} I(\chi,\psi)\, sin\ (\chi) sin^2(\psi)\, d\chi\, d\psi$$

Where $I(\chi,\psi)$ is the X-ray intensity for a basal-pole figure having χ as polar angle and ψ as azimuthal angle, and

$$N = \int_0^{\pi/2} \int_0^{2\pi} I(\chi,\psi)\, sin(\chi) sin^2(\psi)\, d\chi\, d\psi$$

N is a normalization constant.

Kearns' factor of the pole figure in Fig.1 - 25 and Fig.1 - 26 are presented in Fig.1 - 27. Solid symbols indicate results of Z0-series cladding and hollow symbols indicate results of Z7-series cladding. The difference between f_{TD} and f_{RD} is small at low stress condition. The difference of Z7-series is slightly higher than that of Z0-series
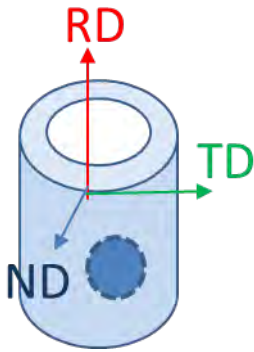
Fig.1 - 24 Principle direction of a 3mm disc used for the analysis of texture evolution after biaxial creep test. It is noted that RD = rolling direction = axial direction, TD =transverse direction = circumferential direction, and ND= normal direction= radial direction.
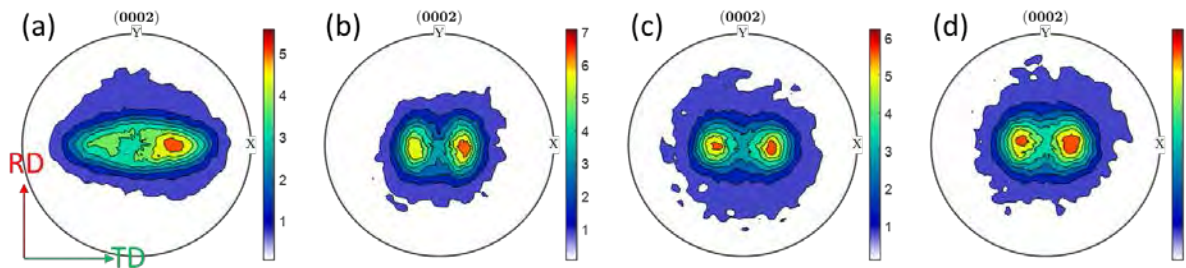
Fig.1 - 25 Texture evolution of Zircaloy-4 tubes without hydride after creep test at 500°C. (a) As-Received (b) Stress at 65 MPa (c) Stress at 55 MPa (d) Stress at 40 MPa. It is noted that RD = rolling direction = axial direction and TD =transverse direction = circumferential direction.
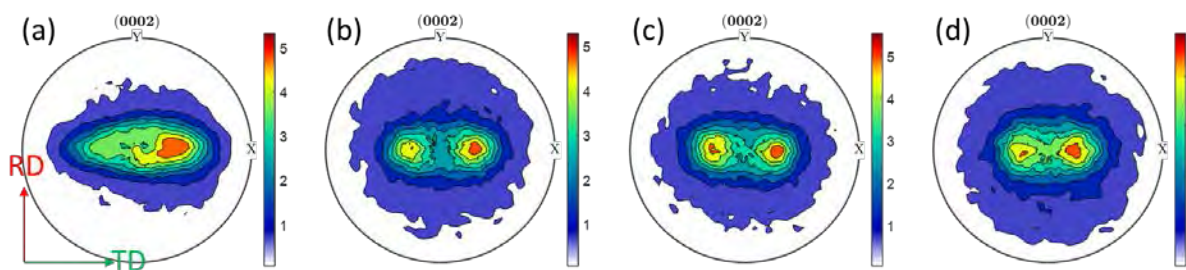
Fig.1 - 26 Texture evolution of Zircaloy-4 tubes with 750 wt. ppm H after creep test at 500°C. (a) As-Received (b) Stress at 65 MPa (c) Stress at 55 MPa (d) Stress at 40 MPa It is noted that RD = rolling direction = axial direction and TD =transverse direction = circumferential direction.
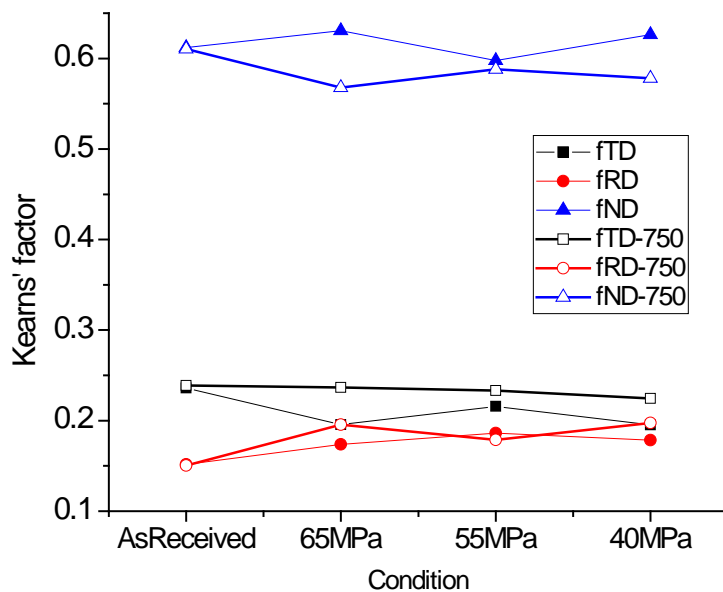
Fig.1 - 27 Kearns factor of Zircaloy-4 tube with 750 wppm H after creep test at 500°C.

A TEM bright field image of Z7D50 cladding failed in 543 hours is demonstrated in Fig.1 - 28. The dislocation network is observed at the left hand side of the image, which could be the interaction of <a> type dislocation gliding on their slip plane.
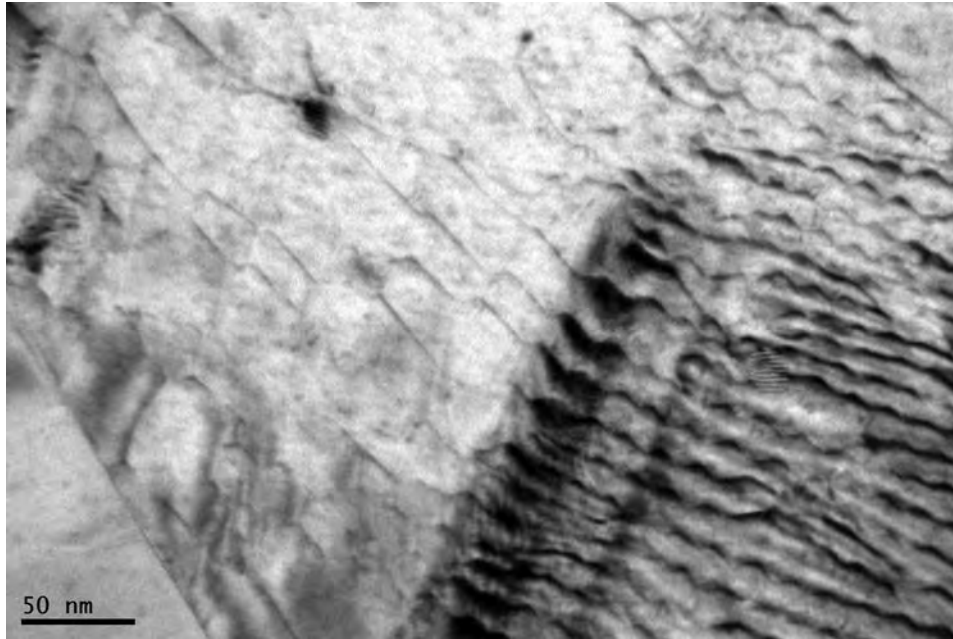
Fig.1 - 28 TEM   bright field image of Zircaloy-4 tube with 750 wppm H after creep test at 40 MPa and 500°C failed in 543 hours.

The characteristic crystallographic texture of cold-worked stress-relieved (CWSR) Zircaloy-4 cladding is the angle $\pm30°$ between two basal poles of α-Zr (002) plane and radial direction, as shown in Fig.1 - 29. This special texture distribution of CWSR Zircaloy-4 cladding are related to improved mechanical properties and corrosion resistance for application in nuclear reactor. Understanding of crystallographic texture evolution of pre-hydrided cladding after creep test would help to evaluate the degradation in mechanical properties in crept material. High energy synchrotron X-ray at beamline 1-ID at Advanced Photon Source (APS) in Argonne National Laboratory allow us to study minor amount of second phase such as zirconium hydride which is not able to be analyzed using in-house XRD on campus, as demonstrated in Fig.1 - 30. It is noted that the crystallographic structure of hydride belong to δ-hydride phase according to the lattice spacing of hydide peaks.
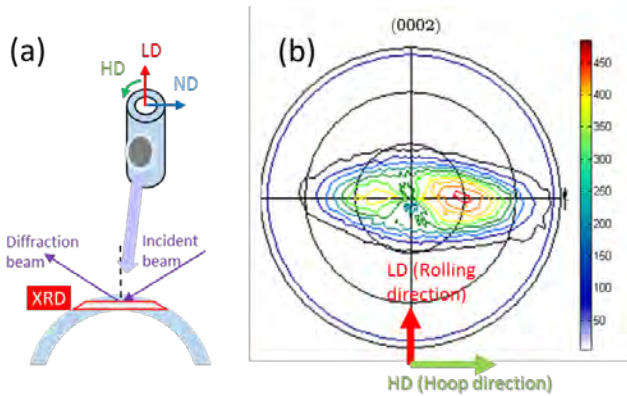
Fig.1 - 29 (a) Indication of a 3mm foil on longitudinal direction (LD)- circumferential direction (HD) plane for pole figure measurement using XRD. (b) (0002) direct pole figure of Zircaloy-4 cladding without hydrogen charge process before creep test.

.
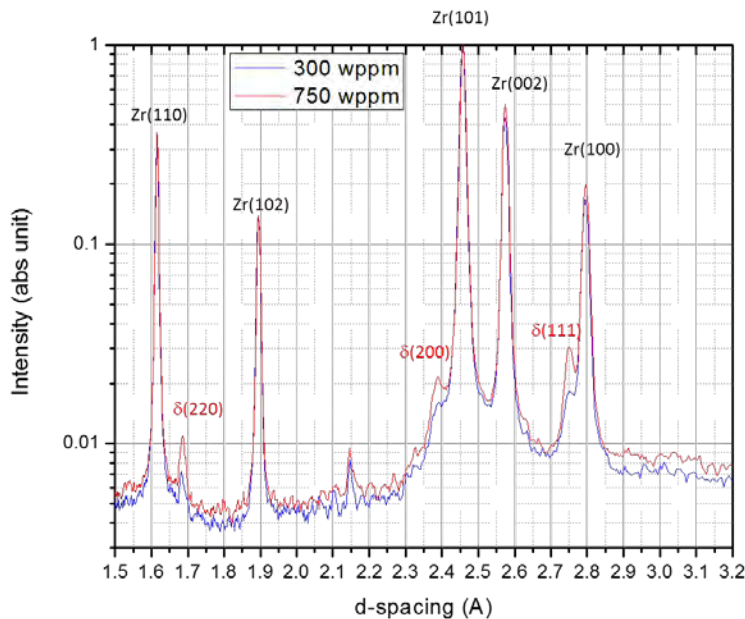
Fig.1 - 30 Pre-creep analysis of Synchrotron X-ray diffraction of Zircaloy-4 with hydrogen content 300 wt. ppm (in blue) and 750 wt. ppm (in red).

Ex-situ synchrotron wide–angle x-ray scattering (WAXS) tests of crept specimen will be used to investigate texture evolution of hydride and matrix phase before and after biaxial creep test. A more detailed setup diagram can be found as Fig.1 - 31. The WAXS signal was

collected by a detector array composed of four identical GE angio type 41 cm × 41 cm 2D detectors, which is named "Hydra" detector array. Crept sample will be rotated along the ω direction (rotate about the vertical direction as well as the longitudinal direction of specimens) with wide-angle X-ray scattering (WAXS). ω angle will range from 0 to 360 degree. A full rotation in continuous mode with a 0.5 degree interval is proposed for the w scan. Pole figures of multiple crystallographic orientation of hydride and matrix phase can be captured in one measurement. In-situ synchrotron heating tests will be conducted to analysis the terminal solid solubility for hydride dissolution of pre-hydrided at 300°C, 350°C, and 400°C. Data analyses are supposed to take 6 months.
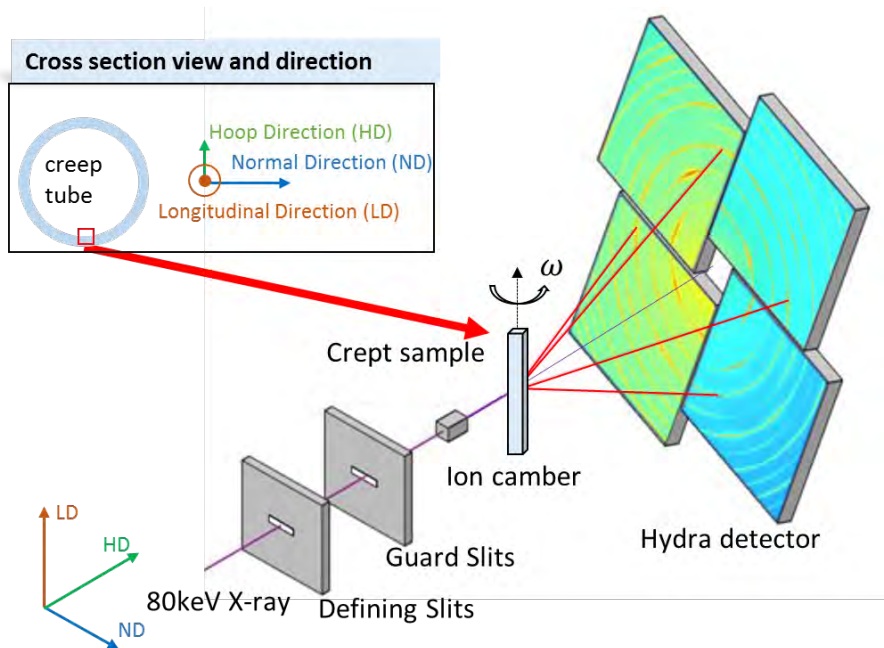
Fig.1 - 31 Synchrotron experiment setup

1.5. Summary and Future Work

The pressurized tube technique successfully achieved on pre-hydrided Zircaloy-4 cladding in this study. Biaxial creep tests on Zircaloy-4 tubes were conducted using internal pressurization of closed-end tubes at 500°C, 400°C, 350°C, and 300°C. The increase in hydrogen level accelerates steady-state creep rate and shortens the lifetime at 500°C air. Zircaloy-4 claddings with high hydrogen content showed a lower creep strain rate at creep temperature below than 500°C.

To provide further understanding of the creep behavior of Zircaloy-4 claddings with high hydrogen content at low temperature, investigation and microstructure analysis for specimen

crept at temperature below 500°C are scheduled and listed as following:

1. Ex-situ synchrotron wide–angle x-ray scattering (WAXS) tests of crept specimen will be used to investigate texture evolution of hydride and matrix phase before and after biaxial creep test.

2. Characterization of Post-Creep Specimen, including tensile tests along radial direction and longitudinal direction to observe the distribution of hydride phase using optical microscopy (OM) and SEM.

3. Investigation of the microstructure around e-beam welded region with low oxidation rate.

2. Evaluation of off normal temperature events in stored nuclear fuel cladding on storage limits utilizing a modified dating code.

2.1. Introduction

Since the mid-1980s when spent fuel pools began to reach their capacity at nuclear plants operating companies have had to find alternative options for spent fuel storage. The main two options consist of increasing the spent fuel pool size and casking the fuel assemblies for dry storage either on site or at a repository. With the closing of Yucca Mountain in 2011 there are no fuel repositories in the United States, as such casked dry storage is becoming more and more significant in the United States as the total fuel amounts will eventually surpass the capacity for wet storage [18].

During storage, fuel cladding is at risk of failure from several processes, among them creep failure is considered the most important [19]. Though the rate at which creep occurs within the cladding is low, over the course of twenty to forty years accumulated damage in the cladding can cause failure. Because temperature and pressure determine the rate at which creep occurs over the lifetime of a cask the Determining Allowable Temperatures in Inert and Nitrogen Gases code (DATING) routine was developed to determine an allowable temperature and pressure combinations for dry storage [19].

During storage the cladding experiences a decreasing internal temperature, and thus a decreasing creep rate throughout its life time. However unexpected temperature events, such as repackaging, re immersion into a fuel pool, or failures of the cask cooling system can occur. These events could potentially cause a temperature spike within the contained assemblies which could spike the creep rate and thus affect the overall expected lifetime of the cladding.

The DATING routine works well for standard cases of storage, however off-normal temperature events are not well incorporated into the system. This study aims to reproduce the DATING routine using updated creep equations in order to look at the effect off normal temperature events have on allowable temperature limits for zirconium based cladding. Zircaloy-4 will be used for several creep tests at varying temperatures and pressures expected to be seen during storage, updated creep equations will be fit to the data to better allow for changing temperature conditions in the code, and finally the effects of several off temperature conditions will be looked at for potential storage risks.

2.2. Background

2.2.1. Overview

Since the early years of nuclear reactor design, zirconium and its alloys have been of interest for cladding design.   The combination of their low macroscopic neutron cross section, good aqueous corrosion resistance, high melting temperature, and ease of fabrication and weldability make it an ideal material for in reactor cladding usage [20].   However, it has only been since the 1960s that databases of creep test results for these alloys have really been put together, and the results of the tests analyzed for better understanding of the materials mechanics.

Zirconium creep data have been accumulated over many different test conditions, there have been several studies in low temperature ranges, 250-400°C, with stresses from 60-250 MPa [18] [20] [21] [22] [23], as well as a large amount of higher temperature studies with temperatures ranging upwards from 500°C [24] [25] [26].   Little has been done below 250°C as the time frames for these tests begin to range into multiple years for noticeable effects to be seen. Because of this being able to use higher temperatures and pressures and extrapolate downwards is of key interest to the industry.   Despite this attempt to apply higher temperature and pressure data to lower temperature and pressure conditions, no universal creep law has been found which applies well to all the creep data at this time.   However several general forms have been made which can be fit to fairly large ranges of conditions.

Currently the NRC review plan for dry storage calls for a very low probability of cladding failure during extended storage [27].   To demonstrate this fuel performance codes are often used to predict and demonstrate the behavior of the cladding over its expected storage lifetime. Because of the long term nature of these predictions accurate creep modeling is of utmost importance in the fuel performance codes which predict over 40 years in some cases.   One of the more used codes in the industry is FRAPCON which utilizes the Determining Allowable Temperatures in Inert and Nitrogen Gases (DATING) code subroutine to evaluate cladding conditions over the course of the time fuel is to be stored.   In order to better understand the workings of this creep performance model a brief overview of the equations utilized in the code will be covered.

2.2.2. Creep Strain Models

Two main approaches to creep modeling are taken by most studies, the first being a mechanistic approach in which differing creep mechanisms such as high-temperature climb, low-temperature climb, grain boundary sliding, Nabarro-Herring creep, and Coble creep to name a few have equations fit to them to understand the expected behavior of the material at given

conditions [20].   The other main approach is to fit a more general creep equation to empirical data, often in the form of several independent functions and constants for each variable in the creep scenario, stress, temp, fluence [28].

Both the Matsuo and Mayuzumi studies utilized a generalized creep equation approach to modeling Zr-4 tubes under internal pressure. Eq.2-1 takes the form of a steady state creep strain determined by experienced stress and temperature, and a primary creep strain based on the calculated steady state rate. The equations utilize fit constants D, n, a, b, A and B, while also using E as the Elastic modulus, T for temperature in °K, and R for the universal gas constant. While both Matsuo and Mayuzumi utilize the same equation forms, it can be seen in Table 2- 1 that different constants are found for the separate cases [21] [24].

$$\varepsilon = \varepsilon_p^s\{1 - \exp(-D(\dot{\varepsilon}_s t)^n)\} + \dot{\varepsilon}_s t \qquad (2.1)$$

Where

$$\varepsilon_p^s = a(\dot{\varepsilon}_s)^b \qquad (2.2)$$

Which represents the primary creep behavior, and

$$\dot{\varepsilon}_s = A\left(\frac{E}{T}\right)\exp\left(\frac{B\sigma}{E}\right)\exp\left(\frac{-Q}{RT}\right) \qquad (2.3)$$

Which represents the secondary creep behavior.

Table 2- 1 Constants utilized in Matsuo and Mayuzumi creep equations [21] [24]

	D	n	a	b	A	B	Q	ε_p^s
Matsuo	52	0.5	2.16×10^{-2}	0.109	1.57×10^{13}	1.13×10^3	272000	
Mayuzumi	10	.0.51			1.02×10^5	4060	233000	0.05

Different approaches utilizing the same base equation can be seen, where Matsuo fits an equation to calculate a saturated primary strain, ε_p^s, Mayuzumi notes that there was no clear tendencies in their data thus they took the average value of .05 for ε_p^s instead of calculating it like the Matsuo study [24].   The remaining values utilized in the equation formula vary drastically by values exceeding 10^8 in the case of constant A.   No absolute reason for the difference between the two studies found constants is known, however the operating regimes for both tests, Matsuo's being 330-420 ^{0}C with hoop stresses of 49-314 MPa and Mayuzumi's being in the range of 454-584 ^{0}C and stresses of 8.5-19.5 MPa, not overlapping could indicate that the equation form used is only valid for conditions which were included in the fitting of constants utilized in the equation [21] [24].

The other approach to creep modeling is to utilize governing equations for different creep mechanisms such as high-temperature climb, low-temperature climb, grain boundary sliding, Nabarro-Herring creep, and Coble creep.   Ashby and Frost state that seven or more mechanisms are factors in the deformation of metals and crystalline structures.   To utilize this information a diagram, or map, of which process dominates a given stress and temperature condition is created based on governing equations tied to those processes [29].   Depending on the source which of the processes, and the equations tied to them can differ.   For example Ashby [30] describes diffusion controlled creep has been theoretically described as

$$\dot{\varepsilon} = \frac{14\Omega}{kT} \frac{D_v}{d^2} \sigma \left(1 + \frac{\pi \delta D_B}{d \, D_b} \right) \tag{2.4}$$

where

    Ω= atomic Volume,
    k= Boltzmann constant,
    d= average grain diameter,
    δ= grain boundary thickness
    D_v= volume diffusivity,
    And D_b= grain boundary diffusivity

Which reduces to the forms for Nabarro-Herring creep and Coble creep when $D_v \gg D_B$ or $D_B \gg D_V$ respectively.

$$\dot{\varepsilon}_{NH} = \frac{14\Omega}{kT} \frac{D_v}{d^2} \sigma \tag{2.5}$$

$$\dot{\varepsilon}_{coble} = \frac{14\Omega}{kT} \frac{\pi \delta D_B}{d^3} \sigma \tag{2.6}$$

Ashby [30] also describes dislocation controlled creep as

$$\dot{\varepsilon}_{climb} = A \frac{D_v \, \mu b}{kT} \left(\frac{\sigma}{\mu} \right)^n \tag{2.7}$$

Where

    μ= sheer modulus and
    b= burgers vector of dislocation

This approach relies upon an understanding of the microstructure of the material being utilized, and the effects each process will have on the crystalline structure. The DATING code developed in 1988 by Pacific Northwest National Laboratory utilizes a similar approach of assigning equations to each creep mechanism. It assigns equations for the following mechanisms: High-Temperature Climb (HTC), Low-Temperature Climb (LTC), Grain Boundary Sliding (GBS), Nabarro-Herring and Coble creep [19]

$$\ln(\dot{\varepsilon}) = A * \ln\left(\frac{\sigma}{E}\right) + B - C * \left(\frac{T_m}{T}\right) + \ln\left(\frac{T_m}{T}\right) + \ln\left(\frac{E}{10^4}\right) \qquad (2.8)$$

Where

σ = stress (MPa)

T_m = melting temperature (K)

E = elastic modulus (MPa)

T = cladding temperature (K)

As can be seen in Fig. 2- 1 each of these processes has a region of the map of temperatures and pressures where it is the dominating mechanism for creep strain in Zircaloy. Using this map each of the equations constants are fit by determining conditions at which two mechanisms contribute equally, and by equating the two processes to each other over the large range of combinations where they are equal the constants found in Table 2- 2 are determined. With these constants similarly to the Ashby equations a creep rate can be assigned to each mechanism for a given temperature [19].

Table 2- 2 Constants for differing creep mechanisms in the DATING code

	A	B	C
HTC	5	55.75	14.15
LTC	7	55.18	10.19
GBS	2	20.74	9.9200
Nabarro Herring	1	18.25	14.15
Coble	1	11.03	9.9200
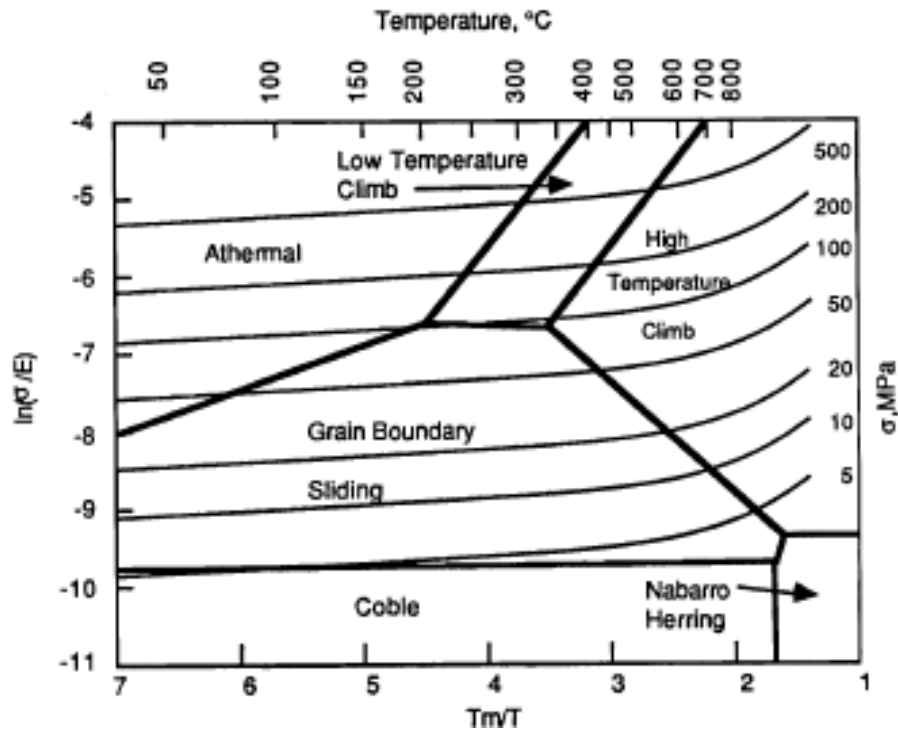
Fig. 2- 1 Creep deformation map for Zircaloy-4 [19].

2.2.3. Temperature Modeling

In order for the performance codes to properly simulate creep strain over years of storage, an accurate representation of the conditions the fuel experiences must be known. In 1987 Levy et al. examined both BWR and PWR fuel assembly designs in order to design a model of the decaying temperatures within storage casks backfilled with helium gas. They found two major regions of decay over the lifetime of the fuel, an initial rapid drop off for the first seven years which transitions to a slower rate from then onwards [31]. The model, shown below, is based around the temperature history of 1 year out of the reactor fuel with a burnup rate of 30 MWd/kgM.

$$T_1 = T_a \left(t^{-.3400}\right) \text{ for } 1 < t < 7 \text{ years} \tag{2.9}$$

$$T_2 = T_b \left(t^{-.0840}\right) \text{ for } t > 7 \text{ years} \tag{2.10}$$

Where

$$T_b = T_a \frac{7^{-.3400}}{7^{-.0840}} \qquad (2.11)$$

T_a is decided based on the initial fuel temperature at the start of storage. Levy et al. determined that both T_1 and T_2 would under predict temperature in the region of the other, so the model is set to choose the maximum between the two separate equations [19]. The DATING code utilizes both the Levy equations in the case of storage in helium as well as a separate set of equations for storage in nitrogen [19]. This equation takes the form

$$\ln(T - 273) = a_0 + a_1 * \ln(time) \qquad (2.12)$$

Where the coefficients a_0 and a_1 are dependent on the burnup, B in MWd/kgU, and similar to the helium storage equations time since removal from the reactor. For times from 2 to 5 years they take the form of

$$a_0(B) = \exp[1.455 + 0.20 * \ln(B) - 0.2391 * 10^{-1} * \ln(B)^2] \qquad (2.13)$$

$$a_1(B) = -1.0339 + .0094 * B \qquad (2.14)$$

And for times over 5 years

$$a_0(B) = \exp[1.167 + 0.169 * \ln(B)] \qquad (2.15)$$

$$a_1(B) = -0.51391 * 10^{-1} - 0.98780 * 10^{-2} * B$$
$$= 0.92362 * 10^{-4} * B^2 \qquad (2.16)$$

Just like the helium case, the larger of the two temperatures calculated is utilized in the model as the temperature for a given time [19].

2.2.4. Creep Failure and lifetime fraction model

Just as creep-deformation maps have been developed to discern which creep mechanism will be prevalent at a given temperature and pressure, creep-rupture mechanism maps have also been created in order to understand which method a given specimen will eventually fail by [19]. The mechanism of failure depends on the expected temperature and pressure experienced by the sample, as can be seen in figure 4 for common dry storage applications of pressures less than 100

MPa the main mechanism by which failure is expected is cavitation diffusion controlled rupture, transitioning to cavitation power law rupture at lower temperatures [19].
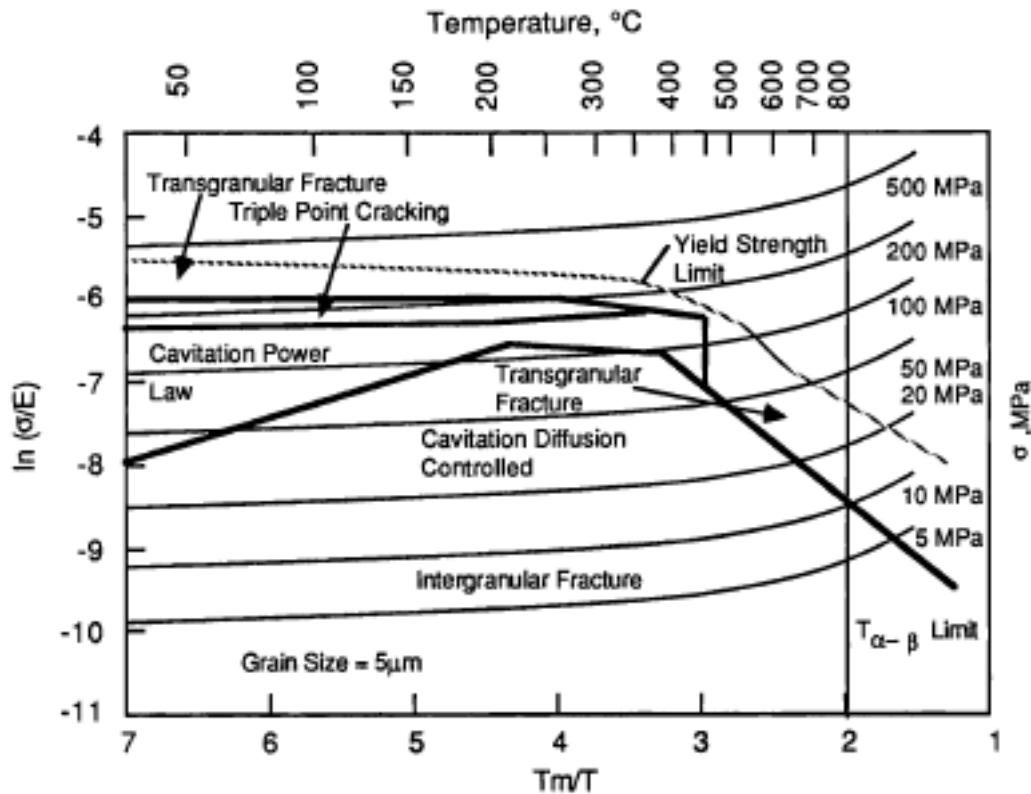
Fig. 2- 2 Creep rupture mechanism map [19].

For each of these mechanisms equations were fit to model the expected failure time of the material taking the reduced form [19]

$$\ln\left(t_{fx}\right) = A - \ln(\dot{\varepsilon}) - B * ln\left(\frac{\sigma}{E}\right) - \ln\left(f(X)\right)$$

(2.17)

Where

A & B are constants

$\dot{\varepsilon}$ is the expected creep rate

σ is the stress

And f(x) depends on the creep rupture mechanism

While initially used in the dating code the approach to failure time calculation was revised in 2001 to utilize a conservative Monkman-Grant relationship [32]. This relation correlates the temperature, creep rate and failure time to a Constant, which then once rearranged into the form

of Eq.2.18 can be utilized to solve for an expected failure time.

$$t_f = \frac{0.02e^{\left(6.2-\frac{4300}{T}\right)}}{\dot{\varepsilon}} \qquad (2.18)$$

In a steady state environment this relationship could be utilized directly to find a temperature and strain rate combination that allows for the desired storage time limit. However, in order to be utilized within the DATING code where temperature conditions are changing a method for monitoring the damage in the material over its cumulative lifetime of conditions must be used. The damage fraction model used in the DATING code solves for a creep rate utilizing Eq.2.8 and the constants from Table 2- 2 at each time step of the desired lifetime for the cladding. These creep rates are utilized with Eq.2.18 to find the expected failure time for the conditions at each time, then using the length of an the individual time step in the code determines the fraction of the failure time the cladding would experience at that given time step. Each of these individual fractions can then be integrated across the entire time length of interest to find a cumulative damage fraction for a given set of starting conditions. Damage fractions greater than one representing failure before the desired lifetime is reached, fractions less than one meaning failure is expected past the desired lifetime [19].

2.2.5. Potential off normal temperature events

As this study is looking at the potential effects of off normal temperature conditions on storage limits, potential events will be discussed here. In the normal course of operation, previously noted equations for temperature profiles have been shown to be accurate [31]. However, in the case of off normal operations, temperatures have been noted to spike which would not be reflected in the base temperature profile utilized by performance codes such as DATING.

An EPRI report from 2001 noted that after fuel is transferred from a wet storage pool and interred in a cask for dry storage, there is a 24 hour drying period during which the encountered temperature will ramp up, dwell, and then ramp back down as the fuel dries and the cask is filled with helium [33]. The amount of the temperature rise for this event is assumed to be 40°C though the report does tie this to the specific case of a 17x17 Westinghouse PWR design, and doesn't elaborate on how it would change depending on burnup differences or fuel design [33].

Mayuzumi and Onchi prefaced several studies on evaluating creep property data for Zircaloy at up to 800°C on the events such as burial accidents, or abrupt drying inside of the cask [24]. This statement of temperatures up to 800°K (526°C), considering average storage temperatures can range from initial storage conditions of 400°C to an average around 290°C [33]

shows the a large potential for change in internal conditions given the right events.

2.3. Equation Fitting and Modified DATING Code

The goal of this work is to evaluate the effects which off normal temperature conditions could have on storage limits for fuel cladding over expected lifetimes. This necessitates the usage of a creep model which is viable over a larger range of temperatures. Due to the differences in the approaches of modeling the generalized and mechanistic models described in the prior section both will be utilized separately in order to verify any effects found in one will are not inherent to the individual modeling approach. For the mechanistic approach Eq. 8 and Figure 2, in the original DATING code will be utilized as they have been reviewed and revised multiple times over several years [19] [31] [32], and the approach on its own is designed to cover the full spectra of temperature and pressure conditions. The generalized equation utilized by Matsuo and Mayuzumi can be seen in Table 2- 1 to have drastically different fit constants depending on the range the data they are mapping occurs in. For this reason several creep strain experiments have been run over the temperature range of 300-500^{0}C, as opposed to limiting it to 100^{0}C ranges the studies use in order to try and increase the range of accuracy when extrapolating the model downwards.

2.3.1. Creep strain modeling

Due to the shape of the temperature profile experienced by the cladding it can be expected that the largest amount of creep strain will be in the initial years of the fuels storage lifetime. Because of this importance is placed on models being accurate across the large range of temperatures experienced at the initial times of storage. Due to the fact that the Mayuzumi study and Matsuo study cover different temperature regimes and the fit constants do not match up across the different ranges, equations used in this study of the same form will be fit to data gathered over a temperature range of 300-500^{0}C and pressures of 40-65 MPa in order to extend the range of predictable creep strain of the equations. Experimental details have been mentioned in chapter 1.

2.3.2. DATING code and modifications

The original dating code is an iterative method by which an allowable initial temperature or stress is determined for dry storage of spent fuel assemblies. In both cases of stress or temperature iteration the user must input the other condition to describe the fuel to be evaluated. In both cases the code then sets a range of temperatures and stresses over which it will iterate, in

the case of temperature this is between 274 K and 1000 K, for stress this range is between 10 and 600 MPa.   Both these ranges are set above zero for the minimum to avoid complications in the code.   The user also enters a desired life time for the fuel, this study utilized 40 years as the time length for the fuel lifetime.   The code then takes the entered life time and will split it into 100 second intervals in order to get a good resolution for changing creep rates, especially at the start where temperature is changing rapidly.   Assuming helium is utilized for the cask at each time step the code will calculate the expected temperature utilize Eq.2.9 - 2.11.   Utilizing Eq.2.8 the code will calculate for each creep mechanism an expected rate and select the highest rate as the creep rate for that time step.   The resulting creep strain rate will then be entered into the Monkman-Grant relationship described by Eq. 2.18 and an expected failure time is then found.   From this the damage fraction of the time step is found by dividing the time step of 100 seconds by the expected life time at the current conditions, it is this step where the time step length determines accuracy of the found temperature limit.   Once each time step has been run the cumulative damage fraction for the conditions is found by integrating the individual fractions found across all the time steps.   If the found cumulative damage fraction is within a tolerance, (.05% in this study) of 1, the code will designate that run's temperature as the allowable limit and returns the value.   If it falls outside of the tolerance an iterative method is used where the program takes the two most recent solved allowable limit conditions, and extrapolates the conditions to find the theoretical point of unity, runs that condition, and potentially continues to extrapolate until the actual point of unity is reached.

Modifications to the DATING code have been made to evaluate the effect of off normal temperature events.   The ability to designate a point at which an event happens has been added to the code, when this point is reached in the life time, a switch is tripped in the code which adds a set temperature value to the calculated value to represent the effects an event may have.   In order to evaluate the worst possible case the temperature addition is maintained throughout the course of the fuel life time.   The other main change to the DATING code is the addition of the generalized creep equations fit to the data found in this study into the program in order to verify any effects of off normal events found.

In this study events occurring at 10%, 20%, 30%, 50%, and 75% of the desired 40 year life time have been evaluated.   For each of these time frames hoop stresses of 20, 30, and 40, and 60 MPa were used

2.4. Results and Discussion

2.4.1. Creep Equation Fitting

As mentioned in section 1.2.3, creep tests have been run at varying temperature and pressures in order to model the creep strain behavior of Zircaloy-4 cladding.   Samples were run until failure for high temperature test (at 500^0C), or a 2000 hour cumulative run time was reached for test temperature at 400^0C, 350^0C, and 300^0C.   The results of the creep tests are displayed in Fig.1 - 9 (a) and Table 2- 3.

Table 2- 3 Values for creep test findings

Temperature (C)	Stress (MPa)	Measured Steady state rate ($\dot{\varepsilon}_s$)	Saturated primary creep strain (ε_p^s)	A
500	65	2.30 E-03	0.01230	9.88E+09
500	60	1.20 E-03	0.00970	5.16E+09
500	55	7.08 E-04	0.01042	3.04E+09
500	40	1.65 E-04	0.00771	7.09E+08
400	65	8.79 E-06	0.00433	6.16E+05
400	55	6.67E-06	0.00204	9.06E+05
350	65	7.57E-07	0.00132	1.01E+06
300	65	1.56E-07	0.00032	2.46E+05

It can be seen that there is a drastic falloff in overall strain rates between the 500^0C cases and below 500^0C cases, for modeling purposes its necessary to split these two cases in order to increase accuracy of each region.

The constants in Eq.2.1- Eq.2.3 to be fit are split between the primary creep Eq.2.2 and the steady state creep rate Eq.2.3.   As the primary creep equation is based off of the found steady state, the constants for the steady state rate are determined first.   A relationship between the steady state creep rate and the normalized applied stress is utilized to find the stress constant B in Eq.2.3. In Fig. 2- 3 this relationship can be seen utilizing the 500^0C case with the large amount of stress cases tested for that temperature.   The slope is found to be 7114 which is then represents the stress dependence of the creep rate in Eq.2.3.   Similarly the activation energy is found from a relationship between the reciprocal of temperature and the natural log of the measure steady state rate, the stress constant B, applied stress, and temperature.   This relationship can be seen in Fig. 2- 4.   The slope found in Fig. 2- 4 corresponds with an activation energy of 202 (kJ/mol).
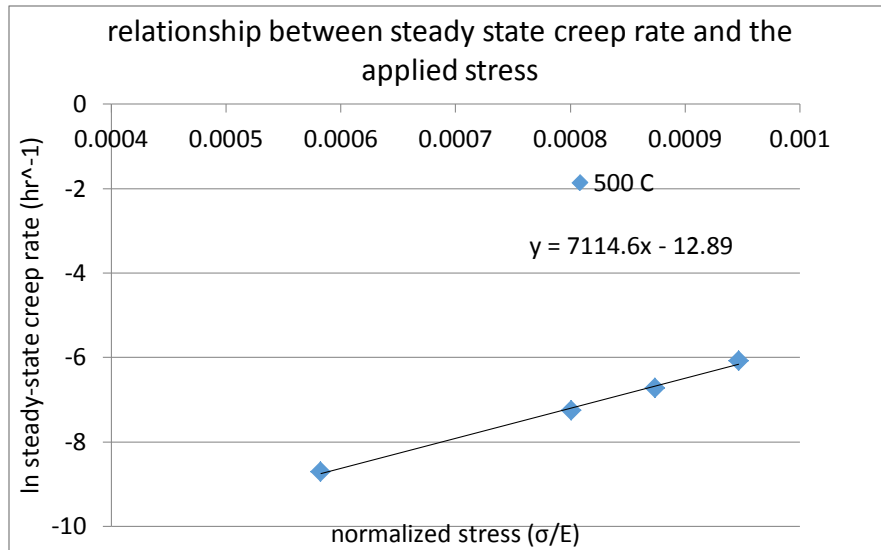
Fig. 2- 3 Relationship between steady state creep rates and the applied stress. The found slope corresponding with constant B in Eq.2.3 is found to be 7114.6
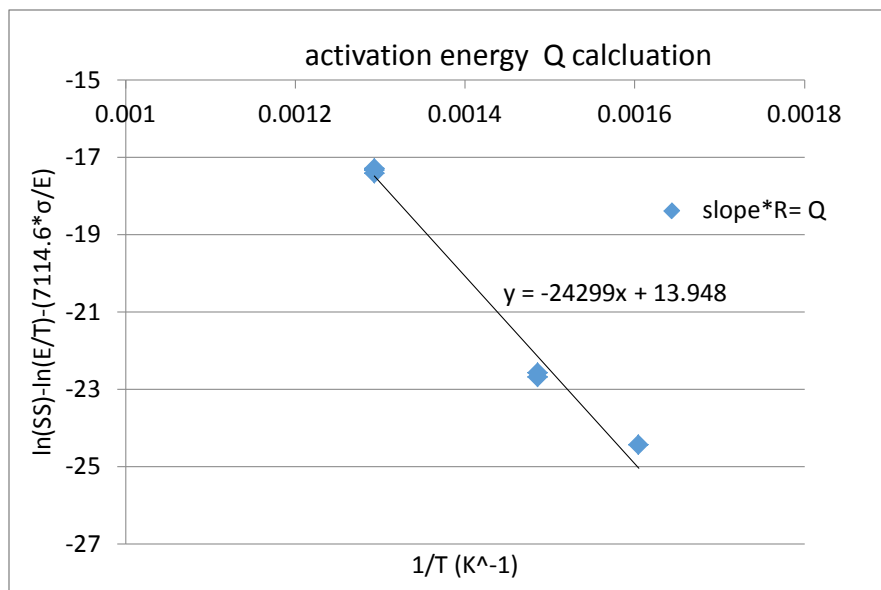
Fig. 2- 4 Relationship used to determine activation energy Q for Eq.2.3. Activation energy if found to be 202 kJ/mol

With values for B and Q, the final component A in Eq.2.3 can be found by direct substitution into Eq.2.3 to find a value for A in for a given condition. Table 2- 3 contains the found A values for each condition. It can be seen that in each case, the value of A does not take on a singular value thus is not truly a constant as is described in the Matsuo and Mayuzumi papers.

The values found all fall inside the range of A values found in the Matsuo and Mayuzumi papers of 1.02E+05 and 1.57E+13, however as they are not a constant, an approach must be taken to incorporate this new variable. For the 500^0C range the A value follows an exponential rate increasing with stress with a good fit as can be seen in Fig. 2- 5, it is suspected this would hold true in lower temperatures with the values in the exponential changing based on the temperature range however below 500^0C the data available are not vast enough to investigate this trend as only 500^0C could run tests at low enough pressure in a manageable time frame. For the below 500^0C case, instead a weak increasing trend can be seen between temperature and the found A values displayed in Fig. 2- 6. The found trend takes the form of:

$$A = 501.78 * e^{.0113*T}$$

(2.19)

Another approach to the A component would be to just take an average of the value and apply it, however this leads to very large errors in the calculated steady state rate thus these relations will be used in Eq.2.3 for the low and high temperature regions of the code.
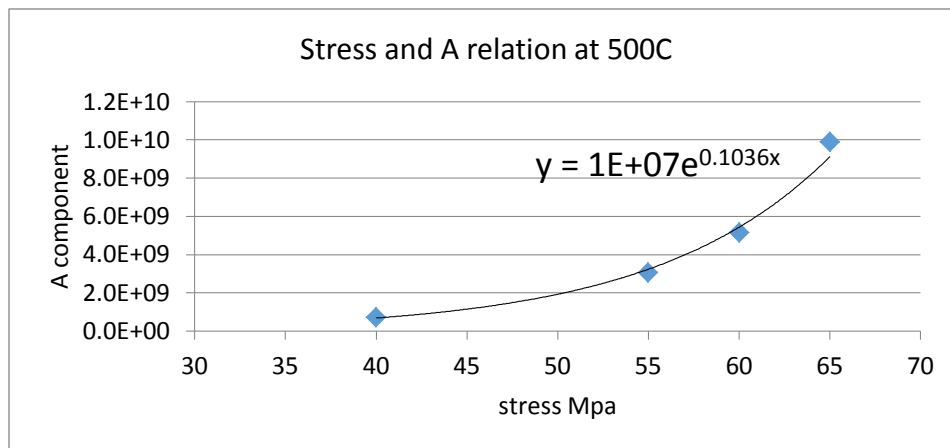

Fig. 2- 5 Relationship between stress and the A components at 500^0C. It can be seen that the data follows a close exponential fit to increasing hoop stress
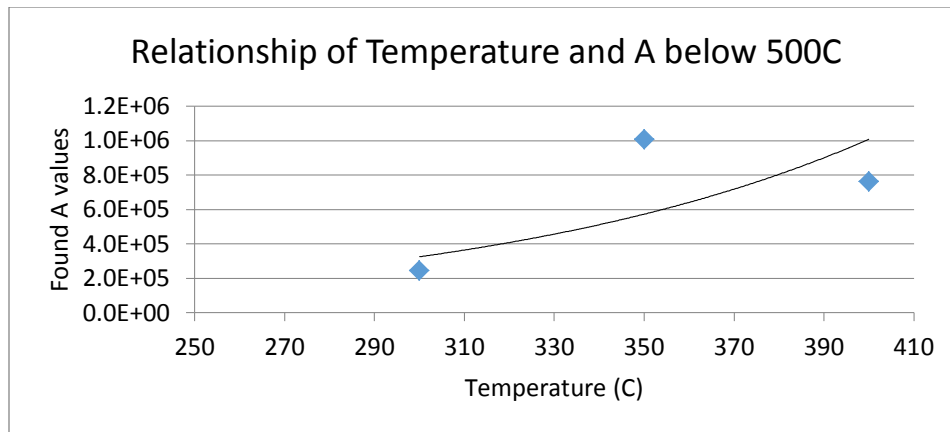
Fig. 2- 6 Relationship between stress and the A components at $500\,^{0}$C.   It can be seen that the data follows a close exponential fit to increasing hoop stress

The saturated primary strain ε_p^s calculated in Eq.2.2 is based on the calculated steady state rate at the conditions found.   Fig. 2- 7 depicts the relation between increasing steady state rate and increasing saturated primary creep.   Two distinct regions can be seen in the data, an initial rapid increase followed by a slower rate beyond a point.   This has been modeled by two separate linear equations which meet at a converging steady state rate of 2.069E-5(h^{-1}). Eq.2.2 has been replaced with this as it better represents this distinct change in rates seen in the experimental data.

Fig. 2- 7 Relationship of primary saturated strain and stead state strain rates for both high and low steady state rates

Matlab was utilized to fit constants D and n in Eq.2.1 through direct substitution of the measured creep values from Fig.1 - 9(a) and Table 2- 3, and the equations for saturated primary
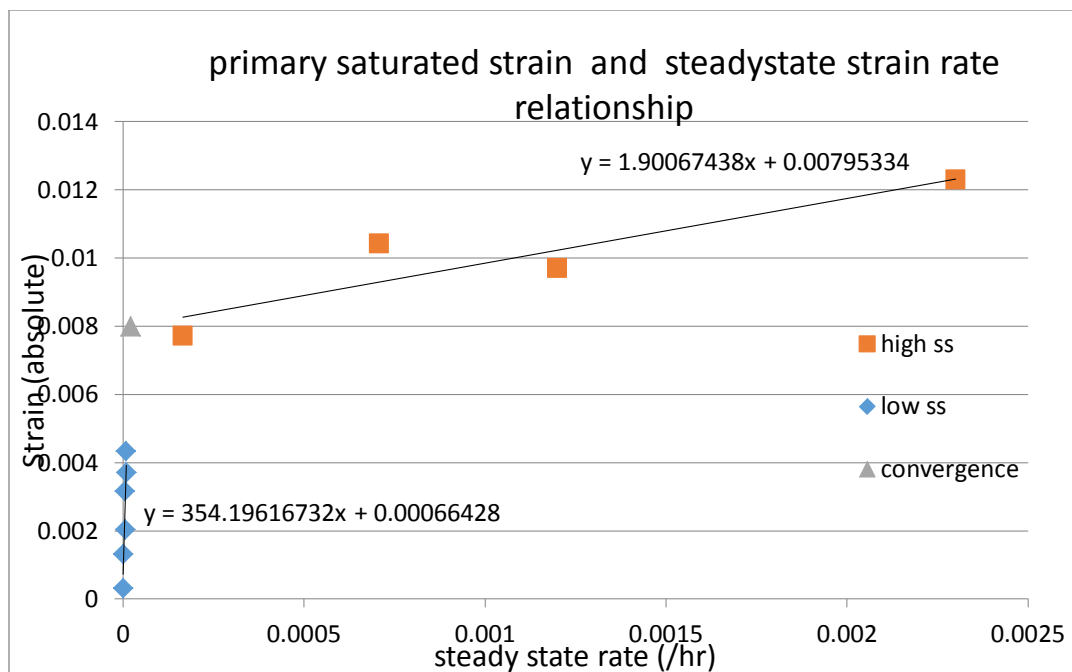
strain and steady state strain rate.   The first 30-100 hours of test time is utilized so that the fit matches the primary strain behavior the constants are meant to fit.   The constants found for D and n are 5.398 and .5199 respectively Fig. 2- 8 displays the fit of the final equation for several pressures and temperatures.   In most cases a good agreement can be seen between the prediction and experimental model.
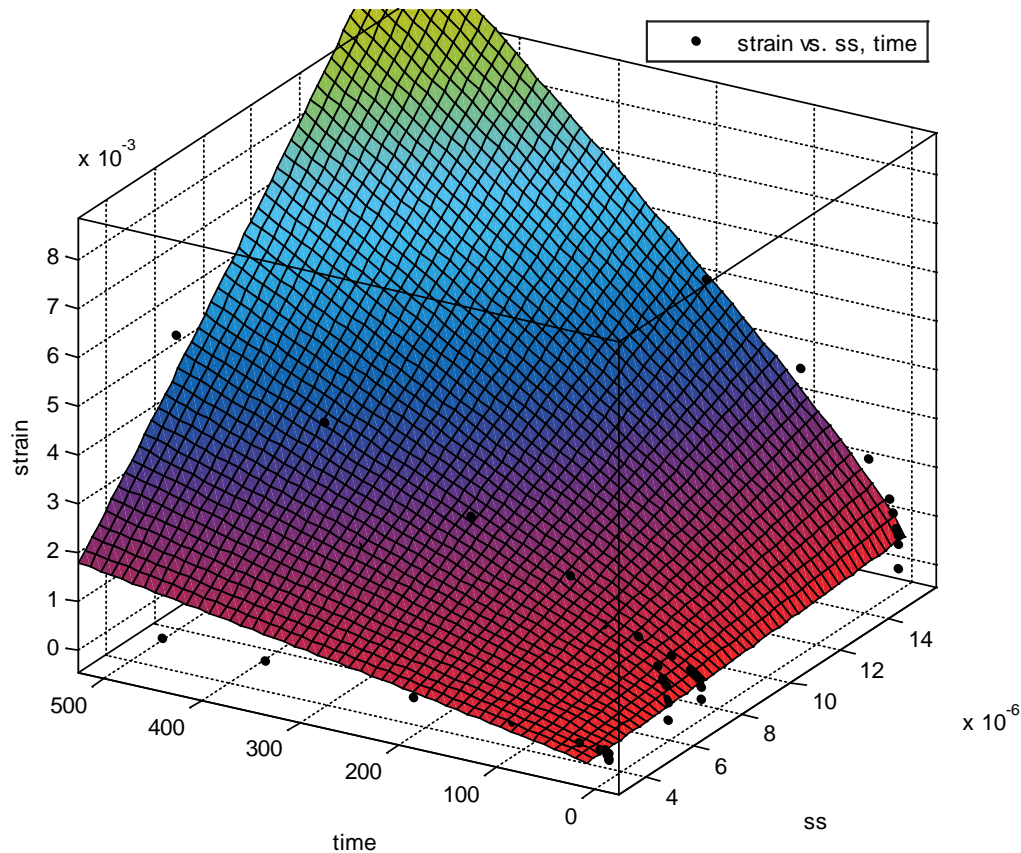
Fig. 2- 8 Matlab fit of constants n and D.   Fit matches well for primary portion of curve and early lifetime.   Though it over predicts once It reaches the steady state region.

It can be seen that for each case, the model does a good job of fitting the primary strain of the experiments.   However in each case it will eventually surpass the experimental data in the secondary region and begin to overestimate the strain.   This is likely due to the method of calculating the A constant in the steady state region not being a perfect fit as it directly modifies the entire value calculated for steady state creep as can be seen in Eq.2.3.   In the event it is too

low the model will under predict the strain, likewise if it over predicts the A value it will over predict in the secondary region. This trade off of over and under prediction is not present in the Matsuo and Mayuzumi models as they trade potential accuracy for consistency in over and under prediction by taking a single average of the value and applying it to all cases.

2.4.2. Finite Element Analysis for Creep Behavior

The experimental results are central to understand material properties at certain temperatures and stresses. However, these experimental conditions are limited and could not directly provide long-term creep life estimations. To develop a simulation equation, we begin with a description of the time-dependent relationship between stress and strain. Creep strain is described as the sum of two strain component: First one describes a linear stress dependence at low stress levels, and second one describes a stronger stress dependence at higher stress levels. The linear portion can be approximated by the relation $\varepsilon = C(t)\sigma$, where t represents time. This fitting line is used to evaluate the slope $C(t)$ and is allowed to intercept the strain axis at nonzero values. The interception value is considered to be a measurement uncertainty. The portion that has a stronger dependence on stress can be represented by $\varepsilon = K(t)\sigma^n$, where, n is the stress exponent. Then, the total stress-strain relationship can be represented by:

$$\varepsilon = C(t)\sigma + K(t)\sigma^n \tag{2.20}$$

As suggested by Swindeman and Pugh [34], $C(t)$ and $K(t)$ can be represented as:

$$C(t) = A \, cosh^{-1}(1 + rt) \tag{2.21}$$

$$K(t) = Pt^m \tag{2.22}$$

where A, r, P and m are temperature dependent constants obtained from curve fitting. Finally, the experimental creep data can be represented as:

$$\varepsilon = A\sigma cosh^{-1}(1 + rt) + P\sigma^n t^m \tag{2.23}$$

A more accurate manner to simulate the creep behavior is to apply finite element method (FEM). FEM is a numerical technique for finding approximate solutions to boundary value problems. The commercial software, ABAQUS, was employed for the FEM analysis. ABAQUS/CAE provides numerical functions for both modeling and analysis of mechanical components and assemblies and allows visualization of the finite element analysis result. Creep, a nonlinear huge deformation problem, is especially suitable for simulation by ABAQUS. The

ABAQUS model of the creep tube before deformation is shown in Fig. 2- 9.

ABAQUS provides three basic models to describe creep behavior: the time-hardening, strain-hardening, and hyperbolic-sine models. However, all these models cannot precisely describe the three-stage creep development, so the implementation of user subroutines is needed to develop better simulation accuracy. The user subroutines in ABAQUS allow the program to be customized for particular applications and projects, and greatly extend the applicability of ABAQUS. With slight modifications to the constants' values, Eq.2.23 is used in the creep subroutine as the constitutive function. The dimension of pressurized tube defined in ABAQUS is of the same size as the one used in the experiment. Since the dimension of a sample near two end caps barely change in our experiment, the two ends are assumed to be fixed in the model as a boundary condition. The subroutine program is attached in the appendix.

The five parameters, A, r, P, n, and m, in Eq.2.23 should be determined before simulation using ABAQUS. Assume that HTC mechanism accounts for creep behavior of Zircaloy-4 cladding without hydride at 500^{0}C and 40 MPa effective stress at wid-wall, the three parameters P, n and m is determined by fitting experimental results with HTC model in Eq.2.8 and parameter listed in Table 2- 2. Then P, n and m is 9.34E-13, 5, and 1, respectively. The effect of true stress was considered for determination of parameter A and r. The true stress will increase with the increase of tube diameter and the decrease of wall thickness of tube. The wall thickness was calculated based on the assumption of volume conservation during creep deformation, and true stress was calculated using measured diameter and calculated thickness. Plug the true stress into Eq.2.23, and then fit the experimental results using creep strain in primary region using into Eq.2.23. Finally, the A equal to 6.54E-5, and r equal 1.94, was determined. Fig. 2- 10 shows the pressurized creep tube deformed after FEM modeling. By using the tool of XY-Data, we can pick a node in the center region of the deformed model and plot its moving magnitude, which can then be compared with our experimental results. Fig. 2- 11 is the comparison between experimental results and strain simulated by using ABAQUS. This figure imply that the steady-state region dominated creep deformation at 500C even though the effect of true stress is taking into account.
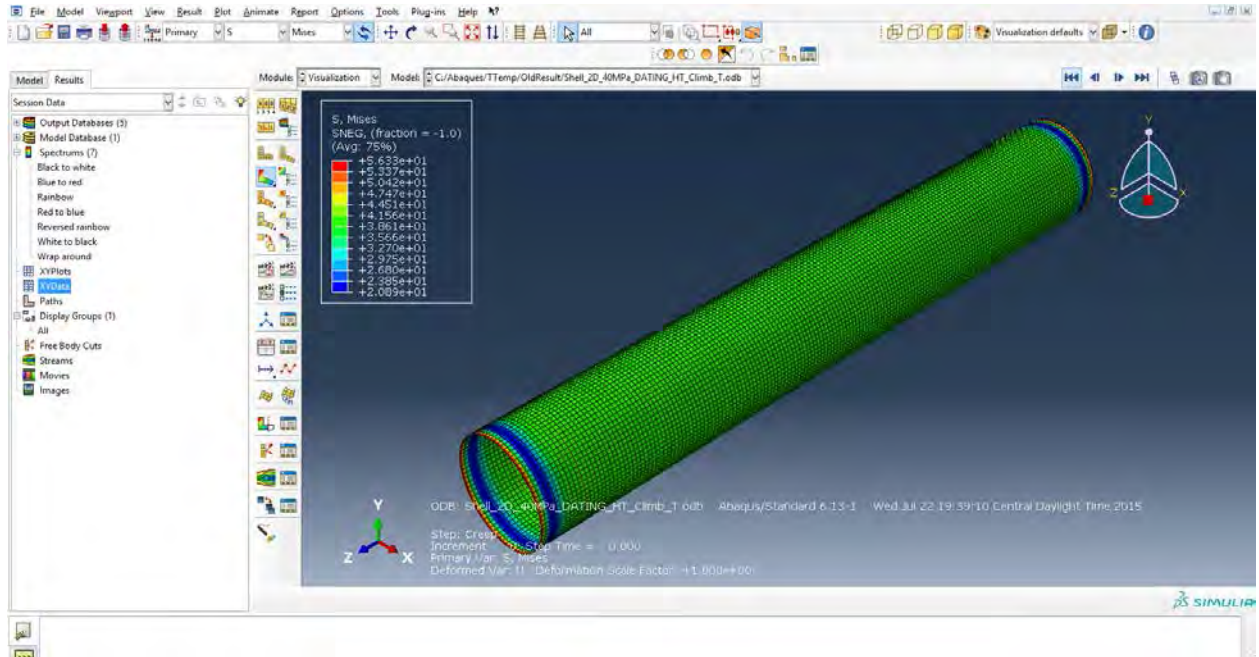
Fig. 2- 9 ABAQUS modeling for a pressurized creep tube.
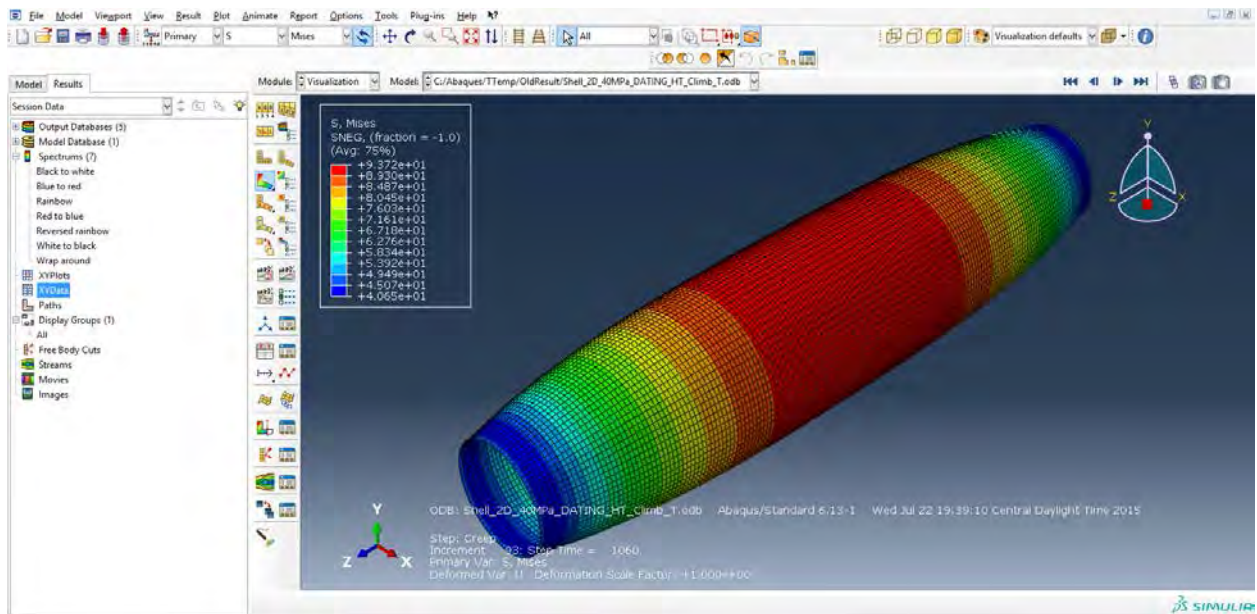
Fig. 2- 10 FEM modeling for creep strain development of a pressurized creep tube.
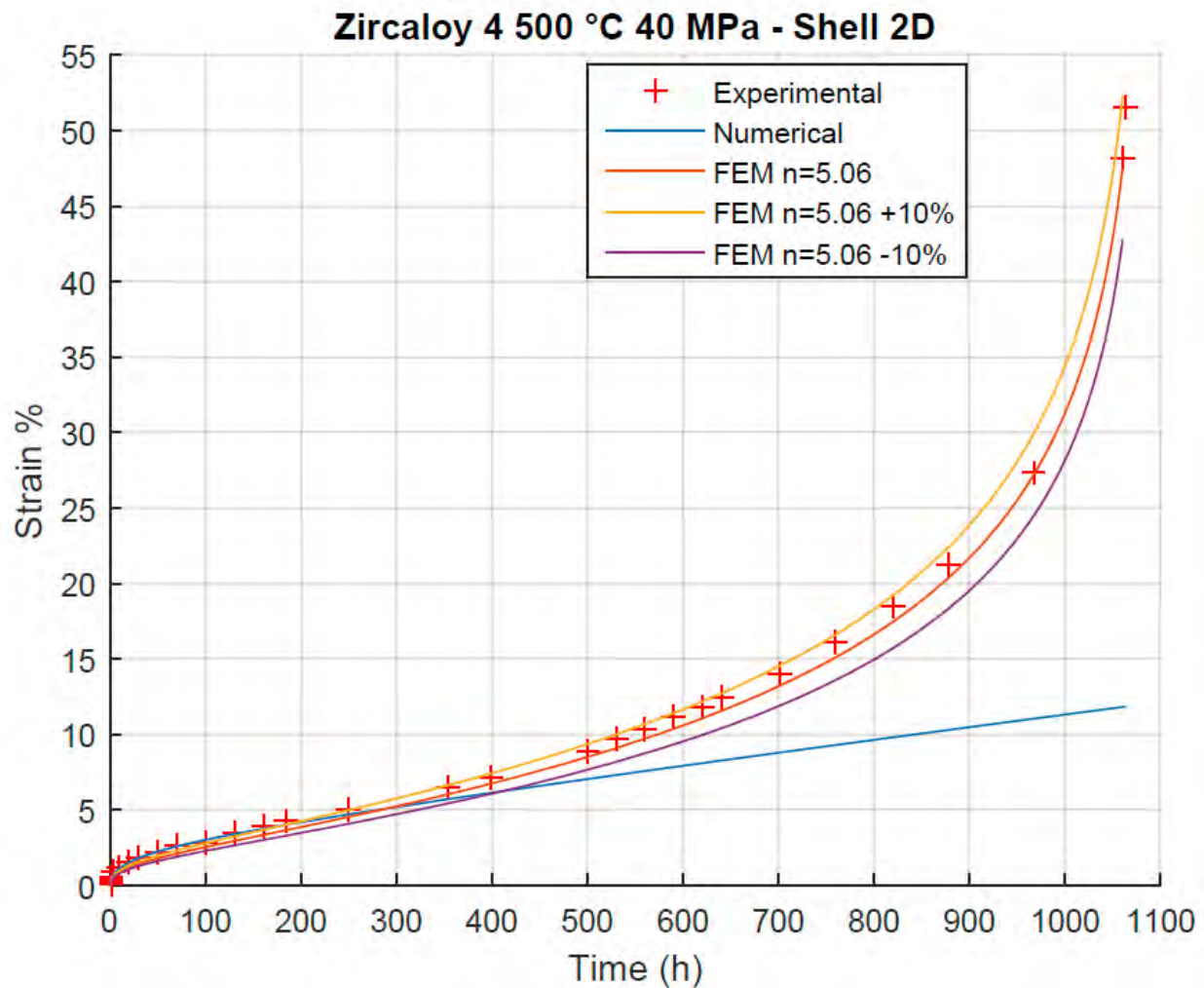
Fig. 2- 11 Comparison of creep strain simulated by ABAQUS and experimental results

2.4.3. Off Normal Temperature Effects

Utilizing the fit equations discussed in 2.4.1, and Eq.2.8 with the constants from Table 2- 1 a base line allowable temperature was established utilizing the modified dating code for hoop stresses of 20, 30, and 40 MPa.   Following this events taking place at 10, 20, 30, 50, and 75% of the expected 40 year lifetime were evaluated for expected effect on the allowable temperature limit.   Events of 10, 20, 30, 40, 60, and 100^0C were tested for effects on allowable temperature limit the results of the events at 10% of the lifetime are tabulated in Table 2- 4.   The list of other events tested is tabulated in the appendix.

Table 2- 4 Table of event effects at 10% of a 40 year life time

	DATING model			Matsuo Mayuzumi model		
	20 MPa	30 MPa	40 MPa	20 MPa	30 MPa	40 MPa
Base line Allowable temp (^{o}C)	463.11	440.42	423.4	158.74	150.94	143.14
100 ^{o}C increase	463.11	440.42	423.4	158.74	150.94	143.14
10 ^{o}C increase	463.11	440.42	423.4	158.74	150.94	143.14
20 ^{o}C increase	463.11	440.42	423.4	158.74	150.94	143.14
30 ^{o}C increase	463.11	440.42	423.4	158.74	150.94	143.14
40 ^{o}C increase	463.11	440.42	423.4	158.74	150.94	143.14
60 ^{o}C increase	463.11	440.42	423.4	158.74	150.94	143.14
100 ^{o}C increase	463.11	440.42	423.4	158.74	150.94	143.14

Changes to the allowable limit are of a magnitude such that they all fall within the 0.5% tolerance on the damage fraction.   Similar to the events tested in Table 2- 4, events occurring later in the lifetime of the cladding likewise do not show any indication of changes in the allowable temperature limits.   This indicates that the effect of an off normal temperature event is minimal to the lifetime damage of the cladding.   It was expected that late in the storage lifetime when the temperature has drastically dropped off the initial amount that a minor increase compared to the change from the initial storage temperature would not cause a noticeable effect. Comparatively at 5% of a forty year lifetime, 2 years in, where for example a 400^{0}C starting temperature will have dropped off a little over 100^{0}C an increase of 100^{0}C would have raised the temperature back to near the starting temperature again.   No change in storage limit can be seen, likely due to the temperature profile still quickly decreasing to the point where even with the added 100^{0}C the damage accumulated will be far below the level that is experienced at initial storage conditions.   Most fuel discharged from the reactor is in wet storage for years before being placed into dry storage, events prior to two years since discharge should not contribute to the allowable limits, thus off normal temperature events evaluated in this study do not show any indication of a significant effect on allowable storage temperature limits in Zircalloy-4 cladding. It can be seen that despite the large difference in expected allowable storage temperatures both cases show no effect on allowable storage temperatures, thus it is unlikely either individual code has inherent properties that are affecting the events effects from being seen.

The vast difference in allowable temperatures predicted by both equation forms must also

be addressed.   Several factors contribute to the difference in allowable limits, likely the largest is the interaction of the primary strain portion of the fit equations with the damage fraction calculation, an interaction which is not present in the mechanistic equations.   During the primary region of creep the equations interpret primary creep as a drastically higher creep rate then the mechanistic models output at the given time.   This directly impacts the damage fraction of the early storage times as Eq.2.18 which predict failure time has the calculated strain rate for that time step in the denominator.   This leads to a portion of the storage life time generating a drastically larger damage fraction then the mechanistic approach would.   Combined with the fact that this occurs during the portion of the storage life where conditions lend towards the highest creep strain rates already and the difference in damage fractions becomes considerable. The code compensates for this large difference in damage levels by reducing the allowed starting temperature, however as the fit code's accuracy and viability is limited by the range which the data it is based upon the further outside of the experiment range it reaches the more error it will encounter in calculating expected damage fractions.   It is likely that the damage calculated at the low temperature ranges is actually lower than the model predicts, it can be seen in Fig. 2- 8 that at the lowest measured rate, 4 E-06 /h the steady state range once reach rapidly begins to overestimate the strain in the model.   As the code extrapolates to the lower temperatures this overestimate will still be present and hinder the capabilities of the fit equations from generating an accurate allowable temperature.   Due to this limitation of accuracy to experimental data available, the Matsuo and Mayuzumi model is not an effective method for modeling large temperature ranges expected during dry storage, though for smaller ranges, or with a very large database of experimental conditions it can be quite accurate for those conditions.

2.5. Conclusion and Future Work

In this study, a database on creep strain of Zircaloy-4 creep tubes over a temperature range of 300-500°C with pressures of 40-65 MPa was created.   This was utilized to attempt to fit a generalized creep equation across a large temperature and pressure range.   Finally the DATING routine from the FRAPCON code has been modified to utilize both the fit equation along with mechanistic equations to evaluate the effect off normal temperature events could have on allowable storage limits for dry storage. The following is a brief summary of conclusions from this study:

1. The DATING code has been modified to allow for off normal events using both mechanistic approaches and generalized equations, with similar findings.

2. The modified dating code shows no expected effect of off normal temperature events of up to 100°C increases occurring during storage time as early a 5% of a 40 year life time.

3. The generalized equation form utilized by the Matsuo and Mayuzumi studies while accurate for a small temperature range. Its accuracy is significantly affected by the sample size of creep data that is utilized to fit the constants within the equation form. For the range of dry storage temperatures and pressures a much larger database size is required then this study had access to for accurate results.

Several aspects of this study could be improved upon to allow for further accuracy and scenario evaluation for dry storage conditions the following is a brief list of possible future work:

1. A larger creep data base could be created with temperature and pressures lower than the current study utilized.   This could allow for better accuracy of the stress constant in the generalized equation, as well as potentially shed light on the nature of the A component's response to changing temperatures and pressure in the generalized equation.

2. An evaluation of the temperature profile for higher burn-ups that current generation fuels are achieving is needed to evaluate the effects that current fuels will undergo as they transition from wet storage to dry storage in the future.

3. Implementation of expected hydride precipitation in stored fuel over changing temperature ranges during events could potentially modify the expected failure lifetime of cladding.   A study on the effects of hydride precipitation effects on damage fraction calculations would allow for this phenomenon to be accounted for in lifetime calculations.

3. References

[1]   A. J. Machiels, "Spent Fuel Transportation Applications: Longitudinal Tearing Resulting from Transportation Accidents--A Probabilistic Treatment," *EPRI, Palo Alto, CA,* vol. 1013448, pp. 3-5, 2006.

[2]   J.-P. Mardon, D. Charquet and J. Senevat, "Influence of composition and fabrication process on out-of-pile and in-pile properties of M5 alloy," in *Zirconium in the nuclear industry, ASTM STP 1354*, 2000.

[3]   B. A. Chin and E. R. GILBERT, "Prediction of maximum allowable temperatures for dry storage of Zircaloy-clad spent fuel in inert atmosphere," *Nucl. Technol,* vol. 85, pp. 57-65, 1989.

[4]   R. 3. Interim Staff Guidance - 11, "Cladding Considerations for the Transportation and Storage of Spent Fuel," NRC Spent Fuel Project Office, 2003.

[5]   R. L. Coble, "A model for boundary diffusion controlled creep in polycrystalline materials," *Journal of Applied Physics (US),* vol. 34, 1963.

[6]   C. Herring, "Diffusional viscosity of a polycrystalline solid," *Journal of applied physics,* vol. 21, no. 5, pp. 437-445, 1950.

[7]   F. R. Nabarro, "Report of a Conference on the Strength of Solids," in *The Physical Society*, London, 1948.

[8]   M. Boiek, P. Hofmann and C. Petersen, "Superplasticity of Zircaloy-4," in *Zirconium in the nuclear industry, ASTM STP 633*, 1977.

[9]   H. L{\"u}thy, R. A. White and O. D. Sherby, "Grain boundary sliding and deformation mechanism maps," *Materials Science and Engineering,* vol. 39, no. 2, pp. 211-216, 1979.

[10]   A. Sarkar, K. Boopathy, J. Eapen and K. L. Murty, "Creep Behavior of Hydrogenated Zirconium Alloys," *Journal of Materials Engineering and Performance,* vol. 23, no. 10, pp. 3649-3656, 2014.

[11]   P. Bouffioux and N. Rupa, "Impact of Hydrogen on Plasticity and Creep of Unirradiated Zircaloy-4 Cladding Tubes," in *Zirconium in the nuclear industry, ASTM STP 1354*, 2000.

[12]   D. S. Shih, I. M. Robertson and H. K. Birnbaum, "Hydrogen embrittlement of a titanium: in situ TEM studies," *Acta Metallurgica,* vol. 36, no. 1, pp. 111-124, 1988.

[13]   H. Chu, S. Wu, K. Chien and R. Kuo, "Effect of radial hydrides on the axial and hoop

mechanical properties of Zircaloy-4 cladding," *Journal of nuclear materials,* vol. 362, no. 1, pp. 93-103, 2007.

[14] E. R. Gillbert and L. D. Blackburn, *J. Eng. Mater. Technol.,* vol. 99, no. 2, pp. 168-180, 1977.

[15] S. Timoshenko and J. N. Goodier, Theory of Elasticity, second ed., McGraw-Hill, 1951.

[16] J. J. Kearns, "On the relationship among f texture factors for the principal planes of zirconium, hafnium and titanium alloys," *Journal of Nuclear Materials,* vol. 299, no. 2, pp. 171-174, 2001.

[17] A. J. Anderson, R. B. Thompson and C. S. Cook, "Ultrasonic measurement of the kearns texture factors in zircaloy, zirconium, and titanium," *Metallurgical and Materials Transactions A ,* vol. 30, no. 8, pp. 1981-1988, 1999.

[18] H. Spilker, M. Peehs, H.-P. Dyck, G. Kaspar and N. Klaus, "Spent LWR fuel dry storage in large transport and storage casks after extended burnup," *Journal of Nuclear Materials,* vol. 250, pp. 63-74, 1997.

[19] E. P. Simonen and E. R. Gilbert, Dating- A Computer Code for determining allowable temperatures for dry storage of spent fuel in inert and nitrogen gases, Vols. PNL-6639, Richland, Washington: Pacific Northwest Laboratory, 1988.

[20] D. G. Franklin and G. E. Lucas, Creep of Zirconium Alloys in Nuclear Reactors, vol. ASTM STP 815, Philadelphia, Pa: American Society for Testing and Materials, 1983.

[21] Y. Matsuo, "Thermal Creep of Zircaloy-4 Cladding under Internal Pressure," *Journal of Nuclear Science and Technology,* vol. 24, no. 12, pp. 111-119, 1987.

[22] R. Limon and S. Lehmann, "A creep rupture criterion for Zircaloy-4 fuel cladding under internal pressure," *Journal of Nuclear Materials,* vol. 335, pp. 322-334, 2004.

[23] C. Cappelaere, R. Limon, C. Duguay, G. Pinte, M. LeBrenton, P. Bouffioux, V. Chabretou and A. Miquet, "Thermal Creep Model for CWSR Zircaloy-4 Cladding Taking into Account the Annealing of the Irradiation Hardening," *Nuclear Technology,* vol. 177, no. 2, pp. 257-272, 2012.

[24] M. Mayuzumi and T. Onchi, "Creep deformation and rupture properties of unirradiated Zircaloy-4 nuclear fuel cladding tube at temperatures of 727 to 857 K," *Journal of Nuclear Materials,* vol. 175, pp. 135-142, 1990.

[25] B. Marple, Y. J. Song, S. Gollapundi and K. L. Murty, "Stress Rupture Characteristics of Zirconium Alloy Cladding Under Closed-End Internal Pressurization," in *Proceedings of the 16th International Conference on Nuclear Engineering*, Orlando, Florida, 2008.

[26] Y. Zhou, B. Devarajan and K. L. Murty, "Short-term rupture Studies of Zircaloy-4 and Nb-modified Zircaloy-4 Tubing using closed -end internal pressurization," *Nuclear Engineering and Design,* vol. 228, pp. 3-13, 2004.

[27] U.S. Nuclear Regulatory Commission, "Standard Review Plan for Dry Cask Storage System: Final Report," NUREG-1536, January 1997.

[28] A. Machiels, "Creep as the Limiting Mechanism for Spent Fuel Dry Storage," EPRI, Palo Alto, California, 2000.

[29] H. J. Frost and M. F. Ashby, Deformation-mechanism maps: the plasticity and creep of metals and ceramics, Universtiy of Michigan: Pergamon Press, 1982.

[30] M. Ashby, "A First Report on Deformation Mechanism Maps," *Acta Metallurgica,* vol. 20, p. 887, 1972.

[31] I. S. Levy, B. A. Chin, E. P. Simonen, C. E. Beyer, E. R. Gilbert and A. B. Johson, Jr., "Recommended Temperature Limits for Dry Storage of Spent Light Water Reactor Zircaloy-Clad Fuel Rods in Inert Gas," Pacific Northwest Laboratory, PNL- 6189, Richland, Washington, 1987.

[32] E. Gilbert, E. Simonen, C. Beyer and P. Medvedev, "Update of CSFM Methodology For Determining Temperature Limits for Spent Fuel Dry Storage in Inert Gas," Pacific Northwest Laboratory, Richland, Wa, 2001.

[33] *Creep Modeling and Analysis Methodology for Spent Fuel in Dry Storage, EPRI, Palo Alto, CA: 2001. 1003135.*

[34] R. W. Swimdeman and C. E. Pugh, "Creep Studies on Type 304 Stainless Steel (Heat 8043813) Under Constant and Varying Loads," ORNL-TM 4427, 1974.

Appendix A: Modified DATING CODE

```
if abs(newdamage-1)>.05
    if newdamage >1 %need lower temp case
deltatemp=abs ((temp-lowesttemp)/2);
temp2= temp-deltatemp; %midpoint established for next loop
hightemp=temp;
    else
deltatemp=abs (temp- hightemp)/2; %need higher stress case
temp2=temp+deltatemp;%midpoint established for next loop
lowesttemp=temp;
end
end
end
newdamage %output
allowedtemp=temp-273.15 %output
hold on
scatter(temphistory,damagehistory)
% scatter(Temphist,timehist)
temphistory;
damagehistory;
% wrong entry
    else
    promptinvalidentry='please choose a valid entry, exiting'
    end
    end
%%% nested dating code
function Datingprogram4
timesteps=(timelength*(3.15569*10^7))/100; %# of time increments
%%% constants
R=8.314;
E=(11.09-11.61*(temp/2125))*10^4;
Tm=2125;
temp=temp;
Stress=Stress;
timelength=timelength;
```

```
timestep=(timelength*(3.15569*10^7))/timesteps; %setting time step for problem.
DH=0;    %drying cycle heat amount
%2.62974*10^6% 1 month in seconds
%%% initialize matricies and values
Creepstrain=0;
Creeprate=0;
damagefraction=0;
Time=3.15569*10^7;
Temp=temp;
Creeprates=zeros(5,1);
damagetotal=0;
totalcreepstrain=zeros(timesteps,1);
raddamagetot=0;    %change1
Damage=0;%initilize damage total
I=1; %set loop start at second timestep.
X=0;
%%% iterative loop
    while I<=timesteps
        Talpha=(temp);
        Tbeta=Talpha*((7^-.34)/(7^-.0840));
        if Time <= (7*(3.15569*10^7))        %start tempsolve
        Temp=Talpha*(Time/(3.15569*10^7))^-.34;
  %# timesteps to 7 years
        else
        Temp=Tbeta*(Time/(3.15569*10^7))^-.0840;
        end                     %end tempsolve
if DH>0;
if (Time-(3.15569*10^7))<28800
Temp= temp+(((Time-(3.15569*10^7))*DH)/28800);
end
if (Time-(3.15569*10^7))>=28800 && (Time-(3.15569*10^7))<57600
Temp=temp+DH;
end
if (Time-(3.15569*10^7))>=57600 && (Time-(3.15569*10^7))<86440
Temp= temp+DH-(((Time-(3.15569*10^7))*DH)/28800);
end
```

```
end
if flag1==1
if (Time-(3.15569*10^7))> (timelength*(3.15569*10^7))*flag2;
    Temp=Temp+flag3;
end
end


E=(11.09-11.61*(Temp/2125))*10^4;
S=Stress/E;
TI=Tm/Temp;
e=E/(10^4);
% Creeprates(1,1)=exp( 5* log(S) + 55.75 - 14.15*(TI) + log(TI) + log(e));
% Creeprates(2,1)=exp( 7* log(S) + 20.18 - 10.19*(TI) + log(TI) + log(e));
% Creeprates(3,1)=exp( 2* log(S) + 20.74 - 9.9200*(TI) + log(TI) + log(e));
% Creeprates(4,1)= exp(log(S) + 18.25 - 14.15*(TI) + log(TI) + log(e));
% Creeprates(5,1)=exp( log(S) + 11.03 - 9.9200*(TI) + log(TI) + log(e));
% Creeprate=max(Creeprates);
% ESP=.0216*(3600^.109)*(Creeprate^.109)*((2-tanh(35500*3600*Creeprate))^-2.05);
% primary=ESP*(1-exp(-52*((Creeprate*(Time-(3.15569*10^7)))^.5)));
A=501.78*exp(.0113*Temp);
D=7114.6;
Q=200741.53;
ESS=A*(E/Temp)*exp(D*S)*exp(-Q/(R*Temp)); %steady state calc
if ESS<2.069*10^-5
    ESP=354.196167+.00066428;
else
    ESP=1.90067438*ESS+.00795334;
end
Cstrain1=(ESP*(1-exp(-5.398*(ESS*(Time/3600))^.5199)))+ESS*(Time/3600);
Cstrain2=(ESP*(1-exp(-5.398*(ESS*((Time+timestep)/3600))^.5199)))+ESS*((Time+ti
mestep)/3600);
Creeprate=(Cstrain2-Cstrain1)/timestep;
        if I<timesteps
            Creepstrain=Creeprate*timestep+Creepstrain;
            totalcreepstrain(I,1)=Creepstrain;
        end
end
```

```
        timefailcalc = (.02 * exp(6.2-(4300/Temp))) / Creeprate;%monkman grant
   timefailcalcrad=timefailcalc*(1-.9*(1/(1+raddamagetot)));    %change 3
            damagefraction=timestep/timefailcalcrad;%damagefraction calc
        Damage=Damage+damagefraction;
   raddamagetot=timestep*(2.332*10^17)*exp(-4*(10^4)/Temp); %change 2
   % Temphist(I)=Temp;
   % timehist(I)=I*timestep;
        I=I+1;
        Time=Time+timestep; %next time step
        end
   Temp
   % plot(timehist,Temphist)
   newdamage=Damage;
   end
   end
```

Appendix B: Subroutine for ABAQUS

```
      SUBROUTINE CREEP(DECRA,DESWA,STATEV,SERD,EC,ESW,P,QTILD,
     1 TEMP,DTEMP,PREDEF,DPRED,TIME,DTIME,CMNAME,LEXIMP,LEND,
     2 COORDS,NSTATV,NOEL,NPT,LAYER,KSPT,KSTEP,KINC)
C
      INCLUDE 'ABA_PARAM.INC'
C
      CHARACTER*80 CMNAME
C
      DIMENSION DECRA(5),DESWA(5),STATEV(*),PREDEF(*),DPRED(*),TIME(2),
     1 COORDS(*),EC(2),ESW(2)
C
      DO 3 KK=1,5
```

```
3 DECRA(KK)=0.D0

   A=

   P=

   Rm=

   Rn=

   r=

C

   DECRA(1)=A*QTILD*r/SQRT(2*r*TIME(1)+r**2*TIME(1)**2)*DTIME+
  1 Rm*P*QTILD**Rn*TIME(1)**(Rm-1)*DTIME
     DECRA(5)=A*r/SQRT(2*r*TIME(1)+r**2*TIME(1)**2)*DTIME+
  1 Rn*Rm*P*QTILD**(Rn-1)*TIME(1)**(Rm-1)*DTIME

C

   RETURN

   END
```

Technical Mission Area 1 – Low Temperature Creep

Atomistic and Discrete Dislocation Dynamics Simulations

Prithwish K. Nandi, Apu Sarkar and Jacob Eapen
North Carolina State University, Raleigh, NC 27695

This mission's focus is on the low temperature creep of UNF cladding enabled by decay heat from fission products and stresses from internal pressures. This section covers atomistic and discrete dislocation dynamics (DDD) simulations to understand the mechanism of creep under dry storage conditions.

The DDD simulations at dry storage conditions complement the experimental investigations that have been conducted at higher temperatures. One of the main conclusion from the DDD simulations is that creep in Zr is dominated by prismatic slip, which is consistent with experimental results. For stresses expected in dry storage thermodynamic conditions, the creep is expected to be controlled by dislocations. The DDD simulations indicate that additional basal plane dislocations, which generally multiply under neutron irradiation, will not affect the creep rate significantly and the creep rate of uniirradiated Zr alloy samples will be bounding for crept samples at dry storage conditions.

PART A: Atomistic Simulations: Defect Accumulation and Microstructure Evolution with Radiation using Molecular Dynamics Simulations

A.1 Introduction

Computer simulations of radiation interactions with materials can complement experimental investigations and can aid in developing models for failure of materials especially under irradiation conditions. Zr has been investigated in the past using molecular statics (MS) as well as molecular dynamics (MD) simulations. Willaime and Massobrio [1] performed MD simulations using a tight-binding approach and reported the Burgers mechanism for the temperature dependent *hcp* to *bcc* phase transition. Morris *et al*. [2] calculated the structure and energy of compression twin boundaries in Zr using a combination of first-principles and embedded atom techniques. Serra and Bacon [3] later proposed a new model for {1012} twin growth in *hcp* metals using MD simulations.

Wooding *et al*. [4,5] performed high energy displacement cascade simulations in α-Zr using a Finnis-Sinclair type many–body potential (AWB) that was proposed by Ackland *et. al*. [6]. de Diego and Bacon [7] later probed the defect structures that are produced by near-surface displacement cascades in α-Zr using the same AWB potential. The temperature dependence of creation and clustering of defects generated by displacement cascades in α-Zr was reported by Gao *et al*. [8]. Willaime [9] obtained the formation energies of self-interstitials in *hcp* Zr using density functional theory (DFT) simulations. The mechanisms of interactions between vacancy dislocation loops with the self-interstitial atoms were later reported by Kulikov and Hou [10]. More recently the structure and properties of vacancy and interstitial clusters in α-Zr were investigated by de Diego *et al*. [11] using the AWB potential. Thus it can be noted that the

AWB potential has been widely employed in cascade simulations in Zr despite a few well-documented limitations [12]. To overcome some of the drawbacks of the AWB potential [6], Mendelev *et al*. [13] proposed a new EAM potential for α-Zr (M10).

The M10 potential is able to predict the α to β phase transformation in Zr. It also predicts the melting point, liquid structure data and several elastic constants with reasonable accuracy. In this investigation, we have used the M10 potential [13] with an additional hard sphere repulsive interaction at interatomic distances less than 0.1 Å (labeled as M10*) to account for the high compressibility anticipated in displacement cascade simulations [14] at very short times. Ongoing work also considers a spline fit to the ZBL potential [15] at short distances that is expected to be more realistic than a hard sphere repulsive potential.

A.2 Computational Methods

Zr has a hexagonal close-packed (*hcp*) structure [space group: 194 (P63/mmc)]. For our simulations, we have chosen the orthorhombic representation of the *hcp* lattice with the unit cell spanned by the vectors $\vec{a}_0 = (1,0,0)$, $\vec{b}_0 = \left(0,\sqrt{3},0\right)$ and $\vec{c}_0 = \sqrt{8/3}\,(0,0,1)$, The orthorhombic unit cell for *hcp* lattice is equivalent to two conventional *hcp* cells with its four basis atoms located at (0,0,0), (1/2,1/2,0), (1/2,5/6,1/2) and (0,1/3,1/2).

A Zr lattice with 256,000 atoms is first relaxed with the conjugate gradient method to its lowest potential energy configuration. It is then equilibrated for 50 ps at constant temperature (300 K) and constant pressure (0 bar) using the LAMMPS [15] MD simulation package. Displacement cascades are then simulated with a 3 keV primary knock-on atom (PKA) introduced close to one of the surfaces of the simulation box. Since it was reported by Wooding et al. [4] that the inclination of the initial PKA direction has no perceptible effect on either the damage state in the collisional phase or the final defect state [4], we have considered the initial PKA momentum perpendicular to the basal plane only. Further investigations will consider other PKA directions. A small set of atoms constituted by three layers of atoms at the system boundary is allowed to absorb the excess thermal energy that crosses into the boundary region using a damped Nose-Hoover thermostat [16]. The boundary atoms also function to attenuate the pressure wave that originates from the radiation knock and prevent it from reentering the simulation box. The atoms in the interior region are allowed to evolve according to the Newton's laws of motion without any constraints. Three different timesteps are used in the cascade simulations – a timestep of 10^{-5} ps is used for the collision phase followed by timesteps of 10^{-4} ps and 10^{-3} ps for the first 3 ps of the annealing phase and the remainder of the annealing phase (25 ps), respectively. For the sequential cascade simulations, the PKA is chosen from the spatial region in the near–vicinity of the first PKA. For each subsequent knock, the PKA momentum and energy are also kept identical to the first knock.

A.3 Identification of Defects

Unambiguous identification of defects in a cascade structure is not straight-forward as there are several criteria available to identify the defected structures. Among the several techniques, Wigner-Seitz cells, the equivalent sphere analysis [17] and common neighbor analysis [18] are widely used for identifying defects in molecular simulations. In this work, we

have used the equivalent sphere analysis (ESA) which is based on the Lindemann criterion [17]. In ESA, a defected configuration of the atoms is compared with a reference crystalline state without any defects.

For identifying the vacant sites, each lattice site of the reference configuration is first associated with a sphere. If no atom is found inside the equivalent sphere in the defective configuration, the corresponding lattice site in the reference configuration is tagged as a vacant site. We have used in our analysis a threshold value of $0.32 \times$ lattice constant [7] for the radius of the sphere. A similar procedure is used to estimate the number of displaced atoms. In summary, the ESA method catalogues the vacant sites and the displaced atoms. Note that in this discussion, the term 'displaced atom' points to an atom which is found to be displaced from its equilibrium lattice site.

A.4 Results and Discussion

Equilibrium Properties: We will first report several equilibrium properties with the M10[*] potential. Table 1 shows the lattice parameters and the cohesive energy of the α-Zr using several potentials including M10[*]. The lattice parameter at 0 K is determined by performing an energy minimization of the system using the conjugate gradient algorithm. The cohesive energy is defined as the difference between the potential energy of the bound state (crystal) and the isolated atoms which is taken as zero.

Table 1. Equilibrium lattice parameters and cohesive energy per atom for α-Zr with different potentials. M10[*] refers to M10 potential [14] with an additional hard sphere repulsive potential at distances less than 0.1 Å.

	Experiments	AWB [6]	PM [21]	IKV [22]	M10[*]
a (Å)	3.232 [19]	3.249	3.232	3.232	3.211
c (Å)	5.147 [19]	5.183	5.149	5.149	5.244
$E_{cohesive}$ (eV)	-6.32 [20]	-6.250	-6.250	-6.250	-6.469

Table 2. Elastic constants, bulk modulus (B), Young modulus (Y), shear modulus (G) and Poisson's ratio (v) for α-Zr with different potentials.

|	AWB [6]	PM [21]	IKV [22]	M10[*]
C_{11} (GPa)	160	146	155	148
C_{12} (GPa)	76	70	67	82
C_{13} (GPa)	70	65	65	63
C_{33} (GPa)	174.7	164.8	173	180
C_{44} (GPa)	36	32	36	48
Y (GPa)				115
Poisson's Ratio (v)				0.3
G (GPa)				44
B (GPa)				96

The stiffness of a material is characterized by its elastic constants which, in the limit of infinitesimal deformation, can be defined as $\sigma_{ij} = \sum_{k,l} C_{ijkl}\varepsilon_{kl}$ where σ_{ij} and ε_{kl} are the elements of the stress and strain tensors, respectively, and C_{ijkl} are the elements of a fourth order elastic constant or stiffness tensor. For a *hcp* system, there are five independent (contracted) elastic constants [23]: C_{11}, $C_{11}+C_{12}$, C_{13}, C_{33} and C_{44}. In the current study, we have estimated the elastic constants at 0 K with the M10* potential and the results are tabulated in Table 2 (along with a comparison to the predictions from the other potentials). We have also tabulated the values of bulk modulus (*B*), Young's modulus (*Y*), shear modulus (*G*) and Poisson's ratio (*v*) with the M10* potential in Table 2.
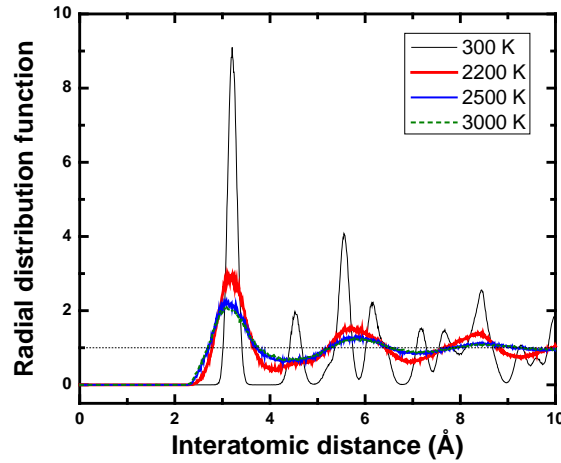

Fig. 1 RDF of Zr at different temperatures.

Radial distribution function: Figure 1 shows the radial distribution function (RDF) of α-Zr at four different temperatures: 300 K, 2200 K, 2500 K and 3000 K with the M10* potential. While the crystalline features are clearly observed at 300 K, the RDF shows a melted disordered state at temperatures above 2200 K. From the changes observed in the RDF, the melting point is estimated to be 2200 K which compares favourably with the experimental value of 2128 K [24].
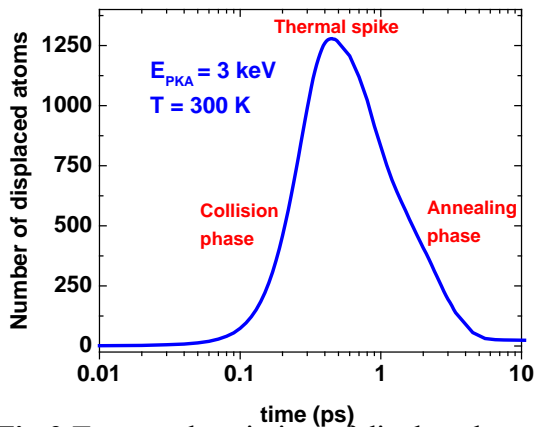

Fig.2 Temporal variation of displaced atoms
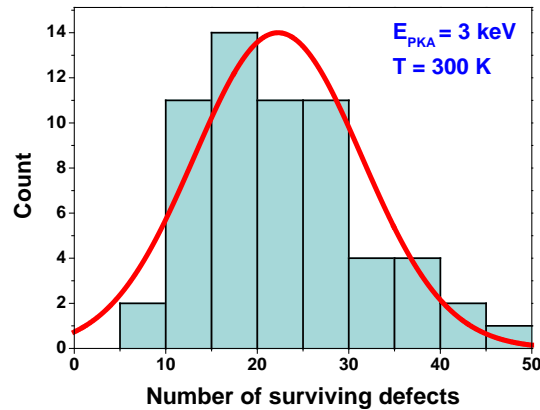
Fig.3 Statistical distribution of displaced atoms

Cascade Simulations: To assess statistically significant defect characteristics, we have employed an isoconfigurational ensemble with copies of the same configuration but with different momenta. The PKA energy (3 keV) and momentum direction (perpendicular to the basal plane) however, remain unchanged in all isoconfigurational copies. The number of displaced atoms (N_D), averaged over 60 independent isoconfigurational copies, is shown in Figure 2 as a function of time. The number of displaced atoms (N_D) increases rapidly upon the PKA impact (collision phase) and reaches a maximum at the 'thermal spike'. This is followed by quenching or annealing of the system which results in a recombination of defects and a reduction in N_D. At the end of the annealing stage, N_D attains a steady state value. Note that N_D at the end of annealing stage is only a small fraction (2%, approximately) of what is generated at the thermal spike. In Figure 3 we have depicted the statistical distribution of N_D obtained from the isoconfigurational runs. We can observe that there is a wide spread in the number of displaced atoms which survive at the end of the annealing phase. Nevertheless there is evidence for an underlying Gaussian distribution for the number of displaced atoms, a trend which is also observed in cascade simulations in other materials such as copper (preliminary results). More simulations are being conducted on Zr to assess the nature of the distribution.

Defect microstructure from cascade overlap: A main objective of the present study is to investigate the evolution of extended defects such as stacking faults and dislocations in Zr under irradiation with cascade overlap. Therefore, we irradiate the same sample several times sequentially after allowing the simulation to achieve a constant number of displaced atoms at the end of the annealing stage for each knock. Typically, the number of displaced atoms becomes constant in approximately 10 *ps*. In addition, the system is allowed to equilibrate for 15 *ps* before the initiation of each subsequent radiation knock. Note that the timescale for these MD simulations are generally smaller than what is accessible in most experiments. The resulting microstructure is analyzed using an in-house code as well as with DXA [25] for identifying point and extended defects.
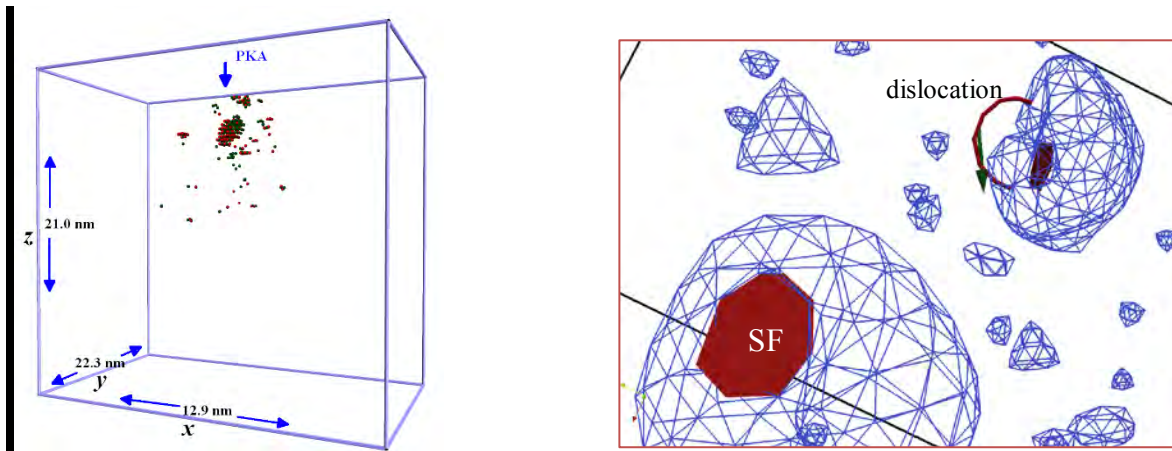
Fig.4 (Left) Defect microstructure from cascade overlap. Green spheres represent interstitials and red spheres represent vacancies. (Right) Stacking faults (SF) (both in the basal and prism planes), and a Shockley partial dislocation with a (1/6)<112> Burgers vector on the basal plane. The small structures shown as blue colored mesh (right) represent an interstitial or vacancy surface.

Figure 4 shows the defects generated from an overlap of six sequential cascades. By and large we have observed that defects are primarily comprised of single interstitials, vacancies and split vacancies following a single knock. With sequential knocks, we see the emergence of stacking faults (SF) both in the basal and prism planes. We have also observed a Shockley partial dislocation having a (1/6)<112> Burgers vector on the basal plane, which is consistent with the experimental observations. In the next section, the role of basal, prismatic and pyramidal slip systems on creep will be assessed through discrete dislocation dynamics (DDD) simulations.

References

1. F. Willaime and C. Massobrio, *Phys. Rev. Lett.* **63,** 2244 (1989).
2. J. R. Morris, Y. Y. Ye, K. M. Ho, C. T. Chan and M. H. Yoo, *Phil. Mag. A* **72,** 751 (1995).
3. A. Serra and D. J. Bacon, *Phil. Mag. A* **73,** 333 (1996).
4. S. J. Wooding and D. J. Bacon, *Phil. Mag. A* **76**, 1033 (1997).
5. S. J. Wooding, L. M. Howe, F. Gao, A. F. Calder and D. J. Bacon, *J. Nucl. Mater.* **254,** 191 (1998).
6. G. J. Ackland, S. J. Wooding and D. J. Bacon, *Phil. Mag. A* **71,** 553 (1995).
7. N. de Diego and D. J. Bacon, *Phil. Mag. A* **80,** 1393 (2000).
8. F. Gao, D. J. Bacon, L. M. Howe and C. B. So, *J. Nucl. Mater.* **294,** 288 (2001).
9. F. Willaime, *J. Nucl. Mater.* **323,** 205 (2003).
10. D. Kulikov and M. Hou, *J. Nucl. Mater.* **342,** 131 (2005).
11. N. de Diego, Y. N. Osetsky and D. J. Bacon, *J. Nucl. Mater.* **374,** 87 (2008).
12. N. de Diego, A. Serra, D. J. Bacon and Y. N. Osetsky, *Modelling Simul. Mater. Sci. Eng.* **19,** 035003 (2011).
13. M. I. Mendelev and G. J. Ackland, *Phil. Mag. Lett.* **87,** 349 (2007).
14. C.A. Becker, "*Atomistic simulations for engineering: Potentials and challenges*" in Tools, Models, Databases and Simulation Tools Developed and Needed to Realize the Vision of ICME, ASM (2011). http://www.ctcms.nist.gov/potentials
15. S. Plimpton, *J. Comp Phys.* **117**, 1 (1995). http://lammps.sandia.gov
16. S. A. Nose, *J. Chem. Phys.* **81,** 511 (1984).; W. G. Hoover, *Phys. Rev. A* **31**, 1695 (1985).
17. D. Terentyev, C. Lagerstedt, P. Olsson, K. Nordlund, J. Wallenius, C. S. Becquart, and Malerba, *J. Nuc. Mater.* **351**, 65 (2006).
18. D. J. Honeycutt, H. C. Andersen, *J. Phys. Chem.* **91**, 4950 (1987).
19. Pearson., *A handbook of lattice spacings and structures of metals* (Pergamon, Oxford, 1967).
20. C. Kittel, , *Introduction of Solid State Physics*, (NY:Wiley, 1986).
21. R. C. Pasianot and A. M. Monti, *J. Nucl. Mater* **264**, 198 (1999).
22. M. Igarashi, M. Khantha and V. Vitek, *Phil. Mag. B* **63**, 603 (1991).
23. S. Pronk and D. Frankel, *Phys. Rev. Lett.* **90**, 255501 (2003).
24. http://www.webelements.com/zirconium/
25. A. Stukwoski and K. Albe, *Modelling Simul. Mater. Sci. Eng.* **18,** 085001 (2010).

PART B: Discrete Dislocation Dynamics Simulations of Creep

B.1   Introduction

Plastic deformation of metals and alloys are primarily governed by the motion of dislocations. Two types of dislocations (edge and screw) are identified in materials depending on the orientation of their line and Burger vector. Dislocations can slip or glide in planes containing both the dislocation and the Burgers Vector. For a screw dislocation, the dislocation and the Burgers vector are parallel, so the dislocation may slip in any plane containing the dislocation. For an edge dislocation, the dislocation and the Burgers vector are perpendicular, so there is only one plane in which the dislocation can slip. There is an alternative mechanism of dislocation motion, fundamentally different from slip that allows an edge dislocation to move out of its slip plane, known as dislocation climb. Dislocation climb allows an edge dislocation to move perpendicular to its slip plane. Fundamental understanding of dislocation motion was developed initially from phenomenological studies and later supported by analytic formulation, microscopic observations and correlation with mechanical test results [1-8]. With the advancement of computational material science [9] different modeling techniques have been employed to simulate the dynamical behavior of dislocations[9-14]. In this section, we perform dislocation dynamics simulations to investigate the creep behavior of copper (for benchmarking purpose) and zirconium at dry storage conditions.

B.2   DDD Simulations

The ParaDiS code developed at Lawrence Livermore National Laboratory is used for the Discrete Dislocation Dynamics (DDD) simulations [15, 16]. In this approach, the dynamics is based on dislocation line decomposition and a nodal formulation of the dislocation segments as represented in Figure 1. Each segment is characterized by its Burgers vector, glide plane normal and the line direction. The force on a dislocation node is calculated by the summation of all Peach–Koehler (PK) forces resulting from an externally applied stress, the local line tension and the stress field due to other dislocation segments. The segment positions are defined by calculating the speed of the node and the local events occurring during the displacement. These can include direct annihilation, junction formation and cross-slip.

In the ParaDiS code [15, 16] the applied PK force **F** acting jointly from different sources on a dislocation segment is related to the segment velocity **V** by

F = BV   (1)

where **B** is the drag tensor acting on the segment. The nodes move according to the first order equation of motion:

$$\frac{d\vec{r}_i}{dt} = M[\vec{f}_i]$$ (2)

$$\vec{f}_i = -\frac{\partial E[\{\vec{r}_i\}]}{\partial \vec{r}_i} \qquad (3)$$

Where f_i is the force on node i, E is the energy of the dislocation network, and $M[f_i]$ is a mobility function giving the velocity of node i as a function of node force f_i. The network energy E includes interaction between all network segments and the applied stress. In addition to moving the nodes, ParaDis evolves the network topology to reflect the physics of dislocation interactions in real crystal by adding or deleting certain nodes.

Figure 1 Nodal representation of dislocations: The dislocation lines are represented by a set of nodes connected to each other by a straight line segment. Each segment has a non-zero Burgers vector.

B. 3   Results and discussions:

B.3.1   Benchmarking with Copper:

First DDD simulations have been carried out on a single crystal block of copper deformed at a constant stress for benchmark purposes. In this simulation, the employed mobility model includes generic mobility law for FCC metals using only dislocation glide on the [111] planes and (b) dislocation climb. In the first set of simulations, the glide mobility values for screw and edge dislocation segments are set to $10^4(Pa\ s)^{-1}$, and climb-to-glide ratio is set to 10. The elastic constants, shear modulus and magnitude of Burgers vector are set to values corresponding to copper. The simulation volume is a $20 \times 20 \times 20\ \mu m^3$ cube with edges aligned along $x = [100]$, $y = [010]$, $z = [001]$ directions. Periodic boundary conditions (PBC) are applied in all three directions. The initial dislocation structure is chosen to mimic that of single crystal copper, consisting of dislocation lines with mixed orientations, as shown in Figure 2, and the simulations are allowed to evolve at a temperature of 373 K at various applied stresses.
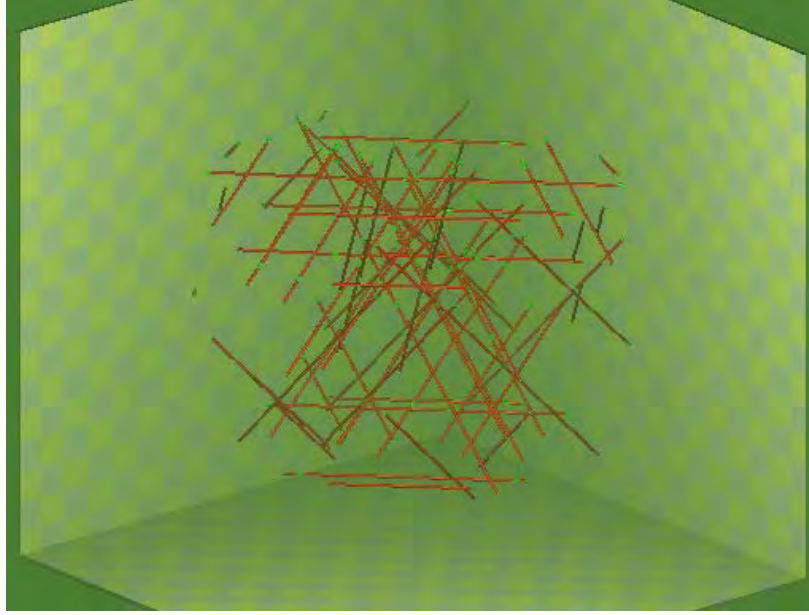
Figure 2 The initial dislocation configuration for the DDD simulation of creep under constant stress.

In the simulations, constant stresses of different magnitudes (50-250 MPa) are applied along the x axis with a mobility of 10^4 (Pa s)$^{-1}$. Figures 3 (a) and 3 (b) depict the evolution of plastic strain and dislocation density with time, respectively, while Figure 4 shows the typical dislocation microstructure after a plastic strain of 0.025 at a stress level of 100 MPa. From Figure 3 (a) it can be observed that the DDD simulation is able to reproduce the expected trend in the creep behavior with increasing stress. It may be noted that the creep rates obtained in these simulations are much higher than those observed in typical experiments. This is due to the low (constant) drag coefficient used in the simulations, which allows reasonable simulation times.
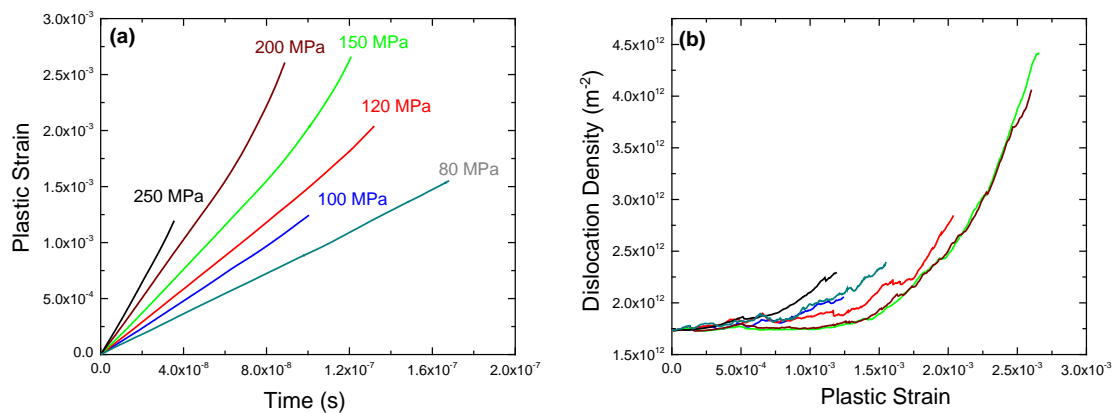
Figure 3 Evolution of (a) plastic strain with time and (b) dislocation density with plastic strain for virtual creep tests conducted on single crystal copper at various stress values using DDD simulations.
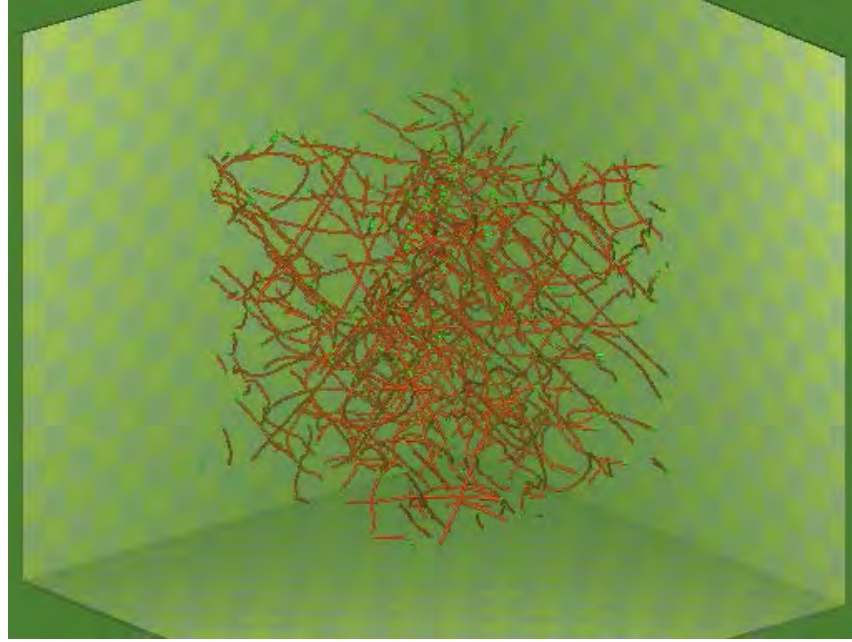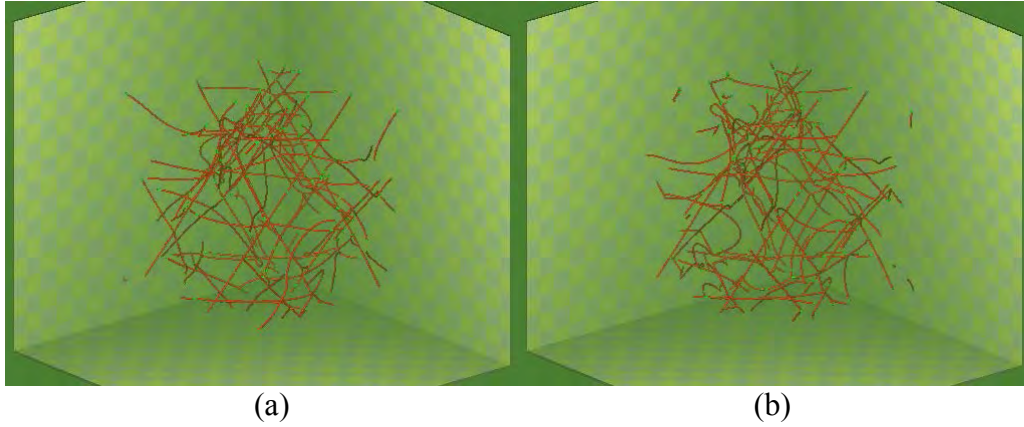
Figure 4 Dislocation microstructure after a plastic strain of 0.025 at stress of 100 MPa.

In next set of simulations, mobility values are changed to 1 (Pa s)$^{-1}$, and climb-to-glide ratio set to 10. Figure 5 (a) shows evolution of plastic strain and creep rate with time for a test conducted at a stress of 80 and 50 MPa. It can be observed that the creep rate is of the order of 1 s^{-1}, which is similar to that obtained in a recent DDD simulation of creep of single crystal nickel [17]. Figure 5 b shows the corresponding evolution of dislocation density with plastic strain.
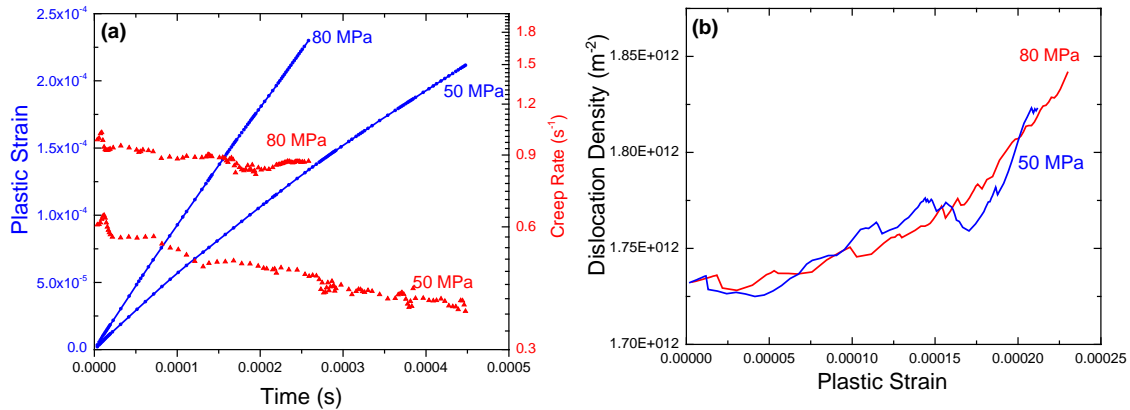
Figure 5 Variation of (a) plastic strain and creep rate with time and (b) dislocation density with plastic strain for a virtual creep test at different applied stress levels using DDD simulations.

Figure 6 (a) and (b) show the dislocation microstructure after a plastic strain of 0.00023 and 0.00021, respectively (corresponding to stress levels of 80 and 50 MPa, respectively).

(a)   (b)

Figure 6 Dislocation microstructure after a plastic strain of (a) 0.00023 at a stress of 80 MPa, and (b) 0.00021 at a stress of 50 MPa.

Climb-to-glide mobility ratio has been reported to have a significant effect on the strain evolution during constant stress DDD simulations [17]. To investigate the effect of climb-to-glide ratio, simulations are run for three different climb/glide ratios – 10, 50 and 100. The stresses are varied between 50 to120 MPa, and glide mobilities for screw and edge dislocations are set at 1 (Pa s)$^{-1}$ for all the simulations. The final strains are averaged over five independent simulations for each condition. It is observed that increasing the ratio of climb to glide mobility, decreases the creep rate. This indicates that, climb may be the rate controlling mechanism during the creep of copper. Figure 7 shows the creep curves of copper at a stress of 50 MPa with different climb-to-glide mobility ratios (10, 50 and 100).
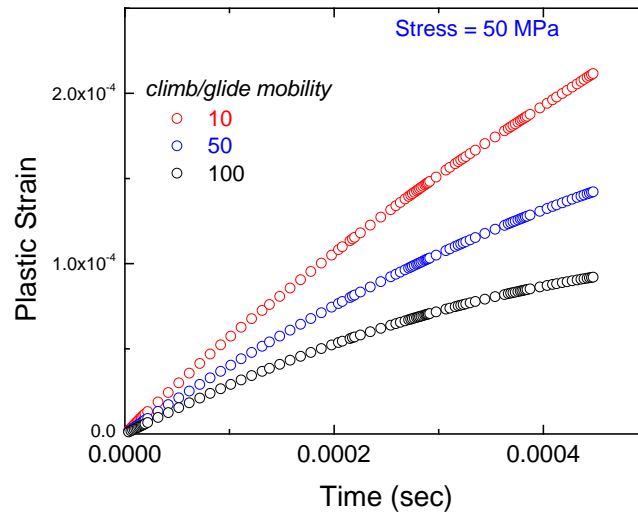

Figure 7 Effect of climb to glide mobility ratio on the creep behavior of copper.

The experimental creep data are in general analyzed in terms of minimum or steady-state creep rate ($\dot{\varepsilon}$); the applied stress (σ) provides the driving force for dislocation mobility. As the stress level is increased, the rate of deformation also increases. In general, it is found that [18]:

$$\dot{\varepsilon} \propto \sigma^n \hspace{6cm} \text{(iii)}$$

where n is termed as the *stress exponent* and its value depends on the deformation mechanism. Figure 8 shows the steady-state creep rate as a function of stress for three different climb-to-glide ratios. Error bars in the plot indicate the standard deviation from the five independent simulation runs. It is evident from the plot that the creep rate is dependent on the climb-to-glide ratio: increasing the climb/glide ratio decreases the creep rate, and *vice-versa*. Moreover, the stress dependence of the creep rate is greater for higher values of climb/glide ratio. Straight line fit of the data points for a particular climb/glide yields the value of the stress exponent (n). The values of n are 6.7±0.9, 4.6±0.3 and 4.0±0.3 for the climb/glide rations of 100, 50 and 10, respectively.

Creep experiments on copper in the stress range used in the current DD simulations typically yields a stress exponent value 6.5, approximately [19, 20]. This value of n is close to that obtained for climb/glide ratio of 100. Experimental results typically indicates that dislocation climb is the rate controlling factor for creep in copper. Thus we demonstrate that the DDD simulations can predict realistic values of creep behavior.
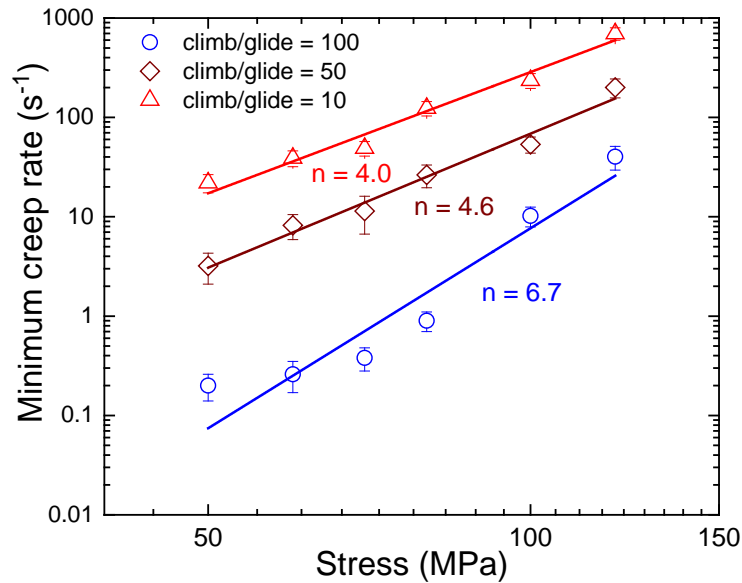
Figure 8 Log-log plot of minimum creep rate versus stress obtained from DDD simulations.

It may be noted that during the course of plastic deformation, dislocations move to new locations, and new dislocations are generated and annihilated too. Thus the dislocation microstructure evolves in a complex manner during plastic deformation. Fig. 9 shows the dislocation microstructure for copper at a strain of 0.00005 obtained at a stress level of 50 MPa. Dislocation junction formation is clearly visible in the early stages of deformation.
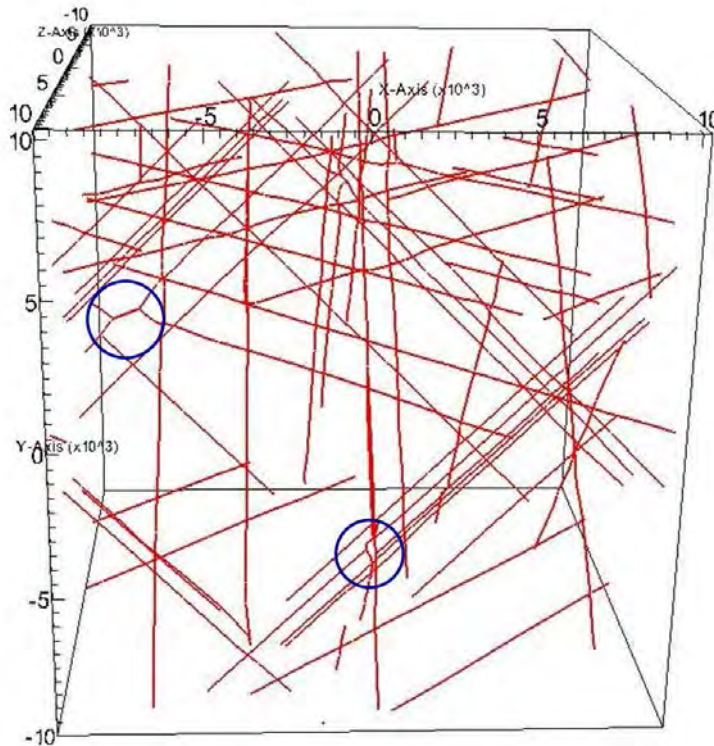
Figure 9 Dislocation microstructure at a strain of 0.00005 obtained from DDD simulations.

B.3.2 Simulations with Zr

Having established that DDD simulations can generate realistic creep behavior, we perform simulations in zirconium at dry storage conditions. Note that the DDD simulations complement the experimental work, which is typically performed at higher temperatures. Constant stress DD simulations have been carried out on Zr at 300 °C using the code *Micromegas* (instead of ParaDis). In these simulations, prismatic, pyramidal and basal slip systems are activated separately as well as jointly.

In the first case, a constant stress of 100 MPa has been applied along the *c*-axis of a Zr block with random dislocation configurations; Figure 10 shows the plastic strain as a function of time. Creep rate is derived from the plastic strain and is plotted in Figure 11. It can be seen that the creep rate initially decreases and then reaches a steady state – a behavior that is not unlike in typical experiments. Some loss of dislocations from the simulation box has also been noticed.

Next, simulations have been carried out to investigate the effect of slip system on the creep strain. Different simulation runs have been carried out using only basal slip, pyramidal slip, and prismatic slip; a combination of prismatic, pyramidal and basal slip with equal contribution is also investigated. Figure 12 shows the plot of the plastic strain as a function of time. It can be observed that the creep strain is low for both basal slip and pyramidal slip. For prismatic slip, the creep strain is higher and is similar to that of the system with combined slip – an observation that is typical in experiments. To our understanding, this is the first simulation that reproduces this effect at the microstructural level in Zr.
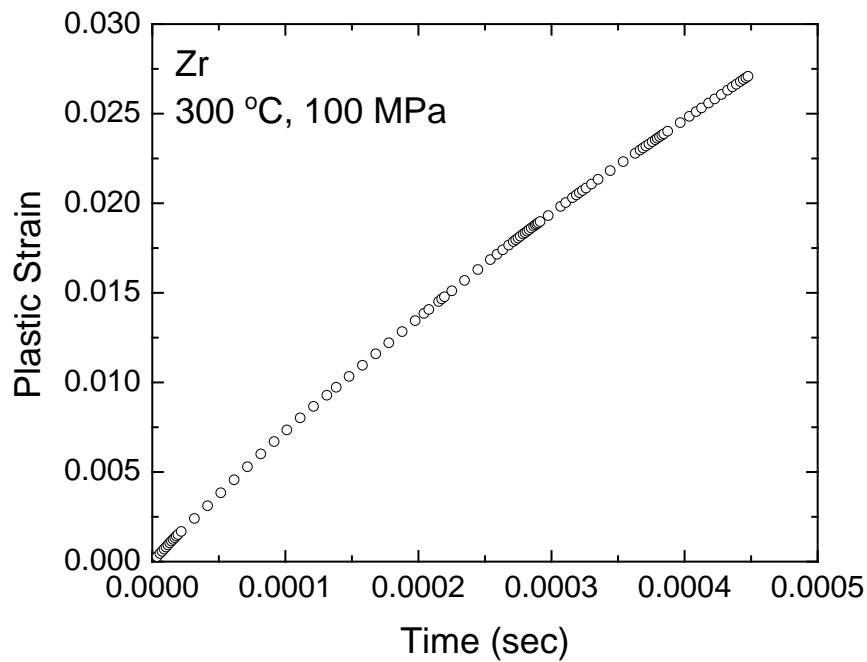
Figure 10 Evolution of Plastic Strain as a function of time in Zr during constant stress DDD simulation.
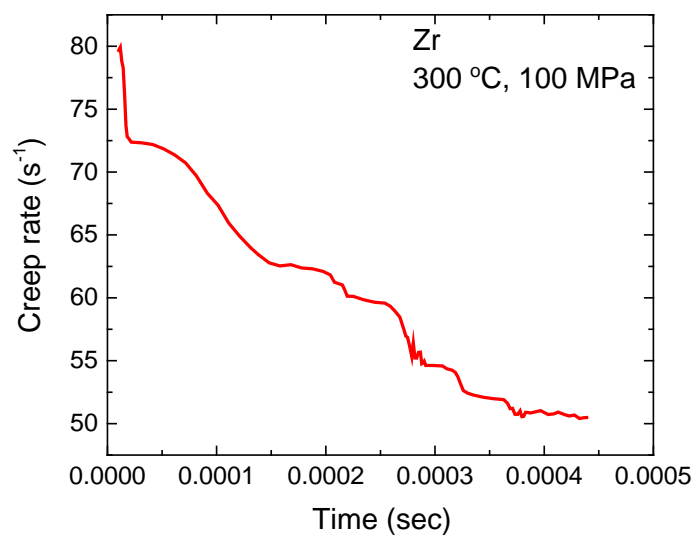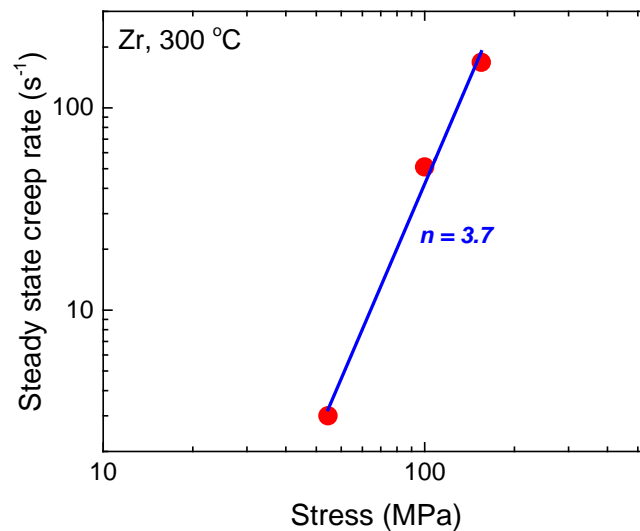

Figure 11 Creep rate as a function of time in Zr using DDD simulations.
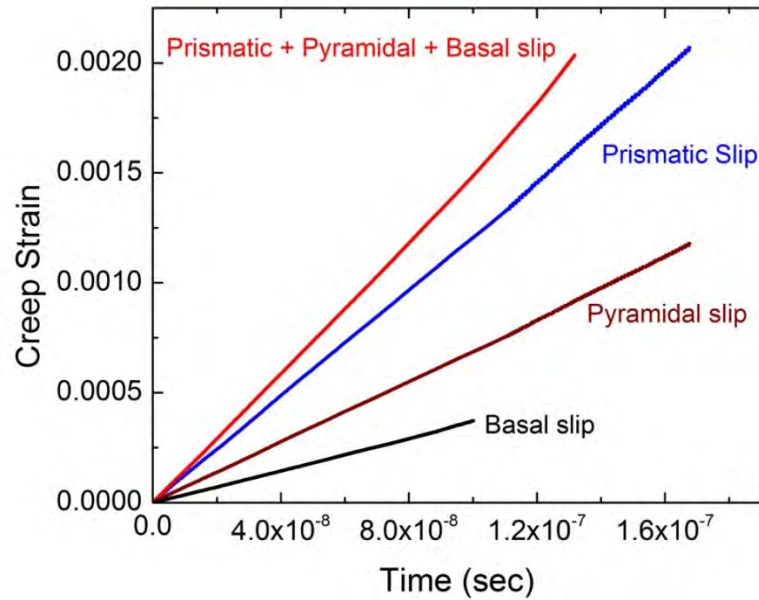
Figure 12 Role of different slip systems in Zr from DDD simulations.

Finally, the steady-state creep rate as a function of stress is plotted in Figure 13 with all the slip system activated at 300 °C. We note that a stress exponent of 3 to 4 is typically observed in Zr alloys at low stresses.

Figure 13 Steady state creep rate as a function of stress in Zr using DDD simulations.

Conclusion

The DDD simulations at dry storage conditions complement the experimental investigations that have been conducted at higher temperatures. One of the main conclusion from the DDD simulations is that creep in Zr at 300 °C is dominated by prismatic slip. For stresses expected in dry storage conditions, the creep is expected to be controlled by dislocations. It is known that irradiation in Zr alloys multiply the dislocations on the basal plane, typically. The DDD simulations indicate that additional basal plane dislocations will not affect the creep rate significantly and the creep rate of un-irradiated Zr alloy samples will be virtually bounding for crept samples at dry storage conditions.

References

[1]   C. Domain, G. Monnet, Physical review letters, 95 (2005) 215506.
[2]   K. Otsuka, C. Wayman, Vol. II, (1977) 81.
[3]   F.R. Nabarro, (1967).
[4]   F.R.N. Nabarro, Z.S. Basinski, D. Holt, Advances in Physics, 13 (1964) 193-323.
[5]   J. Hirth, J. Lothe, John Willey and Sons, NewYork.
[6]   H.M. Zbib, M. Rhee, J.P. Hirth, International Journal of Mechanical Sciences, 40 (1998) 113-127.
[7]   J.R. Greer, W.D. Nix, Physical Review B, 73 (2006) 245410.
[8]   J. Horton, S. Ohr, Journal of Materials Science, 17 (1982) 3140-3148.
[9]   K.G.F. Janssens, D. Raabe, E. Kozeschnik, M.A. Miodownik, B. Nestler, Computational materials engineering: an introduction to microstructure evolution, Academic Press, 2010.
[10]   E.B. Tadmor, M. Ortiz, R. Phillips, Philosophical Magazine A, 73 (1996) 1529-1563.
[11]   V. Yamakov, D. Wolf, S.R. Phillpot, A.K. Mukherjee, H. Gleiter, Nature materials, 1 (2002) 45-49.
[12]   M. Koslowski, A.M. Cuitino, M. Ortiz, Journal of the Mechanics and Physics of Solids, 50 (2002) 2597-2635.
[13]   L. Nicola, E. Van der Giessen, A. Needleman, Materials Science and Engineering: A, 309 (2001) 274-277.
[14]   H.M. Zbib, T. Díaz de la Rubia, M. Rhee, J. P Hirth, Journal of Nuclear Materials, 276 (2000) 154-165.
[15]   A. Arsenlis, W. Cai, M. Tang, M. Rhee, T. Oppelstrup, G. Hommes, T.G. Pierce, V.V. Bulatov, Modelling and Simulation in Materials Science and Engineering, 15 (2007) 553.
[16]   V. Bulatov, W. Cai, Computer simulations of dislocations, Oxford University Press, 2006.
[17]   S. Hafez Haghighat, G. Eggeler, D. Raabe, Acta Materialia, 61 (2013) 3709-3723.
[18]   G.E. Dieter, Mechanical metallurgy, McGraw-Hill New York, 1976.
[19]   R. Sandström, Acta Materialia, 60 (2012) 314-322.
[20]   I. Saxl, M. Svoboda, Rev. Adv. Mater. Sci, 25 (2010) 233-240.

2.0 Summary of Key Results and Findings from TMA-2: Hydrogen Behavior and Delayed Hydride Cracking

This mission focused on the characterization and understanding of delayed hydride cracking (DHC) in spent Zircaloy cladding. The DHC mechanism is generally attributed to local hydride precipitation at stress risers present on the surface of the cladding. Samples with low and high hydrogen loadings were prepared and studied using various methods.

The following sections are detailed reports presented from TMA2 contributors in their original format (to maintain clarity).

Hydrogen Interactions in Zirconium Alloys for Nuclear Applications
John Calvin Martinez and Sean M. McDeavitt, Texas A&M University

Excerpted from J.C. Martinez M.S. Thesis, May 2015

<u>Overview</u>

The absorption of hydrogen in zirconium-based nuclear fuel cladding alloys is one of the most significant contributors to its degradation during long-term storage. The goal of this work was to perform a detailed study of the behavior of hydrogen in two zirconium-based alloys used in nuclear applications. Specimens were prepared through low temperature cathodic charging using an electrochemical hydrogen insertion technique. Analysis was carried out through electron microscopy, X-ray diffraction, and differential scanning calorimetry.

The two alloys studied in this work were HANA-4 and Zircaloy-4. The electrochemical charging system was operated at 65 ± 5 °C, using a $0.2 - 0.4$ A/cm^2 current density, in a 0.2 M sulfuric acid solution. An electrode of platinum mesh was used as the anode, and the zirconium alloy samples were used as the cathode. Specimens were hydrogen charged to 170 wppm, Zircaloy-4, and 1600 wppm, HANA-4. The resulting hydride phases were measured through X-ray diffraction. The observed hydride phases were ε-hydride in HANA-4 and δ-hydride in Zircaloy-4.

Annealing was carried out at 530 °C, 440 °C, and 350 °C on sections of both alloys. The heat treatment resulted in a range of bulk hydrogen concentrations. Differential scanning calorimetry was then utilized to measure the hydride dissolution temperature in each coupon. These measurements however proved inconclusive, as the differential heat flow signals of charged and uncharged samples were difficult to distinguish.

1.0   Introduction

Zirconium alloys have a crucial function in the nuclear power industry. Due to the high corrosion resistance and favorable neutronic properties of zirconium alloys, they have been widely employed as cladding for fuel in light water and heavy water nuclear reactors [1]. The cladding is the first containment barrier in reactor design. It holds the fuel in place, within the fuel bundles that make up the core, and confines fission products within the fuel. Criticality in a reactor is a function of materials and geometry. Thus, the geometric stability of the fuel, provided by the cladding, is an important part of criticality control. The cladding; therefore, performs an important role in the complete life cycle of nuclear fuel. The performance of zirconium based cladding alloys has been the subject of much investigation over the years [1-6]. Performance issues range from corrosion and degradation of mechanical properties during burnup to hydrogen embrittlement and delayed hydride cracking during post irradiation storage. To address these issues, new cladding alloys and fabrication techniques are being developed to extend the service life of the fuel cladding [7-9]. A partial list, of zirconium cladding alloys and their compositions, is given in Table 1.1 below.

Table 1.1 Compositions of Various Zirconium Alloys

Alloy	Sn wt%	Fe wt%	Cr wt%	Nb wt%	Ni wt%	Mo wt%	O wppm
Zircaloy-2	1.5	0.12	0.1		0.05		1250
Zircaloy-4	1.3	0.2	0.1				1250
Zr-2.5Nb				2.4-2.8			900-1300
Zirlo	1.1	0.1		1.1			1200
M5		0.038		1.0			0.135
Excel	3.8			0.8		0.9	N/A*
E110		0.009		1.0			600
HANA-4	0.4	0.2	0.1	1.5			N/A**

[7] K.W. Song *et al*, (2008).
[8] D. Khatamian, *et al*,(1995).
[9] M. Billone, *et al*, (2008).
  * Not reported in [8] Khatamian *et al*, (1995)
 ** The HANA-4 material used in this study was found to contain 1000 wppm O.
*** wppm: Parts per million by weight, equivalently μg/g.

To further the understanding of the impact of hydrogen on zirconium and its alloys, the zirconium alloys HANA-4 and Zircaloy-4 were employed in the experiments performed in this study. The work was funded by the Department of Energy and conducted as part of the Fuel Aging and Transportation (FAST) Integrated Research Program (IRP).

The HANA-4 alloy is one of six HANA, 'High-performance Alloy for Nuclear Applications' alloys being developed at the Korean Atomic Energy Research Institute (KAERI) in South Korea. HANA-4 is being developed as part of a national research program to develop materials for high burnup fuel (HBF) [7]. Zircaloy-4 is an established alloy and has been used for many years in pressurized light-water reactors (PWRs) [10]. It was developed through a nuclear technology research and development program by the U.S. Navy [10, 11].

The objectives of this research are particularly concerned with the impacts of hydrogen on zirconium alloys used in nuclear applications. Hydrogen absorption is one of the most significant contributors to the degradation of the cladding throughout its service lifetime. Hydrogen is absorbed by zirconium through corrosion. The oxidation of the cladding in water evolves hydrogen, a fraction of which is absorbed by the cladding. Hydrogen has a low solubility in zirconium, only about 1 wppm (wppm: Parts per million by weight, equivalently μg/g) at room temperature and ~200 wppm at 400 °C [12]. When the absorbed hydrogen exceeds the solubility limit, excess hydrogen precipitates as a second phase, zirconium hydride. Hydrogen accumulates in the cladding during burnup, with bulk hydrogen concentrations reaching between 350 wppm and 800 wppm in high-burnup fuel [5]. High burnup is the term applied to fuel assemblies with burnup greater than 45 GWd/MTU [5], where GWd/MTU is a unit of energy released per metric ton of uranium in the fuel. At reactor operating temperatures 250 – 300 °C for CANDU [13], 285 °C for BWR, and 275 - 315 °C for PWR, less than 100 wppm of hydrogen can be maintained in solid solution [12, 14]. Therefore, a significant portion of the hydrogen in high burnup fuel is precipitated as hydride during in core service. Upon cooling, after removal from the core, nearly all the hydrogen is precipitated as hydride.

The hydride phase is brittle and its presence reduces the ductility and fracture toughness of the cladding [9, 15, 16]. The severity of the embrittlement is increased when hydrides are radially oriented. This makes the dissolution of hydrides a concern, because of the potential reorientation of hydrides upon re-precipitation [16, 17]. The presence of hydrogen in solution or in hydrides can lead to component failure through a process known as delayed hydride cracking (DHC).

Delayed hydride cracking is a below yield stress failure mechanism. It poses a significant threat to the integrity of the cladding. Because DHC results from hydride precipitation at the tip of a crack or flaw, it is directly connected to the terminal solid solubility of hydrogen in the zirconium alloy being considered. As the terminal solid solubility describes the conditions under which hydride dissolution and precipitation occurs, knowledge of the TSS for an alloy is important when considering its susceptibility to DHC [8].

While the terminal solid solubility (TSS) of hydrogen in irradiated and un-irradiated material is known and has been widely reported for many zirconium alloys such as Zircaloy-2, Zircaloy-4, Zr-2.5%Nb, and others [8, 14, 18-20], TSS data is not widely available for the HANA alloys. As several studies have already been made to evaluate other characteristics of HANA-4 and Zircaloy-4: steam oxidation under loss of coolant accident conditions (LOCA) [21], corrosion [22], and creep [7]; one of the goals of this work is to add to this growing evaluation by taking the first step toward measuring the TSS of hydrogen in HANA-4. The corresponding measurements made in Zircaloy-4 enable baseline comparison.

In order to study the impacts of hydrogen at the elevated concentrations found in high burnup fuel, hydrogen was inserted into the zirconium alloy specimens through cathodic charging. Charging resulted in 170 – 220 wppm H in Zircaloy-4, and 800 – 1600 wppm H in the HANA-4 alloy. The sections of the charged specimens were annealed at 540 °C to create uniformly distributed hydrides within these samples. Charged and annealed samples were characterized through electron microscopy and X-ray diffraction (XRD). The XRD measurements showed a change from the high-density ε-hydride (ZrH_2) phase, post charging, to the lower density δ- hydride ($ZrH_{1.66}$) phase, post annealing, in the HANA-4 specimens. The phases measured in the Zircaloy-4 specimens changed from the post charging δ- hydride to α-zirconium in the annealed sample; even though the specimen contained 170 wppm H.

To measure and compare the terminal solid solubility of these two alloys, the hydride dissolution temperature was measured for samples prepared under select annealing conditions. Annealing was carried out at 530 °C, 440 °C, and 350 °C. Measurements of the hydride dissolution temperature in this study were performed using differential scanning calorimetry (DSC), following the work of Khatamian [23] and others [20, 24]. However, these measurements were inconclusive. In uncharged specimens of both alloys, there was a feature in the DSC curve at ~350 °C, making it difficult to measure hydride dissolution in the samples annealed at that temperature. While the high and middle temperature measurements in HANA-4 contained features near the annealing temperatures, 530 °C and 440 °C respectively, the features in the low temperature measurement could not be separated from that mentioned above in the uncharged specimen. In Zircaloy-4 only in the sample annealed at 440 °C was a corresponding feature observed, no features corresponding to the annealing temperature were observed in the highest temperature measurement. As in HANA-4, no feature near the annealing temperature could be distinguished from the uncharged specimen.

The following chapters provide a more in depth look at relevant background information, the methods employed, and results of this study. Chapter II provides an overview of background information motivating this study. Chapters III and IV discuss the experimental methods and results; with discussion and conclusions given in chapters V and VI.

2.0   Background

Hydrogen absorption is one of the limiting factors on cladding lifetime, due the resulting degradation. This Chapter presents a sequence of discussions describing relevant phenomena and literature that provide the foundation for the work performed here. Section 2.1 describes the hydrogen-zirconium binary phase diagram. Section 2.2 introduces the terminal solid solubility behavior of hydrogen in zirconium. Section 2.3 describes in more detail how hydrogen is absorbed into Zr-based nuclear cladding during normal operation, and Section 2.4 describes laboratory methods of charging zirconium alloys with hydrogen. Sections 2.6 and 2.7 discuss hydrogen embrittlement and hydride reorientation, which leads to delayed hydride cracking, Section 2.8.

2.1   The Hydrogen-Zirconium Binary Phase Diagram

The hydrogen zirconium system has been studied for over 60 years, yet ambiguity remains regarding the nature and formation of certain hydride phases [25-28]. Figure 2.1 shows the Zr-H binary phase diagram, as reported by Zuzek and Abriata, 1990 [28].
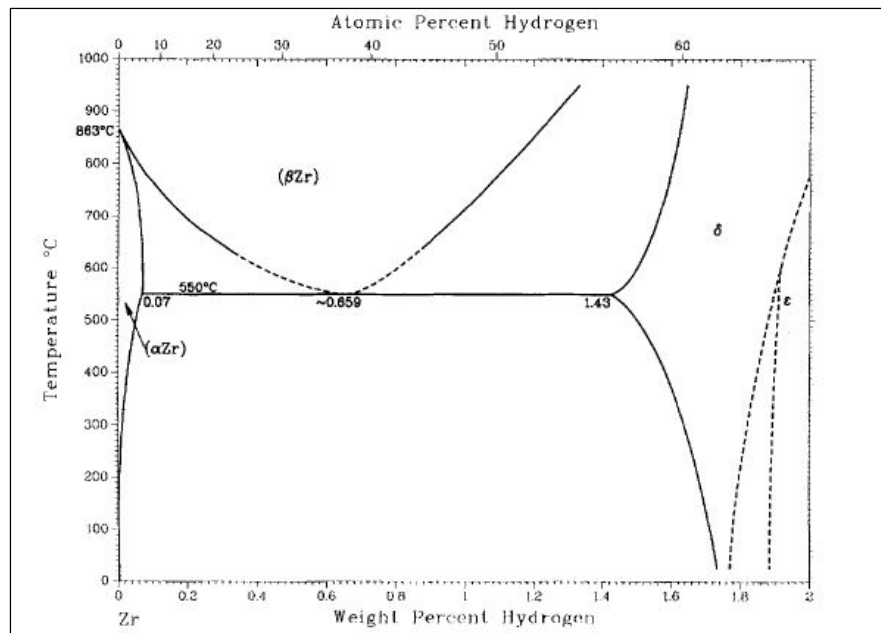
Fig. 2.1 Zr-H Phase Diagram[28].

There are five primary phases in the Zr-H system, see Figure 2.1, in the region from 0 – 1000 °C, and 0 – 2 wt% hydrogen. These are: α-Zr, β-Zr, γ-ZrH, δ-ZrH$_{1.66}$, and ε-ZrH$_2$ [29]. The γ phase is not shown in the phase diagram because it is considered by many to be a metastable phase [28-30], though some authors argue for its stability as an equilibrium phase[27].

Lanzani [26] suggested that the stability of the γ phase may be dependent on the purity of the zirconium and which alloying elements are present. The δ-hydride is reported to preferentially precipitate in zirconium alloys with elevated concentrations of α stabilizers (e.g., O, Hf, Sn), while the γ-hydride preferentially precipitates in high purity zirconium or alloys containing β stabilizers [26].

The formation of the γ- and ε-hydride phases is proposed to result through martensitic like transformations of the δ-hydride [30]. Unlike diffusionless martensitic transformations, theses transformations require a change in hydrogen concentration [30]. Only the 1 to 1 stoichiometric composition for the γ-hydride (ZrH), is exact, since the δ and ε phases have a broad range of stable stoichiometries [30].

Pure Zirconium in the α-Zr phase has a hexagonal close packed (HCP) crystal structure, and is stable below the β transition temperature, 863 °C [28, 31]. The β phase, is body centered cubic (BCC) and metastable below 863 °C [28, 30]. Certain alloying elements, such as hydrogen and niobium, act as β stabilizers, lowering the β transition temperature and inhibiting decomposition of the β phase [26, 32]. The β-Zr phase is reported to have a greater affinity for hydrogen than α-Zr and an increased terminal solid solubility [32-34]. Higher TSS means more hydrogen can be absorbed before the precipitation of embrittling hydrides, resulting in a longer component lifetime in-core [32].

As described in §2.3, hydrogen absorption by the cladding takes place at elevated temperatures. The hydride phases precipitated in the cladding upon cooling depends upon the hydrogen concentration and the rate at which it is cooled [35]. Because higher hydrogen concentrations, and cooling rates less than 10 K/min, lead to preferential precipitation of the δ-hydride phase, the δ-hydride phase is the dominant phase present in the cladding of spent nuclear fuel (SNF) during wet storage [5, 26, 29, 35]. By adopting cooling rates less than 10 K/min, the author was able create the δ-hydride phase in annealed portions of cathodically charged zirconium alloy sections, replicating the dominant hydride phase in SNF.

2.2 Terminal Solid Solubility

The terminal solid solubility (TSS) is an important property of the Zr-H system. Terminal solid solubility represents the phase boundary between dissolved hydrogen in solution and the precipitation of hydrides as a second phase. It is termed the terminal solid solubility because it marks the initiation and termination of phase transformations mentioned above [36]. The terminal solid solubility of hydrogen in Zircaloy, as measured by DSC, is given below in Figure 2.2.

In the measurement shown below there are two curves. This is because there is a hysteresis between the terminal solid solubility for dissolving hydrides (TSS_d) and precipitating hydrides (TSS_p). The lower curve is the dissolution solvus, and gives the temperature at which all the hydrogen is in solid solution, for a given hydrogen concentration. The upper curve is the precipitation solvus and it denotes the temperature at which hydrogen precipitates to form the hydride phase or phases [36, 37].
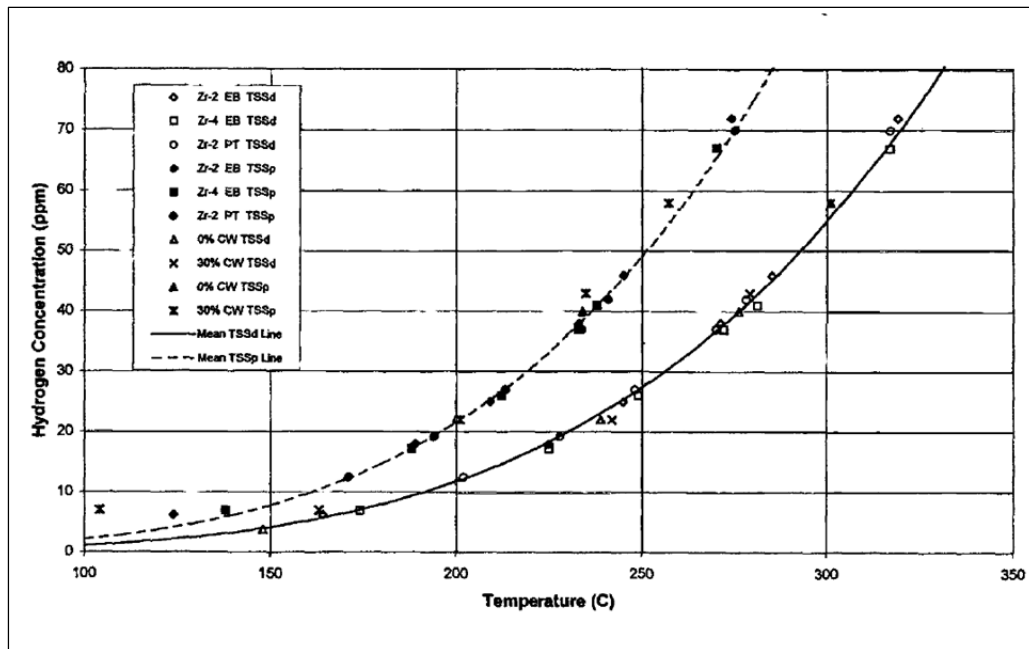
Fig. 2.2 Terminal solid solubility of hydrogen in Zircaloy material. Measured by DSC. Reprinted, with permission from <u>ASTM STP 1354 Zirconium in the Nuclear Industry: Twelfth International Symposium</u>, 100 Barr Harbor Drive, West Conshohocken, PA 19428. [37]

The hysteresis between the solvi is the result of a difference in matrix accommodation energies for precipitating and dissolving hydrides. Because the hydride phases are less dense than α-phase zirconium, there is 17% volume change when α-Zr transforms to δ-hydride. The zirconium matrix must be expanded to accommodate the increase in volume associated with hydride growth [2, 38]. The matrix accommodation energy is the work that must be done expanding the matrix.

The accommodation energy depends on the elastic modulus and the shape of the precipitated hydride. As the yield stress is temperature dependent, the matrix accommodation energy is also temperature dependent [30, 38, 39]. This hysteresis is crucial to observations of crack velocity in delayed hydride cracking [2, 38].

It has been observed that TSS may be impacted by the addition of particular alloying elements [14, 32, 33] and irradiation damage [20]. In assessing the impact of irradiation on TSS, Vizcaino *et al*, [20], reported a significant increase in TSS for Zircaloy-4 irradiated for 10 full effective power years in a heavy water power reactor (HWPR). Une *et al*, [18], reported no change in TSS between un-irradiated Zircaloy-2 and Zircaloy-2 irradiated for 3 – 5 cycles in a commercial boiling water reactor (BWR). Both studies used DSC to measure the TSS in their respective materials; however, the in-core service times differed for the irradiated materials [18, 20].

The variation in TSS between un-alloyed zirconium and the Zircaloys is slight, prompting Kearns [14] to represent TSS for these materials as a single curve, *Eq.* (2.1).

$$TSS_d = 1.2 \times 10^5 e^{-\frac{Q}{RT}} \qquad\qquad (2.1)$$

$Q = 8550\, \frac{Cal}{mol}$ Q is the activation energy.

$R = 1.987\, \frac{Cal}{mol \cdot K}$ R is the Universal Gas Constant

$T = Temperature\ in\ K$

Equation (2.1) is referred to as the Kearn's line, and is referenced in many TSS studies [18, 20, 33, 37]. Une *et al* [24] found no difference in TSS between Zircaloy-2 and high Fe (0.26wt%) Zircaloy. However, Khatamian *et al* [8] found that the TSS for the Excel alloy, composition in Table 1.1, was significantly higher than for either Zircaloy-2 or Zr-2.5wt%Nb alloys. This result led to several studies by Khatamian [32-34] to re-evaluate niobium bearing alloys. Khatamian [32-34] reported an increase in the TSS of niobium bearing alloys. Khatamian found that niobium increased the TSS by stabilizing the β phase, which exists as a small fraction in an α + β mix, nominally 90% α and 10% β. Khatamian and Ling [34] reported that the solubility limits of hydrogen in the β phase is two orders of magnitude higher than in α-Zr. Due to its higher solubility, the presence of β phase Zr was found to significantly increase TSS (Figure 2.3) [32-34].

Figure 2.3 shows that increasing niobium content results in increased TSS$_d$. As mentioned in §2.1, the β phase is metastable below 900 K. Khatamian and Ling [33, 34] found that the TSS decreased as the fraction of BCC β phase transformed back to the HCP α phase by aging at 400 – 500 °C for 1 – 100 hrs, Figure 2.4 [33, 34].
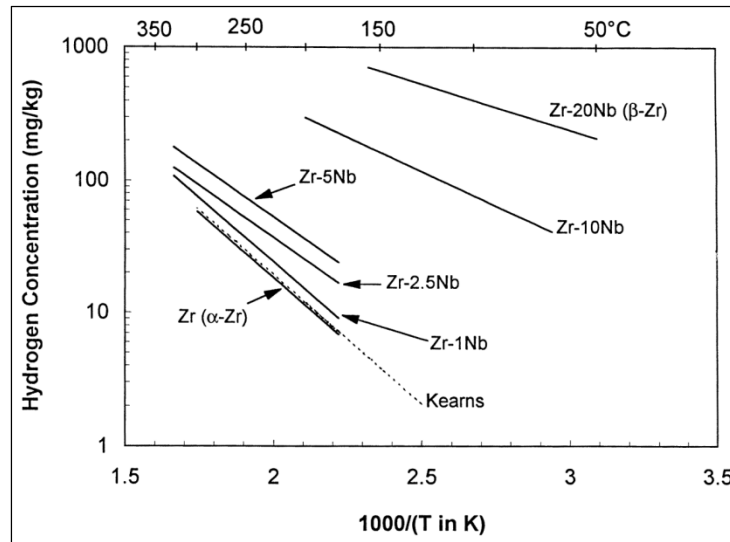
Fig. 2.3 Increase in TSS$_d$ with increasing niobium content in Zr-Nb alloys [32].
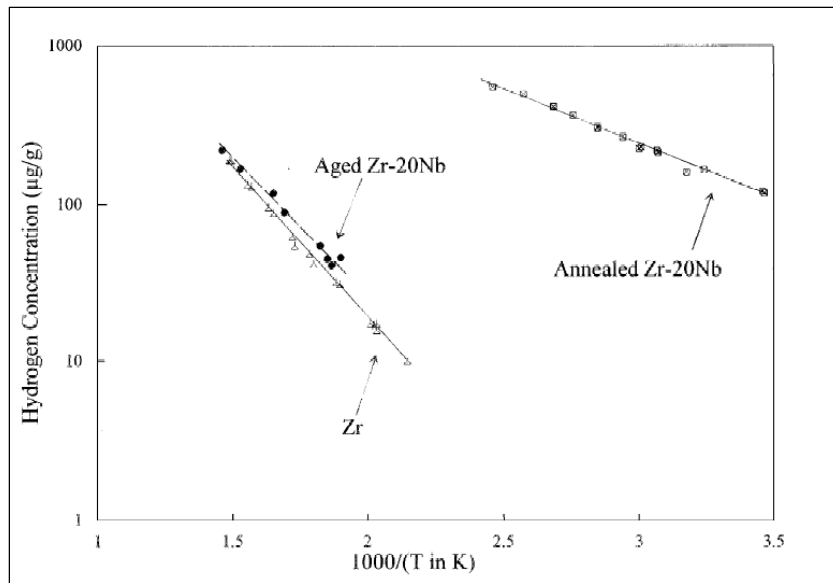
**Fig 2.4** Change in TSS for Zr-20Nb with β-Zr fraction. Annealed, fully regenerated β-phase. Aged, fully decomposed to α phase [34].

Figure 2.4 shows that the TSS for Zr-20Nb approaches that of pure zirconium as aging decomposes the β phase to α-Zr. This is why the Zircaloys, in which only the α-Zr phase is present, retain a TSS equivalent to that of unalloyed α zirconium [5, 33, 34]. The niobium stabilization of the β-Zr phase raises the TSS in Zr-Nb alloys by partitioning the hydrogen into the β phase, with its greater hydrogen solubility limit.

As the TSS of different alloys may vary, due to its dependence on crystal structure and alloying elements, it is essential that an alloys TSS be known, in order to know the conditions under which hydride dissolution and precipitation occur [8, 14, 40].

2.3 Hydrogen Absorption During Reactor Operation

As noted in Chapter I, the corrosion of zirconium alloy components during reactor operation is a critical performance-limiting phenomenon. The extreme harshness of the in-core environment poses significant challenges to cladding performance. The performance degradation during irradiation negatively impact the integrity of the cladding and its post irradiation performance in wet and dry storage. The severity of degradation to cladding integrity is closely related the level of burnup in the fuel [5].

The mechanical properties of the cladding are influenced by the absorption of hydrogen into the cladding through corrosion; which can be represented as a function of burnup [22, 41]. On the waterside of the cladding, corrosion occurs primarily in the form of oxidation: $2H_2O + Zr \rightarrow ZrO_2 + 4H$ [12, 41]. See Figure 2.5.
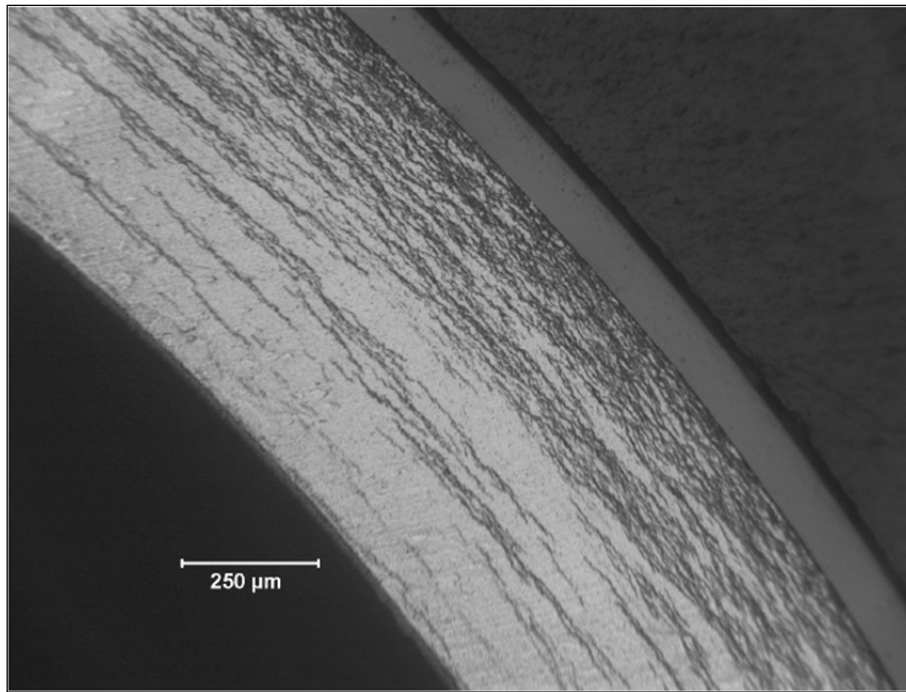
Fig. 2.5 Example of hydrogen absorption during aqueous corrosion: 740 wppm H [9].

During the waterside-oxidation process, a thick oxide layer forms on the outer surface of the cladding, dark region in Figure 2.5. A portion of the evolved hydrogen is absorbed into the cladding and diffuses under the influence of stress and thermal gradients. In Figure 2.5, the absorbed hydrogen has precipitated to form circumferential hydrides. The majority of the hydrides have precipitated near the outer surface, but hydrides are present throughout the specimen. The evolved hydrogen, not absorbed by the cladding, is carried away by the coolant [9].

The ratio of hydrogen absorbed to total hydrogen evolved during the oxidation process is called the hydrogen pickup fraction [12]. The hydrogen pickup fraction depends on alloying constituents and fabrication methods [9, 42]. When the amount of hydrogen absorbed by the cladding exceeds the precipitation solvus, zirconium hydride is precipitated as a second phase [29, 35, 43, 44]. In order to limit hydrogen uptake by the fuel cladding, the Nuclear Regulatory Commission (NRC) limits total cladding oxidation to 0.17 times the total cladding thickness before oxidation (10 CFR 50). However, within these limits, high burnup fuel accumulates between 350 wppm and 800 wppm H, leading to hydrogen embrittlement and the potential for component failure through delayed hydride cracking [5].
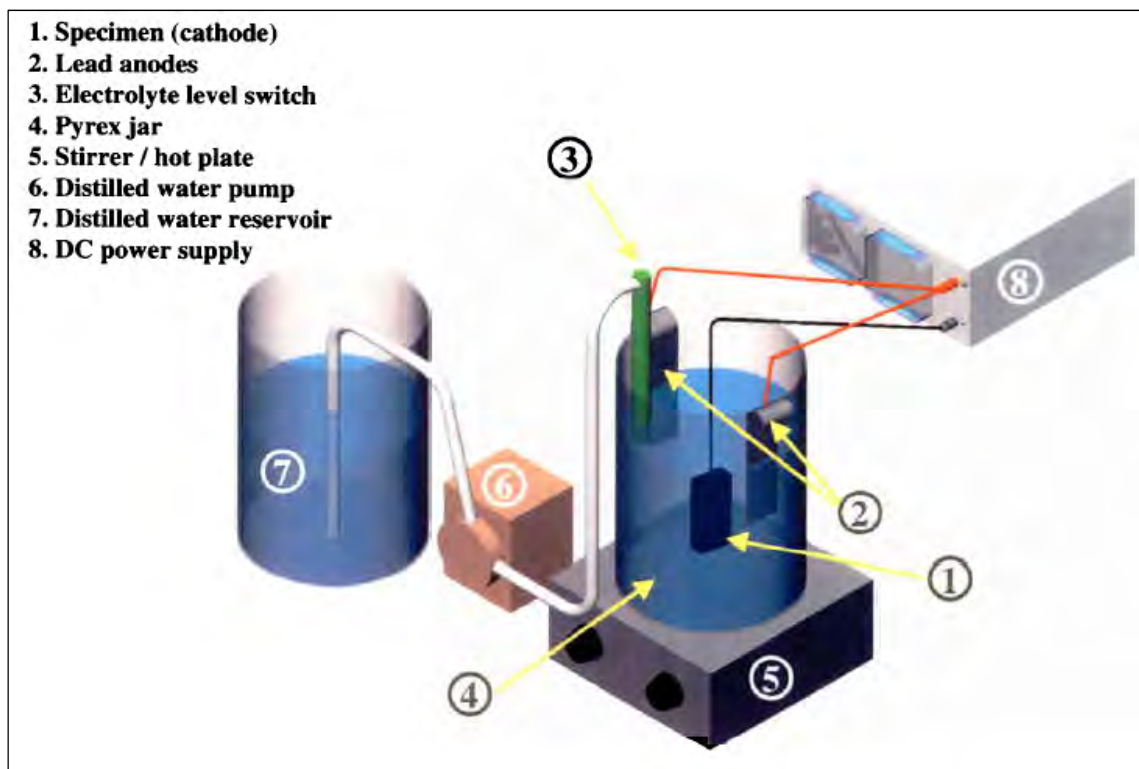
2.4 Methods of Charging Zirconium Alloys with Hydrogen

Zirconium alloys typically have a small amount of hydrogen impurities after fabrication. The amount of hydrogen varies by alloy. Some Zircaloy-4 alloys have around 20 wppm hydrogen [45]; while other alloys, such as HANA-4, typically have less than 10 wppm hydrogen after fabrication [21]. These trace amounts of hydrogen have little effect on cladding properties

and behavior. Therefore, hydrogen must be inserted into samples, in order to study the elevated hydrogen concentrations seen in cladding at the end of life (EOL) in reactor operation.

There are four methods to insert hydrogen into zirconium reported in literature. These are: cathodic charging, gas phase insertion, aqueous corrosion, and diffusion through a weld from a metal in which hydrogen has a higher activity [12]. As cathodic charging was the method of hydrogen insertion selected for this project; the basic principles of this method are presented in detail below.

Cathodic charging requires simplistic equipment: a reaction vessel, direct current power supply, and a suitable electrolyte and electrode pair. Cathodic systems for charging zirconium with hydrogen are roughly divided between two categories: low temperature cathodic charging, as seen in Hindle and Slattery [46] and Lepage *et al*, [40], see Figure 2.6, and high temperature cathodic charging systems (HTC), such as those used by John *et al* [47] and Choi *et al* [48].

1. Specimen (cathode)
2. Lead anodes
3. Electrolyte level switch
4. Pyrex jar
5. Stirrer / hot plate
6. Distilled water pump
7. Distilled water reservoir
8. DC power supply

Fig 2.6 Example of the cathodic charging system described in Lepage *et al*, 1998 [40].

Low temperature charging takes place below 100 °C [40, 46]. A variety of electrolytes can be used in these systems. Sulfuric acid (H_2SO_4) was chosen as the electrolyte in this project, as done in [40, 43, 46]. Potassium-hydroxide (KOH) is another commonly used electrolyte for this purpose [49, 50]. In both cases hydrogen is evolved through the decomposition of water during electrolysis [43]. An example of sample charged through low temperature cathodic charging is presented in Figure 2.7. Low temperature cathodic charging results in the creation of a dense surface hydride layer. The hydride concentration in the rim appears uniform.
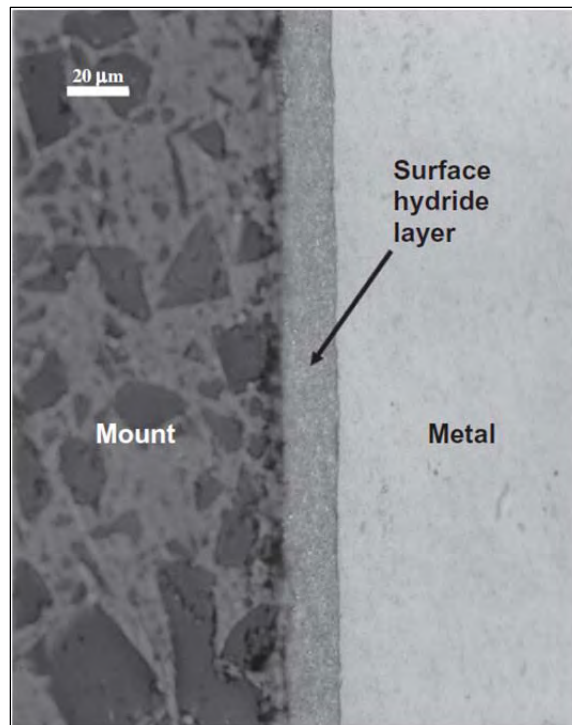
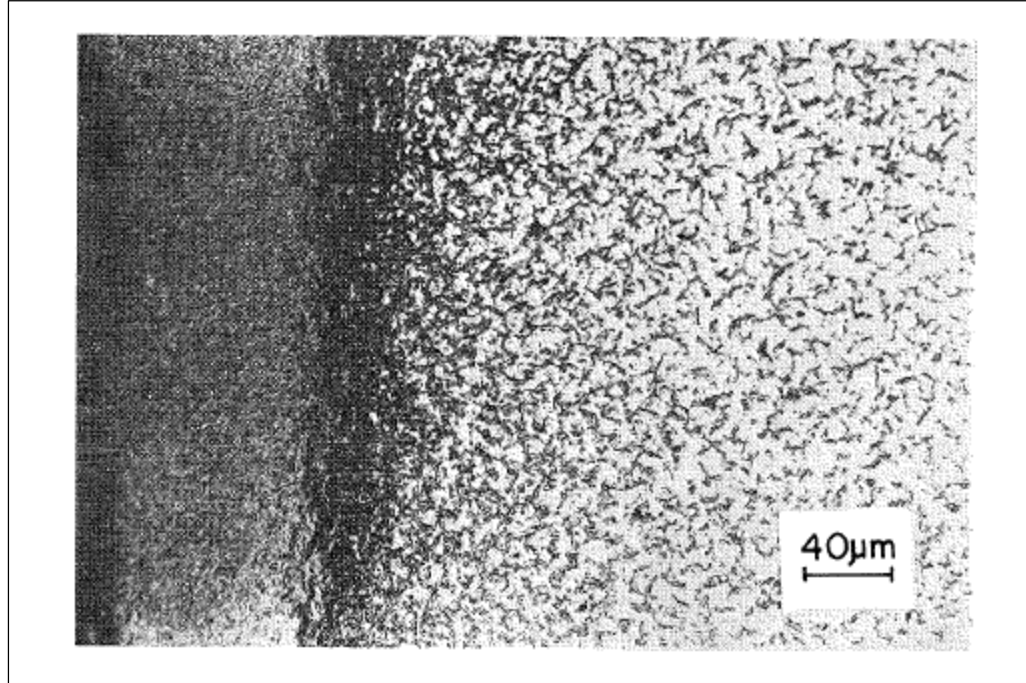**Fig. 2.7** Example of surface hydride layer from low temperature cathodic charging [23]

The HTC process uses an aqueous salt or molten salt electrolyte, with temperatures greater than 250 ℃, see Figure 2.8.
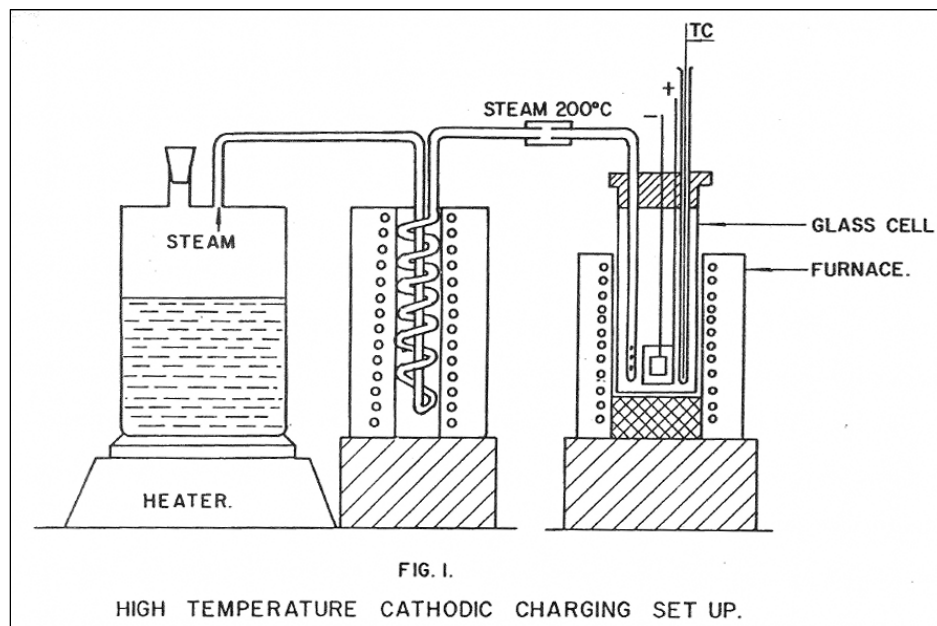
Fig 2.8 System diagram for High Temperature Cathodic Charging [47].

As seen in the diagram above, HTC requires the addition of a steam line and an additional heater [47]. John *et al*, [47] tested nine salt mixtures as electrolytes using potassium sulfate (K_2SO_4), potassium hydrogen sulfate ($KHSO_4$), sodium sulfate (Na_2HSO_4), and sodium hydrogen sulfate ($NaHSO_4$). An example of a specimen charged by high temperature cathodic charging is given in Figure 2.9.

Fig 2.9 Example of surface hydride layer from high temperature cathodic charging [47].

Due to increased hydrogen mobility at the higher operating temperature of high temperature cathodic charging systems, hydrides form well into bulk, far from the surface. This results in a hydride concentration gradient, and hydrides being precipitated in a less localized manner than seen in specimens charged at lower temperature.

Equation (2.2), from Lepege *et al*, [40] gives the minimum thickness of the hydride rim required to produce the desired bulk hydrogen concentration, for a sample of known thickness. It is noted in [40] that if the hydride layer is present on both sides of the sample, only half the thickness per side is required.

$$T_{hydride}(\mu m) = 7.232 \times 10^{-2} \, H_{Zr} \, T_{Zr}(mm) \tag{2.2}$$
$$T_{hydride} = Thickness \ of \ the \ hydride \ layer \ in \ \mu m$$
$$H_{Zr} = hydrogen \ level \ required$$
$$T_{Zr} = Thickness \ of \ Zirconium \ alloy \ sample \ in \ mm$$

Rearranging *Eq.* (2.2), the bulk hydrogen concentration that may be obtained in a sample can be estimated from the observed hydride rim thickness, *Eq.* (2.3).

$$H_{Zr} = \frac{T_{hydride}(\mu m)}{7.232 \times 10^{-2}(T_{Zr}(mm))} \tag{2.3}$$

The form found in $Eq.\,(2.3)$ was one method used to estimate bulk hydrogen concentration in charged samples.

In addition to $Eq.$ (2.3), hydrogen concentration estimates were made using $Eq.$ (2.6). Equation (2.6) is derived from $Eq.$ (2.4) and $Eq.$ (2.5). This method requires knowing the rim thickness and the hydride phase present in the sample. Equation (2.4) is the definition of wt% for hydrogen. Equation (2.5) approximates the mass of hydrogen based on rim thickness, the volume of the hydrided region, and the density of the hydride phase present in the sample. When combined with $Eq.$ (2.4), to form $Eq.$ (2.6), it can be seen that the apparent volume dependence drops out, as the hydride volume and zirconium volume have the same length. Thus the volume terms in $Eq.$ (2.6) effectively become area fractions.

$$wt\% \, H = \frac{m_H}{m} \tag{2.4}$$
$$= \frac{m_H}{m_{ZrH_x} + m_{Zr}}$$
$$= \frac{m_H}{\rho_{ZrH_x} V_{ZrH_x} + \rho_{Zr} V_{Zr}}$$

$$m_H = x \, \rho_{ZrH_x} V_{ZrH_x} \left(\frac{M_{M_H}}{M_{M_{ZrH_x}}} \right) \tag{2.5}$$

where:
$m = Total\ mass$
$x = Stoichiometric\ factor\ of\ hydride\ phase$
$\rho_{ZrH_x} = Density\ of\ hydride\ phase$
$V_{ZrH_x} = Volume\ of\ hydride\ phase$
$M_{M_H} = Molar\ mass\ hydrogen$
$M_{M_{ZrH_x}} = Molar\ mass\ of\ hydride\ phase$

Thus:

$$H \, wt\% = \frac{x \, \rho_{ZrH_x} V_{ZrH_x} \left(\frac{M_{M_H}}{M_{M_{ZrH_x}}} \right)}{\rho_{ZrH_x} V_{ZrH_x} + \rho_{Zr} V_{Zr}} \tag{2.6}$$

where:
$\rho_{Zr} = Density\ of\ Zirconium$
$V_{Zr} = Volume\ of\ Zirconium$

2.5 Hydride Homogenization

The homogenization process involves annealing the charged sample in a furnace. The annealing time should be sufficient for the hydrogen to approach an equilibrium concentration throughout the specimen. Literature reports annealing in air, an inert atmosphere, or under vacuum [23, 29, 40, 46, 49, 51]. Homogenization is governed by the terminal solid solubility behavior described in §2.2. During heating the hydrides at the rim begin to dissolve as the temperature increases. The hydrides continue to dissolve until the TSS_d at the homogenization temperature is reached. See Figure 2.10.
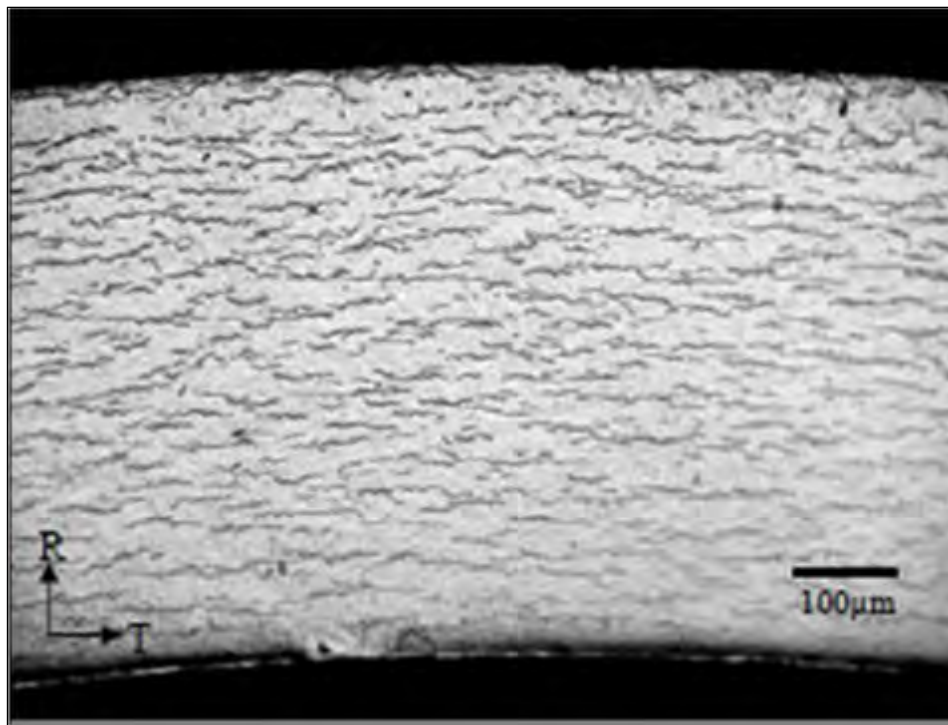
Fig. 2.10 Example of homogenous hydride distribution. (200 wppm H) [3]. Reproduced with permission of the IAEA.

As the hydrogen dissolves into solution, it diffuses throughout the sample; eventually reaching a uniform distribution [52]. Upon cooling this results in the uniform precipitation of hydrides in the sample.

2.6 Hydrogen Embrittlement

The absorption of hydrogen results in a degradation of mechanical properties, known as hydrogen embrittlement. When combined with the potential for hydride assisted cracking (delayed hydride cracking) the cladding is put at risk of failure in reactor operation and extended storage [5, 53].

Hydrogen embrittlement is the degradation of mechanical properties due to the formation of hydrides in the cladding [5]. Embrittlement of Zircaloy or other nuclear cladding increases with burnup as the associated increase in oxidation leads to higher hydrogen content. As noted in Chapter 1, for reactor operating temperatures around 315 °C, less than 100 wppm of hydrogen is soluble. Continued hydrogen absorption creates an increased weigh fraction of zirconium hydride, and increasing embrittlement.

Upon precipitation the zirconium hydride forms platelets with highly textured radial or circumferential orientation, the orientation is related to the internal stress of the cladding tube. An example of circumferential hydrides in cladding is given in Figure 2.11, and radial hydrides are shown in Figure 2.12.
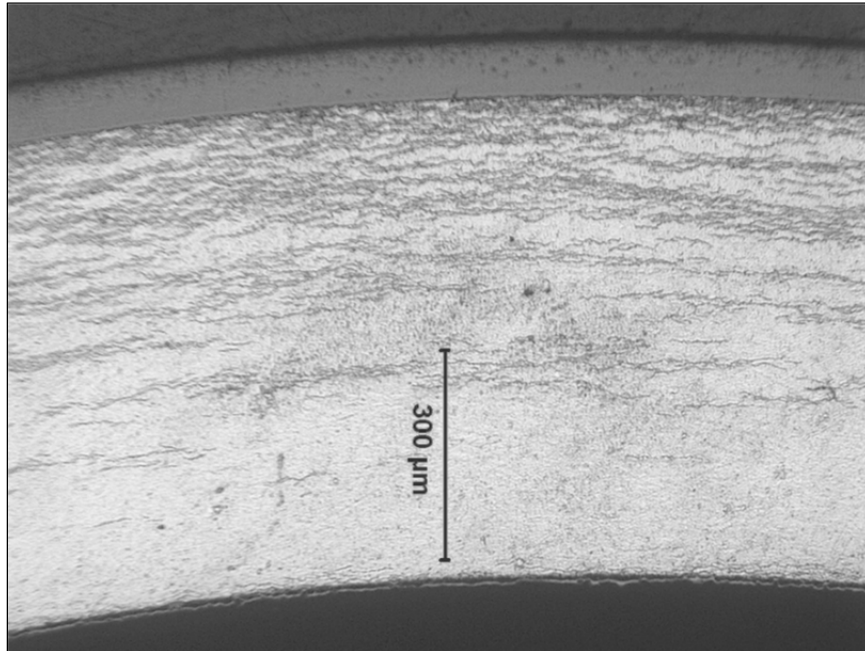
Fig 2.11 Outer oxide layer with a gradient of circumferential hydrides in the bulk [9].
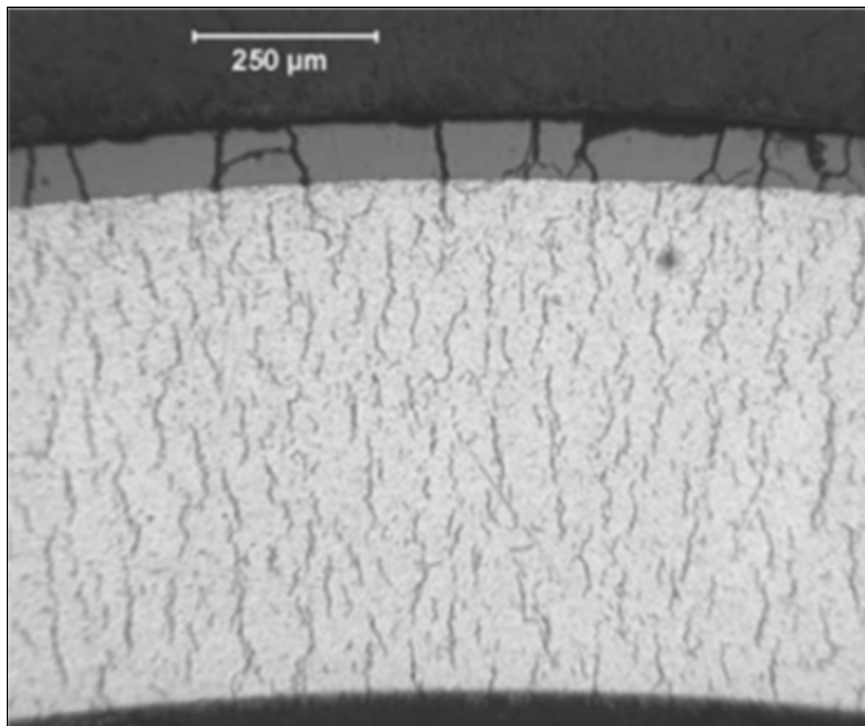
Fig. 2.12 Outer oxide layer with radial hydrides in the bulk [5].

The severity of embrittlement is strongly related to the orientation of the hydrides [16]. Radial hydrides negatively impact the integrity, ductility and fracture toughness of the cladding. The presence of hydrides results in loss of ductility and a rapid decrease in yield strength at temperatures up to 150 °C [54]. These effects are increased at low temperatures, making it a concern during dry storage. The rate of embrittlement increases rapidly at elevated temperatures, making it an important factor in evaluating cladding performance under a postulated loss of coolant accident (LOCA) or during the drying process [5, 9].

The susceptibility of zirconium cladding alloys to hydrogen embrittlement has been reduced by improving their corrosion resistance and controlling the preferred hydride orientation. Corrosion resistance was improved through a combination alloy composition and fabrication techniques [1, 7, 15, 46, 55-57]. Research in the 1960's, showed that the hydride orientation in zirconium alloys is dependent on internal stress, grain structure, and texture[55]. Hindle and Slattery [46] determined that even though tube fabrication processes consist of several steps, the last step is most important for determining the orientation of precipitated hydrides. As a result, current cladding production methods are designed to reduce embrittlement by preferentially precipitating circumferentially oriented hydrides, through control of the texture and residual stress in the material after fabrication [5, 46, 53, 55]. New alloys and techniques continue to be developed to improve the performance and lifetime of cladding alloys for HBF [7, 8].

2.7 Hydride Reorientation

Although cladding fabrication methods directly impacts the preferential precipitation of circumferential hydrides, as discussed in the previous section, a change in the stress field can lead to the reorientation of hydrides [16]. Reorientation occurs when previously precipitated hydrides dissolve back into solution and then re-precipitate under the influence of the current internal tensile stress. Such dissolution is caused by an increase in cladding temperature, which can occur during normal operation, reactor starts and stops, a loss of cooling accident, and during vacuum drying, when fuel is being transferred to dry storage. It has been observed that for hydride reorientation to occur the applied stress must exceed a threshold value [16, 53]. The reorientation stress threshold has been measured for various zirconium alloys to lie between $75MPa - 220MPa$ in the temperature range from $250 - 550$ °C. This variation is due to differences in microstructural texture and hydrogen concentration, though may depend on other factors as well [53, 58, 59].

The reorientation process is of particular concern during the fuel drying process. After an extended storage period in a spent fuel pool, fuel assemblies are moved from the wet condition, placed in a dry storage canister (still underwater), which is then sealed and drained. The canister then undergoes several cycles of evacuation and backfilling with high purity argon gas.

At the time of transfer and drying, nearly all the hydrogen in the cladding will be in the form of circumferential hydrides [1]. The evacuation of the canister leads to a rise in cladding temperature due to residual decay heat in the fuel. Because evacuation removes convection as a means of heat transfer, it is physically possible for the decay heat to raise the cladding temperature above 450 ℃ [5]. This would cause a significant portion of hydrogen, about 300

wppm in Zircaloys, to dissolve back into solution [58]. Hydrogen dissolved upon heating is available to re-precipitate as radial hydrides upon subsequent cooling. The drying process also changes the internal stress state of the cladding, Figure 2.13.
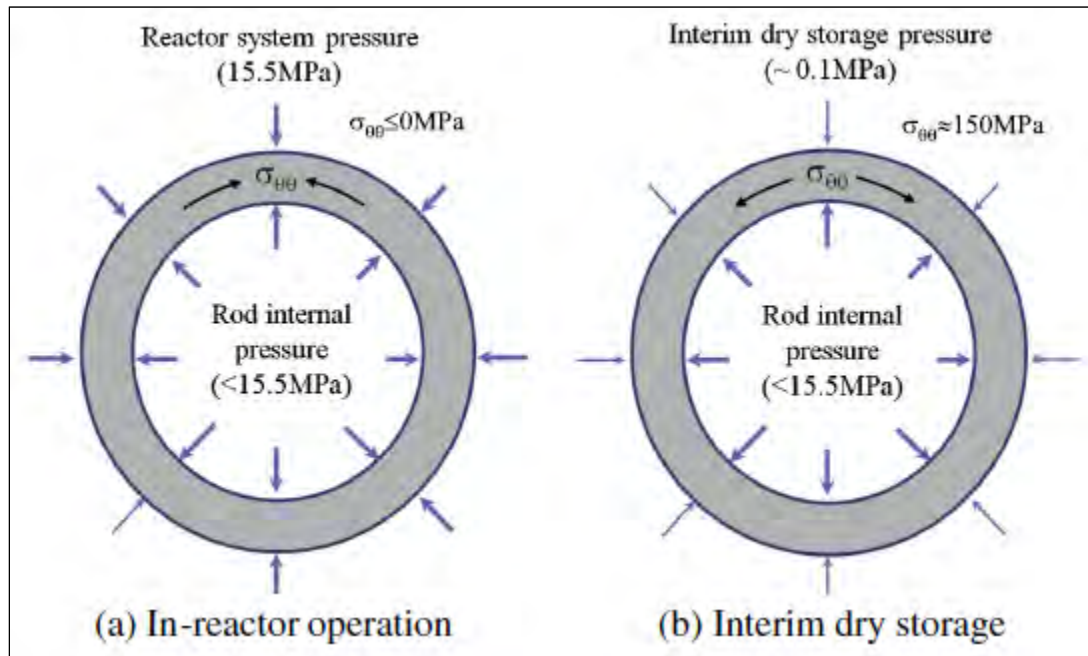

Fig 2.13 Change in cladding stress state from compressive to tensile hoop stress [59].

Figure 2.13 illustrates that, while in the reactor core and during wet storage, external pressure balances the internal pressure in the fuel rod, and the cladding retains its compressive hoop stress. When the canister is evacuated the internal rod pressure exerts a tensile hoop stress on the cladding. Upon cooling, hydrides precipitate such that the platelet normal is aligned parallel to the internal tensile stress as radial hydrides [16, 58, 59]. Thus re-precipitation during the drying process puts the cladding at significant risk of forming radial hydrides and suffering severe embrittlement. To reduce the potential for embrittlement, the Nuclear Regulatory Commission (NRC) has established a 400 °C limit on peak cladding temperature (PCT) at any point during storage or the drying process [5, 60],

2.8 Delayed Hydride Cracking

As noted above, used nuclear fuel cladding becomes embrittled by zirconium hydride formation. As the fuel assemblies are moved into dry storage, the drying process has the potential to cause hydride reorientation in response to internal stresses. As the fuel ages in storage, a further challenge arises as hydrogen may continue to migrate within the cladding and a phenomenon known as Delayed Hydride Cracking (DHC) becomes operative [2]. As a failure mode, DHC is a below yield strength failure due to stable crack growth through a hydride embrittled region. Delayed hydride cracking has been responsible for several failures of zirconium components within reactors, and is a further concern during interim dry storage [2, 61]. Figure 2.14 illustrates the DHC process.
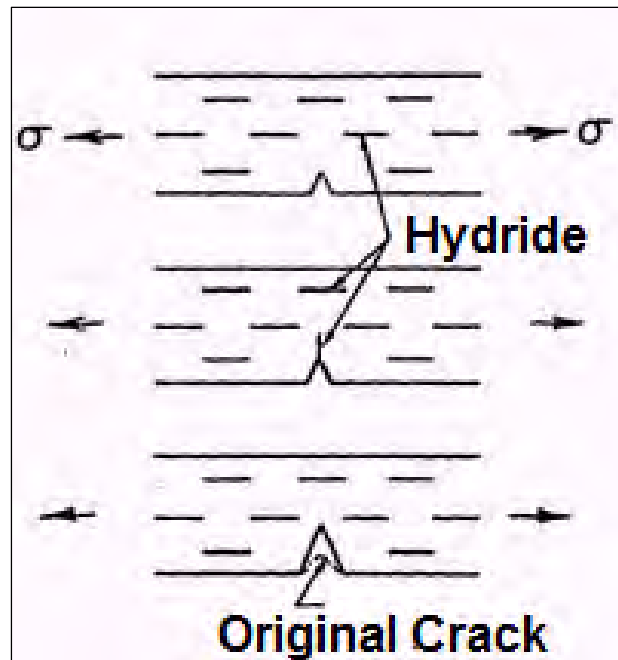
Fig 2.14 Illustration of the DHC process. Begins with a crack or flaw creating a region of high stress intesnsity (top). Brittle hydride precipitates at crack tip (middle). The hydride fractures and the crack grows through the embrittled region (bottom). [2]
Reproduced with permission of the IAEA.

2.8.1 Models of Delayed Hydride Cracking

There are two models for the thermodynamic basis of delayed hydride cracking (DHC). The older model, referred to by some, McRae *et al* [61], as the diffusion first model (DFM), was developed by Dutton and Puls in 1975 [62]. Over the years this model has been developed and refined by many authors as more accurate results were obtained for terms affecting the solvus, and other parameters important to modelling DHC [62].

More recently, a new model has been proposed by Kim *et al* [63-66]. This model is referred to in literature as Kim's Model, Kim's New Model, or as the precipitation first model (PFM) [61, 63, 65, 66]. The two models present a different physical basis for DHC and make different predictions about the process through which DHC is begun.

The DFM predicts that the difference in chemical potential for hydrogen, between the stressed and unstressed regions, will result in hydrogen diffusion to the high stress region, to restore the chemical potential to equilibrium. The diffusion of hydrogen to the stressed region raises the local hydrogen concentration at the crack tip until either chemical equilibrium or the precipitation solvus is reached. If the concentration reaches the precipitation solvus, hydrogen precipitates to form hydrides or grow on an existing crack tip hydride, eventually allowing the crack to grow through the embrittled region [61, 62]. A complete derivation of the DFM is given by Puls [39], and a discussion of the DFM with supporting experimental evidence is given by

McRae *et al* [61]. The DFM was also extended to cover the case of a thermal gradient by Sagat *et al*, [67].

In the precipitation first model (PFM), proposed by Kim [66], the stress state induces precipitation of hydrides at the crack tip, without raising the hydrogen concentration to the precipitation solvus at the test temperature or lowering the solvus itself [63]. The precipitation of hydrides at the crack tip leads to a lower concentration of hydrogen in solution at the crack tip. This concentration gradient provides the driving force for diffusion of hydrogen from the bulk leading to hydride growth and DHC [63]. It is suggested by Kim that dislocations, generated in the plastic zone of the crack tip assist the precipitation of hydrides, even though the precipitation solvus has not been reached [63]. Kim *et al* has proposed that a transformation from γ hydride, ZrH, to δ hydride, $ZrH_{1.66}$, may also play a role in creating the concentration gradient between the crack tip and the bulk [65].

These two differing models have been mentioned for completeness, the following description of delayed hydride cracking is given in terms of the diffusion first model, as this model is more prevalent in the literature regarding delayed hydride cracking [2, 61, 67-69].

2.8.2 Description of Delayed Hydride Cracking

Delayed hydride cracking (DHC) begins at an initial crack tip or defect [70]. The stress concentration at the crack tip lowers the chemical potential of hydrogen. The difference in chemical potential between the stressed and unstressed regions drives the diffusion of hydrogen to the crack tip [2, 61-64, 68, 70]. The hydrogen concentration increases at the crack tip, in the stressed region. Under a sufficient stress intensity, the driving force from the chemical potential difference is strong enough to for the hydrogen concentration to reach the precipitation solvus[2]. The precipitation of additional hydrogen, migrating from the bulk, embrittles the region of increased stress-concentration, resulting in fracture upon reaching a critical condition. The critical condition leading to fracture and crack growth is related to the length of the hydride and the applied stress intensity factor. This process is then repeated at the new crack tip [2].

Delayed hydride cracking is a threshold phenomenon, as mentioned above, in order for cracking to occur the stress intensity at the tip of the crack must exceed a threshold value [2, 68]. Once cracking has begun; however, the crack growth rate, or crack velocity, is nearly independent of the stress intensity factor at the crack tip, see Figure 2.15 below [2].
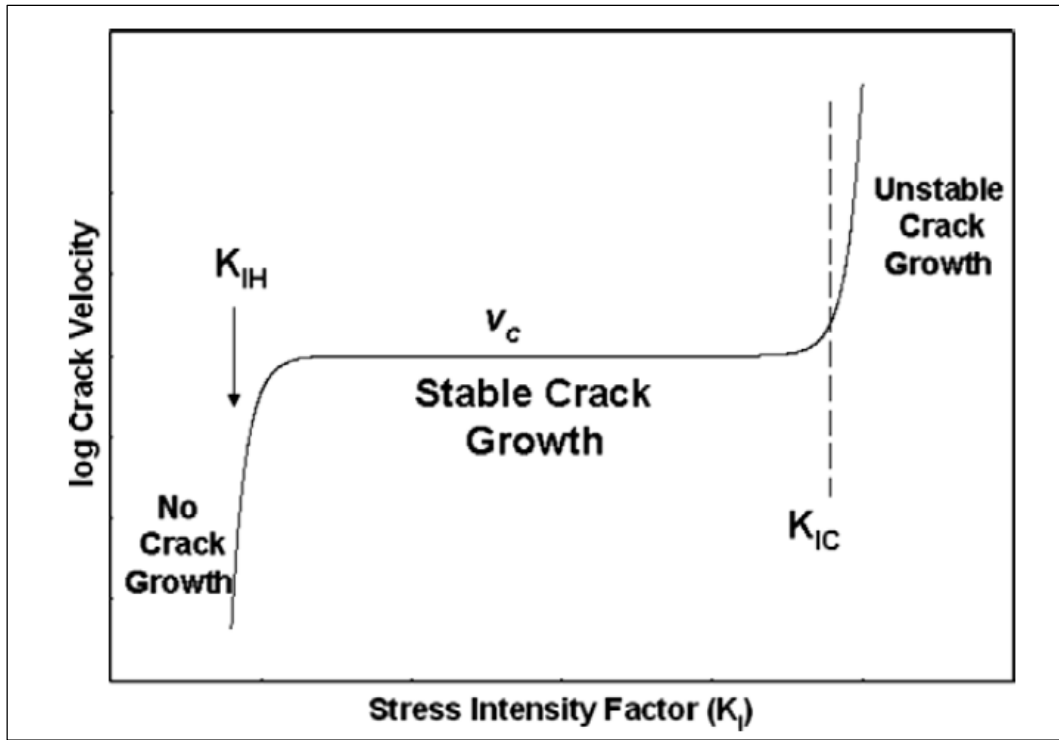
Fig. 2.15 DHC crack velocity dependence on stress intensity. (Fig 2.2 in [2]).

The stress intensity factor is a concept from fracture mechanics used to describe the stress state at a crack tip or flaw. In delayed hydride cracking, the stress is dependent on the solubility of hydrogen in the cladding, temperature, and the yields stress of the material [2, 70]. The embrittlement, caused by the precipitation of hydrides, allows the crack to grow by stages through the embrittled region until it is arrested in the Zr-matrix [2]. After each fracture the crack holds stable during what is termed 'the incubation time'. During the incubation time hydrogen diffuses to, and precipitates at, the new crack tip until the hydride reaches the critical length (estimated to be between 1.92 and 5.33 μm) and the fracture repeats [2, 3, 38]. The incubation time is controlled by the rate of hydrogen diffusion, from the bulk, to the crack tip. Equation (2.7) is an analytical equation for the average crack velocity during DHC [2].

$$V = G D_H C_H e^{\frac{V_H^h \Delta p}{RT}} \tag{2.7}$$

Where:
G is a geometric function that includes geometry factors as well as the molar   volumes of zirconium and zirconium hydride;
D_H is the diffusion coefficient of hydrogen in zirconium(a function of temperature);
C_H Is the solubility of hydrogen in zirconium in a stress free state;
V_H^h is the partial molar volume of hydrogen in zirconium;
Δp is the difference in hydrostatic tensile stress between the crack tip and the bulk at a distance equal to the characteristic hydride spacing away from the crack tip;
R is the gas constant;
T is the absolute temperature.

2.8.3 Influence of Terminal Solid Solubility

While hydrides provide the mechanism for crack propagation, delayed hydride cracking can occur even when no hydrides are present in the bulk [61]. This is because the hydrogen concentration only needs to locally exceed the solvus at the crack tip for hydrides to form there. Delayed hydride cracking is a complicated phenomenon with many dependencies, as detailed above. The dependencies on stress intensity, hydride length, hydrogen concentration, and temperature, are all influenced by the nature of the TSS of the hydrogen zirconium system [2, 38, 65, 70].

The hysteresis in TSS curves for precipitating and dissolving hydrides, described in section 2.2, is responsible for the sensitivity of DHC crack velocity to test temperature and direction of approach to test temperature; that is, whether the test temperature is approached by heating or cooling [2, 3, 38, 65]. Measurements of DHC crack velocity have shown that specimens tested at the same temperature will have different crack velocities if they differed in maximum temperature reached during the test [2].This relationship is shown in Figure 2.16.
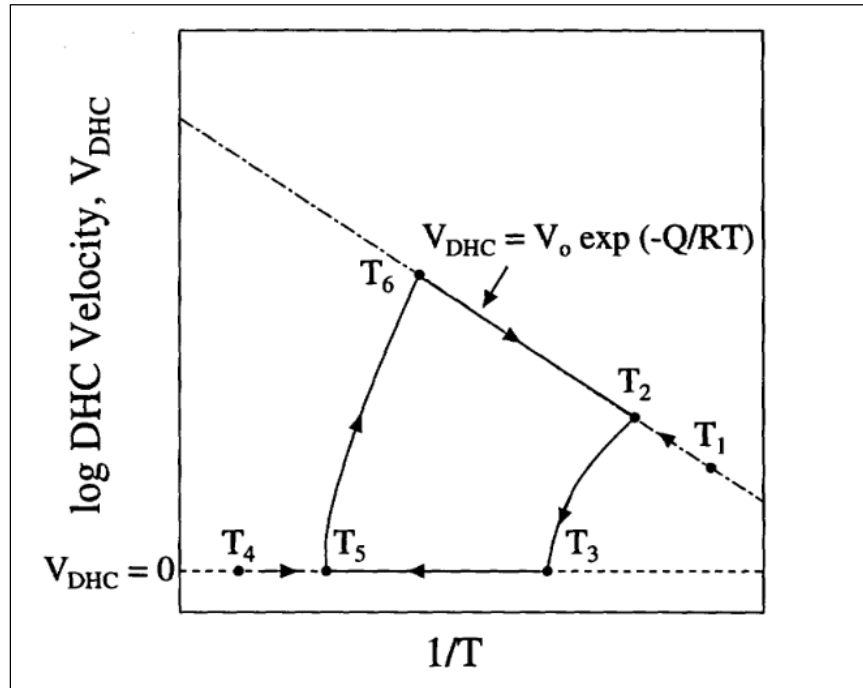
Fig 2.16 The sensitivity of DHC crack velocity to the thermal history [71]**.**

The highest crack velocities are measured, upon cooling, in the specimens with the most hydrogen in solution at the maximum temperature during testing. This is because the crack velocity depends on the amount of hydrogen available to diffuse to the crack tip, and concentration of hydrogen in solution is governed by TSS [2]. What Figure 2.16 shows, is that reaching the test temperature on heating (approaching test temperature from below) results in lower crack velocities than if the test temperature is reached upon cooling (approached from above) [2]. If the crack velocity is measured on heating at successively higher temperatures, then it follows T_1, T_2, T_3, T_4. After T_2 there is insufficient driving force to concentrate hydrogen at the

crack tip and precipitate or grow the hydride, so the cracking velocity goes to zero. If the test temperature is approached from above the crack velocity follows T_4, T_5, T_6, T_2. At T_4 all hydrogen is in solution, precipitation cannot occur the specimen is cooled to near the precipitation solvus. At T_5 the specimen is near enough to the precipitation solvus to precipitate hydrides at the crack tip, and the crack velocity becomes measureable. Cooling from T_4 to T_6 results in the highest crack velocity because the T_6 is very close to the precipitation solvus, increasing the driving force for hydrogen diffusion to the crack tip. At T_6 only a small increase in hydrogen content is required to precipitate hydride at the crack tip [2, 38, 61, 68, 69, 71]. Therefore, accurate knowledge of the TSS is necessary to preclude DHC from occurring under reactor operating conditions [8].

3.0 Experimentl

This section describes the materials, equipment, and procedures employed in the conduct of this research. The materials used for this study are described in section 3.1. Section 3.2 describes the cathodic charging system and the modifications made to it over the course of this study. Section 3.3 provides a detailed operating procedure for the cathodic charging system. The equipment and procedure for homogenizing hydrogen in charged specimens is given in section 3.4. Analytical methods used to characterize samples are described in 3.5.

3.1 Materials

Two zirconium alloys were selected for this study: Zircaloy-4 and HANA-4. Zircaloy-4 is a Zr-Sn alloy, and the industry standard cladding for PWR's [3]. Because of this, Zircaloy-4 has been extensively studied [14, 15, 20, 21, 44, 52, 72]. HANA-4 is a newer cladding alloy being developed by the Korean Atomic Energy Research Institute (KAERI) for high burnup fuel applications [7, 56, 73-75]. The designation, HANA, stands for' High-performance Alloy for Nuclear Applications'. HANA-4 is one of six HANA alloys [7, 56, 73]. Unlike the Zircaloys, HANA-4 is Zr-Nb alloy, with small amounts of tin, iron, and chromium. The respective compositions of Zircaloy-4 and HANA-4 are given in Table 3.1.

Table 3.1   Major Alloying Elements of Zircaloy-4 and HANA-4 in wt%.

Alloy	HANA-4		Zircaloy-4	
	Reference[7]	Measured	Reference[15]	Measured
Cr	0.1	0.06	0.07 - 0.13	0.07
Fe	0.1 - 0.2	0.12	0.18 - 0.24	0.12
Nb	1.5	1.47		
Sn	0.4	0.35	1.2 – 1.7	1.32
O	Not Reported	0.10	0.09 – 0.16	0.13
H	~ 7 wppm	0.001	> 0.003	0.001

Measurements of alloy composition performed by IMR Test Labs, 131 Woodsedge Dr. Lansing, NY. 14882.

The measurements of alloy composition were performed by IMR test labs. The composition was measured by a combination of the following techniques: combustion-infrared absorbance, inert gas fusion-thermal conductivity, and inert gas fusion-infrared absorbance..

The Zircaloy-4 sheet material was procured as part of the larger research program[1]. A strip was cut from the sheet, and this strip was used to fabricate specimens to be charged with hydrogen and undergo post charging analysis. An illustration of the sample size and geometry is given in Figure 3.1. Measurements were made with a high precision caliper and averaged as a normal distribution to obtain uncertainties.

Fig. 3.1 Zircaloy-4 Material: (Left) Dimensions. (Right) Post Charging.

The HANA-4 material was also provided by a member of the larger research program[2] and was received as 30 cm long cladding tubes. The tube dimensions were measured with a high precision caliper and statistically averaged as before. The inner diameter was measured to be 8.20 ± 0.06 mm, and the outer diameter as 9.53 ± 0.01 mm; with wall thickness of 0.62 mm. Examples of as received and post charging HANA-4 are shown in Figure 3.2.
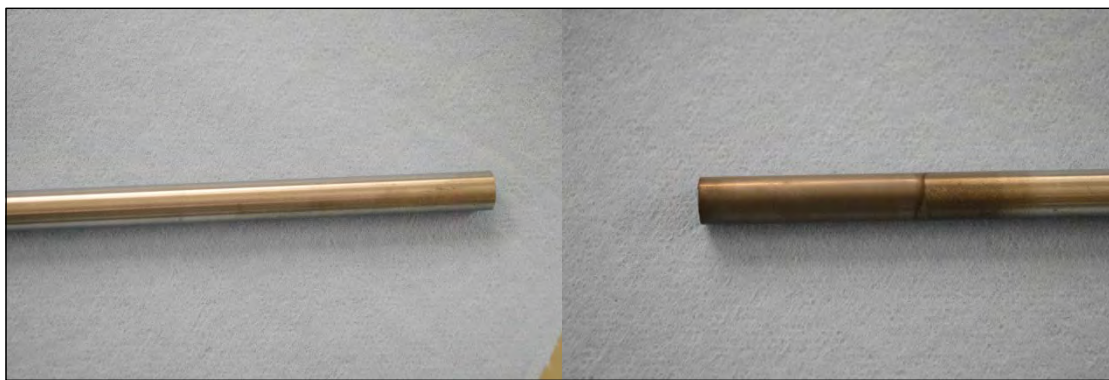
Fig. 3.2 HANA-4 Material: (Left) As Received. (Right) Post Charging 680 $A \cdot h$.

---

[1] Purchased by Dr. Yong Yang at the University of Florida.
[2] Received from KAERI through Dr. K.L. Murty at North Carolina State University.

The geometric difference in the form of the as received alloys proved to have a significant impact on attempts at comparison. The solid cross section of the Zircaloy-4 samples resulted in a lower surface area per gram of material. Therefore, hydride rims of a similar thickness correspond to a much lower bulk hydrogen concentration in the Zircaoly-4 specimens as compared to those in HANA-4. The geometric difference impacted the electric potentials (Figure3.3) during charging and the Zircaloy-4 annealing times, as these samples had a longer diffusion path to reach homogenization than the HANA-4 samples.
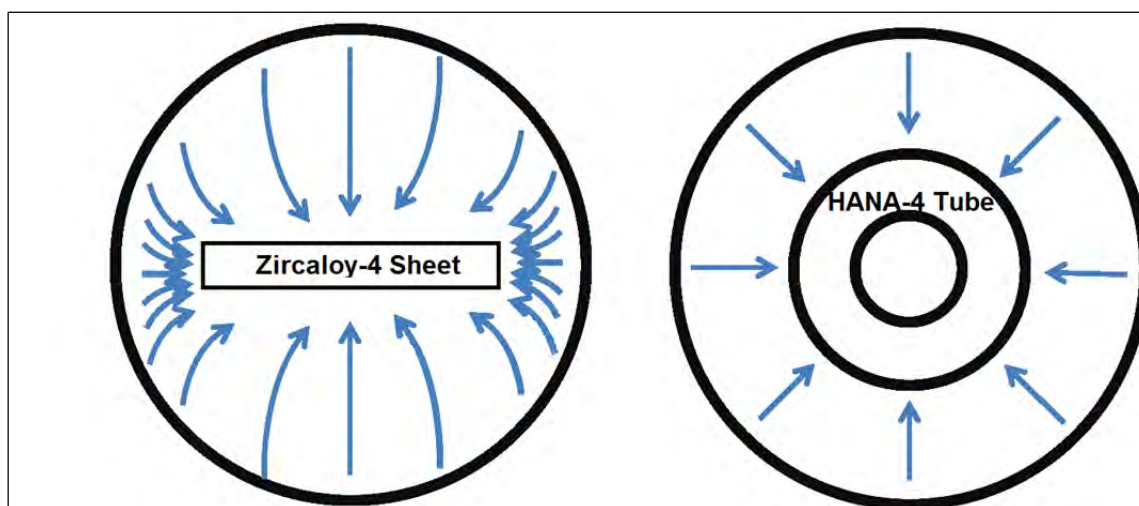
Fig 3.3 Illustration of differences in electric field strength during charging. [76]

Figure 3.3 illustrates the differences between the Zircaloy-4 sheets and HANA-4 tubes during charging. Specimens were prepared for charging by pickling for 3 minutes in a solution comprised of 50 % H_2O, 45 % HNO_3 and 5 % HF; percentages are by volume. The pickling solution and procedure was taken from Berry *et al* [77]. Pickling was chosen over mechanically cleaning, with 1200 grit emery paper, as suggested by Lepage *et al* [40], because pickled samples have been reported to have a hydriding rate two to four times higher than samples cleaned by grinding [2].

3.2 Cathodic Charging

A number of system configurations were tested based on literature sources by this author. The first design employed in this study was developed by Kuhr [78], and that system was based on work by John *et al*, [47] and Choi, [72].

Electron microscopy and x-ray mapping were employed to assess the effectiveness of this system. Early results showed that the system was not inserting enough hydrogen into the samples to form a visible surface hydride layer; at magnifications up to 2000X. This led to the further modification of this system; which was heavily influenced by Lepage *et al* [40] and Hindle and Slattery[46]. The original system and that used for the principle experiments in this research are described in the following sections.
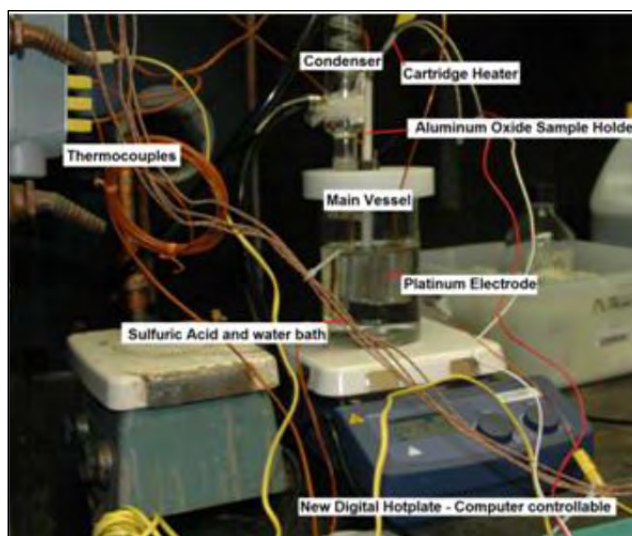
3.2.1 Initial Cathodic Charging System

The electrochemical hydrogen charging system, developed by Kuhr [78] consisted of a: pyrex reaction vessel, platinum mesh electrode, alumina (Al_2O_3) sample holder, hotplate (with a magnetic stirrer), 10 volt DC power supply, four K-type thermocouples, and an automated data recording system. Figure 3.4. A list of model numbers for commercial components is given in Table 3.2.

Table 3.2Components of the Cathodic Charging System

Power Supply	TDK-Lambda ZUP 10-80
Hot Plate	SCILOGEX MS7-H550-Pro 7x7
DAQ	Omega OM-USB-TC-AI DAQ

Fig 3.4 Initial cathodic charging system (ECH-TG System), designed by Kuhr [78]

This setup allowed a cartridge heater to be inserted into the alumina sample holder. This was part of the original work by Kuhr [78], the cartridge heater was not utilized in any experiments in this work. In later experiments by Kuhr [78], an aluminum sleeve was placed between the sample holder and the zirconium alloy sample.

The thermocouples were placed to measure the hotplate, solution, and condenser inlet and outlet temperatures. The four temperature signals and the voltage and current signals from the power supply were recorded by an Omega OM-USB-TC-AI DAQ. The operating parameters and system components were modified due to repeated failure to achieve the desired result.

3.2.2 Final Cathodic Charging System

Initial modifications to the system focused on reducing components in the reaction vessel. The aluminum sleeve, between the sample and sample holder, was removed before the first experiment in this work. Further changes were introduced after several unsuccessful attempts at hydrogen charging. The final configuration of the hydrogen charging system, Figure 3.5, designated the low-temperature cathodic-charging system (LCS), is shown below.
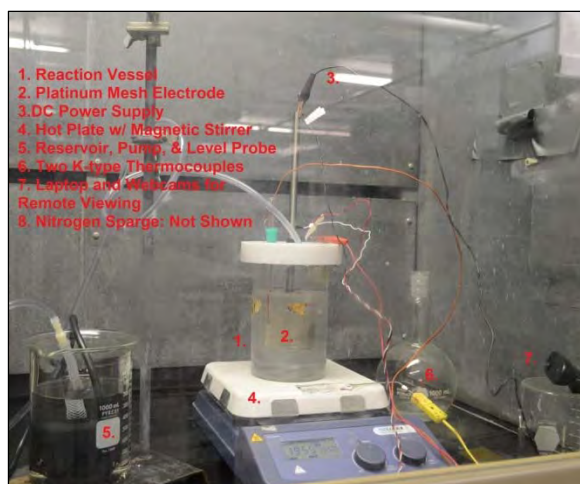
Fig. 3.5 Low Temperature Cathodic Charging System.

As shown above, the LCS retained the reaction vessel, platinum mesh electrode, hot plate, and power supply. The other components were replaced or removed. The condenser was replaced with a makeup water supply system, after the system was moved to a fume hood without the necessary plumbing for it. The condenser thermocouples were removed with the condenser, leaving only two thermocouples, which were used to monitor the solution and hot plate temperatures during electrolysis. The aluminum oxide sample holder was removed as a potential barrier to hydrogen insertion. It was also incompatible with the HANA-4 and Zircaloy-4 geometries. A nitrogen gas sparge was added to remove excess oxygen from the solution, prior to electrolysis. The automated data acquisition system was abandoned after the DAQ malfunctioned. Instead, temperatures and voltages were recorded manually.

The makeup water supply system created for this work consisted of a reservoir, pump, and a solid state relay connected to a probe. The relay controlled the pump, turning it on when the probe lost contact with the solution and turning it off when contact was restored. A schematic of the pump controller is provided in Appendix E.

With the removal of the aluminum oxide sample holder it was necessary to modify the connection between the sample and the power supply. Examples of the connection methods used are shown in Figure 3.6.
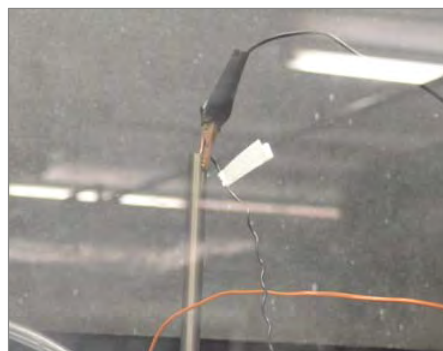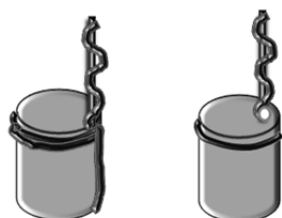
Fig. 3.6 Methods of connecting samples to the power supply.

Initially, the connection between the sample and power supply was established by wrapping a zirconium wire around the specimen to be charged. Pliers were used to twist the zirconium wire, in an attempt to pull it tight against the sample surface. This is illustrated on the far left in Figure 3.6. An effort was made to improve the connection by drilling a hole in the sample tube and passing the wire through before wrapping, illustrated in the middle of Figure 3.6. This proved to be more effective than the first method; however, the absence of the sample holder made it difficult to center the sample within the platinum anode. Both issues were resolved in the final connection method, show at right of Figure 3.6. By using a longer section of sample, the power supply was able to be connected, via an alligator clip, directly to the sample. The sample was held at the desired height inside the reaction vessel by a Viton stopper in the Teflon lid. This enabled good electrical contact between the sample and the power supply, while allowing easy adjustment of the position of the sample with respect to the platinum anode. This method was only used during the charging of the HANA-4 and Zircaloy-4 samples.

The nitrogen sparge was constructed from a piece of stainless steel tubing, closed at one end, with holes drilled in the lower portion of the tube (see Figure 3.7).

Fig. 3.7 Nitrogen sparge.

It was introduced to minimize oxygen contamination of charged samples. Analysis via x-ray mapping of a rim structure on the outer surface of a sample revealed elevated oxygen content in the rim. The presence of oxygen made the nature of the observed structure uncertain. It was suggested by personnel at Savannah River National Laboratory (SRNL) that bubbling nitrogen through the solution before electrolysis may remove excess oxygen from the electrolyte

solution. The nitrogen sparge was used for 30 – 60 minutes prior to placing the sample in the electrolyte.

3.3 Operating Conditions

The original operating conditions followed those used by Kuhr [78]. The system employed 50 wt% sulfuric acid (H_2SO_4), as the electrolyte, and the solution temperature was set between $85 - 120$ ℃. The current density was fixed at $0.5 \frac{A}{cm^2}$. Charging times were between 6 – 25 hrs, 20 – 79 A-hrs.

After EAN-7 operating conditions were changed to follow those reported by Lepage *et al* [40]. A 0.2 M sulfuric acid (H_2SO_4) electrolyte, solution temperature 65±5 °C, and current density $0.2 \frac{A}{cm^2}$. Eventually, charging times were increased to greater than 95 hrs, ranging from 95 – 219 hrs, 325 – 680 A-hrs.

Due to some ambiguity regarding what surface area to use for current density calculations, actual current densities varied. For tube specimens, the surface area used was the active surface. Early tests showed hydride formation on both the inner and outer surfaces of tubes, and so the surface area calculations included both surfaces. With the change in connection methods, utilizing the longer tube sections for HANA-4, charging only affected the outer surface. As only the outer surface area was active during charging, in this configuration, the current density was effectively doubled on the active surface. This was discovered post charging, thus the HANA-4 samples were created with an effective current density that was roughly twice the targeted current density. This necessitated an increase in the target current density for the final Zircaloy-4 sample, in order to maintain consistency in charging parameters between HZrH-2 and Zr4H-3.

3.3.1 Cathodic Charging Procedure

System Preparation:
1. Anode Preparation:
   a. Different anodes may be used, preparation may vary.
      i. If using a platinum, Pt, anode, clean the anode by rinsing with ethanol in a sonic bath for 5 minutes, followed by 10 minutes with distilled water in a heated sonic bath.
      ii. If using a lead, Pb, anode; clean Anode surface by removing the surface layer with sand paper or an abrasive flap wheel on a hand drill. (This must be done in the fume hood.)
2. Electronics:
   a. Turn on power supply and hot plate/magnetic-stirrer.
      i. For 65 °C, set the hot plate temperature to 200 °C.
      ii. Temperature may need slight adjustment based on current.
   b. Open Stirrer software, the short cut is named "Stirrer Software" and select the appropriate com port, currently com port 4.
      i. Open remote viewing software, currently TeamViewer 9.0.
3. Nitrogen Tank:

a. Fill an appropriately sized container with water. Place nitrogen sparge in the container. Ensure all valves on the nitrogen system are closed. Open the main valve (Tank Valve). Then carefully open the regulator valve. When desired nitrogen flow is achieved, close the main valve. The regulator is now set to a safe operating pressure.

4. Electrolyte Solution:
   a. This procedure requires a 0.1-0.2 Molar solution of H_2SO_4. This is achieved by mixing distilled water with concentrated H_2SO_4.
   b. Before mixing, know the concentration of the H_2SO_4 and how to mix a 0.2 Molar solution.
      i. If using 1.0 molar (Equivalent to 2.00 Normality) then the ratio of water to acid is 8 ml H_2O to 2 ml H_2SO_4.
   c. Typically, 600 ml of electrolyte is used.
   d. To mix H_2O and H_2SO_4, pour the required amount of H_2O into the reaction vessel. Next, carefully and slowly add the required amount of H_2SO_4 to the reaction vessel. (The mixing of H_2O and H_2SO_4 is very exothermic.)
   e. Once electrolyte is mixed, insert the nitrogen sparge for $30 - 60$ min.
   f. While nitrogen sparge is running, calculate current needed to achieve desired current density over sample surface.
      i. $\rho = \dfrac{I}{S_{A_{eff}}}$, where $\rho =$ Current Density, $I =$ Current, and $S_{A_{eff}} =$ Effective Surface Area of the Sample.

5. Setting up the Anode:
   a. Turn off and remove nitrogen sparge at this point.
      i. Remove the sparge and place it in a beaker of distilled water.
      ii. Turn on the sparge to clean any fluids out of the line.
      iii. Turn off, dry and store sparge.
   b. If using Platinum
      i. Pass the wire on the Pt anode through the appropriate hole in the lid of the reaction vessel.
      ii. Set position of anode relative to sample.
   c. If using Lead.
      i. The Pb anode, typically $2 - 4$ strips of Pb, are placed around the reaction vessel according the marks around its rim.
      ii. Connect the anode strips together, in series, with alligator clips.
   d. Connect anode wire from power supply to the anode.

6. Final Check:
   a. With anodes in place, check that all thermocouples are appropriately positioned.

Sample Preparation:
1. Attach Cathode to Power Supply:
   a. On small samples, this should be done with zirconium wire by spot welding or drilling and tapping with screws to connect the wire to the sample. For a large section, wait till step 4.
2. Cleaning:
   a. Chemical:

       i.   Carefully mix 5 ml of HF, 45 ml HNO$_3$, and 50 ml H$_2$O in an appropriate plastic container.[3]

      ii. Place sample in solution and wait 3 minutes.

     iii. Remove sample from solution and place in water to quench pickling process.

  b. Manual

       i.   Clean sample by removing surface oxide layer with sand paper. Be sure not to heat up sample while removing surface layer, as an increased temperature increases the oxidation rate.

3. Sample is now clean, be careful not to touch or otherwise contaminate sample. Place sample in solution as soon as possible.

4. Once sample is in solution, attach the cathode wire to the power supply.

Run the System by engaging the power supply.

3.4 Homogenization Procedure

Homogenization was carried out in an inert argon atmosphere. Large samples were annealed in a tube heater, contained in an argon atmosphere glove box. Samples to be characterized by DSC were homogenized in a flowing argon environment with a Netzsch STA 409 simultaneous thermal analysis unit. Homogenization times were calculated from $Eq.(3.1)$ provided in Lepage *et al* [40], using hydrogen diffusion data from Kearns [51] $Eq(3.2)$. Equation (3.1) is the solution to the diffusion problem of hydrogen through a plate, of thickness $2L$, with hydride on both surfaces. The solution represented by $Eq.(3.1)$ corresponds to a mid-plane concentration that is 97% of the TSS$_d$ [40].

$$t = 1.5\frac{L^2}{D} \tag{3.1}$$

$t = Diffusion\ time\ (s)$
$2L = Thickness\ of\ the\ plate\ (cm)$
$D = Diffusion\ Coefficient\ \left(\frac{cm^2}{s}\right)$

The diffusion coefficient used in $Eq.(3.2)$ is the average diffusion coefficient, reported by Kearns [51], for zirconium, Zircaloy-2, and Zircaloy-4. This coefficient was also used for diffusion calculations in HANA-4; diffusion data for HANA-4 was not available.

$$D = D_0 e^{-\frac{Q}{RT}} \tag{3.2}$$

$D = 7.00 \times 10^{-3} \left(\frac{cm^2}{s}\right)$
$Q = 10650 \left(\frac{cal}{mol}\right)$
$R = 1.987 \left(\frac{cal}{mol \cdot K}\right)$
$T = Temperature\ (K)$

Samples were annealed four to eight times longer than the calculated homogenization times, in order to assure that the desired homogenization conditions were achieved.

---

[3] HF will dissolve glass/pyrex containers.

3.5 Characterization Methods

3.5.1 Electron Microscopy: Sample Preparation

The effects of cathodic charging, and subsequent heat treatments, were checked by imaging sections of the treated samples. A combination of back scattered electron (BSE) and secondary electron (SE) microscopy was used for metallographic examination. Optical microscopy was limited to examination of samples during polishing prior to electron imaging.

Electron imaging, BSE/SE, was performed using the CAMECA SX50 electron microprobe in the Department of Geology and Geophysics, at Texas A&M University. This instrument was capable of analysis via x-ray mapping for elements above atomic number 12. Analysis via X-ray mapping led to the discovery of oxide formation on some early samples; which led to the changes in the system described in §3.2.2 Optical imaging was performed using a Hirox KH-1300 digital microscope.

The preparation of samples for metallographic analysis proceeded as follows. Charged Specimens were sectioned, mounted in epoxy, and mechanically polished. Some samples were chemically etched, particularly the annealed samples; as etching reveals the hydrides during imaging. Samples that were examined by electron microscopy required the application of a carbon coating, via sputtering, prior to imaging.

Samples were sectioned with a LECO VC-50 diamond saw, and mounted in a cold set epoxy. Once cut and mounted in epoxy, the sample is ground with silicon-carbide paper through a progression of finer grit [79]. The procedure varied over the project, in an attempt to attain a cleaner polish. However, it nominally consisted of a progression from: 180, 240, 320, 400, 600, and 800 to 1200 grit silicon carbide papers; on the CAMI scale. Each grinding step should take less than 5 minutes [76]. Grinding was followed with rough polishing, using a 3μm diamond suspension on a micro-cloth. The final polish was applied with a 1 μm diamond suspension. It is unnecessary to proceed to a finer polish, as the chemical etching leaves a surface roughness that is on the 1200 scale. Some researchers do not polish beyond 1200 for this reason [80].

The etchant used to prepare samples for metallographic examination was taken from Raynaud [81] and Colas *et al* [53, 80]. The etchant consists of 10 parts H_2O, 10 parts HNO_3, and 1 part HF. The sample is swab etched for 5 seconds, then submerged for 10 seconds. The sample is them removed and immediately washed with cool water.

Measurements of rim thickness were made by recording the length of lines drawn perpendicular to the surface with MS Paint. The average length was determined and multiplied by a conversion factor from pixels to μm, derived from the length of the scale bar.

3.5.2 X-ray Diffraction

Further analysis of as received, post charging, and post annealing material was carried out, via X-ray diffraction (XRD). The system used was a Rigaku Geigerflex Powder X-ray Diffractometer, located in the Department of Geology and Geophysics at Texas A&M University. The X-ray analysis employed CuKα X-rays. The X-ray beam section is

approximately 1 cm^2 and 90% of the diffracted intensity comes from a layer 2–11 μm under a solid flat surface, depending on 2θ.

3.5.3 Differential Scanning Calorimetry

Hydride dissolution measurements were performed via DSC with two different thermal analysis units; the results were inconclusive and often dissolution was not observed, as reported in §4.4. The first instrument, was a Netzsch STA 409, and the second, was a TA SDT Q600. Both systems are of the heat flux design and both simultaneously carry out DSC and TGA (thermogravimetric analysis) measurements.

A heat flux DSC uses a single furnace. The sample and the reference are maintained in thermal contact, and the respective temperatures and heat flow between them are measured. In a heat flux system, during an exothermic event, the sample temperature is higher than the reference. The sample temperature is being measured against the reference, thus exothermic events result in an increase in sample temperature over the reference and positive difference between the sample and reference temperatures. Thus exothermic events are naturally plotted as positive peaks on a heat flux DSC; though the direction may be changed if the operator desires.

3.5.4 DSC Measurement of the Hydride Dissolution Temperature

When the terminal solid solubility for dissolution (TSS$_d$) for an alloy is known, specimens of known concentration may be prepared through the following procedure. First, the alloy specimen is cathodically charged until the hydride rim is thick enough to supply the desired hydrogen concentration, after subsequent annealing. The specimen is then annealed at a temperature corresponding to that concentration; taken from TSS$_d$. Any excess hydrogen, in the rim, is removed by dry grinding with 600 grit paper; after the homogenization step [23, 29, 40]. When the TSS$_d$ is unknown, it can be determined by preparing several samples in the same manner, with a range of homogenization temperatures. The temperatures are selected over the range for which TSS$_d$ is to be measured. Once the samples are prepared, the hydride dissolution temperature (HDT) and corresponding hydrogen contents are measured [8, 20, 23, 24]. Plotting hydrogen concentration (C$_H$) against HDT, as log C$_H$ vs inverse temperature (1/T), linear regression may be used to determine a best fit for the TSS$_d$ curve [18, 20, 33, 34]. Thus, measuring HDT for HANA-4 and Zircaloy-4, is the first step toward determining TSS for these alloys.

3.5.5 Homogenization for DSC Measurements

Three temperatures, 350 °C, 450 °C, and 540 °C were selected, at which specimens of both alloys would be homogenized. Temperature selection was governed by the desire to study specimens with hydrogen concentrations between 300 and 800 wppm, as this matches the hydrogen content of cladding from high burnup spent nuclear fuel (SNF) [5]. Table 3.3 lists the diffusion parameters, calculated, and actual annealing times used to create samples for hydride dissolution temperature (HDT) measurement.

Table 3.3   Diffusion Parameters and Annealing Times

Sample	T_{Target} °C	$T_{Meas.}$ °C	D cm^2/s	L (cm)	t_c (min)	t (min)
HTSS-1	540	533	9.59×10^{-6}	0.062	15	240
HTSS-2	450	442	4.22×10^{-6}	0.062	25	250
HTSS-3	350	346	1.28×10^{-7}	0.062	75	375
ZTSS-6	540	530	9.59×10^{-6}	0.024	1.5	60
ZTSS-7	450	438	4.22×10^{-6}	0.024	3.4	60
ZTSS-3	350	345	1.28×10^{-7}	0.162	510	2040

After homogenization the specimens are subjected to an appropriate temperature profile in a DSC to measure the HDT. Details of the DSC measurements are given in Chapter 4. Sections for HDT measurements were cut from charged and uncharged specimens of both alloys. Measurements in HANA-4 were given the identification key HTSS, and those in Zircaloy-4 ZTSS.

The sections were cut to fit into the sample cups of the Netzsch STA 409 unit which have a 6 mm diameter. For the HANA-4 alloy, sections were cut from a thin ring of tubing. The Zircaloy-4 sections were cut so as to provide sufficient hydrogen concentration for comparison with the HANA-4 samples.

The samples were sectioned using the diamond saw. Sections of HANA-4 were then straightened, by hammering, to remove curvature. This allowed better contact between the specimen and the STA 409 sample cup. It also aided the uniform removal of residual surface hydride, after homogenization by annealing. The Zircaloy-4 sections were cut in two manners; illustrated in Figure 3.10.
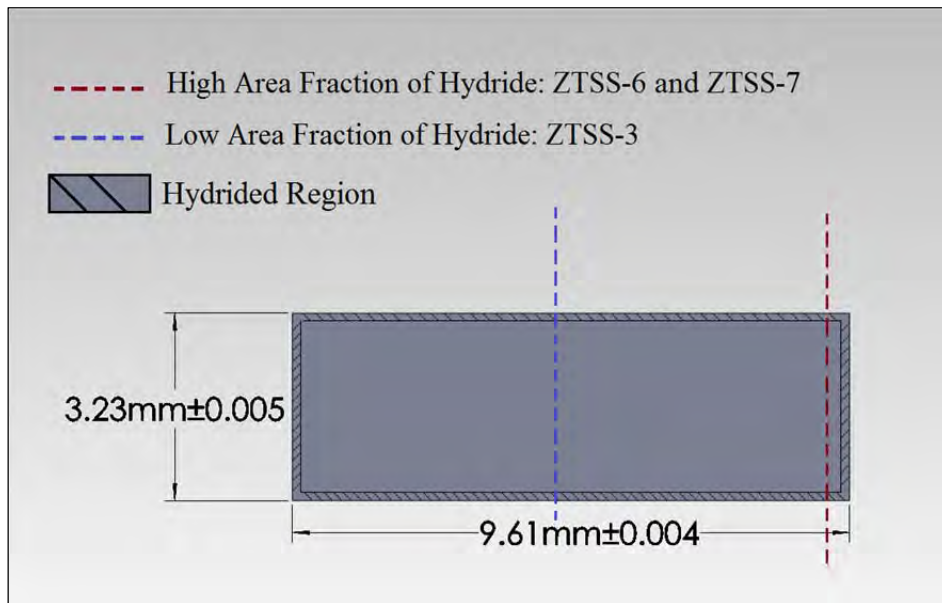
Fig. 3.10 Methods of Sectioning Zircaloy-4 for TSS measurements.

Specimen ZTSS-3 was cut from the end of Zr4H-3, cross section shown in Figure 3.10. The blue line in Figure 3.10 shows roughly where ZTSS-3 was cut, to enable it to fit into the DSC sample cups. This method of sectioning limited the potential bulk concentration of the sample to less than the estimated 170 wppm; because, hydride was only present on three of the outer surfaces. This method of cutting has a higher volume fraction of bulk zirconium. However, it was noted that the potential bulk hydrogen in a thin section depends on the thickness (volume fraction) of the hydride rim and the thickness of the specimen. (See *Eq.* (2.3)). The hydride thickness is fixed, post charging. Therefore, in order for a sample to have a higher bulk concentration, the volume fraction of the zirconium must be reduced. Specimens ZTSS-6 and ZTSS-7 were cut down the red line, taking advantage of the observation above. This created a plate with hydride on one side, and by controlling the thickness of the plate the potential bulk concentration was increased to an estimated 860 wppm.

3.5.6 Operating Conditions Netzsch 409 STA

Prior to performing measurements, the Netzsch STA 409 was calibrated for temperature and enthalpy. The calibration was performed using the melting points of six metal standards: indium, tin, bismuth, zinc, aluminum, silver, and gold. The calibration procedure followed the Netzsch Calibration Manual. Prior to calibration, it was necessary to select the operating conditions that would be used during the sample measurements. The purge flow and protective flow rates were selected to match those suggested in the Netzsch operations manual. Vizcaino *et al* [20] reported that heating rates, 5-30° K/min, had negligible impact on the system. However, it was also noted that an increased heating rate, improved signal definition [20, 24]. The choice of heating/cooling rate attempted to balance the sensitivity of the measurement with hydride precipitation kinetics. Therefore, 10 K/min was chosen as the heating/cooling rate. As noted in §2.1, a cooling rate greater than 10 K/min changes the primary hydride precipitate from δ to γ hydride [18, 29, 35]. As δ hydride is the primary hydride phase found in SNF, it was desirable to retain it as the primary phase in the samples [5, 26]. However, other studies have reported heating and cooling rates greater than 10 K/min [20, 23].

The operating conditions used with Netzsch, during annealing and HTD measurements, are given in Table 3.4. Each sample was measured once. Upon completion of this first test series, ZTSS-3 was measured again, with variable heating and cooling rates. Parameters for the HDT measurements with the Netzsch 409 are given in Table 3.5.

Table 3.4   Netzsch 409 STA Operating Conditions

Sample	$\dot{T}$ K/min	Purge Flow	Protective Flow	Gas
HTSS-1-3 ZTSS-6,7, and 3	10	20 mL/min	10 mL/min	UHP-Ar
ZTSS-3 Mk. II	30, 20, 10	20 mL/min	10 mL/min	UHP-Ar

Table 3.5   HDT Measurement Parameters for Netzsch 409

Sample	Mass mg	T_{set} °C	T_{max} °C	T_{anneal} °C	No. Cycles	Reference
HTSS-1	31.9	565	546	533	6	Empty
HTSS-2	29.6	550	532	442	4	Empty
HTSS-3	32.6	550	531	346	4	Empty
ZTSS-6	7.3	565	544	530	4	Empty
ZTSS-7	9.2	500	484	438	4	H free Zircaloy-4
ZTSS-3	38.2	400	401	345	4	Empty
ZTSS-3-Mk II	38.2	400	392	----	6	Empty

3.5.7 Operating Conditions TA SDT Q600

The second series of hydride dissolution temperature (HDT) measurements was performed with a TA Q600 DSC/TGA, at Texas A&M University's Materials Development and Characterization Center (MDC^2). The calibration and operation of the unit was handled by the MDC^2 staff[4]. The heating and cooling rate for these measurements was changed to 20 K/min; following the recommendation of Vizcaino *et al* [20], who reported that the dissolution peak was not observed at 5 °K/min, and was not well defined at 10 K /min. Vizcaino *et al* reported that 20 K/min resulted in a well-defined dissolution peak. The measurement conditions used with the TA Q600 are given in Table 3.6. These measurements utilized the same samples as the measurements performed with the Netzsch unit. To distinguish between measurements on the different instruments the suffix Q added to sample designations after measurement with the TA Q600.

Table 3.6   HDT Measurement Parameters for TA Q600

Sample	Mass* mg	$T_{Meas.}$ °C	$\dot{T}$ °C/min	No. Cycles	Reference
HTSS-1Q	330.458	545	20	3	Empty
HTSS-2Q	334.851	480	20	3	Empty
HTSS-3Q	331.774	380	20	3	Empty
HTSS-0Q	353.426	480	20	3	Empty
ZTSS-6Q	325.844	545	20	3	Empty
ZTSS-7Q	322.772	480	20	3	Empty
ZTSS-3Q	327.426	380	20	3	Empty
ZTSS-0Q	323.717	480	20	3	Empty

*Mass includes mass of sample cup

---

[4] Dr. Anup K. Bandyopadhyay

4.0 Experimental Results

Table 4.1   Charging Parameters and Results for all Samples

Experiment	Electrolyte		Current Density	Run Time	Hydride	H
Sample	Temp.	Concentration	$\frac{A}{cm^2}$	$A \cdot h$	μm	$wppm$
EAN-S	120 °C	50 wt % H_2SO_4	0.5	20.10		
EAN-1	120 °C	50 wt % H_2SO_4	0.5	26.43		
EAN-2	120 °C	50 wt % H_2SO_4	0.52	33.60		
EAN-3	120 °C	50 wt % H_2SO_4	0.487	17.46		
EAN-4	120 °C	50 wt % H_2SO_4	0.5	75.20		
EAN-5	85 °C	50 wt % H_2SO_4	0.508	72.94		26**
EAN-6	90 °C	50 wt % H_2SO_4	N/A	*		0
EAN-7	90 °C	50 wt % H_2SO_4	N/A	*		0
EAN-8	65 °C	0.2 M	0.21	79.31		81**
LAE-1	65 °C	0.16 M	0.096	6.49	3.1 ± 0.7	58
LAE-2	65 °C	0.16 M	0.195	8.03	5.8 ± 0.7	109
EAN-9	75-80 °C	0.16 M	0.200	326.80	17	326
ZrH-1	75-80 °C	0.2 M	0.240	340.21	6.3 outer 8.1 inner	270
ZrH-2	75-80 °C	0.2 M	0.240	575.47		0
HZrH-1	65-71 °C	0.2 M	0.387***	342.00	33.8 ± 1.8	754
HZrH-2	65-69 °C	0.2 M	0.387***	679.98	51.2 ± 1.0	1227
Zr4H-1	63-68 °C	0.2 M	0.266	344.72	19.3 ± 1.2	82-110
Zr4H-2	63-68 °C	0.2 M	0.266	>584.4	12.3 ± 0.3	53
Zr4H-3	63-69 °C	0.2 M	0.37	680.21	14.9 ± 1.2	64-85

* Potentiostatic Tests.
** Hydrogen Concentrations Measured at UIUC.
*** The target current density was 0.2 $\frac{A}{cm^2}$.

4.1 Charging System Definition

The first six samples charged in this configuration were EAN-S through EAN-5. The designation EAN stands for, Electrolysis-Acid-No Thermal Gradient. Post charging analysis on these samples showed no indication of a hydride layer being deposited on the sample surface (Figure 4.1).
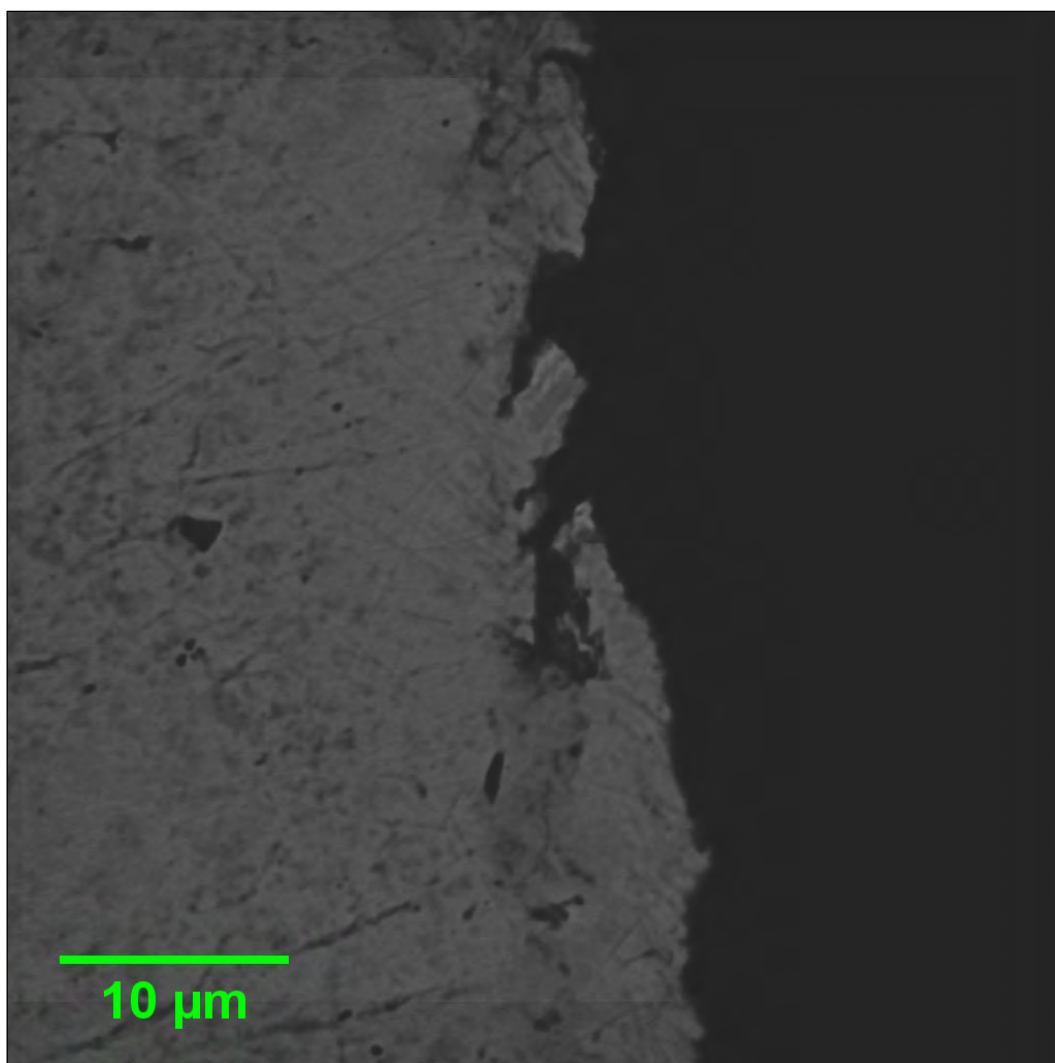
Fig. 4.1 EAN-4: Un-etched micrograph of outer sample surface. 75 A-hrs.

From Table 4.1, sample EAN-4 was charged for 75 A – hrs, at 0.5 A/cm^2, in a 120 °C 50 wt% H_2SO_4. In the above micrograph it is plain that no hydride formation is evident in the rim. After the first six runs proved unsuccessful, two more samples, EAN-6 and EAN7, were run as crude potentiostatitic tests to characterize the relationship of current to voltage in the system, for two different sample holder materials. See Figure 4.2 .

Fig. 4.2 Potentiostatic Testing Results.

The two sample holders were made of alumina (Al_2O_3), which was used for all previous samples in the EAN series, and boron-nitride (BN) which was used for some samples in previous work by Kuhr [78]. These tests both terminated in when the current, in excess of 10 amps, caused the zirconium wire connecting the power supply to the sample to fail. The results indicated that the sample holders were not parasitic to the hydride reaction; which had been considered as a reason for the failure of previous charging runs.

In light of the failure to attain a hydride rim on previous samples, the charging conditions were modified according to Lepage *et al* [40]. In the updated charging procedure the electrolyte concentration was reduced to a $0.2\,M$ sulfuric acid solution, (H_2SO_4), and the solution temperature was reduced to $65 \pm 5\,°C$; with a target current density of $0.2\,\frac{A}{cm^2}$. Two tests were performed under these conditions, LAE-1 and LAE-2, in which strips of lead, Pb, were employed as the anode.

Electron microscopy of these samples hinted at the formation of small hydride rim, less than $6\,\mu m$, which corresponds to an estimated bulk hydrogen concentration of $\sim 110\,wppm$ (Figure 4.3).

Fig. 4.3 LAE-2:Etched micrograph, first indication of hydride formation, 8 A-hrs.

In order to increase the bulk hydrogen concentration the charging time was increased from less than 24 hr to greater than 96 hr. All subsequent runs were employed the platinum mesh anode, used previously, so as to avoid potential complications from the rapid oxidation of the lead strip anodes. The alumina sample holder tube was also removed for this test. Post charging analysis of the first such sample, EAN-9, revealed a 17 μm hydride rim; approximately 330 $wppm$ of bulk hydrogen concentration, Figure 4.4.
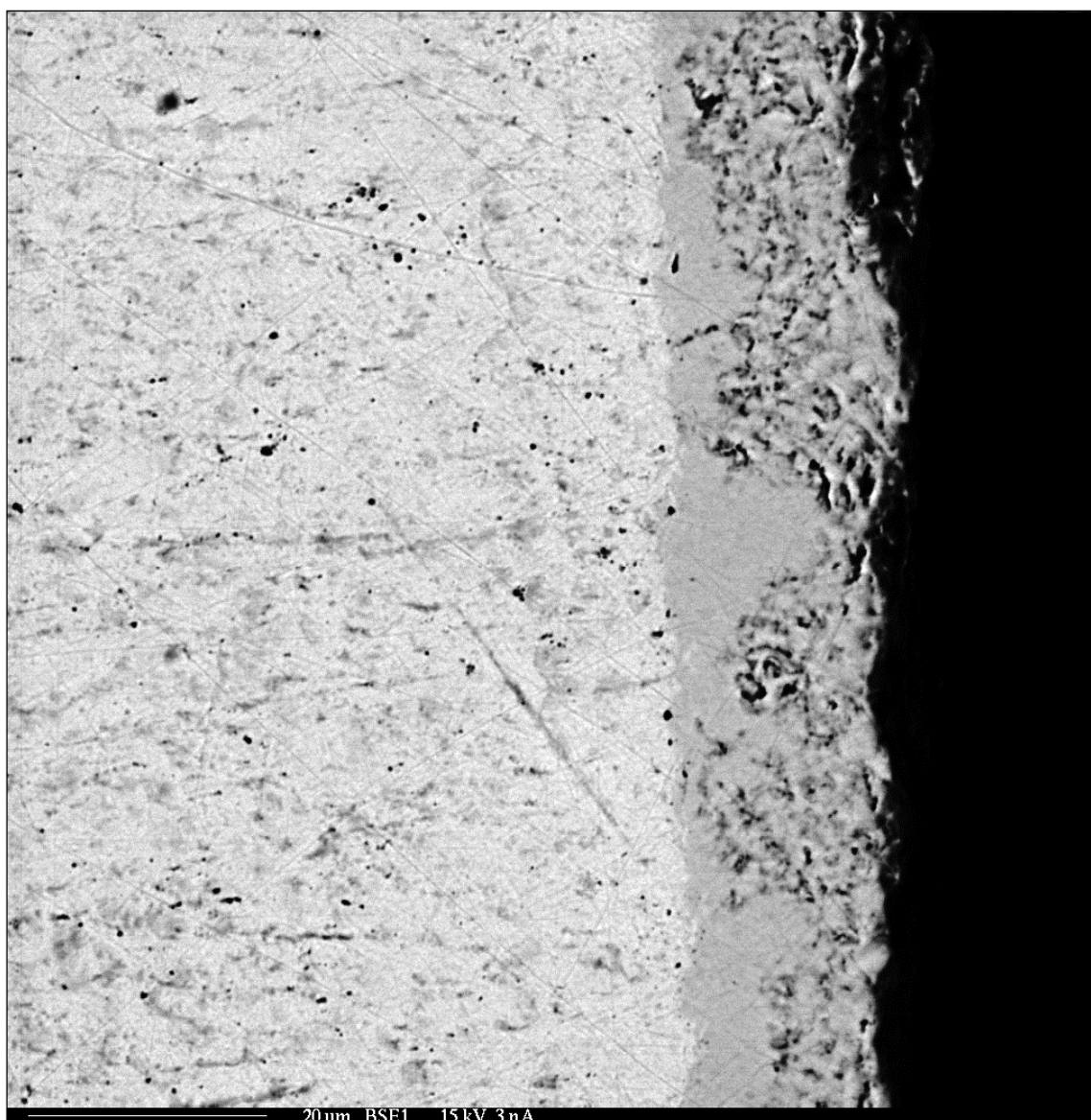
Fig. 4.4 EAN-9: Un-etched micrograph, 17 μm hydride rim, 326 A – hrs.

After the successful charging of EAN-9, two further samples, ZrH-1 and ZrH-2, were created to demonstrate repeatability and to set the charging parameters to be used for Zircaloy-4 and HANA-4. The first specimen, ZrH-1, showed good agreement with EAN-9; however, the hydride layer was split between the inner and outer surfaces. The second, ZrH-2, showed no indication of hydride formation. It is thought that connection between the zirconium wire and the sample was inadequate, which may be the primary reason for previous failures. A second possibility lies in the Alumina sample holder, which was reintroduced in ZrH-2, to prevent the sample on the cathode with from making contact with the anode.

4.2 Parametric Study

After achieving successful hydrogen insertion in EAN-9 and ZrH-1, the focus of the study shifted from proving the charging method to a parametric study of hydrogen charged Zircaloy-4 and HANA-4. Table 4.2 reproduces the list of charging conditions, resulting hydride thicknesses, and estimated bulk hydrogen concentrations for these samples. The hydrogen concentration estimates are based on $Eq.$ (2.3), taken from [40].

Table 4.2   Charging Parameters and Results

Experiment	Electrolyte		Current Density	Run Time	Hydride	H
Sample	Temp.	Concentration	$\frac{A}{cm^2}$	$A \cdot h$	μm	$wppm$
HZrH-1	65-71 °C	0.2 M	0.39**	342.0	33.8 ± 1.8	840
HZrH-2	65-69 °C	0.2 M	0.39**	680.0	51.2 ± 1.0	1260
Zr4H-1	63-68 °C	0.2 M	0.27	344.7	19.3 ± 1.2	160-220*
Zr4H-2	63-68 °C	0.2 M	0.27	>584.4	12.3 ± 0.3	110***
Zr4H-3	63-69 °C	0.2 M	0.37	680.3	14.9 ± 1.2	130-170*

 * The larger value includes hydride contribution from all four faces.

 ** The target current density was $0.2 \frac{A}{cm^2}$. The effective current density was twice the target current density; because, the inner surface was inactive during charging.

*** Charging was interrupted by a power failure.

To carry out this study, two HANA-4 samples, HZrH-1 and HZrH-2 and two Zircaloy-4 samples, Zr4H-1 and Zr4H-2 were created. However, during the charging of Zr4H-2, power was lost for indeterminate amount of time and the number of amp-hours charged was unknown. A third Zircaloy-4 sample, Zr4H-3 was run to replace Zr4H-2.

As the thickest hydride rim, and higher potential bulk hydrogen concentration was achieved in sample HZrH-2, it was decided that characterization and analysis would focus on HZrH-2 and Zr4H-3. Zr4H-3 was charged with the same current density and for an equivalent number of amp-hours as HZrH-2. Thus, the target current density for Zr4H-3 was increased to $0.4 \frac{A}{cm^2}$.

Examples of as received and charged HANA-4 and Zircaloy-4 are shown in Figure 4.5 and Figure 4.6.

4.2.1 Parametric Studies in HANA-4

Charging HZrH-2 for 680 A-h, with a current density of $0.39 \frac{A}{cm^2}$, resulted in a $51 \pm 1 \mu m$ hydride rim. A back scattered electron (BSE) image of the charged specimen is shown in Figure 4.7. This specimen was not chemically etched prior to imaging.
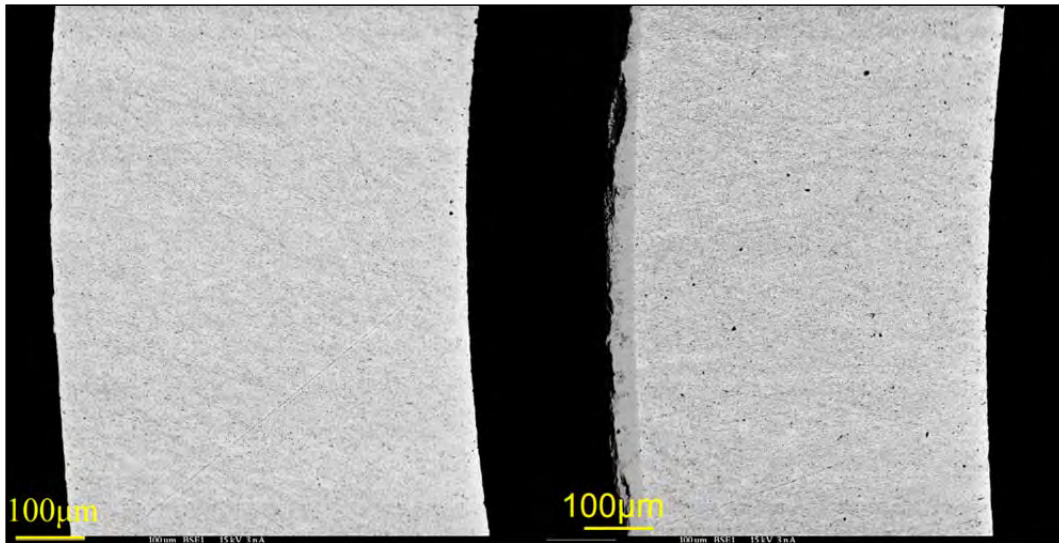
Fig. 4.5 Pre and Post Charging HANA-4 (BSE): (Left) As received HANA-4. (Right) Hydrogen charged HANA-4.
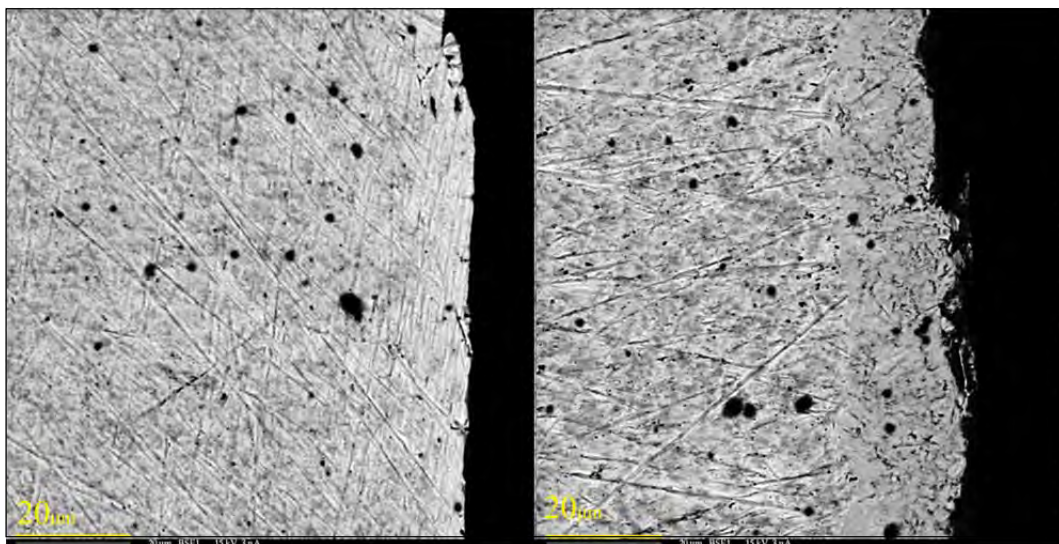
Fig. 4.6 Pre and Post Charging Zircaloy-4 (BSE): (Left) As received Zircaloy-4. (Right) Hydrogen charged Zircaloy-4.
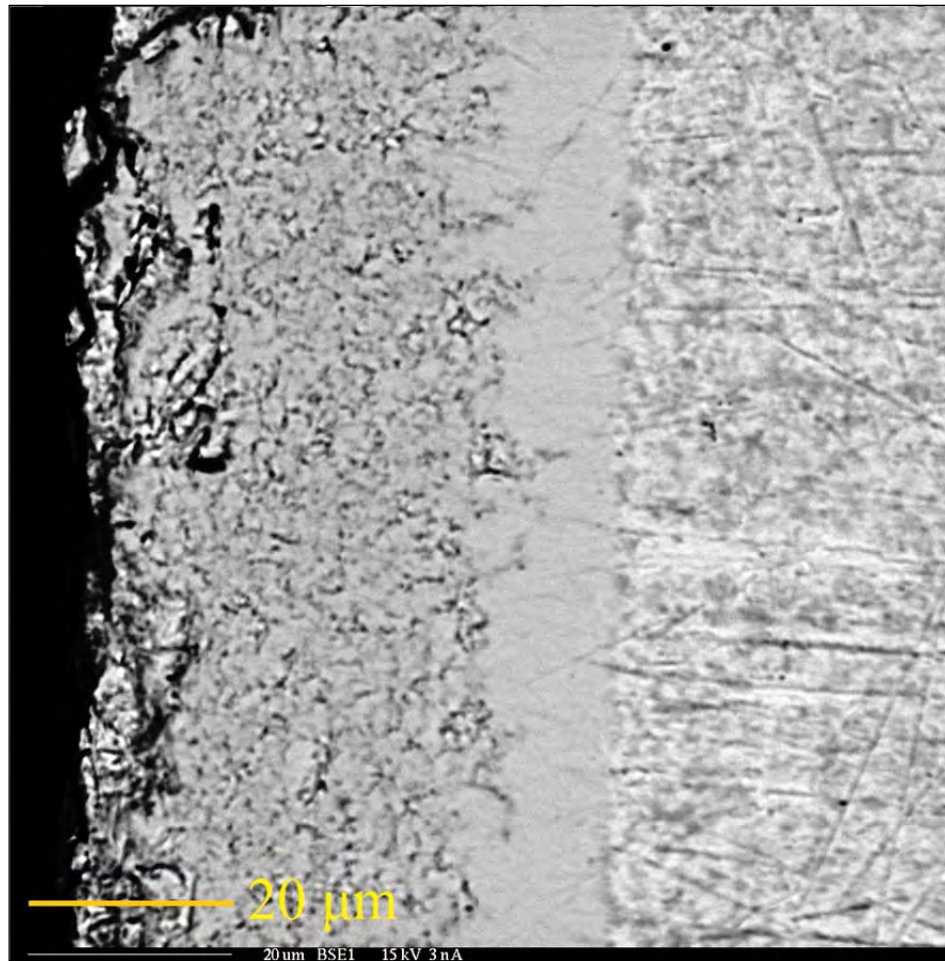
Fig. 4.7 HZrH-2: 51μm thick hydrided region, 680 A-h, 0.39 A/cm^2.

The image shows three distinct phase regions in the sample. The inner region, at right, is the bulk zirconium alloy. The darker region, to the left, is a dual zoned hydride rim. The hydrided region exhibits two topologies: rough and porous at far left, and smooth toward the middle of the image. The rough area is may be the region of greatest hydrogen concentration, as hydrogen ingress occurs from the outer surface and hydrogen diffusion is slow at the charging temperature 65 °C. The roughness is likely due to material loss from the brittle hydride phase during the grinding step in metallographic preparation.

A portion of the charged sample, HZrH-2, was annealed for 1 hour at 540 °C. The annealing process comprised ramping from ambient to 540 at 25 °C/min, followed by a 60 minute hold, and furnace cooling back to room temperature. This homogenization was only partially successful, as seen in Figure 4.8. Annealed specimens were chemically etched to provide greater contrast between the bulk and the hydrides. Etching used the solution and technique described in §3.4.
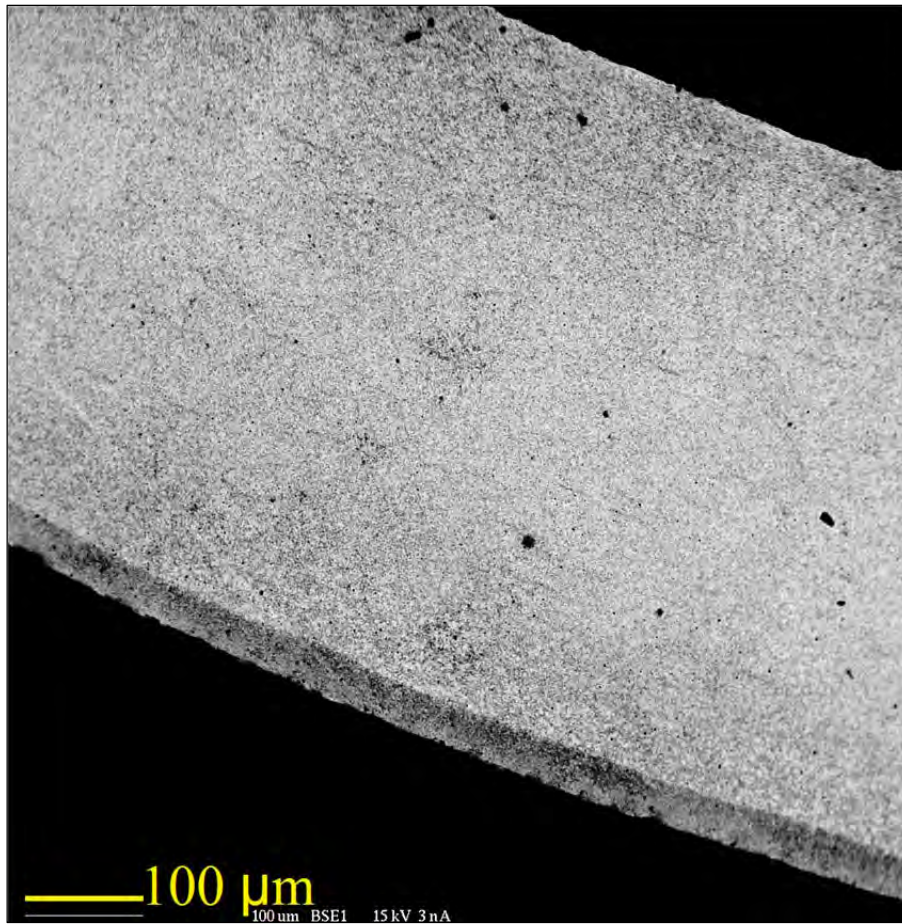
Fig. 4.8 HZrH-2: Post annealing 60 min at 540 °C.

From the figure, it is apparent that the majority of hydrogen remained in the hydride rim. A small number of faint hydride platelets are visible in the bulk; however, analysis of the image revealed that the hydride thickness at the rim was unchanged. This was not expected. The hold time, 60 minutes, was chosen to be a factor of four greater than the 15 minutes that should have been sufficient to reach 97% of the equilibrium concentration throughout the sample, as done by Khatamian [23]. The 15 minute diffusion time was calculated using *Eq* (3.1) and the average diffusion coefficient for zirconium, Zircaloy-2, and Zircaloy-4 reported coefficient reported by Kearns [51], *Eq* (3.2).

A possible explanation for this unexpected outcome could be that there was more hydrogen in the rim than could diffuse to the bulk under the applied annealing conditions. The bulk hydrogen content, obtainable from the rim, was estimated to be between 1260 and 1600 wppm. Estimates were made using *Eq* (2.3) and *Eq*(2.6) respectively. Using TSS_d data for the average of zirconium, Zircaloy-2, and Zircaloy-4 from Kearns [14] Eq(2.1), TSS_d at 540 °C is 600 wppm , which means that it would be expected for the Zr solution to saturate at 600 wppm if HANA 4 were to behave in a similar manner to Zricaloy 4. However, the relatively small

number of hydride platelets visible in Figure 4.4, suggests a bulk concentration well below the possible 600 wppm (see Figure 2.10 for comparison).

A second piece of HZrH-2 was annealed, because of the incomplete hydride redistribution seen in the previous sample, the annealing conditions were changed to 4 hrs at 550°C, Figure 4.9.
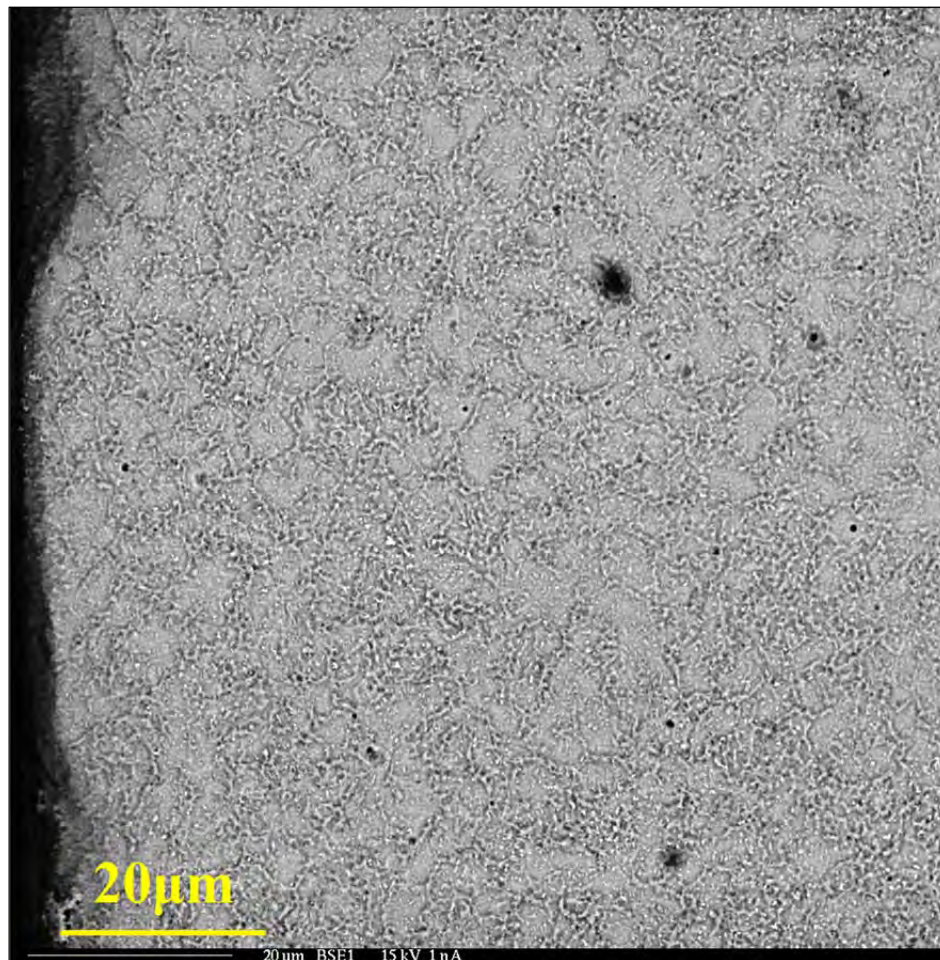
Fig. 4.9 Post annealing rim removal, prior to H measurement. Annealed 550 °C for 4 hrs.

The sample shown in Figure 4.9 was cut from the material sent to IMR Test labs for hydrogen content measurement. This sample was ground with silicon carbide papers, post annealing, to remove any remaining rim prior to hydrogen concentration measurements by IMR. From the figure it is clear that grinding has completely removed any hydride rim that might have remained after the extended anneal.

4.2.2 Parametric Studies in Zircaloy-4

The Zircaloy-4 sample, Zr4H-3, charged with the same current density, for an equivalent number of A-hrs as HZrH-2, see Table 4.2 for details, developed a thinner hydride rim,15±1 μm, as seen in Figure 4.10. As with the HANA-4, a diffusion time was calculated, using *Eq.* (3.1) and the Kearns [51] data. The estimated diffusion time was multiplied by four, yielding a furnace dwell time of 270 mins. Similarly, a ramp rate of 25 °C/min was used, and the sample was furnace cooled to room temperature. However, unlike the HZrH-2 sample, the homogenization successfully produced a uniform distribution of readily visible hydride platelets leaving no visible hydride rim behind, Figure 4.11.
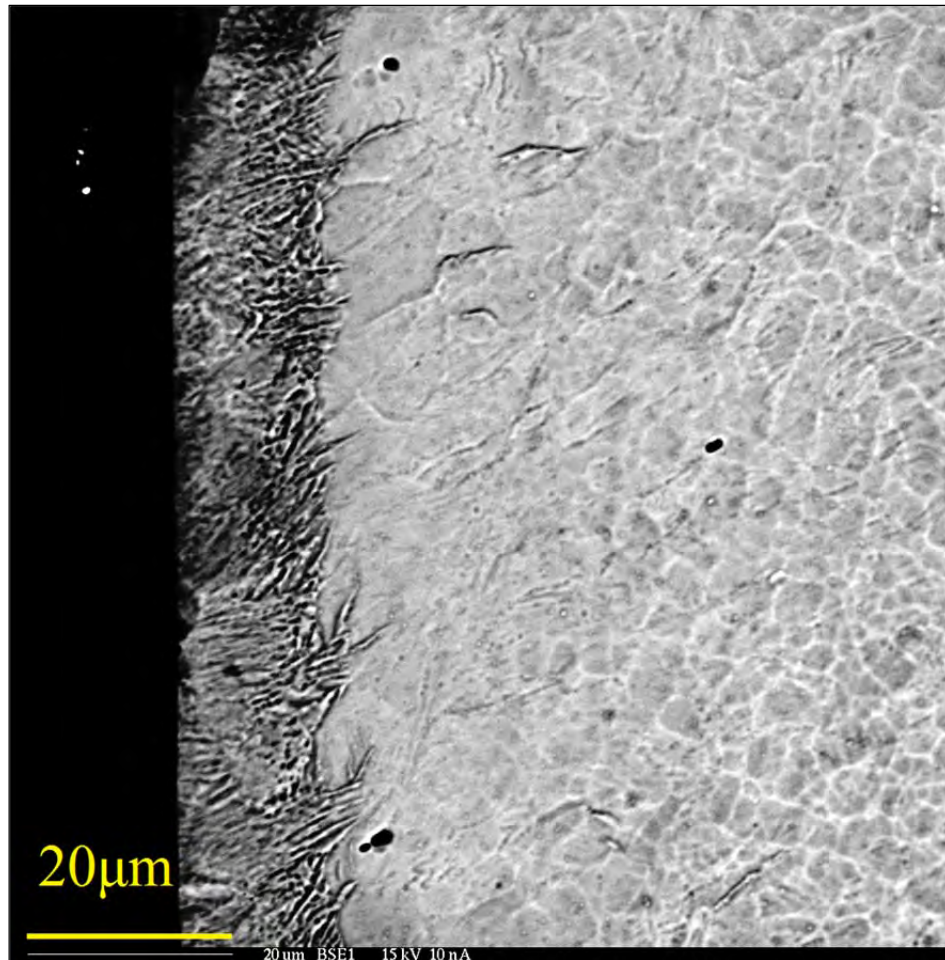
Fig. 4.10 Zr4H-3: 15μm thick hydrided region, 680 A-h, 0.39 A/cm^2.
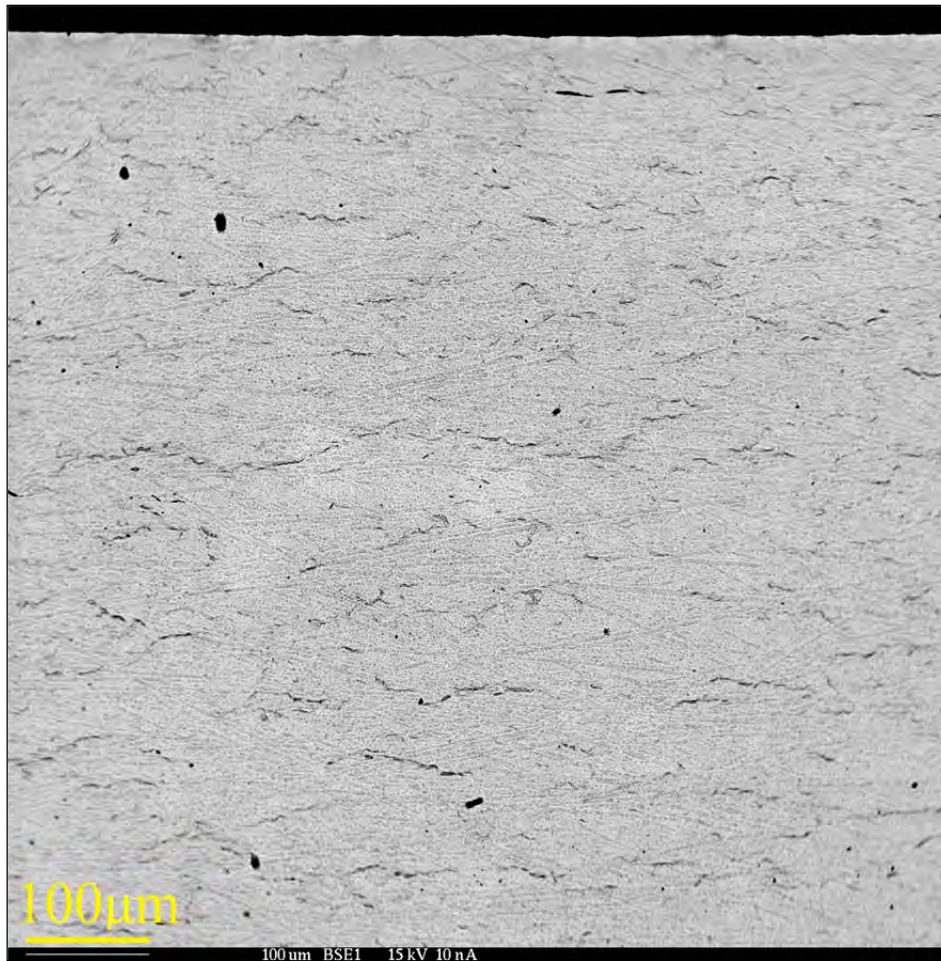
Fig. 4.11 Zr4H-3: Post Annealing, 270 min at 540 °C.

In contrast to the HZrH-2 sample, where the estimated bulk concentration from the rim exceeded the solvus concentration from Kearns TSS_d data, Zr4H-3 had an estimated hydrogen concentration of 170-200 wppm, by Equations (2.3) and (2.6). A concentration of even 200 wppm is well below the solvus concentration of 600 wppm at 540 °C. Hence, the homogenization parameters were sufficient to dissolve the hydride rim, and redistribute the hydrides in a uniform manner.

4.3 X-Ray Diffraction

Charged samples were further characterized through X-ray diffraction. Table 4.3 lists the peaks for phases of interest; within the range of measurement. File numbers 05-0665 (α-Zr), 34-657 (β-Zr), 34-0690 (γ-ZrH), 34-0649 (δ-ZrH$_{1.66}$), and 17-314 (ϵ-ZrH$_2$) from the Joint Committee on Powder Diffraction Standards (JCPDS) were used to index the diffractograms. The zirconium-oxide peaks listed in Table 4.1 were taken from the Standard X-ray Diffraction Powder Patterns, published by the National Bureau of Standards [82]. X-ray diffractograms for post annealing HZrH-2 and Zr4H-3 are given in Figures 4.12 and 4.3.

Table 4.3   XRD Peaks for Zirconium, Zirconium Hydride, and Zirconium Oxide

Zirconium and Zirconium Hydrides Peaks: Range 48-72 in 2θ								
Zr	Intensity	δ-ZrH$_{1.66}$	Intensity	γ-ZrH	Intensity	ε-ZrH$_2$	Intensity	ZrO
α-48.0	17	54.2	37	54.3	24	51.9	12	56.1
β-51.5	17	64.6	43	56.6	11	55.3	18	67.1
α-56.9	17	67.8	12	62.9	16	62.5	20	70.6
α-63.5	18			67.0	14	67.8	8	
β-64.3	33			69.0	13	68.6	8	
α-66.8	3							
α-68.5	18							
α-69.6	12							

Fig. 4.12 Post Annealing HANA-4: 48° – 72° in 2θ. Sample, HZrH-2
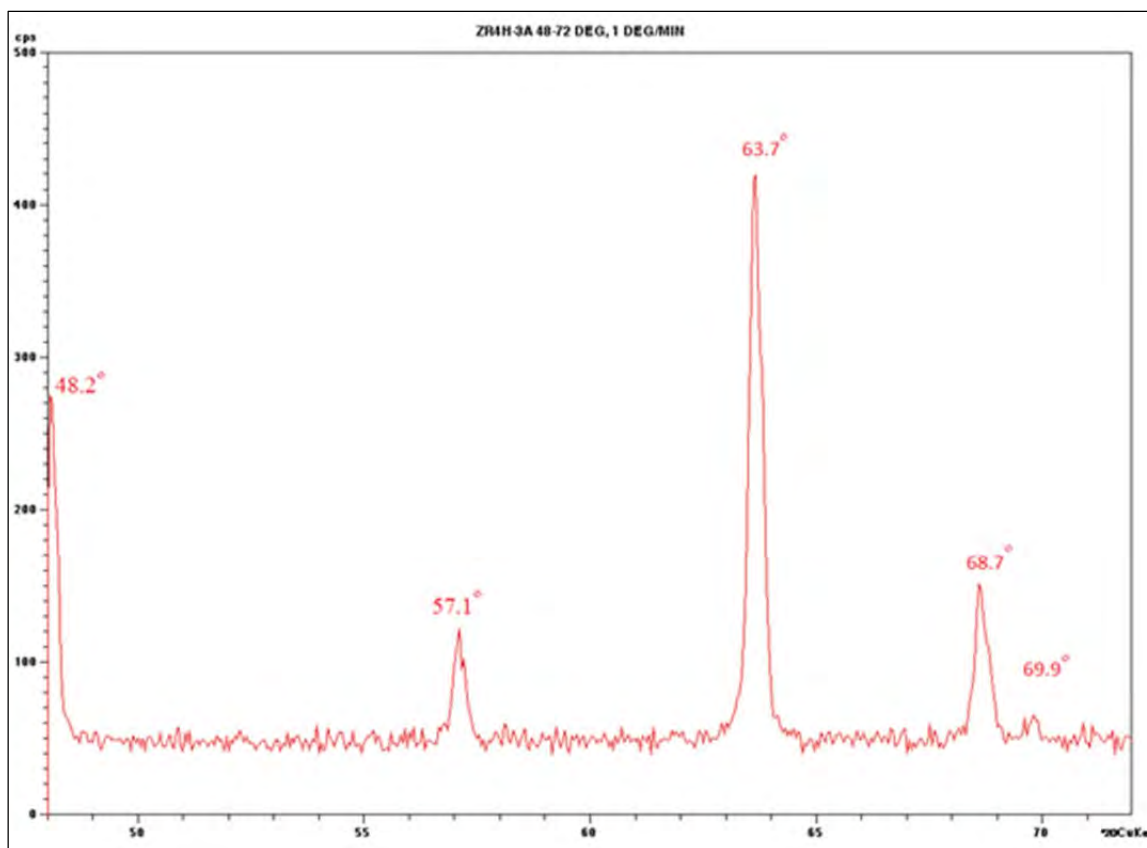
Fig. **4.13** Post Annealing Zircaloy-4: 48° – 72° in 2θ. Sample Zr4H-3A.

Additional X-ray diffraction plots of HZrH-2 and Zr4H-3, pre and post charging, are provided in Appendix A. The phases identified and the peaks measured, pre and post charging, for each sample are given in Table 4.4.

Table 4.4   Phases Identified as Received and Post Charging: Angle in 2θ

α-Zr		ε-ZrH2		δ or δ+α	
HZrH-0*	Zr4H-0*	HZrH-1	HZrH-2	Zr4H-1	Zr4H-3
	48.0	52.1	52.2	54.2	54.1
56.7	56.9	54.9	55.0	64.3	64.2
63.2	63.5	62.7	62.8	67.8	68.0
68.2	68.5	67.6	67.2	68.7	

*Numerical designation zero indicates as received alloy.

Uncharged HANA-4 and Zircaloy-4 both exhibited pure α-Zr peaks in their diffraction patterns. Although HANA-4 is reported to contain β-Zr, no β peaks were observed. This is likely due to the volume fraction of the β-Zr being below the detection limit. For charged and annealed samples the presence of β-Zr is potentially masked by hydride peaks, see Table 4.1. Charged HANA-4 had sufficient hydrogen concentration in the rim that XRD revealed pure ε-hydride

peaks, corresponding to a hydrogen wt% > 1.8, see Figure 2.1 for Zr-H phase diagram. By comparison, the δ or δ+α phase was identified for the Zircaloy-4 specimens, which corresponds to a large region of the phase diagram, 0 wt%< C_H < ~1.7 wt%; where C_H is hydrogen concentration.

The observed hydride phases in both HANA-4 and Zircaloy-4 were transformed after annealing. Due to the closely spaced peaks of the H-Zr system, it was difficult to determine exactly which phases were present. It appears that some of the metastable γ-phase may have formed in the HANA-4 samples during cooling. The post annealing Zircaloy-4 appears to be pure zirconium, despite metallographic evidence to the contrary. Post annealing peaks and corresponding phases are given in Table 4.5.

Table 4.5   Phases Identified Post Annealing: Angle in 2θ

γ+δ or α+δ		α	
HZrH-1A	HZrH-2A	Zr4H-1A	Zr4H-3A
54.0	54.1	48.2	48.2
56.7	56.7	57.1	57.1
63.2	63.3	63.7	63.7
64.5	64.5	68.7	68.7
68.2	68.2	69.9	69.9

4.4 Hydrogen Concentration Measurements

4.4.1 External Laboratory Measurements

Charged sections from annealed portions of HZrH-2 and Zr4H-3 were sent to IMR Test Labs, 131 Woodsedge Dr. Lansing, NY. 14882, for hydrogen content measurement. The full reports are given in Appendix B. The HANA-4 required the remaining hydride rim to be removed, as the goal was to measure the bulk concentration after annealing at 550 °C for 4 hrs (Figure 4.9). This was not necessary for the Zircaloy-4, as BSE imaging showed no remaining rim under identical annealing conditions (540 °C 270 min) Figure 4.11. Measurement of hydrogen concentration was performed via inert gas fusion-thermal conductivity. The measurement required a minimum of 2 grams of material. The results of the hydrogen concentration measurements by IMR are given in Table 4.6.

Table 4.6   Measured Hydrogen Content

Sample	Hydrogen wt%	Hydrogen wppm	Est. H wppm *Eq*(2.6)
HZrH-2	0.16	1600	1600
Zr4H-3	0.017	170	200

Measurements of alloy composition performed by IMR Test Labs, 131 Woodsedge Dr. Lansing, NY. 14882.

These measurements are in good agreement with the hydrogen concentration estimates based on observed hydride thickness and the density of the observed hydride phase, yet unexpectedly high for the annealed HANA-4 sample HZrH-2. As noted in the discussion of Figure 4.9, the Kearn's line [14] *Eq* (2.1), gives the TSS_d of Zircaloy-4 at 540 °C as 600 wppm

hydrogen. The presence of 1600 wppm hydrogen in the annealed portion of HZrH-2 suggests that HANA-4 may have a significantly higher TSS than Zircaloy-4.

4.5 Annealing and Differential Scanning Calorimetry

4.5.1 Measurements with Netzsch 409 STA

As discussed in §3.5.5 , the Netzsch 409 was used to load hydrogen from the charged rim into the bulk of the sample as preparation for hydride dissolution temperature (HDT) measurement. It was also used for the first series of HDT measurements in both alloys. Measurements with the Netzsch 409 proved to be inconclusive, as the DSC signal was dominated by the baseline behavior of the system, see Figure 4.14.
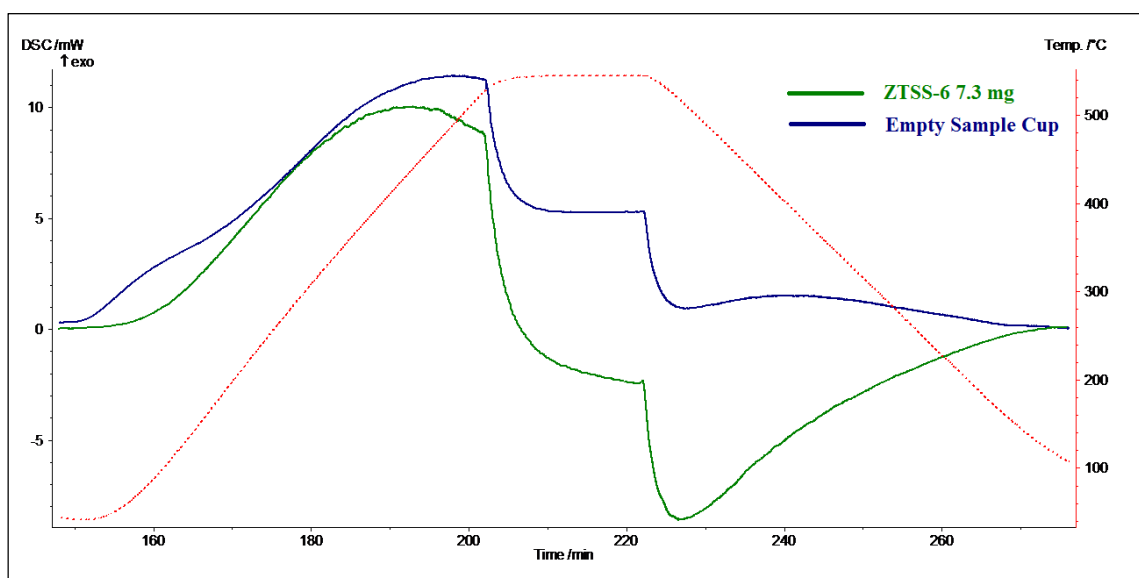
Fig. 4.14 Typical heat flow response over 1 cycle: with sample and empty.

As seen in Figure 4.14, the sample curve, green, and empty system curve, blue, follow a similar pattern. All significant changes in the signals are related to changes in the temperature profile, red. This behavior was typical of results obtained with the Netzsch. None of the HDT measurements attempted with the Netzsch instrument were successful, as no dissolution or precipitation peaks could be definitively identified in the DSC signal. The heating curves for each alloy are shown in Figures 4.15 and 4.16.
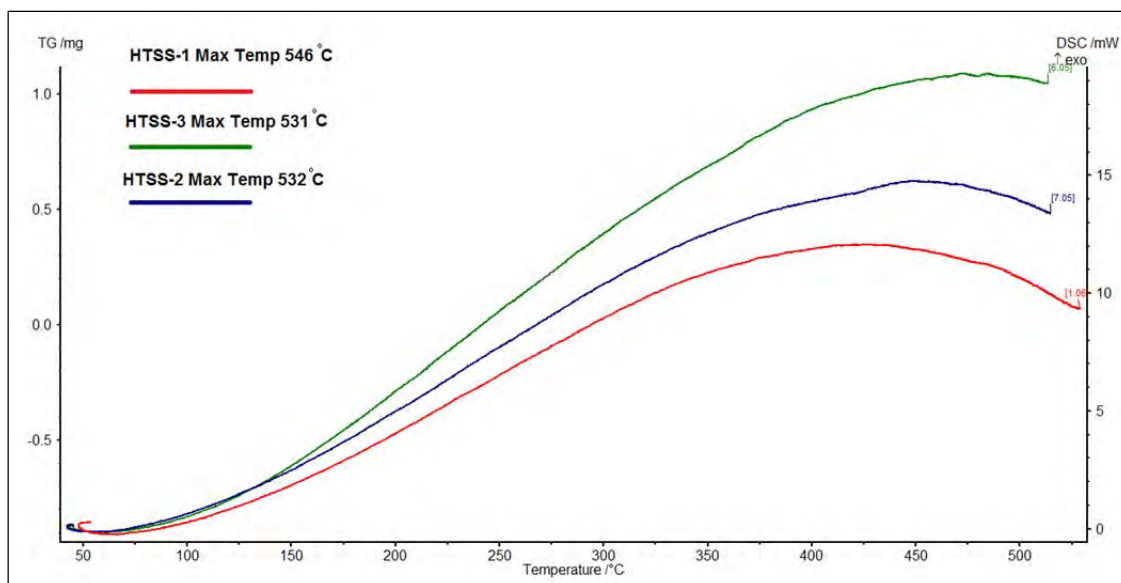
Fig. 4.15 Heating curves, HTSS-1, HTSS-2 and HTSS-3: heating/cooling 10 °C/min.

In both alloys the heating curves appear smooth; giving no indication of a hydride dissolution peak. The heating curves for Zircaloy-4 are given in Figure 4.16.
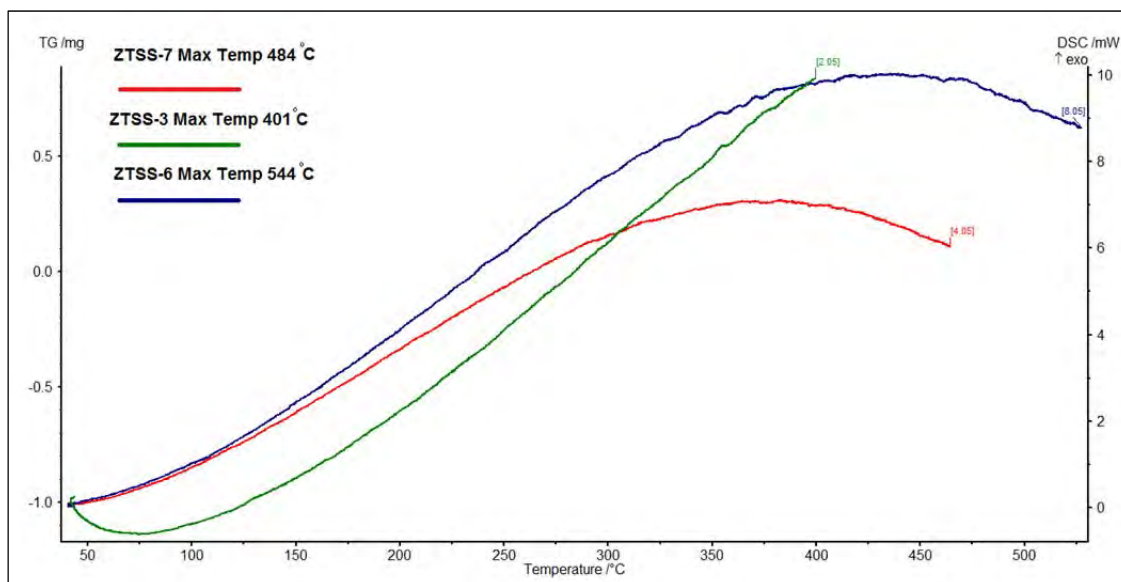
Fig. 4.16 Heating curves, ZTSS-1, ZTSS-2 and ZTSS-3: heating/cooling10 °C/min.

Samples HTSS-2 and HTSS-3, exhibited small exothermic peaks during cool down from max temperature, of the HDT measurement, Figure 4.17. Likewise, sample ZTSS-3 contained a similar exothermic peak during the homogenizing anneal, but no peaks were seen during the cooling portion of the HDT measurements for this sample, see Figure 4.18.
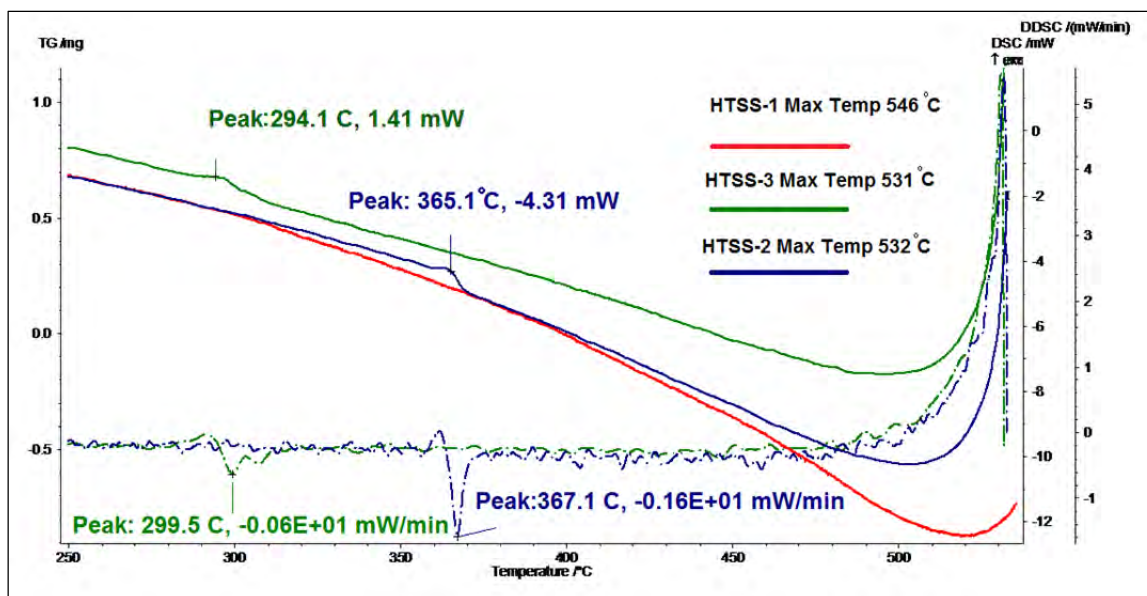
Fig. 4.17 Cooling curves, HTSS-1, HTSS-2 and HTSS-3: heating/cooling10 °C/min..
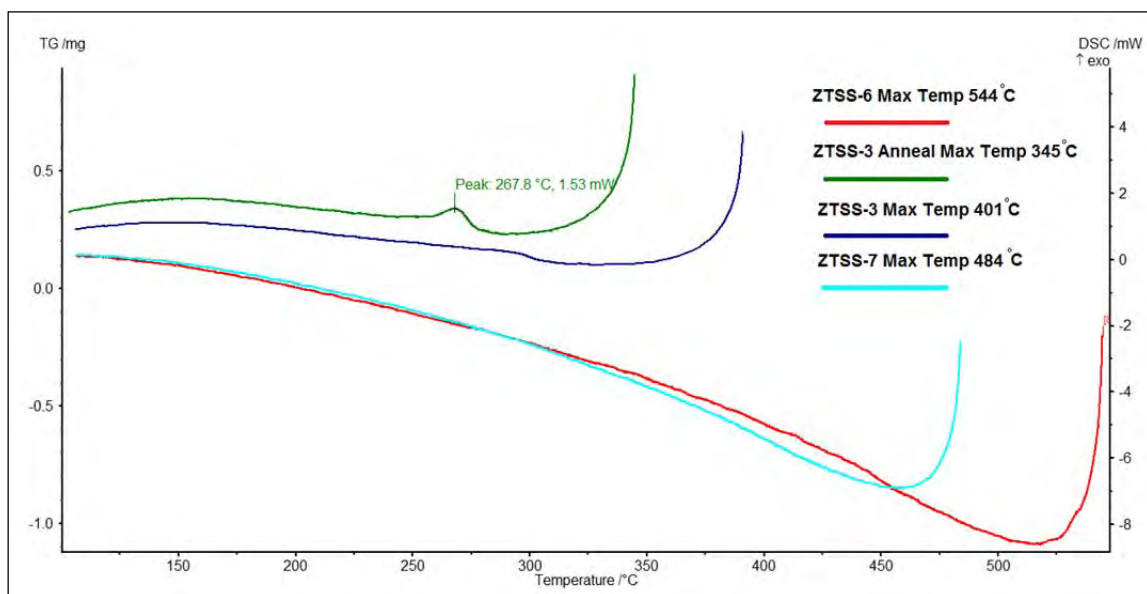
Fig. 4.18 Cooling curves, 10 °C/min: Zircaloy-4.

These small peaks are unlikely to be hydride precipitation peaks; especially in light of the HDT measurements made with the TA Q600. Other reasons suggesting they are not dissolution peaks include the following: they are not present in all samples, nor are they present in all the runs of a single sample. As noted above, ZTSS-3 exhibited a cooling peak during the annealing, but did not in either of the two HDT measurement runs. Additionally, these peaks are very small and blunted compared to precipitation peaks reported in literature [8, 18, 20].

The peak temperatures (PT) and maximum slope temperatures (MST), for these peaks are listed in Table 4.7.

Table 4.7   Netzsch: Peaks Observed During Cooling

Sample	PT °C	MST °C
HTSS-2	365.1	367.1
HTSS-3	294.1	299.5
ZTSS-3	267.8	273.6

4.5.2 Measurements with TA SDT Q600 DSC/TGA

The results from the TA Q600 DSC/TGA measurements are markedly different from those performed on the Netzsch STA 409, in that some changes in the DSC signal are independent of the temperature profile, Figure 4.19. The results of these measurements are presented below; for HANA-4 and Zircaloy-4. For completeness, an attempt was made to analyze the peak temperature (PT), onset temperature (Onset), and maximum slope temperature (MST) for all significant features in the DSC signal. However, the hydride dissolution temperature is the primary feature of interest, with secondary consideration being given to the hydride precipitation temperature, in this study.
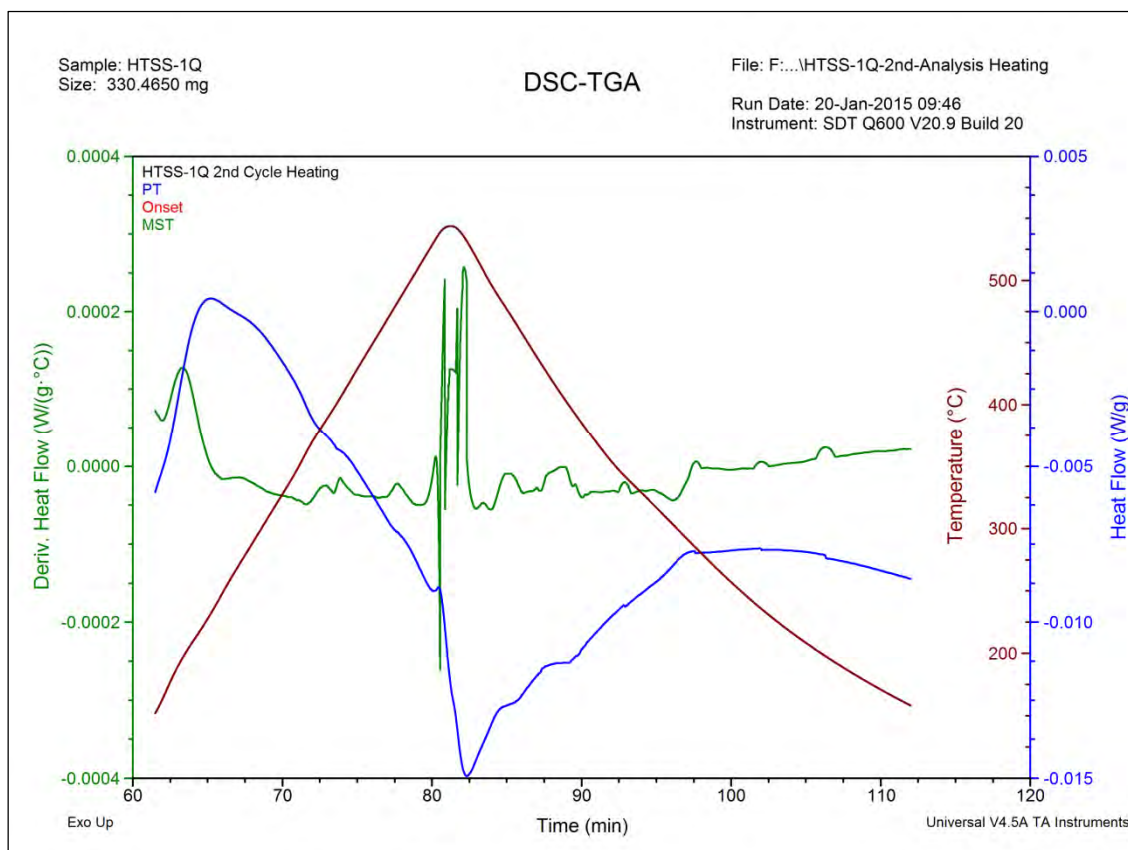
Fig. 4.19 Example of DSC signal over 1 cycle: TA Q600.

Hydride dissolution is an endothermic event, and occurs upon heating above the dissolution temperature, TSS_d. Hydride precipitation is an exothermic event, and occurs upon cooling at a temperature below the dissolution temperature. These are the criterion by which

potential hydride dissolution and precipitation peaks were judged. Characteristics of peaks, observed during heating, that are close to the annealing temperature are given in Table 4.8 below.

Table 4.8   Hydride Dissolution Temperature Measurements Q600. DSC (°C)

HTSS-1	Cycle-2	Cycle-3	Anneal	ZTSS-6	Cycle-2	Cycle-3	Anneal
PT	528.60	528.31	533	PT	391.90	394.16	530
Onset	527.22	526.97		Onset	389.47	390.39	
MST	534.26	533.81		MST	405.19	404.91	
HTSS-2	Cycle-2	Cycle-3	Anneal	ZTSS-7	Cycle-2	Cycle-3	Anneal
PT	429.57	429.48	422	PT	455.51	456.26	438
Onset	430.23	422.91		Onset	432.59	452.29	
MST	438.44	422.39		MST	443.43	466.88	
HTSS-3	Cycle-2	Cycle-3	Anneal	ZTSS-3	Cycle-2	Cycle-3	Anneal
PT	371.06	373.01	346	PT	354.56	351.49	345
Onset	352.08	355.73		Onset	355.68	352.25	
MST	363.71	364.94		MST	363.52	362.75	

Hydrogen free specimens of HANA-4 and Zircaloy-4 were measured under the same conditions, max temp 480 °C, 20 °C/min heating and cooling, for 3 cycles with 1 minute holds between dynamic segments, as HTSS-2Q and ZTSS-7Q. Analyzed heating curves for hydrogen charged and hydrogen free samples of each alloy are presented in Figures 4.20 – 4.23.
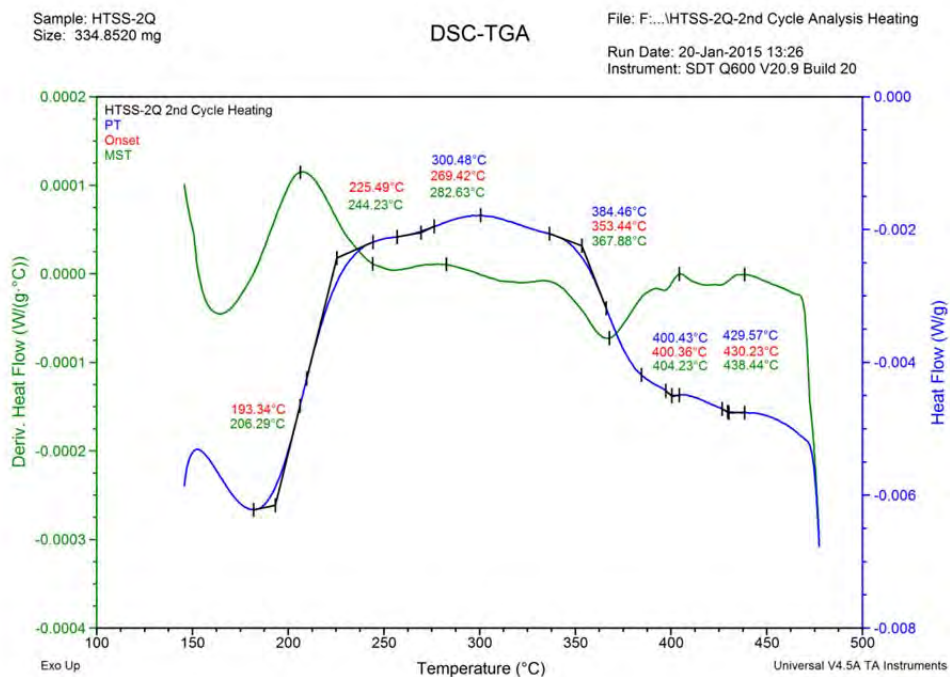
Fig. 4.20 HTSS-2Q: Heating curve, Max Temperature 480°C.
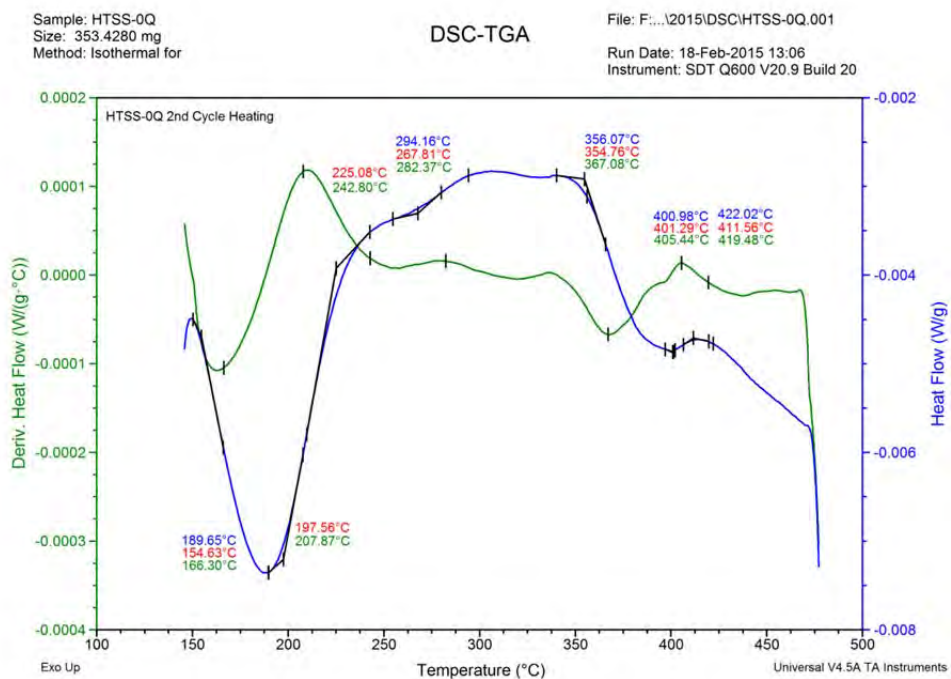
Fig. 4.21 HTSS-0Q: As received material: Heating curve, Max Temperature 480 °C.
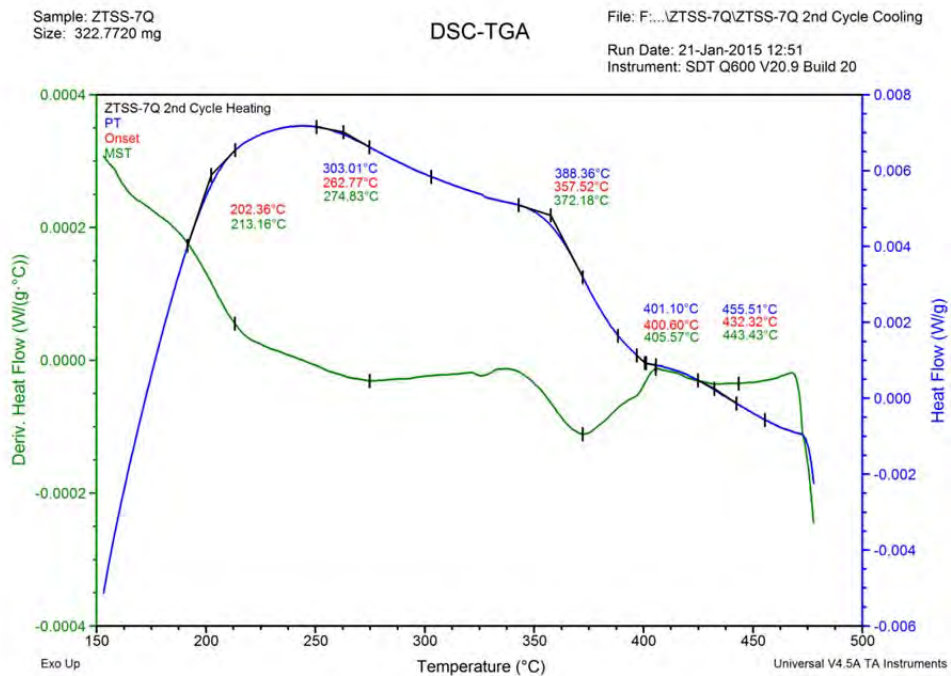
Fig. 4.22 ZTSS-7Q: Heating curve, Max Temperature 480 °C.
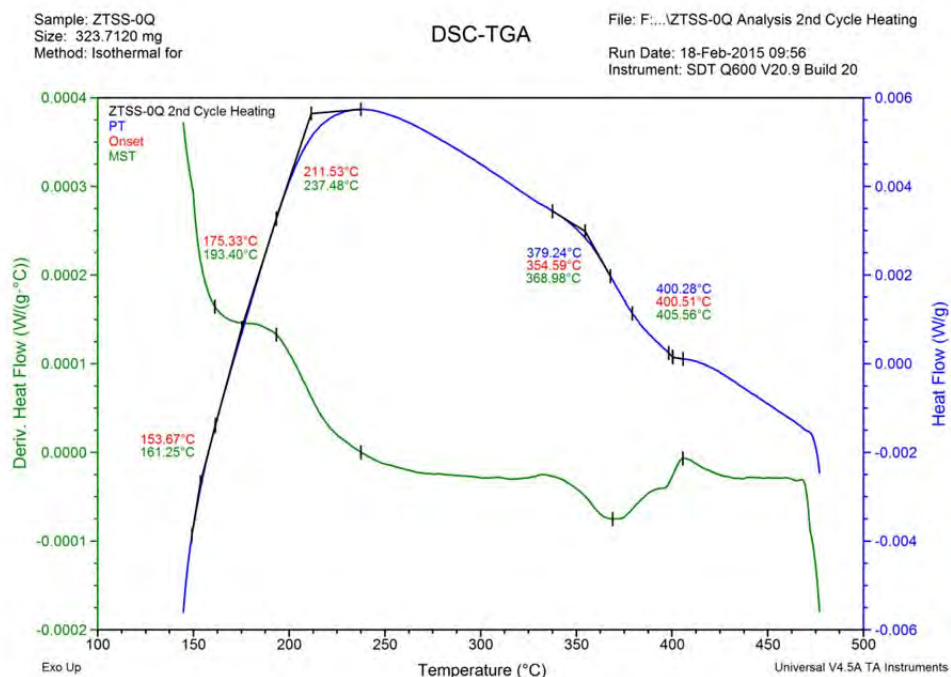
Fig. 4.23 ZTSS-0Q As received Material: Heating curve, Max Temperature 480 °C.

The above figures show that the general shape of the DSC curve is the same for hydrogen charged and hydrogen free specimens of the same alloy. The hydrogen charged specimens contain additional features, endothermic dips in the DSC signal potentially indicating a hydrogen related reaction. Though the DSC signal for the two alloys differ in appearance, in both the charged and uncharged specimens there is an endothermic event that begins at an onset temperature around 350 °C and finishes near 400 °C. This event is present in all samples, charged or uncharged, though it is truncated in the samples that only reached 380 °C.

5.0 Discussion

Though the early attempts at cathodic charging were largely unsuccessful, they provided an opportunity to gain experience with the characterization methods employed in this study. Analysis of the inconclusive results led to modifications in the cathodic charging system and procedure; ultimately resulting in a system capable of consistently charging zirconium alloys with hydrogen concentrations above 1000 wppm.

5.1 Comparison and Analysis of Parametric Studies

A notable difference was observed in the post charging hydride rim thicknesses in the two alloys. In HANA-4 the observed rims were 30 – 50 μm thick, while in Zircaloy-4 the observed rims were only 10 – 20 μm thick. Samples HZrH-2 and Zr4H-3 were charged for an equivalent number of amp-hours, with the same target current density. Despite this, HZrH-2 had a 50 μm rim compared to the 12 μm rim of Zr4H-3. Estimating the mass of hydrogen contained

in each sample using *Eq*(2.4) and *Eq*(2.5) suggests that HZrH-2 contained up to four times the mass of hydrogen as Zr4H-3.

However, the difference in rim thickness between Zr4H-3 and HZrH-2 may not be due entirely to a difference in materials or geometry. Zr4H-3 ran for twice as many *A-h*, at twice the current density of Zr4H-1. This should have resulted in a thicker rim on Zr4H-3 than Zr4H-1, as both the run time and increased current density should have resulted in increased hydrogen content. Yet, as seen in Table 4.2, the hydrided region on Zr4H-3 is approximately 4 μm thinner than the one on Zr4H-1. Thus, while geometry likely plays a significant role in the effectiveness of hydrogen charging, as suggested by Figure 3.3, it also appears that some variation in charging conditions is introduced from run to run. This is in part due to difficulty with the level switch. On occasion, the level switch would fail to turn off the pump, resulting in a dilution of electrolyte concentration.

The annealing results of the HANA-4 samples, taken from HZrH-2 proved interesting. The first attempt at annealing, 540 °C for 60 minutes, had no measureable effect on the thickness of the hydride rim. However, X-ray diffraction measurements on the annealed sample revealed that the hydride in the rim had transformed from the hydrogen rich ε-hydride phase (ZrH_2) to the δ-hydride ($ZrH_{1.66}$) phase. This explains why some hydride platelets were observed in the bulk, even though the rim thickness appeared unchanged. When a second section was annealed (Figure 4.9), 550 °C for 240 minutes, electron microscopy revealed a uniform network of fine hydrides distributed throughout the matrix. This section was from the material that was measured by IMR Test Labs. In order to measure the concentration of hydrogen in the bulk, the surface layer is was removed after annealing. The hydride rim was originally 50 μm thick, and a minimum of 250 μm was removed from the surface post annealing. This would be sufficient to remove the rim and prevent excess hydrogen from impacting the measured concentration. Hydride rim removal was confirmed via BSE/SE imaging of a section of the sample sent to IMR, Figure 4.9. IMR Test Labs reported a hydrogen concentration in this sample of 1600 wppm. The terminal solid solubility limit of hydrogen in Zircaloy-4, *Eq* (2.1), at 550 °C is approximately 640 wppm [14]. If the TSS_d of HANA-4 is consistent with that of Zircaloy-4, then the measured hydrogen concentration is expected to be 640 wppm after annealing, but was measured to be 1600 wppm. This interesting result indicates that HANA-4 has a significantly higher terminal solid solubility under dissolution (TSS_d) than Zircaloy-4.

It was noted earlier, §2.2, that β-Zr has been shown to have a higher TSS_d than α-Zr [33]. Park *et al* [83], reported that HANA-4 is heat treated to retain some of the meta-stable β phase, although the β phase was not detected in XRD measurements of the as received HANA-4. This is likely due to the volume fraction being too low for the β phase to be distinguished in the XRD measurements. If the β phase is present, as HANA-4 is a niobium bearing alloy, a niobium stabilized β phase could be increasing the TSS_d of HANA-4, as reported by Khatamian [32] for other Zr-Nb alloys [7].

The annealing temperature, 550 °C, is the reported α→β transition temperature, at elevated hydrogen concentration, in the H-Zr system. This is the high temperature limit of the Kearns line [14]. Because the β phase is metastable, and its stability is impacted by temperature, it is unclear how annealing may have impacted the HANA-4 microstructure. Annealing may have caused decomposition of the β phase, as discussed by Khatamian [32], this is especially true for the first anneal of 60 minutes at 540 °C. As described in §2.2, Figure 2.8, aging at

elevated temperatures decomposes the β phase, lowering TSS$_d$ to be consistent with Zircaloy-4. Alternatively, as the second anneal, 240 minutes at 550 °C is at the transition temperature, it may have partially regenerated the β phase resulting in an increase in TSS$_d$.

Only a small piece of the sample sent to IMR was retained, and that piece was mounted and polished to produce the micrograph shown in Figure 4.9. Thus the author was unable check for the presence of β phase through XRD. Even if enough material had been available, the β-Zr peaks would be difficult to distinguish from neighboring peaks in the Zr-H system, particularly δ-hydride.

5.2 Analysis of Differential Scanning Calorimetry Results

During the heating cycle most samples had an endothermic peak close to the annealing temperature. At first this seemed a good indication that these peaks are associated with hydride dissolution. The peak temperature (PT), onset, and maximum slope temperature (MST) for these peaks are plotted against the annealing temperature for HANA-4, Figure 5.1, and Zircaloy-4, Figure 5.3.
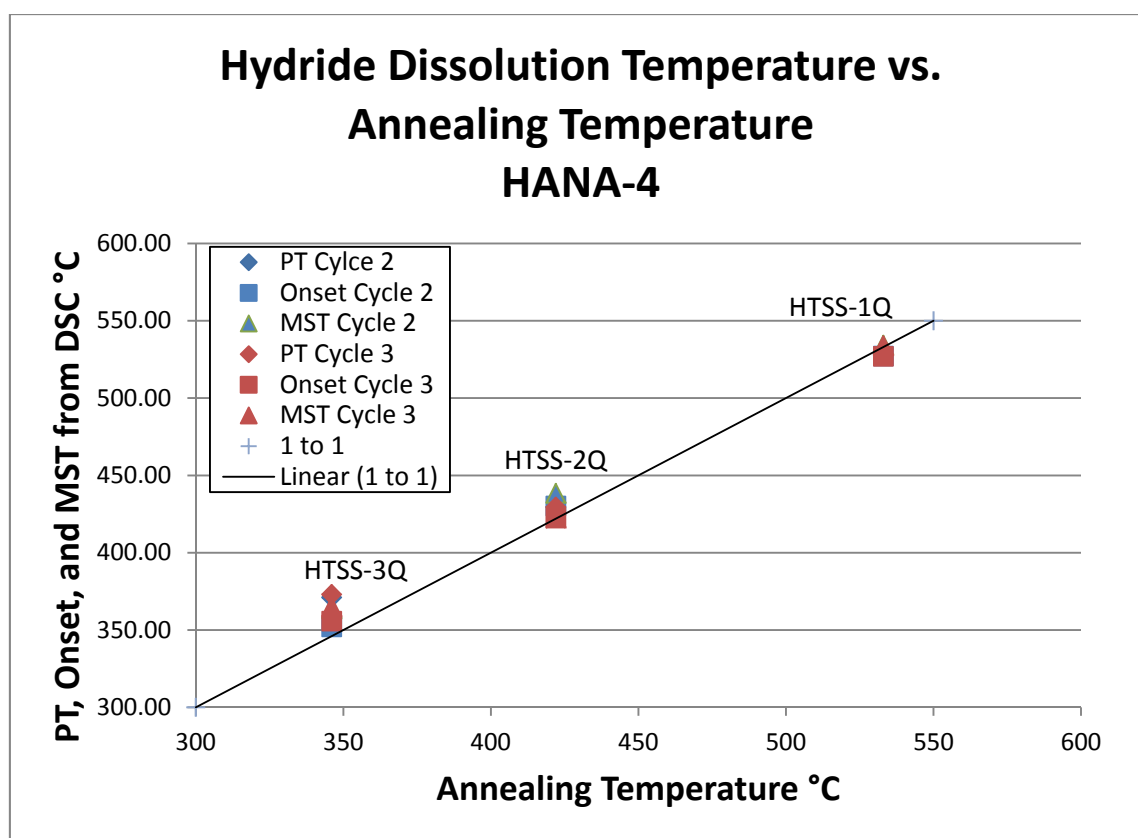
Fig. 5.1 HANA-4: Measured PT, Onset, and MST. Potential hydride dissolution peaks.

The plot shows a good agreement between the proposed hydride dissolution temperature and the annealing temperature. However, after comparison to peaks measured in a hydrogen free reference, §4.4.2 Figures 4.20 – 4.23, peaks associated with the uncharged alloys were removed (Figure 5.2).
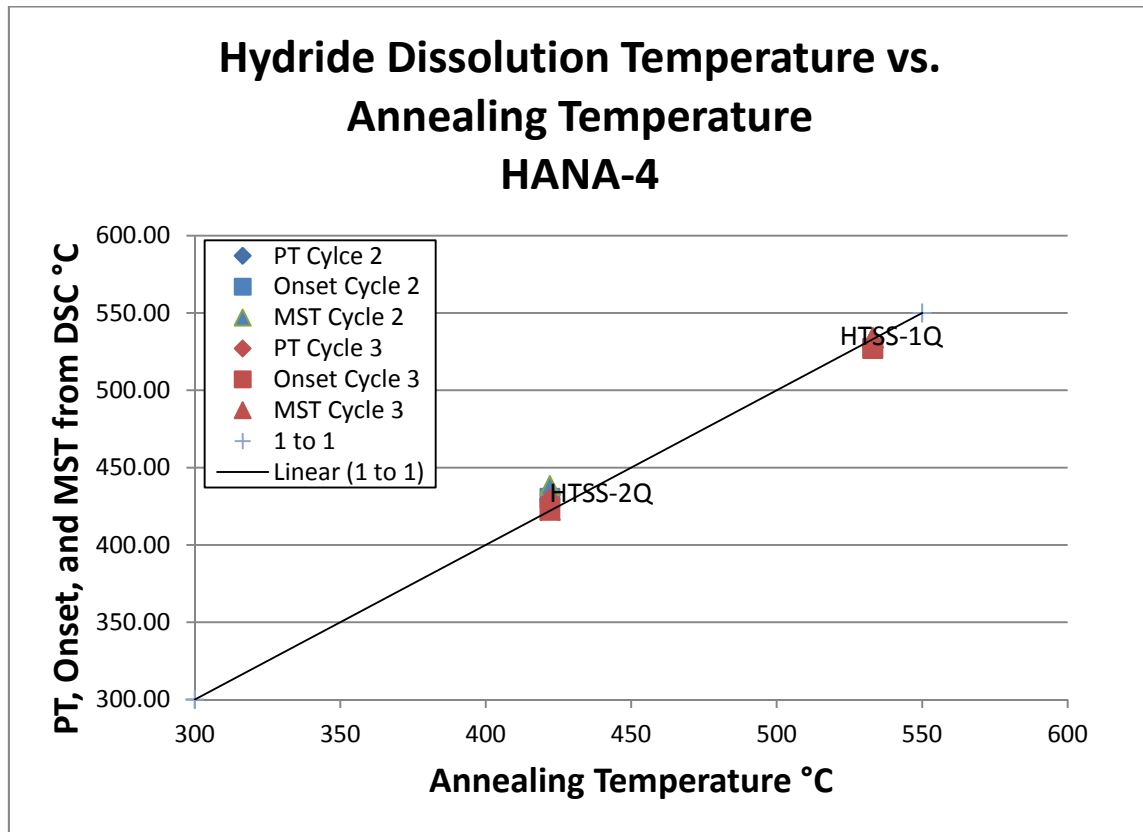
Fig. 5.2 HANA-4: Peaks attributable hydrogen dissolution.

Similarly, the potential hydride dissolution peaks observed in Zircaloy-4 are plotted against the annealing temperature (Figure 5.3), then peaks associated with the hydrogen free reference are removed (Figure 5.4).
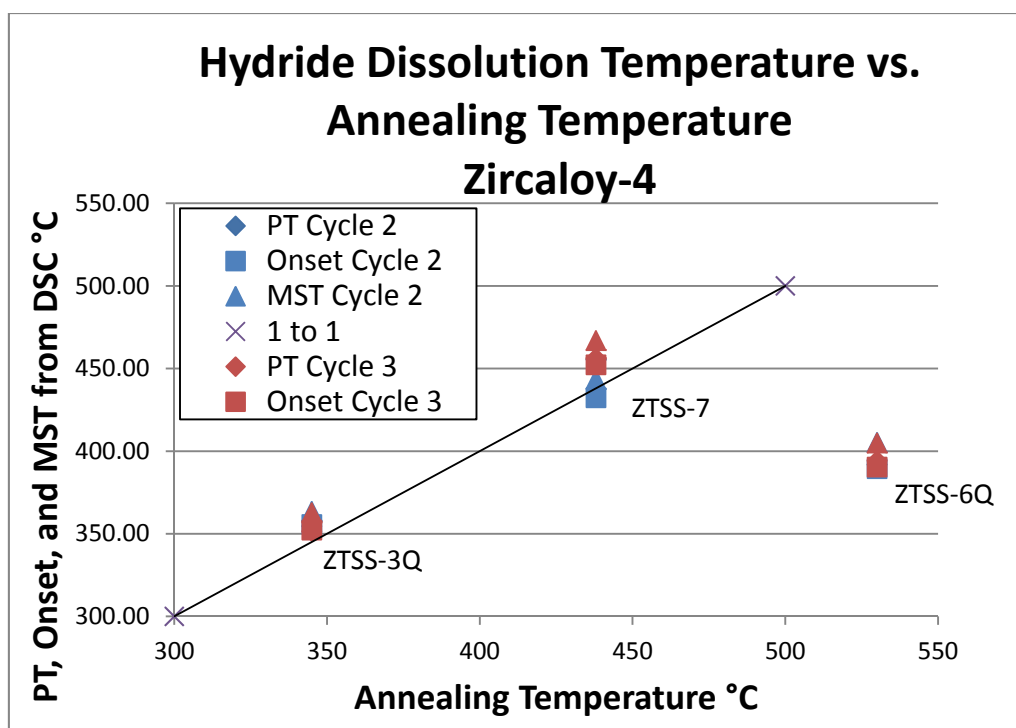
Fig. 5.3 Zircaloy-4: Measured PT, Onset, and MST. Potential hydride dissolution peaks.
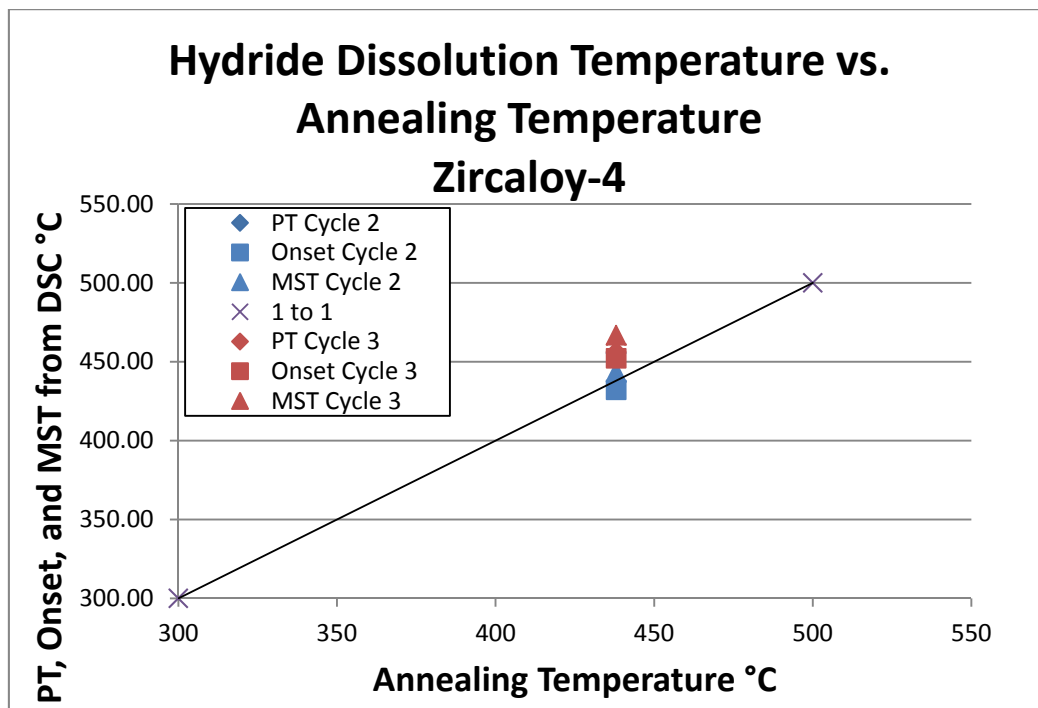
Fig. 5.4 Zircaloy-4: Peaks attributable hydrogen dissolution.

In ZTSS-6Q, which was annealed at 530 °C, the last peak is located near 390 °C. No peak corresponding to the annealing temperature is present. The last peak in this sample starts down at 359 °C (onset temperature) and levels off at 389 °C. This is similar to what is seen in HTSS-0Q and ZTSS-0Q, the as received reference samples. As would be expected, given their appearance in the reference samples, these features are present in all other samples. The feature is incomplete in HTSS-3Q and ZTSS-3Q, as the temperature program only went to 380 °C; short of the turning point at 400 °C. Sample HTSS-1Q does not have the sharp drop at 350 °C, but there are inflections in the curve at 353 °C and 400 °C, matching the behavior of the other samples. Therefore, although the dip at 355 °C corresponds to the annealing temperature of 345 °C used for HTSS-3Q and ZTSS-3Q, its appearance in all the samples, especially the as received references, is indicative of something intrinsic to the system, independent of hydrogen concentration and alloy. It is unclear to this author what this feature may represent. It is present in both alloys in the charged and uncharged condition, but seems absent in the work of other researchers K. Une *et al*, [18]. A complete list of onset temperatures for all features observed during heating and cooling is given in Appendix C, Table C.1 and Table C.2. The average onset temperatures of features, in each sample, that are not seen in the hydrogen free references are listed in Table 5.1. Table 5.1 excludes features that were only present in one cycle during heating.

Table 5.1   Average Onset Temperatures of Hydrogen Bearing Samples: Heating (°C)

HTSS-1Q	476	495	528
HTSS-2Q	427		
HTSS-3Q			
ZTSS-6Q	266		
ZTSS-7Q	262	442	
ZTSS-3Q	274	322	

Thermal analysis is a difficult technique to master [84, 85]. Though every attempt at care was made with these measurements, the results proved inconclusive. The importance of establishing a baseline for the system cannot be overstated [84, 85]. The difficulty with the Netzsch measurements was the manner in which the signal was dominated by the baseline behavior of the system. The baseline behavior of the system should be thoroughly recorded for each temperature profile using hydrogen free reference samples within 1 mg of the hydrided sample mass. It may be necessary to place such a hydrogen free reference in the reference sample cup, as reported by Khatamian [23] and Vizcaino *et al* [20]. This was attempted once using the Netzsch instrument, but the result proved inconclusive. However, it may help hydride peaks stand out if the difference in temperature between the two samples is due entirely to the presence of hydride in the sample.

Additionally, greater care should be taken to remove oxide layers formed on samples during previous heating runs. As noted in Gmelin and Sarge [85], oxide layers must be removed prior to measurement in metal samples. While the post annealing oxide layer was removed on samples before DSC measurement in the Netzsch, removal of any post measurement oxide was not attempted prior to measurement with the TA Q600 instrument.

6.0 Summary and Recommendations

Zircaloy-4 and HANA-4 were successfully charged with hydrogen through low temperature cathodic charging. Enough hydrogen was inserted through cathodic charging to create samples with hydrogen concentrations up to 860 wppm in Zircaloy-4 and 1600 wppm in HANA-4. These concentrations are consistent with cladding from high burn up fuel, C_H 300 – 800 wppm, where C_H is hydrogen concentration. The charged specimens were annealed to create specimens with uniform bulk-hydrogen concentrations and hydride morphology. Annealing was carried out at 540 °C, 450 °C, and 350 °C, resulting in a range of bulk hydrogen concentrations, within the range of interest for nuclear fuel cladding in reactor and during dry storage.

During each phase of sample development, hydride morphology and hydride phases were characterized through back scattered electron imaging and x-ray diffraction. Hydride dissolution measurements, via differential scanning calorimetry, proved inconclusive, though there appeared to be a correlation between observed features and the annealing temperature in some specimens, in other specimens the observed features could not be distinguished from features in the uncharged alloys.

A continuation of this effort requires the completion of the TSS measurements in HANA-4 and Zircaloy-4. The low temperature cathodic-charging system (LCS) has been shown to effectively insert hydrogen. Hydrogen charged zirconium alloy specimens are foundational to studying the impacts of hydrogen on zirconium alloys. Future work from this project could include the following.

1. Completion of the terminal solid solubility of hydrogen in HANA-4 and Zircaloy-4. To complete a measurement of TSS, the hydrogen concentrations of the DSC samples must be determined. Hydrogen concentration measurements are difficult with small sample sizes. IMR test labs required 2 g of material for hydrogen content analysis, and another lab required 6 g. With DSC coupons on the order of 50 mg or less, it is necessary to find a facility or instrument capable of measuring hydrogen in small samples.

2. The geometric difference between alloys should be removed. While it did not prevent charging, this additional variable made it difficult to determine the cause of differences in the materials charging behavior.

3. The low temperature cathodic charging system (LCS), would benefit from modifying or replacing the current level switch probe; in order to make the level control more reliable. The difference in rim thickness between the Zircaloy-4 samples is likely due to dilution of the electrolyte during the charging of Zr4H-3. This dilution resulted from a malfunction in the level switch probe, which caused the pump overfill the reaction vessel. The probe was also prone to shorting the level switch circuit by making contact with the sample. In such situations, the electrolyte level was depleted, due to evaporation.

REFERENCES

[1] B. Cox, R. Peter, Hydriding Mechanisms and Impact on Fuel Performance, ZIRAT, Advanced Nuclear Technology, Uppsala Sweden, 2000.

[2] Delayed Hydride Cracking in Zirconium Alloys in Pressure Tube Nuclear Reactors, International Atomic Energy Agency, Vienna, 2004.

[3] Delayed Hydride Cracking of Zirconium Alloy Fuel Cladding, International Atomic Energy Agency, Vienna, 2010.

[4] R.E. Einziger, H. Tsai, M. Billone, B.A. Hilton, Examination of spent PWR fuel rods after 15 years in dry storage, NUREG, Division of Systems Analysis and Regulatory Effectiveness, Office of Nuclear Regulatory Research, U.S. Nuclear Regulatory Commission, Washington, D.C., 2003.

[5] D.B. Rigby, Evaluation of the Technical Basis for Extended Dry Storage and Transportation of Used Nuclear Fuel, U.S. Nuclear Waste Technical Review Board, Washington D.C., 2010.

[6] M.A. McKinnon, M.E. Cunningham, Dry Storage Demonstration for High-Burnup Spent Nuclear Fuel-Feasibility Study., Pacific Northwest National Laboratory, Richland, WA, 2003, p. 112.

[7] K.W. Song, Y.H. Jeong, K.S. Kim, J.G. Bang, T.H. Chun, H.K. Kim, K.N. Song, Nuclear Engineering and Technology 40 (2008) 21-36.

[8] D. Khatamian, Z.L. Pan, M.P. Puls, C.D. Cann, Journal of Alloys and Compounds 231 (1995) 488-493.

[9] M. Billone, Y. Yan, T. Burtseva, R.S. Daum, Cladding Embrittlement During Postulated Loss-of-Coolant Accidents
NUREG/CR-6967, Office of Nuclear Regulatory Research, U.S. Nuclear Regulatory Commision, Argonne National Laboratory, 9700 South Cass Avenue, Argonne, IL 60439, 2008.

[10] C.L. Whitmarsh, Review of Zircaloy-2 and Zircaloy-4 Properties Relevant to N.S. Savannah Reactor Design, U.S. Atomic Energy Commission, Washington D.C., 1962.

[11] R. Krishnan, M.K. Asundi, Indian Academy of Sciences 4 (1981) 41-56.

[12] Waterside Corrosion of Zirconium Alloys in Nuclear Power Plants, International Atomic Energy Agency, Vienna, Austria, 1998.

[13] D. Khatamian, J.H. Root, Journal of Nuclear Materials 372 (2008) 106-113.

[14] J.J. Kearns, Journal of Nuclear Materials 22 (1967) 292-303.

[15] R.S. Daum, Hydride-Induced Embrittlement of Zircaloy-4 Cladding Under Plane-Strain Tension, Materials Science, vol Ph.D, Pennsylvannia State University, 2007.

[16] R.N. Singh, R. Kishore, S.S. Singh, T.K. Sinha, B.P. Kashyap, Journal of Nuclear Materials 325 (2004) 26-33.

[17] S.-J. Min, J.-J. Won, K.-T. Kim, Journal of Nuclear Materials.

[18] K. Une, S. Ishimoto, Y. Etoh, K. Ito, K. Ogata, T. Baba, K. Kamimura, Y. Kobayashi, Journal of Nuclear Materials 389 (2009) 127-136.

[19] S. Yamanaka, M. Miyake, M. Katsura, Journal of Nuclear Materials 247 (1997) 315-321.

[20] P. Vizcaíno, A.D. Banchik, J.P. Abriata, Journal of Nuclear Materials 304 (2002) 96-106.

[21] J.H. Baek, Y.H. Jeong, Journal of Nuclear Materials 361 (2007) 30-40.

[22] Behaviour of high corrosion resistance Zr-based alloys, Proceedings of a Technical Meeting on the State of the Art in Zirconium Alloys Development, Buenos Aires, Argentina, 2005, p. 200.

[23] D. Khatamian, Journal of Nuclear Materials 405 (2010) 171-176.

[24] K. Une, S. Ishimoto, Journal of Nuclear Materials 322 (2003) 66-72.
[25] R.S. Daum, Y.S. Chu, A.T. Motta, Journal of Nuclear Materials 392 (2009) 453-463.
[26] L. Lanzani, M. Ruch, Journal of Nuclear Materials 324 (2004) 165-176.
[27] W.M. Small, J.H. Root, D. Khatamian, Journal of Nuclear Materials 256 (1998) 102-107.
[28] E. Zuzek, J.P. Abriata, Bulletin of Alloy Phase Diagrams 11 (1990) 11.
[29] J.S. Bradbrook, G.W. Lorimer, N. Ridley, Journal of Nuclear Materials 42 (1972) 142-160.
[30] M.P. Puls, The Effect of Hydrogen and Hydrides on the Integrity of Zirconium Alloy Components: Delayed Hydride Cracking, Springer London, 2012.
[31] B.A. Cheadle, S.A. Aldridge, Journal of Nuclear Materials 47 (1973) 255-258.
[32] D. Khatamian, Journal of Alloys and Compounds 293–295 (1999) 893-899.
[33] D. Khatamian, Journal of Alloys and Compounds 356–357 (2003) 22-26.
[34] D. Khatamian, V.C. Ling, Journal of Alloys and Compounds 253–254 (1997) 162-166.
[35] B. Nath, G.W. Lorimer, N. Ridley, Journal of Nuclear Materials 58 (1975) 153-162.
[36] Z.L. Pan, I.G. Ritchie, M.P. Puls, Journal of Nuclear Materials 228 (1996) 227-237.
[37] A. McMinn, E.C. Darby, J.S. Schofield, The Terminal Solid Solubility of Hydrogen in Zirconium Alloys, in: G.P. Sabol, G.D. Moan (Eds.), Zirconium in the Nuclear Industry: Twelfth International Symposium, vol ASTM STP 1354, West Conshohocken, PA, 2000, pp. 173-195.
[38] M.P. Puls, Metallurgical Transactions A 21 (1990) 2905-2917.
[39] M.P. Puls, Journal of Nuclear Materials 399 (2010) 248-258.
[40] A.D. Lepage, W.A. Ferris, G.A. Ledoux, Procedure for Adding Hydrogen to Small Sections of Zirconium Alloys, Materials and Mechanics Branch, Chalk River Laboratories, Chalk River, Ontario, 1998.
[41] B. Cox, Journal of Alloys and Compounds 256 (1997) 244-246.
[42] P.A.C. Raynaud, A.S. Bielen, Cladding Hydrogen Based Regulations in the United States, Water Reactor Fuel Performance Meeting, United States Nuclear Regulatory Commission, Chengdu, China, 2011, p. 9.
[43] Y. Liu, Q. Peng, W. Zhao, H. Jiang, Materials Chemistry and Physics 110 (2008) 56-60.
[44] A.J. Parkinson, Hydride production in zircaloy-4 as a function of time and temperature, Texas A&M University, College Station, Texas, 2010.
[45] P. Vizcaino, P.C. Fagundez, A.D. Banick, Engineering 2 (2010) 573-579.
[46] E.D. Hindle, G.F. Slattery, Journal of the Institute of Metals 94 (1966) 245-249.
[47] J.T. John, P.K. De, H.S. Gadiyar, High Temperature Cathodic Charging of Hydrogen in Zirconium Alloys and Iron and Nickle Base Alloys, B.A.R.C External, Bhabha Atomic Research Centre, Bombay India, 1991.
[48] Y. Choi, J.W. Lee, Y.W. Lee, S.I. Hong, Journal of Nuclear Materials 245 (1998) 124-130.
[49] M.A. Martín-Rengel, F.J. Gómez Sánchez, J. Ruiz-Hervías, L. Caballero, A. Valiente, Journal of Nuclear Materials 429 (2012) 276-283.
[50] J. Wei, P. Frankel, M. Blat, A. Ambard, R.J. Comstock, L. Hallstadius, S. Lyon, R.A. Cottis, M. Preuss, Corrosion Engineering, Science and Technology 47 (2012) 516-528.
[51] J.J. Kearns, Journal of Nuclear Materials 43 (1972) 330-338.
[52] J.J. Kearns, Journal of Nuclear Materials 27 (1968) 64-72.
[53] K.B. Colas, A.T. Motta, M.R. Daymond, M. Kerr, J.D. Almer, S.W. Dean, Journal of ASTM International 8 (2011) 103033.
[54] M.P. Puls, S.-Q. Shi, J. Rabier, Journal of Nuclear Materials 336 (2005) 73-80.
[55] J.J. Kearns, C.R. Woods, Journal of Nuclear Materials 20 (1966) 241-261.
[56] H.-G. Kim, I.-H. Kim, B.-K. Choi, J.-Y. Park, Y.-H. Jeong, K.-T. Kim, Corrosion Science 52 (2010) 3162-3167.

[57] A. Strassar, R. Adamson, F. Gararolli, The Effect of Hydrogen on Zirconium Alloys Properties, ZIRAT, vol I, Advanced Nuclear Technology International, Skultuna, Sweden, 2008.

[58] R.S. Daum, S. Majumdar, Y. Liu, M. Billone, Journal of Nuclear Science and Technology 43 (2006) 1054-1067.

[59] S.-J. Min, J.-J. Won, K.-T. Kim, Journal of Nuclear Materials 448 (2014) 172-183.

[60] Interim Staff Guidance-11 Revision 3 Cladding Considerations for the Transportation and Storage of Spent Fuel, Nuclear Regulatory Commission, Washington, DC, 2003.

[61] G.A. McRae, C.E. Coleman, B.W. Leitch, Journal of Nuclear Materials 396 (2010) 130-143.

[62] M.P. Puls, Journal of Nuclear Materials 393 (2009) 350-367.

[63] Y.S. Kim, Materials Science and Engineering: A 490 (2008) 146-150.

[64] Y.S. Kim, S.B. Ahn, Y.M. Cheong, Journal of Alloys and Compounds 429 (2007) 221-226.

[65] Y.S. Kim, K.S. Kim, Y.M. Cheong, Journal of Nuclear Science and Technology 43 (2006) 1120-1127.

[66] Y.S. Kim, S.J. Kim, K.S. Im, Journal of Nuclear Materials 335 (2004) 387-396.

[67] S. Sagat, C.K. Chow, M.P. Puls, C.E. Coleman, Journal of Nuclear Materials 279 (2000) 107-117.

[68] D.A. Scarth, E. Smith, Modelling Delayed Hydride Cracking in Zirconium Alloys, in: B.L. Karihaloo (Ed.) IUTAM Symposium on Analytical and Computational Fracture Mechanics of Non-Homogeneous Materials, vol 97, Springer Netherlands, 2002, pp. 155-165.

[69] A.A. Shmakov, B.A. Kalin, Y.G. Matvienko, R.N. Singh, P.K. De, Materials Science 40 (2004) 764-771.

[70] R.N. Singh, S. Roychowdhury, V.P. Sinha, T.K. Sinha, P.K. De, S. Banerjee, Materials Science and Engineering: A 374 (2004) 342-350.

[71] S.-Q. Shi, M.P. Puls, Advances in the Theory of Delayed Hydride Cracking in Zirconium Alloys, Materials and Mechanics Branch, Scientific Document Distribution Office, Chalk River, Ontario, Canada, 1994.

[72] Y. Choi, J.W. Lee, Y.W. Lee, S.I. Hong, Journal of Nuclear Materials 256 (1998) 124-130.

[73] H.-G. Kim, B.-K. Choi, S.-Y. Park, Y.-I. Jung, D.-J. Park, J.-Y. Park, Journal of Nuclear Materials 426 (2012) 173-181.

[74] J.-Y. Park, S.J. Yoo, B.-K. Choi, Y.H. Jeong, Journal of Alloys and Compounds 437 (2007) 274-279.

[75] J.-Y. Park, S.J. Yoo, B.-K. Choi, Y.H. Jeong, Journal of Nuclear Materials 373 (2008) 343-350.

[76] J. Wei, Effect of Hydrogen on the Corrosion Performance of Zirconium Alloys, School of Materials, Ph.D Dissertation, Manchester, 2012, p. 281.

[77] W.E. Berry, D.A. Vaughan, E.L. White, Corrosion 17 (1961) 109-117.

[78] S.H. Kuhr, An Electrolytic Method to Form Zirconium Hydride Phases in Zirconium Alloys with Morphologies Similar to Hydrides Formed in Used Nuclear Fuel, Texas A&M University, College Station, Texas, 2012.

[79] The Science Behind Materials Preparation, A Guide to Materials Preparation and Analysis, Buehler SUM-MET, United States, 2004.

[80] K.B. Colas, Kinetics of Zirconium Hydride Precipitation and Reorientation Studied Using Synchrotron Radiation, Mechanical and Nuclear Engineering, MS Thesis, Pennsylvania State University, State College, Pennsylvania, 2009.

[81] P.A.C. Raynaud, Crack Growth Through the Thickness of Thin Sheet Hydrided Zircaloy-4, Materials Science and Engineering, Ph.D Dissertation, Pennsylvania State University, State College Pennsylvania, 2009.

[82] H.E. Swanson, H.F. McMurdie, M.C. Morris, E.H. Evans, Standard X-ray Diffraction Powder Patterns: Section 5. Data for 80 Substances, NBS Monograph Series, U.S Department of Commerce. National Bureau of Standards, Washington, D.C, 1967.

[83] J.-Y. Park, B.-K. Choi, Y.H. Jeong, Special Issue on the Water Reactor Fuel Performance Meeting 2008 41 (2009).

[84] D. Chen, A. Green, D. Dollimore, Thermochimica Acta 284 (1996) 429-433.

[85] E. Gmelin, S.M. Sarge, Pure & Appl. Chem 67 (1995) 1789-1800.

[86] H. Zou, G.M. Hood, J.A. Roy, R.J. Schultz, J.A. Jackman, Journal of Nuclear Materials 210 (1994) 239-243.

[87] H. Zou, G.M. Hood, H. Nakajima, J.A. Roy, R.J. Schultz, Journal of Nuclear Materials 223 (1995) 186-188.

[88] R.L. Hervig, F.K. Mazdab, G. Moore, P.F. McMillan, Analyzing hydrogen (H2O) in silicate glass by secondary ion mass spectrometry and reflectance Fourier transform infrared spectroscopy, in: V. Benedetto De, J.B. Robert (Eds.), Developments in Volcanology, vol Volume 5, Elsevier, 2003, pp. 83-103.

Hydride Phase Behavior in Zircaloy: Simulated Rim Structure, Hydride Re-Orientation, Elastic Response, Particle Morphology, and Analysis of Thermal Cycling Behavior

Brent J. Heuser and Jun-Li Lin

University of Illinois

Introduction

Experimental activities related to hydrogen phase behavior in Zircaloy was performed across an extensive parameter space that included hydrogen concentration, *in situ* loading conditions, *ex situ* loading conditions, and hydride morphology. Our activities were focused on hydride re-orientation with a simulated hydride rim structure. The experimental investigations relied heavily upon X-ray diffraction using both synchrotron (the APS) and neutron sources (the SNS). In addition, small-angle neutron scattering has been used to study deuteride morphology.

General sample preparation for simulated hydride rim structure

Ni coating was used to facilitate hydrogen absorption from the gas phase and preferential hydride formation at the near surface (RIM structure). Ni coating was deposited via magnetron sputtering to ~1μm thickness at ambient temperature. The following procedure was used to prepare hydrogen-loaded Zy samples with near-surface hydride particles (RIM structure):

Polishing following the below recipe:

4-Step Method for Zirconium and Hafnium					
Surface	Abrasive/Size	Load lb. (N)/Specimen	Base Speed (RPM)	Relative Rotation*	Time
CarbiMet 2	320- (P400) Grit SiC (wax-coated)**	5 (22)	240-300	>>	Until Plane
UltraPad	9-μm MetaDi Supreme Diamond	5 (22)	150-200	><	5:00
Trident	3-μm MetaDi Supreme Diamond	5 (22)	120-180	>>	3:00
ChemoMet	0.02 – 0.06-μm MasterMet Silica	5 (22)	100-150	><	7:00

*>> = Complimentary (platen and specimen holder rotate in the same direction)
 >< = Contra (platen and specimen holder rotate in opposite directions)
**Rub candle wax lightly across the rotating disc prior to grinding

Hydrogen loading from the gas phase was measured using a Sievert's apparatus at 400 ˚C. Two hydrogen pressure versus time plots are shown in Figure bjh1. The kinetics of hydrogen absorption are far superior to those without Ni coating (not shown), are reproducible, and consistently require approximately one hour to reach equilibrium.
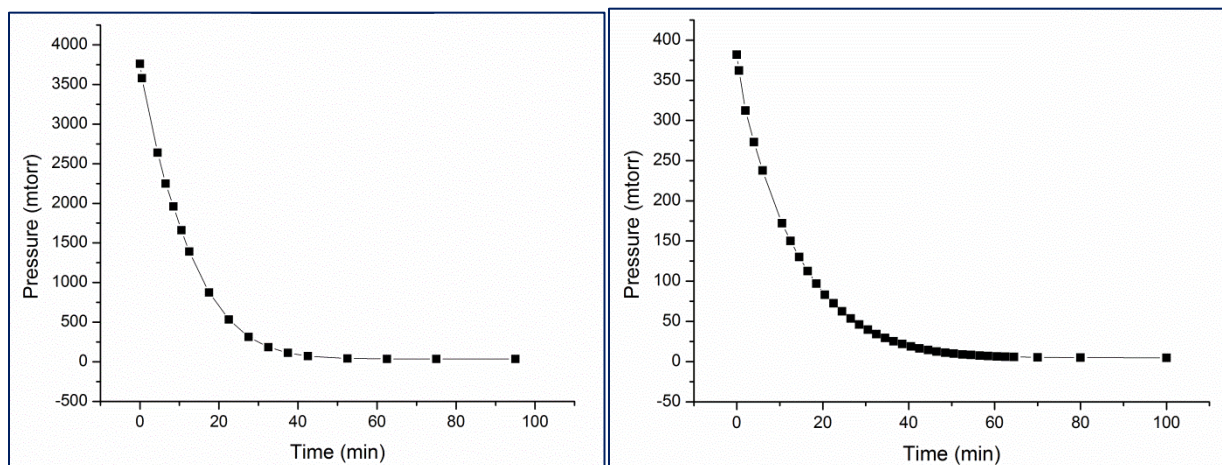
Figure bjh1. Hydrogen gas pressure change in constant volume versus time for Z-4 samples 24+26 (LHS) and 27 (RHS). The bulk hydrogen concentration is 500 and 100 wppm, respectively, corresponding to $ZrH_{0.05}$ and $ZrH_{0.01}$, respectively.

Neutron Diffraction using the VULCAN Instrument

In situ neutron diffraction measurements have been performed using the SNS VULCAN instrument. Applied loads at temperature were used to study the response of the Zr-D system with a simulated rim structure. The experimental setup is shown in Figure bjh 2. Samples were slowly cooled from 400 ºC to the room temperature with the rate of 1 ºC/min. A 80 MPa tensile load was applied along the rolling direction.

The deuterium concentration of the sample with data shown in Figure bjh3 was 1054 wppm. Reitveld refinement was applied to obtain evolution of the weight fraction and the lattice parameter of each phase (δ-deuteride and zirconium). The precipitation activation energy (Q) could be estimated by plotting the concentration of deuterium in the solid solution versus the temperature then fit with the classic exponential equation. The measured Q is ~24k J/mol and ~22k J/mol in the RD and the ND, respectively. Considering the uncertainty of the Q is ~5k J/mol, the measured Q is nearly identical between the two directions. This Q value is also close to the published values where no load was applied, implying that the load has very limited effect on the Q.

Using offset method on a lattice strain evolution curve is used to quantify the starting temperature of the phase transformation, which is also known as the TSSP in a case of cooling in Figure bjh4. A linear line is draw parallel to the linear thermal expansion line then offset by the amount of measured uncertainty. The intersection between the offset line and the data curve is then determined as the transition temperature. The measured TSSP is ~320 ºC (Known TSSP without stress ~ 450 ºC). This might indicate that the external stress decreases the TSSP. However this value should be treated cautiously due to large temperature range covered by one neutron data point.
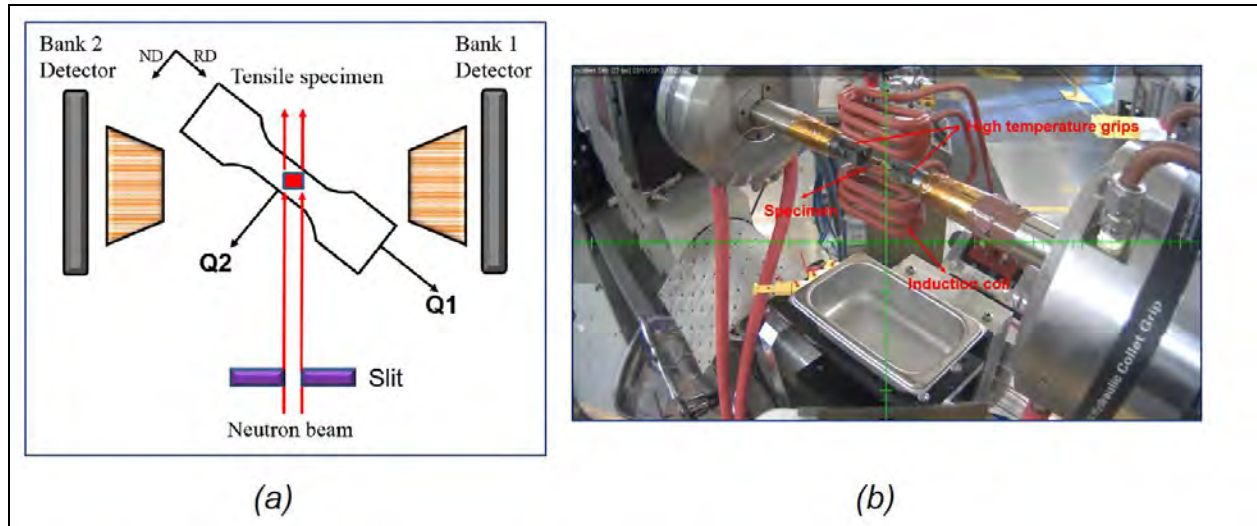
Figure bjh2. (left) Schematic representation of the detector geometry of the VULCAN instrument. The reflection of lattice planes which have normal directions parallel and perpendicular to the load direction are recorded by Bank 1and Bank 2, respectively and (right) experimental setup in VULCAN instrument with induction coil *in situ* heating.
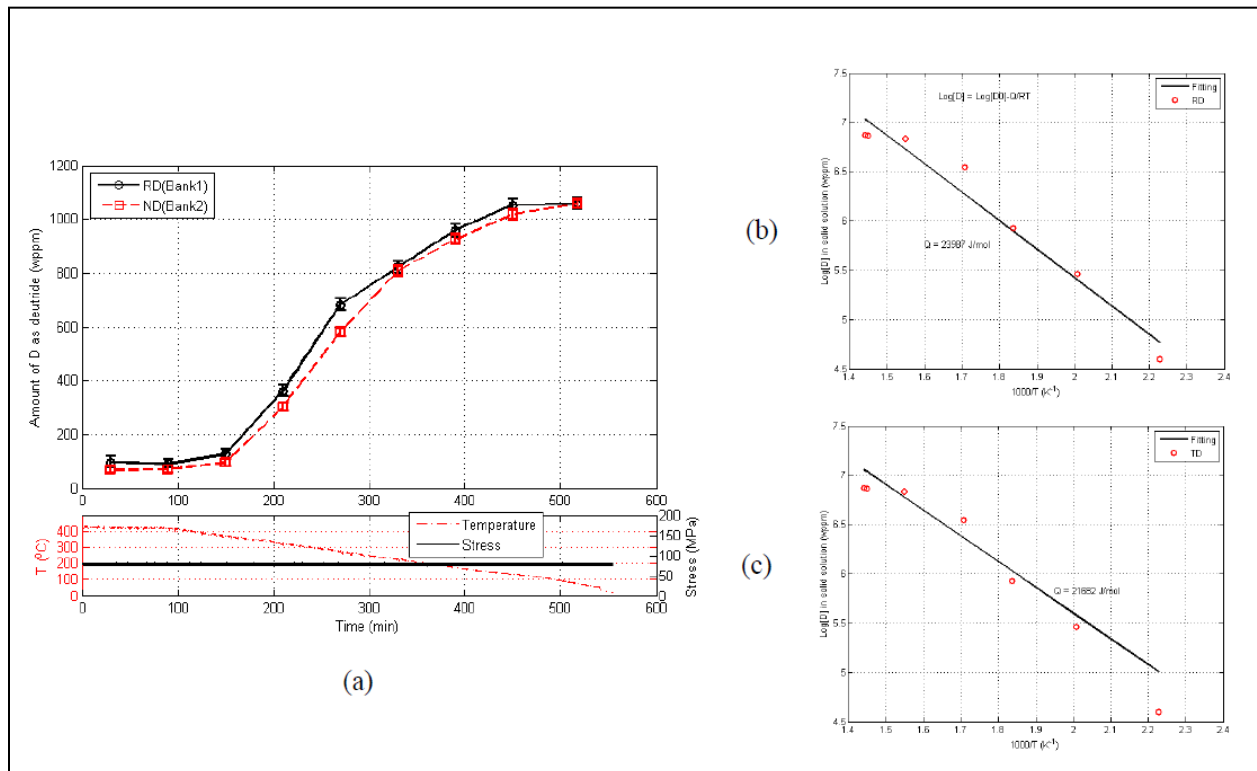
Figure bjh3.   Evolution of the phase fraction in the (a) deuteride and in (b,c) the solid solution. The behaviour can be fitted to a classical exponential equation. The obtained Q is similar to published values where no stress was applied.
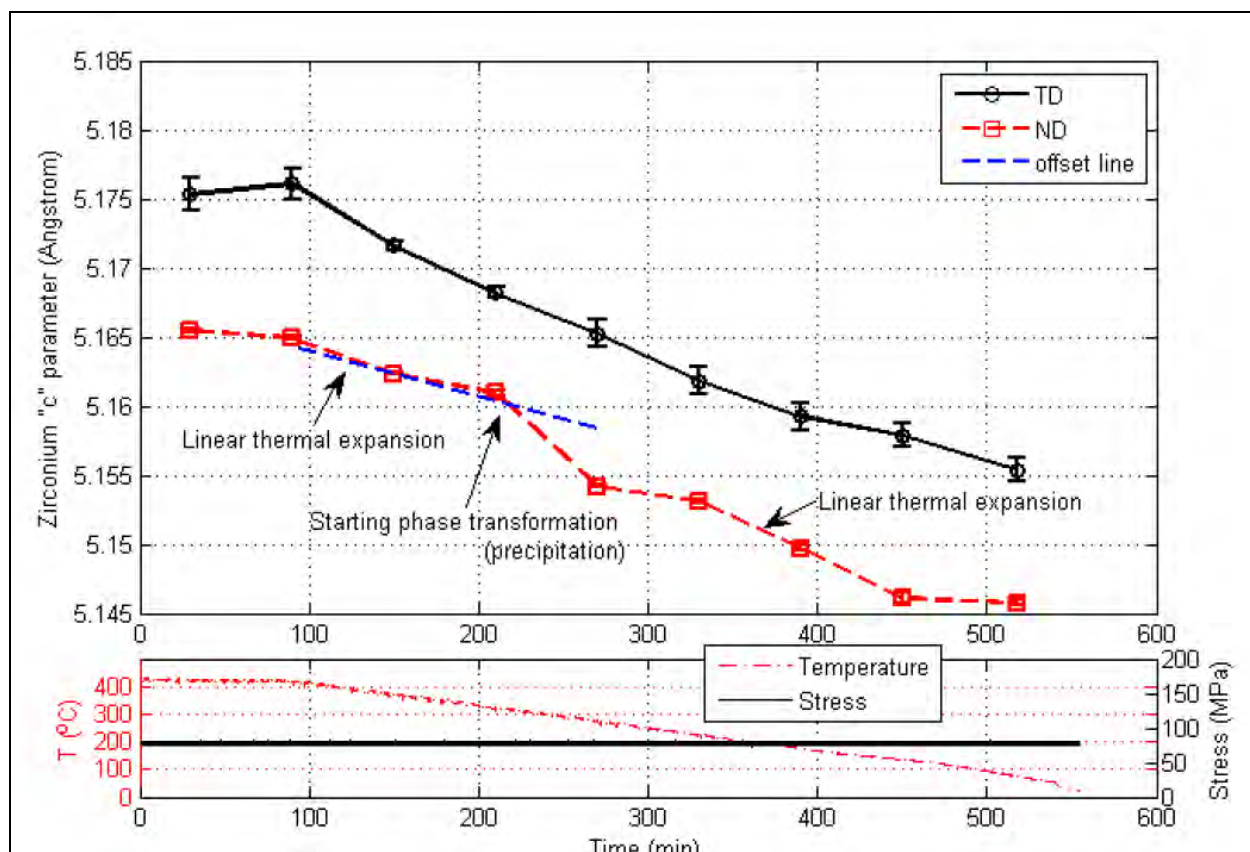
Figure bjh4. Evolution of the c lattice parameter during the ramping. An offset method was used to determine the TSSP. Because most of the Zr grains have basal plane oriented close to the ND, the effect of phase transformation on the lattice strain is therefore more pronounced in the ND.

Thermal cycling under a constant applied load was studied as well; these results are shown in Figure bjh5. This is a different sample from slowly cooling test, but with identical deuterium concentration (1054 wppm deuterium) and was thermal cycled between 420 ºC and 120 ºC with an applied tensile load of 90 MPa tensile load along the TD. Since the hydride morphology is a plate and will generate lattice strain, the largest induced compressive stresses are in the long axis direction of the plate (the in-plane direction), causing the smallest lattice parameter in this direction. Therefore, the continually increase of the lattice spacing in the TD and the decrease in the ND might indicate hydride reorientation during the cycling.
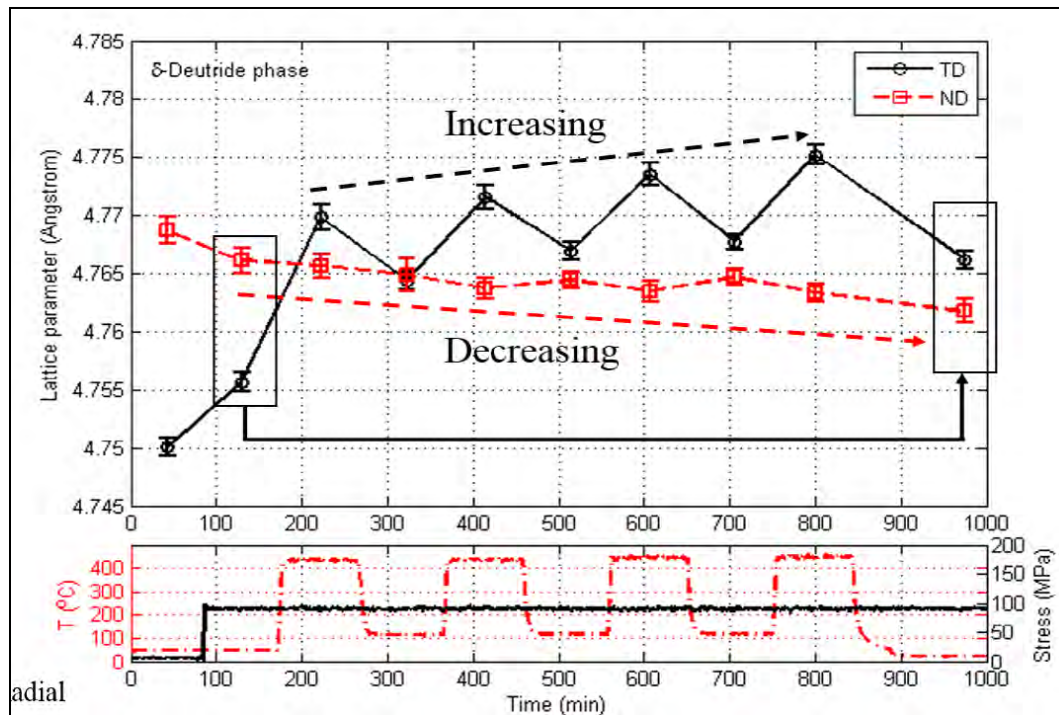
Figure bjh5. Evolution of the deuteride lattice parameter during thermal cycling.

Analysis of *In Situ* Thermal Cycling (Synchrotron XRD)

Theoretically, lattice strain response of the Zr phase is a combination of several sources: thermal + external load + H in solid solution + hydride. Pure lattice transformation model is commonly used to describe strain induced by the precipitation of hydride. A simple model which includes these strain sources successfully predicts the evolution of Zr a-axis strain. However, the model overestimates the strain evolution of the c-axis. The application of this model is shown in Figure bjh6.
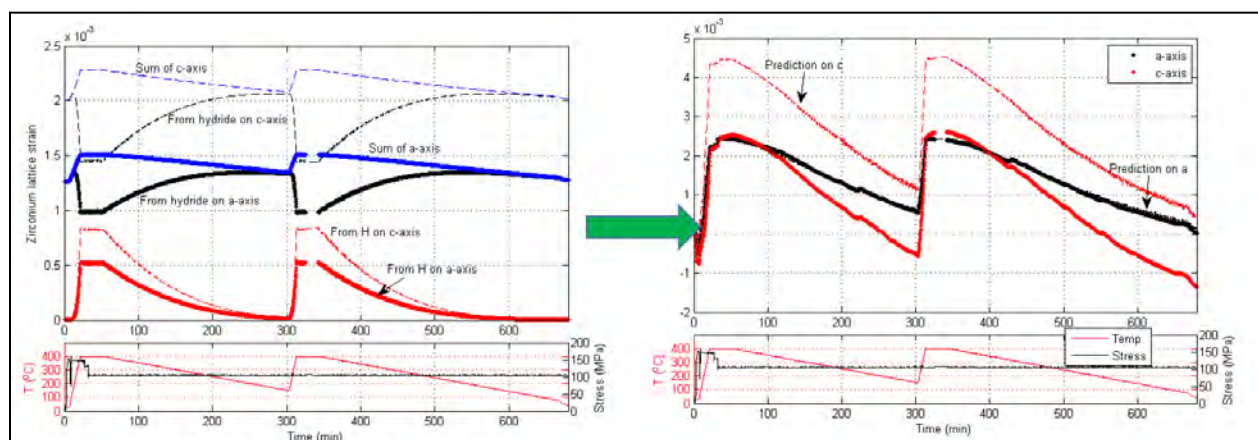
Figure bjh6. (left) Evolution of lattice strain induced by H in solid solution and hydride precipitation during the cycle and (right) Evolution of the Zr-matrix lattice strain data during the cycle, as well plotted is the lattice strain calculated by the model (dashed line).

Appendix bjh1—Publication of Synchrotron XRD Experiment and Analysis

Study of the mechanical behavior of the hydride blister/rim structure in Zircaloy-4 using *in-situ* synchrotron X-ray diffraction

Jun-li Lin [a], Xiaochun Han [a], Brent J. Heuser [a, *], Jonathan D. Almer [b]

[a] Department of Nuclear, Plasma, and Radiological Engineering, University of Illinois at Urbana-Champaign, Urbana, IL, USA
[b] Advanced Photon Source, Argonne National Laboratory, Argonne, IL, USA

ABSTRACT

High-energy synchrotron X-ray diffraction was utilized to study the mechanical response of the f.c.c δ hydride phase, the intermetallic precipitation with hexagonal *C14* lave phase and the α-Zr phase in the Zircaloy-4 materials with a hydride rim/blister structure near one surface of the material during *in-situ* uniaxial tension experiment at 200 °C. The f.c.c δ was the only hydride phase observed in the rim/blister structure. The conventional Rietveld refinement was applied to measure the macro-strain equivalent response of the three phases. Two regions were delineated in the applied load versus lattice strain measurement: a linear elastic strain region and region that exhibited load partitioning. Load partitioning was quantified by von Mises analysis. The three phases were observed to have similar elastic modulus at 200 °C.

© 2016 Elsevier B.V. All rights reserved.

NOTE: Pages 235 through 243 were extracted from the final report. Please refer to the journal article above to review the deleted information.

Appendix bjh2—Poster for the 2016 Zirconium in the Nuclear Industry Conference (poster was selected as a finalist for Best Poster award).
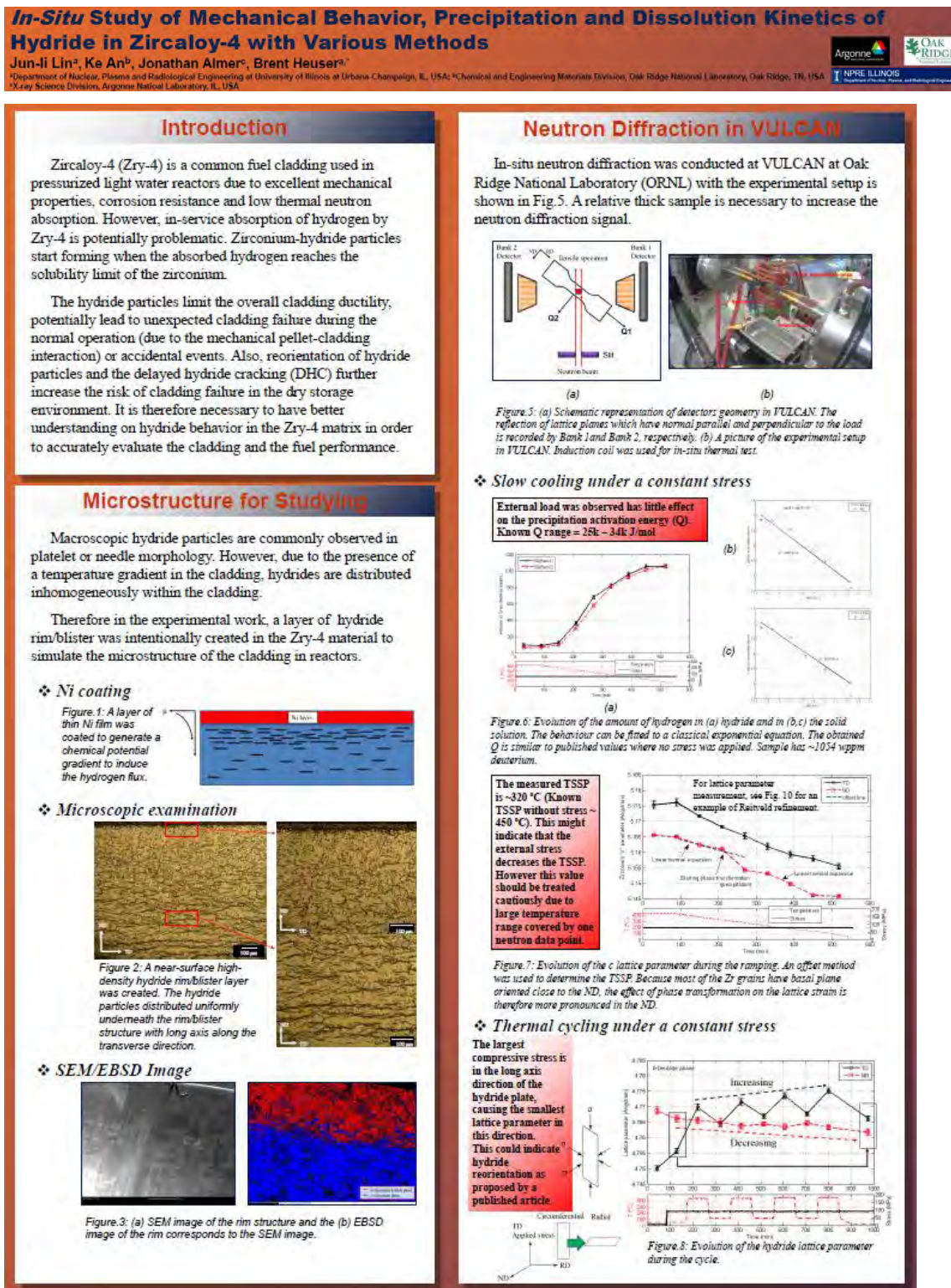
Synchrotron Diffraction in APS 1-ID

Synchrotron diffraction is a powerful tool for minor phase characterization. For the case of hydride study, synchrotron source in Advanced Photon Source can detect hydride with concentration as low as 17 wppm.

Figure 9: Synchrotron experiment setup at beam 1-ID at APS in Argonne National Lab.
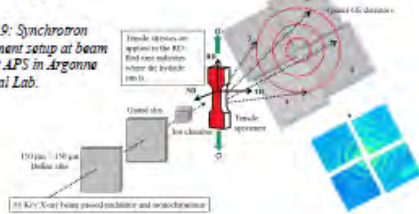
❖ Mechanical behavior when loaded

Diffraction data were extracted along two relevant directions: TD and RD. RD represents strain along the loading direction while TD contains information of Poisson's effect. Reitveld refinement was performed to obtain macroscopic representative strain after been carefully assessed

Reitveld fitting
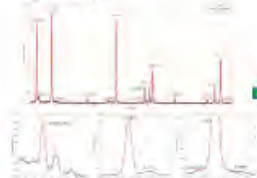
Lattice strain

Figure 10: Reitveld fitting on whole spectrum. Also shown are the resolvable hydride and second phase particles peaks.
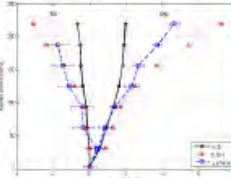
Figure 11: Lattice strain evolution as a function of applied stress for sample with 997 wppm hydrogen.

Rietveld refinement is necessary if the goal is to measure bulk representative strain. Full detail can be found in J. Lin et al. J. Nucl. Mater., 471 (2016), 299-307.
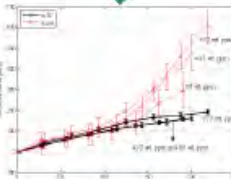
Figure 12: Evolution of von Mises stress as a function of applied stress in Zr and Zr-hydride phases.

❖ Thermal cycling under a constant stress

Strain response of the Zr phase is now a combination of several sources – thermal + external load + H in solid solution + hydride. Pure lattice transformation model is commonly used to describe strain induced by the precipitation of hydride.
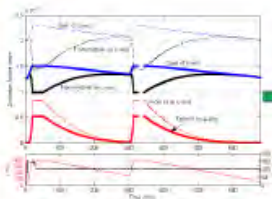
Figure 13: Evolution of strain induced by H and hydride during the cycle.
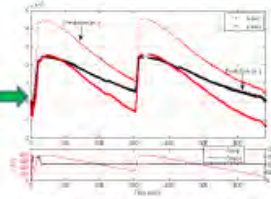
Figure 14: Evolution of the Zr-matrix strain during the cycle.

A simple model which includes several strain sources successfully predict the evolution of Zr a-axis strain while thermal cycled. However, the model overestimated the strain evolution of the c-axis.

Hyrax – Phase Field Simulation

Phase field model is a powerful tool for simulating variety of material processes. Generally saying, the evolution driving force is to reduce the total free energy of the system.

Hyrax is created by Dr. Jokisaari and Dr. Thornton from the University of Michigan. Please see report of CASL-U-2013-0346-000 for more details.
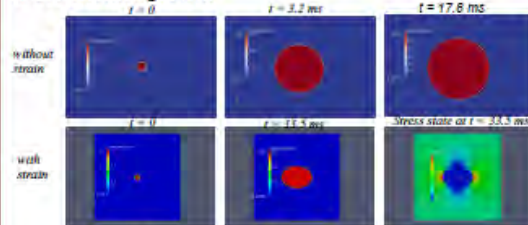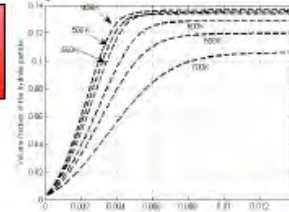
❖ Isothermal growth

Figure 15: Evolution of a single hydride particle in a zirconium matrix with supersaturated hydrogen concentration at 600k.

The growth rate increases as the increase of temperature. Also observed is that more hydrogen remains in the solid solution at high temperature.

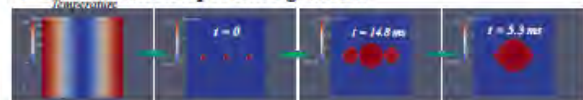### ❖ Growth with temperature gradient

Figure 16: Evolution of single hydride particle in a zirconium matrix with supersaturated hydrogen and non-uniform temperature distribution.

Conclusion

- The hydride in the blister/rim structure has similar texture relationship with the Zr as the uniformly distributed hydrides. The δ is the only hydride phase observed in the rim.

- The load partitioning between the hydride and the Zr phase was observed, which can be quantified using Reitveld analysis and von Mises equation.

- From the experimental observation, the external stress decreases the TSSP of the hydride phase in the Zircaloy.

- From the thermal cycle experiment, the c-axis was observed to have smaller strain than the a-axis, which is controversial to most of the studies that show anisotropic strain is usually higher on the c.

Acknowledgement

Appendix bjh3—SANS Analysis of Deuteride Stability (manuscript submitted to J. Applied Crystallography, June 2016).

Small-Angle Neutron Scattering Measurements δ-Phase Deuteride (Hydride) Particle Stability in Zircaloy 4

Brent J. Heuser and Jun-Li Lin

University of Illinois at Urbana-Champaign

Department of Nuclear, Radiological and Plasma Engineering

Urbana, IL 61801 USA

Changwoo Do

Biology and Soft Matter Division

Neutron Sciences Directorate

Oak Ridge National Laboratory

Oak Ridge, TN 37831 USA

Small-angle neutron scattering (SANS) measurements have been performed under ambient conditions to investigate deuteride (hydride) particle stability in Zircaloy 4, a fuel cladding material used in pressurized light-water nuclear reactors. Hydrogen pickup by the cladding leads to a rim structure in which large circumferential hydride plate-like particles preferentially form on the cooler water-side region of the cladding. We simulate this rim structure and substitute deuterium to increase the coherent response and decrease the incoherent background. Four bulk deuterium concentrations were investigated, 100, 400, 500, and 1000 parts per million by weight (wppm) deuterium, as well as zero-concentration reference sample. The SANS response from the deuteride phase was observed at all concentration values. The effect of *ex situ* applied stress at elevated temperature on deuteride phase stability was investigated in the 400 and 1000 wppm samples. The SANS response of all samples, including the reference sample, consisted of strong Porod scattering plus an incoherent background over the entire measured Q range (0.005 to 0.4 Å^{-1}). Anisotropic Porod scattering was observed at concentrations greater than 100 wppm and was especially strong at 1000 wppm. Evidence of hydride reorientation along the applied load direction was observed 400 wppm during isothermal static loading at 200 ºC.

1

Introduction

Zirconium-based alloys are used as fuel cladding in light water nuclear reactors (LWRs) throughout the world. The cladding must maintain adequate strength and ductility to prevent rupture during in-core service, post-service pool storage, and long-term dry cask storage. LWR cladding undergoes radiation hardening and embrittlement during service and experiences significant tensile hoop stress evolution due to fission gas release from the fuel and from fuel swelling leading to mechanical contact. In addition, a water-side oxide layer and large circumferential hydride platelets form in the Zr matrix (Lemaignan and Motta, 1994; Sawatzky, 1960; Courty *et al.*, 2014). A temperature gradient exists within the cladding wall and preferential hydride precipitation occurs on the cooler water-side portion during in-service hydrogen pickup; this non-uniform distribution is known as a hydride rim structure. Radiation hardening, embrittlement, tensile hoop stress evolution, corrosion, and hydride formation all act to limit the service lifetime of the cladding.

An open fuel cycle is currently employed in the U.S., mandating long-term storage of used nuclear fuel for geological time periods of order 10^5 years. Mechanical integrity of the cladding against rupture must be sustained during this storage period. One mechanism that could potentially lead to post-service failure is delayed hydride cracking (DHC) resulting from hydride particle reorientation under tensile hoop stress (Kearns and Woods, 1966; Puls, 1990; Coleman, 1982; Kim, 2008; Puls, 2009). Hydride reorientation has been extensively studied in an effort to understand dependencies on stress, hydrogen concentration, and thermal history (Kearns and Woods, 1966; Singh *et al.*, 2004; Hong and Lee, 2005; Daum *et al.*, 2006; Desquines *et al.*, 2014). Technical specifications for drying procedures prior to dry-cask storage exist to mitigate hydride reorientation and potential DHC. In addition, newest class of Zr-based LWR cladding has been developed to limit corrosion and hydride formation during service (Bossis *et al.*, 2006; Billone *et al.*, 2008).

Hydride dissolution and precipitation as function of temperature and applied load is effectively studied *in situ* with synchrotron X-ray diffraction (XRD) at 3rd generation photon sources (Tulk *et al.*, 2012; Colas *et al.*, 2010; Zanellato *et al.*, 2012). High incident X-ray energy (~10^2 keV) results in appreciable transmission through samples with thickness up to 10^0 cm, enabling Laue geometry diffraction measurements. Furthermore, the high incident energy contracts reciprocal space and entire Debye-Scherer rings can be imaged with excellent solid angle resolution using pixelated two-dimensional area detectors. The quantification of hydride phase texture in the clad material (Daum *et al.*, 2009; Zanellato *et al.*, 2012) and the mechanical response of the Zr-hydride system, with both uniform (Kerr *et al.*, 2008) and non-uniform hydride distribution (Lin *et al.*, 2016), has been effectively studied by the synchrotron X-ray diffraction. Synchrotron X-ray diffraction was also applied to study the hydride reorientation in Zr-based alloys by many authors. For example, Colas *et al.* (2010) and Colas *et al.* (2013) studied the (111) peak line broadening of the δ-Zr hydride phase and correlated this to a strain broadening effect due to reorientation. Alvarez *et al.* (2012) suggested that hydride reorientation could be studied by d-spacing measurements of the δ(111) reflection along different orientations relative to the matrix, since radial hydrides (reoriented) and circumferential hydrides (non-reoriented) have different preferred growing directions.

2

The utility of XRD measurements using high-brilliance 3rd generation X-ray sources to study the hydride phase in Zr-alloys rests with adequate sensitivity to minor second phases with weak diffraction contrast. Small angle scattering techniques also transform real-space structure into reciprocal space, but with measured intensity at much small wavevector transfer values than wide-angle diffraction. Ensemble-averaged particle size, shape, and size distributions can be determined in the small-angle regime (Gerold and Kostorz, 1978; Glatter and Kratky, 1982; Heuser and Althauser, 1999). Small-angle X-ray scattering (SAXS) measurements of the hydride phase in Zircaloy are difficult, however, because of the weak contrast and more importantly strong Porod scattering from intermetallic second phase particles (SPPs). We know of no examples of SAXS applied to the study hydrides in Zircaloy in the published literature. The intermetallic SPPs in Zircaloy increase the strength and creep resistance of the matrix, both extremely important mechanical properties of LWR cladding. Accordingly, control of the SPP size distribution via thermo-mechanical processing used in fabrication is critical and proprietary. Characterization of SPP size distributions in Zircaloy using SAXS has been performed (Uno *et. al.*, 1996; Sen *et al.*, 2000; Srirangam *et al.*, 2014) and complements microscopy because of the inherent ensemble averaging.

Much stronger hydride particle-matrix contrast exists for neutron scattering techniques and small-angle neutron scattering (SANS), for example, finds application in the study of metal hydrides (Fong and Spooner, 1994; Heuser and Althauser, 1999; Chen and Heuser, 2001). The substitution of deuterium for hydrogen to increases the coherent foreground and decreases the incoherent background, facilitating SANS analysis of metal hydrogen (deuterium) systems. We present *ex situ* SANS measurements of Zircaloy 4 loaded with deuterium and placed under tensile stress at elevated temperature to investigate deuteride stability associated with hydride reorientation.

Experimental

Cold-work, stress relieved (CWSR) Zircaloy 4 (Zy4) was supplied by ATI Specialty Alloys and Components as β-quenched, 3mm thick rolled plate. This material had nominal Zy4 composition by weight (1.20−1.70 Sn, 0.18−0.24 Fe, 0.07−0.13 Cr, balance Zr and the total Fe+Cr composition of 0.28−0.37) as specified by ASTM Standard B353−12 (ASTM, 2012). Samples were double-side mechanically polished with the final step using a 0.05 μm silicon dioxide suspension. Deuterium loading and a simulated rim structure was facilitated by the deposition of a thin (~0.2 μm) Ni coating on both sides of the samples. The Ni coating enhances the near-surface deuterium chemical potential and results in reproducible time-pressure loading behavior. A Sieverts-type apparatus gas charging system (Chen and Heuser, 2000) was used to load the samples with deuterium by exposure to the gas phase at 400 ℃. Samples were cooled to ambient temperature at a rate of 1 ℃/minute to promote the precipitation of δ-deuteride particles (Bradbrook *et al*., 1972). The presence of the δ-hydride (deuteride) phase has confirmed with XRD (Lin *et al*., 2016) and optical microscopy presented below. Deuterium loading was performed with all samples under a stress-free environment. Overall deuterium concentration was determined from the total pressure change using the known sample mass and the ideal gas law (Chen and Heuser, 2000). A list of the samples investigated is given in Table 1. The sample identification nomenclature is: material−sample number−deuterium concentration in wppm−tensile stress value. This table contains sample gauge thickness, deuterium concentration values, and applied tensile stress conditions, as described below.

3

Cold-rolled Zy4 has a known texture in which two basal plane (0002) poles aligning ± 30–40º from the normal direction (ND) toward the transverse direction (TD) and residing in the ND-TD plane (Lemaignan and Motta, 1994). The texture of the as-received material used here was characterized by XRD and agreed with the known texture; details of this analysis can be found elsewhere (Lin *et al*., 2016). The 400 ºC deuterium loading temperature is below the recrystallization temperature of Zircaloy (~600 ºC) and has no effect on the matrix CWSR microstructure. The FCC δ–hydride (deuteride) phase is known to have a preferred lattice orientation relationship with the Zr matrix, $(111)_\delta\|(0001)_{Zr}$ (Perovic, 1983; Yuan, 2016). This preferred orientation has been confirmed for our samples as well (Lin *et al*., 2016). Optical microscopy was performed to examine the deuteride morphology in our samples. Contrast between the Zircaloy matrix and the δ-deuteride phase was achieved by swabbing an etchant consisting of de-ionized water, nitric acid, sulfuric acid, and hydrofluoric acid with a ratio of 10:10:10:1 for a 10 s.

Two *ex situ* temperature-stress loading conditions were used to study deuteride stability. One consisted of a constant tensile load applied at 200 ºC for 20 hours. The tensile load was applied along the transverse direction (TD), the tensile hoop stress direction during service. These samples were oriented with the incident neutron beam along the normal direction (ND), with the TD vertical and the rolling direction (RD) horizontal. A second set of samples were cycled between 150 and 400 ºC under constant tensile load (tensile load values listed in Table 1). The temperature cycling procedure involved heating to 400 ºC quickly (25 ºC/min), holding for 1 hour, cooling at 1 ºC/min to 150 ºC, and immediately repeating for a total of eight or ten cycles. The tensile stress was continuously applied along the RD for this loading condition and this direction was oriented vertically during SANS analysis with the incident beam along the ND.

The Spallation Neutron Source (SNS) at Oak Ridge National Laboratory is a time-of-flight neutron source optimized for neutron scattering measurements. All detected neutrons are digitally recorded as discrete events. The SNS was operating at approximately 1 MW during the course of our two measurement runs which used approximately four total days of beam time. The Extended-*Q* SANS instrument at the SNS (Zhao, 2010) was used to measure the absolute differential macroscopic cross section $d\Sigma/d\Omega$ over a wavevector transfer range of $0.005 \le Q \le 0.4$ Å^{-1}. The wavevector transfer is given by $Q=(4\pi/\lambda)\sin(\theta/2)$, where λ is the neutron wavelength and θ is the scattering angle. Two sample-to-detector distances were used, 1300 mm and 4000 mm, to record high and low *Q* ranges, respectively. The respective wavelength bandpass ranges were λ:6–9.5 Å (high *Q*) and λ:9.5–13.1 Å (low *Q*). Samples were measured in air at ambient temperature. The PorSi B standard was used to determine the calibration factor at low *Q* to convert measured intensity to absolute differential macroscopic cross section. The radial-averaged high *Q* data were scaled to the low *Q* data over the overlapping range of *Q* values (~0.02 to 0.05 Å^{-1}) to create $d\Sigma/d\Omega$ versus Q plots across the entire wavevector transfer range. All data at both detector settings were corrected for the known sample thicknesses, the detector sensitivity, area background, empty beam background, and λ–dependent sample transmission.

We resolve the net SANS response between Zy4 samples with and without deuterium loading and Zy4 samples with the same deuterium concentration with and without applied tensile stress. As discussed in the Introduction, significant scattering from Zircaloy intermetallic SPPs occurs in the small angle scattering regime. Resolution of the *net* SANS response from the deuteride phase and from changes in the deuteride phase induced by applied tensile stress at-temperature therefore requires very good counting

4

statistics. The intensity from two-dimensional area detector is typically radial averaged and this averaging greatly improves the statistics of a $d\Sigma/d\Omega$ vs Q one-dimensional format used for analysis. The counting statistics of the sample transmission measurements are equally important to resolve small net scattering intensities, especially at low Q where a longer wavelength bandpass (significantly lower incident beam intensity) is used. We recorded the sample transmission for the low Q measurements for 30 minutes, five to six times longer than typically done. The area detector scattering measurements were two to four hours in duration.

Results of SANS Analysis

A comparison of the SANS response from three reference samples (zero deuterium loading, no applied tensile stress) is shown in Figure 1. These responses are not net scattering curves as defined in the previous paragraph, but have been corrected for detector sensitivity, empty beam background, area background, sample transmission and placed on an absolute cross section scale. A Zircaloy 2 reference sample (Zy2–4–00d–00MPa) is included in this comparison but this material was not part of our investigation of deuteride stability. The absolute cross sections in Figure 1 follow the Porod power law given by,

$$\frac{d\Sigma}{d\Omega}(Q) = 2\pi \frac{\Delta\rho^2}{Q^4} \frac{S}{V} = \frac{A_P}{Q^4} , \qquad [1]$$

where $\Delta\rho$ is the scattering length density ($\rho=Nb$, where b is the scattering length and N is the atomic number density) contrast between the structural inhomogeneity (the SPPs in this case) and the matrix and S/V is the total surface area to volume ratio. Porod scattering is the asymptotic small-angle scattering response from interfaces defined by a discontinuity in Nb, such as the interfaces defining embedded SPPs. Generally, the small-angle scattering response can be divided into two Q regimes; the Guinier regime so that $Ql\sim2\pi$ and asymptotic regime so that $Ql \gg 1$, where l is the characteristic length scale of the scattering object or structural inhomogeneity. The Q-dependence within the Guinier regime is determined by the single particle form factor and the inter-particle structure factor, the latter becoming insignificant in dilute solution. The asymptotic response is independent of the particle form factor, with magnitude determined by the scattering length density contrast and the total surface area to volume ratio, as indicated by Equation 1. However, anisotropic Porod scattering can result from oriented anisometric particles, such as aligned embedded plate-like particles [Heuser and Althauser, 1999]. The Porod amplitude A_P includes the particle size distribution via the S/V ratio; this distribution can be determined if the particle shape and $\Delta\rho$ are known *a priori* or assumed [Srirangam *et al*., 2014]. We list the A_P values determined over a constricted Q range of 0.018–0.023 Å^{-1} for our samples in Table 1.

The SANS responses shown in Figure 1 follow the Porod law, with a high-Q incoherent background. The three Zy4 reference samples (Zy4–36–00d–00MPa, Zy4–47–00d–00MPa, and Zy4–49–00d–00MPa) have nearly identical scattering responses (Porod amplitudes in Table 1 agree to within the quoted statistical uncertainty). These three measurements were performed during two separate experimental runs separated 18 months (IPTS-9077 and IPTS-10566) and this comparison establishes the reproducibility with respect to all corrections needed for absolute intensity.

5

The low Q rollover is either the result of an over subtraction of the empty beam (the beam stop penumbra is not properly corrected for) or a particle size effect. The SPP size distribution in Zircaloy has been measured with small-angle scattering (Uno *et. al.*, 1996; Sen *et al.*, 2000; Srirangam *et al.*, 2014). The work by Srirangam *et al.* extended into the ultra-small-angle regime with X-rays, capturing the effect of the particle form factor for SPPs in Zy4 and revealing a bimodal size distribution. The rollover in Figure 1 occurs at $Q\sim6\text{x}10^{-3}$ Å^{-1}. The corresponding characteristic length from the $Ql\sim2\pi$ Guinier condition is $l\sim10^3$ Å, consistent with the main peak in the β-quenched SPP bimodal size distribution of Srirangam *et al*. We therefore attribute the rollover to the size of the SPPs and the beginning of Guinier-type scattering at lowest Q.

The purpose of our work is to study deuteride stability and we do not present additional analysis of the Zircaloy SPP scattering. However, we note the approximate factor of two lower Porod scattering from Zy2 compared to Zy4 in Figure 1 (also compare the Porod amplitude values in Table 1) is consistent with the $\Delta\rho$ values we calculate for the two common SPPs, $Zr_2(Ni,Fe)$ in Zy2 ($\Delta\rho$=1.23 x 10^{10} [1/cm^2]) versus $Zr(Cr,Fe)_2$ in Zy4 ($\Delta\rho$=1.76 x 10^{10} [1/cm^2]). This difference can therefore be explained by the SPP $\Delta\rho$ (Porod amplitude scales with $\Delta\rho^2$) values assuming the same *S/V* ratio exists in Zy2 and Zy4.

The SANS response from the three deuterium loaded and the reference samples (all without *ex situ* applied tensile load) are shown in Figure 2. A systematic trend of increasing response with deuterium concentration is evident, as is the general Porod behavior of the scattering response. The *net* SANS response, defined as the difference between the with-deuterium measurement and the reference (both without *ex situ* applied stress) is shown in Figure 3. The ability of SANS to resolve increasing deuteride phase small scattering as a function of concentration is demonstrated by these net data. The SANS responses follow the Porod law, with a high-Q background.

The effect of applied *ex situ* tensile load is examined for the 394 wppm deuterium loaded sample in Figure 4, the net response defined as the with-tensile load minus the without tensile load at the same deuterium concentration. The applied tensile load (*ex situ* at 200 ˚C for 20 hours) affected the deuteride phase morphological, causing an increased SANS response. On the other hand, temperature cycling at approximately the same concentration (473 versus 394 wppm) had little effect on the Porod intensity, while a significant reduction is induced by temperature cycling at low deuterium concentration (Zy4−43−100d−80MPa versus Zy4−31−98d−00MPa in Table 1). The effect of static tensile loaded of the 1034 wppm sample was also a significant reduction in the SANS intensity (Zy4−34−1034d−163MPa versus Zy4−35−1034d−00MPa in Table 1). The effect of the different tensile loading conditions at different deuterium concentrations is captured in Figure 5, a histogram plot of Table-1 Porod amplitudes.

Some samples exhibited anisotropic scattering that is evident in the 2-D SANS area detector images shown in Figure 6. Isotropic scattering is observed in the reference (Zy4−36−00d−00MPa) and lowest deuterium (Zy4−31−98d−00MPa) samples. The Zy4−33−394d−00MPa sample exhibits weak anisotropy along the TD, while very strong anisotropy is observed at highest deuterium concentration (Zy4−35−1034d−00MPa) along the TD. Static loading of the 400 wppm deuterium sample at 200 ˚C induced scattering anisotropy that was not present at the same concentration without loading. The 2-D detector image for the net subtraction (394d with tensile load minus 394 without load) shows this anisotropy. While this net response is weak, it is an indication of change in the deuteride phase induced by the *ex situ* tensile load.

6

Further analysis of the scattering anisotropy can be achieved by performing sector averages as a function of azimuthal angle ϕ within the detector plane. Sector-averaged analysis of representative samples is shown in Figure 7. These data represent the SANS response within a ±5˚ $\Delta\phi$ sector pie-shaped wedge over a Q range of 0.02 to 0.08 Å^{-1}. Scattering anisotropy is demonstrated by the variation of sector-average intensity as a function of azimuthal angle. Weak anisotropy is observed for the reference zero-deuterium, no applied load sample along the RD for this sample ($\phi=0$˚). Very strong anisotropy along the TD ($\phi=\pm90$˚) is observed at highest deuterium concentration. Static load at 200 ˚C in the Zy4−33−394d−00MPa sample induces noticeable anisotropy along TD.

Optical microscopy has been performed to image the deuteride phase particles, at least within the resolution of the microscope (~5 μm). A series of optical micrographs are shown in Figure 8 for the reference material (left-hand micrographs) and the static loaded samples (right-hand micrographs). All micrographs show the ND-TD plane with the RD normal to these directions. The sample orientation during SANS analysis was an incident beam direction along the ND with the TD-RD plane coinciding with the measured Q plane. Overall, the deuteride particle morphology appears courser for the reference, undeformed material. This is best seen at lower and intermediate magnification. The anisotropic net Porod scattering from deuteride particles after static at-temperature loading will be due to platelets with a component of the normal direction along the TD. It is difficult to determine if reorientation has induced this deuteride morphology based on a comparison of the highest magnification micrographs in Figure 8.

Discussion and Summary

The SANS response from the reference zero-concentration and deuterium-loaded samples exhibits a systematic trend of increasing Porod intensity with solute concentration. Porod scattering is the result of interfacial discontinuities within the sample; for example, the interfaces associated with embedded second phase particles. Two types of SPPs exist in our samples, χ phase particles and deuteride phase particles. The χ phase particles dominate the SANS response from all Zircaloy 4 samples, except at 1000 wppm deuterium. The fact net scattering is observed in deuterium-loaded samples that increase with deuterium concentration is a demonstration of the utility of SANS to study the Zircaloy-hydride (deuteride) system. In fact, 100-wppm sample, with a hydrogen-equivalent concentration of 50 wppm, has a concentration approximately twice the allowable limit for as-fabricated Zircaloy LWR cladding. The net SANS response at this low solute concentration therefore represents the lower limit of resolvable deuteride scattering.

200 ºC isothermal tensile loads cause a change in the Porod amplitude. At 394 wppm deuterium (Zy4−32−394d−170MPa) Porod scattering increases and noticeable anisotropy develops. On the other hand, the Porod amplitude decreases for the 1034-Zy4 sample (Zy4−34−1034d−163MPa) after isothermal tensile loading. Temperature cycling under constant tensile load decreases the Porod response in all cases, even the zero concentration reference Zy4−48−00d−80MPa. Dislocation recovery at 400 ºC could occur and, while this would be a small effect, it could reduce the observed SANS response. The more important point is that cycling reduced the Porod amplitude in the reference material; this reduction is therefore is convoluted with deuteride phase-induced changes in the SANS response.

7

Table 1. Zircaloy sample characteristics used in this study.

Sample ID[†]	D Conc. [wppm]	Gauge Thickness [mm]	σ/T conditions	A_P[††] x10^{-7} [cm^{-1}Å^{-4}sr^{-1}]
Zy2–4–00d –00MPa	zero	1.07	no applied load	1.08
Zy4–36–00d–00MPa	zero	2.81	no applied load	2.36
Zy4–47–00d–00MPa	zero	2.81	no applied load	2.29
Zy4–49–00d–00MPa	zero	3.12	no applied load	2.32
Zy4–48–00d–80MPa	zero	2.61	80 MPa/RD/10 cycles	2.20
Zy4–31–98d–00MPa	98	2.89	no applied load	2.52
Zy4–43–100d–80MPa	100	2.74	80 MPa/RD/8 cycles	1.89
Zy4–33–394d–00MPa	394	2.92	no applied load	2.70
Zy4–32–394d–170MPa	394	2.72	170 MPa/TD/200˚C	3.09
Zy4–45–473d–77MPa	473	2.71	77 MPa/RD/8 cycles	2.74
Zy4–46–473d–128MPa	473	2.68	128 MPa/RD/8 cycles	2.57
Zy4–35–1034d–00MPa	1034	2.84	no applied load	5.23
Zy4–34–1034d–163MPa	1034	2.83	163 MPa/TD/200˚C	4.54

[†]3X series of samples measured during IPTS-9077 (September, 2014); 4X series during IPTS-10506 (February 2015).

[††]Uncertainty in Porod amplitude $\sigma \sim 10^{-9}$ [cm^{-1}Å^{-4}sr^{-1}] for all measurements.

8

9
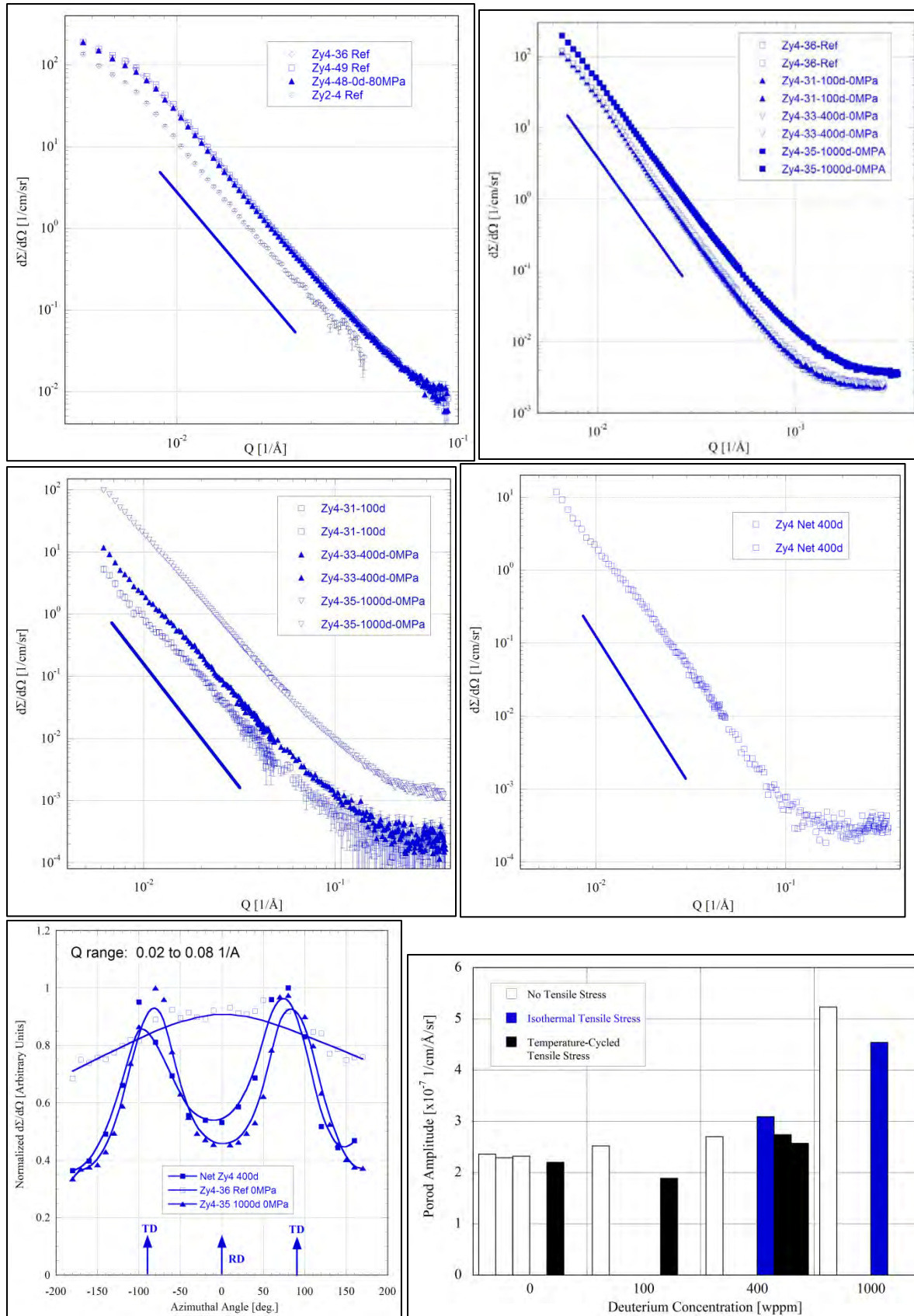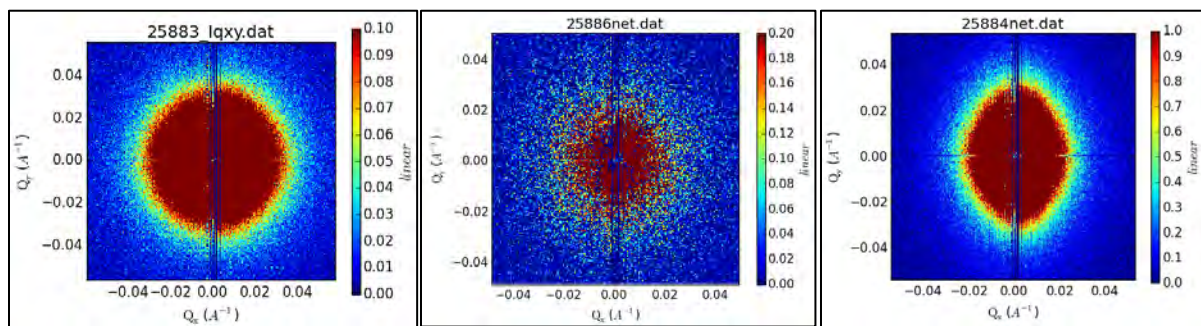
Zy4-36_Ref_nosig   Zy4-31_Net_100d_nosig_ref   Zy4-35_Net_1000d_nosig_ref
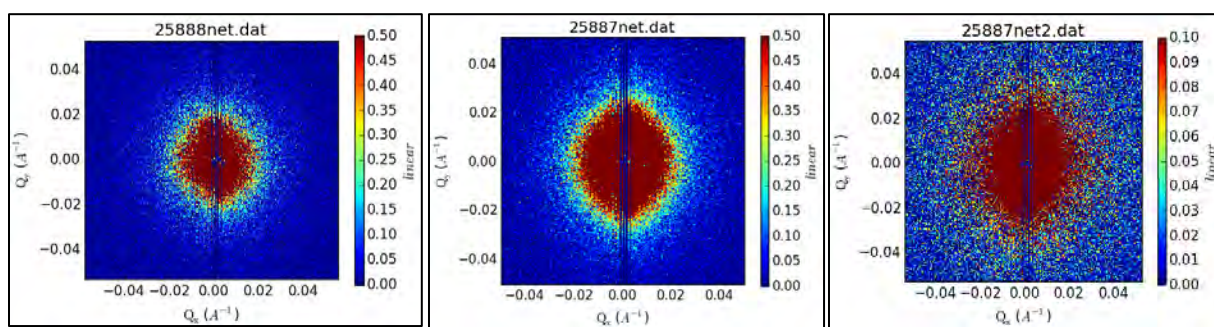
Zy4-33_Net_400d_nosig_ref   Zy4-32_Net_400d_sig_ref   Zy4_Net_400d_sig_nosig

10
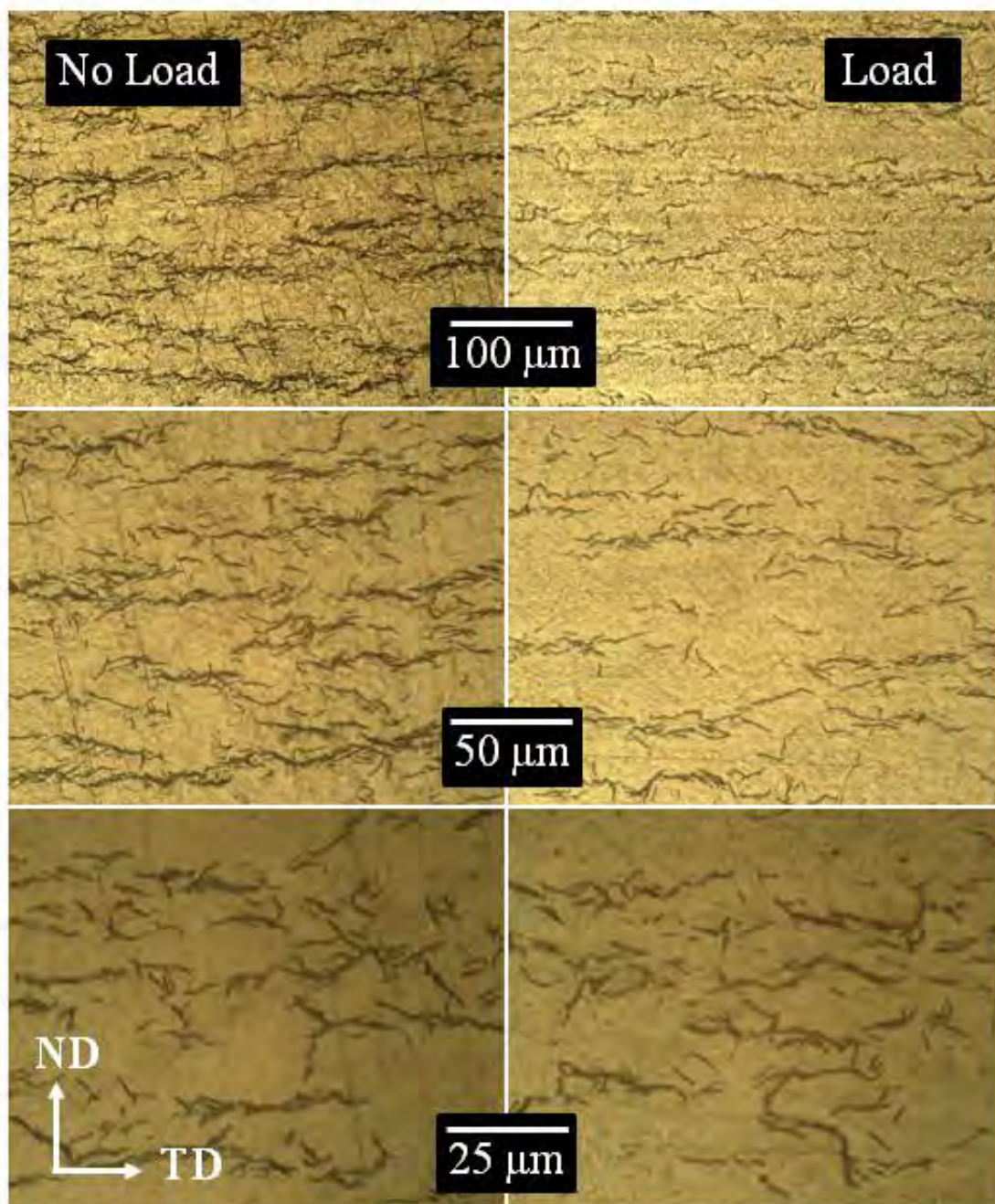
References

Alvarez, M. V., Santisteban, J., Vizcaino, P., Flores, A., Banchik, A. and Almer, J. (2012). Acta Materialia, 60(20), 6892–6906.

ASTM Standard B353-12 (2012), Specification for Wrought Zirconium and Zirconium Alloy Seamless and Welded Tubes for Nuclear Service (Except Nuclear Fuel Cladding).

Bradbrook, J., Lorimer, G., and Ridley, N. (1972). J. Nucl. Mater., 42, 142–160.

Billone, M., Yan, Y., Burtseva, T., Daum, R. *et al*. (2008). Cladding embrittlement during postulated loss-of-coolant accidents. Tech. rep. Argonne National Laboratory.

Bossis, P., Pecheur, D., Hanifi, K., Thomazet, J. and Blat, M. (2006). In 14th International Symposium on Zirconium in the Nuclear Industry, 3, 494–525.

Chen, W.C. and Heuser, B.J. (2000). J. Alloys Compd., 312, 176–180.

Chen, W.C. and Heuser, B.J. (2001). Phys. Rev., 65, 014102–014108

Colas, K., Motta, A., Almer, J., Daymond, M., Kerr, M., Banchik, A., Vizcaino, P. & Santisteban, J. (2010). Acta Materialia, 58, 6575–6583.

Colas, K. B., Motta, A. T., Daymond, M. R. & Almer, J. D. (2013). J. Nucl. Mater., 440, 586–595.

Coleman, C. (1982). Zirconium in the Nuclear Industry: Fifth International Symposium. ASTM STP, 754, 393–411.

Courty, O., Motta, A. T. and Hales, J. D. (2014). J. Nucl. Mater., 452, 311–320.

Daum, R., Chu, Y. and Motta, A. (2009). J. Nucl. Mater., 392, 453–463.

Daum, R. S., Majumdar, S., Liu, Y. and Billone, M. C. (2006). J. Nuc. Sci. Tech., 43, 1054–1067.

Desquines, J., Drouan, D., Billone, M., Puls, M.P., March, P., Fourgeaud, S., Getrey, C., Elbaz, V., and Philippe, M. (2014). J. Nucl. Mater., 453, 131-150.

Fong, R.W.L. and Spooner, S. (1994). Script Met., 30, 649-654.

Gerold, V. and Kostorz, G. (1978). J. Appl. Cryst., 11, 376–404.

Glatter, O. and Kratky, O., (1982). Small Angle X-ray Scattering, Academic Press, London.

Heuser, B.J. (1994). J. Appl. Cryst., 27, 1020-1029.

Heuser, B.J. and Althauser, J.W. (1999). J. Phys.: Condens. Matter, 9, 8945–8961.

Hong, S. and Lee, K. (2005). J. Nucl. Mater, 340, 203–208.

Kearns, J. and Woods, C. (1966) J. Nucl. Mater. 20, 241–261

Kerr, M., Daymond, M., Holt, R. and Almer, J. (2008). J. Nucl. Mater., 380, 70–75.

Kim, Y.S. (2008). J. Nucl. Mater. 378, 30–34.

Lemaignan, C., and Motta, A. T. (1994). Zirconium Alloys in Nuclear Applications, Materials Science and Technology.

Lin, J.-l., Han, X., Heuser, B. J. and Almer, J. D. (2016). J. Nucl. Mater. 471, 299–307.

Perovic, V., Weatherly, G.C., and Simpson, C.J. (1983). Acta Metall., 31, 1381-1391.

Puls, M.P. (1990). Metall. Trans. A, 21, 2905–2917.

Puls, M.P. (2009). J. Nucl. Mater., 393, 350-367.

12

Sawatzky, A. (1960). J. Nucl. Mater. 2, 321–328.

Sen, D., Mazumder, S., Tewari, R., De, P.K., Amenstsch, H., and Benstorff, S. (2000). J. Alloys Compd., 308, 250–258.

Singh, R., Kishore, R., Singh, S., Sinha. T. and Kashyap. B. (2004). J. Nucl. Mater. 325, 26–33.

Srirangam, P., Idrees, Y., Ilavsky, J., and M.R. Daymond (2014). J. Appl. Cryst. 48, 52–60.

Tulk, E., Kerr, M. and Daymond, M. (2012). J. Nucl. Mater., 42, 93–104.

Uno, M., Kamiyama, T., Anada, H., Miyake, C., and Suzuki, K. (1996). J. Nucl. Mater., 231, 34–38.

Yuan, G., Cao, G., Yue, Q., Yang, L., Hu, J., and Shao, G. (2106). J. Alloys Compd., 658, 494-499.

Zanellato, O., Preuss, M., Buffiere, J.-Y., Ribeiro, F., Steuwer, A., Desquines, J., Andrieux, J. and Krebs, B. (2012). J. Nucl. Mater.,420(1), 537–547.

Zhao, J.K., Gao, C.Y., and Liu, D. (2010). J. Appl. Cryst., 43, 1068-1077.

13

Hydrogen Rim Development and Reorientation Characterization in ZIRLO Under Dry Storage Conditions

Yong Yang, University of Florida

Abstract

Hydride rim testing has determined that the most optimal surface treatment involves shot peening. This process leaves large amounts of residual stress that strongly promotes the formation of hydrides along the outer surface in large clusters and density. A hydride gradient can also be observed with this treatment. Hydride reorientation experimentation has yielded further results. Exploration of the reorientation threshold has shown that even at hoop stresses as low as 60 MPa, reorientation can occur. While the degree of reorientation is low, further characterization on the effect it has of the mechanical properties will be needed to be done before it can be considered negligible. It seems apparent that the testing temperature for the mechanical tests will be crucial in characterizing this. One of the most critical factors on reorientation is the hydrogen content, at higher concentrations the hydrogen does not entirely go into solution and is therefore not eligible to reorient.

1. Introduction

The need for energy in the United States is continuously on the rise. Nuclear power is expected to continue to grow in use for the foreseeable future in order to continue to meet the demand. However, a growing concern is the spent nuclear fuel (SNF) that comes from nuclear power. Currently, the plan for handling the fuel involves indefinite long-term storage of the SNF. As it stands, the SNF is expected to be able to sit in long-term dry storage facilities without having any issues. This may not necessarily be the case. As the SNF sits in dry storage there are several modes of degradation that can occur. These degradation mechanisms include: corrosion of the canister or SNF, stress corrosion cracking, hydrogen embrittlement, etc.

The main focus for this research and experimentation revolves around the hydrogen behavior in SNF at the dry storage conditions. The testing conditions will start at the point that the SNF begins to be placed into dry storage. These conditions include a maximum temperature of 400°C (temperature from vacuum drying process), hoop stresses ranging from 60-90 MPa, and slow cooling rates of 1C/min or lower. It is known that SNF cools significantly slower than 1C/min and techniques are being developed to achieve slower cooling rates.

Apart from testing hydrogen behavior under these conditions methods are being developed in order to generate material that resembles the hydride structure of SNF as it would normally be. Currently most lab procedures for hydriding material (placing hydrogen into the metal matrix and having it precipitate) have a uniform distribution. The distribution of hydrides is normally more of a rim-like structure with a gradient towards the inner surface. Obtaining material that has the same structure as SNF would be crucial for making more direct comparisons on the hydrogen behavior in zirconium alloys and determining the extent of degradation, if any.

2. Experimental Methods

2.1 Hydride Rim Testing

The first step for hydride rim development involves the generation of an oxide layer. The oxide layer is created by placing samples into a bath of LiOH and heating for several hours. This generates an oxide layer on the inner surface and outer surface, the outer oxide layer will be removed. The inner oxide layer will act as a diffusion barrier and significantly reduce the likelihood of hydride formation near the inner side of the sample.

Removal of the outer oxide layer is done by both chemical and mechanical means. The outer oxide layer is grinded off with varying silicon carbide grit sand paper in order to also leave some residual stress on the outer surface. The residual stress will help to promote hydride formation on the outer surface. Afterwards the outer surface is cleaned with a bath of Alconox, followed by chemical etching with an acidic mixture of HF, HNO3, and DI water.

Once the sample is prepared it will be placed into the furnace for testing. Current testing temperatures for hydride rim development are focused on lower temperatures (270-290°C) to

mitigate the diffusion of hydrogen. The desired result is to obtain a structure similar as to what is shown below in figure 1.
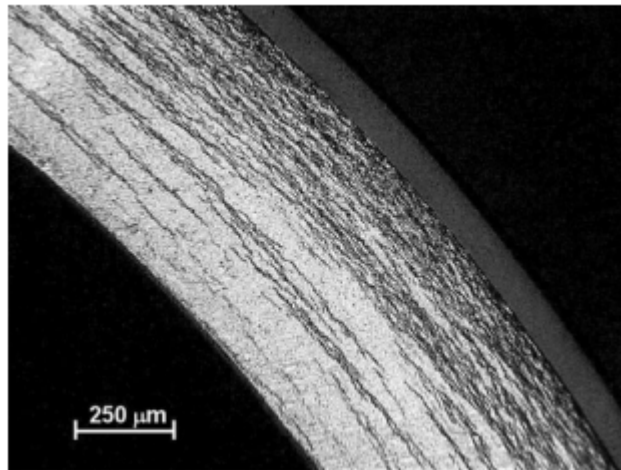

Figure 1 - Hydride rim structure [1]

2.2 Hydride Reorientation Testing

Sample development for reorientation testing is similar to hydride rim testing. Hydride reorientation testing has been carried out over a range of hoop stresses that would be expected in dry storage conditions with a focus on lower stresses. The purpose of focusing on lower stresses is to clarify and determine what the reorientation threshold is. Previously the reorientation threshold has been characterized to be at different stresses, with different materials, and varying hydrogen content. Characterization of the reorientation threshold will continue specifically for conditions that spent nuclear fuel would be expected to be. These conditions include hoop stresses ranging from 60-110 MPa, and possibly lower depending on the hydride behavior. However, for our experimental purposes the max hoop stress to be tested is at 90 MPa. The NRC has recently been investigating these degradation mechanisms and has set a limit on the highest possible hoop stress SNF should be. The temperature for these experiments will always start at 400°C and be furnace cooled to achieve a slow cooling rate.

3. Results

3.1 Hydride rim
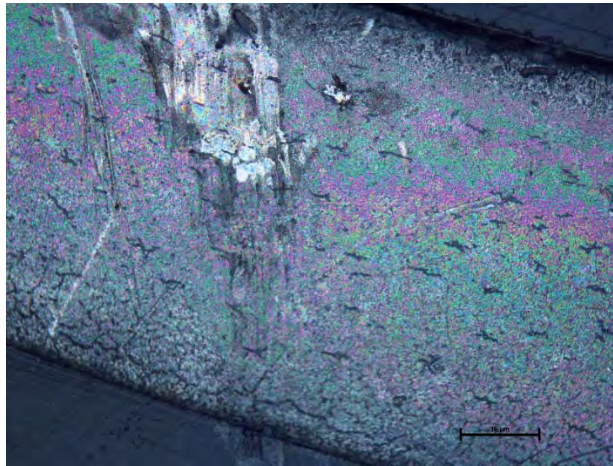
Figure 2 - Hydride rim experimental result

It can be observed from figure 2, that a uniform distribution is still apparent. Compared to previous results the length of hydrides is typically smaller, particularly deeper into the tube where there is less residual stress. This experiment was done at a lower temperature of 290°C with a hydriding time of 24 hours. Small clusters of hydrides and larger hydride growth can be observed near the outer surface. This is likely due to the surface treatment leaving residual stress on the outer surface which promotes hydride growth [1]. However, it can be seen that efforts must be put into applying more stress on the outer surface to generate a larger cluster of hydrides.

The inner surface of the tube has about a 5-6 micron area where no hydrides have precipitated. In general most samples have about an area of 5-8 microns in length where no hydrides have precipitated near the inner surface.
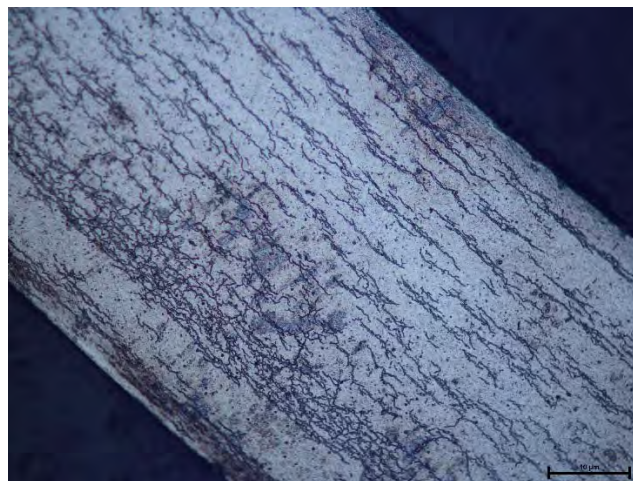
Figure 3 - Shot peened hydride rim

Figure 3 shows the hydride formation after shot peening and chemical cleaning of the outer surface. The shot peening process was done primarily to induce larger amounts of residual stress on the outer surface. The hydride clustering near the outer surface shows a significant improvement and can easily be seen as well as a gradient of hydrides rather than a uniform distribution. This sample was done at 290°C and 48 hours hydriding time.
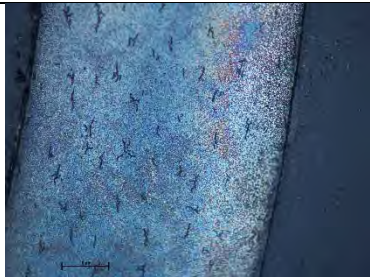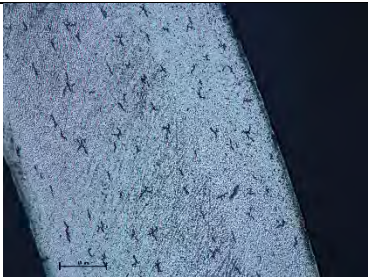
The spacing of hydrides near the outer surface may be explained by the chemical cleaning process, during etching about 1-3 microns of material can be lost. By reducing the etching time this may not be an issue. Additionally, by reducing the hydriding time a lesser amount of hydrogen can be absorbed and reduce the diffusion into the material. Although reorientation can also be observed within the hydrides, by applying a thermal cycle at the end of the hydriding process the radial hydrides can be turned into circumferential hydrides.

Further optimization of these shot peened samples can lead to the full development of a hydride rim.
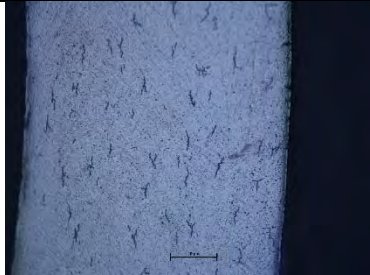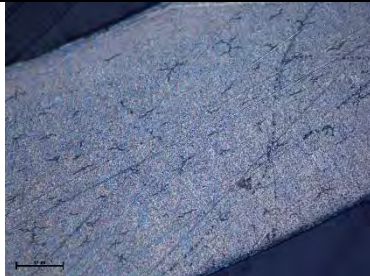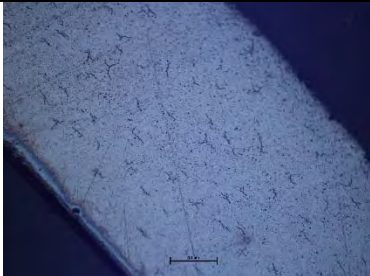
3.2 Reorientation

Table 1 below shows results for reorientation at low hydrogen content values (30-36 ppm). Reorientation can be easily observed in the samples with low hydrogen content. Table 2 shows the samples at hydrogen contents (155-160 ppm) where reorientation can also be observed.
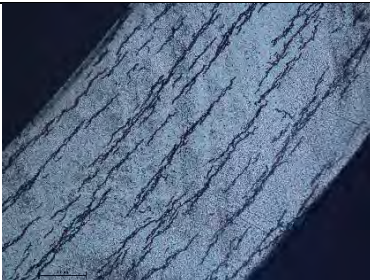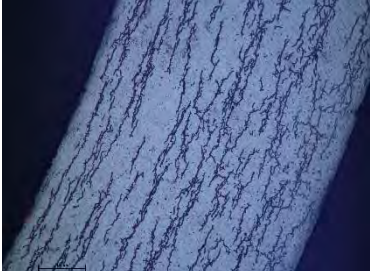
Table 1 - Reorientation of low hydrogen content (34 ppm) Zirlo

	6 hour hold	24 hour hold	Reorientation degree
60 MPa			12% / 16%

	6 hour hold	24 hour hold	
70 MPa			14% / 16%
90 MPa			16% / 18%

Table 2 - Reorientation of higher hydrogen content (160 ppm) Zirlo

	6 hour hold	24 hour hold	Reorientation degree
60 MPa			4% / 5%
70 MPa			7% / 8%
90 MPa			8% / 14%

Close examination of the samples pressurized to a hoop stress of 60 MPa reveals that reorientation did occur. This indicates that the reorientation threshold under these conditions can still possibly be at lower hoop stresses. However, the degree of reorientation is considerably low.

In order to get an idea of the significance radial hydrides can have on the mechanical properties of materials, look at the results from some experiments done by Hsu et al. He performed X-specimen testing in order to get an idea of the impact radial hydrides could have on the material. In the figure shown below, the left shows result from tests done at 25°C and the right tests at 300°C. It can be deduced that at higher temperatures the impact of radial hydrides is less significant, but the presence of any hydrides at all can severely reduce the load bearing capacity at lower temperatures [2,3]. Further testing at varying temperatures expected during dry storage conditions should be done in order to clarify any possible damage or degradation from hydrogen embrittlement.
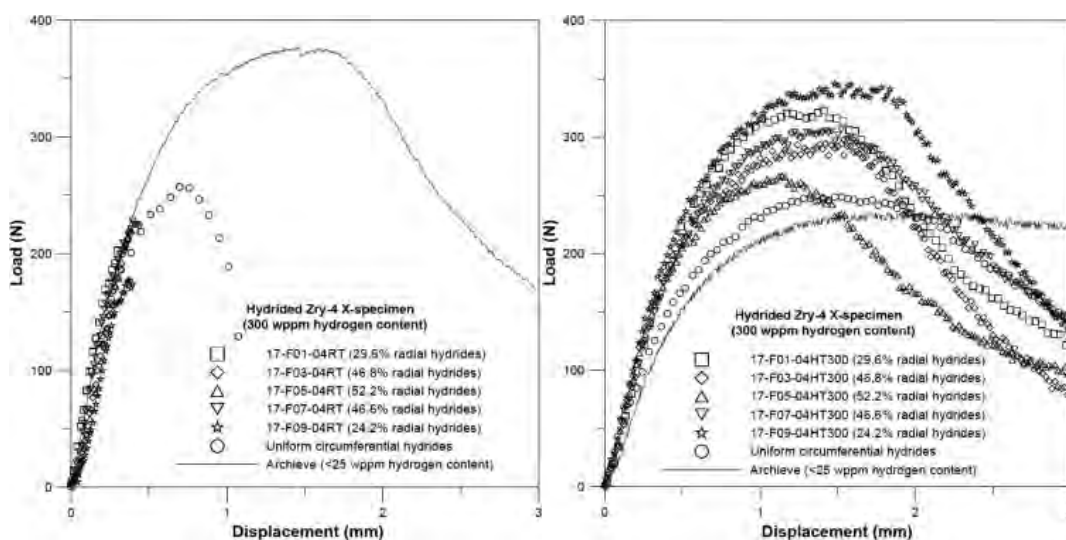

Figure 4 - X- specimen testing results, left test done at 25°C and right test done at 300°C [2]

It can also be noticed that in the samples with lower hydrogen content the reorientation degree is observed to be higher. This is due to the fact that the length of the radial hydrides is comparable to the length of the circumferential hydrides. When measuring the degree of reorientation, the total length of the radial hydrides was measured over the total length of all hydrides. Typically, quantification of hydrides and hydride reorientation was done by measuring the total number of hydrides and the total length of all hydrides [4]. However, more recent research has focused primarily on the total length of hydrides since the hydride length of radial hydrides can be significantly different than the circumferential length as observed in the samples in Table 2.

In order to quantify the degree of radial hydride formation, image processing with ImageJ freeware was used. In this report the area fraction of radial hydrides occupying the total area in the tube was taken as the degree of reorientation. This was done by converting the images to a grey scale and setting the program to delete the circumferential hydrides leaving only the radial hydrides. At this point the area fraction of the hydrides was taken and used to quantify the degree

of reorientation. The area fraction measurement effectively takes into account the total length of the hydrides in relation to the tube to give an accurate degree of reorientation. Although it must be noted that these numbers may be inflated. The main reason for this is that during the etching process some dimples were formed that show as black specks that the program also treats as hydrides. By discriminating against particle size many of the dimples can be removed but some still remain and add to the total area fraction.

4. Conclusion

Hydride rim experimentation has shown that the inner oxide layer acts as a sufficient diffusion boundary. Most samples are similar to the one shown in which there is a large region where no hydrides are formed near the inner surface. Grinding of the outer surface has shown small clustering of hydrides near the outer surface. However, a uniform distribution can still be observed.

The shot peened sample shows significant improvement on hydride clustering near the outer surface. By reducing and changing several parameters optimization of the hydride rim can be achieved.

Reorientation has been observed at hoop stresses as low as 60 MPa. Further characterization to determine the reorientation threshold under the same temperatures and hydrogen contents would require testing at lower hoop stresses. As of now, the degree of reorientation seems insignificant on the effect it would have the materials mechanical properties.

At lower hydrogen contents it was observed that there was a larger degree of reorientation. The reason for this can be explained by the total dissolution of hydrides at lower hydrogen contents at 400°C [5]. At higher hydrogen contents it would be expected that there is only partial dissolution leading to a smaller degree of reorientation [4,5,6]. However, at higher hoop stresses it can be observed that the degree of reorientation becomes larger.

5. Future Work

Continuous efforts on further enhancing the hydride rim structure will be done. By using more rigorous processes to induce larger residual stresses on the outer surface it is expected for there to be a larger region for more hydride formation.

Testing accounting for much lower cooling rates will be explored in the future. It is expected that at lower cooling rates this will allow more time for the hydrogen to be able to dissolve and reorient, despite knowing that only partial dissolution will occur. Mechanical testing and delayed hydride cracking tests will be performed on all the materials and conditions mentioned in this paper. This will determine if the radial hydride content will have a significant effect on the material properties or not.

More importantly, with the complete reorientation system developed and several samples already generated and experimented on, testing notched samples will begin. Testing of the notched samples will generate data on how hydrogen behaves near areas of higher stress. It is known that hydrides preferentially precipitate in regions of higher stress, this can be observed in the radial hydride formation near the ends of circumferential hydrides. Small notches will be made to mimic possible damage the zirconium alloys can face during operation in a power plant such as from pellet clad interactions. These areas of high stress may increase the likelihood of radial hydride formation, and more notably have a large local density of radial hydrides. Having a large local density of radial hydrides may have a more significant effect on the materials mechanical properties and will be investigated to determine if this would be a cause of concern.

References

[1] Shimskey R., Hanson, B., MacFarlan, P. "Optimization of Hydride Rim Formation in Unirradiated Zr-4 Cladding" Pacific Northwest National Lab. PNNL-22835. September 2013.

[2] Hsu, H., Tsay, L. "Effect of hydride orientation on fracture toughness of Zircaloy-4 cladding". Journal of Nuclear Materials. Vol. 408 Issue 1 pgs 67-72. Janaury 2011.

[3] Dutton, R., Nuttal, K., Puls, M. P., Simpson, L. A. "Mechanisms of Hydrogen Induced Delayed Cracking in Hydride Forming Materials." Metallurgical Transactions A Volume 8A. October 1977.

[4] Motta, A., Masaki A, Toshikazu, B., Toshiyasu, M., Katsuichiro, K., Takayoshi, Y., Yasunari, S., Takeda, T. "Evaluation of Hydride Reorientation Behavior and Mechanical Properties for High-Burnup Fuel-Cladding Tubes in Interim Dry Storage". Journal of ASTM International. Vol. 5, No.9. JAI101262. 2008.

[5] IAEA. "Delayed hydride cracking in zirconium alloys in pressure tube nuclear reactors". IAEA-TECDOC-1410. 1998-2002.

[6] McRae, G.A., Coleman, C.E., Leitch, B.W., "The first step for delayed hydride cracking in zirconium alloys". Journal of Nuclear Materials. Vol. 396 pgs 130-143. Janurary 2010.

3.0 Summary of Key Results and Findings from TMA-3: Canister Corrosion

This mission was focused on recognized gaps in understanding mechanisms relevant to the corrosion degradation of the UNF canisters in various environments. The methods employed included: 1) electrochemical corrosion testing, 2) stress corrosion cracking (SCC) studies, 3) characterization of the corrosion of welds, bolted joints, and seals under prototypic conditions, and 4) integration the results of corrosion tests and microstructural analyses.

The following sections are detailed reports presented from TMA3 contributors in their original format (to maintain clarity).

1 Background

1.1 Introduction

With the termination of Yucca Mountain nuclear waste repository by United States Congress in 2011, new long term storage solutions are being sought for storing spent nuclear fuels. United States Nuclear Regulatory Commission (NRC) was tasked to examine the current storage conditions and identify the knowledge gap for the continued storage of nuclear fuels. Currently over 65,000 tons of spent fuel are stored in over 1400 dry casks, with an ongoing production of 2,400 tons of spent fuels annually. The dry casks have a stainless steel housing or canister that is surrounded by concrete. The canisters are made of type 304 or 316 stainless steels by forming and welding. However, these austenitic steels are susceptible to corrosion and stress corrosion cracking (SCC). It was reported by the NRC [1] that canister corrosion and pitting, which can cause SCC, are areas of concern and there is a knowledge gap in regards to their initiation in dry cask storage conditions. It is known that pitting corrosion can evolve into SCC and may cause canister failure, particularly in the regions of welds due to the presence of residual stresses in these regions. SCC is of particular importance in coastal regions where concentration of corrosive chloride ions in the environment is particularly high. The stainless steel canister in dry cask storage is the last defense to avoid radiation leaking and therefore it is important to understand and predict the degradation mechanisms for corrosion and SCC of stainless steel and its welds in canister relevant conditions.

1.2 Dry cask designs

There are five licensed canister vendors in the United States with a multitude of dry cask storage designs among them [1-3]. The primary design features of concern in SCC are storage orientation and canister seal. Canisters can be stored horizontally or vertically. Figure 1 shows two different canister designs (HI-STORM 100 and Transnuclear TN-68) and storage orientations. In vertical storage, a concrete over-pack surrounds the canister with a minimum annular gap (no larger than 2 inches) for airflow and the surface temperatures of the canister at the beginning of life are between 170°C and 200°C. The ventilation holes at the top and bottom of the concrete over-pack provides natural convection cooling. In horizontal storage, canisters are stored horizontally on guiderails within a concrete structure with air ventilation pathways. This may lead to galvanic corrosion and crevice corrosion between stainless steel canister and guiderails. The different airflow patterns between vertical and horizontal storages are expected to affect the temperature distribution and aerosol deposition and therefore affect the kinetics of corrosion and stress corrosion cracking.

Canister seals can also affect corrosion. The welded seals produce heat affected zones that may be more rapidly attacked by corrosion than the surrounding base material. The residual stress resulting from welding can accelerate the stress corrosion cracking. Bolted seals provide sites for crevice corrosion and galvanic corrosion, though bolted seals may allow easier fuel assembly retrieval later.

1
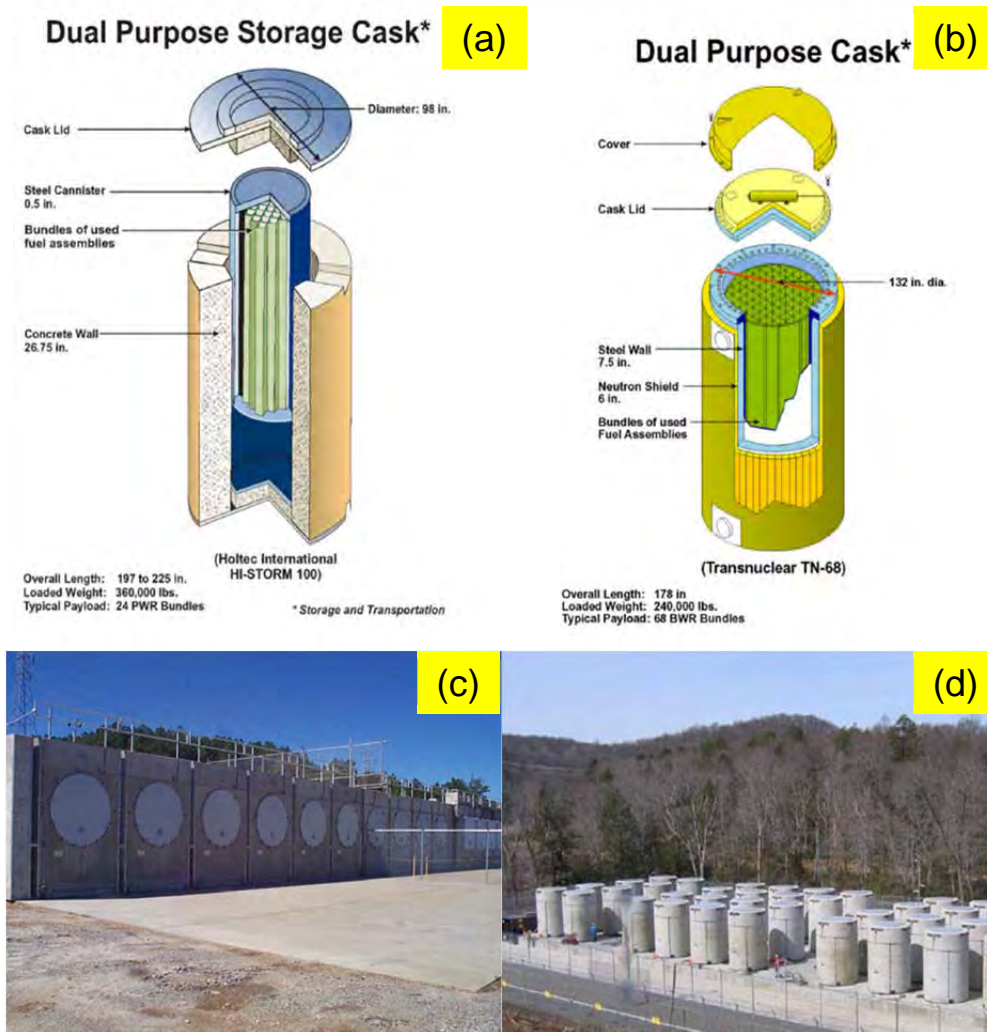
Figure 1. Canister design and orientation, (a) Holtec HI-STORM 100, (b) Transnuclear TN-68 dry cask storage, (c) Horizontal dry storage at Connecticut Yankee, and (d) vertical dry storage at Oconee. The Holtec design (a) is a welded stainless steel canister while the Transnuclear cask lid (b) is bolted. The neutron shielding placement and stainless steel containment thickness also vary between designs.

1.3 Corrosion and SCC testing

Although the SCC phenomenon has been studied extensively, there were relatively few studies on the initiation and propagation of SCC of stainless steel for canister applications when the IRP project started. Due to the unique stress conditions, varying environments, and specific modes of salt deposition onto the canister surface, the mechanism and parameter space for SCC were not clearly defined. In particular, the kinetics of SCC after initiation stage was not known, which is critical for prediction of the lifetime of the canisters.

Environmental exposure tests performed by CEA [2] with varying levels of relative humidity (RH) between 40 to 100% showed that the corrosion of canister occurs in two phases: a dry and a wet condition. When the temperature is above 41°C in a dry phase, corrosion is not favored. But when the canister temperature is below 41°C, a wet regime starts due to condensation and deliquescence and corrosion can

2

occur if RH is below 40%. Equilibrium thermodynamics were used to determine the required temperature for the dry to wet phase transition.

Japan's Central Research Institute of Electric Power Industry (CRIEPI) [3] studied corrosion and SCC of low carbon 304 stainless steel samples under constant load in saline envirnments over months. By varying the levels of initial chloride deposition on the tensile samples, it was found that a minimum chloride concentration of 0.8g/m^2 was needed to initiate SCC and the critical concentration was dependent on the canister temperature. The constant load tests were also used to determine the needed stress intensity factor or Kc to initiate the SCC at 35% RH. When the canister temperature was 83ºC, Kc was found to be 30MPam^0.5. It was also noted that after a regime of rapid crack growth, the average crack propagation rate decreased to 1.6×10^{-11} m/s, as shown in Figure **2**. Some compact tension (CT) samples tested by Turnbull [14] showed similar SCC crack propagation rate under corrosive conditions, 2.1×10^{-11}m/s in chloride solution at 40ºC when the stress intensity factor was 20MPa m^0.5.
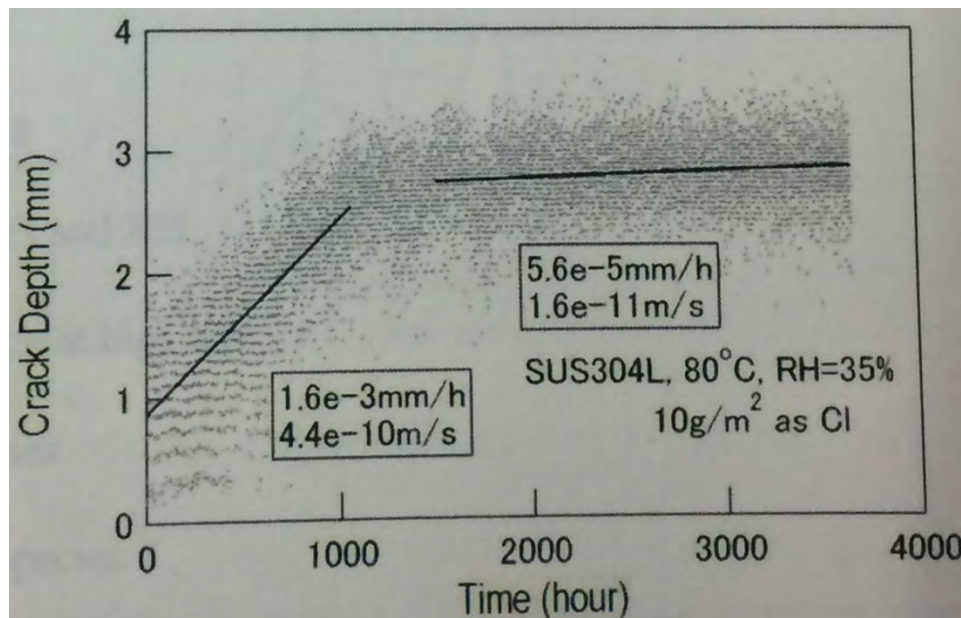
Figure 2 SCC growth rate (crack depth vs time) of 304L 4-point bend samples (under constant load) exposed at 80ºC, with 35%RH and 10 g/m^2 Cl⁻. A rapid crack growth rate of 4.4×10^{-10} m/s was followed by a much slower growth rate of 1.6×10^{-11} m/s.

South West Research Institute (SWRI) [4] studied corrosion and SCC of weld samples using U-bend with about 15% strain at the bend apex and C-rings with a lower strain of 0.5 and 1.5%. ASTM U-bend and C-rings were used. It was found that SCC initiated with salt loadings as low as 0.1 g/m^2 on the U-bend surface, which is consistent with findings of other researchers. SCC was more severe on sensitized samples - the as-received specimens were attacked to a much lower extent than sensitized and welded samples.

Potentiondynamic tests have been widely used in characterizing corrosion and SCC susceptibility under varying conditions. In particular, passivation tests were used to determine the onset of corrosion and pitting of steels in sodium chloride solutions, however some caution must be exercised in electrochemical measurements. Scan rate can cause dramatic differences in the potentiodynamic measurements. Other important control parameters include solution concentration, and composition and aeration, as detailed in ASTM G108-94 [5]. It has been shown that the heat affected zone of weld region is more susceptible to corrosion than the weldment or base material when exposed to 0.5M H_2SO_4, plus

3

0.01 M KSCN solution [4]. Higher passivation current (-3×10^{-5} vs 1×10^{-6} A/cm^2)was observed in the HAZ than in the base material or weldment.

1.4 Canister surface conditions

In 2013, EPRI [6] conducted an analysis of canister surface that had been in service for 19 years at Calvert Cliffs in Southern Maryland. Atmospheric deposits on the canister surface were collected and analyzed but showed unexpected compositions. Two different methods were used to analyze the compositions of the deposits on the canister's surface: a wet method using SaltSmart^{TM} device which measured the conductivity of the dissolved solution, and a dry method using Scotch-Brite sponge with filter paper on a removable cartridge - the sponge was scraped against the surface and the residue was analyzed with x-ray diffraction, x-ray fluorescence, gas chromatography and ion chromatography. It was found the dry method provided more reliable data. Table 1 lists the compositions measured by the two methods. As can be seen, a relatively small amount of sodium was detected, which indicates the largest portion of deposits were in the form of clay.

Table 1. Deposit composition on a canister exterior surface from Calvert Cliff dry cask storage after 19 years of service.

	Wet method using SaltSmart, mg/m^2	Dry method using Scotch-Brite sponge, mg/m^2
Ca	463	67
Mg	13.9	1.2
K	48.4	13
Na	5	0.33
Cl	5.2	0
S	12	3.4
Al	27.7	3.7
Si	134	13
P	5.9	0.76
Ti	23.4	0
Cr	3.1	215
Mn	8	29.1
Fe	256	1077
Ni	2	102
Cu	0	6
Zn	34.3	17.4
Zr	2	0
Total	1043.9	1548.9

4

## 2 Corrosion and stress corrosion cracking experiments

2.1 Materials and salt used

Both 304L and 316L stainless steel grades were both used in this research. Early canisters were made of 304L, however the more recent ones are made of 316L because of its enhanced corrosion resistance. The 316L contains higher molybdenum which imparts higher corrosion resistance. Both alloys were low carbon grades to mitigate carbide formation during welding process. The materials were obtained from Penn Stainless with a cold rolled, annealed, and pickled finish. The composition and heat number of the both 304L and 316L are shown in Table 2.

Table 2. Compositions (in wt%) of the 304L and 316L stainless steel used in this research.

	Heat	C	Co	Cr	Cu	Mn	Mo	N	Ni	P	S	Si
304L	D5L6	0.0148	0.1595	18.06	0.443	1.74	0.2925	0.0802	8.054	0.033	0.0022	0.3250
316L	X216	0.0155	0.2465	16.73	0.5455	1.64	2.031	0.0469	10.05	0.0355	0.0038	0.362

Materials were tested in the as-received (AR), sensitized, or welded conditions. To induce sensitization, the samples were heated to $675^{o}C$ for 24 hours to simulate the HAZ during welding. Figure 3 shows the optical images of the as received and sensitized 304L.

(a)   (b)
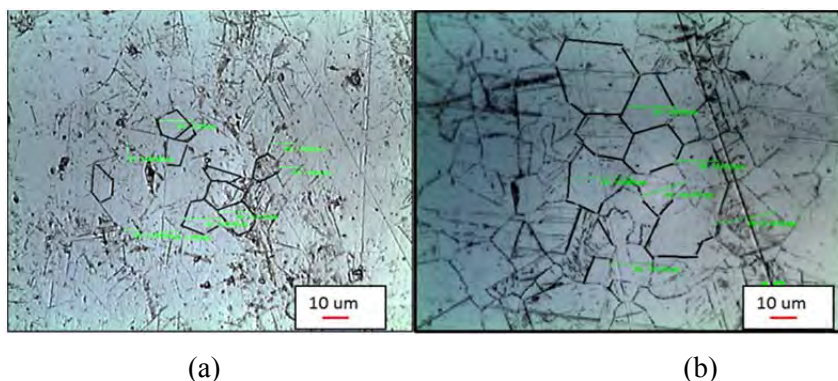
Figure 3. Optical images of (a) as-received and (b) and sensitized 304L.

Two welded materials were also used. One was a sheet of 1.27mm thick 304L welded in-house at the University of Wisconsin. The sheet was saw cut and welded using 308 filler metal with 35A DC current. The second was a welded plate supplied by Idaho National Laboratory (INL) and prepared under more prototypic canister conditions. The base material was a 5/8" thick 304L plate and it was welded using 308 stainless steel filler metal and welded with a DC current range of 50-200A. The base metal (Heat F8W9) was obtained from Diversified Metal Inc and the 308 filler metal (Heat 256828) was obtained from Norco. The compositions of the 304L base metal and 308L filler metal are shown in

5

Table 3. The photograph of the two different 304L welds is shown in Figure 4. Figure 5 shows the schematic of the 304 weld prepared by INL.

Table 3. Compositions of 304L and 308 filler used in the weld material provided by INL.

	Heat	C	Co	Cr	Cu	Mn	Mo	N	Ni	P	S	Si
304L	F8W9	0.0198	-	18.04	0.465	1.64	0.3405	0.0808	8.036	0.0345	0.001	0.2735
308L filler	256828	0.010	-	20.16	0.13	2.09	0.09	0.033	9.67	0.022	0.016	0.46
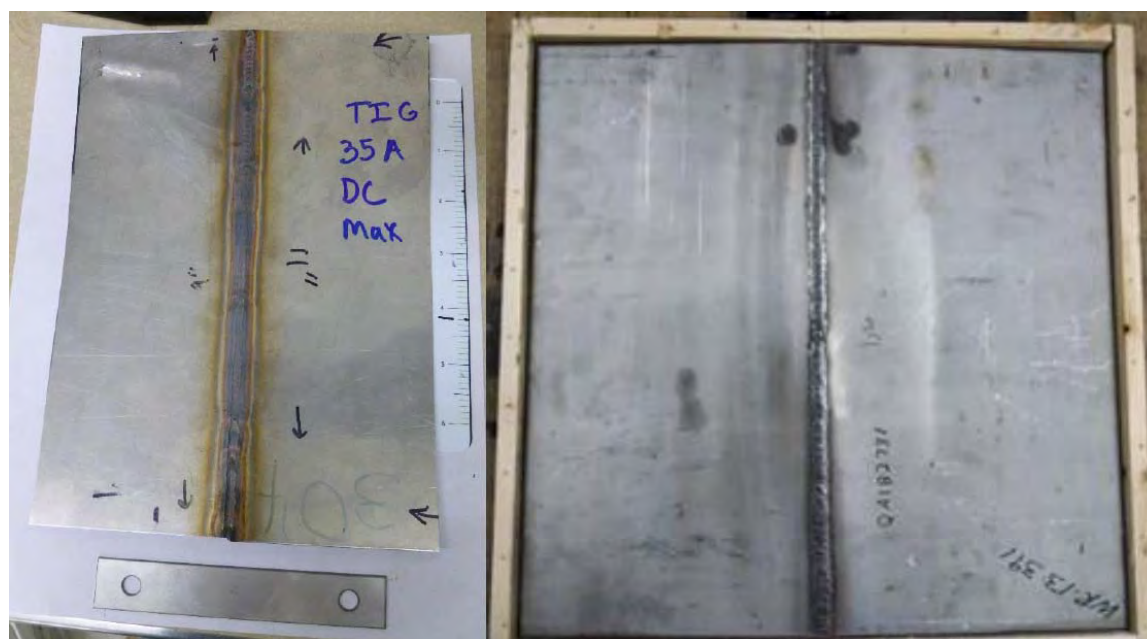
Figure 4. Weld plates used in this study. (a) in-house 304L stainless steel from which U-bend samples and polarization samples were sectioned. (b) 304L stainless steel weld plate from which U-bend samples were prepared.

6
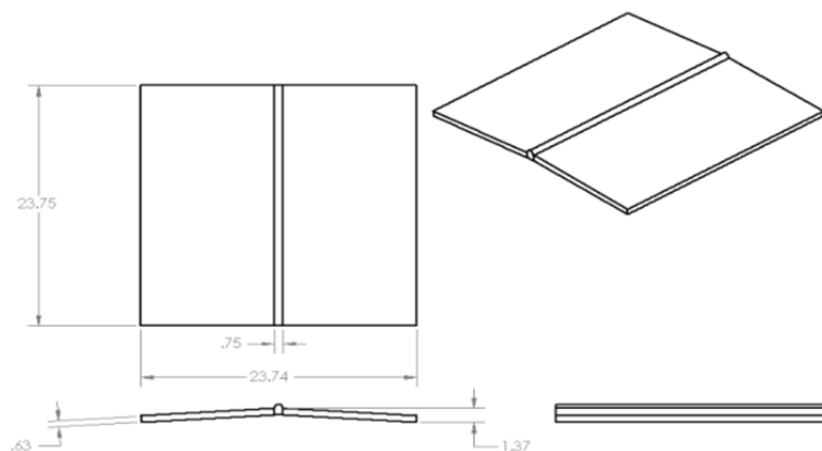
Figure 5. Schematic of prototypic weld plate obtained from INL.

This 304 weld plate prepared by INL was welded to best simulate the welding conditions in fabricating the canisters for spent nuclear fuels, though the stress level may be different from the canisters welding. This 304 weld plate was water jet cut along the weld line as seen in Figure 6. The typical weld microstructure is shown in Figure 7. The weld metal, heat affected zone and base material are shown in Figure 7.

Figure 6. Water jet cutting of the weld plate procured from INL.
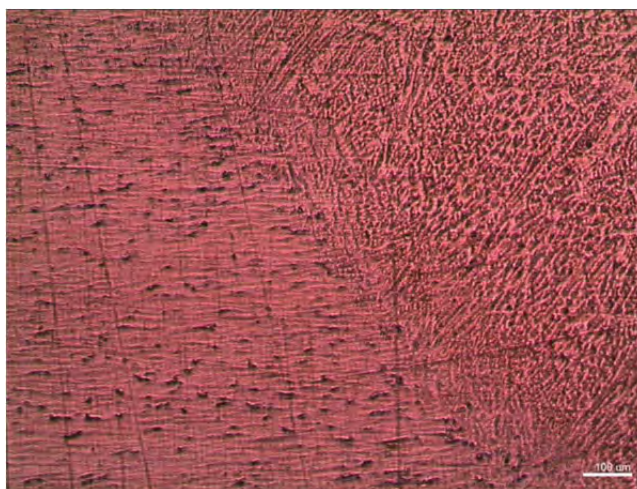
Figure 7. Optical micrograph of weld structure.

This water jet cut material was then EDM wire cut to create strip samples as shown in Figure 8. These strip samples are mirror polished for corrosion testing and for preparing U-bend SCC samples.

7
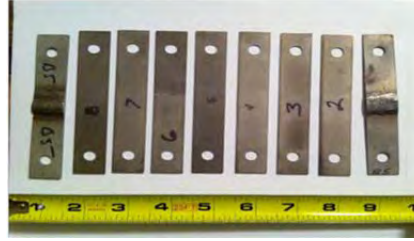
Figure 8. EDM wire cut sections of the weld plate.

ASTM synthetic sea salt [7] was used to induce corrosion for all corrosion and SCC experiments. The composition of the dry ASTM synthetic sea salt is shown in Table 4. 1N synthetic sea salt water was prepared by adding 41.953 grams of dry sea salt to 1 liter of deionized water. The weight percent of sodium chloride after mixing in the water was 2.453%.

Table 4. ASTM D 1141-98 sea salt composition (in wt%).

NaCl	58.490%
MgCl2 6H2O	26.460%
Na2SO4	9.750%
CaCl2	2.765%
KCl	1.645%
NaHCO3	0.477%
KBr	0.238%
H3BO3	0.071%
SrCl2 6H2O	0.095%
NaF	0.007%

2.2 Introduction of the corrosion and SCC experiments

A variety of experiments were conducted in this research for understanding potential corrosion mechanisms in dry cask storage canisters. Pitting experiments included salt on sample hydration (SOSH) exposure, salt spray exposure, pitting profiling, and electrochemical polarization. SCC experiments included compact specimen (CT) fatigue cycling, CT constant loading, and U-bend environmental exposure tests.

2.2.1 Salt on sample hydration (SOSH) exposure test

SOSH testing was conducted to determine pit size, and pit surface density over the course of 96 hours. SOSH test samples were discs of 16 mm diameter and 1 mm in height with a mirror-polished surface. The discs were placed in a 10 inch diameter acrylic chamber with a Teflon flooring and metallic dust cover. A hydrometer and thermometer were introduced in the chamber to record average temperature and RH, which remained at ambient conditions (~20% RH, 21°C). The acrylic chamber was loaded with a large number of samples at the beginning of each experiment. Two salt application methods were used, solid and liquid deposition. For solid deposition, two salt crystals were loaded on the surface of each sample. A specified volume of deionized (DI) water; either 0.1 or 0.2 ml, was dropped onto the surface of each sample to promote the dissolution of the salt crystals. Every 8 hours, the same volume of DI water was dropped onto the surface. In the case of liquid deposition, a specified volume (0.05 ml) of concentrated

8

sea salt water (1N, 2N, or 4N) was dropped onto the surface only at the beginning of the test. All liquid deposition tests lasted for 96 hours.

For both solid and liquid deposition tests, two samples were removed from the chamber every 24 hours to provide a snapshot of the corrosion process for that time period. The two samples were cleaned and weighed to determine mass change. SEM images were then taken at 13 locations on each sample. Images were then compiled in ImageJ 1.38e to obtain visual data regarding pit size and pit surface density. A 50% threshold mask was used in ImageJ to convert from color to black and white binary data. **Figure 9** demonstrates this process.

Two pit profiles on separate samples were modeled through incremental polishing. Samples were polished between 10 and 30 microns, and then examined under SEM to image the pit perimeter. This step was repeated until the depth of the pit had been polished past. In addition to two incrementally polished pits, another pit had been ion milled to visualize its entire depth profile.
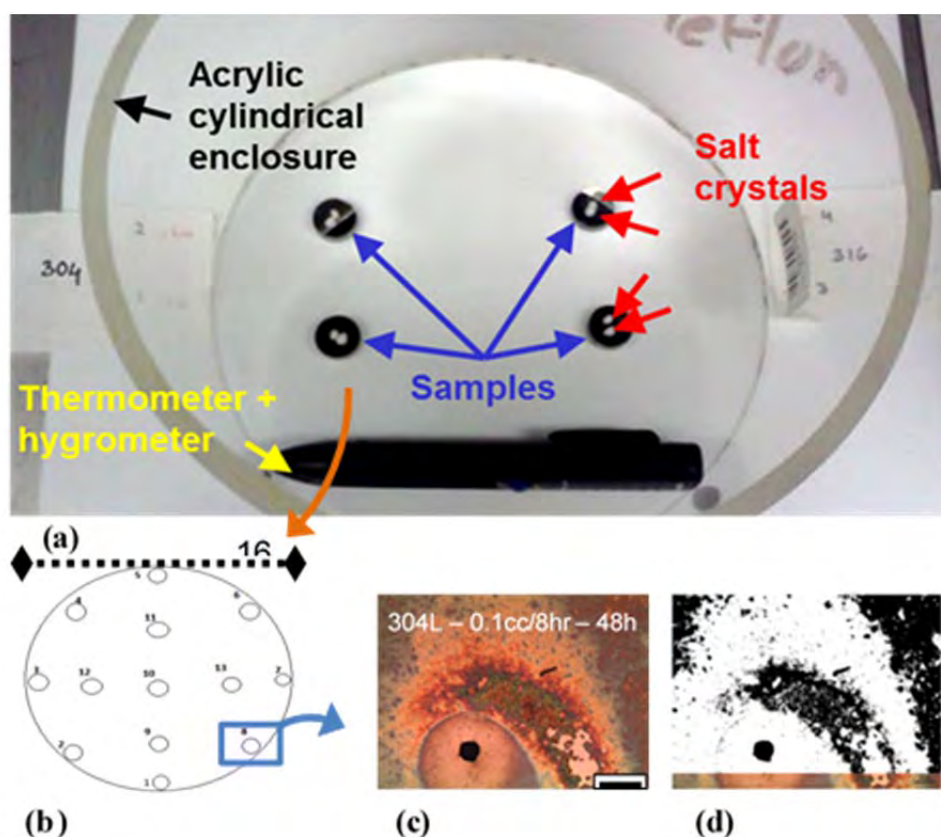
Figure 9. SOSH test procedure. (a) Overhead profile of the acrylic chamber loading. A 96 hour test would typically have 8 samples with salt loading, removing two samples every 24 hours. (b) A single disc sample was imaged in 13 locations with an optical and SEM microscope. (c) An example of a corrosion site with 0.1 cubic centimeters DI water hydration every 8 hours. (d) Image conversion to a black and white binary signal to calculate pit sizes.

2.2.2 Salt spray exposure test

Salt spray testing was carried out using samples similar to the SOSH samples. However, samples were suspended in a chamber rather than resting horizontally. Figure 10 shows the salt spray nozzle and chamber. To spray the salt, compressed air was blown into a glass nozzle to force water out of a sealed

9

reservoir and combine it with the air flow. ASTM sea salt water was sprayed for 5 minutes, followed by 55 minutes without spray. This continued for 8 hours, followed by 16 hours without spray. Each week, a 1-day examination was conducted on the samples. During examinations, each sample was removed from the spray test chamber, cleaned, weighed, and re-entered into the chamber.
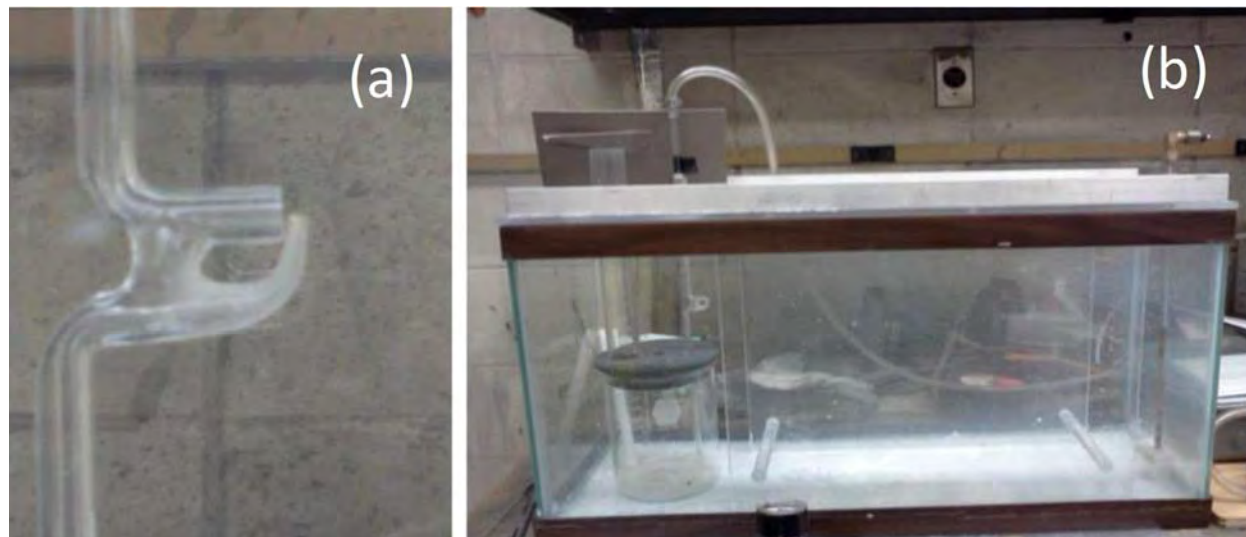

Figure 10 Salt spray testing. (a)The salt spray nozzle (aspirator tube) was custom made by Wild Rose Glass. (b) The salt spray chamber. Samples were suspended from rungs at the top of the chamber. A timer allowed for eight spray intervals over a 24 hour time span

2.2.3 Electrochemical polarization

Potentiodynamic tests were conducted on several materials to compare corrosion resistance. A potentiodynamic polarization scan technique developed by CRIEPI [8] was used to compare repassivation potential for three different materials including base metal SS304L, a weld bead section of the SS304L sheet produced in-house, and a HAZ region from the same sheet. Samples were surrounded by a circular Teflon housing to minimize crevice corrosion. Experiments were conducted in non-deaerated synthetic seawater with a pH of 7.6. A Solartron 1287A potentiostat with a 1 L corrosion cell were used. Measurements were taken using a Saturated Calomel Electrode (SCE) as reference. Figure 11 shows the electrochemistry cell.

The experiments began by breaking down the passive layer and initiating crevice corrosion of the sample near the edges of the Teflon holder. This was done by controlling the current, holding it at 200 uA for 2 hours. Potential (voltage) decreases very rapidly at the beginning of this current hold, due to a loss of resistance from the breaking of the passive layer. After holding the current for 2 hours, potential became the control variable. Every 2 hours the potential was stepped down by 10 mV while monitoring the current. This caused the current to decrease for nearly 1 hour before rising to its value before the voltage step-down. Decrements of voltage continued until current dropped in a potential step without recovery. This voltage step is the repassivation potential, represents the recovery of the passive layer.
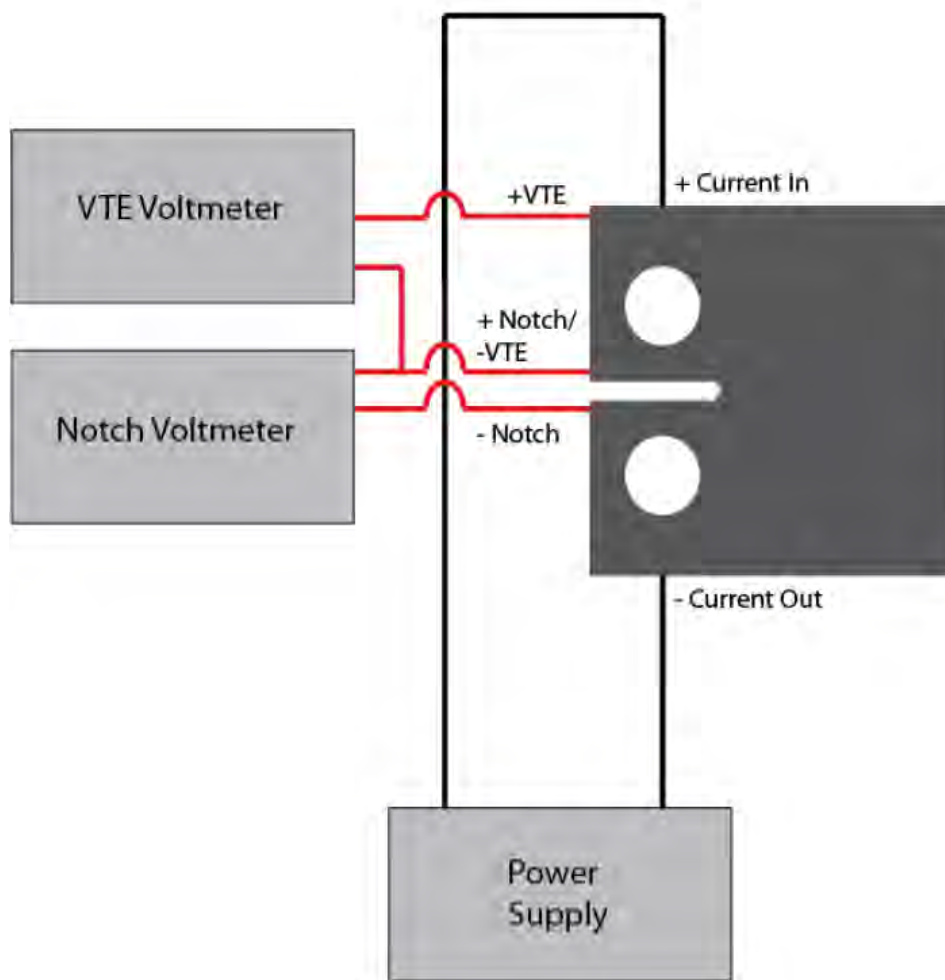
10
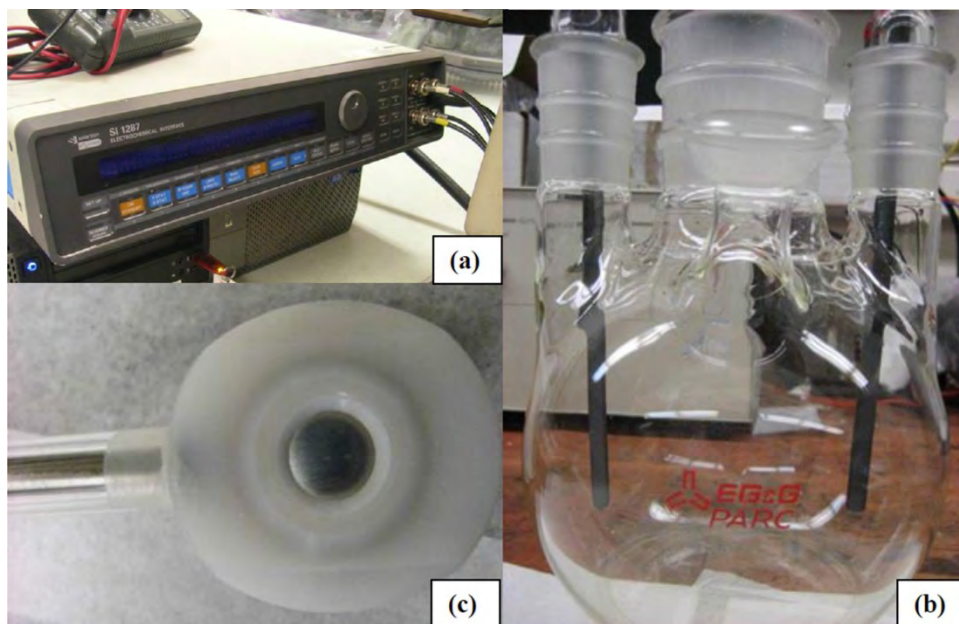
Figure 11. Electrochemistry cell. (a) A Solartron 1287A potentiostat with (b) 1 L corrosion cell was used. Measurements were taken with an SCE reference electrode on (c) 16 mm disk samples surrounded by a Teflon seal.

2.2.4 SCC tests using compact tension (CT) specimen fatigue cycling

Compact tension specimens were first used to determine SCC crack growth rates under various treatment conditions. Samples were electron discharge machine (EDM) cut from 6.35 mm SS304L by Adron Tool in Menomonee Falls, WI. Specimen design and crack measurements were performed in accordance with ASTM E647-00 [9] . The width of CT specimen was 25.4 mm to ensure the hydraulic load frame would be capable of fracturing the specimen. The surface of samples was ground with 320 grit paper to ensure consistency across all samples. It was assumed this 320-grit ground surface would approximate the surface roughness of the canister. Dimensions of the CT are shown in Figure 12.

Figure 12 Dimensions of compact tension specimen. All dimensions are in mm.

The direct current potential drop (DCPD) method was used to measure crack length while the samples were in an Instron 6601 Load Frame. By applying a constant 1.5 Amp current across the CT, potential changed with a growing crack length. A reference voltage was also measured to compensate for temperature drifts. The DCPD method is shown in Figure 13 schematically.

12

Figure 13 Schematic DCPD measurement method. Power was supplied to the sample above and below the loading pin holes. The VTE Voltmeter read a reference voltage to compensate the Notch Voltmeter in case of a temperature excursion.

The ASTM equation for calculating crack length is given as

$$\frac{a}{W} = B_0 + B_1 * \left(\frac{V}{V_r}\right) + B_2 * \left(\frac{V}{V_r}\right)^2 + B_3 * \left(\frac{V}{V_r}\right)^3$$

where a is the crack length, W is the specimen width, V is the voltage read by the voltmeter, Vr is the initial voltage across the notch without crack propagation, and the B values are constants, B_0= -0.5051, B_1= 0.8857, B_2= -0.1398, and B_3= 0.0002398. For the specimen dimensions, crack length values were only valid for lengths over 1.2 mm. The DCPD method required that copper leads be connected to the CT samples. Initial connections were made by soldering the copper wires to the stainless steel samples. However, these bonds were weak and caused inaccurate data collection. Leads were later brazed to the stainless steel samples using a BAG-24 filler metal, containing silver. A propane torch was used to heat the base metal and filler to 750°C, slightly above the liquidus point of the braze metal. This created a good metallic bond between the CT specimen and the copper wire. After connecting the leads, samples were ground with 320 grit paper again to remove the surface damage caused by the torch. Leads were

13

then electrically insulated with a resin coating to prevent circuit shorting to load frame and corrosion at the connections.

After the CT specimens were prepared using the above methods, samples were loaded into an Instron 6601 load frame with lower arm actuator with a 100 kN maximum load. Grips and load arms were designed specifically for this project. Adjustable lock nuts ensured that the load chain components were properly aligned. The components were made of plain-carbon steel to ease the machining process.

An environmental chamber was designed to fit around the load chain to heat the sample and control salt vapor RH. A polycarbonate tube surrounded the CT specimen and was sandwiched by two corrosion-resistant aluminum disks. A concentric aluminum cylinder was positioned between the load chain and polycarbonate tube. This cylinder was wrapped with a 150 watt silicon heating tape and perforated to enhance heat transfer to the chamber air. A thermocouple located near the CT communicated with the temperature controller for the heating tape. Salt vapor was created with a commercial sonication-type humidifier. A PET plastic tube directed vapor flow into the chamber. A hygrometer located in the chamber measured in-situ RH. The full system is shown in Figure 14 .
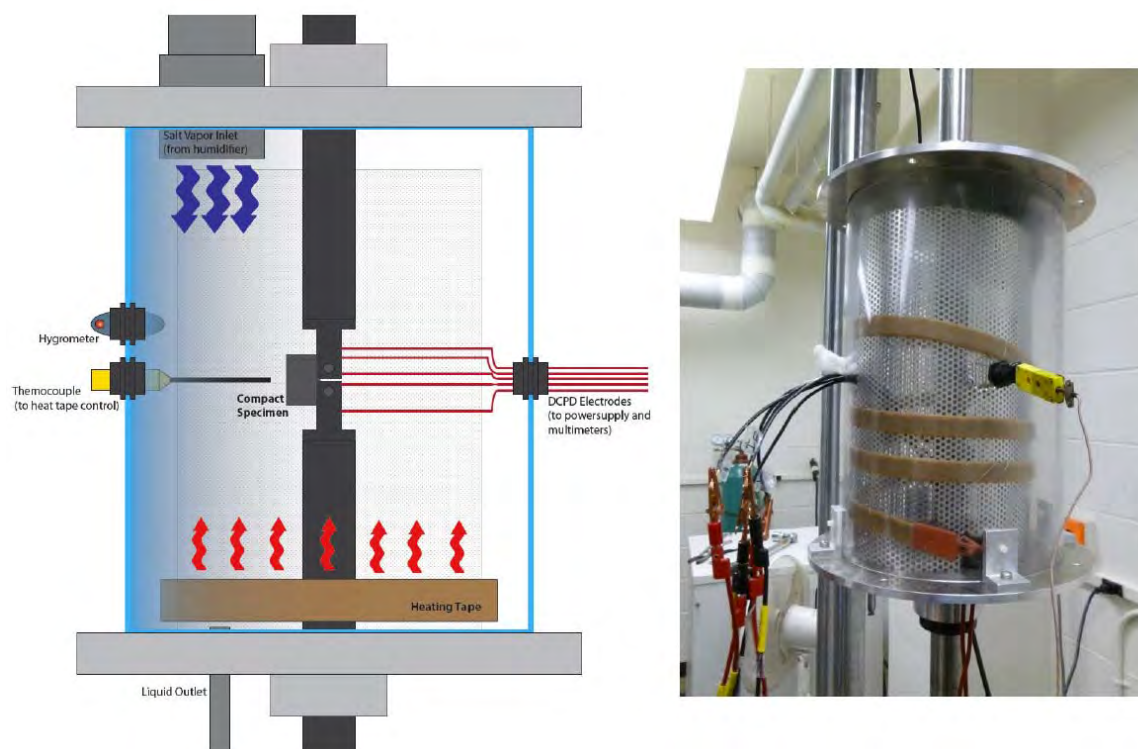
Figure 14. Environmental Chamber for DCPD measurement of compact tension (CT) specimen.

Prior to conducting experimental trials, the DCPD method was verified with several tests. Short circuiting the CT across the notch was a primary concern. A dry CT was first cracked by fatigue cycle cracking to approximately 1.2 mm. It was then visually measured and DCPD measured. With a 1.5 Amp current, the DCPD crack size was within 9.0 microns of the visually inspected crack size. The sample was then immersed in a synthetic seawater solution and measured, once again measuring within 9.0 microns of the inspected size. Finally, the sample was allowed to dry in a saturated salt solution and read after drying. Once again, the crack size was within 9.0 microns of the optical measurement.

Following the salt solution verification, another CT specimen was fatigue cracked, unloaded, and visually inspected five times to determine standard error between DCPD crack length and true crack length. In this case, three separate DCPD correlations were tested. In addition to the ASTM correlation, a

14

modified ASTM correlation was used with a least-squares fitting technique between the known crack lengths and B constants. Another correlation was also tested based upon the use of in-situ reference voltage. Optical microscope images were compiled over each other in cases where crack length extended beyond the view field. Final standard error was found to be +/- 10.0 microns. The next series of images demonstrates this process.

After determining the standard error in DCPD measurements, CT samples were fatigue cracked under various conditions to determine the effects of temperature, sensitization, and salt vapor on SCC. All CT specimens were initially pre-cracked approximately 1.2 mm (18,000 precrack cycles) under cyclic loading. The minimum and maximum loading was 4.1 kN and 10.4 kN, with a cycle frequency of 1 Hz. At the end of pre-cycling, samples were held in tension at 7.25 kN for 2 hours before cycling to near failure. The minimum and maximum loading during the second cycling phase was 4.8875 kN and 9.6125 kN.

Both sensitized and AR samples were fatigue cracked. Tests were carried out in one of four environmental conditions: ambient, heated to 80°C, heated to 120°C, and heated to 80°C with 80% RH salt vapor. For heated samples, loading began at the end of the pre-cycling phase before the second fatigue loading. Salt vapor was introduced to the systems at the beginning of the second fatigue loading. A total of seven fatigue tests were conducted. The load frame was programmed to end the test when the CT specimen mouth had vertically opened by 50 mm. Generally this occurred when the crack length of CT specimen was 5,000 microns and began to rapidly fail.

2.2.5 SCC tests using constant loaded CT specimens

After completing fatigue-induced SCC tests, it was thought that constant loading of CT specimens would better simulate actual canister conditions. Thus, a series of constant load tests were conducted using CT specimens. Constant load specimens were pre-cracked with the same conditions as the fatigue cracking specimens. After pre-cracking, the samples were held at 7.25 kN for 2.0 hours, and heated during this time frame if needed. After holding at 7.25 kN, the loading force was ramped to 12 kN in one minute. Four total tests were completed. These were at ambient and 80°C salt vapor conditions for both AR and sensitized material.

2.2.6 U-bend environmental exposure tests

U-bend tests were generally used to most closely simulate prototypic canister conditions. These samples were favorable due to the inherent stresses in the samples without dynamic loading. All U-bends were mirror polished prior to bending and environmental exposure so that developing pits and cracks could be easily characterized. The specimens were 1.2 mm thick with a 25.4 mm bend diameter and water jet cut by Penn Stainless. Samples were bent using a Bayleigh Industrial Bar Bender such that spring back was observed after bending, as described in ASTM G30-97(R2015) [10]. A metal bolt was slid through both holes and tightened to recover the bend shape and maintain geometry throughout exposure testing. Teflon insulators prevented metal-on-metal contact between the U-bend and hardware so that galvanic corrosion is avoided. The U-bend geometry and the bending process are shown in Figure 15.

15
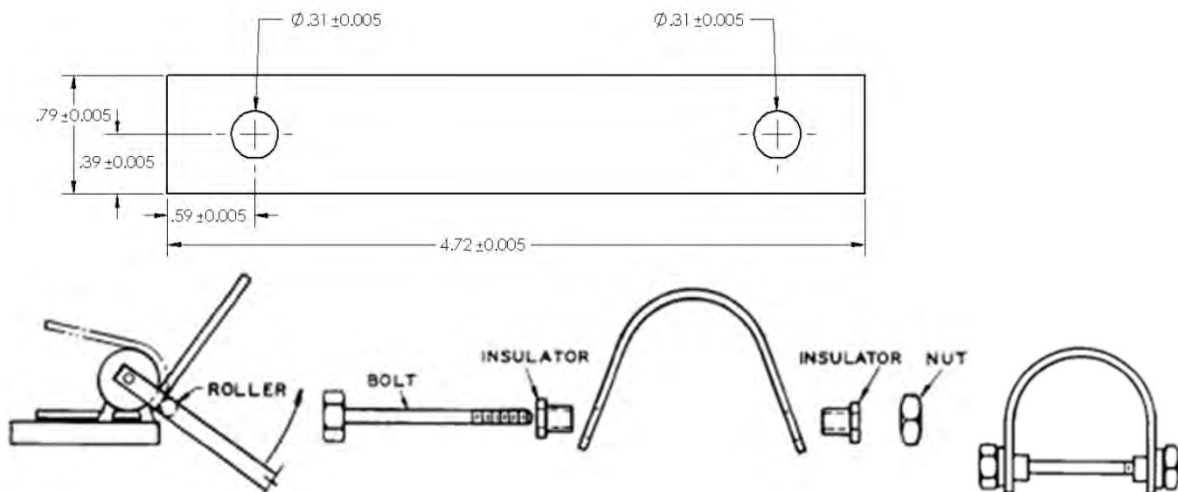
Figure 15. U-bend geometry and bending process. A Bayleigh Industrial manual bender was used to bend the specimens using the two-stage method described in ASTM G30.

As mentioned previously, U-bends were made from three types of material; as-received (AR), sensitized, and welded stainless steels. Five long-term exposure tests were conducted to analyze pitting and cracking rates. At least ten U-bend samples were prepared for each type of exposure test. Three of the exposure tests were held at 80°C with 80% RH salt vapor. Each of these three used a different U-bend material. The remaining two tests both used AR material exposed to 80% RH. One test was held at 60°C and the other at 30°C to determine bounds for the critical pitting temperature. U-bends were placed in the same environmental chamber used for CT samples after removing the chamber from the load frame.

U-bend samples were sequentially removed from the environmental chamber at specific time intervals over the course of the experiment lifetime. After removal, each sample was sonicated in DI water followed by acetone and methanol. This allowed the pits and cracks to be imaged by optical microscopy and SEM. Once removed, samples were not re-entered into the corrosion chamber.

The rates of pitting attack and crack growth were determined from optical data. Each U-bend sample was imaged at 1000x in a JEOL JSM-6610 SEM with Energy Dispersive X-ray Spectroscopy (EDS) capability. Six images were taken from the top plane of each sample. Each series of images was taken from the areas of highest damage after inspecting the U-bend. This region was typically 12.11 degrees offset from either side of the U-bend peak or +/- 3.0 mm from the peak. Images were taken every 2.75 mm across the width of the sample so they would be in sequential order and at uniform locations across all samples.

After obtaining SEM images, pitted regions were counted for each image using ImageJ 1.38e. Minimum pit resolution was 0.2 micron diameter so that any features smaller than this were not counted. Crack lengths were also counted across samples. Cracks were not considered to be significant if their length was less than 100 microns. Crack-like features that were less than 100 microns in length but within a specified circularity limit were considered to be crack initiation sites. This circularity was $0.15 \leqslant$ circularity $\leqslant 0.685$. Calculation of this value is given below as well as the roundness calculation. Because roundness utilizes a major axis value, which is subjective for each feature, it was determined that circularity would be a better distinction for crack initiation sites. Percentage of area pitted, number of crack initiation sites, and total crack length were analyzed.

16

$$circularity = 4 * \pi * \frac{area}{perimeter^2}$$

$$roundness = 4 * \frac{area}{\pi * major\ axis^2}$$

3 **Results and discussion**

3.1 SOSH

Figure 16 shows the pit size distribution of SS316L to SS304L. As expected, SS304L had experienced more corrosion than SS316L, due to increased nickel and molybdenum content in SS316L. SS304L exhibited a larger number of pits for every pit size after the 48 hour experiment when compared to SS316L for 0.1 ml hydration tests. These results also showed that higher salt- concentrated solution yields higher corrosion rates. Finally, the distribution of pit sizes was as expected, with a high concentration of large area pits followed by trailing concentrations of smaller sized pits fitting an exponential distribution.
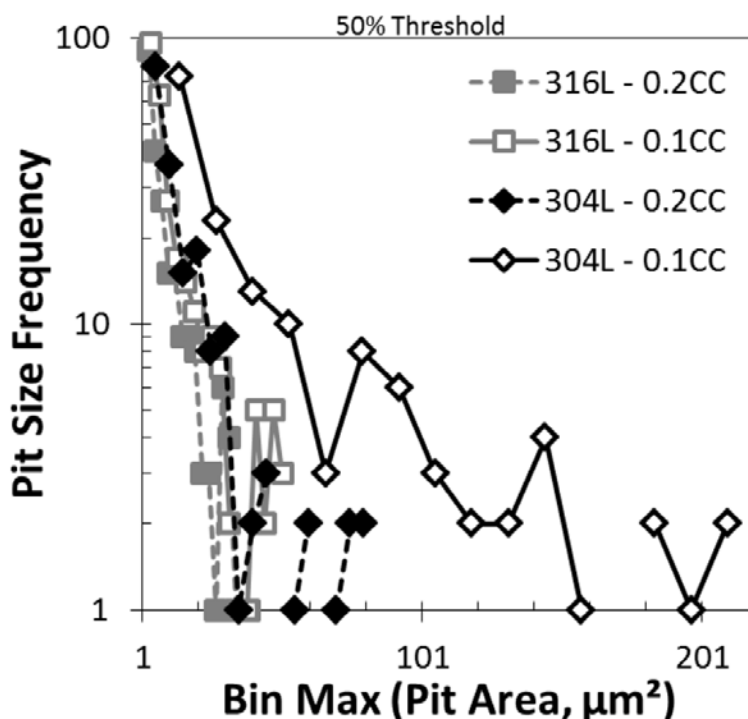
Figure 16. Distribution of pit size after SOSH tests in various concentrations of salts. Four tests were performed over 48 hours. SS304L exhibited more corrosion susceptibility compared to SS316L when tested under similar conditions.

Figure 17 shows the pit size distribution of 1N, 2N, and 4N concentration liquid deposition SOSH tests. A volume of 0.05 ml of sea salt water was applied once to the samples at start of the tests. The highest concentration of pit size for any time step with any concentration was between 0.02 and 0.152 μm^2 in area except for the 96 hour 1N concentration exposure test. A Weibull distribution of pit size appears evident in the 1N concentration samples. Higher concentration tests assume an exponential

17

distribution. The Weibull distribution has two shaping parameters and can exhibit a maximum at a non-zero point in time, unlike the exponential distribution. The exponential distribution is a special case of the Weibull distribution as shown below

$$f(t;\ \lambda, k) = \frac{k}{\lambda}\left(\frac{t}{\lambda}\right)^{k-1} e^{-\left(\frac{x}{\lambda}\right)^{k}} \qquad When\ k = 1 \qquad f(t;\lambda) = \frac{1}{\lambda}e^{\frac{t}{\lambda}}$$
,

The variables and k are both shaping functions. It is commonly accepted [11, 12] that pit initiation can be modeled by these two statistical distribution functions. For pit area distribution to take the same form as either of these functions, it would be implied that pit area growth is a square root function of time or an Arrhenius function of time. It is more likely that the latter is true as indicated in previous work. As mentioned before, the Weibull distribution takes exponential form when k is 1. Therefore, this parameter exhibits dependence on salt concentration. When holding all other conditions constant, pit area size demonstrated both distribution types.
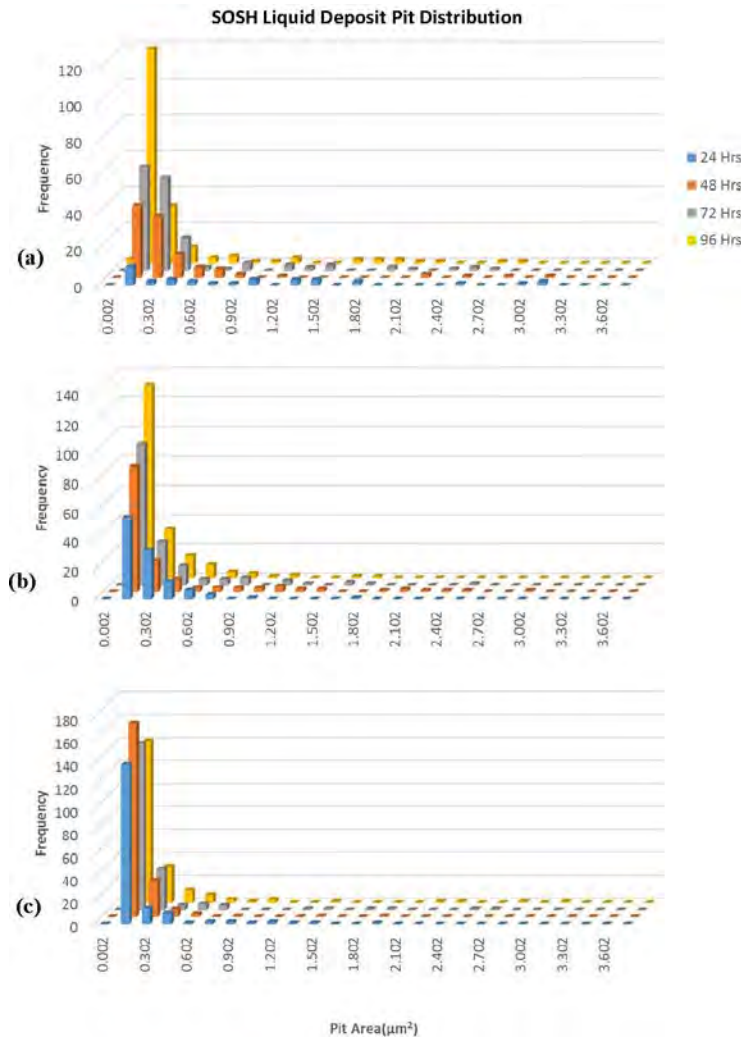
Figure 17. Pit size distributions as a function of salt concentration (a) 1N, (b) 2N, (c) 4N salt solutions were deposited on the samples in a volume of 0.05 ml.

18

Cross-sectional image of a pit from SOSH tests as produced by the focused ion beam (FIB) technique using a gallium source is shown in Figure **18**. The near-surface volume of the pit is nearly hemispherical in shape, however, the cross section shows a much deeper tear-drop shaped section. This is likely due to an increase in chloride ion concentration within the pit. Using electrochemistry pitting kinetics, corrosion rate can be determined from the solution pH. A lower pH will increase pit growth kinetics. In the pit geometry shown, it is likely chloride ions could not leave the local system easily due to restricted flow or an oxide cap. The chloride would bond with hydrolyzing hydrogen to form HCl and continue to drive corrosion by lowering pH.
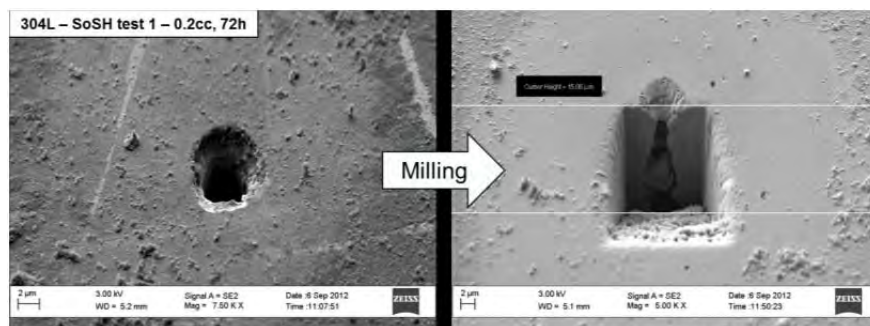
(a)   (b)

Figure 18. Pit profile. (a) Pit surface on SS304L after salt crystal deposit and 0.2 cm3 deionized water applications per 8 hours for 72 hours. (b) Pit profile cut using focused ion beam (FIB) technique. The pit depth was 15 microns, with a mouth that was 5 microns in diameter.

Two examples of incrementally polished pits are shown in Figure **19** and Figure **20**. Like the ion-milled pit, these pits are much deeper than they are wide; with width to depth ratios of about 1/3. Many sources in literature suggest that pits' profile can be estimated as hemispherical in geometry, however the profiles of these pits show a structure that is more cylindrical.
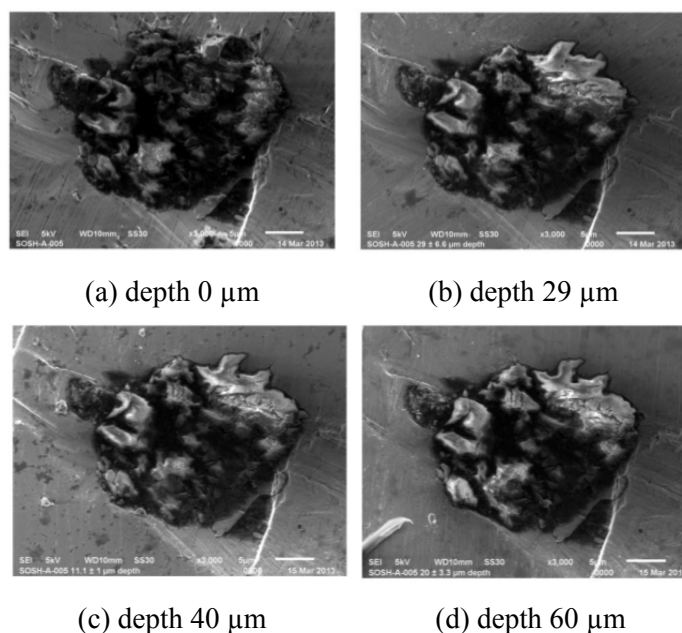
(a) depth 0 μm   (b) depth 29 μm

(c) depth 40 μm   (d) depth 60 μm

Figure 19. Incrementally polished pit. Incremental polishing to estimate shape as a function of depth. The final polishing step removed a total of 80 microns of materials removal and the pit depths estimated to be between 60 and 80 microns.

19

(a) Depth: 0 um   **(b) Depth: 29 um**

(c) Depth: 40 um   **(d) Depth: 60 um**
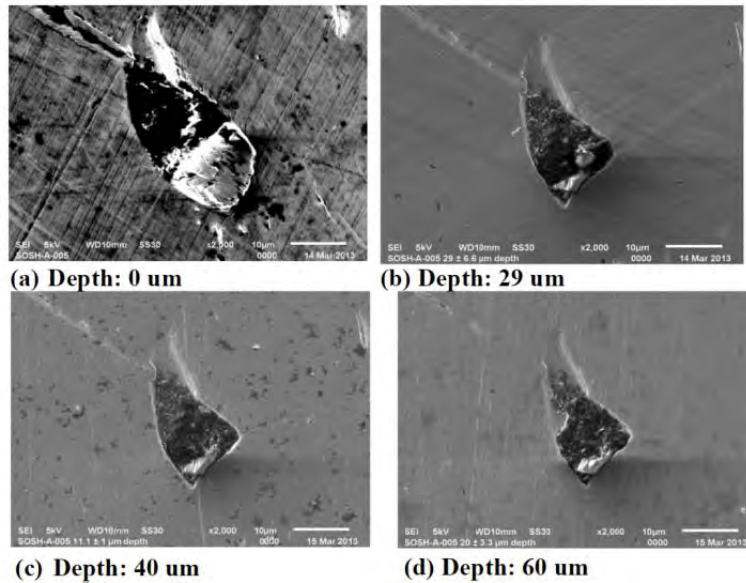
Figure 20 Incrementally polished pit. These images show incremental removal of the sample surface to determine pit depth and geometry. The final polishing step removed a total of 80 microns from the material so that the actual pit depth was between 60 and 80 microns.
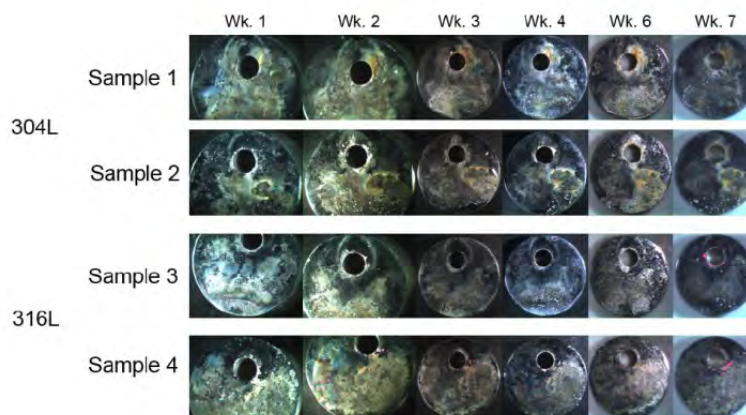
3.2 Salt spray tests

Mass gain results as shown in Figure **21** indicate that the corrosion rate for SS304L is higher than SS316L, as expected. At the end of 5 weeks, the mass gain of SS304L was over triple that of SS316L (0.55 mg compared to 1.9 mg). Mass gain came from the combination of salt deposition and corrosion product formation. The first two measurements of SS316L salt spray tests indicate a mass loss between week 1 and week 2. This is likely due to corrosion products forming on the surface and remaining after cleaning. Optical imaging of the salt spray samples indicated a tendency for corrosion sites to reinitiate after cleaning as indicated by the recurring patterns of red rust shown on the samples from week to week, as shown in Figure **22**.
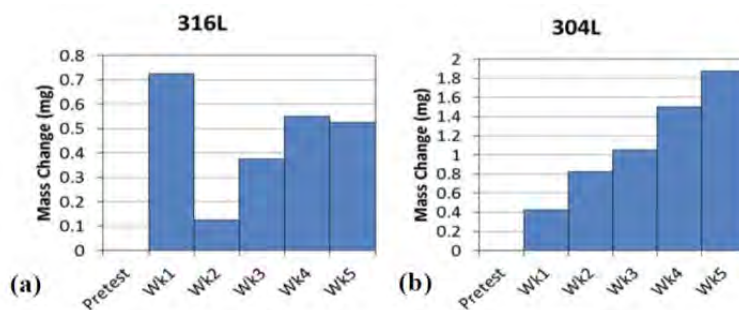
Figure 21. Mass change for (a) 316L and (b) 304L after salt spray tests

Figure 22. Images of samples from salt spray tests shown at the end of each week prior to cleaning, weighing, and re-immersion into the salt spray chamber.

3.3 Electrochemistry

Repassivation tests demonstrated that the weld bead with HAZ sample was most susceptible to corrosion. The sample of SS304L had the highest repassivation potential, and the sample with only a HAZ region had a repassivation potential between the two. Generally, a higher repassivation potential means a material is more noble and has a higher resistance to corrosion. The repassivation plots for these three tests are shown in Figure **23**.

| (a) | (b) | (c) |
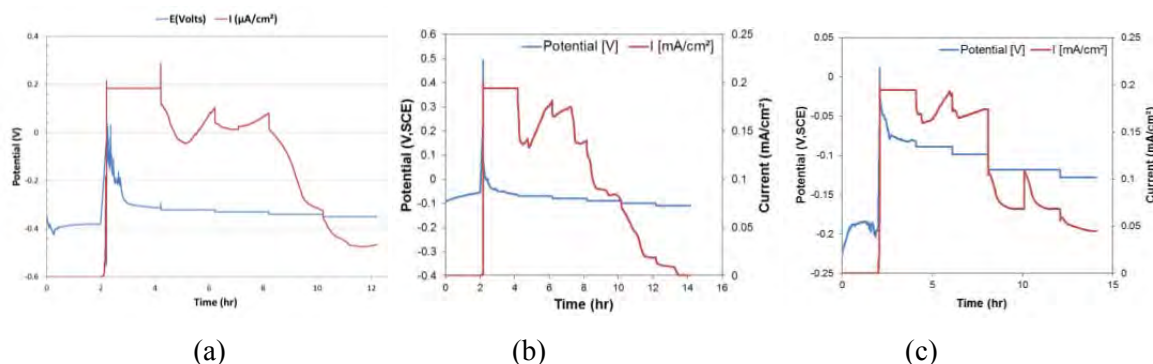
Figure 23 SS304L linear repassivation scans. Non-deaerated synthetic seawater with pH of 7.6 was used as the solution. (a) SS304L base metal. (b) SS304L HAZ. (c) SS304L HAZ with weld bead. Repassivation is shown where the current crosses the potential. The weld bead sample had the lowest repassivation potential and therefore the lowest resistance to corrosion

3.4 SCC fatigue cycling

Compact Tension (CT) Specimens were first tested by fatigue cycling. Samples typically failed after cracking beyond 5,000 microns. Failure was determined to be the point when the DCPD voltage changed by over 50 mV in 0.5 second. Temperature and prior material processing treatment was shown to affect fatigue life. A corrosive environment that included 80% RH sea salt vapor and a temperature of 80°C caused the sensitized material to fail the fastest after 11 hours of fatigue cycling. The as-received (AR) material showed no signs of accelerated failure associated with corrosion when exposed to these conditions. A temperature increase from 21°C to 80°C caused failure to occur 5 hours sooner for both AR

21

and sensitized material. However, a further increase to 120°C had no distinct effect. Therefore temperature had the highest impact on failure, followed by corrosion of sensitized material.
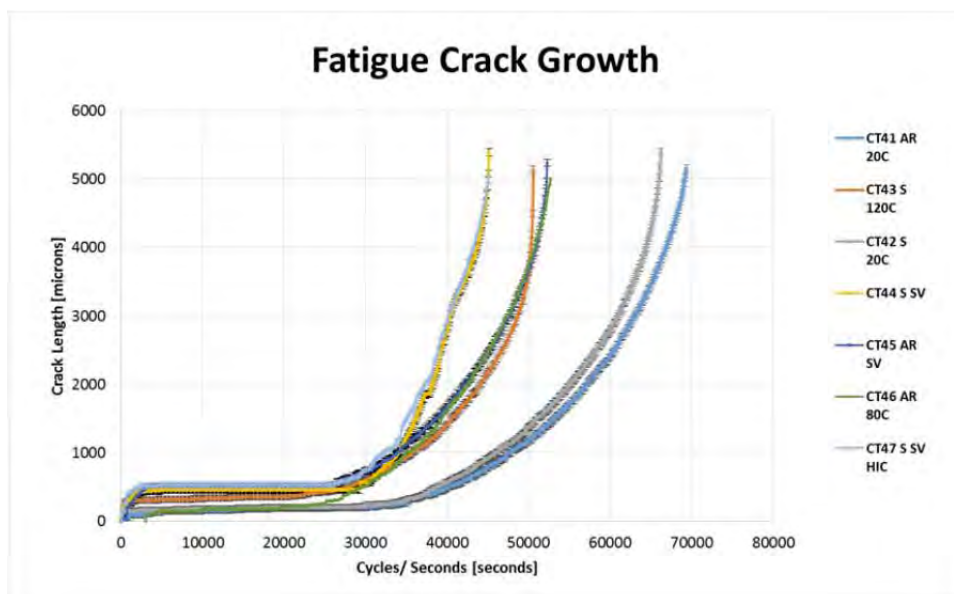
Figure 24. SCC fatigue crack growth of different 304L tested different environments. At 19 hours, AR and sensitized CTs failed in ambient conditions. At 14 hours, AR CT failed in 80°C, 80% RH salt vapor conditions. Two sensitized CTs failed at 80 C and 120 C with no salt vapor. At 11 hours, sensitized CTs failed in 80°C, 80% RH salt vapor conditions. A 1N and 2N solution was used, resulting in similar time failures at 11 hours.

3.5 Constant loading SCC tests

Unexpectedly, the SCC constant load tests produced highly variable results and probably required long test times to acquire any meaningful data. In agreement with previous data by Turnbull and Tani [13, 14], crack growth rates decayed rapidly. At the end of 117 hours (7,000 minutes), crack growth rates were approximately 9.2×10^{-8} m/s. Figure **25** presents the AR material cracking for longer times before a stunted growth regime. Because tests were not taken to failure, the constant loading data is not considered to be representative SCC. Ductility of the steels prevented rapid fracture.
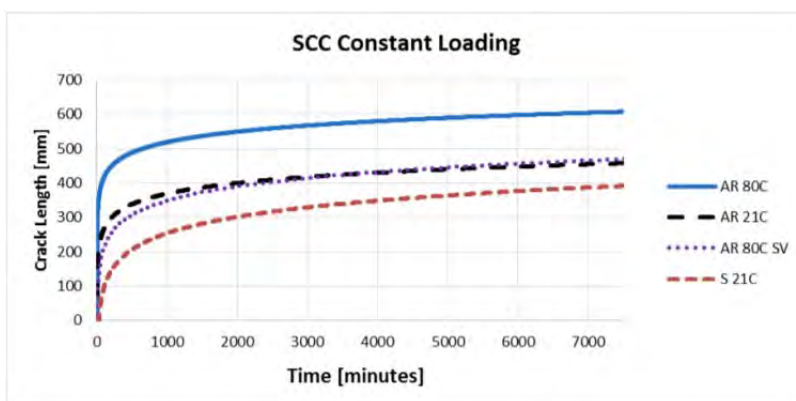
Figure 25. SCC constant loading. Crack growth rates decayed logarithmically as shown in the literature. Because of time constraints, tests were terminated before failure of any CT specimen. The data from these tests is not regarded as accurate.

22

3.6 U-Bend exposure tests

U-bend testing was carried out on three materials as per ASTM standard ASTM G30-97(R2015): AR, sensitized, and welded SS304L. Three environmental conditions were studied: 30°C, 60°C, and 80°C, all with 80% RH salt vapor produced from the atomization of ASTM synthetic sea salt. Typical evolution of the U-bend surface in these tests is shown in Figure 28. At the beginning of the corrosion process, pits nucleated separately but later stages became interconnected with cracks. Longer exposure times caused these cracks to grow beyond pit sites, and propagate in a direction perpendicular to the applied stress. Crack direction was observed to remain within 45 degrees of the main axis, deviating only to meet a nearby pit.
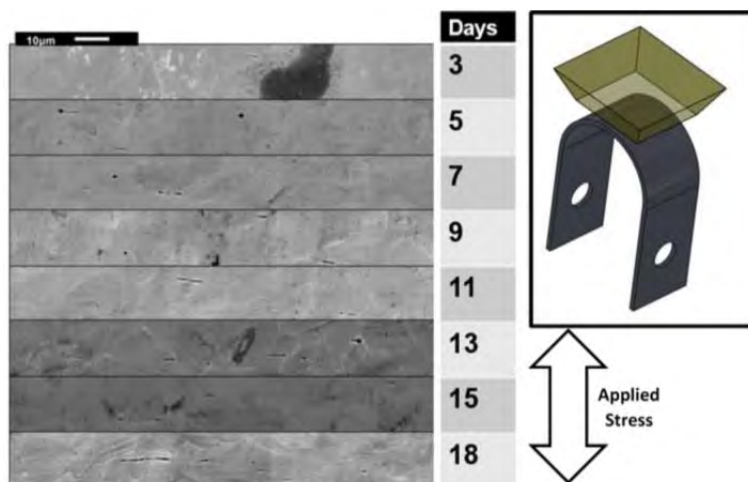
Figure 26. Progression of surface corrosion in U-bend tests over an 18 day exposure test. Eight separate U-bend surfaces are shown at their respective days of removal from a 30° C, 80% RH salt vapor environment. Images show rectangular sections of the top portion of the U-bend near the peak. Pits tend to grow into one another as cracks begin to nucleate and propagate.
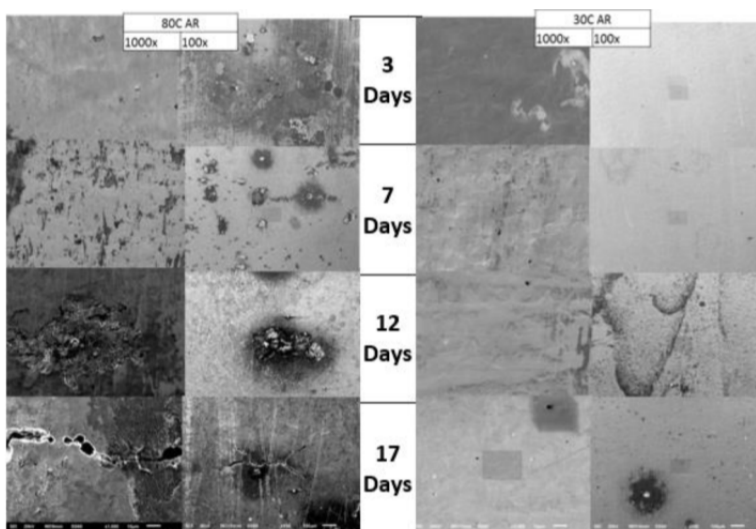
Figure 27. SCC of AR Material for 80°C and 30°C, 80% RH salt vapor tests.

Figure **27** demonstrates surface damage differences of U-bends tested at 80°C and 30°C , both held at 80% RH. The 30°C specimens were generally unaffected by corrosion at the end of 20 day tests whereas

23

the 80°C specimens had undergone significant pitting, SCC, and sodium chloride deliquescence. The largest pits discovered on the 30°C samples shopwed high sulfur concentrations at their centers and in rings around the pit. EDS mapping also showed halos of molybdenum around such pits, which provides more evidence of preferential manganese sulfide (MnS) dissolution induced corrosion at 30°C. As demonstrated by Pardo [15], the dissolution of MnS can drive local pH below 2, at which point Mo from the steel matrix dissolves and MoO_3 readily forms. The pH level outside of the pit can be higher in the range of 4 to 6, causing MoO_3 to become unstable and form $FeMoO_4$ on the flat surface surrounding the pit mouth. This indicates that corrosion selectively initiates at inclusion sites under these conditions. This process is shown in Figure **28**.

(a)   (b)
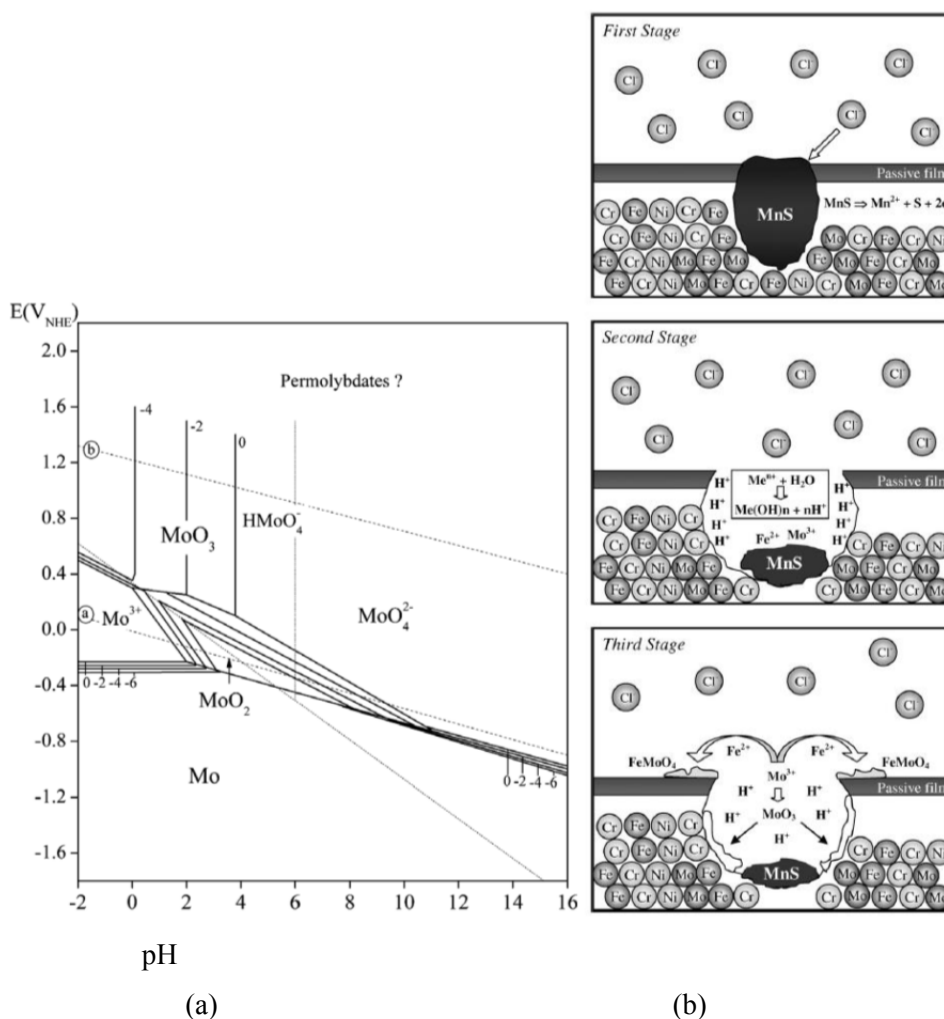
Figure 28. (a) Pourbaix diagram of molybdenum-oxygen stability and (b) possible corrosion mechanism near MnS inclusions. According to the Pourbaix diagram, at higher pH, MoO_4 species are favored, which can form $FeMoO_4$ on the steel surface. Within the pit, pH can be lower and favor the formation of MoO_3. This lower pH is caused by the dissolution of MnS inclusions. As shown in (b) the corrosion mechanism can be explained in three stages:in the first stage, MnS inclusions are thermodynamically unstable and dissolve to reveal a bare steel surface; the second stage sees dissolution of the steel matrix elements and continued water hydrolysis; the third stage results in molybdenum becoming highly oxidized and stable. The formation of deposits around the pit can in some cases prevent contact of chloride ions with the steel matrix.

24

An EDS map of a corroded inclusion zone is also shown in Figure **29**. It should be noted that the formation of $FeMoO_4$ results in a highly stable and insoluble species. This compound can prevent chloride ions from driving further dissolution of the steel matrix. Formation of this oxide likely slowed the corrosion of $30^{o}C$ U-bend samples.
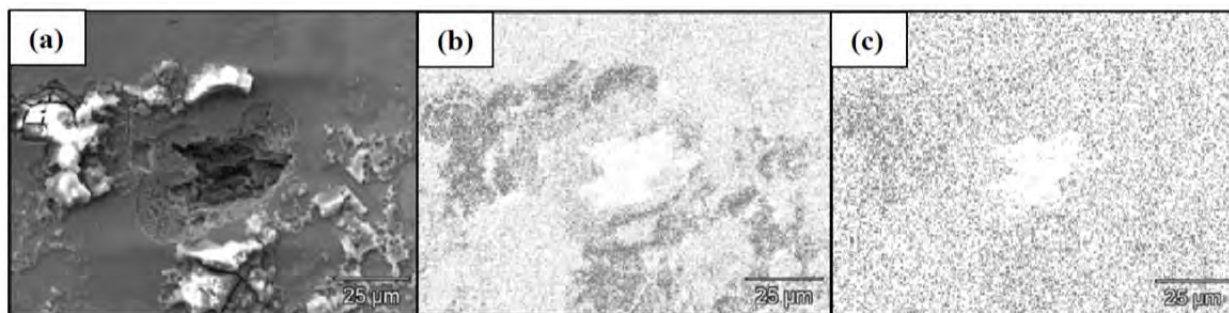
Figure 29. Corrosion of an MnS inclusion in 17 day 30oC 80% RH U-bend tests for 304L stainless steel. (a) SEM of pitted area (b) EDS map of oxygen shows large oxide deposits around the pit. (c) EDS molybdenum map confirms transport of molybdenum oxide from the pit to the surrounding area.

Much like the $30^{o}C$ 80% RH U-bend, the $60^{o}C$ 80 % RH U-bends exhibited very little corrosion and no SCC at the end of 20 days. However, large amounts of calcium were found on the surface of these samples. This indicates that calcium chloride ($CaCl_2$) from the sea salt may have deliquesced on the U-bend surface. Deliquescence studies by Enos et al have shown that conditions of $30^{o}C$ and 80% RH are possible thermodynamic conditions for this to occur. $CaCl_2$ is often used as a desiccant and may have prevented water from hydrating the U-bend surface. EDS mapping suggests that the $CaCl_2$ may have further formed CaO_2. If this occurred, then the U-bend surface was under high chloride concentration throughout the 20 day exposure and still exhibited minimal corrosion. Therefore, these results indicate that corrosion is much more sensitive to temperature than salt concentration in 80% RH conditions. A critical pitting temperature exists between $60^{o}C$ and $80^{o}C$ that causes pits to initiate and rapidly grow without repassivation. The idea of a critical pitting temperature has been studied by Soltis and Laycock [16] and generally describes an initiated pit entering a state that thermodynamically favors rapid growth. It is possible that the surface of the U-bend samples contain initiated pit regions that are undetected with the current SEM image resolution. Regions of lace-like structures may also indicate early signs of corrosion as shown in Figure **30**.

25
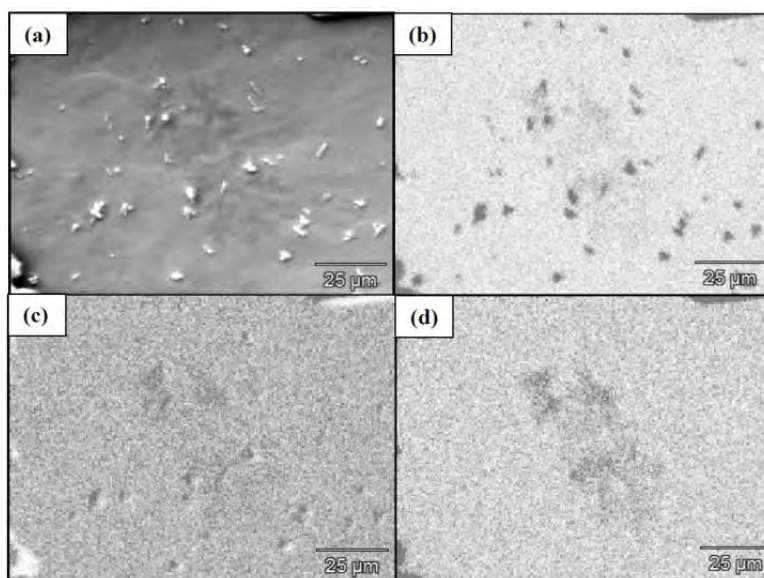
Figure 30. 20 day exposure of 60°C 80% RH U-bend for 304L stainless steel. (a) SEM image. (b) Calcium EDS map (c) oxygen EDS map (d) sulfur EDS map. Sulfur concentrations in the lace-like feature may be indicative of corrosion initiation.

U-bend tests conducted at 80°C exhibited the most corrosion damage. Among these tests, the sensitized specimens were attacked the most and the AR specimens were attacked the least. Welded U-bend samples exhibited corrosion the most in the HAZ next to the weld bead, indicating that corrosion of the filler metal is of less consequence than the heat-treated base material in the HAZ. Cracks also propagated faster in the welded and sensitized samples compared to the AR samples. This is caused by carbide precipitates embrittling grain boundaries in the HAZ during welding. After 11 days of exposure, the welded and HAZ samples had developed a crack across the entire width of the U-bends. The case of sensitized samples corroding faster than welded samples is in agreement with studies by Mintz [4].

Deliquescence of sodium chloride was also significant in the 80°C samples. Conditions for sodium chloride deliquescence are possible at temperatures slightly below 80°C in 80% RH. Once solutionized, sodium chloride easily dissociates into chloride ions and drives faster metal dissolution. The negative charge of the chloride anions build up at defects in the stainless steel's steels passive layer, eventually overcoming the energy needed to hydrolyze water resulting in the formation of hydrochloric acid as well as iron oxide. Optical imaging has also shown multiple crack initiation sites branching from these deliquescence locations, attributing to faster pitting attack in these 80°C specimens.

A final analysis of the U-bend data is presented in Figure **31**. Three trends are shown which include percentage of pitted area, density of crack initiation sites, and total crack length. Evidence suggests that corrosion is minimal for 60°C and under in 80% RH environments. There is also a tendency for HAZ and sensitized material to crack faster than AR material for these conditions. Cracks did not propagate in the 30°C and 60°C tests, which indicate that pitting may be a necessary precursor to SCC. Such a case is also supported in optical evidence of cracking paths connecting pit sites in 80°C samples. Pitting rate had slowed at the end of 80°C AR testing. Such behavior is expected for highly corroded surfaces. This is due to concentrations of cathodic charging that occur around the pit mouth. A high density of cathodic charging on the surface will prevent new pits from forming new cathodic regions next to existing pits.

U-bend tests provided valuable insight to the SCC process. A clear temperature dependence was observed for the pitting kinetics of SS304L. Corrosion products on the samples were likely composed of hydrated Iron III Oxide (Fe_2O_3 xH_2O) and iron molybdenum oxide ($FeMoO_4$). Pitting was either absent in samples or had likely repassivated after initiation to prevent growth to detectable levels. Pitting that did

26

occur in the lower temperature samples had deposits of Mo nearby, suggesting dissolution of a sulphide inclusion. Calcium deposits were also prevalent in the 60°C samples, which may have been the result of calcium chloride deliquescence. There were many regions of corrosion due to sodium chloride deliquescence on the 80° C samples. Thus it is likely that sodium chloride deliquescence occurs between 60°C and 80° C at 80% RH. Samples without pits larger than 1 micron diameter did not exhibit cracking. As shown by several authors Weeën and Acuña [17, 18], pit walls can be a source of stress concentration and will initiate SCC in these regions. Cracking may not have initiated on the 60°C and 30°C samples due to the lack of stress concentration sites. Therefore, SCC was only a concern for 80°C tests over a 20 day period. This temperature dependence was also shown in the fatigue cycled compact specimens.
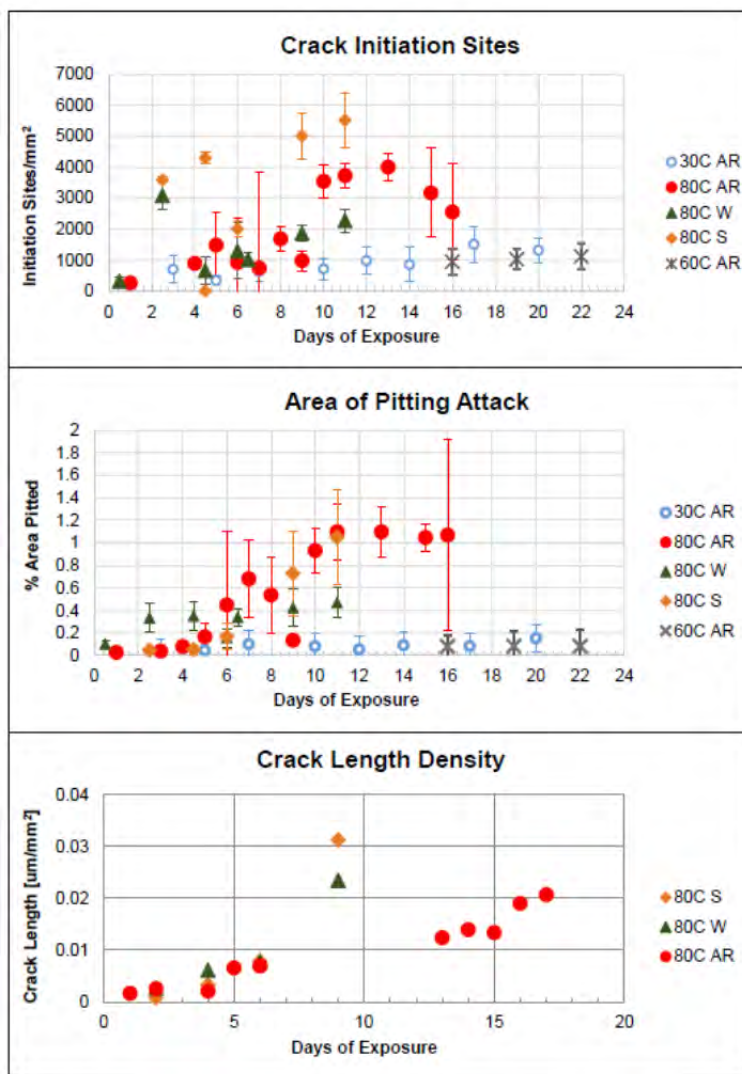
Figure 31. Progression of SCC in U-bend tests for SS304L (a) % area corroded. (b) crack initiation sites. (c) total crack length.

27

3.7 Exposure test of 304L weld samples procured from INL

Two atmospheric salt spray chambers were developed. One chamber was tested to reach a maximum temperature of 50°C and is fully operational, though some minor upgrades were needed such as installing new in-situ humidifier to ensure constant humidity without any interruption. In order to evaluate the stress corrosion cracking (SCC) of 304 stainless steel at higher temperatures, a second corrosion chamber was assembled later in the project. The second chamber was made with polycarbonate materials that can be used at higher temperatures. This chamber can reach temperatures up to 80°C. Both chambers utilize a Labview program so that they can log continuous temperature data through thermocouple inputs, as well as maintain a stable temperature through controlled heaters within the chamber.

Figure 32 shows that first corrosion chamber. The three heating bands in the chamber are clamped by two aluminum plates for improving the heat transport. Salt vapor was pushed into the chamber through the ultrasonic humidifier with the use of a compressed air. This chamber built was able to reach a stable and sustained atmospheric temperature of 50°C, at a sustained humidity of 80% humidity. However, the limit of the output of the heaters was governed by the transition temperature of the acrylic material, which was around 90°C. Higher temperatures showed a level of softening in the acrylic material.
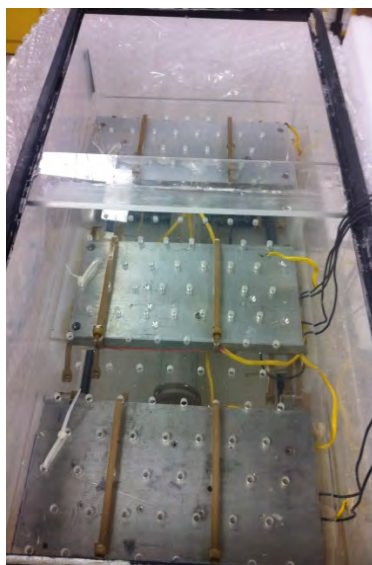

Figure 32. First corrosion testing chamber built to simulate dry cask storage conditions.

Three ASTM U-bend samples made with 304 stainless steel (without weld) were tested in the chamber at about 50°C at 80% relative humidity for 100 hrs. Although the temperature in the chamber is not very uniform, it can be seen clearly that the corrosion of 304 stainless steel is strongly dependent on the temperature. Higher temperature can result in more severe corrosion. After 100hrs, some corrosion occurred in the 304 stainless steel U-bend sample at 54°C. But no stress corrosion crack was observed in the sample under SEM. And almost no corrosion visually occurred in the U-bend sample at 45°C.

28
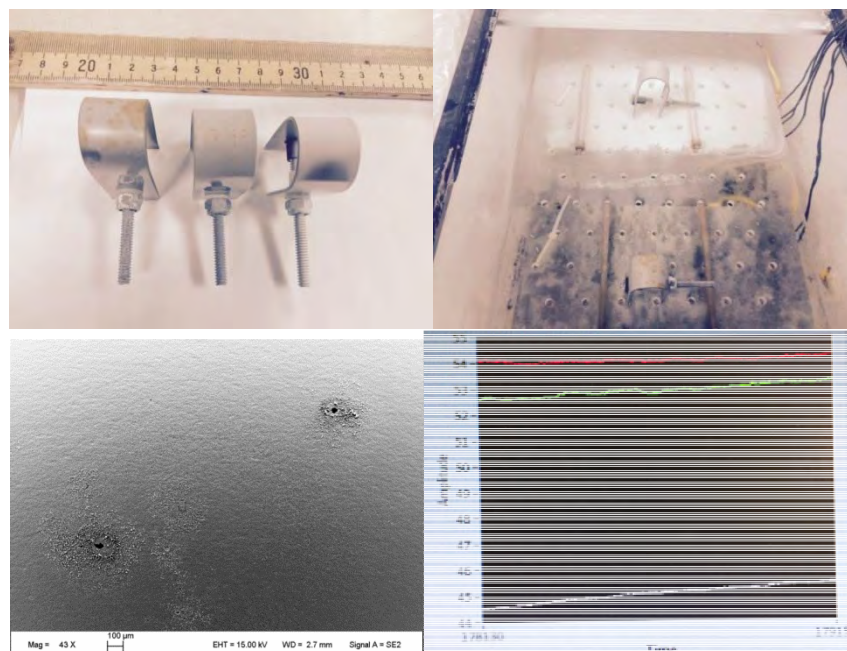
Figure 33. A corrosion test performed in the first chamber on plain 304 stainless steel U-bend samples. The test conditions were at 50°C and 85%RH. The results showed instability in the temperature caused by the high amount of air flow coming from the salt spray input. However, even at 50°C there was a notable level of corrosion in the samples.

The first chamber was limited by the material used in its construction, which led to the construction of the second chamber whose capabilities were successfully tested for temperatures up to 80°C at 80% humidity. Figure **34** shows the temperature graphs in a test showing a temperature of 80°C that was reached. The chamber has the capability to disperse humidified salt spray throughout the chamber and onto the samples. This humidity was monitored and logged using an insertable data drive. Figure 35 show a picture of a 304 flat sample and SEM image of the weld area. Some slight pitting corrosion occurred
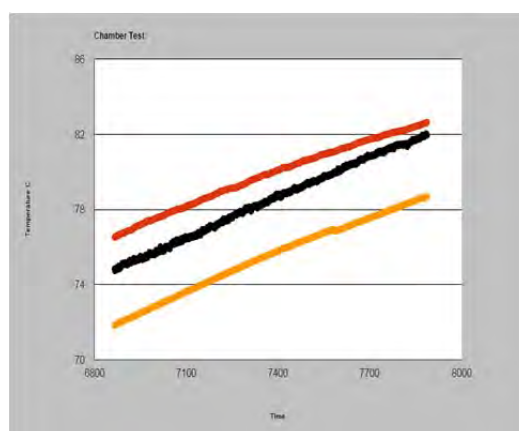
Figure 34 Temperature graph during a corrosion test in the second environmental chamber. The temperature can reach 80°C, though there were some variations on the temperature.

29

Figure 35. Photograph and SEM image of weld metal for a 304 flat weld sample after 40°C/100hr corrosion test for 100 hrs.

Temperature has significant effects on pitting corrosion of 304 stainless steel. Figure 36 shows the SEM images of 304 base material that was tested in 80% RH at 50ºC and 60ºC for 100hrs. Significantly more pitting corrosion occurred in the sample tested at 60C. Expansive patches of deliquescence were observed at 60C.

For both 60°C and 50°C, the weld microstructure displayed a higher level of corrosion as anticipated, as shown in Figure 37. At 50°C some regions of deliquescence were observed, and intense surface corrosion occurred at 60ºC. The same trend was observed for pitting corrosion of heat affected zone of 304 weld, as shown in Figure 38. It appears that 50°C-60°C appears to be the region where deliquescence starts to become significant.
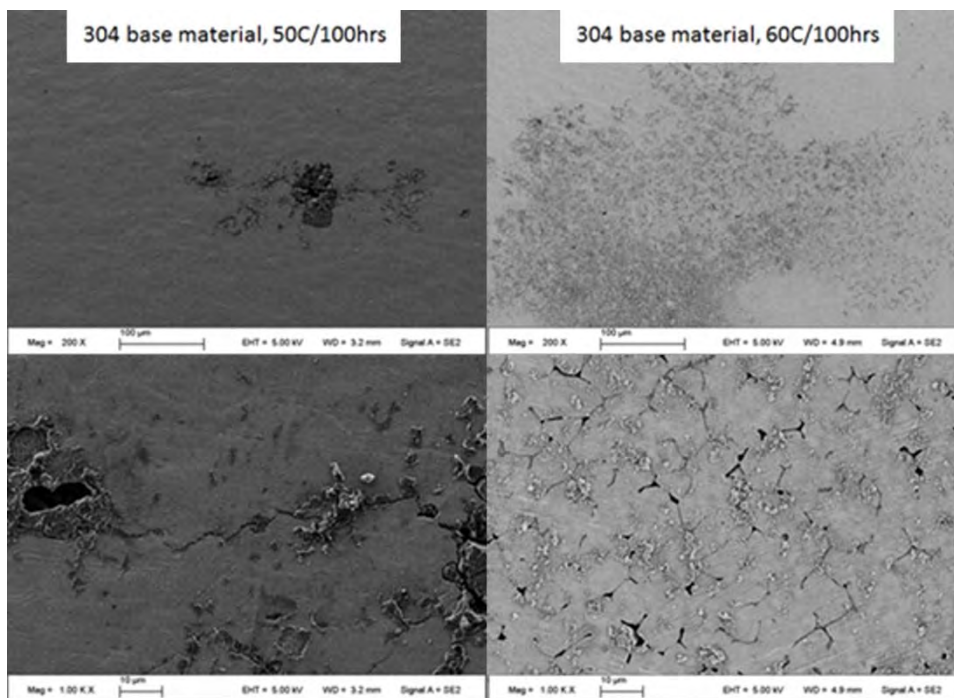
Figure 36. SEM images of 304 base material tested in 80% RH at 50°C and 60°C for 100hrs.

30
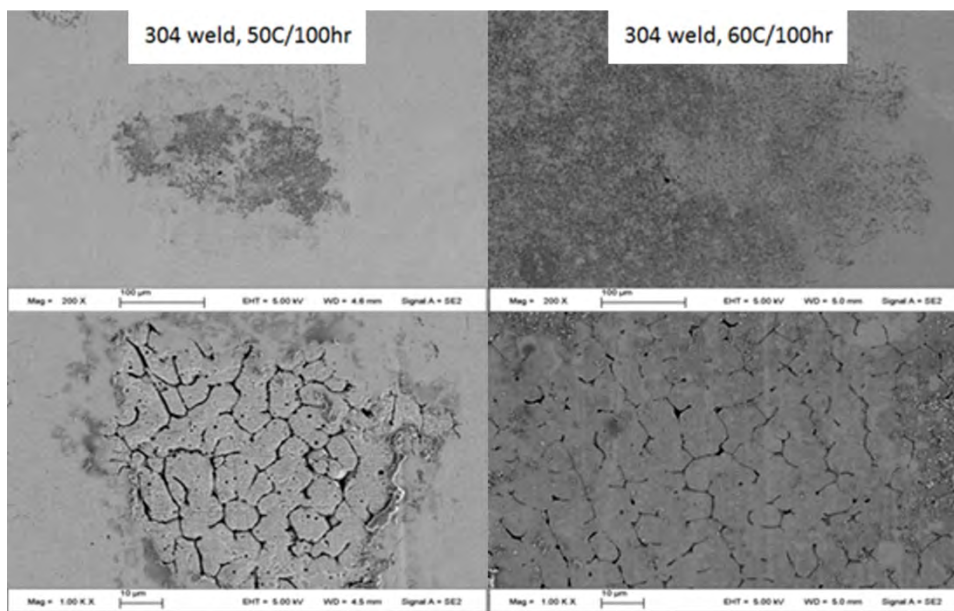
Figure 37. SEM images of 304 weld material tested in 80% RH at 50°C and 60°C for 100hrs.
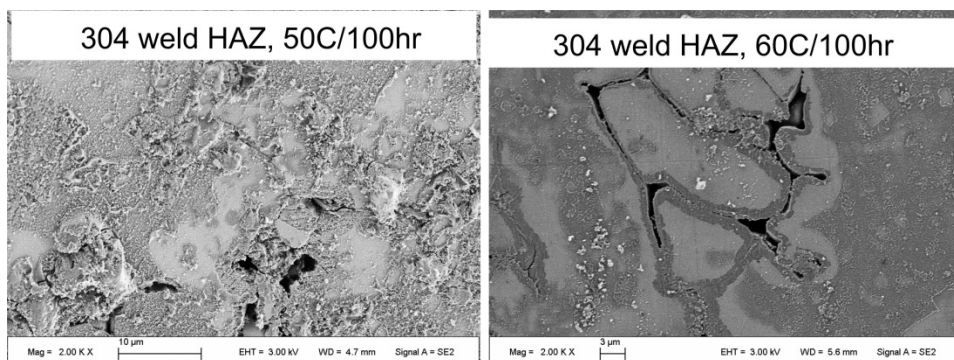

Figure 38. SEM images of heat affected zone of 304 weld material tested in 80% RH at 50°C and 60°C for 100hrs.

Because of the ductility of 304 weld is significantly lower than the base material, some micro-cracks occurred in U-bends made from 304 weld. To avoid the micro crack of 304 welds, some samples were bent to a lower degree and tested. It was found that different bending angles revealed extensive differences in corrosion. Figure 39 shows the samples with different extents of bending in the environmental chamber. As shown in Figure 40, corrosion increased as bending or strain increased. This test also clearly showed that weld is more susceptible to pitting than the base material.

31

Figure 39. Photographs of of 304 weld samples with different degrees of bending.
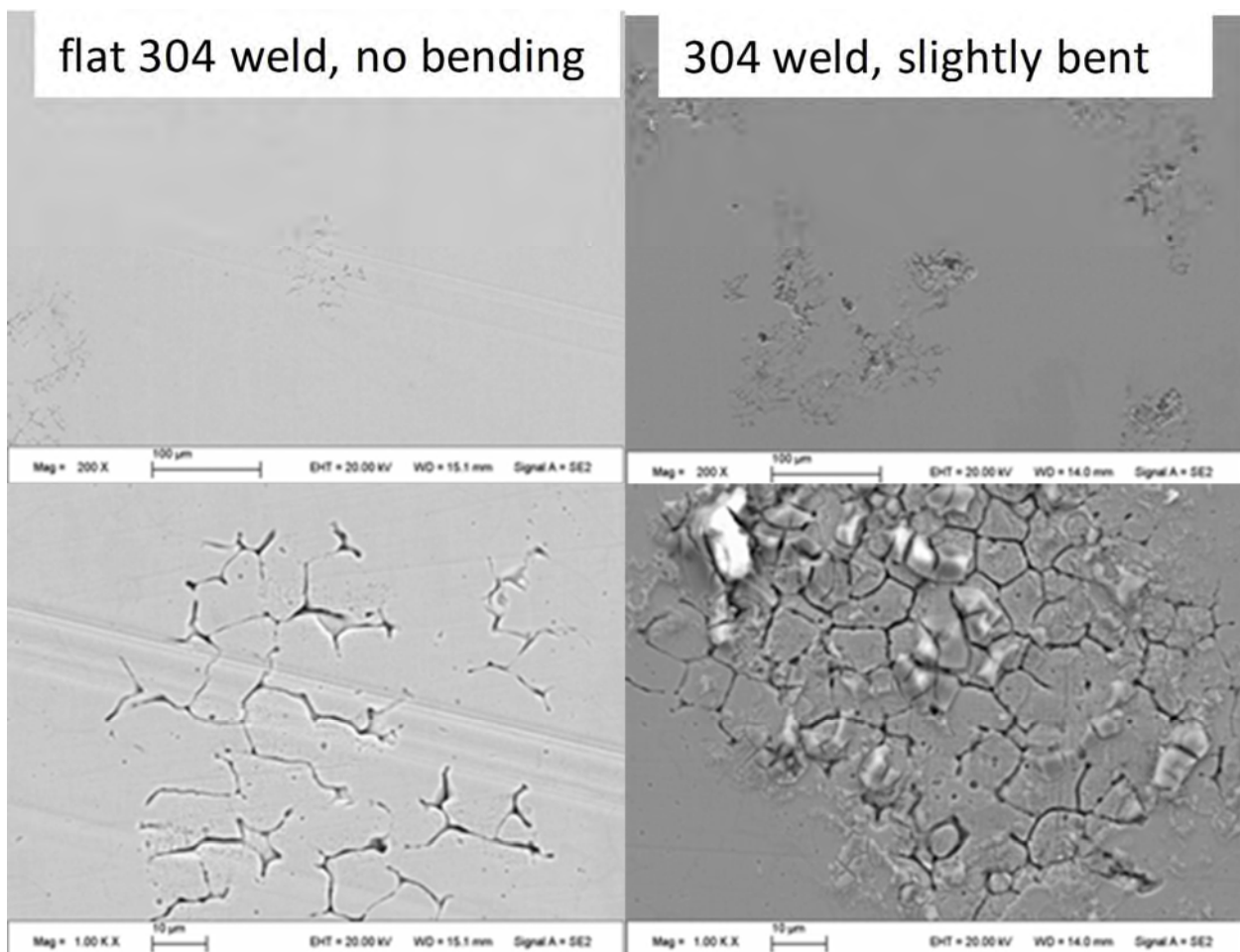
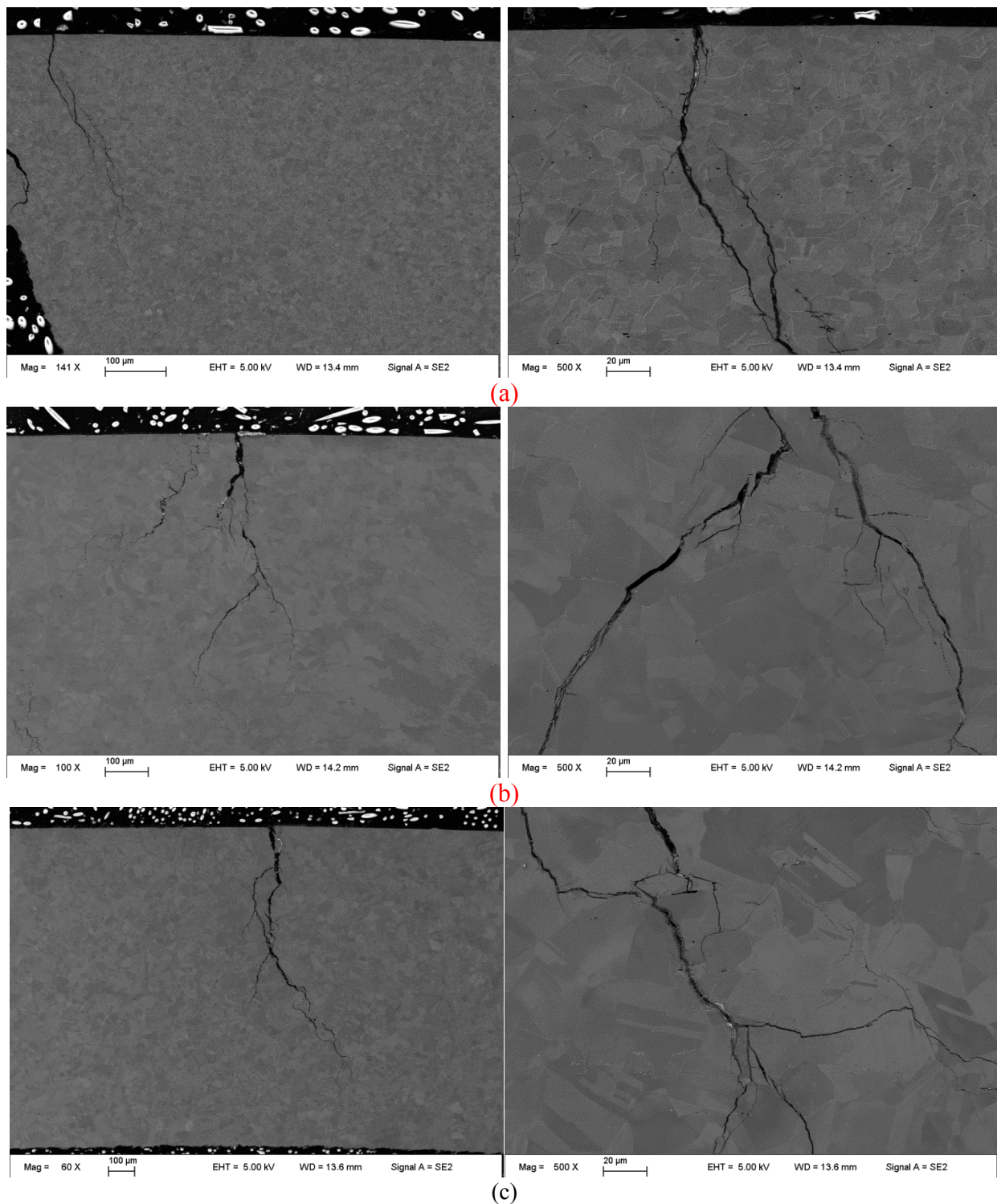**Figure 40. SEM image of prototypic weld samples at various bending angles.**

32

The actual canisters temperatures have been measured to be in the ranges of 49°C to 118°C, while the calculated temperatures ranged from 60°C to 105°C [19]. It is expected that at higher temperatures, SCC may initiate sooner and propagate faster because of faster corrosion rate at higher temperatures. Therefore, two U-bend samples made from as-received 304L and 304L INL weld were exposed to 80°C for up to 2 weeks. Because of the ductility of the 304L weld is lower than the 304L material, some cracks occurred during preparing the standard U-bends with 1-in diameter, therefore some U-bend samples with a much larger diameter (2.25 in) were prepared. No cracks occurred during bending process by observing the samples under SEM at 200x magnifications.

Figure 41a and b shows the overall picture that clearly shows the SCC cracks on both 304L and 304L INL weld. SEM was used to identify the major SCC crack and nearby cracks as shown in Figure 41c and d. Severe SCC cracks were observed in both 304L and 304L INL weld U-bends. Figure 42 shows the SEM images of the cross sections of the U-bends. Figure 42a is for 304L and Figure 42b and Figure 42c are for the cross sections of the weld zone and heat affected zone of 304L INL weld. From Figure 42 , it can be seen that all the SCC cracks propagated transgranularly and multi SCC crack branches were formed during the propagation process.

The severe SCC cracks observed in 304L and 304L welds indicated that 304L stainless steel may be susceptible to SCC at 80°C synthetic sea water fog with 30% RH or higher. Therefore the canisters must be monitored carefully if they are exposed to the high end of temperature ranges, that is 80°C or higher.

33

Figure 41. Overall SCC crack of 304L (a) and 304L INL weld (b) and SEM tracing of the major SCC crack in 304L (c) and 304L INL weld (d) after exposure synthetic sea water at 80°C with 30% RH for two weeks.

34

Figure 42. SEM images of the SCC cracks in (a) 304L, (b) weld zone of 304L INL weld and (c) heat affected zone of 304L INL weld, after after exposure synthetic sea water at 80°C with 30% RH for two weeks.

35

4   Conclusions

Pitting and stress corrosion cracking experiments were conducted on two stainless steels, SS316L and SS304L. These experiments used prototypic canister materials and storage conditions. The SS304L alloy exhibited higher corrosion rates than SS316L in parallel tests. Samples under stress were highly susceptible to SCC in an 80°C 80% RH salt vapor environment when compared to samples at 60°C, 30°C, and 21°C. Higher concentrations of sea salt caused increased pit density and pitting rate on flat steel samples. However, there appeared to be a maximum pit density of the surface of samples after which surface corrosion was inhibited. This maximal pit density was observed on salt-on- sample hydration tests and the U-bend exposure tests. Two explanations for this behavior are possible. Pitting in an aqueous environment is an electrochemical process that results in an anodic pit mouth and cathodic region around the pit. As more pits are created, large cathodic regions are established which prevent new areas of negative charge from forming. Another possibility is that pits growing in a region consume chloride ions or other necessary reaction products faster than they can accumulate for new pit initiation. However, it is unknown how deep pits had grown under the substrate surface during certain time lengths. For samples that had been corroded for 4 days, pit depths of at least 60 microns were identified.

When comparing high and low concentration salt water, the high concentration water had initiated more pits over the course of 4 days. However, these pits maintained a size that was primarily under 0.302 μm^2. Lower concentration sea salt water exhibited larger pit growth. Therefore, high salt concentration water leads to higher pitting rates but lower pit growth which may be beneficial in preventing growth to a critical pit size in which cracking initiates. Pit size distribution had been shown to exhibit a Weibull distribution that was dependent upon salt concentration in water. The most common pit area size for hydrated samples was between 0.152 and 0.302 μm^2 throughout four days of corrosion. This indicates a decaying pit growth rate with respect to time.

Both sodium chloride and calcium chloride deliquescence was observed in synthetic sea salt water vapor at 80% RH. Sodium chloride deliquescence was not seen at 60°C or below, implying it is bounded between 60°C and 80°C at 80% RH. Similarly, calcium chloride deliquescence is bounded between 30°C and 60°C at 80% RH. The dissolution of sodium chloride was destructive to the SS304L substrate, causing regions of intergranular attack and crack initiation sites. The dissolution of calcium chloride had left calcium deposits which were presumed to be calcium oxide from EDS inspection. This oxide would serve to protect the steel surface, preventing water from hydrating the surface.

It is likely that a critical pitting temperature exists between 60°C and 80°C at 80% RH for SS304L. The critical pitting temperature is a thermodynamic condition that favors stable pit growth and prevents repassivation of pits that may initiate on the surface. U-bend and compact specimen tests both exhibited accelerated surface corrosion at 80 °C. Pits resulting from sulphide inclusions were also found in the samples regardless of temperature conditions. Thermodynamic data shows that these compounds are unstable and prone to dissolution. Because large pits were not found at the 60°C and 30°C samples, it is likely that these inclusion sites regrew a passive layer after dissolution.

Stress corrosion cracking appeared to require pit sites for initiation. Surfaces with observable cracks always contained a pit site, deliquescence site, or were formed by pit connections. This cracking was likely the cause of stress concentration located in pit walls. Samples with pits smaller than 1 micron diameter did not exhibit SCC. Therefore, only the U-bends tested at 80°C had cracked during exposure to 80% RH sea salt vapor. Crack growth rarely propagated more than 45 degrees from the line perpendicular to stress application. When propagation did exceed 45 degrees, it was between two pit locations. Sensitization and welding can make stainless steels more prone to SCC. Electrochemical testing showed that heat affected zones near weld beads had lower repassivation potential than SS304L base material. U-bend exposure tests demonstrated faster crack initiation and crack growth in sensitized samples than as received samples. Carbide precipitation and chromium diffusion reduces ductility and corrosion resistance. These contribute to faster SCC rates in the sensitized and welded materials.

36

Further evaluation of SCC in SNF canister materials should include welded samples under stress at conditions near the critical pitting temperature. Studies on humidity levels lower than 80% are important to observe so that deliquescence effects of other salts can be studied. While sodium chloride deliquescence yielded detrimental effects, calcium chloride deliquescence appeared to deposit onto the surface and act as a desiccant. Other salt species such as magnesium chloride is known to deliquesce between 10% and 50% RH.

It should also be mentioned that SNF canister storage environments are far more dynamic than those tested in this work. Night and day temperature cycling could be simulated in future testing to compare against steady state conditions. Pitting initiation requires a breakdown in the stainless steel passive layer. The steel may repassivate if temperature conditions are changed, requiring another initiation period before continued growth of a pit. Pit growth may also be halted through the buildup of salts and clays on the canister surface. Layers of salt had deposited on the U-bend samples over time which may have acted like a desiccant similar to calcium oxide. Most importantly, stresses similar to those in the canister must be studied at the critical pitting temperature. Constant load tensile sample tests have been known to exhibit decreasing crack growth rates while U-bend testing shows no impediments to SCC.

Significant increase in crack density was observed between 50°C and 60°C for weld samples. Temperature range of 50°C-60°C appears to be the region where deliquescence starts to matter. Strain in the U-bends can accelerate the pitting corrosion of 304 welds. Type 304L alloys are very susceptible to SCC at 80°C synthetic sea water fog with 30% RH or higher. This suggests that the canisters must be monitored carefully if they are exposed to the high end of temperature ranges.

37

FAST-IRP Thrust Area 3: Monitoring the Corrosion of Nuclear Fuel Cladding Using Optical Approaches

Another aspect of research at the University of Wisconsin has been in the area of optical monitoring of corrosion products as they form on the materials surface. Although the canister application involves steel we initiated this work with Zircaloy-4 (Zr-4) because it forms a uniform oxide layer that greatly facilitates the development of optical monitoring techniques. The technique can then be readily extended to stainless steel, the material of the canister. The overarching goal of this phase of the work was to develop a compact on-line diagnostic for monitoring corrosion of canisters.

We present results of optical monitoring of surface corrosion products on Zr-4 using two approaches: Raman scattering and infrared (IR) interference. For this study, Zr-4 alloy was oxidized in air at 500 °C and investigated by micro-Raman spectroscopy and Fourier Transform Infrared (FT-IR) spectroscopy to detect the oxidation process. Systematic Raman scans and FT-IR scans were performed to study the relationship between typical Raman spectra/FT-IR spectra and various oxidation corrosion degrees. The thicknesses of the oxide layers developed for various exposure time were measured by cross-sectional Scanning Electron Microscopy (SEM) examination. The results of this work reveal that oxide layer thickness can be directly related to the Raman scattering characristic peaks and the IR interference. The study provides the basis for an accurate, non-destructive, and sensitive method to monitor the degree of corrosion on stainless steel canisters.

1.   Sample Oxidation

The Zr-4 cladding samples were cut by a diamond saw to dimensions of 1 cm×1 cm and 1 mm in thickness. The samples were ground and polished by a Struers TegraForce-5 polish machine on one side using Allied High Tech SiC papers from 120 grit to 1200 grit to remove the native surface oxide layer and provide a smooth sample surface. The morphology of the oxide may be affected by the cold-worked nature of the polished surface. Future work will have to address the comparison of our oxide thickness sensor for cold-worked and stress-relieved samples. The samples were introduced in a quartz tube 5 cm diameter and were oxidized in a Thermo Scientific F79335-70 furnace chamber at 500 °C in flowing air. Because the oxide layer thickness increases with the oxidation time, samples were oxidized for 5 hours, 10 hours, 20 hours, 50 hours and 100 hours respectively in order to get different oxide layer thicknesses for measurement with the Raman technique. After oxidation, the polished side of each oxidized sample was ready for further Raman laser scattering investigation.

## 2.   Scanning Electron Microscopy (SEM) Examination

Sample Preparation

After Raman spectroscopy measurements, the oxidized Zr-4 samples were prepared for cross-section measurement by SEM in order to compare to the Raman results. Each sample was held vertically in an Allied High Tech sample clip and mounted with phenolic powder. Each mounted sample was ground and polished by Allied High Tech SiC paper from 120 grit to 1200 grit to provide a smooth surface, then was further fine polished by a Struers MD Mol plate with 3 μm Polycrystalline Diamond suspension, Struers MD Nap plate with 1 μm Polycrystalline Diamond suspension, and Struers MD Chem plate with 0.04 μm colloidal Silica suspension in order to achieve mirror cross-section surface. The mirror-polished sample cross-sections were examined with a LEO 1530 Scanning Electron Microscope in SE2 mode with 5 kV gun voltage.. Following this procedure, the zirconium oxide region could be identified in the cross-section SEM images. In the cross-section SEM images of each oxidized sample, the scale measurement function in the SmartSEM software was carried out to measure the zirconium oxide layer thickness accurately at different positions of cross-section.

Examination Results

To investigate the thicknesses of the oxide layers grown for different times, the cross-section of each sample was checked by Scanning Electron Microscopy as previously described. Fig.43(a) shows samples after mounting with phenolic. The SEM images of the cross-sections of the samples are shown in Figs.43(b)-(f). In these SEM images, phenolic, zirconium oxide, and Zr-4 are clearly distinguished by white-black color contrast due to their differing material properties. The SEM images were taken in more than 20 different regions over the whole cross-section of each sample, so they can be representative for the sample oxide layer thickness. Based on the thickness of the top oxide layer as measured by the scale function using the Smart SEM software, the statistical average thickness and standard deviation of the top oxide layer is shown in Fig. 44. The mean thickness of the oxide layer for the 5 hour sample is about 0.55 μm with a deviation of about 0.066 μm. But for the 100 hour sample, the mean thickness of the oxide layer is about 10.13 μm with a deviation of about 3.08 μm. This suggests that during oxidation, the growth rate of the oxide layer varies across the sample and the oxide layer will have an uneven profile.

39
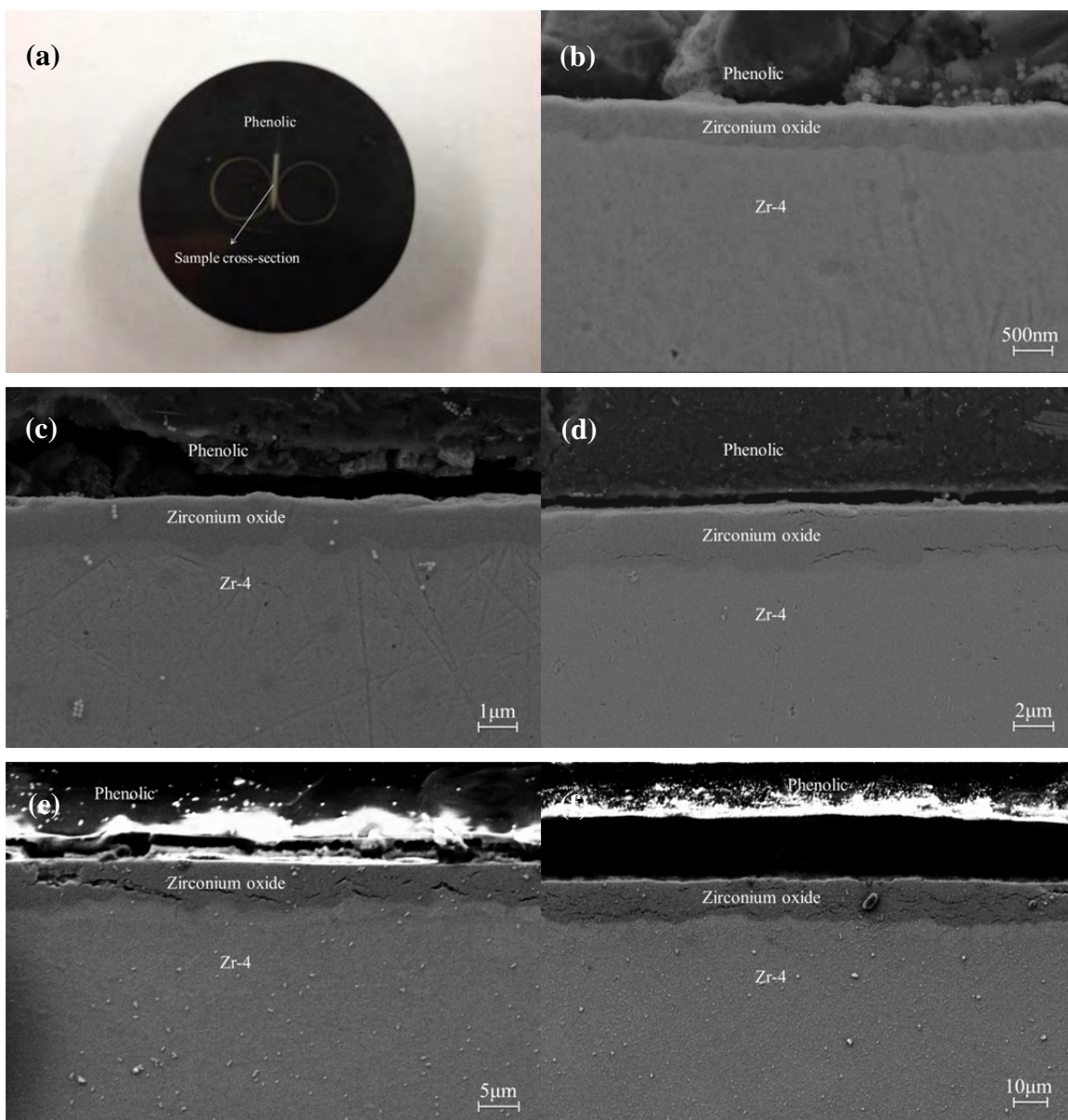
Fig. 43 (a) Optical image of Zr-4 sample after mounted by Phenolic. The cross-sectional SEM images of Zircaloy-4 samples oxidized at 500 °C in ambient air for (b) 5 hours, (c) 10 hours, (d) 20 hours, (e) 50 hours, and (f) 100 hours.
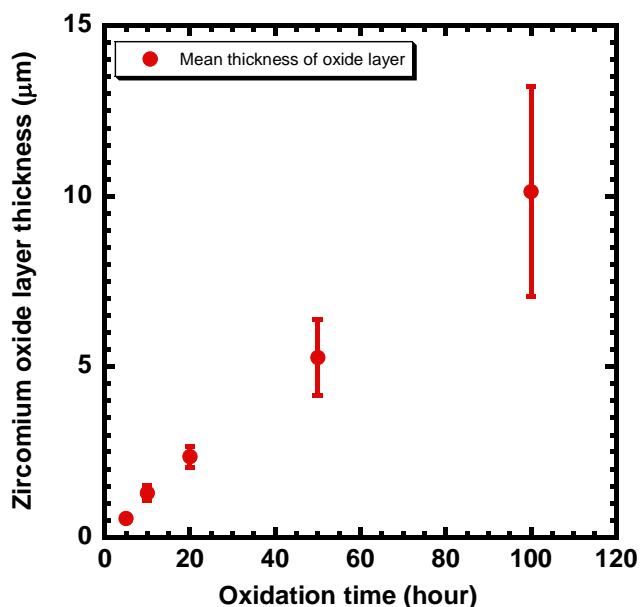
Fig. 44. The calculated statistical average thickness and deviation of all oxidized samples as a function of oxidation time.

3.   Raman Scattering Investigation

The Raman spectra of the oxidized samples were measured with a Thermal Scientific DXR micro-Raman spectrometer. The excitation laser source is a DXR 532 nm green laser and the output power was 10mW. The spectra were acquired by a 50 μm aperture. The objective of the microscope was chosen to be 10×, which corresponds to a laser beam spot size diameter of 2.1 μm. Raman spectra were collected from the entire 2.1 μm diameter spot. The scans were implemented by a 900 lines/mm grating to obtain full range spectra and find the spectrum range of interest for further study. The x-axis scan was chosen as Raman shift. For each sample, systematic scans for several spots randomly selected at different region on sample were carried out. Then, the representative spectra which appeared most frequently were chosen for further analysis. These representative Raman spectra can effectively detect the sample properties of interest.

Raman Characteristic Spectra

Raman scans were performed at different spots on bare Zr-4 as well as samples oxidized for 5, 10, 20, 50, and 100 hours. From the full range scanned Raman spectra of these samples, it appears that the characteristic scattering peaks appear between wave number of 160 cm^{-1} and 800 cm^{-1}. Fig. 45 shows the selected representative Raman spectra in this wave number range of the samples. In Fig. 45, a baseline has been subtracted from each spectrum, which allows all the spectra to be put at the same level to permit selection of the best peaks for measuring the oxide layer thickness. As the Raman spectra reveal, the characteristic Raman scattering peaks become more obvious as the sample's oxidation time increases. In

40

the spectrum from the non-oxidized sample, there is only one peak around 480 cm^{-1},with a very weak intensity. The spectrum from the 5 hour sample exhibits the 480 cm^{-1} peak, which is similar to the bare sample. Meanwhile, two weak peaks around 180 cm^{-1} and 630 cm^{-1} appear with a broad peak width. In the spectrum from the 10 hour exposed sample, the peaks at 180 cm^{-1}, 480 cm^{-1} and 630 cm^{-1} become stronger and wider. In addition, two peaks at 340 cm^{-1} and 380 cm^{-1} appear. The spectrum from the 20 hour sample is similar to that of the 10 hour sample, but the intensity of each peak increases slightly. The peaks at 180 cm^{-1} and 630 cm^{-1} begin to split into two sub-peaks at 175 cm^{-1} and 187 cm^{-1}, 613 cm^{-1} and 638 cm^{-1} respectively. In the spectrum from the 50 hour exposed sample, all these peaks still exist at the same positions, but with much stronger intensities. New peaks at 220 cm^{-1}, 540 cm^{-1} and 580 cm^{-1} also appear within this spectrum. The spectrum from the 100 hour exposed sample contains all the peaks in the 50 hour sample's spectrum, but each of them displays an increase in intensity. Furthermore, there are two new peaks at 280 cm^{-1} and 300 cm^{-1} with weak intensities.

As the oxidation time increases, thicker oxide layer is grown on top of Zr-4 and in turn the Raman spectrum of this sample can show stronger Raman scattering signals. Comparing all of these Raman spectra in detail, some characteristic peaks are helpful in identifying bare and oxidized samples. As discussed previously, there are 12 characteristic peaks coming out or enhanced in the spectra of the tested samples. In the spectra of the bare and 5 hour samples, the differences are only observed for peaks at 180 cm^{-1} and 630 cm^{-1}, which do not exist in bare sample spectrum. These two peaks exist in all the spectra of the oxidized samples (from 5 to 100 hours) and their intensities increase consistently as the oxidation time increases, although there is splitting in these two peaks for long time oxidized samples. These split peaks at 175 cm^{-1} and 187 cm^{-1}, 613 cm^{-1} and 638 cm^{-1} correspond to the existence of the zirconium oxide tetragonal and monoclinic polymorphs in the oxide layer. When an oxide layer grows thicker, there will be more zirconium oxide in these polymorphs. Oxide layers grown in environments other than air will likely have a different morphology than those studied here. Future work is necessary to establish whether approach used successfully in this study will apply to oxides grown under other conditions.
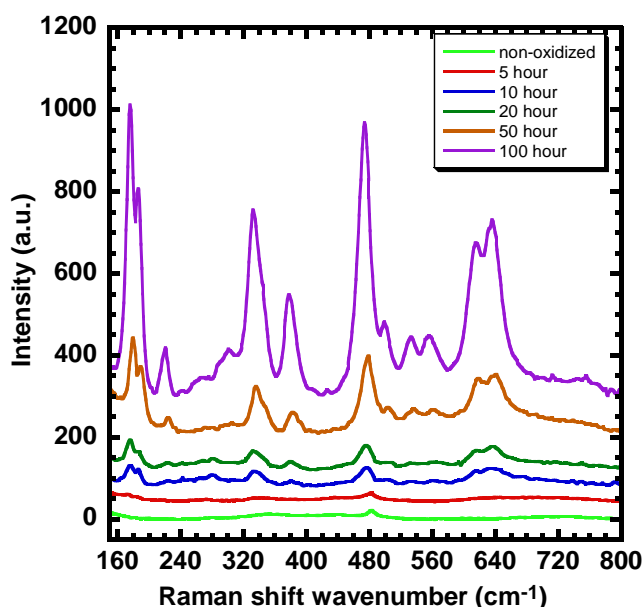

41

Fig. 45. The selected representative Raman spectra of the non-oxidized, 5 hour, 10 hour, 20 hour, 50 hour and 100 hour oxidized Zr-4 cladding samples. 12 characteristic peaks appearing in the in the spectra for thick oxide layers.

Data Analysis and Discussions

As discussed in the previous section, there are two characteristic peaks at 180 cm^{-1} and 630 cm^{-1} in the spectra and these can be candidates as signals for detecting the Zr-4 cladding oxide layer thickness. In order to analyze these two peaks quantitatively, using Gaussian-Lorentzian mode deconvolutions. Fig. 46 shows the deconvolution processes of these two characteristic peaks from the selected representative spectra of the 10 hour and 100 hour exposed samples (same data as Fig. 45) as examples. In all cases, spectra are taken from multiple spots on each sample to minimize the effects of spatial variability in surface morphology. After deconvolution, the two sub-peaks can be replaced by individual peaks at the 175 cm^{-1} and 187 cm^{-1}, and 613 cm^{-1} and 638 cm^{-1} positions respectively. The intensities of these four peaks from the representative Raman spectra of all oxidized samples are shown in Fig. 47 as a function of the average thickness of the oxide layer. The intensities of all of these four deconvoluted peaks increase consistently as the oxide layer becomes thicker. For the 10 hour sample with average oxide layer thickness of 1.30 μm, the intensities of the deconvoluted peaks are 44.1, 26.6, 21.3 and 39.5. For the 100 hour sample with average oxide layer thickness 10.13 μm, the intensities have increased greatly to 645.5, 405.5, 264.9 and 356.5.

42
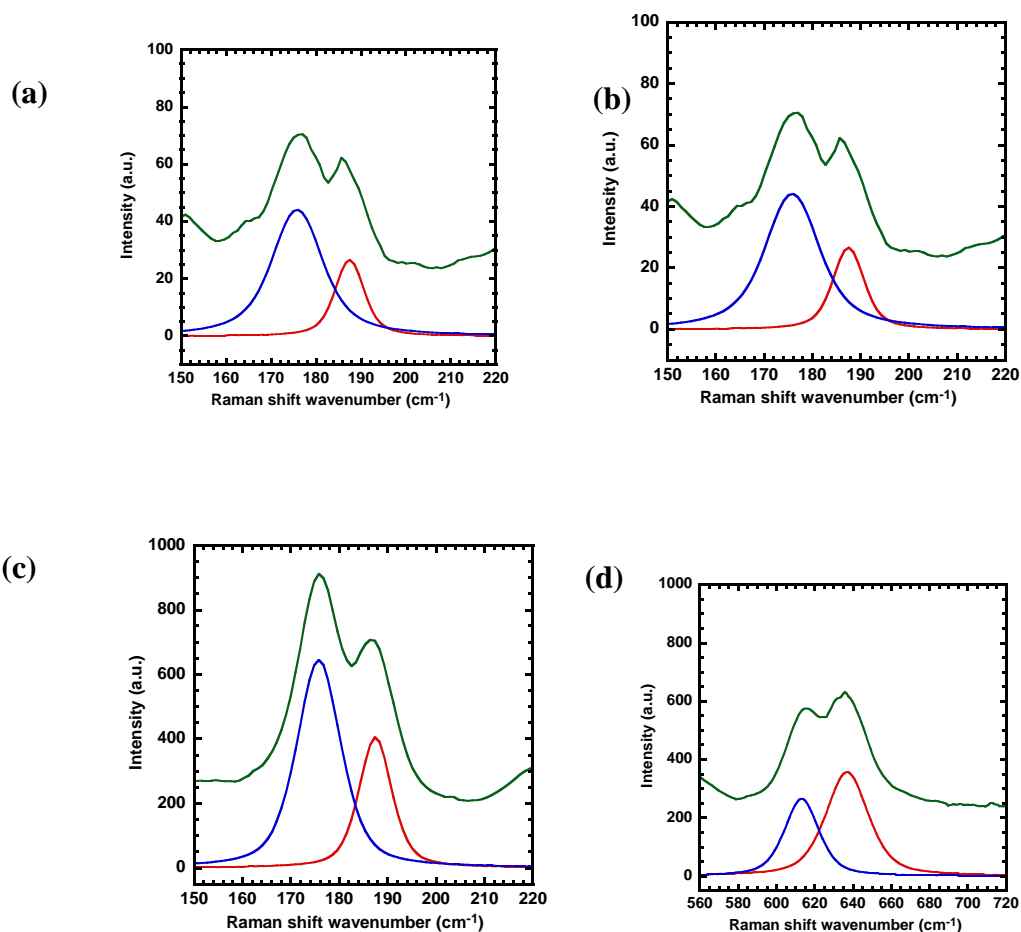
Fig. 46. The Gaussian-Lorentzian deconvolution processes of characteristic peaks at 180 cm-1 and 630 cm-1 from the selected representative Raman spectra of the 10 hour (a) (b) and 100 hour (c) (d) oxidized samples. The peaks at 180 cm-1 and 630 cm-1 are deconvoluted into peaks at 175 cm^{-1} and 187 cm^{-1}, and 613 cm^{-1} and 638 cm^{-1} positions respectively.
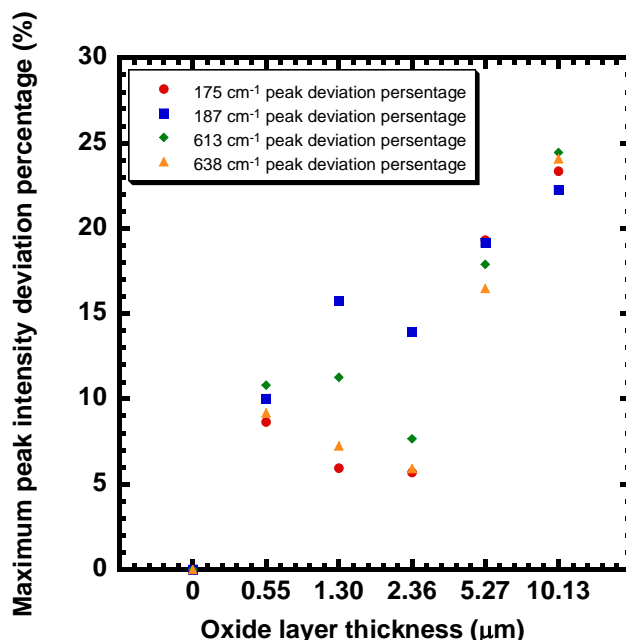
The deconvoluted characteristic peaks have been related to the oxide layer thickness as shown in Fig. 47. The difference in intensities of the peaks at 175 cm^{-1}, 187 cm^{-1}, 613 cm^{-1} and 638 cm^{-1} are clear enough to identify each sample with the corresponding oxide layer thickness. Taking the peak at 175 cm^{-1} as an example, the peak intensity increases from 0 for a bare sample to 3.5, 44.1, 63.2, 186.6 and 645.5 for 0.55 μm, 1.30 μm, 2.36 μm, 5.27 μm and 10.13 μm oxide layer thicknesses. Because there is no peak at these positions for the bare sample, it is easy to distinguish it from the oxidized samples, even for the 5 hour sample with a 0.55 μm thick oxide layer. Among the oxidized samples, the average thickness difference between 5 hour and 10 hour samples is only about 0.75 μm, but the signal intensity of the 10 hour sample is almost 10 times higher than that of the 5 hour sample. This result reflects the fact that during the oxidation process at 500 °C, as oxidation time increases, the components of the monoclinic and tetragonal (metastable) polymorph zirconium oxide increase, and consequently, they show much stronger characteristic peaks in the Raman spectra.
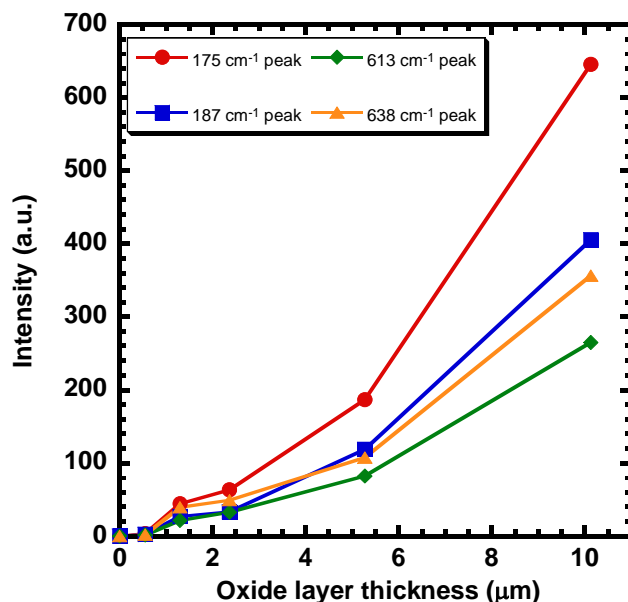
Fig. 47. The intensities of the deconvoluted peaks at 175 cm-1, 187 cm-1, 613 cm-1 and 638 cm-1 from the selected representative Raman spectra as a function of the average thickness of the oxide layer. All of these peaks are enhanced when the oxide layer thickens.

The deconvoluted characteristic peaks at wave numbers of 175 cm^{-1}, 187 cm^{-1}, 613 cm^{-1} and 638 cm^{-1} were collected and studied for all tested Raman spectra from different positions of each oxidized sample. In Fig. 48, the maximum intensity deviation percentages of each characteristic peak for all oxidized samples are plotted as a function of the average thickness of the oxide layer. Here, in order to maintain consistency, the intensities of the deconvoluted characteristic peaks from the selected representative Raman spectra are taken as reference. It is observed that the maximum intensity deviations for these

43

characteristic peaks are in the range from about 5% to a little lower than 25% for all tested positions on the surfaces for all oxidized samples.

Fig. 48. The maximum intensity deviation percentages of the deconvoluted characteristic peaks as a function of the average thickness of the oxide layer.

This intensity variation comes from the difference in the thickness of the oxide layer. This result means that the uneven condition of the oxide layer thickness for the sample can be roughly reflected in intensity variation of the characteristic peaks. After analysis of these characteristic peaks, they can be confidently considered as sufficient scattering signals to detect the oxide layer thickness on Zr-4 alloy, and further employed to finish the task of converting the oxide layer thickness to detectable optical signals.

4.   IR Interference Investigation

The optical interference spectra of the oxidized samples were measured using a Nicolet Magna 550 series II FT-IR spectrometer coupled with an optical/IR microscope using a Globar light source. A KBr beam splitter and an MCT/A detector were selected. The spectra were acquired through a 95 μm aperture, which produced a light beam diameter approximately of 100 μm. The scans were implemented to obtain reflection spectra with optical interference from 1000 to 4000 cm^{-1}. For each sample, systematic scans for several spots, randomly selected at different regions on the surface, were carried out. The representative spectra were chosen to effectively correlate with oxide film thickness.

IR Interference Spectra

Figure 49 shows the representative IR interference spectra in the wavenumber range from 1000 to 4000 cm^{-1} for the Zr-4 samples oxidized from 0 to 100 hours. As seen from the FT-IR spectra, the interference patterns vary with the degree of oxidation. The spectrum for bare Zr-4 (Fig. 49(a)) is a nearly straight line with no vertical oscillations. In the case of the 5 hour oxidized sample, the spectrum begins to

show an interference oscillation pattern and this test range only covers one and half full periods. The interference spectra of the 10 and 20 hour samples are similar to that of the 5 hour sample, but with more oscillation periods and smaller peak-to-peak amplitudes. There are more than two and approximately three full periods in this range for the 10 and 20 hour samples, respectively. The peak-to-peak amplitudes begin to decrease for these two samples as the wavenumber increases. Moreover, the peak-to-peak amplitude of the 20 hour sample is a little smaller than that of the 10 hour sample. In the spectrum of the 50 hour sample, there are more than four full oscillation periods. The peak-to-peak amplitude is smaller than those of the previous three oxidized samples and damps faster with increasing wavenumber. The spectrum of the 100 hour sample gives the largest number of oscillation periods, the smallest peak-to-peak amplitude and the fastest peak-to-peak decay. Thus for thicker oxide layers (i.e. longer oxidation times), the FTIR spectra show more oscillation periods in the test range and smaller peak-to-peak amplitude with a higher damping rate with wavenumber.

45
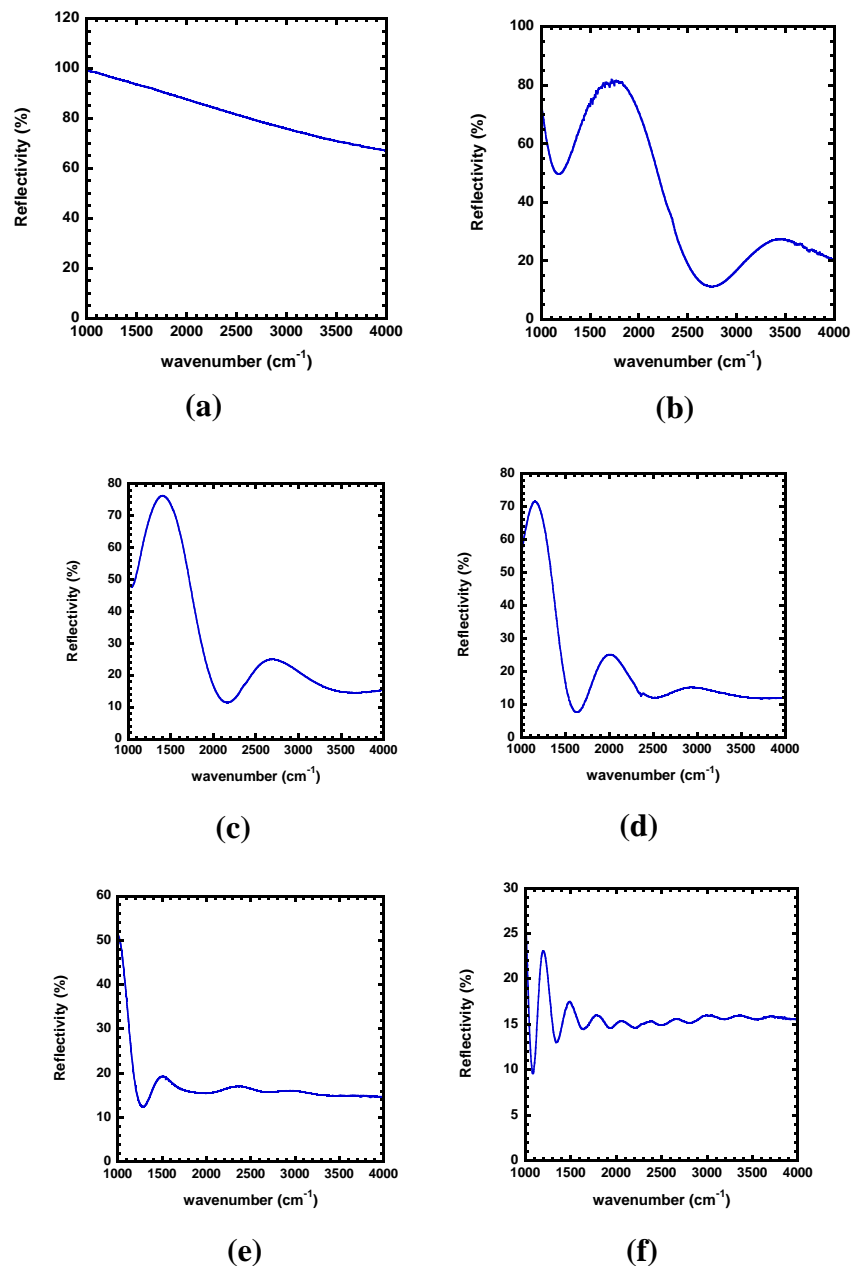
Fig. 49. **IR interference spectra for (a) bare Zircaloy-4 sample and for samples of this alloy exposed at 500 °C in ambient air for (b) 5 hours, (c) 10 hours, (d) 20 hours, (e) 50 hours, (f) 100 hours.**

The optical interference of the reflected light waves is related to the distance between the two reflected interfaces. In this study, the top surface of oxide layer and the interface of oxide layer and the underlying Zr-4 are the reflected interfaces. Therefore, the interference patterns from these spectra are affected by oxide thickness and provide a measurement of the degree of oxidation. There is no interference patterns in the spectrum of the bare Zr-4 sample but the samples with different oxidation times show different oscillation periods. The oscillation periods from the measured spectra of the oxidized samples are shown in Fig. 50 as a function of oxidation time.

46
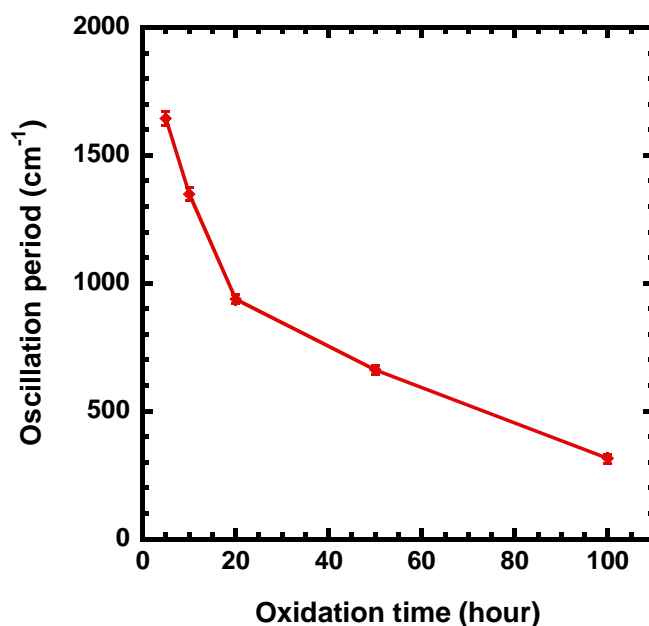
Fig. 50. The oscillation periods of the various oxidized samples in the test wavenumber range as a function of oxidation time.

Data Analysis and Discussions

As discussed in the previous section, the optical interference spectrum is a function of the oxide layer thickness for the oxidized Zr-4 samples. The reflected light waves from the outer oxide surface and the interface between the oxide layer and the underlying Zr-4 substrate are from the same light source, so they are coherent to each other and have the same frequency. The total displacement magnitude at the intersection of these two waves is equal to the vector sum of the displacement magnitude of each individual wave. When a crest of one wave meets that of the other wave, a constructive interference occurs with a wave magnitude equal to the sum of each wave's magnitude. However, if a crest of one wave meets with a trough of the other wave, the interference will be destructive and the resultant wave magnitude is the difference of the magnitude of the two waves. In the case of the oxide layer on Zr-4, the interference patterns are decided by the difference of the optical paths of two reflected waves. If the oxide layer makes the two reflected light waves have an integral number of periods difference in optical paths, then constructive inference occurs. However, if the oxide layer makes a half period behind or ahead of the previous case, the inference is destructive. The other oxide layer thicknesses produce the interference between constructive and destructive cases. In the scanned FTIR spectra, the light waves covering wavenumbers from 1000 to 4000 cm^{-1} were reflected from two interfaces of the oxide layer. They can superimpose to form the interference patterns at each individual wavenumber and then to produce the IR interference spectra in the test wavenumber range. Therefore, these interference spectra can present the thickness of oxide layers. In these interference spectra, there is a range from 0 to 9 oscillation periods, from 1000 to 4000 cm^{-1}, corresponding to the range from a bare sample to a sample oxidized for 100 hours.

For a weak absorbance thin film, the thickness, t, can be quantitatively extracted from the interference spectra using the following relationship:

47

$$t = \frac{M \times \lambda_1 \times \lambda_2}{2 \times (n_1 \times \lambda_2 - n_2 \times \lambda_1)} \tag{1}$$

where M is the number of oscillations between the two crests or troughs, and n_1, λ_1 and n_2, λ_2 are the corresponding refractive indices and wavelengths at the crests or troughs. The refraction indices, n, of zirconium oxide have been studied and the values are between 1.6 and 2.1 in the 1000 to 4000 cm^{-1} wavenumber range. For the 100 hour oxidized Zr-4 sample, if an oscillation period around 2000 cm^{-1} is chosen and because the refraction indices, n, are assumed to be 2, then the oxide layer can be calculated as 9.4 μm by equation 1 from the representative spectra. The thickness of the oxide layers for the other samples can be obtained in a similar fashion. Fig. 51 shows the average calculated oxide layer thicknesses and corresponding standard deviations from the measured interference spectra for each sample compared to those obtained from previous SEM cross-section measurements. There is actually a good agreement for the results of two approaches and the differences in thickness may be primarily attribute to the roughness existing in the two interfaces of the oxide layer and the material property difference between the oxide under this test and the those studied in previous studied due to the oxide formation process difference. Additionally, the diameter of the incident IR beam is approximately of 100 μm and it is evident from SEM images that the thickness of the oxide layer varies spatially to some extent in this area, so the obtained interference spectrum actually represents the average thickness of oxide layer in this beam-covered region.
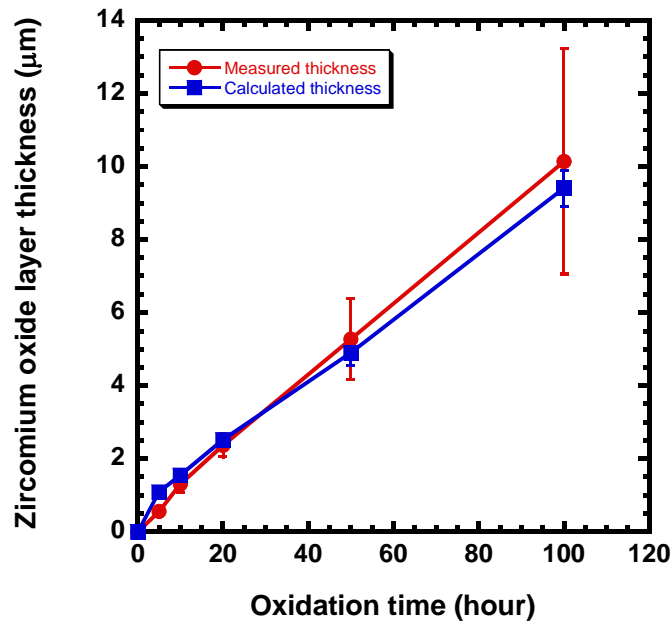

Fig. 51. Comparison of oxide layer thicknesses from the direct SEM image measurements and calculated thickness values from FT-IR data, including the corresponding standard deviations.

From the interference spectra of the oxidized samples in Fig. 49, the amplitudes of the interference pattern decrease and damp faster with wavenumber as the oxidation time and oxide layer thickness increase. In the SEM cross-sectional images, as the oxide layer thickens the roughness of the interfaces increases. The rougher interface results in less effective light reflection and more scattering. Therefore, as the oxidation progresses, the interference between the two reflected light waves becomes weaker, and the amplitude of the interference becomes smaller. Meanwhile, as the wavenumber increases, the wavelength

of the incident light gets smaller and closer to the interface roughness of the oxide layer, especially for the 50 and 100 hour samples. Hence, the interference can be reduced and observable damping of the interference occurs with increasing wavenumber.

5. Current Work

Despite the ending of the grant we are continuing work in this area. A Ventus 50: 50mW 532nm DPSS Laser system. A schematic illustration of this system on optical table shown in Fig. 52. A photograph of the system is shown in Fig. 53.
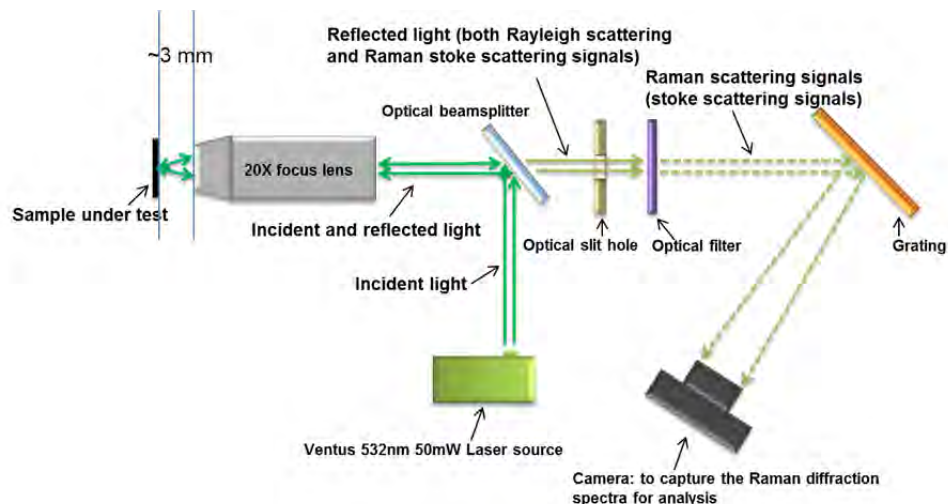
Fig. 52. Schematic illustration of discrete Raman scattering system on optical table.
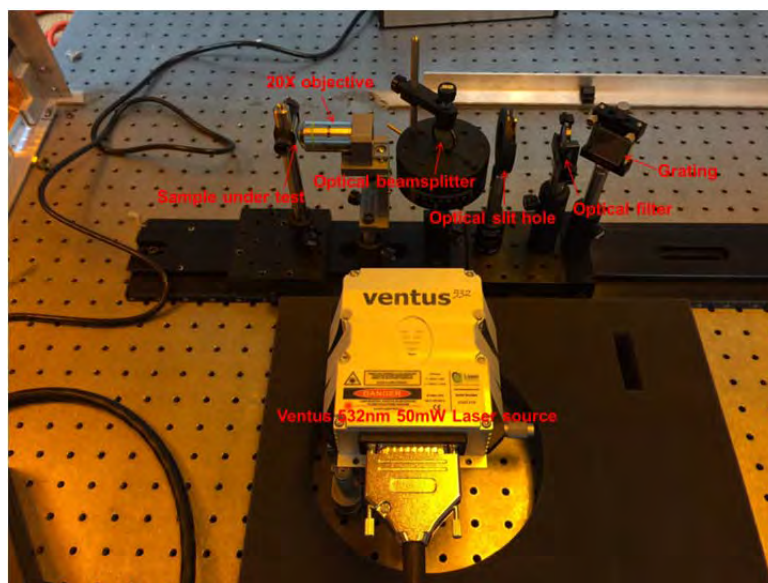
Fig. 53. Photograph of discrete Raman scattering system on optical table.

We have finished preliminary alignment for the optical system on optical table and confirmed that the optical path can be confined in the same plane. Presently, we are working on the scattering spectrum acquisition and data analysis.

49

5   References

[1] R. Einziger and D. Dunn, Identification and Prioritization of the Technical Information Needs Affecting Potential Regulation of Extended Storage and Transportation of Spent Nuclear Fuel: Draft Report for Comment (NRC, Washington, D.C., 2012b).

[2] M. Hélie, C. Desgranges, and S. Perrin, in Prediction of corrosion behavior of HLW containers in the framework of the French interim storage concept, Proceedings of the Regulatory Information Conference, Maryland, 2012, pp. 120-132.

[3] EPRI Technical Report 1025209, Calvert Cliffs Stainless Steel Dry Storage Canister Inspection, 2014.

[4] X. He, T. Mintz, R. Pabalan, L. Miller, and G. Oberson, Assessment of Stress Corrosion Cracking Susceptibility for Austenitic Stainless Steels Exposed to Atmospheric Chloride and Non-Chloride Salts (USNRC, Texas, 2014).

[5] ASTM G108-94, Standard Test Method for Electrochemical Reactivation (EPR) for Detecting Sensitization of AISI Type 304 and 304L Stainless Steels

[6] EPRI Technical Report 1025209, Calvert Cliffs Stainless Steel Dry Storage Canister Inspection, 2014.

[7] ASTM D1141, 1998 (R2013) Standard Practice for the Preparation of Substitute Ocean Water.

[8] J-I. Tani, M. Mayuzumi, N. Hara, "Initiation and propagation of stress corrosion cracking of stainless steel canister for concrete cask storage of spent nuclear fuel," Corrosion **65** (3), 187-194 (2009).

[9] ASTM E647-2015, Standard Test Method for Measurement of Fatigue Crack Growth Rates

[10] ASTM G30-1997 (R2015), Standard Practice for Making and Using U-Bend Stress-Corrosion Test Specimens

[11] T. Shibata and T. Takeyarna, "Pitting Corrosion as a Stochastic Process," Nature **260,** 315-316 (1976).

[12] A. Valor, F. Caleyo, L. Alfonso, D. Rivas, and J. Hallen, "Stochastic modeling of pitting corrosion: A new model for initiation and growth of multiple corrosion pits," Corrosion Science **49** (2), 559-579 (2007).

[13] H. Kaieda, K. Suzuki, Y. Shiba, Y. Aoyagi, K. Kubota, D. Wyborn, and A. McMahon, in Evaluation of the underground structure and progression mechanism beneath the Cooper 57

[14] A. Turnbull and S. Zhou, "Impact of temperature excursion on stress corrosion cracking of stainless steels in chloride solution," Corrosion Science **50** (4), 913-917 (2008).

[15] A. Pardo, M. Merino, A. Coy, F. Viejo, R. Arrabal, and E. Matykina, "Pitting corrosion behaviour of austenitic stainless steels – combining effects of Mn and Mo additions," Corrosion Science **50** (6), 1796-1806 (2008).

[16] J. Soltis, N. Laycock, and D. Krouse, "Temperature dependence of the pitting potential of high purity aluminum in chloride containing solutions," Corrosion Science **53** (1), 7-10 (2011).

[17] P.Van der Weeën, A. Zimer, E. Pereira, L. Mascaro, O. Bruno, and B. De Baets, "Modeling pitting corrosion by means of a 3D discrete stochastic model," Corrosion Science **82**, 133-144 (2014).

[18] N. Acuña, J. González-Sánchez, G. Kú-Basulto, and L. Domínguez, "Analysis of the Stress Intensity Factor around Corrosion Pits Developed on Structures Subjected to Mixed Loading," Scripta Materialia **55,** 363-366 (2006).

[19] http://publicservice.vermont.gov/sites/dps/files/documents/general/ Dry%20Cask%20Rebuttal%20Material%20from%20Sally%20Shaw%202015-03-26.pdf

50

4.0 Summary of Key Results and Findings from TMA-4: Novel System Monitoring

The focus of this mission was to develop in-situ prognostic monitoring methods to verify the condition of the UNF and the internal canister environment without having to break the seal of the inner cask. This included the development of self-powered sensing methods to continuously monitor the cask system and provide physical, safety, and security information during.

The following sections are detailed reports presented from TMA4 contributors in their original format (to maintain clarity).

U.S. Department of Energy, Idaho Operation Office
Consolidated Innovative Nuclear Research, NEUP IRP

Integrated Research Project Report

Novel System Monitoring of Spent Nuclear Fuel Canisters

IRP TMA 4 Lead:
Dr. Darryl P. Butt
Boise State University,
Dept. of Materials Science and Engineering
1910 University Drive, Boise, ID 83712
208-426-1054, darrylbutt@boisestate.edu

Address Change: Dr. Darryl P. Butt, University of Utah, College of Mines and Earth
Sciences, 115 South 1460 East, Room 205, 801-581-8767, darryl.butt@utah.edu

IRP TMA 4 Team:

Dr. Darryl P. Butt, Boise State University, Dept. of Materials Science and Engineering, Boise, ID
Dr. Sin Ming Loo, Boise State University, Dept. of Electrical and Computer Engineering, Boise, ID
Dr. Mike Hurley, Boise State University, Dept. of Materials Science and Engineering, Boise, ID
Dr. Brian Jaques, Boise State University, Dept. of Materials Science and Engineering, Boise, ID
Mr. Vikram Patel, Boise State University, Dept. of Electrical and Computer Engineering, Boise, ID
Dr. John Youngsman, Boise State University, Dept. of Materials Science and Engineering, Boise, ID
Mr. Drew Lysne, Boise State University, Dept. of Materials Science and Engineering, Boise, ID
Dr. Kumar Sridharan, University of Wisconsin, Dept. of Engineering Physics, Madison, WI
Dr. Jack Ma, University of Wisconsin, Dept. of Electrical and Computer Engineering, Madison, WI
Dr. Jake Blanchard, University of Wisconsin, Dept. of Electrical and Computer Engineering, Madison, WI
Dr. Howie Choset, Robotics Institute, Carnegie Mellon University, Pittsburgh, PA (not funded)
Dr. Sean McDeavitt, Department of Nuclear Engineering, Texas A&M University, College Station, TX

1

1.0 Introduction

1.1 The Need for Surveillance and Prognostic Health Monitoring

On-site storage of spent nuclear fuel (SNF) at reactor sites was intended to be a relatively short term, interim stage of the U.S. plan for long-term storage and disposition of nuclear waste. However, the absence of a permanent, central repository for spent nuclear fuel or reprocessing scheme in the U.S. has necessitated longer-term storage of spent nuclear fuel on-site or at distributed Independent Spent Fuel Storage Installations (ISFSIs). Regulations for ISFSIs for the initial storage period up to 20 years with the potential for an extension of an additional 20 years were given in 1998.[1] Until a permanent solution is determined through policy enactment, dry storage is effectively the current final stage of the life-cycle of nuclear reactor fuel in the U.S. Consequently, in order to address the potential issues associated with onsite, dry storage the Nuclear Regulatory Commission (NRC) and (DOE), in cooperation with organizations such as the Energy Research Policy Institute (EPRI) as well as several national laboratories, universities and the various vendors, have attempted to identify and characterize expected degradation modes of the fuel and containment materials at times beyond 20 years.[2-6] Validation of models and stewardship of SNF, in addition to maintaining public confidence, requires tools and science-based approach to surveillance and prognostic health monitoring of SNF storage.

This development effort was part of multi-university collaboration to address understanding and monitoring potential degradation mechanisms in SNF containers. The effort was organized into four teams, or technical mission areas (TMAs) as depicted below in the original proposed matrix. This report addresses TMA-4, Novel System Monitoring.

Low Temperature Creep
J. Tulenko (UF)***
K.L. Murty (NCSU)
J. Eapen (NCSU)
G. Fuchs (UF)
Y. Yang (UF), 25%
J.F. Stubbins (UIUC), 50%
Carl Beyer (PNNL)

Hydrogen Behavior & DHC
B. Heuser (UIUC)***
J.F. Stubbins (UIUC), 50%
S.M. McDeavitt (TAMU)
L. Shao (TAMU)
Y. Yang (UF), 75%
T. Adams (SRNL)

UNF Canister Corrosion
K. Sridharan (UW)***
T. Allen (UW)
D. Butt (BSU), 50%
M. Hurley (BSU), 75%

Novel System Monitoring
D. Butt (BSU), 50% ***
M. Hurley (BSU), 25%
S.M. Loo (BSU)
J. Blanchard (UW)
J. Ma (UW)

2

1.2 Background on Spent Fuel Storage Containment

Following their useful life in a reactor, fuel assemblies are transferred temporarily to wet storage pools for cooling, generally for a period lasting several years due to the high level of decay heat which can be on the order of 6% of the power output of the reactor. The duration of wet storage depends on the amount of burnup as this will dictate decay heat load and the resulting thermal profile of a SNF dry assembly. Following wet storage, the fuel assemblies are dried and loaded in to one of a large variety of different types of SNF dry storage canisters, such as vertical and horizontal variations illustrated in Fig. 1. However, there are certain similarities among designs. Generally, the inner canisters, which hold the SNF, are fabricated from cold-rolled stainless steel (304 or 316 varieties). The inner canisters are sealed and backfilled with helium to prevent cladding oxidation, and are generally sealed by welding, although some containers are mechanically sealed with bolts.

These sealed containers are then covered with a concrete overpack, which serves as a secondary barrier. The overpack is designed to have strategically placed several centimeter-sized openings or vents, both at the base and top of the overpack, to allow for convective cooling and removal of decay heat. Consequently, in addition to the heat and radiation produced by the SNF, both the overpack and the inner canister, which are simply stored outdoors on concrete pads, are exposed to the elements.

Dry storage systems for SNF are typically aggregated and located either on- or off-site at independent storage installations (ISFSI). Vertically oriented dry storage containers are sited on an isolated concrete pad while horizontally oriented storage canisters are typically located in a modular concrete bunker, regardless of orientation the storage sites are typically above ground and surrounded by a fenced perimeter. Above ground storage sites are subject to ambient environmental conditions and hence, the specific environmental conditions (temperature, relative humidity, atmospheric impurities, etc.) a SNF dry storage will experience during its operational lifetime are dependent on geographic location.

To ensure long-term safe storage of SNF or should it need to be transported or retrieved in the future it is necessary to know the conditions of the canister interior components including the fuel, cladding, moderators, and support assemblies. For example, prior to retrieving a fuel assembly from a sealed canister it would be of interest to know whether a cladding breach or fuel rearrangement due to pellet degradation has occurred. Such changes in the fuel assemblies are important to understand for the safe transfer of the fuel to other storage environments or for possible reprocessing.

It is of greater importance to have the ability to continuously understand the conditions of the SNF canister and overpack materials, since there are relatively greater potential consequences the public and environment should there be a breach of the primary confinement barrier. Specifically, as noted and prioritized by Hansen *et al.*[4], the weld zones of the inner canister are of most concern. The focus of this proposed work is to develop surveillance and monitoring systems for the exterior of a SNF canister. In addition to monitoring the environmental conditions and canister degradation modes, exterior canister monitoring can also provide information about the condition of the internals. Significant degradation of any of the

3

internal components will affect the radiation and temperature profiles on the canister exterior. Hence spatially resolved monitoring of the external conditions can be used to also infer conditions on the interior, without breaching the container or placing a separate monitoring system in the very tightly-confined interior of the sealed canister.
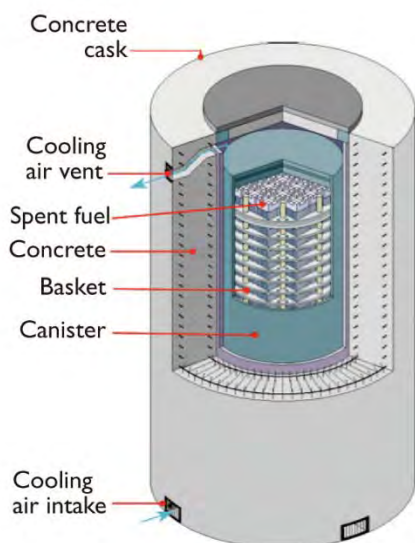
Figure 1. Cut away view of a typical spent nuclear fuel dry storage system including the canister and concrete overpack.

A goal of any surveillance program should be to provide both an early warning and detection of initiation and propagation of expected failure modes as well as to provide information on normal as well as anomalous environmental conditions. In the case of the stainless steel canisters, the primary degradation concern is atmospheric, stress corrosion cracking near heat affected weld zones on the canister exterior surface generated during container fabrication.[4] To verify container integrity it would be desirable to directly measure the weld zone corrosion kinetics using electrochemical techniques, combined with visual and non-destructive flaw detection such as guided ultrasonic waves or eddy current techniques for the detection of corrosion products and/or cracks.[7] To most accurately monitor the condition of a sealed SNF storage canister the sensor system should be located on or adjacent to the canister wall in the annular space between the canister and the vented concrete overpack. However the complexity of implementing a full-scale, direct assessment inspection for the entire container and all circumferential and longitudinal weld zones is currently prohibitive given the current container designs and the lack of inspection tools with the flexibility to penetrate each design geometry. The small amount of available space between the container wall and concrete overpack as well as the expected harsh sensor operating conditions strongly constrain the design of sensors, delivery systems and necessary accompanying communications electronics. Any future container designs should consider internal monitoring.

4

1.3 Relevant Operating Conditions

The environmental conditions, namely temperature, radiation, and atmosphere, experienced by the sensor and delivery systems will of course differ substantially from the local ambient conditions due to heat and radiation generated from decaying spent nuclear fuel. Relevant operating conditions affecting survivability of the sensor system were determined to be temperature, radiation level, and composition of the atmosphere near to the SNF canisters.

The temperature on the canister surface depends on the quantity and extents of burn-up of used fuel assemblies as well as the heat transfer properties of the storage system. Canister surface temperature measurements have been conducted at both the Idaho National Laboratory (INL) dry storage demonstration project and more recently at on-site dry storage installation at Calvert Cliffs.[8, 9] In addition, multiple efforts to model the canister surface temperature profile have been performed for both vertical and horizontal dry storage schemes with different assumed spent fuel loads.[9-13] Based on these assessments, we can assume that during normal conditions the maximum canister surface temperature is conservatively less than 250°C and generally less than 200°C.[9-13] The canister surface temperature will decreases with time as the fuel decays and varies significantly depending on location, with the highest temperatures seen on the middle to upper portions of the canister. The bottom and edges of the canister see relatively lower temperatures due to geometry of the container and arrangement of the fuel assemblies within the canister. Temperature is an important operating constraint because the sensors and electronics must survive and reliably perform in the highest expected temperature range. However, the areas on the canister that see lower temperatures are expected to enter the window of corrosion susceptibility, where the temperature is sufficiently low enough to allow formation of a thin electrolyte layer through salt deliquesce or condensation, earlier than hotter regions on the canister.

The expected radiation level is a significant concern for design of supporting electronic hardware. The electrical components are expected to be the most susceptible part of the sensor system to potential radiation damage. Radiation levels at the exterior canister surface remains under-characterized in part because primary concerns are managing total worker dose during drying and loading operations and maintaining an insignificant offsite public dose during storage. However, it is known that the radiation will be pure gamma radiation and, based on external measurements on the container, it is expected that the radiation levels will be much greater than 1 Rad/hour. Therefore, any sensor or deliver system electronics inserted into the canister channels must be able to survive these dose levels for prescribed durations and it would be desirable to have a system capable of monitoring radiation levels.

The dry storage system provides passive cooling by drawing in ambient air through bottom cask vents, across the canister surface, and exhausting through top vents. The composition of organic and inorganic airborne particulates and pollutants in the ambient air will eventually promote the development of an aggressive chemical environment on the canister surface that could produce degradation of the container components. The exact composition of eventual surface deposits will be dependent on location; with storage sites in coastal regions typically experiencing more aggressive conditions then in-land sites. The amount of moisture in the ambient air and temperature profile on the canister surface will determine when accumulated

5

deposits may become hydrated and eventually deliquesce, forming a concentrated electrolyte on the canister surface. For metallic components the primary degradation mode that could become active during dry storage is atmospheric induced corrosion and SCC. Experimental corrosion and SCC testing as well as assessment of the expected environmental conditions has shown that corrosion and SCC may be expected during the duration of dry storage,[4] as the canister eventually cools enough to allow deliquescence and moisture on the surface. In addition, corrosion associated with microbial activity can not be ruled out. Microbes are known to create byproducts such as H_2S and S^{2-}, which can also contribute to corrosion, and SCC. Consequently, an important objective of any surveillance program should be to monitor these atmospheric and surface products in order to anticipate conditions that could cause degradation.

1.4 Technical Mission Area Objective

The objective of this proposed program mission area was to develop a monitoring approach to enhance the safety, confidence, and science-based assessment of dry cask storage of spent nuclear fuel (SNF). Although not in the original scope, the team also investigated sensor delivery options, in particular, the possible use a novel snake robot design to place and service sensor packages. The specific technical objectives of the program were subject to change as they were partly driven by feedback from the IRP external advisory committee, which consisted of members from DOE National Laboratories, EPRI, and the NRC. Their guidance, combined with other analyses lead our team to focus initially on developing monitors for assessing the environmental conditions near the weld zones of the inner container, i.e., on the outer wall of the inner steel container where there are known residual stresses and the potential for heat affected zones. Thus, monitoring would include assessing the conditions between the inner container and outer cask adjacent to the weld. In order to monitor this region, which has limited accessibility, it would be necessary to insert a monitoring package within the channel between the two containers. Thus, we sought to develop a sensor package that could potentially be self-powered with dimensions on the order of the size of a cell phone. In the later stages of the program, the advisory committee recommended that the team focus on developing a weather resistant sensor module that could also be attached to the vent ports of the outer cask, essentially a small weather station adjacent to the vent port that could not only measure radiation levels but would provide real time data on the atmosphere and temperature entering and exiting the container.

Below, we describe the project scope and provide summary discussions of the technologies that were both considered and implemented. We then describe the final generation sensor package, and its operation and communications. Because this research has ended and the team is no longer funded to work in the area, we provide information below that might allow a followup team to advance our sensor module design, including a few technologies that we could not pursue due to funding and time limitations. Where possible, we provide information on suggested vendors and sensor models.

2.0 Technical Scope

In the course of this project the team identified key monitoring needs, identified potential monitoring and communication technologies to address those needs, developed and selected

6

technologies for demonstration, and developed integrated monitoring packages though an evolutionary process. The overall scope is described in the table below.

Vision Summary	
Year 1: Technology design and ambient demonstrations	**Years 2 and 3: Radiation hard systems construction and pilot demonstrations**
Identify Technologies	Develop Rad Hard Monitoring Technology
"Ambient" Demonstrations	Develop Communications Technology and Protocols
Define Engineering Challenges	Identify Engineering Issues to Implementation
Design Novel Rad Hard Prototypes	Demonstrate Selected Technologies
Develop External Team	Develop IP as Appropriate
Complete Plan for Radiation Pilot Phase	

In the sections below we describing the various technologies considered for monitoring of SNF storage including radiation monitors, thermal monitors, atmospheric sensors, corrosion and stress corrosion cracking sensors, as well as other inspection and delivery systems.

2.1 Monitoring Radiation Levels

It was an objective of this research to develop radiation sensors for monitoring spent fuel storage conditions. At the advice of our external advisory board, radiation sensing was omitted from the final sensor package. However, we did investigate potential gamma radiation sensors for possibly implementation in future devices. Monitoring radiation on the exterior of the overpack is straightforward and has already been done. Monitoring levels inside the overpack is quite challenging and probably unnecessary as it is possible to estimate these values through a combination of calculations and external measurements. Sensors are currently available that could function in the SNF environment of interest. For example, LND, Inc., manufactures a GM tube that can operate in the expected environment for moderate times. It is 158 mm long with a diameter of 16 mm and is constructed of a 446 SS body and filled with Ne. There is also a small amount of a halogen gas (not specified) as a quencher. The interior of the 446 SS body is plated with Pt in order to enhance the production of photoelectrons from the wall during a radiation event. It requires an operating voltage between 850-1200 V, with a recommended value of 900 V. The inclusion of the halogen gas as a quencher (unlike earlier aromatic species) provides an extremely long shelf life. When the GM tube is used within the parameters specified it should provide a useful life of 5×10^{10} counts. This sensor provides the best available solution to survive the operating conditions and provide acceptable radiation level data. However, the high operating voltage presents a challenge to develop on-board electronics using the limited available power. Thus, the use of this detector might require hard wiring of external power.

2.2 Temperature Monitors and Thermal Imaging

Temperature can be measured using a variety of methods including bi-materials thermometers, resistance temperature detectors (RTDs), thermistors, thermocouples, semiconductor junction thermometers, infrared, pyroelectric thermometers, liquid-in-glass, and manometric thermometers. Based on the needs for low power consumption, limited physical access, remote access to data, temperatures up to 250°C, and gamma radiation all but two of the considered options appear to be viable solutions for long term monitoring needs: thermocouples

7

and RTDs. Type K thermocouples have proven to be robust, stable, and reliable temperature probes in extreme radiation environments.[26] Consequently, we chose to use K thermal couples in all sensor packages. These thermocouples are inexpensive, available with small dimensions, and easily shaped, joined and inserted into sensor packages. We also incorporated an RTD on to our internal electronics in order to monitor internal temperatures in the interior of the sensor modules.

Thermal imaging sensors can potentially interface with the SoC over a standard video interface, or over a lower bandwidth interface for low resolution devices. Small, inexpensive, low resolution imagers may be useful with data overlaid from an optical sensor. FLIR Systems makes a couple of different thermal imaging sensors that fit the application. The Quark camera core, depicted in Fig. 2, for example, has small 22 x 22 x 35 mm lens. It features a maximum resolution of 640 x 512 and can display at a maximum of 7.5Hz (due to export control restrictions). It is available in limited quantities at at this date, but has potential to be quite useful in inspections. While it would fit within the packaging envelope, it would potentially take a lot of space away from other sensors. It features an analog video interface that would require an analog to digital converter external to the CCIP SoC.

Figure 2. FLIR Quark thermal imaging camera.

The FLIR Lepton camera, shown in Fig. 3, has lower resolution than that of the Quark at 80 x 60 pixels, however it is significantly smaller. It measures at 8.5 x 8.5 x 5.9 mm, which makes it small enough to easily integrate with other sensors into the housing. It also features a standard MIPI CSI-2 camera interface, along with an optional SPI interface, which would require no extra hardware to interface with the CCIP. The downside of this camera is that it is a new product, and FLIR has expressed that they only want to sell it in volume. Fortunately, the FLIR is releasing a thermal imaging cell-phone add-on called the FLIR One, which features the Lepton sensor. The FLIR camera would not survive in the interior channels between the overpack and inner steel SNF container, but could be used for brief visual inspections through the vent ports.

Figure 3. FLIR Lepton thermal imaging camera.

8

There are also other small thermal imaging sensors, with resolutions that are lower than the FLIR Lepton. The Melexis MLX90620 and Panasonic Grid-EYE sensors, shown in Fig. 4 , both only feature a total of 64 pixels. However, they are both very inexpensive and readily available through regular channels.
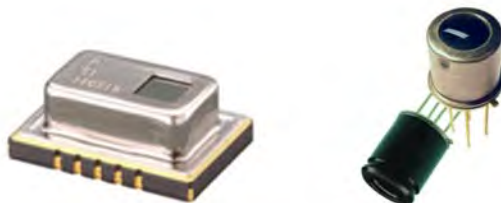
Figure 4. Left Panasonic Grid-EYE, right Melexis MLX90520

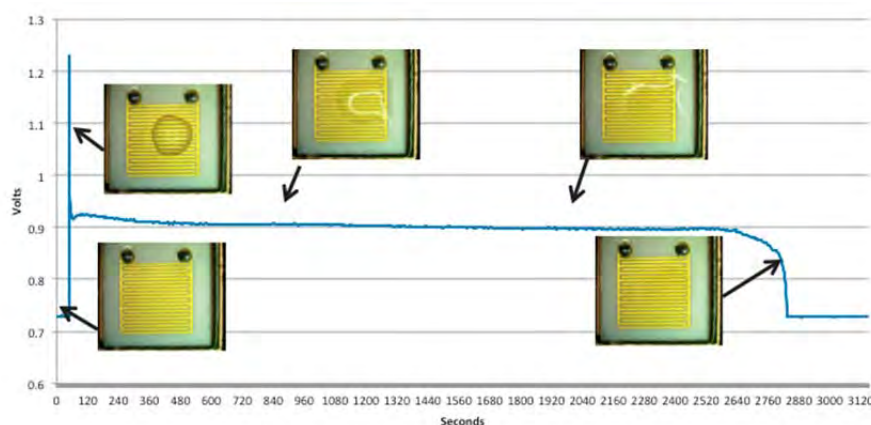*2.3 Sensing Electrolyte Concentrations and Relative Humidity*

An expected primary source of SNF canister degradation is corrosion due to exposure from the atmosphere surrounding the canister. As humidity and temperature fluctuate over time, favorable conditions will be encountered where moisture can condense on the surface of the container forming an electrolyte layer, allowing to corrosion to occur. In order to measure the time that the canister is susceptible to atmospheric corrosion, a time-of-wetness sensor is included in the sensor system. This sensor measures the amount of time when an electrolyte layer is present and the canister is therefore potentially susceptible to corrosion activity. The output signal may be voltage, current, or resistance/impedance.

Generally, the time of wetness is used to measure two parameters, an environmental parameter and a surface parameter. When treated as an environmental parameter, the time of wetness sensor would be used to monitor the conditions around the canister, such as humidity and temperature effects. It could, for example, be used to measure the "wetness" or the time the humidity is at 80% or higher at a temperature greater than 0°C (i.e., conditions where an aqueous electrolyte is present. When treated as surface parameter, time-of-wetness can be in measured two ways. The first approach is to use two, interdigitated noble metals (such as gold) electrodes and measure the time that an electrolyte bridges the gap between the electrodes, detected by the absence of resistance between the electrodes. An example of such a design tested in our laboratory is shown in Fig. 5. The second approach is to have two non-noble metals that act as a galvanic corrosion monitor. As a liquid electrolyte is formed between the two metals, corrosion occurs, and duration of corrosion activity is measured. An advantage of this type of monitor is that it requires no power and is a directed indicator of corrosivity. A disadvantage is that the sensors are by design sacrificial and therefore must be replaced periodically in order to maintain their usefulness. We will discuss this type of monitor in more detail in the preceding section.

Boise State University has experience in custom designing robust sensors of this type through previous research programs, including research for Pratt & Whitney where we developed similar sensors to monitor conditions in the hostile environment of the Joint Strike Fighter engine. However, such sensors are now available commercially, for example through Campbell Scientific. The ultimate electrolyte sensor is expected to consist of a robust ceramic

9

substrate such as alumina, and very likely platinum or gold electrodes. These sensors will be sufficiently robust to use both outside and inside the overpack. There are also a range of inexpensive humidity sensors commercially available, for example, through Ohmic Instruments and Michell Instruments. The later company sells a capacitive sensor that can be used to 200°C. While an absolute measurement of humidity levels between the overpack and inner canister would be desirable, positioning sensors at the entrance and exit of the container vents (Fig. 1) will enable us to very accurately calculate water vapor partial pressures within the channels as a function of position.

Figure 5. Au/Alumina time to wetness sensor showing sensor response (voltage vs. time) as a function of electrolyte concentration, in this illustration, a droplet of water.

2.4 Monitoring Corrosivity and the Propensity for Environmentally Induced Cracking

In addition to monitoring the atmospheric conditions near the canister (i.e. humidity and time of wetness), it is useful to more directly monitor corrosion processes directly or at least the propensity for corrosion. For atmospherically induced corrosion the rate is strongly influenced by the chemical composition of the atmosphere as well as humidity and temperature. For example, dry storage installations sited in coastal regions will be exposed to different and generally more severe corrosion conditions than sites located far inland where the compositions of airborne particulates and aerosols are less influenced by airborne chlorides. Relative corrosivity data will provide an indication of the potential influence of atmospheric composition on not only general corrosion rate, but also more localized phenomena such as pitting and stress corrosion cracking (SCC).

2.4.1 Galvanic Corrosion Monitor

Similar to the previously described interdigitated time-of-wetness sensor, a corrosivity sensor has the ability to sense when an electrolyte layer forms on the surface. However, due to the dissimilar electrode materials selected and trace geometries of the electrodes, it is also able to indirectly assess the relatively severity of the corrosive atmosphere. A corrosivity monitor functions by placing two dissimilar metals, often one of the metals is the material of interest, in

10

proximity but isolated from one another by an electrical insulator. When atmospheric conditions promote the formation of an electrolyte layer on the surface of the sensor, the insulator gap is bridged by the conductive film and the two dissimilar metal electrodes become electrically connected. As a result, a galvanic couple is formed which generates a potential and allows for the flow of a corrosion current. The magnitude of the current depends on the relative difference in potential between the metals and the corrosivity of the electrolyte deposit. If the base metal (anode) is selected based on the canister system of interest and the conductive layer (opposite of or deposited above the insulator) is a noble metal, the corrosion current will correspond to a corrosion rate of the base metal under galvanically driven corrosion conditions as illustrated in Fig. 6. While the sensor is not designed to directly identify either the specific electrolytes or their concentrations, only a measure of the relative aggressiveness of the environment, it may provide information on the potential corrosion rate of the canister. Such sensors are extremely robust and can survive and provide data both on the interior and exterior surfaces of the container.
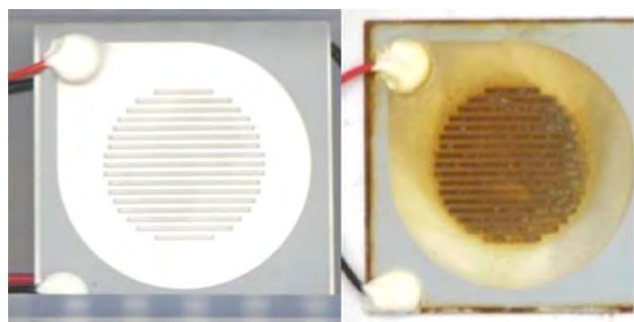
Figure 6. Dissimilar metal corrosivity sensor before (left) and after (right) a seven day exposure in a salt water environment.

2.4.2 Novel Stress Corrosion Cracking Sensors

While the propensity for corrosion is of concern, it is the resulting pits and ultimately cracking that is of most concern. To that end, BSU has developed a new method for monitoring SCC in stainless steel. The method is quite simple in concept, but requires significant bench marking. The essence of the method involves measuring the resistivity of an array of stainless steel wires and ribbons, in some cases with sensitized microstructures. Figure 7 shows an experimental array manufactured at BSU for subsequent testing and benchmarking at UW. This particular sensor package was designed in a modular fashion to enable testing of a variety electrode geometries and microstructures under atmospheric conditions. The package shown in Fig. 7 is partially assembled using eight SCC modules, further illustrated in Figs. 8 and 9.
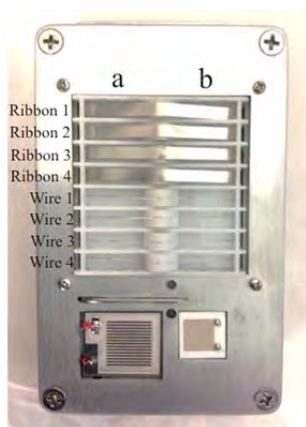
Figure 7. Photograph of a late prototype sensor package ("BSU barnacle") showing eight exposed SCC sensors. This particular sensor array package includes internal and external sensors for measuring temperature, humidity, radiation levels, the presence or absence of an electrolyte, and the propensity for corrosion including stress corrosion cracking.[7]

11
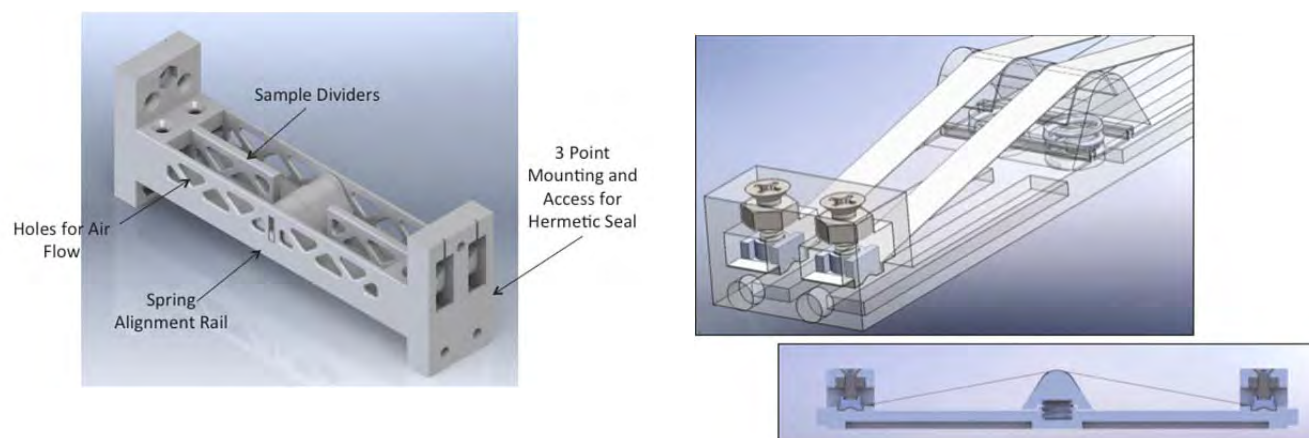
Figure 8. CAD image of an SCC sensor module. Each module holds one or two electrodes.[7]
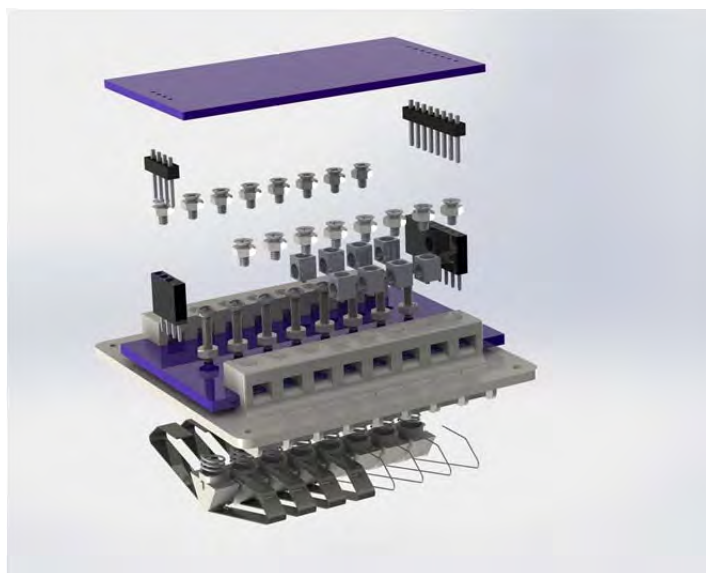
Figure 9. CAD image of the various parts and interfaces included in a second generation SCC sensor module showing mounted ribbon electrodes.[7]

12

The effectiveness of these novel SCC sensors was demonstrated through accelerated testing. While undergoing corrosion, the electrode resistivities are continuously measured. As the electrodes undergo oxidation, the resistivity will increase as the oxide grows and the metal cross section decreases. These values can be correlated with a corrosion rate. As pitting occurs, cracks nucleate and ultimate the electrodes fail. An example of such data is shown in Fig. 10 for two ribbon electrodes exposed to salt water environments. These were accelerated tests resulting in cracking (shown in Figure 11) and failure after approximately 1200 to 1500 min of exposure. Fractography (Fig. 12) of the electrodes clearly demonstrated that failure was associated with environmentally induced cracking. Further discussions of pilot testing of these SCC sensors and the entire sensor package are covered later in this report. Specific details of the testing of individual SCC sensors are provided in Appendix A.
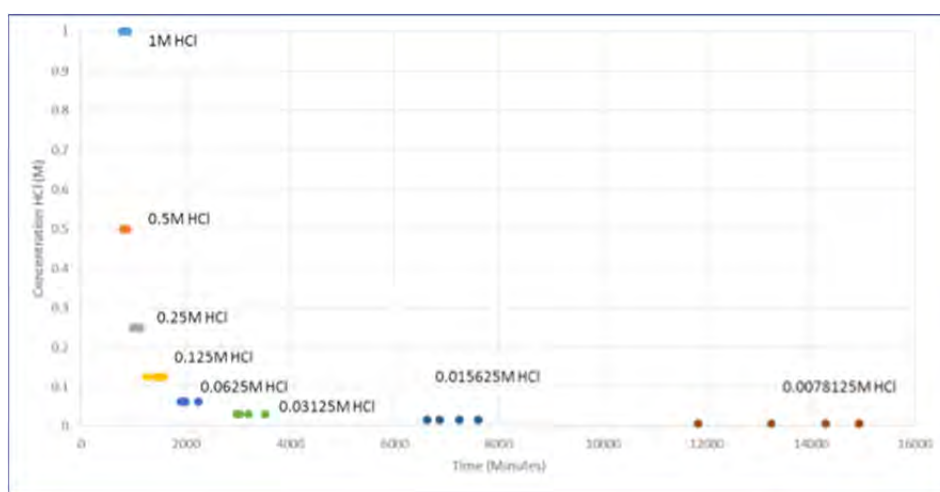
Figure 10. Experimental measurements of the response of stainless steel SCC electrodes sensors exposed to 1 and 2M NaCl (unpublished data, BSU). The data show time to failure of SCC sensors as a function of environmental chloride concentration.

Figure 11. Cracking in a stainless steel-ribbon SCC sensor after exposure to a salt water environment.

13
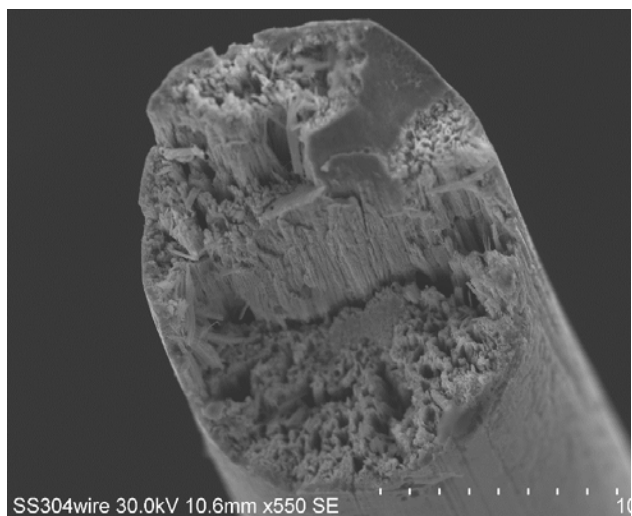
Figure 12. Fracture surface of a SCC sensor electrode after exposure to a salt water environment showing evidence of environmentally induced crack growth.

2.5 Characterization of Corrosion Products and Foreign Deposits

While there are variety of analytical methods that can potentially be used to analyze corrosion products and foreign deposits within the canisters, the cost of implementing an array of technologies was beyond the scope and funding available to this project. The team did, however, investigate various options and selected Raman as an initial focus. The University of Wisconsin team was responsible for this particular activity and worked on miniaturizing and demonstrating a "Raman on a chip" device. Raman is a method that can be used to characterize the nature of bonding in many materials as long as they have a Raman active mode. This does mean that certain materials, such as those with a rock salt structure, can not be characterized with our proposed laser system. Raman is not a good technique for identifying unknowns. However, Raman combined with other could give us a relatively complete understanding of the nature of oxide films and various possible corrosion products or contaminants. Portions of this work have been published.[8]

The University of Wisconsin developed a miniature (~20 x 20 mm) Raman-scattering sensor. The sensor included all system components including a laser source, focus lenses, optical filter, reflection mirror and photodetector (CCD). The sensor was designed to detect the Raman scattering signal and convert it to computer-readable spectra to identify the oxide thickness and/or deposit composition. This sensor could be designed so that it can be either mounted inside the cask on a sensor array package, providing continuous monitoring, or onto a robot, discussed below, for the purpose of routine canister inspections.

The University of Wisconsin demonstrated the feasibility to significantly miniaturize a Raman system. Figure 13 shows a first generation sensor that was built on an alumina/copper substrate. A schematic of the design is shown in Fig. 14. This particular sensor included a 515 nm-30 mW laser diode as a signal source, optical filter for blocking of incident light, and a high sensitivity photodetector. Although this was not a fully functioning detector system, UW demonstrated the ability to obtain Raman signals from this system.

14
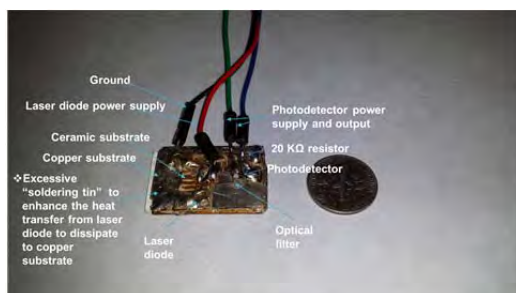
Figure 13. Miniature Raman sensor prototype shown next to a dime for scale.
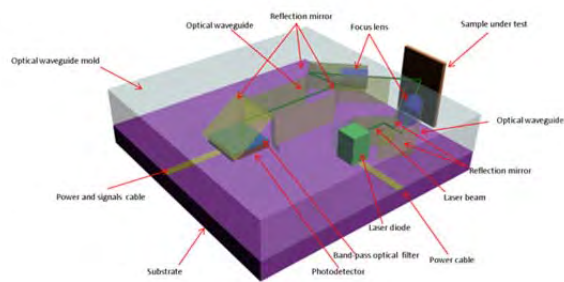

Figure 14. Schematic of UW miniature Raman sensor components.

As depicted in Fig. 14, the Raman sensor is designed to be built on a heat-sink substrate. The optical components include an incident laser source (laser diode), focus lenses, band-pass optical filter and photodetector (CCD). An evaporated-metal mold is applied to the substrate to form an optical waveguide for the light signal transmission. The incident light from the laser diode goes through the focus lens to reach the surface of the sample as a focused beam providing high spatial resolution. The reflection signals, including Raman scattering from the sample surface, go through the collection lens and become a parallel beam. The parallel beam is reflected from a 45 degree mirror to reach the band pass optical filter which blocks the incident laser signals and allows only the wavelength containing a useful Raman scattering signal to pass.

The passing Raman scattering signals ultimately reaches the photodetectors (CCD) and are converted to the spectra such as that shown in Fig. 15. While we were not able to develop additional analytical methods due to scope and cost, the team did investigate other potential, complimentary methods for assessing corrosion products. One method that has significant potential is laser induced breakdown spectroscopy (LIBS). LIBS is essentially a variation of the technique of atomic emission spectroscopy, but uses a laser pulse rather than an electrical or thermal source to excite atomic species to a plasma state. The optical emission spectra are subsequently collected in a monochromator or polychromator and can be relatively easily analyzed. The technique is currently used, for example, on the Mars Rover for characterizing the

15

chemical composition of minerals on the planet and thus has been demonstrated to be useful for unknowns and can be miniaturized. While LIBS is a powerful technique for characterizing the chemistry of corrosion products or foreign deposits, it does not provide information on bonding or crystal structure. Therefore, LIBS is most useful when combined with a structure sensitive tool such as Raman.
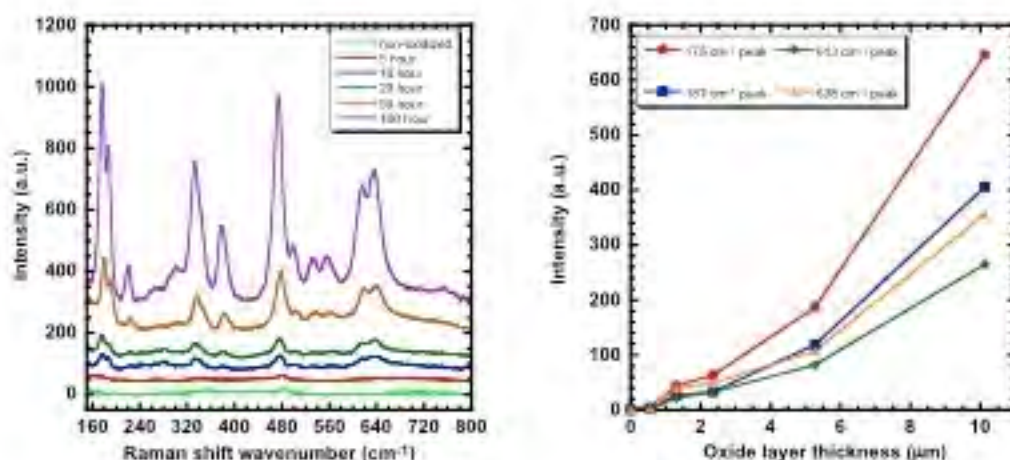
Figure 15. Raman spectra (left) of the surface of Zirc-4 cladding with varying oxide thicknesses. The intensities of the deconvoluted peaks at 175, 187, 613, and 638 cm^{-1} correlated with measured values of oxide thickness.[8]

2.6 Visual Observations of Corrosion Products and Cracking

The prevalence of imaging and video in the cellphone industry has opened the market to a wide variety of small, inexpensive, high resolution camera sensors. Because of the chosen SoC architecture for the CCIP, the cellphone camera interface (MIPI CSI-2) is already present and integrated into the system. Many of the cameras already have existing Linux drivers that are freely available.

Two potential options are the Omnivision OV5460, and the Sony FCB-MA130. The OV5640 is a 5 megapixel camera that can stream 1080p video at 30 frames per second. It is available in a small module that features built-in autofocus. It is not a new camera; however it has the benefit of having full support and documentation for integration with the i.MX 6 processor. There is already driver support and there are development boards that are readily available.

The FCB-MA130 is a 13MP camera that can also stream 1080p video at 30 frames per second. Like the OV5640, it comes available with autofocus. It does not feature built in support for the i.MX 6, however it is well documented making driver development feasible. It is a newer camera, and besides the higher resolution, it features a higher quality optical path. These cameras are of course not designed to be rad hard. At this date, we are not aware of a miniature rad hard

16

camera. There are, however, demonstrated methods for visual inspections of highly radioactive and high temperature areas using optical fibers which could be used for brief inspections.
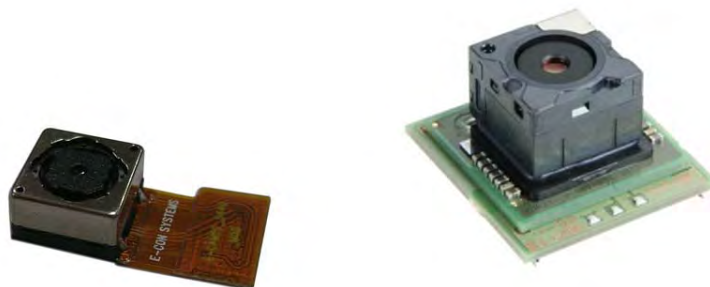
Figure 16. Left - Omnivision OV5640, right - Sony FCB-MA130 miniaturized cameras.

There are additional, more advanced sensors for imaging, not only in 2D, but also in 3D. We already know that several 3D sensors can interface with the SoC (described below) over a USB connection, high speed data bus such as MIPI, or can work in tandem with the optical sensor in the case of structured light. There are different available options that can fit within the packaging constraints. Structured light is a viable option that would work in tandem with the included camera. A line laser could be used in combination with the standard camera to generate distance scans. This would be a very simple, robust solution to imaging although vulnerable to interference from ambient light.

Another option is to use a 3D Time of Flight (ToF) sensor. There are a several companies that make sensors packages that are small enough to fit within the space constraints of the sensor package, one from PMD Technologies and one from Espros Photonics. PMD Technologies developed a single chip 3D ToF sensor that is commercially available. A small evaluation board called the CamBoard Pico XS, shown in Fig. 26, was created for hardware development. This system includes the 3D sensor and required high brightness LED. The CamBoard Pico XS is small enough to fit within the sensor package. Although the CamBoard Pico XS is not available at the time of writing this report, PMD Technologies expressed that they could provide samples of the chipset, which would allow for an even smaller design. The CamBoard Pico XS has a sensor with a resolution of 160 x 120 pixels, with the company is also manufacturing an IC (with a partnership with Infineon) that has a resolution of 352 x 288 pixels. The interface to the CCIP would most likely be over a MIPI CSI-2 interface.
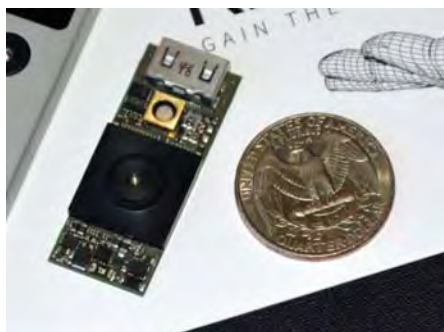

Figure 17. CamBoard Pico XS.

17

Another option comes from Epros Photonics, which is the epc610 IC. They have developed an 8x8 pixel ToF sensor that is available as a standard product. There is more available information about the sensor, and it is only 2.6 x 2.6mm without the lens. The interface to the IC is over an SPI serial link, which would be easy to integrate into the CCIP. Also, the company is in the process of developing a ToF sensor with a resolution of 320 x 240 pixels.

Figure 18. epc610 time of flight sensor mounted to a PCB.

2.6 Atmospheric Particulate Characterization

Although often ignored in the analysis of corrosion, the deposition of particulates on material surfaces can cause localized degradation. Particulate monitoring was outside the scope of this projection. However, current and formal funding from FAA and NIH at Boise State University has led to the development optical particle counters for home and airliner cabin environment monitoring.[9,10] The goal of the optical particle counter design was to create an inexpensive implementation that provides results similar to those of commercial particle counters. Achieving this goal potentially opens up many applications for particle counting that are not obtainable with devices that can cost thousands of dollars each. The optical particle counter design operates on the principles of Mie scattering, wherein a single particle intersecting a beam of light scatters photons onto an optical sensor. The optical sensor converts the photons into a measurable signal, which is analyzed to determine the particle size. The amount of light received at the sensor will be dependent on the particle size, shape, and index of refraction. The count of particles in each size range is divided by the volume airflow through the measurement area to determine the particle concentration. The airflow and optical path are shown in Figure 19. Air enters the sensor from the flow inlet, moves past the laser and photodiode, and exits through the outlet fan area. The fan is not shown in the drawing, normally fitting into the outlet fan area. The laser light passes the photodiode and enters the light trap area where it is absorbed. Because debris entering the canister ventilation system can have deleterious consequences, we recommend including a particle monitoring system in future sensor array. The current monitor design will need to be miniaturized and modified in order to be more environmentally robust.

2
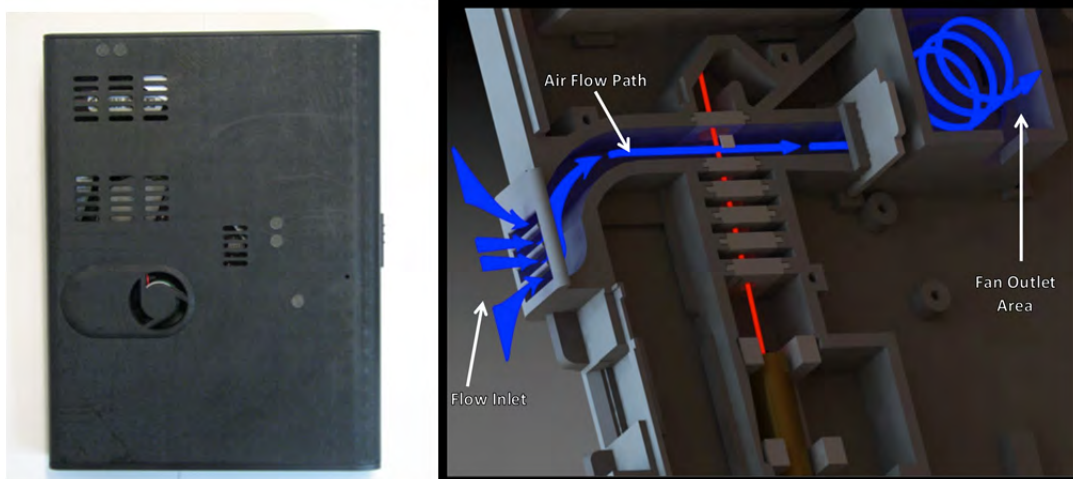
Figure 19. Airliner cabin environment monitor designed and constructed at BSU showing its airflow channel.

2.7 Robotic Sensor Package Delivery System

Although beyond the scope of our original proposal, it became apparent that feasibility of monitoring relies on the ability to maintain low radiation dose levels to workers. The ultimate goal of the proposed work is to place sensors in hard to reach locations. Consequently, a robotic deliver system is more desirable than a human delivery system. This need naturally lead to the development of a relationship between the original research team and Carnegie Mellow University, a leading robotics research university. In particular, we identified a snake robot design (Figs. 20 and 21) developed by Prof. Howie Choset as having a range of demonstrated attributes ideal for sensor package delivery.

Snake robots are highly articulated mechanisms that can thread through tightly packed volumes reaching locations that people and machinery otherwise cannot. The great number of variable degrees of freedom associated with snake robots is what sets their mobility characteristics apart from other types of robotic vehicles. Moreover, the snake robot's small cross section, flexibility, and unique locomotion and climbing capabilities make them ideal tools for inspecting narrow pipes of virtually any geometry, both from the inside and out. The CMU team has developed snake robots that can traverse a variety of terrains, including flat ground and pipes, as shown in Fig. 21. The physical and operating parameters of the robot depicted in Figs. 20 and 21 are summarized in Table 1.

2
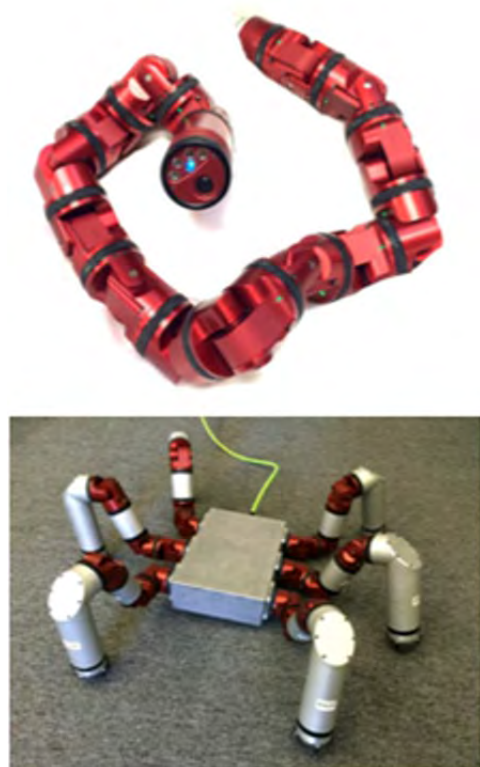
Figure 20. Photograph of a Carnegie Mellon "Snake Robot" (left, top)—see also, e.g., *https://www.youtube.com/watch?v=wMsDg_1TQxA*. Robots such as these have been used to reactor inspections, search and rescue operations, and archeological explorations. Below is a recently developed spider robot (left, bottom) illustrating the modularity and flexibility of the design—see also, e.g., *https://www.youtube.com/watch?v=AMVO6rI5mL4*.


Figure 21. Examples of a CMU snake robot capabilities, clockwise from top left: side winding, rolling, pole-climbing, and inspection from a pole climb.

3

Table 1. Overview of CMU Snake Robot Specifications.

Dimension	- Diameter: 5.1 cm - Length (module): 6.4 cm - Length (full 16 module robot): 1.174 m
Mass	- Module: 205 g - Full 16 module robot: 3.657 kg
Actuation	- Max Torque: 7 N-m - Max Speed: 33 RPM
Power	48 V - Current (resting): 0.64 A - Current (max): 9.6 A
Communication	100 Mbps Ethernet
Sensing	- Angular Position and Velocity - Output Torque 3-axis Accelerometer 3-axis Gyro - Temperature - Voltage - Current

CMU's snake robots contain a series of single degree-of-freedom revolute joints, or modules, connected in a chain where each axis of rotation is offset by 90 degrees such that half of the joints actuate in the vertical plane and the other half in the horizontal plane; this geometry allows for motion in three dimensions. A typical robot consists of 16 modules linked together, with unique head and tail modules. In addition to the 16 rotary DOF design, modules can be added, removed, interchanged, or replaced with novel mechanisms. Any device meeting the interface requirements can be included in the chain.

The housing of each module is machined from 7075 aluminum and anodized to prevent wear and corrosion. Components are densely assembled inside to minimize volume, as illustrated in the module cross-section in Fig. 22. O-rings laid in machined grooves seal the module at each interface. The robot meets IP66 standards, meaning it is splash-proof.
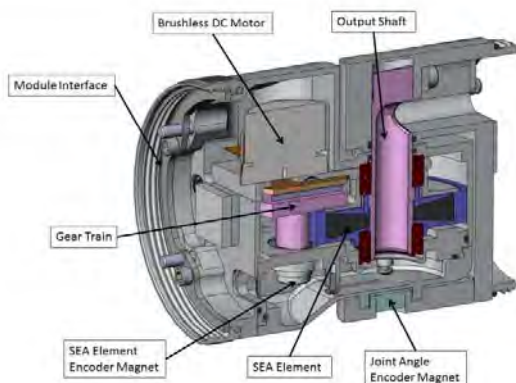
Figure 22. CAD model cross-section of a CMU snake robot module.

4

This design has an inter-module interface which features a rugged, tool-less design allowing for assembly without any tools. Modules are aligned with dowel pins and matching recesses. A freely-spinning threaded collar, held in place by a retaining ring, is turned by hand to lock adjacent modules together. An electrical connection is made between two modules with spring-pin connectors on the interface board touching target areas on the control board. O-rings seal the collar at both ends. Modules can be connected and disconnected quickly and repeatedly. The connections are secure and resist shock and stress. Any device with matching threads, 48V and Ethernet compatibility can be interfaced with a module, allowing for freedom of design and customization.

Both a head and tail module were designed utilizing the custom modular interface and they are pictured in Fig. 23. In addition to providing their specialized functions, these modules demonstrate the potential for the use of other modules that could easily be integrated into the CMU snake robot system.

The head module, shown in Fig. 24, includes a high-definition camera to provide the user with a live video feed while the four LEDs are available for illuminating darker environments. The head module housing is designed with fins to increase surface area and improve heat transfer from the electronics to the surrounding environment. The LEDs are protected by an O-ring sealed acrylic window, while the camera's lens is protected by an O-ring-sealed sapphire glass window.

Figure 23. Photo (left) of the CMU snake robot interface. Dowel pins provide alignment while the threaded collar mechanically secures and seals the modules. The electrical connection is made with spring-pin connectors touching target areas on the control board.

5
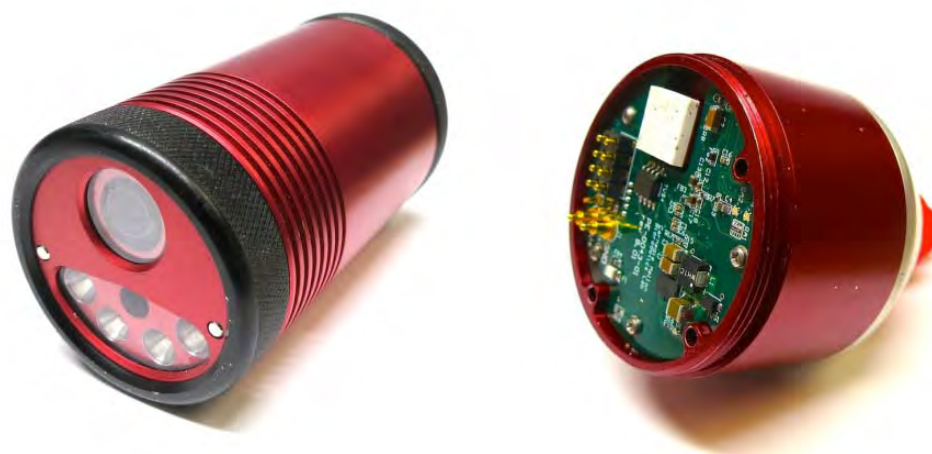
Figure 24. Photos of Carnegie Mellon snake robot head and tail modules

The use of Ethernet as the standard communication interface between modules enables the use of readily available, IP security cameras as the basis for the head module of the snake. The bandwidth that is needed to transmit a high definition video stream is a fraction of the total bandwidth available on the system, paving the way for the use of multiple cameras and additional sensors. The camera module that has been designed to be used for the snake robot is primarily built around the circuit board and camera that were harvested from a commercially available security camera. A custom circuit board was designed to provide power to the camera, to support additional sensors such as an IMU and a pressure sensor, as well as to control high-brightness LEDs for camera illumination. The camera and electronics were packaged into a simple aluminum tube featuring the same standard mechanical and electrical interface as the regular snake modules.

The development effort that went into the Carnegie Mellon snake robot architecture provides an excellent basis for a modular sensor interface. The standardization of the electrical and mechanical interfaces makes it easy to design interchangeable sensor heads for varying applications. Each sensor head may have different requirements, such as small windows or openings, however the snake interface end can remain identical. Thus we envision that one could create a sensor head technology that is flexible and scales as new needs are identified and refined. Instead of building a specific sensor head for a particular use, one could create a generic interface, as illustrated in Fig. 25, that would be built into a sensor head which will readily allow for rapid design and re-design of sensor heads as needs change. Fortunately, the existing snake robot has proven to be stable, both for use and further development, it will remain this way for a long time. Moreover, this interface will "run" Ethernet and therefore, a Common Computing/Interface Platform (CCIP) can be designed once and then reused for different sensors. Likewise, mechanically, the back half of the module could remain the same, with only the front half necessitating a redesign to accommodate different sensors.
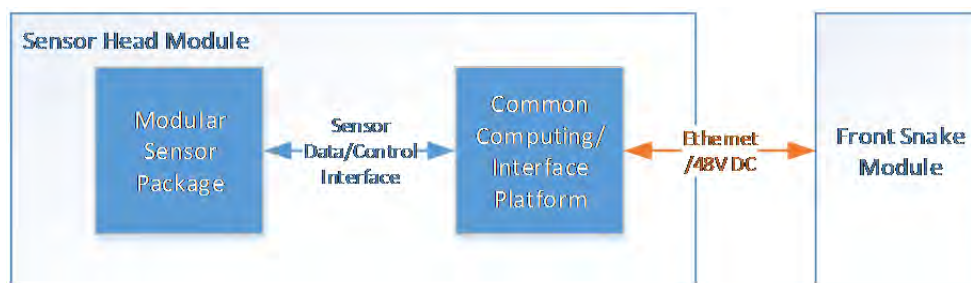
Figure 25. Sensor head interface diagram.

The interface may be viewed as having two ends: the snake robot side and the sensor side. The snake robot interface end of the proposed sensor head will feature the universal interface developed for the Carnegie Mellon snake robot. The mechanical interface would consist of a lock ring, with O-ring seals, dowel pins to provide mechanical alignment, and an electro-mechanical interface featuring spring pins. In front of the electrical interface will be the mounting required for the CCIP electronics. This makes the robot a truly modular device. The sensor end of the proposed head will depend on the type of sensor package that is being used, and if that package needs to be releasable. The rearward facing part of the sensor package can feature standardized connectors to connect to the CCIP. The casing for the sensor head will remain within the two-inch diametric profile of the robot. The length of the sensor head is unrestricted but poses issues with locomotion if it is too long.

The Common Computing/Interface Platform (CCIP), depicted in Fig. 26, will be the computing module that is responsible for collecting data from the sensors, processing and packaging the data and then sending the data over the TCP/IP Ethernet link. It is desirable to make this interface as flexible as possible to suit the different interface requirements of the potential sensors. In its basic function, the CCIP only needs to have the capability of forwarding data. However, for very high data rate applications where the Ethernet link could potentially become saturated, it needs to have the ability to compress data, or to make smart decisions about what data is sent back. This is already the case for sending a digital video stream over the Ethernet link, as the desired 1920 x 1080 resolution would require a 1.49 Gbps link in its uncompressed state; however it can be made to use a fraction of the available 100 Mbps bandwidth if it is compressed. The latency of the sensor data may also be of concern. For video feedback, low latency is important as the snake robot is a remotely operated vehicle. To give the operator an intuitive feel for the motions of the robot, the visual link has to appear to be real-time. The CCIP needs to be able to have enough processing capability to handle the maximum data output of the sensor with the highest data rate, which for most applications will be the video stream from the camera.

33
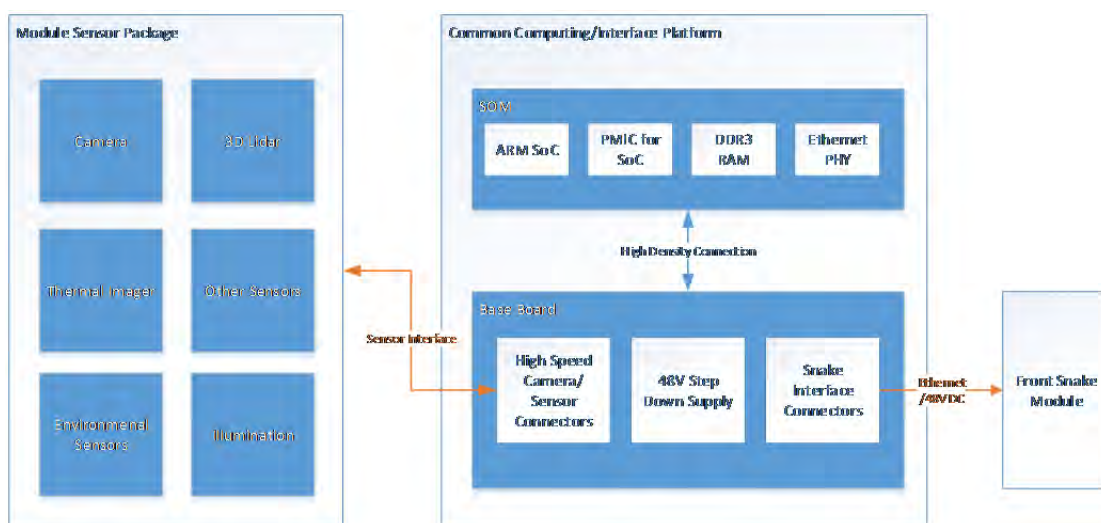
Figure 26. Sensor package/CCIP diagram.

There are many different methods for compressing video, ranging from specialized hardware to open-source software. On the hardware end, a Digital Signal Process (DSP) or Floating Point Gate Array (FPGA) can be used to run the specialized algorithms needed for video compression very efficiently; however the development effort is high and potentially require expensive software packages. These devices also tend to lack the industry standard MIPI CSI-2 camera interface required for most cellphone cameras, necessitating more development. On the software end, there exist readily available software packages for video compression; however they are inefficient and not able to run fast enough or with a low enough latency on a processor that can fit the tight space and power constraints. There is also still the issue of the camera interface, which will again involve additional development.

These same issues are faced in the mobile electronics industry, which turned to a System on Chip (SoC) type architecture that includes specialized video processing hardware, together with a general purpose processor for running regular applications. This allows for an easy software interface, as well as providing the efficient and fast hardware to easily process and compress the video. The type of SoCs that power cellphones and tablets in today's market are extremely powerful and versatile. Not only do they include the aforementioned ability to compress video, most also include interfaces to the other required sensors, feature high speed memory interfaces as well as 3D capable Graphics Processing Units. Most also include the required camera interface without any extra hardware.

The proposed basis for the CCIP is to use a standard ARM SoC that is designed to be used commercially in tablets and cellphones. The features of interest are all available within a single chip:

- Designed for space-constrained applications
- Designed for low power, efficient operation
- Hardware video encoding

34

- Camera interfaces/image processing
- Low speed sensor interfaces (I2C, SPI, GPIO, etc.)
- High speed interfaces (MIPI, parallel, USB, etc.)
- High speed memory interface (DDR3 SDRAM)
- Support for off-chip storage (Removable SD card, flash, etc.)
- Ethernet connectivity (Some provide this, easy to add with USB)
- Support for Linux. Windows, Umbutu, and MacOS

Due to the space restrictions inside mobile devices, most SoCs come in a high density Ball Grid Array (BGA) package. While these packages are excellent from a density perspective, they require very complex and expensive circuit board design and layout. Also, for SoCs that do not have integral RAM, or RAM included using a package-on-package design, a high speed external memory interface needs to be routed to the external RAM chips. A common practice for using SoCs and other processors that have complex high-speed layout requirements is to package them onto a so-called connectorized module, called a System on Module (SOM). The SOM can then be jacked into a base board that is less complex to design and manufacture. The base board can be specific to the target application; however the SOM can be generalized for use in many applications. This means that the cost of developing and manufacturing the SOM can be absorbed by making them in quantity, and then reusing them in different applications.

The easiest path forward for the SoC proposed for the CCIP is to use a SOM and baseboard type architecture. If a commercially available SOM exists and it fits the requirements, it would significantly speed up development, however due to the extremely tight space requirements, this may not be the case. Building a custom SOM would allow for the most efficient use of space for the given application, and due to the modularity proposed in the platform, it could be designed once and reused for many different sensor heads. The SOM baseboard would be designed to provide both the standard Ethernet interface to the snake end of the module as well as the specialized interfaces to the sensors. It would also include the power circuitry required to drive the SOM from the high voltage bus, as well as provide power to the sensors.

Perhaps CMU's most significant contribution to the snake robot field is not the device, but the controllers, sometimes called gaits, that coordinate the motion of the snake robot.[14-17] More specifically, a gait is a controller whose cyclic inputs generate net motion for a locomoting systems. CMU's gait model is at the forefront of those for snake robots (an area in which other prominent researchers include Hirose[11, 12] and Yim,[13, 14] and others[15-17]) in that it provides motion in three dimensions. Assume that the even numbered modules are responsible for propagating vertical waves and the odd for propagating lateral waves, we use the terms $offset_{even}$, $offset_{odd}$, $amplitude_{even}$, and $amplitude_{odd}$ to denote the parameters affecting the two orthogonal waves. Finally, we assume that both offset parameters are set to zero, unless otherwise noted. Essentially, all of our gaits are described by the curvature of a curve passing through the mechanism at any given point. Since the curve is "discretized" by links, all of the gaits can be described by an angle of the nth module at time t as

$$angle(n,t) = \begin{cases} offset_{even} + amplitude_{even} * \sin(\theta), & n = even, \\ offset_{odd} + amplitude_{odd} * \sin(\theta + \delta), & n = odd, \end{cases} \quad (1)$$

35

$$\theta = \left(\frac{d\theta}{dn} * n + \frac{d\theta}{dt} * t \right), \qquad (2)$$

Different sets of parameters describe different types of gaits, such as sidewinding and linear progression. These parameters were initially determined by a large number of experiments and in the recent years, Carnegie Mellon developed techniques, based on geometric mechanics, to design the gaits, i.e., chose the gait parameters. These techniques essentially divide the configuration space Q into two subspaces: a position space G and a shape space M. A closed loop path in the shape space corresponds to a gait and the goal of gait design is to derive the closed loop path in the shape space that corresponds to a desired displacement in the position space. Our gait-design techniques, as well as all others, never placed any joint limits or workspace limits into the shape space. In other words, they simply assumed that the robot was operating in an open space or the robot always had enough space to execute its gait.

Some of our gaits have been demonstrated to work inside a confined space, say a pipe or tube, but these gaits were adaptations of existing gaits whose parameters were empirically derived from related motions. In order to address the complications associated with delivering sensors to an SNF canister, one would need to create a new family of gaits that are specifically designed to operate in confined spaces. No rules have been determined for gait design mainly because existing gait design techniques are generally based on differential relationships and hence have no way of incorporating objects, from which the snake may locomote, into their formulation. Carnegie Mellow has already developed gaits that have no difficulty traversing pipes whose diameters range from 3 to 6 inches. These pipes can have bends and in some cases junctions. However, the robot cannot be steered into a desired branch of a junction; currently it can only go down a particular branch of a junction based on the initial conditions of the robot and the shape of the junction. Essentially, the robot drives blindly through a pipe junction. One of the goals of future work, therefore, would be to develop a robust behavior for navigating junctions in channel networks. This is a challenge because the robot can no longer "blindly" interact with the surrounding channel to propel itself forward.

2.8 Packaging and Communications

As noted above, an objective of this TMA was to develop packaging and communications for sensor array packages to be mounted on the exterior of the overpack as well as in the channels between the overpack and inner canister. Several communications methods were investigated including both hard and wireless. The sensor package design went through a number of interations based in large part on feed back from our external advisory committee. Below we will provide some highlights on the design evolution, but will largely focus on the final module.

2.8.1 Spent Nuclear Fuel Sensor Array Packaging Design

The first generation of the BSU spent nuclear storage monitor prototype,[7] the so-called first generation "Boise State barnacle", was designed in year 1 to hang off the top of the inner canister after it is placed within the casket (Fig. 27). The prototype case was 3D printed at BSU with 0.55 inch thick walls to accurately represent the thickness of titanium shielding required to

36

protect the internal electronics from the radiation. This early version of the barnacle contained twelve K-type thermocouples for placement across the canister, relative humidity, corrosion, time-of-wetness, alpha-beta-gamma Geiger Muller tube, and five stress corrosion cracking (SCC) sensors.

The barnacle had its own local processor, which preprocesses locally captured data and reports back to the motherboard. This allows for an increased amount of control of each sensor node and the use of digital filters when collecting data. The central cavity of the system contains positions for up to twelve SCC sensors of varying geometries. A goal of this research will be to further reduce the size of the sensor, further harden the package for the thermal and radiation environment, and assist in conducting real demonstrations on spent fuel storage containers.

Figure 27. Images of the first prototype of the BSU barnacle sensor array for monitoring of temperature, radiation levels, humidity, time to wetness, and corrosion of spent nuclear fuel storage.

The first generation barnacle required no local microprocessor to function. Instead, all sensor data was digitized and sent over a weather resistant Ethernet cable, which also supplied power. The Ethernet cable terminated at a motherboard (Atmegaton Motherboard, see Fig. 28) which was designed at BSU to be mounted external to the canister. This motherboard uses a 32-bit Atmel processor to process the data received from the sensors. This data is stored locally on a SD card and transmits the data over a secure Zigbit mesh network to a central coordinator for storage and analysis. The motherboard also supports long-term battery backup and all stored data can be access locally via USB.

Figure 28. BSU's Atmegaton motherboard

Following the successful development of the first generation barnacle, efforts focused on further reducing the size of the unit (e.g., to the approximate dimensions of a cell phone) while also increasing the number of sensor components. Specifically, the packaging was re-designed, reduced in size, made to be modular (allowing sensors to be added and removed easily), and designed to hold approximately 20 sensors. This second generation prototype is shown in Fig. 28. Details of the operations of this sensor package are described below, and Appendix B provides a relatively detailed discussion on the fabrication and assembly procedures.
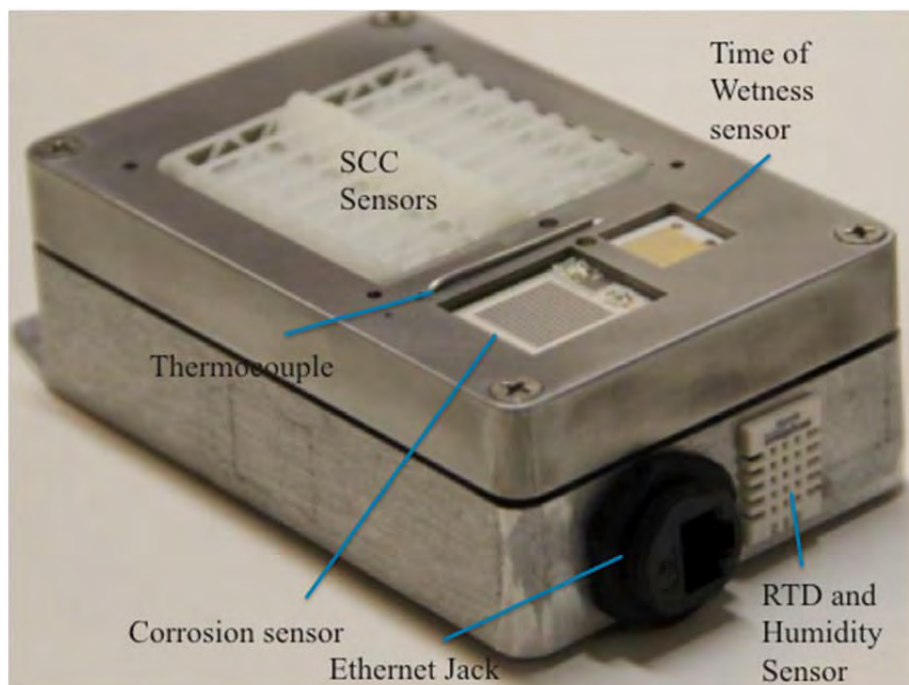
Figure 29. Photograph of a second generation BSU barnacle showing several exposed sensors. This particular sensor array package includes 17 sensors for measuring temperature, humidity, radiation levels, the presence or absence of an electrolyte, and the propensity for corrosion including stress corrosion cracking. The package is similar in size to a cell phone.

38

2.8.2 System Security and Communications

Although we have not been given guidance on security issues associated with sensor data, we have maintained the view that the data are confidential to vendors. Securing embedded systems such as ours is a challenging task.[18,19] One might be tempted to port workstation-based security techniques directly on the devices to make them secure. However, embedded systems have characteristics that differentiate their security architecture from that of workstations and servers. The design of security for embedded systems differs from traditional security design, because these systems are resource-constrained in their capacities and easily accessible to adversaries at the physical layer. One can group embedded security into two categories: resource limitation and physical accessibility. To secure the proposed monitoring system, we will need to consider how to physically secure the sensing system and how the firmware will be hardened.

For securing the sensing system, there are a few things that we have to consider. First is the physical security of sensing system. The sensing system will be installed at a secured storage site. It is anticipated that other security systems will be in placed to protect the storage. Even with this in mind, we will employ "potting" the sensing system as a security measure, as well as protecting it from environmental elements. The potting will make it difficult for someone to extract the hardware and easily recognize and access the components in the systems.

Within the sensing system, the firmware (software running in a embedded system is usually called firmware) will need to be secured. Firmware will be analyzed with off-the-shelf source code security analyzer. The analysis will point us to what portions of the code should be re-written. The boot loader will be secured. One of the most common security holes is buffer overflow. The trigger of buffer overflow could allow an attacker to take control of the sensing system.

The next level securing the system is the wireless communication. For the data to be received in tact, the monitoring systems must be able to send the data securely and deliver it uncorrupted to the monitoring center. This will require encryption. It is highly possibly that someone will be able to acquire/tampering the monitoring hardware and break-in to extract information, including encryption key. This means that symmetric key encryption is out of the question. A symmetric key encryption system is where the same key is used to encrypt and decrypt. The key needs to be kept confidential. The loss of hardware could result in loss of an encryption key. The use of a public key encryption is necessary. With a public key encryption system, one key is used to encrypt the data and another key is needed to decrypt the data. The critical issue is keeping the decrypting key confidential. The increased level of security, not all monitoring nodes will be using the same encryption keys.

Independent Spent Fuel Storage Installations (ISFSIs) normally place multiple canister systems in close proximity in a repeating geometric pattern such as a grid. A large number of canisters can be concurrently monitored by deploying sensor nodes across an entire storage facility. These sensor nodes communicate and report data via a wired or wireless sensor network with a central coordinator. This data is then transmitted by various means to a server with a

sensor measurement database. This data can then be viewed by querying the database using various devices. Figure 30 shows a sample configuration of a deployed sensor network.
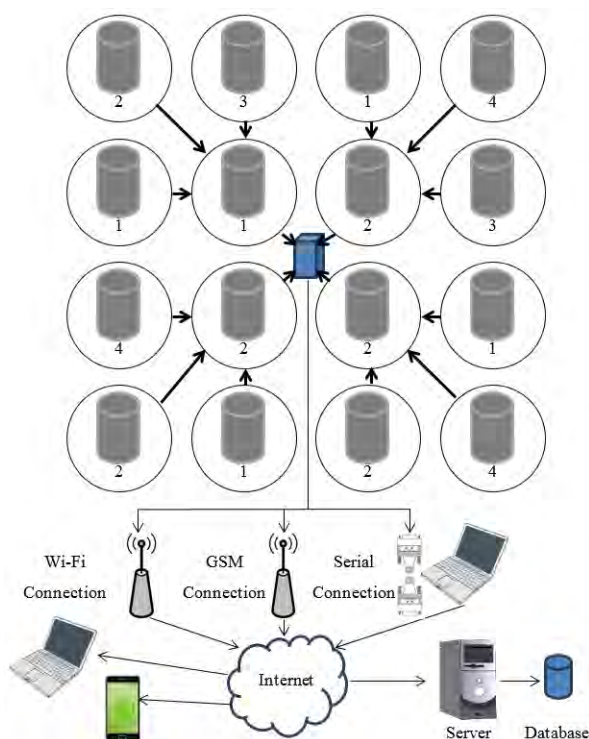

Figure 30. Example Sensor Network Configuration. This example network contains 16 SNF storage systems (grey cylinders) with a various number of nodes at each system. All of these nodes report to the central coordinator (blue box), which then manages the data by storing and/or transmitting it by various means to a server.

Each sensor node may communicate with the coordinator by wired or wireless means. If a wireless mesh network is implemented, such as a ZigBee network, adjacent nodes may "piggyback" transmissions across the network to reach the coordinator. This allows the network topology to be malleable and reduces infrastructure costs to implement the network. Sensor measurements taken at each node can be analyzed on the server side for events such as the presence of water, corrosive elements in the atmosphere, and changes in the SCC sensors. If an abundance of corrosive elements and water are present, the odds of SCC occurring increase. Predictive algorithms can detect data trends and predict the time of failure for each SCC sensor element at each node. This can be used prognostic health monitoring of an individual canister.

The contents of each canister can vary considerably, and therefore, the sensing needs may vary for each canister. In some instances a single sensor node can be used to monitor a critical location on a canister, such as the circumferential closing weld at the top of the each vertical

storage system. Figure 31(A) shows a sample deployment of a single node designed to monitor a single closing weld by being placed in close proximity.
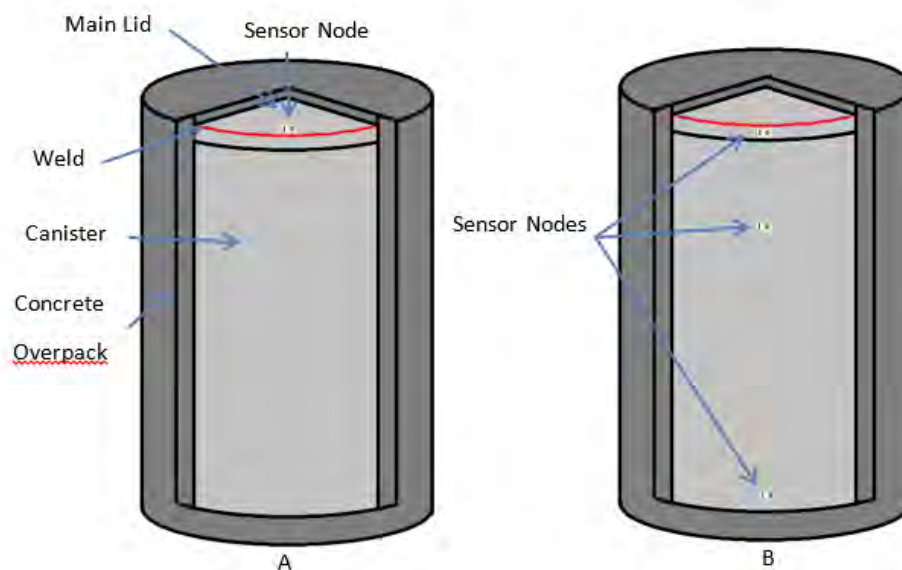
Figure 31. Single Sensor Node and Multi-Sensor Node Deployment. (A) shows the example deployment of a single sensor node near the closing weld (red line) of a vertical canister system. (B) shows the example deployment of a multi-sensor node system over the body of a canister.

Multiple nodes on a single canister have the ability to deduce information about the health of a SNF storage system that a single node could not such as the state of the internal fuel rod configuration. According to a report released by the U.S. Nuclear Waste Technical Review Board (NWTRB) the location of hottest spot on the exterior of the steel canister in vertical storage systems upon initial loading is approximately two thirds the way up the canister.[20] This is assuming the internal structure (see basket in Fig. 1) has not deteriorated and the majority of the SNF contained within has not fallen to the bottom of the canister. Should this occur, it is theorized that the lower sections of the canister would become hotter and that the canister would no longer be safe to move. This increased heat would also increase the rate of deterioration in the lower extremities of the canister.[20] An example sensor node configuration as depicted in Fig. 31(B) would be able to monitor the temperatures at various points over the body of the canister, and over time, show a trend of moving peak temperatures that may signify internal deterioration.

3.0 SCC Sensor Benchmarking and Pilot Testing of Sensor Modules

As described above, a sensor module (barnacle) was designed through multiple iterations. A final sensor package was assembled in year four of this project for subsequent pilot testing. In the absence of a willing vendor, Boise State University procured an environmental chamber for pilot testing. To date, two modules have been used to generate long-term data under highly accelerated conditions. Four additional modules have been built and are being retained for future

tests by vendors should the opportunity be provided. Figure 32 below shows one of the sensor packages following three months of extreme testing.
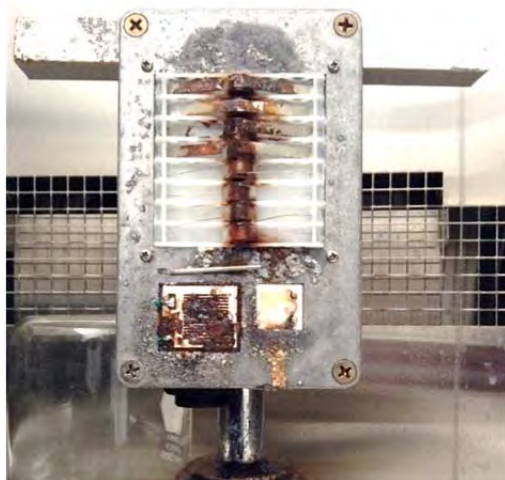
Figure 32. Sensor module following three months of extreme testing.

3.1 SCC Sensor Benchmarking

As described above, the primary sources of dry storage canister degradation are expected to be SCC of the welded lid region and atmospheric induced pitting or crevice corrosion of the container wall. The other environmental sensors mentioned above will allow an estimation of when and how fast corrosion is occurring. However, the novel indirect-assessment corrosion sensors will provide complimentary information on the actual extent of corrosion from identical container materials including the complex influence of weld metallurgy. For long term testing, a multiple electrode sensor was designed using electrical resistance change as a corrosion sensing technique. This technique allows accurate, reliable measurements over a long period of time and does not require extensive electronic hardware or experimental setups associated with full-scale electrochemical corrosion measurements. When metal is oxidized and converted into oxides or hydroxides during active corrosion, the resistance across the electrode will change according to Ohm's law. The measured electrode resistance, $R(\Omega)$, can be compared to calculated resistance values (Equation 1) using the known material resistivity, ρ (Ωcm) compensated for temperature, for the electrode geometry considered, $L(cm)$ is electrode length and $A(cm^2)$ is cross section area, to yield a measurement of the effective extent of corrosion on the electrode.

$$R = \rho \frac{L}{A} \tag{3}$$

Careful design of the electrodes was conducted to provide accurate corrosion data over a long period of time and isolate and characterize the effect of stress and sensitization. Details of the procedures developed for SCC wires and ribbons are provided in Appendix A. Corrosion sensor electrodes were constructed from similar stainless steel as used for canister construction. Electrodes of varying thickness were used to provide data on extent of corrosion of the container wall, which when monitored over time can be converted to a corrosion rate. Thin sensor electrodes will have a greater resistance change over short time periods and will corrode though earlier than thicker electrodes. Figure 33 shows an image take with a Scanning Electron Microscope (SEM) of one corroded stainless steel electrode.
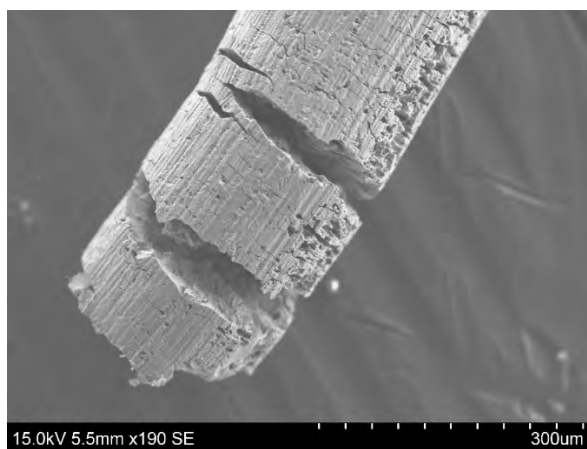
Figure 33. SEM Image of the Effects of SCC on a Stainless Steel Wire. In this image large cracks due to SCC have reduced the cross sectional area of a stainless steel wire. One of these cracks has caused the wire to break.

In Equation 3, the cross sectional area A is inversely proportional to the resistance of the wire. As these cracks form, the sections of the wire begin to lose their cross sectional area. Therefore, the resistance of the wire as a whole increases. Eventually one of the cracks will break the wire and the resistance will increase to a theoretical infinity. Mechanically, there are several methods of creating and holding the electrode samples such that they can be exposed to the environment in which they can corrode. Figure 34 shows a cross-sectional rendering of a device that was created to rapidly test various electrode geometries.
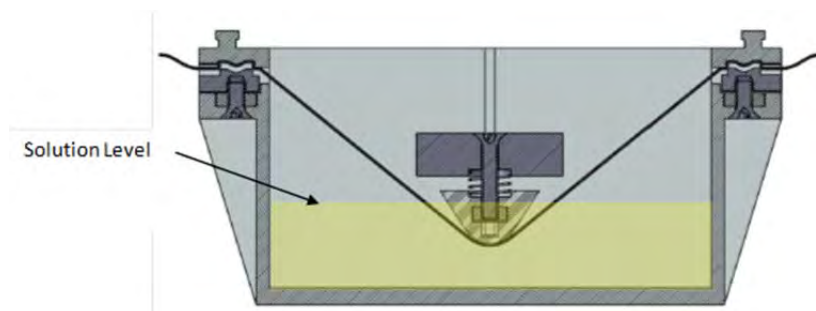
Figure 34. Schmatic of a cross sectional view of an accelerated SCC electrode cell. A single SCC test electrode can be placed within this apparatus for corrosion testing.

The electrodes are placed under constant tension via a spring and the areas of highest stress are submerged within a test solution of HCl and/or NaCl. The resistance of each electrode is monitored by a four wire ohm meter and recorded over time as the material corrodes. Figure 35 shows the recorded graph of four electrodes tested concurrently.
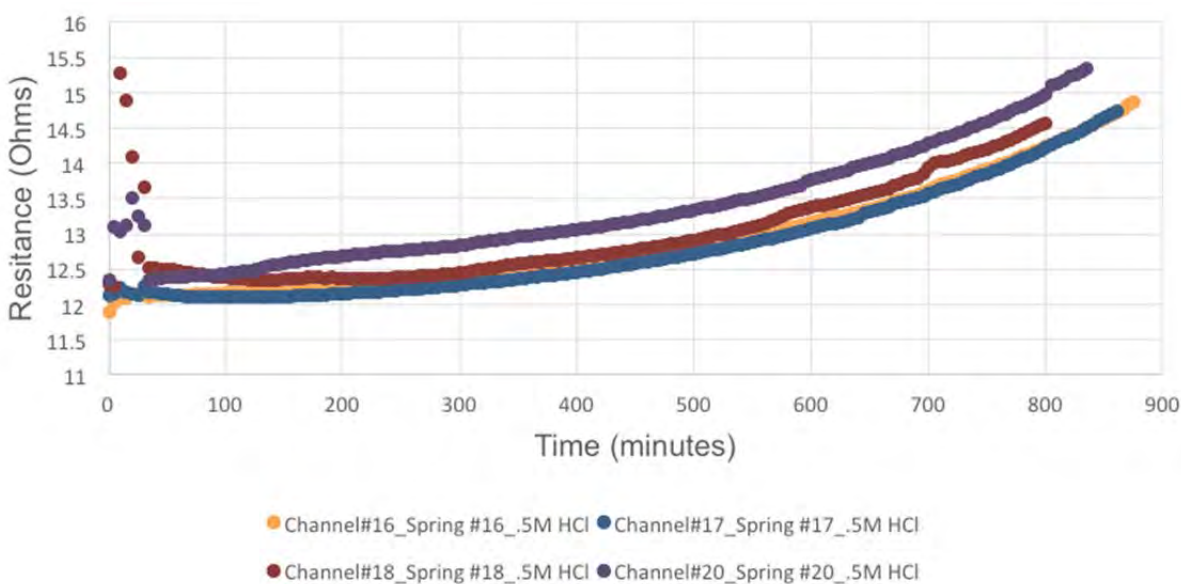
Figure 35. Accelerated Corrosion Testing Data: Time to Failure of .004 in SS304 Wires in 0.5 M HCl Solution (3.5 M NaCl). Four 4 mil wires were tested in the same solution concurrently.

The stress on the electrode is fairly uniform across its length, but during testing only small portion of the wire is exposed to the liquid chlorides. This submerged area has the highest chance of forming a crack and breaking. The actual fracture in the wire occurs when the cross sectional area of the wire becomes so small that the further deformations occur due to the wire tension. Steel is a ductile material so all deformations beyond the elastic region are plastic in nature. These deformations do not return to their original shape when the material tension is

unloaded. When cracks occur the cross sectional area of the wire reduces until the material surpasses its ultimate strength while under the constant tension. Once this occurs the electrode will begin necking, which rapidly reduces the cross section of the material until a rupture occurs and the electrode breaks.

To test for SCC in an open air environment a novel sensor mount was created to hold up to 8 electrodes of various geometries. This mount was created with the use of 3D printing and was made to be as compact as possible. Figure 36 shows a cross-sectional rendering of this sensor.
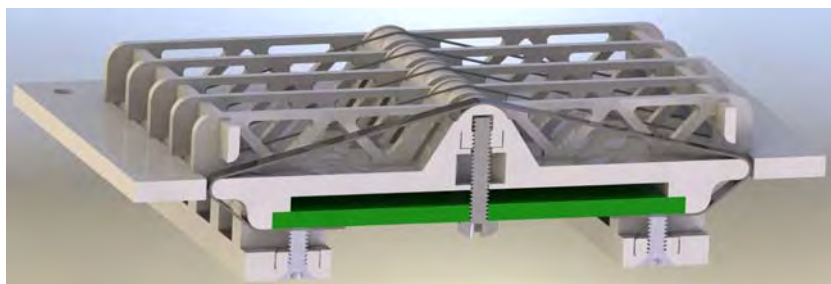
Figure 36. SCC sensor module cross section rendering.

The truss sections of the sensor mount are designed to restrict bending of the entire mount when each electrode is placed under tension. These trusses also prevent broken electrodes form touching neighboring electrodes and promotes airflow around each electrode. The green section is the printed circuit board (PCB) which contains the majority of the resistance measuring electronics as well as the microcontroller interface. The PCB is mechanically integrated into the mount and assists in keeping the mount from bending when under tension. The electronics have been designed to allow the vast majority of commercially available microcontrollers to interface with the sensor and read each channel.

In the case of stainless steel, the presence of chlorides can initiate crack growth. The higher the localized stress is on surface of the metal the higher the chances of a crack forming. Weld locations are a very common failure point due to SCC because of the residual stress and chromium depletion introduced during the welding process, but even bending points can provide the required start point. Crack growth in a stainless steel forms perpendicular to the direction from which the stress is applied. The presence of both water and heat influences the rate at which SCC occurs in open atmosphere. Because of this, the presence of chlorides, water (liquid and gas), and temperature must all be monitored.

The presence of chlorides is monitored by an atmospheric corrosion sensor made from galvanically coupled metals. In this case, stainless steel and silver are used. When the sensor is exposed to a corrosive environment it begins to create a small current which can be used to track the rate of corrosion. These sensors are much more sensitive to corrosion then the electrodes and give an early warning indication that potentially corrosive compounds are present.

Water can be present in both liquid and gas form and therefore different sensors are required to detect each phase. A time of wetness sensor is used to monitor the presence of liquid water. This sensor uses interdigitated combs to detect the presence of liquids between the combs. Should liquid water fall or condense onto the sensor the resistance between the combs will change and can be monitored. Water in gas form can be monitored using an off the shelf humidity sensor which reports back the relative humidity of the environment and temperature can be measured using thermocouples mounted near the electrodes.

All of these sensors require power and need a microcontroller to read them and process the information. A motherboard was created to dispense power and house all the support electronics for the sensor package. This included power regulation, data processing, and communications. The electronics require a housing to safely operate within a corrosive environment and one was created out of aluminum with mounting points for all the above mentioned sensors. Figure 37 shows this enclosure, the final sensor package, with all external sensors integrated.

Figure 37. Assembled sensor module. A complete assembly of the sensor module included the SCC sensor, corrosion sensor, time of wetness sensor, humidity sensor, and thermocouple.

The enclosure is sealed from the ambient environment with a rubble gasket along its circumference and silicone along the sensor cutouts. A weather proof Ethernet jack is used to provide power, programming, and communications with a computer via a serial connection. In order to observe SCC and to monitor the contributing factors of SCC the entire sensor module was placed into a temperature and humidity environmental chamber for long term testing. During this time all sensors were read and recorded once every two seconds. These results are described below.

SCC Sensor modules were placed into an environmental chamber for up to 2 days in order to assess there functionality and survivability. These tests were designed to take the module to the testing extremes to ensure its ability to survive long term testing. A super saturated salt and isopropyl alcohol solution was applied to each electrode and the corrosion sensor to determine if SCC or corrosion activity could be detected. Figure 9 shows a graph of the temperature and humidity levels throughout the test.
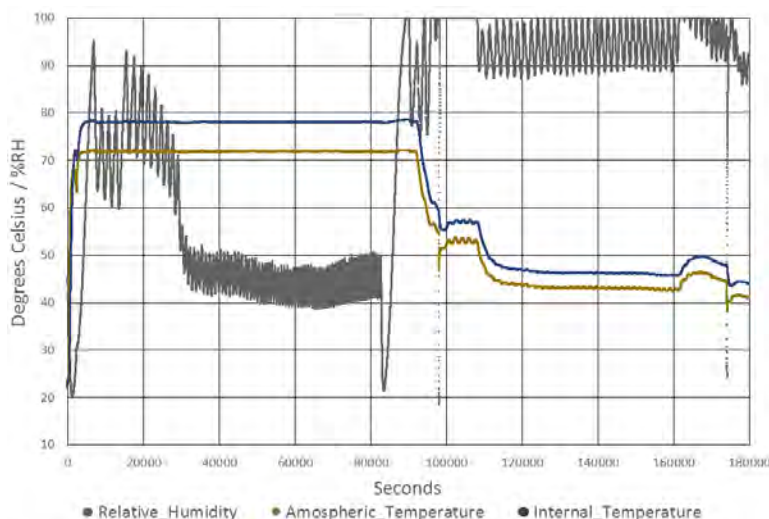
Figure 38. Environmental conditions of survivability test.

The sensor module's external thermocouple and internal temperature sensor tracked very closely throughout the test. The lowest maximum operating temperature of any individual electrical component used in the sensor module is 125°C which is much higher than the expected testing temperature. The momentary dips in humidity were detected when the chamber was opened to physically inspect the module for damage.

The test progresses though several stages. The first is high temperature and humidity, the second is high temperature and lower humidity, and the last is extreme humidity. The extreme humidity test was done to test the water seals on package and to increase the rate of corrosion by allowing water to continuously condense and evaporate. The corrosion sensor was able to clearly detect the presence of a corrosive substance and was affected by the changes in temperature and humidity. Figure 39 shows the readings from the corrosion sensor.
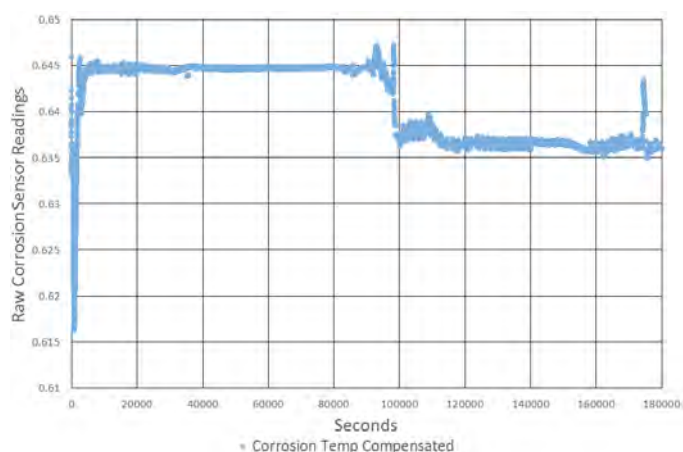
Figure 39. Corrosion sensor output of survivability test.

The corrosion sensor immediately rises at the beginning of the test when the salt solution is added to indicate the presence of a corrosive material and only drops when the temperature decreases. At the conclusion of the test, visible signs of corrosion were apparent on the corrosion sensor. This shows that the proper environment to initiate corrosion on the SCC sensors can be reached.

Crack initiation is random, and when using multiple electrodes of the same geometry the time until initiation can vary drastically. Each electrode may be the same length but have a different resistance based on the unique grain boundaries and microcrystalline structure. This is especially true of electrodes with small cross sectional areas as small defects result in larger changes in resistance. Figure 40 shows representative readings from the SCC sensors.
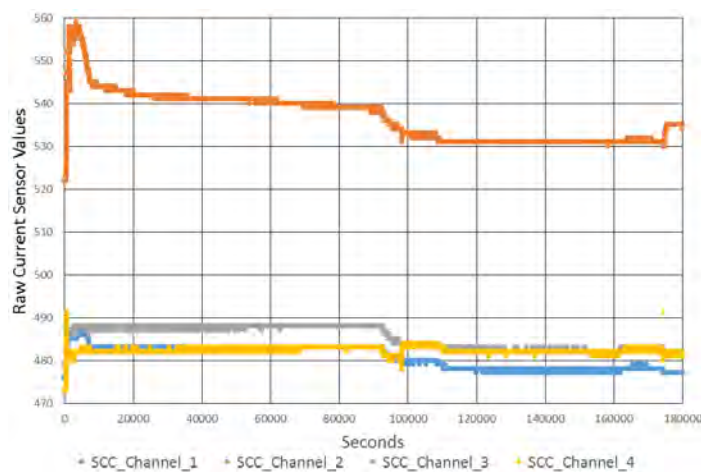
Figure 40. SCC Sensor output of survivability test.

The raw analog to digital readings from the current sensors show that three of the electrodes have a similar starting resistance and one has a slightly higher starting resistance. All electrodes respond as predicted to the change in environmental conditions. Unfortunately, within these test parameters, 50 hours is not enough time for SCC to progress enough to be detectable on any of the electrode lines and requires a longer test. In order to address this we chose to move directly to the final sensor packages in order to carry out full scale module testing. This is described below. An image of one of these modules following three months of testing was shown above in Fig. 32.

3.2 Pilot Testing of Sensor Modules

Two modules of the design shown in Fig. 37 we exposed under relatively severe electrochemically active corrosion conditions in order to demonstrate the durability of the module and functionality of the various sensors. A photograph of the chamber is shown in Fig. 41. Samples were exposed to highly concentrated, periodic salt water spray, humidity levels near 100% RH (except during periodic inspections), and temperatures between 25 and 36°C (Fig. 42) for times up to 3 months. Thus, the samples experienced exposure to a continuous chloride rich electrolyte layer. Any breaches in the packaging (not observed) would also have exposed the inner electronics to the atmosphere and thus could cause malfunctioning of the sensor package. Conditions were varied during the tests (simulating what might be observed in nature) and the chamber door was opened at least weekly to visually inspect the condition of the package and apply salt water. All sensors were monitored and functioned continuously during the exposures as expected.

Figure 41. Environmental chamber (left) adjacent to an electrochemical (ac/dc) spectroscopy system.
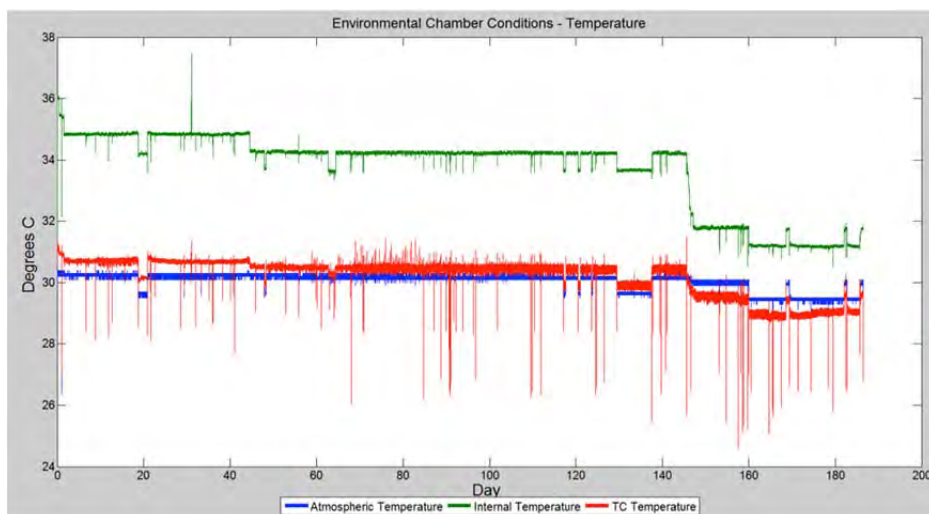
Figure 42. Temperature comparisons showing the measured values of the chamber (blue), external sensor package K-thermocouple (red), and the internal RTD (green) during 188 days of environmental testing. The internal sensor package ran approximately 2°C higher than the outer surface due to heating from the electronics.

Figure 43 shows an example of data collected continuously from the sensor package where the resistivity of SCC sensors was measured. The figure shows the data for a wire SCC electrode and two strip electrodes. In the case of the 8 mil wires (data for only one shown) both wires failed within two days of each other and both failures were sudden and did not give much warning. This is interesting because as it may be an early indicator of corrosion.   In the case of the 6 mil strips, the behavior was as predicted. There was an exponential increase in resistance with time, eventually resulting in a failure.   The 2 mil strip did not behave as predicted. This strip appeared to fail prematurely, but then became operational again over a period of four days. It then continued to slowly corrode until failure. This was the thinnest strip and was the first sample to visibly corrode. It is likely that we lost electrical contact with this strip during testing and then regained the connection for reasons that are unclear.
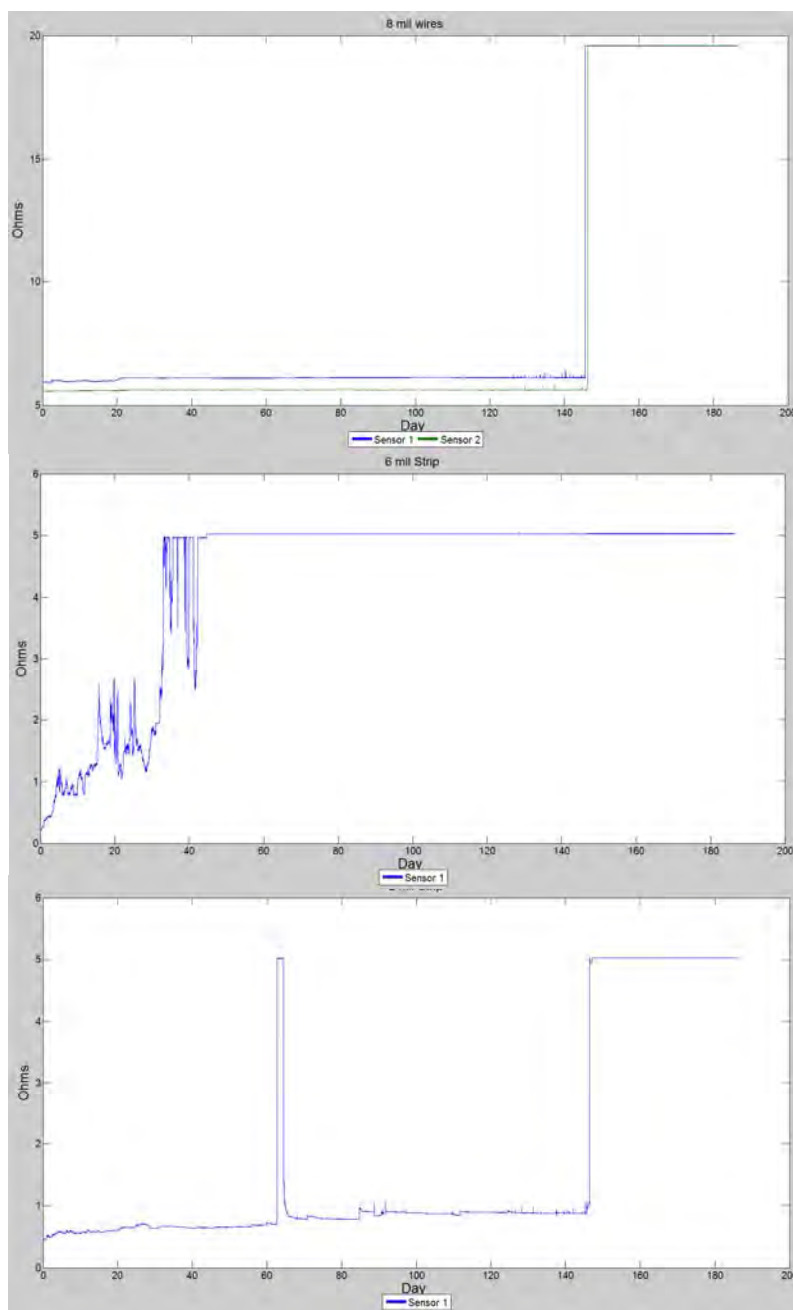
Figure 43. Example of SCC data collected during pilot testing of a monitoring system showing data from an 8 mil wire (top), a 6 mil strip (middle), and a 2 mil strip (bottom).

4.0 Summary

On-site storage of spent nuclear fuel (SNF) at reactor sites was intended to be a relatively short term, interim stage of the U.S. plan for long-term storage and disposition of nuclear waste. However, in the absence of a permanent, central repository for spent nuclear fuel or reprocessing scheme in the U.S. has necessitated longer-term storage of spent nuclear fuel on-site or at distributed Independent Spent Fuel Storage Installations (ISFSIs). Regulations for ISFSIs for the initial storage period up to 20 years with the potential for an extension of an additional 20 years were given in 1998. Until a permanent solution is arrived at through policy enactment, dry storage is effectively the current final stage of the life-cycle of nuclear reactor fuel in the U.S. Consequently, in order to address the potential issues associated with onsite, dry storage, the NRC and DOE, in cooperation with organizations such as EPRI as well as national laboratories, universities and the various vendors, have attempted to identify and characterize expected degradation modes of the fuel and containment materials at times beyond 20 years. Validation of models and stewardship of SNF, in addition to maintaining public confidence, requires tools for and a science-based approach to surveillance and prognostic health monitoring of spent nuclear fuel storage. This research sought to do that through the development of sensors and monitoring technologies. Specifically, a module was developed that enables monitoring of temperature, atmospheric conditions, and susceptibility to corrosion and stress corrosion cracking. Six final module packages were fabricated, two of which have been pilot tested.

5.0 References

1. Nuclear Regulatory Commission, 10 CFR Part 72, *Licensing Requirements for the Independent Storage of Spent Nuclear Fuel and High-Level Radioactive Waste*, Washington D. C., 1998.
2. P. McConnell, et al., "Extended Dry Storage of Used Nuclear Fuel: Technical Issues: A U.S. Perspective," *Nucl. Eng. and Tech.*, **43** [5] 405-412 (2011).
3. Commission, N.R., *Cladding Considerations for the Transportation and Storage of Spent Fuel. SFST-ISG-11 (2003a), Rev. 3, U.S. Nuclear Regulatory Commission, Washington DC. 2003.*, 2003.
4. B. D. Hanson, et al., *Used Fuel Disposition Campaign - Gap Analysis to Support Extended Storage of Used Nuclear Fuel, Rev. 0*, 2012.
5. R. M. Meyer, B. Hanson, and K. Sorenson, *Detecting and Monitoring of Atmospheric SCC in Dry Cask Storage Canisters for Used Nuclear Fuel*, in *CORROSION 2013*2013, NACE International: Orlando, Florida.
6. W. C. Bare and L.D. Torgenson, *Dry Cask Storage Characterization Project-Phase I: Castor V/21 Cask Opening and Examination, INEEL/EXT-01-00183 Rev. 1*, 2001, Idaho National Lab: Idaho Falls, Idaho.
7. M. F. Hurley, D. P. Butt, S. M. Loo, V. Patel, B. J. Jaques, and J. M. Youngsman, "Condition Monitoring System for Spent Nuclear Fuel Dry Storage Containers," U.S. Patent 19975.034US00, 2013, reissue, 2014.
8. H. Mi, S. Mikael, T. Allen, K. Sridharan, D. P. Butt, J. P. Blanchard, and Z. Ma, " Monitoring the oxidation of nuclear fuel cladding using Raman spectroscopy," *J. Nucl. Mater.*, 445, 1-3, 7-11 (2014).

9. J. Hall, M. Pook, J. Kiepert, S. M. Loo, *Monitoring Aircraft Cabin Particulate Matter Using a Wireless Sensor Network*, AIAA 43rd International Conference on Environmental Systems, July 14 - July 18, 2013.

10. J. Hall, S. M. Loo, Dale Stephenson, Ross Butler, Michael Pook, Josh Kiepert, Jordan Anderson, Nicholas Terrell, *A Portable Wireless Particulate Sensor System for Continuous Real-Time Environmental Monitoring*, AIAA 42nd International Conference on Environmental Systems, July 15 - July 19, 2012.

11. S. Hirose, *Biologically Inspired Robots: Snake-Like Locomotors and Manipulators*. Oxford University Press, Oxford (1993).

12. Y. Umetani and S. Hirose, Biomechanical study of serpentine locomotion, in: *Proc. 1st RoManSy Symp.*, Udine, Italy, pp. 171–184 (1974).

13. M. Yim, S. Homans and K. Roufas, Climbing with snake-like robots, in: *Proc. IFAC Workshop on Mobile Robot Technology*, Jejudo Island (2001).

14. M. Yim, Locomotion gaits with polypod, in: *Video Proc. IEEE Int. Conf. on Robotics and Au- tomation*, San Diego, CA (1994).

15. 1. K. Lipkin, I. Brown, A. Peck, H. Choset, J. Rembisz, P. Gianfortoni and A. Naaktgeboren, Differentiable and piecewise differentiable gaits for snake robots, in: *Proc. IEEE/RSJ Int. Conf. on Intelligent Robots and Systems*, San Diego, CA, pp. 1864–1869 (2007).

16. G. Miller, http://www.snakerobots.com/index.html

17. Y. Umetani and S. Hirose, Biomechanical study of serpentine locomotion, in: *Proc. 1st RoManSy Symp.*, Udine, Italy, pp. 171–184 (1974).

18. P. Koopman, *Embedded System Security*, IEE Computer, Vol. 37, No. 7, pp. 95-97, July 2004.

19. D. Hwang, P. Schaumonth, K. Tiri, I. Verbauwhede, *Securing Embedded Systems*, *IEEE Security and Privacy*, **4** [2] 40-49 (2006).

20. H. E. Adkins, *Modeling Used Fuel Storage Temperatures*, in *Presented at Nuclear Waste Technical Review Board Meeting Oct. 2012*, U.S. Department of Energy: Idaho Falls, Idaho.

Appendix A: Mini-Specimen Stress Corrosion Cracking Experimental Tester
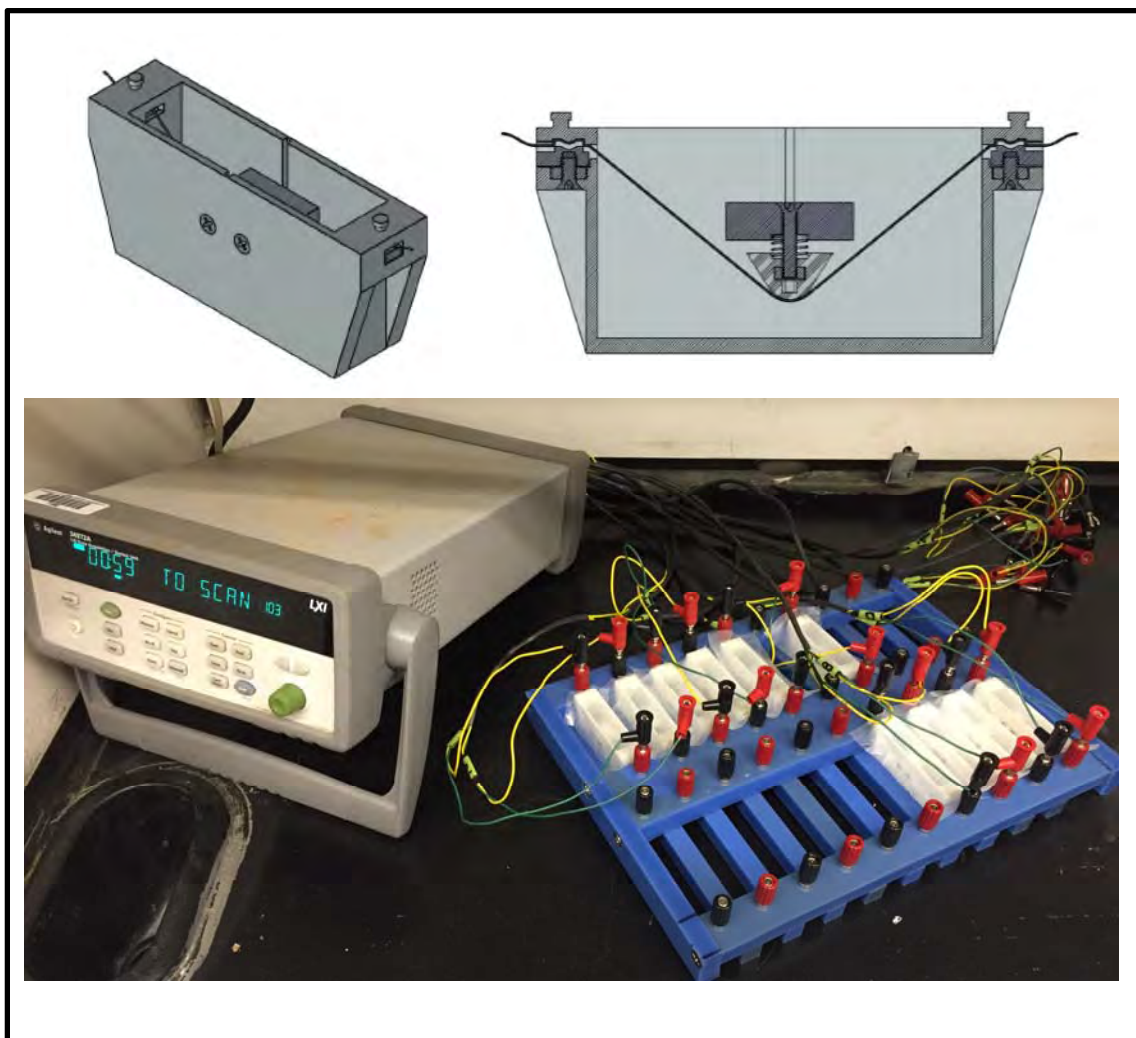
1. Parts List

Probably want to include a slice cross-section rendering so we can add arrows/number for part here:
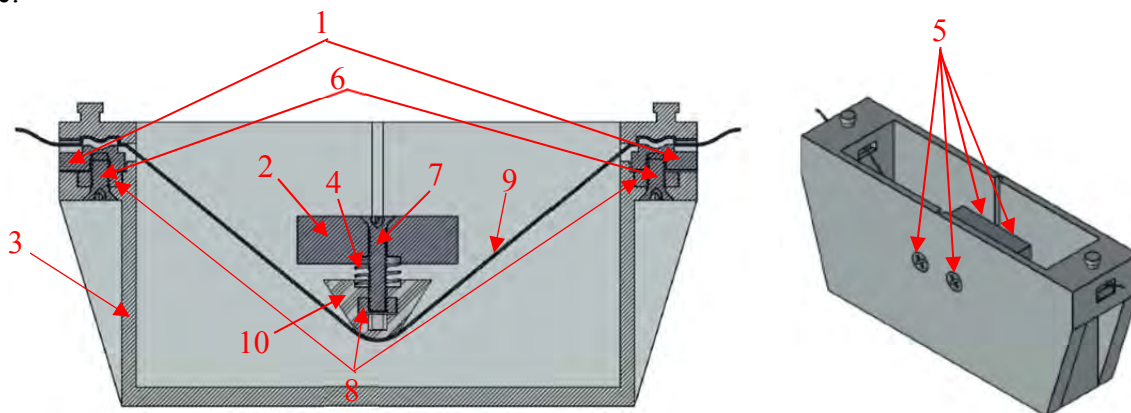
Part #	Description	Quantity	Details	Vendor	Part Number
1	Tabs/inserts	2	3-D Printed	BSU New Product Development Lab http://www.techhelp.org/npdlab/	
2	Support Block	1	3-D Printed	BSU New Product Development Lab http://www.techhelp.org/npdlab/	
3	Trough	1	3-D Printed	BSU New Product Development Lab http://www.techhelp.org/npdlab/	
4	Spring	1		Associated Spring RAYMOND http://www.asraymond.com	C0180-020-0380-I
5	Screw Fastener	4	M2x5		
6	Screw Fastener	2	M2x10		
7	Screw Fastener	1	M2x12		
8	Hex Nuts (Size?)	3			
9	Test sample	1	Wire or thin strip >12cm length	User supplied	
10	Wedge	1	3-D Printed	BSU New Product Development Lab http://www.techhelp.org/npdlab/	

Required Tools and Equipment

a) Small Philips screwdriver
b) Small Flat head screwdriver
c) Parafilm
d) Data acquisition system with milli-ohm resistance measuring capability
e) Wire lead attachment for **d)** or alligator clips to attach to sample ends
f) Tweezers

g) Epoxy or hot-glue gun

Assembly Procedure

This assembly procedure documents the set-up of a wire sample (typically 25 to 250μm in diameter) for SCC testing in the mini-specimen test fixture. Other sample geometries such as thin strips (up to 8 mm wide) will also fit in the test fixture. Test sample length should be >12 cm.

Test Fixture Assembly

1) Begin assembly by clearing any small plastic debris from the hump opening or trough tab openings. This can be done using a small flat head screwdriver. This will allow the nuts to be inserted without applying too much force.
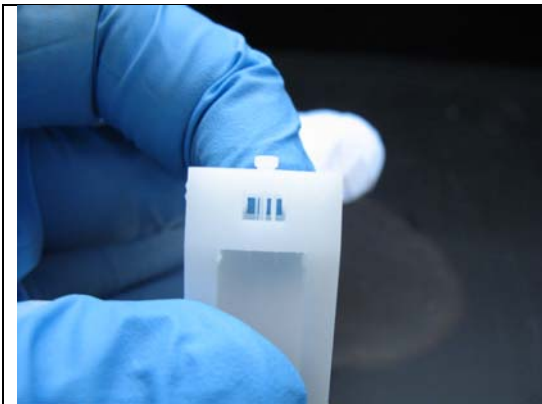
Plastic debris shown in the tab openings of the trough	Breaking debris loose with a flat head screwdriver.
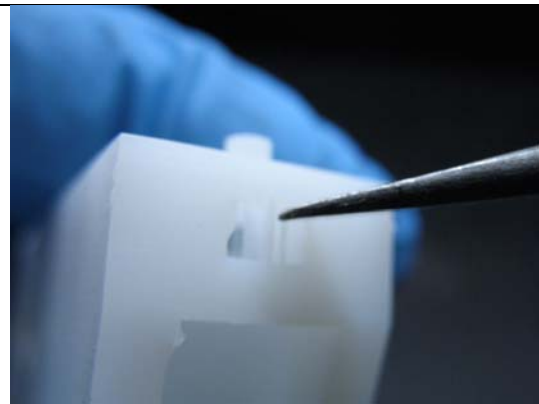
2) When the openings have been cleared one nut should be inserted into each opening. In the case of the hump, the nut should be pushed to the end of the canal where the threads should mesh with the hole on the reverse side of the hump. In the case of the trough, the nuts should be pressed into their designated hexagonal seating located on the bottom of each wing.
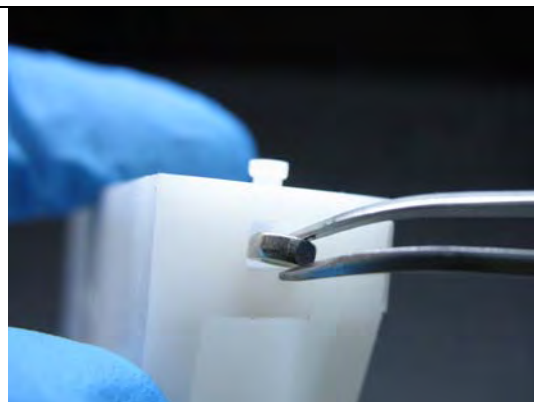
Inserting the nut into one of the trough	Inserting a nut into the hump opening
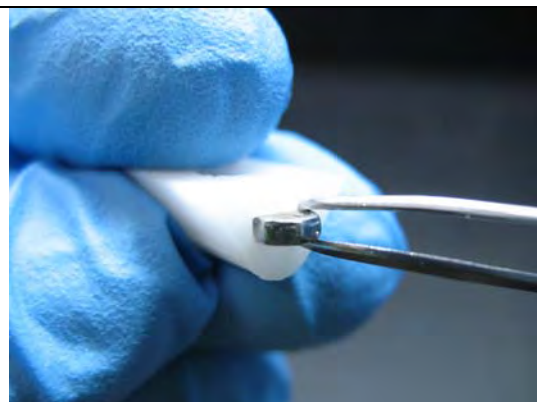
openings	

3) After the nuts are positioned, set aside the trough and focus on the hump assembly. In some cases one might want add a little protection to the nut inside the hump so that it keeps from getting too exposed to the prospective solution. In this case look section 2.4 before moving on.

4) The hump assembly will consist of the nutted hump, a spring, the block and the M2x10 fastener. Thread the fastener through the block so that the fastener head is seated in the chamfered inset on the one side of the block and protrudes through the side with the circular cut.
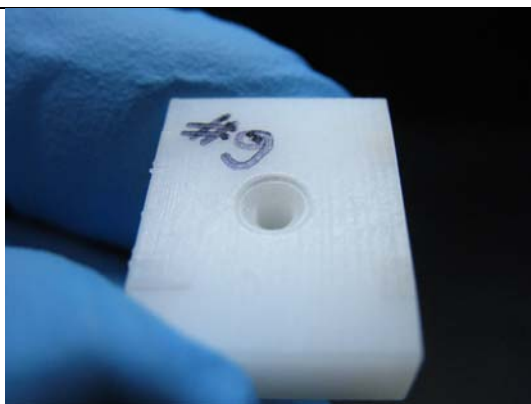
| Chamfered inset side of the block | Fastener configured in opening the correct direction |

5) Now thread the protruding end of the fastener through the circular axis of the spring while keeping them concentric and bringing the spring flush with the end of the circular cut out.

Spring flush with block	Circular cut-out in block
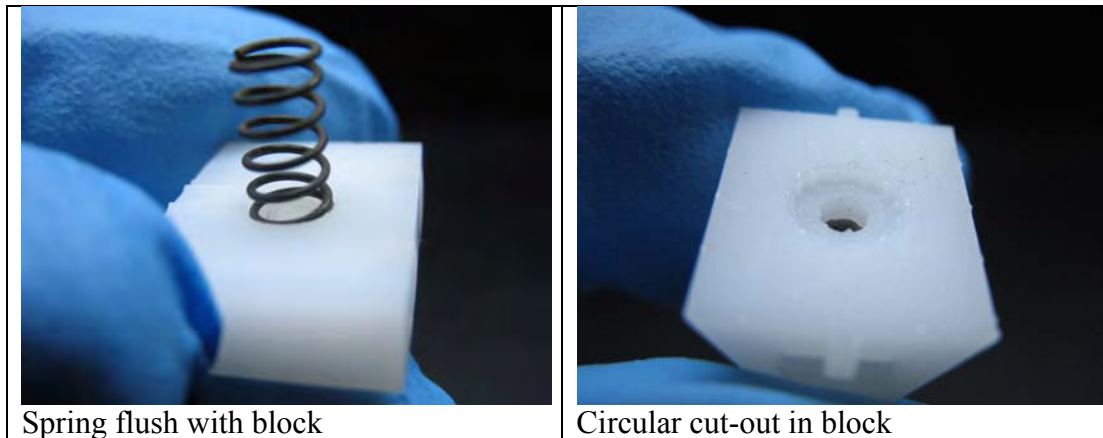
6) Holding the block, fastener, and spring, bring the nutted hump to bookend the assembly by first matching up the other end of the spring flush with the circular cut in the hump. Compress the spring while keeping the key side faces/planes on the hump and the fastener opening faces/planes parallel.

Block, hump, spring and fastener assembled but untightened
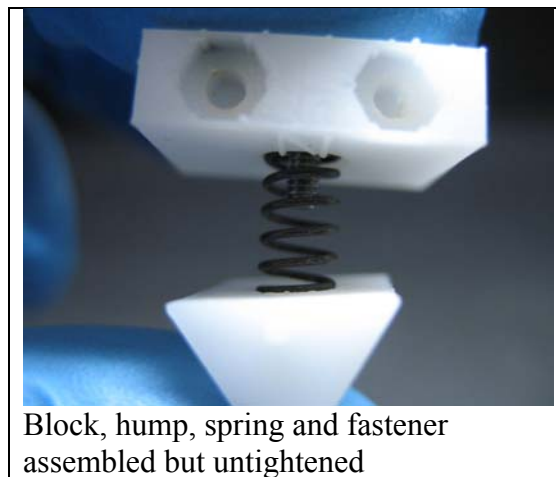
7) As the spring is compressed the protruding fastener should be navigated into the hole at the top of the hump. Once the fastener has been guided into place, a small Philips head screwdriver can be used to secure the nut and fastener in order to keep the assembly together.

Block, hump, spring, and fastener
assembled and tightened
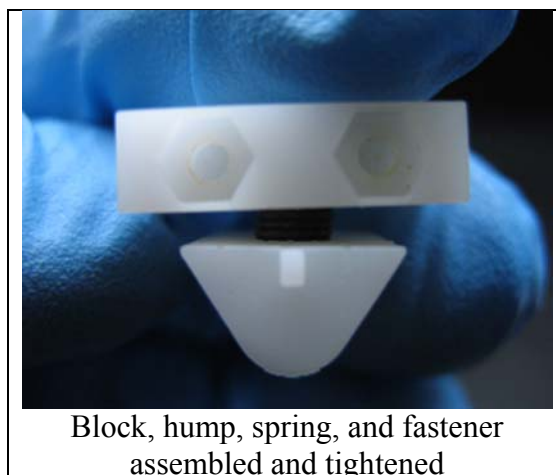
8) Set aside the hump assembly and refocus on the trough assembly.

9) The M2x12 fasteners should be threaded flush with the end of the nuts without unseating them from the wing.

While screwing fastener the nut
becomes un-seated

After the fastener is flush with the nut it
may be re-seated
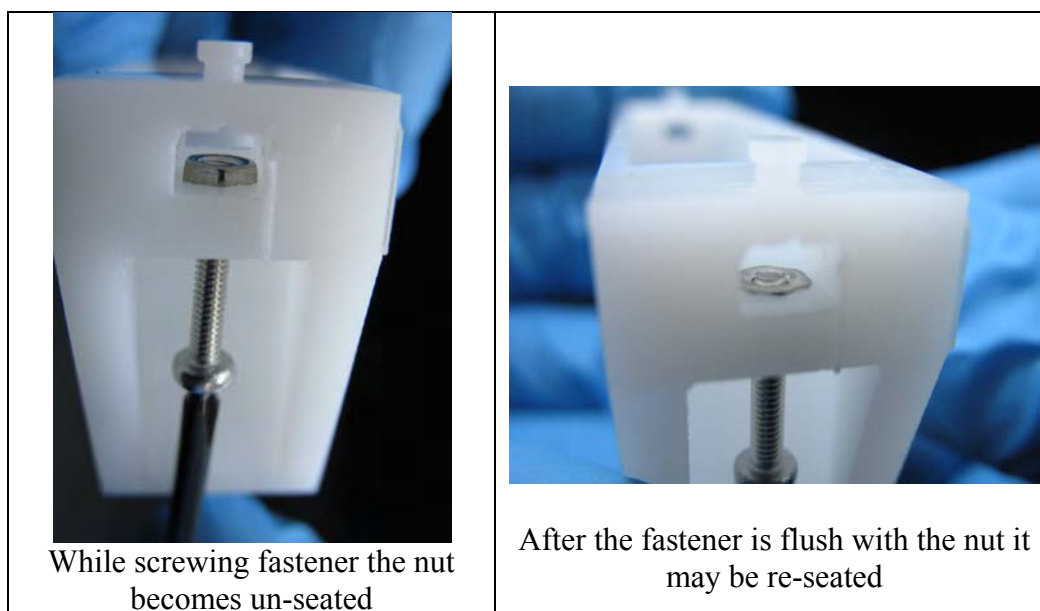
10) Thread the wire sample (see section on Sample Preparation) through each opening. Insert tabs into each wing making sure that the wire is centered.

| Wire threaded through openings on both sides of the trough | Tabs inserted into trough while ensuring the wire stays in the middle |
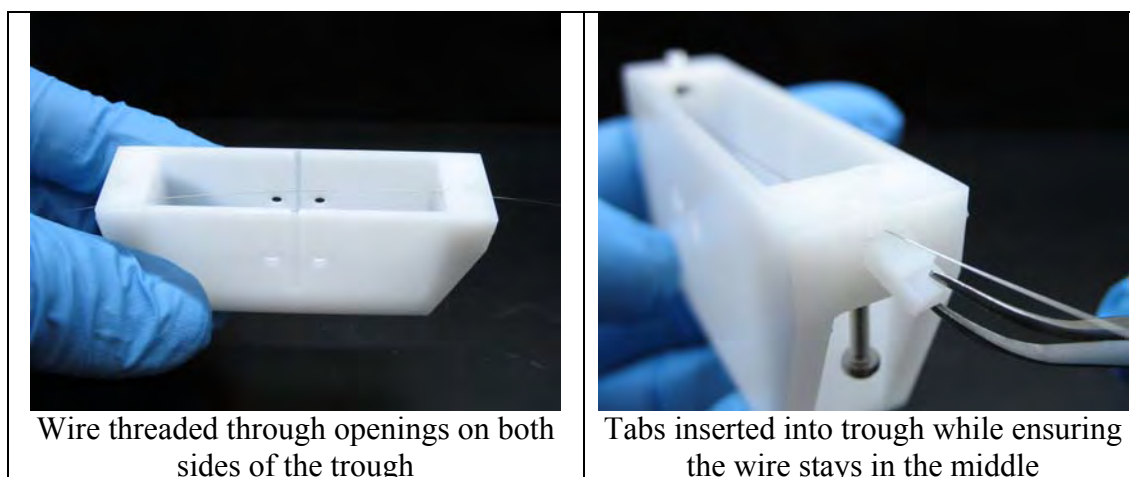
11) Adjust the sample so that enough excess is protruding through one side as to connect with the lead, the excess wire protruding the other side should be comparatively longer. Tighten the fastener on just the one side with the shorter amount of excess. It should be tight enough to keep the wire from slipping with tension.

Tab tightened on one side
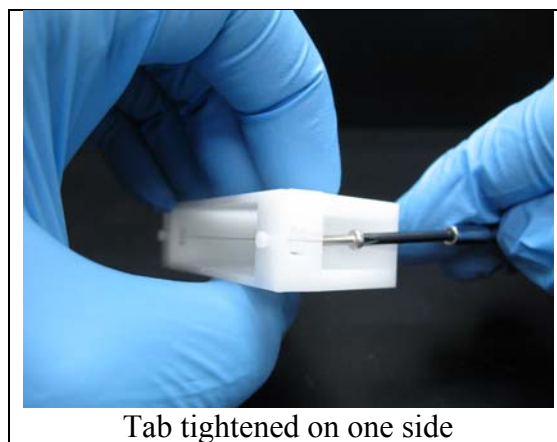
12) Now insert the hump assembly sliding the keys on the hump into the grooves of the trough.

Hump assembly inserted into the trough

13) The assembly should sink far enough so that the fastener openings on the block mesh with the fastener openings in the side walls of the trough.

| Fastener openings do not mesh | Fastener openings mesh |
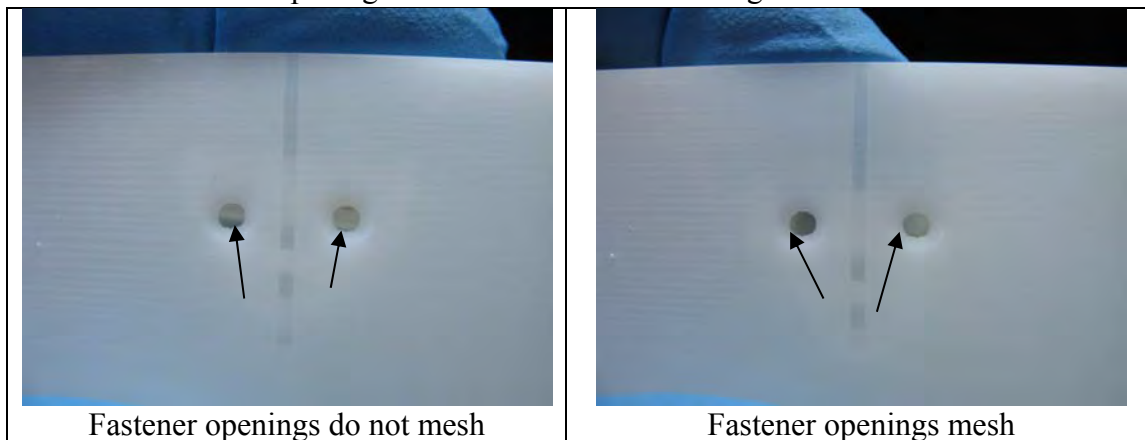
14) Once the openings are aligned, the 4 M2x5 fasteners may be inserted into the openings to secure the assembly in place.

| Openings are aligned | First fastener inserted |
| Second fastener inserted | Both fasteners inserted on one side |
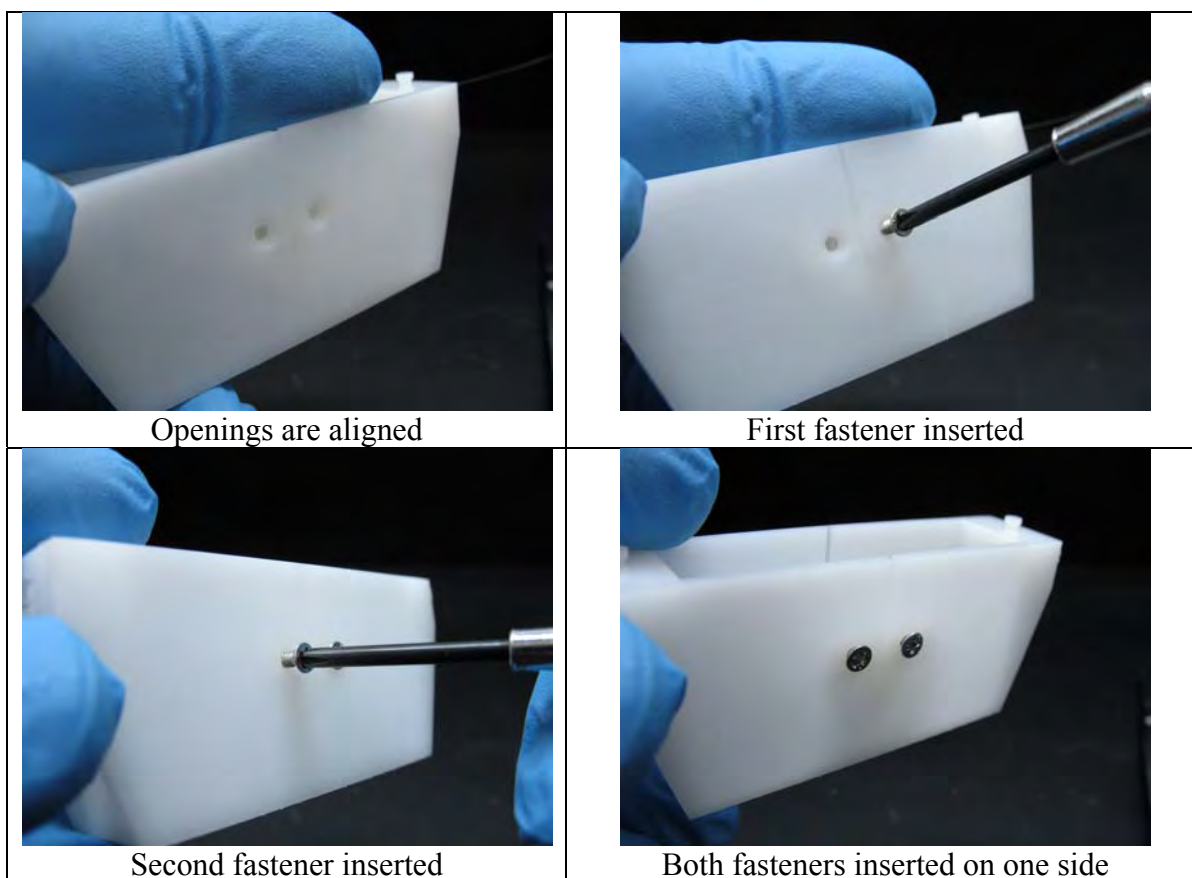
15) By this point the excess wire on the untightened side should have shortened up to match the excess on the tightened side.

Both sides show similar length long enough to attach to leads
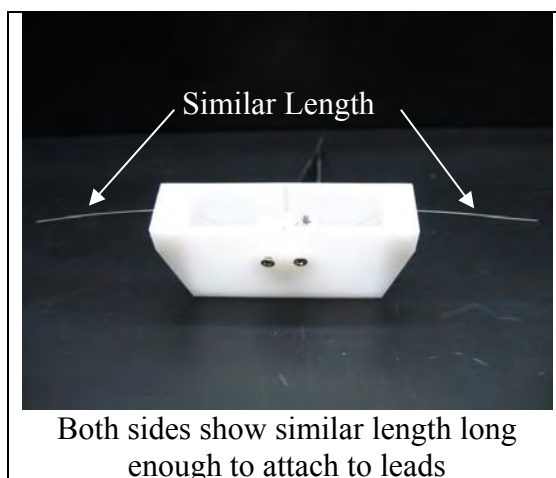
16) Ensuring that the wire is centered over the hump and through the untightened opening, pull the wire sample taut while tightening the untightened fastener.

The wire is pulled tightly while the fastener is tightened
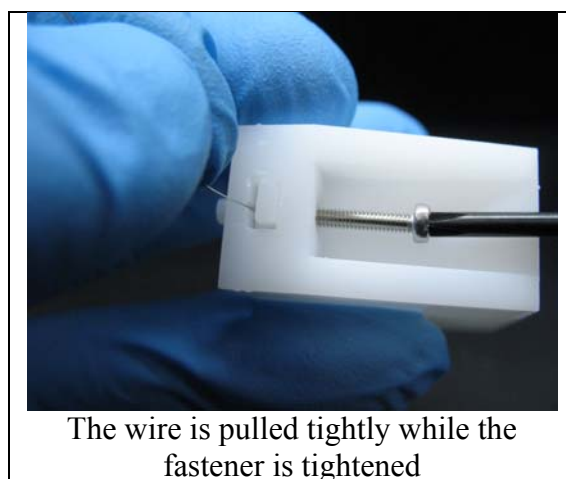
17) Remove the fastener securing the hump to the block. This will release the load of the spring and apply a tensile stress to the wire.
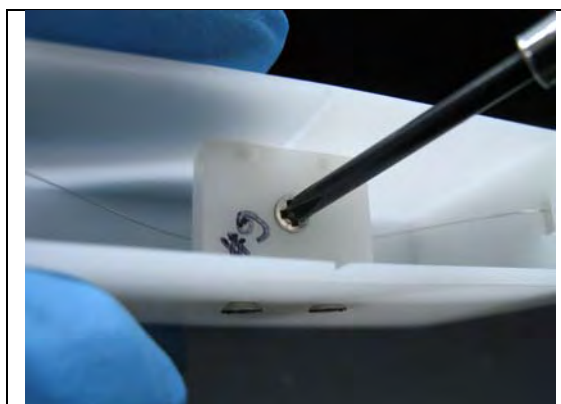
The fastener securing the hump assembly together is removed

18) Ensure that there is no slippage, if there is then the assembly must be retightened and steps x-y must be repeated. Set the trough in the organizational tray and attach the leads.
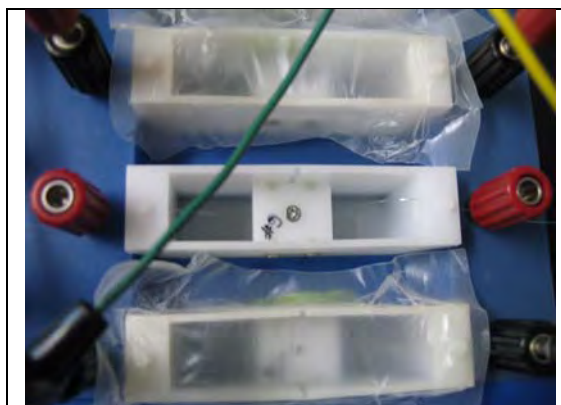
Trough set in tray and connected to leads

19) Set the software to collect resistance data from the leads that are wishfully acquired.

20) Fill the trough with roughly 6-9mL of desired solution without pouring it between the hump assembly and trough wall to reduce the spring assembly exposure to corrosive solution.
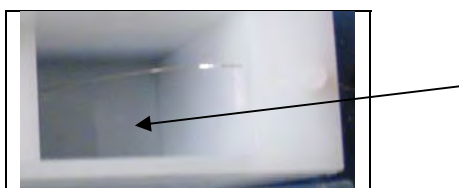
21) When the samples break the springs will shoot the humps into the solution causing a splash for the reason it would be safe to apply parafilm to the top of each fixture. (If

nothing else the parafilm should also help reduce exposure of the leads to the solution vapor.)
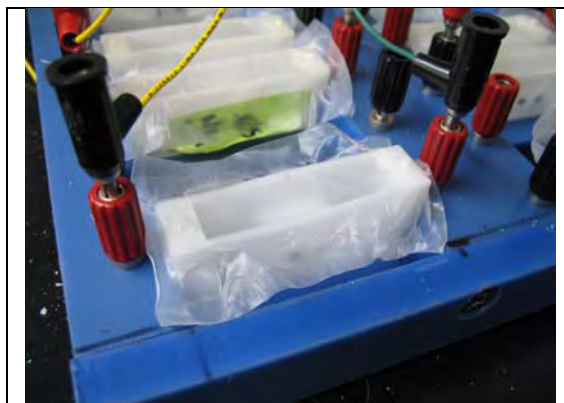
22) Begin data acquisition on the resistance logging instrument and wait until breakage before quickly removing the sample from solution for cleaning.

Sample Preparation

The surface condition of the samples to be tested can effect SCC behavior. For testing of wires or strips it is recommended to polish and clean samples prior to testing. We polished samples to 800 or 1200 grit with SiC polishing papers, then rinsed with DI water and finally cleaned with Acetone and dust-free laboratory wipes.

Following polishing and cleaning the sample surface may be additionally prepared to test for surface treatment effects on SCC behavior such as coating or paints. Also, for atmospheric conditions testing, salt deposits may be applied to the sample surface prior to loading in the test fixture.

Environmental Conditions Set-up

For full immersion testing the test trough should be filled with the solution of interest such that a portion of the test sample covered (see section on Test Fixture Assembly, step 20). In order to minimize exposure of the spring to corrosive conditions the test solution should not be filled above the top of the wedge:
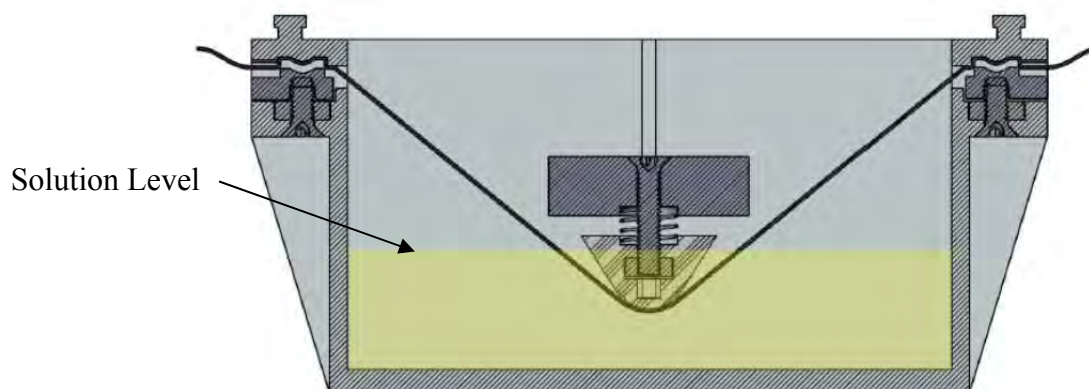
For atmospheric-type testing solution may be added to the trough so that the solution level is low enough that it is not in direct contact with the sample. Covering the test fixture with parafilm will ensure that a high humidity level is maintained with in the test fixture trough, provided a reservoir of liquid solution remains in the bottom.

Adhesive Hint

To limit the amount of exposure of corrosive solution to the nut within the hump as well as the spring, hot glue is can be used to seal the opening in the hump and the excess glue cut away as not to hinder its sliding motion within the trough.


Glue is applied to the hump opening

Appendix B: Sensor Module Assembly Instructions

This appendix gives abbreviated instructions for the assembly of the Boise State Barnacle V3 Sensor Module. Note, a full description of the procedures and operations of the module will be published shortly in the doctoral dissertation of Vikram M. Patel, tentatively entitled "Monitoring and Predicting Stress-Corrosion Cracking of Spent Nuclear Fuel Storage Canisters".

Step 1. PCB Assembly

There are six PCBs to assemble for each unit. The motherboard, SCC sensor, TOW sensor, corrosion sensor, Ethernet adapter, and programmer. These are pictured below. Eagle schematics will contain exact part numbers and component values.
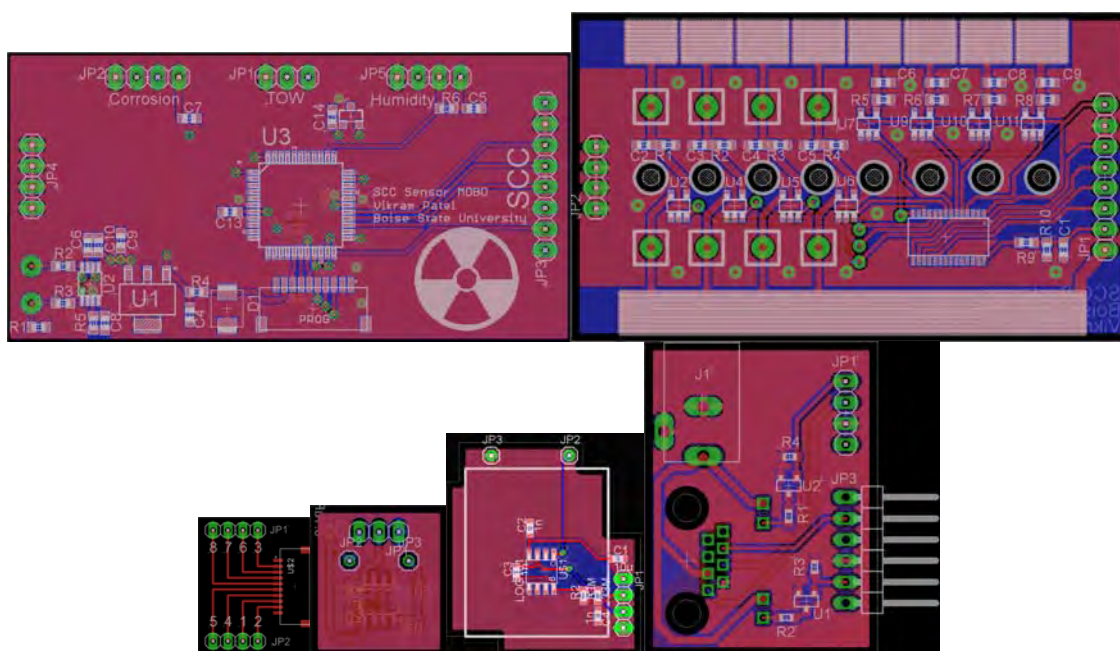
Above: six PCBs. These are the six PCBs that are needed to construct a single sensor module.

Step 2. Select Sensor Gain

The SCC sensors use fixed gain current sensors to operate. The selection of which gain to use is dependent on the geometry of the sensor electrode. Smaller cross sections require less gain as the resistance of these electrodes are higher. Larger cross sections have a lower resistance and require a larger gain. SCC channels 1-4 are designed for wires and will have smaller gains while channels 5-8 are designed for strips which will have higher gain. Each current sensor has a corresponding resistor which must also be selected in order to limit the total current flowing through the sensor element.
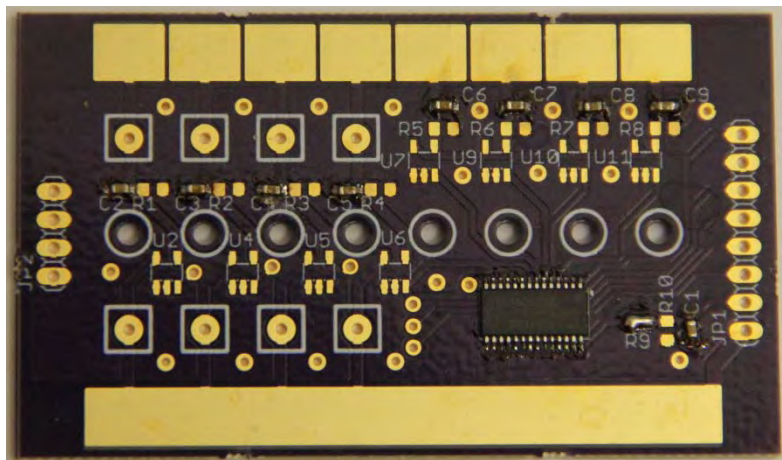
Step 3. Wiring

The TOW sensor, corrosion sensor, humidity sensor, and Ethernet adapter PCBs all require wiring to carry signals to and from the motherboard. The TOW sensor and corrosion sensor require ribbon cable to be soldered to the connection header and terminated in a right angled header. The humidity sensor leads need to be bent 90 degrees as close to the sensor case as possible and crimp connecters need to be used to solder the wires. The Ethernet adapter has eight connections that need to be soldered with short 22 gauge wire. The connections match the numbering on the side of the jack and the silk on the board. Attach a flat flex cable (FFC) to the motherboard and the Ethernet adapter.
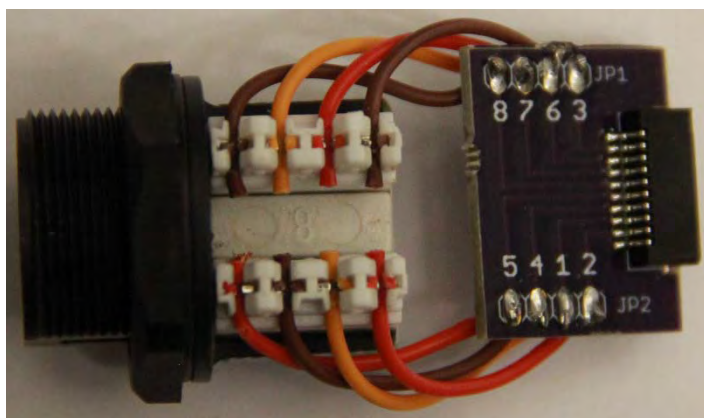
Step 4. Program and test all sensors

Attach all sensors to their respective headers. Connect the Ethernet adapter and programming board with an Ethernet cable. Attach the PICKIT 2 programmer and serial cable to the programming board. Set external power supply to 5V and 100mA and attach to the barrel jack on the programming board. Monitor current consumption for shorts and open circuit conditions. If

current draw is normal, initialize serial terminal to 9600 Baud, 8-bits, no parity, and no flow control. Program the board and observe the terminal output. Correlate each sensor's reading with laboratory standards and confirm proper operation.

<u>Step 5. PCB Cleaning</u>

Once the system is verified all remaining flux must be removed from the PCBs. Use the aerosol PCB cleaner to remove the flux. The SCC sensor pads should be scrubbed clean using a q-tip.


<u>Step 6. Conformal Coating</u>

Each PCB need to be environmentally sealed from liquids and contaminants. Automotive grade conformal coating must be applied to each board to prevent damage. Before conformal coating each female header must be sealed using silicon caulking. The capillary action of the conformal coating can damage the female headers by clogging them and preventing electrical contact. Once these are sealed a paint brush may be used to apply the conformal coating. A UV light may be used to overserve the coating in progress and assist in proper coverage. The SCC contact pads must remain uncovered for proper operation.

<u>Step 7. Clean SCC Sensor SLA</u>

The SCC sensor mount may contain remnants of the 3D printing process which will interfere with operation. These can be cleaned out using tweezers and other small hand tools. The center span of mount may require filing in order properly slide the SCC board in and out of the mount. This should be done by holding the file stationary and moving the mount across the file until the desired material is removed.
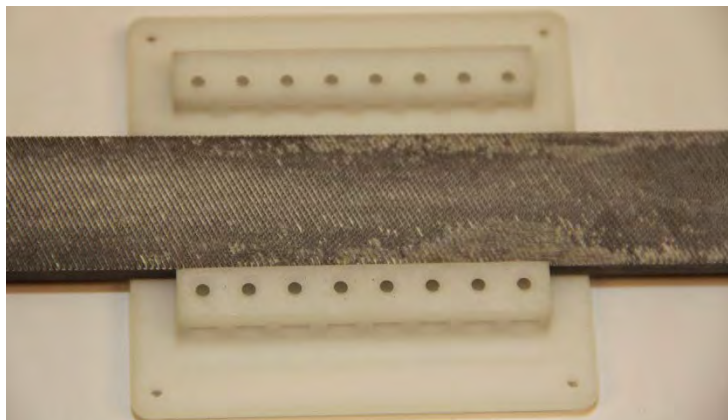
Step 8. Clean Humps

The SLA humps may also require cleaning before use. These can also cleaned using tweezers, but it may become necessary to use a small file to remove excess material.
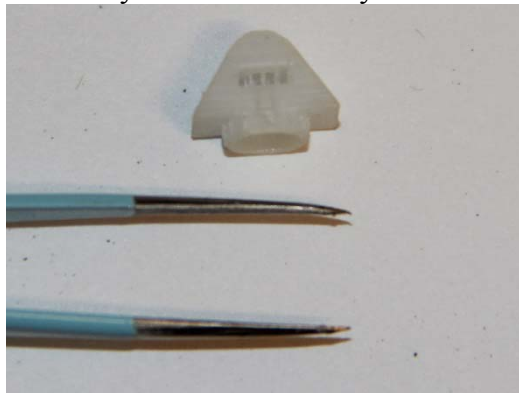

Step 9. Insert Nuts into Humps

Once cleaned the M2 nuts must be inserted into each hump and centered. The alignment of each nut must be maintained as it is inserted into each hump by used a vice to slowly squeeze it into place. Once inserted, the nut may be tapped into place by using a file to adjust its orientation.

Step 10. Insert Springs

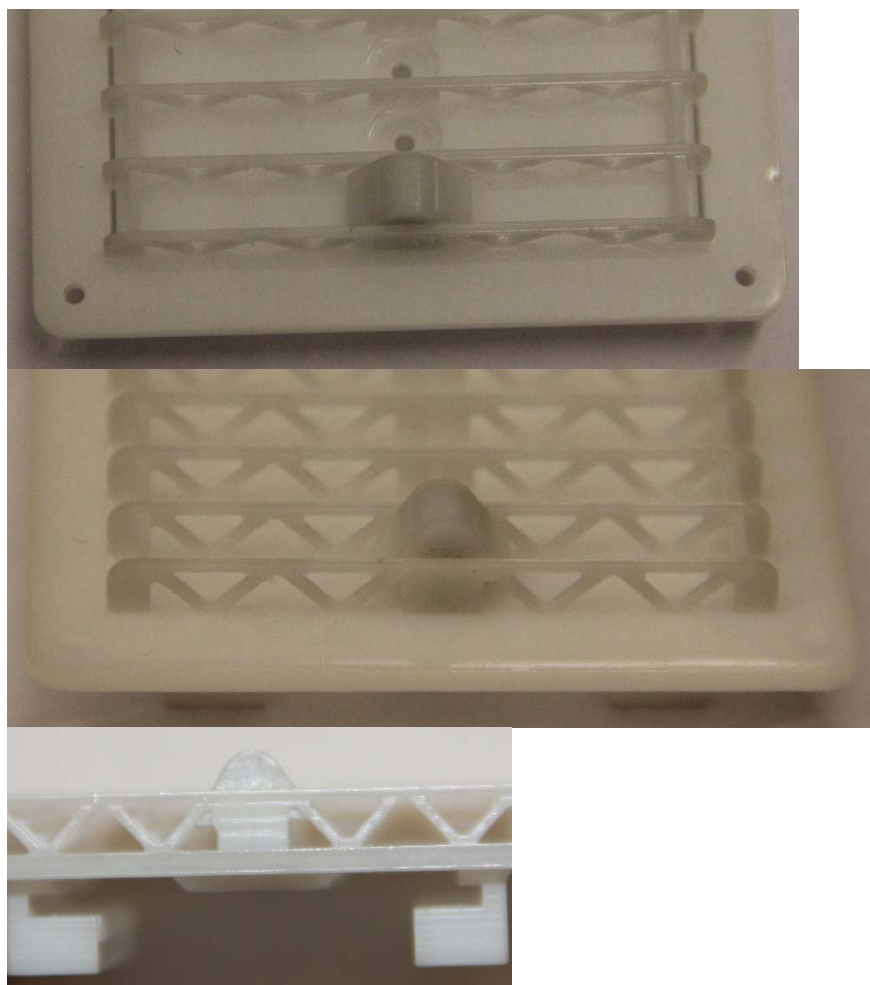Each spring should be inserted into the circular opening at the bottom of each hump.
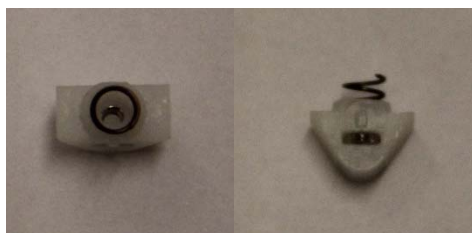
S

tep 11. Mounting Humps

Each hump must snap into each slot on the SCC sensor mount. The hump should move freely and bounce back when depressed.
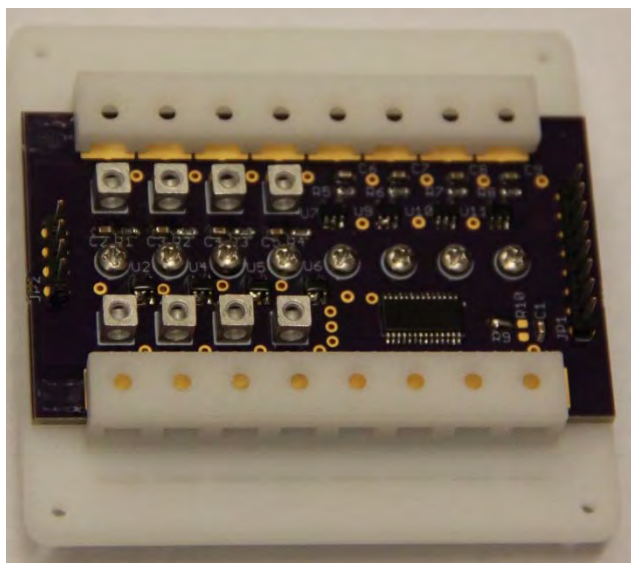
Step 12. Install SCC Sensor PCB

The populated and conformal coated SCC Sensor PCB should now slide into the back of the SCC sensor mount. Align the board such that all the mounting holes match up.
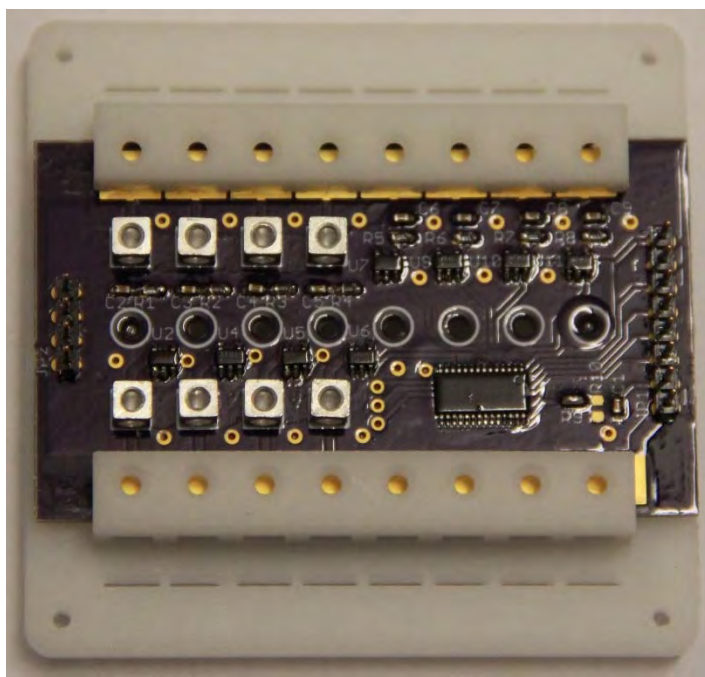
Step 13. Secure Humps with Screws

Use the pan head M2x10 machine screws to tighten down all eight humps to the SCC sensor mount.

Step 14. Insert strip locking nuts and screws

The strip locking nuts press the strips against the PCB pads and prevent the strip from moving out of position. There are eight locking positions for the strips which require the use of 8 M2 nuts and 8 M2x6 countersunk screws. Slide each nut into the SLA opening above each PCB pad and tread the screw onto the nut such that it gets pulled into the hexagonal recess.

Step 15. Load Wires

The wire SCC sensor electrodes mount into channels 1-4 and uses the screw terminals located on the SCC sensor PCB. Cut a six inch section of wire and thread it though each end of the channel mount such that three inches remain on each side of the humps. Using tweezers feed the wire into each of the screw terminals and insert and tighten the screw. Wrap one of the wire ends around the screw such that it no long slips then tighten the wire onto the hump by pulling the other end. Wrap this end around the remaining screw terminal. The wire should have very little slack over the hump.

Step 16. Bend Strips

The strips need to be pre-bent to both correctly fit on the hump and to be pre-stressed in order to increase the chances of SCC occurring on or near the hump. To do this, place the center of each strip on the rubber eraser pad and use the metal cylinder to depress it. This will place a crease into the strip that will be aligned to the hump. The strip is longer then required and will be trimmed when mounted into the sensor.
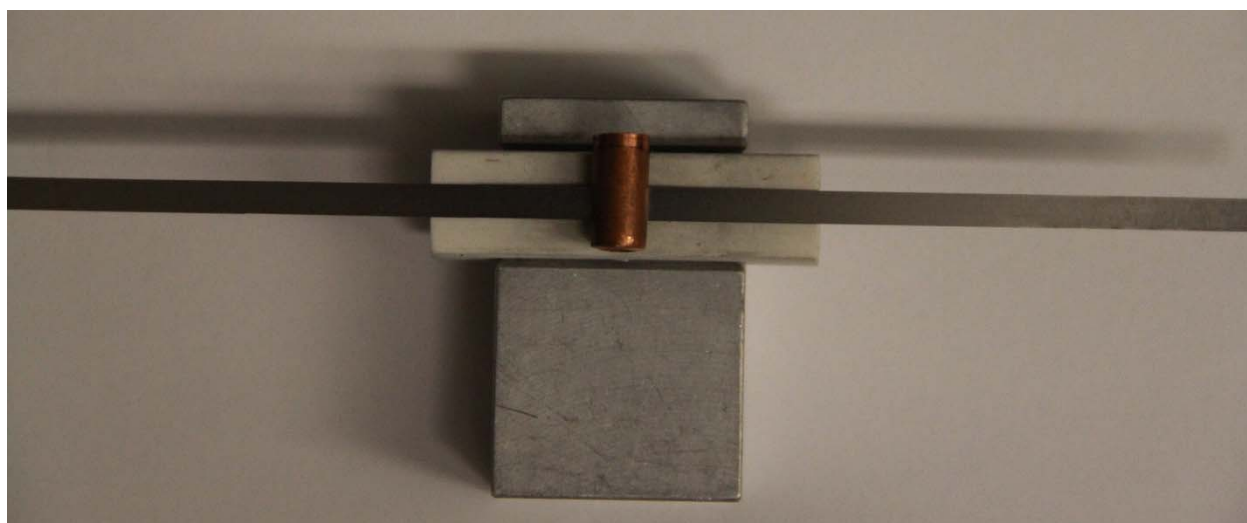
Step 17. Load Strips

Each strip must be loaded carefully and excessive bending should be avoided at all costs. Feed the ends of the strips into the slots of the SCC sensor channel. These must then be fed into the slot containing the screw and pulled through. Depending on the thickness of the strip, this part may or may not be difficult. If the strip is thick, grabbing the tip of the strip with needle nose pliers is an option to help feed the strips into position. When in place, the pre-bent section should be resting on the hump. Tighten the strip mounting screws such that the strip is sandwiched between the screw and the PCB pad. Do not over tighten the screw as this can crack the SLA. Trim the excess strip material to prevent shorts.

Step 18. Remove Hump Screws

When all channels are loaded and all sensor electrodes are secured the hump screws may be removed to place the electrodes under tension. Once removed, preform a continuity check to ensure that all the electrodes remain functional and are making good contact.

Step 19. Mount SCC sensor assembly with Silicone (screws)

Apply a thin layer of silicon around the edge of the SCC sensor and then place it into the cutout located on the aluminum case lid as shown below. Use the M2x10 screws and M2 nuts to secure the SCC sensor. Place additional silicone around the edge of the SLA where the SLA and aluminum meet.

Step 20. Foam Tape TOW and Corrosion PCBs

The TOW sensor and corrosion sensor PCBs are conformal coated, but there is still a potential for shorting if they are placed in direct contact with the aluminum case (which is conductive). The case is also thick such that placing the sensors directly onto the PCBs would make them recessed into the case, which would cause electrolyte buildup within the recess, potentially skewing the results. To fix this, place a layer of double sided foam tape on the PCB and onto the back of each sensor. The tape should not cover the sensor connection vias! Leave the protective film on the tape for now. See the pictures below.
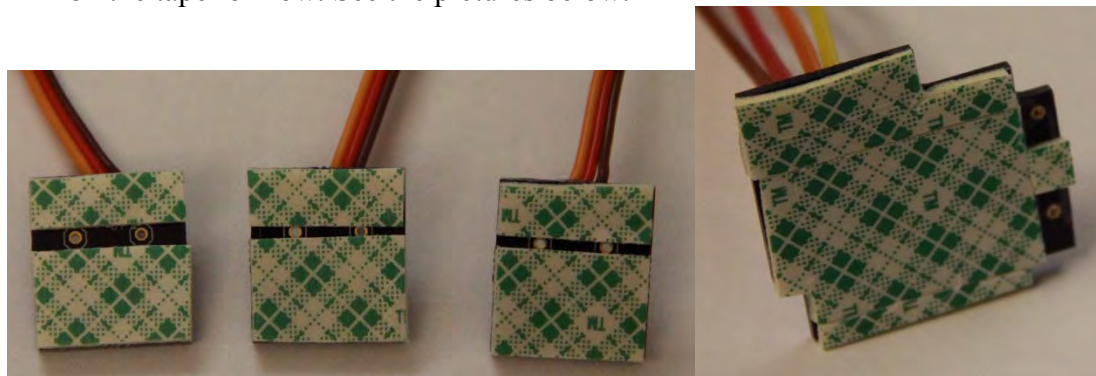


Step 21. Solder TOW Sensor onto PCB

Place a square of foam tape on the back of the TOW sensor and remove areas of tape covering the vias. Remove the protective film from the tape on the TOW sensor PCBS and attach the TOW sensor such that the vias line up. Using a bright light can help with properly lining up the vias on the sensor and PCB. Once attached, place a strand of solid 26 AWG wire through the vias and solder both sides (PCB and TOW sensor). Use care when soldering the gold pads and use silver solder. Trim the nubs on the leads and inspect the TOW sensor for damage.

Step 22. Clean and Conformal Coat TOW Solder Joints

The solder joints on the TOW sensor will be exposed to the corrosive environment and need to be protected. Trim them down using clipping pliers and then conformal coat them. Be sure to only conformal coat the pads and not the comb section of the sensor or it will not function correctly.

Step 23. Mount TOW Sensor

Insert the TOW sensor into the lid opening as shown below. The foam tape should now evenly adhere to the inside surface of the lid. A thin layer of conformal coating may be added at this point around the edges of the foam tap to further secure it and prevent leaks.
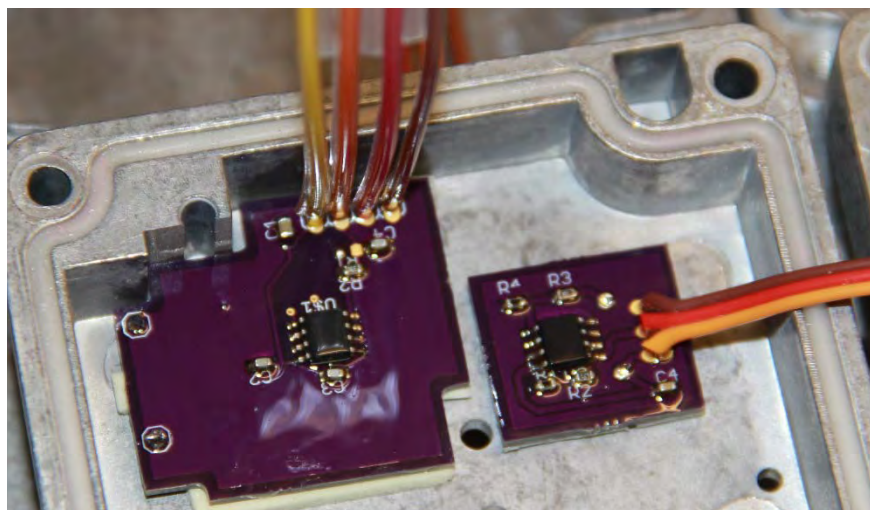
Step 24. Cut Notches into Corrosion Sensor

The atmospheric corrosion sensor is a galvanic sensor that will begin to corrode the moment it is exposed to any electrolyte and the water in the air. Once the sensor is exposed, there is a time table in which the assembly must be completed and placed within the testing chamber. For this reason steps 24-27 may be completed later after step 39.
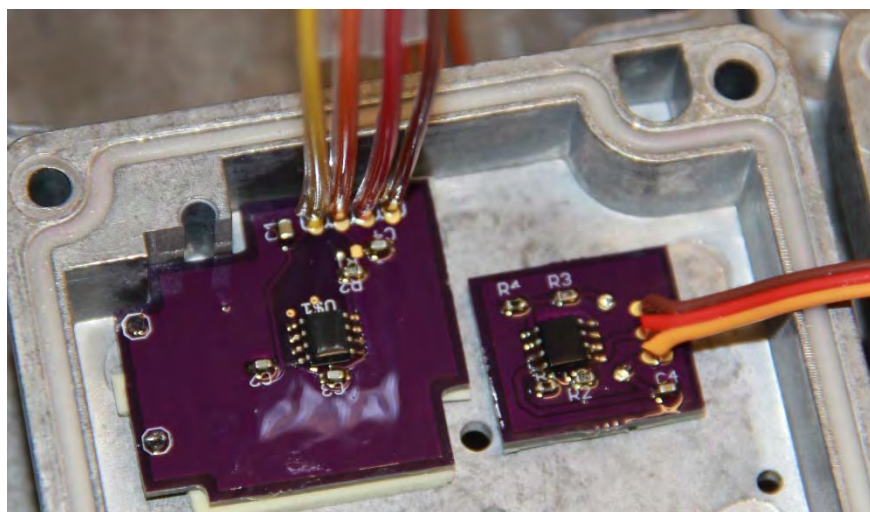The atmospheric corrosion sensor cutout is exactly the correct size to fit the sensor, but the contact wires for the sensor are on the exposed side. To connect these sensors properly, two grooves are needed to be cut to allow the sensor wires to reach the pads. Using a Dremel cutting disk, place two notches into the sensor near the connecting pads as shown in the figure below. These will allow the two contact wires to reach the exposed side of the sensor from inside the case.
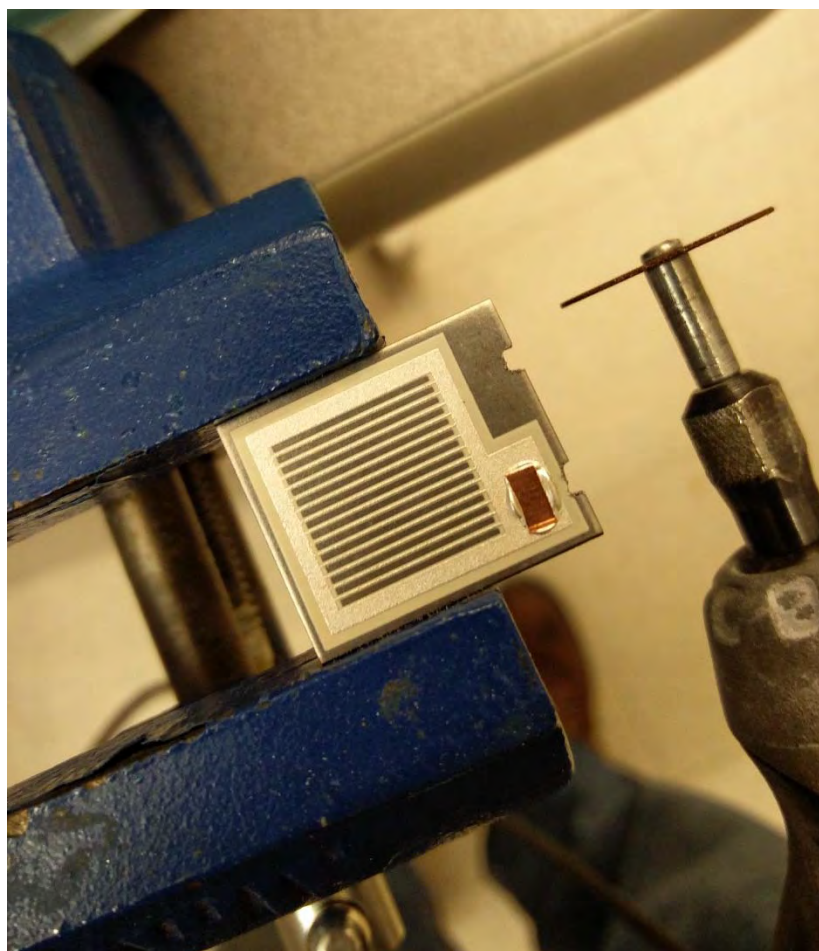
Step 25. Mount Corrosion Sensor

The white square on the top surface of the corrosion sensor board shows the outline of where the atmospheric corrosion sensor will be. Place foam tape on this surface of the PCB and trim the tape such that the entire surface of the PCB is covered, minus the sensor contacts. Remove the protective film and mount the sensor into the case as shown below. Apply foam tape to the back of the atmospheric corrosion sensor such that the entire surface is covered minus the notched area. Place the sensor in the cutout and guide the wires through the notches as shown below. Trim and strip the wires so only a small amount of exposed wire reaches the pads on the senor. Solder these wires to the pads quickly and do not let the plastic coating on the wires melt.

Step 26. Conformal coat corrosion sensor

Trim and clean the soldered contacts on the atmospheric corrosion sensor. Conformal coat these joints without covering the remaining portion of the sensor.

Step 27. Test for Shorts

At this time, check for shorts across all of the connected sensors and fix any problems found. Additional silicone my now be applied to ensure that liquids will not be able to enter the sensor module case.

Step 28. Sand Ethernet Jack

The weather proof Ethernet jack needs to be sanded in order to fit properly into the case. When looking at the jack one can see that the port is not a perfect circle, but more of a "D" shape. This flat part of the jack must be evened out by sanding it down as shown below. Using a long flat file works well, but ensure that the wires are not damaged. If sections of the wire coating are damaged then conformal coat them and double check conductivity.

Step 29. Mount Ethernet Jack

Place a strip of electrical tape in the slot near the Ethernet jack cutout so the wires will not rub against the aluminum housing. Place the rubber washer onto the jack and insert it into the cutout. Push it forward until it snaps into place. Screw the retaining nut on the jack and tighten it to the point where the rubber washer makes a good seal against the aluminum. It will be fine if the jack is slightly twisted.

Step 30. Mount Humidity Sensor

The humidity sensor is mounted on the bottom facing side of the sensor module to prevent liquid water from saturating the humidity element. The four wires coming from the sensor will be in very close quarters with the aluminum case which presents the possibility of shorting. To prevent this, place electrical tape both in the sensor cutout as well as the area in front of the cutout. The plastic casing of the humidity sensor should be flush with the exterior of the aluminum case. Once in this position, use silicone to secure the sensor in place. Prevent silicon from coming in contact with the sensor element, but ensure that the wire contacts in the case are completely covered in silicone and protected.

Step 31. Install Motherboard

Connect the motherboard PCB to the SCC sensor PCB by aligning the headers on each board and connecting them together. Make sure that none of header pins have bent, and that once inserted, the male pins have been completely covered by the female shrouds.

Step 32. Install TOW and Corrosion Sensors Wires

Connect the TOW and atmospheric corrosion sensors to the motherboard by plugging them into their corresponding headers. Placing bends into the wires will keep tension off of the solder joints and prevent the cables from pressing against each other.

Step 33. Strip Thermocouple Leads

The thermocouples have enameled wires that need to be stripped in the areas that need to be conductive. It should be noted that only the section of the wire going into the thermocouple screw terminal should be stripped. Extra stripped wire may lead to shorting the sensor. Use very fine sand paper to strip the enamel off the wires and test the conductivity of the sensor using an ohm meter. If the thermocouple registers as open on the ohm meter then further enamel must be removed from the sensor.

Step 34. Mount Thermocouple

The thermocouple groove on the top of the aluminum case lid is shorter than the full length of the sensor. Thread the thermocouple through the hole at the end of the groove on the lid such that the wires are inside the case. Bend the thermocouple such that the tip of the thermocouple rests at the end of the grove and the rest of the sensor is flush with the lid.

Step 35. Install Thermocouple Wires

Place a piece of electrical tape over the TC to prevent it from moving. Tread the thermocouple wires into the thermocouple screw terminals on the motherboard and lock them in. Test for

conductivity and verify that there are no shorts with the aluminum case. Silicone the TC form the inside of the aluminum case such the liquids would not enter case through the hole. Once this silicone is dry, add a small amount of conformal coating to the thermocouple hole from the outside of the case. The thermocouple leads are very susceptible to corrosive material and should be conformal coated as well up to the screw terminals.

Step 36. Connect FFC Cable between Ethernet Port and Motherboard

Connect the ten pin FFC cable from the Ethernet jack PCB board to the motherboard. Double check that the friction lock is holding and the cable is not bent in the receptacle.

Step 37. Install Humidity Sensor Wire

Connect the humidity sensor to the motherboard by plugging it into the corresponding header. Placing bends into the wires will keep tension off of the solder joints and prevent the cables from pressing against each other.

Step 38. Test for Dead Short

Install the test Ethernet cable and tool chain into the Ethernet jack. Do not power the system on. Check for a dead short between VDD and ground on both the 5V rail and 3.3V rail. If there is a problem then track it down. The overall system load will vary depending of the geometry of the SCC sensor elements used.

Step 39. Power Up Test

Supply the sensor module with 5V at 150mA via the barrel jack on the programming board. Check to see if the current draw is acceptable and check all voltage rails. Debug any problems found.

Step 40. Program Board and Confirm All Sensors

Program the board using the provided hex file and the tool chain. Look for the startup message on the serial terminal using the following settings:
- 9600 baud
- 8-bit
- No parity
- No hardware flow control

Observe the data coming from each sensor and verify the atmospheric sensor readings with the lab standard (temperature and humidity).

Step 41. Seal Aluminum Enclosure

Seal the enclosure using the four case screws. Be very careful not the pinch any of the wires when closing the case. The rubber seal should be flush around the entire seam of the case. Double check steps 40-42 after the case is sealed to ensure nothing was damaged in this step.